Andrey W. Golubkov, Dipl.-Ing.

Safety of Li-ion Batteries for Electric Vehicles

Doctoral Thesis

to achieve the university degree of

Doktor der technischen Wissenschaften

submitted to

Graz University of Technology

Supervisor

Assoc. Prof. Dipl-Ing. Dr.techn. Viktor Hacker

Institute of Chemical Engineering and Environmental Technology
Head: Univ.-Prof. Dipl.-Ing. Dr.techn. Wolfgang Bauer

Graz, January 2021

Affidavit

I declare that I have authored this thesis independently, that I have not used other than the declared sources/resources, and that I have explicitly indicated all material which has been quoted either literally or by content from the sources used. The text document uploaded to TUGRAZonline is identical to the present doctoral thesis.

Date	Signature

If you don't make stuff, there is no stuff.
—Elon Musk, Joe Rogan's podcast

Note of Thanks

I want to thank my family for the support during my years in the university and later at Magna Steyr and at the Virtual Vehicle Research.

Many thanks to my wife Наталья Ванцова for her giving me motivation.

Thanks to Prof. Viktor Hacker, the supervisor of this work, for scientific support and for allowing me to build the first test stand in the laboratory of Institute of Chemical Engineering and Environmental Technology (CEET). Without the first test-stand the whole project would not be possible. I appreciated the support by the team of CEET and especially support from Michael Lammer, Bernhard Marius and Gernot Voitic.

Further I want to thank all my co-workers at Virtual Vehicle Research GmbH (VVR): Alex Thaler, head of the battery group, for the overall project support starting in 2009 and for him urging me to finish the thesis. René Planteu for many years of experimental work, the designing and running the complicated experimental setups and for the management of the battery laboratory. Bernhard Rasch for practical approaches for test stand design and help during experiments. Oliver Korak for conscientious experimental work. Christiane Essl for her activities to get new industrial contracts and for her tireless work to improve the gas analysis. Niels Köster for his motivation to do develop new simulation models with good mathematical foundations. Franz Pichler for initial simulation models and for overall simulation support. Philip Kargl for initial model fitting tools. Jelena Rubesa-Zrim for good model discussions. Matthias Sharrer for the help to select the right software tools. Oskar Schweiger for experimental work and for managing of the test stand to measure heat conductivity. Oliver Mariani for the valuable tips to build test stand hardware. Dino Hrvanovic for discussions about functional safety. Lukas Schweighofer for our discussions. Lauritz Seifert for experimental work. Christian Groß for simplifying the model framework in Dymola/ Open Modellica. David Fuchs and Sebastian Scheikl for initial experimental work. Phillip Krohn

for the work on the first test series with automotive batteries. Schober Markus for initial model with Open Modellica. Hannes Haberl for support during test-stand improvements. Lukas Pusterhofer and Benjamin Weiß for the improvement of the heat-conductivity test-stand. Anna Pichler and Simon Erker for initial work on 3D simulation models.

Figure 1: Partners of the project SafeBattery.

Acknowledgement

This work was conducted as part of the COMET research project Safe Lithium-Based Traction Batteries (SafeBattery). The K-project SafeBattery is funded by Austrian Federal Ministry for Climate Action (BMK), Ministry of Digital and Economic Affairs (BMDW) Austria and the Province of Styria within the framework of the Competence Centers for Excellent Technologies (COMET) programme. The COMET programme is administered by the Austrian Research Promotion Agency (FFG). The author thanks the consortium members of the SafeBattery project (fig. 1) for their valuable input to this work.
The publication was written at VVR and at Graz University of Technology in Graz, Austria. The author would like to acknowledge the financial support of the COMET K2 programme of the BMK, BMDW, the FFG, the Province of Styria (Dept. 12) and the Styrian Business Promotion Agency (SFG).

Abstract

Recent Li-ion battery technology enables mass production of affordable electric vehicles. Typical sizes of battery packs for new models of electric cars are 45 kW h to 77 kW h (VW ID.3.). The energy density of the battery pack reached 160 W h kg^{-1} (Tesla Model 3). The packs have a typical voltage of 400 V. Those packs give a driving range of 300 km to 500 km making the car practical, but when such a pack fails, the large amount of stored energy might be released inside the battery, causing excess heat, gas release and possibly a fire.

The process of unwanted energy release of a Li-ion battery is called thermal runaway. The aim of this thesis was to quantify the different characteristics of the thermal runaway and to generate a foundation to derive appropriate safety measures in battery packs.

At the beginning of the doctoral work a test stand for testing of smaller cells (<5 A h) was build. It was used to test easily available cylindrical cells at different state of charge. In the test series the cells were exposed to over temperature and it was recorded if thermal runaway occurred, at which temperature exothermic reaction started, the temperature rate, the maximum temperature as well as the composition and amount of released gas. Three cell types with different cathodes were compared.

Based on experience with smaller cells a second much bigger test stand was build to test larger automotive Li-ion cells which are used by European car manufacturer. The second test stand can be used with Li-ion cells up to 420 A h, it can accommodate cell holder for different cell types and allows testing of different cell-failure cases. It includes a significantly upgraded gas analysis equipment and more channels for temperature measurement.

Test results from two types of larger cells are included in this work. The first large test cell (prismatic metal can, 50 A h) was tested with different over temperature modes. Different failure mechanisms were observed. The second cell type (pouch cell, 42 A h) was tested extensively at different state of charge and with different heating modes including localized hot-spots on the cell surface. Critical parameters to trigger a thermal runaway and the propagation of the exothermic reaction along the cell were recorded.

Kurzfassung

Moderne Li-Ionen Technologie ermöglicht die Massenproduktion leistbarer Elektrofahrzeuge. Batterien für neue Elektrofahrzeuge speichern 45 kW h bis 77 kW h an Energie (VW ID.3.). Die Energiedichte der Batteriesysteme erreichte 160 W h kg^{-1} (Tesla Model 3). Die typische Systemspannung beträgt 400 V. Solchen Batteriesysteme ermöglichen eine praktikable Reichweite von 300 km bis 500 km. In einem Fehlerfall kann sich die gespeicherte Energie aber auch innerhalb des Batteriesystems in Wärme umwandeln. Dabei wird durch die exotherme Reaktion brennbares Gas freigesetzt, welches einen Fahrzeugbrand verursachen kann.
Diese interne Energiefreisetzung in einer Li-Ionen Batterie wird als thermisches Durchgehen oder Thermal Runaway bezeichnet. Das Ziel der Doktorarbeit ist die Quantifizierung der verschiedenen Eigenschaften des Thermal Runaway und der Aufbau eines Wissensfundaments um Sicherheitsmaßnahmen für Batteriesysteme abzuleiten.
Zu Beginn der Doktorarbeit wurde ein erster Prüfstand für kleine Zellen (<5 A h) gebaut. Er wurde benutzt, um kleine einfach erhältliche Rundzellen bei verschiedenen Ladezuständen zu testen. Die Zellen wurden in Testserien Übertemperatur ausgesetzt und es wurde aufgezeichnet, ob die Zelle in den Thermal Runaway gegangen ist, bei welcher Temperatur die exotherme Reaktion eingesetzt hat, die Temperaturrate, die Maximaltemperatur, die Zusammensetzung und die Menge des emittierten Gases. Es wurden drei Zelltypen mit verschiedenen Kathodenmaterialien verglichen.
Mit den gewonnenen Erfahrungen an kleinen Zellen wurde ein zweiter vergrößerter Prüfstand gebaut, um auch große automotive Zellen von europäischen Autoherstellern zu testen. Der zweite Prüfstand ist für Li-Ionen Zellen bis 420 A h ausgelegt, er kann verschiedene Zellhalter für verschiedene Zellformate aufnehmen und erhöht das Portfolio testbarer Zellfehler. Er beinhaltet eine signifikant erweiterte Gasanalytik und 32 Kanäle für Temperaturmessung.
Diese Arbeit enthält Ergebnisse aus Testserien an zwei Typen automotiver Li-Ionen Zellen. Der erste große Zelltyp (prismatisch, Metallgehäuse, 50 A h) wurde in verschiedenen Arten von Übertemperaturversuchen getestet. Es wurden verschiedene Fehler und Auswirkungen während des Thermal Runaway beobachtet. Der zweite Zelltyp (prismatisch, Gehäuse aus Verbundfolie, 42 A h) wurde ausführlich bei

verschiedenen Ladezuständen und mit verschiedenen Heizmethoden (auch punktuelle Übertemperatur) getestet. Es wurden kritische Parameter für das Auslößen des Thermal Runaway ermittelt und es wurde die Propagation der exothermen Reaktion durch die Zelle quantifiziert.

Contents

1 Introduction

1.1 Structure of This Work

The topic of this doctoral thesis is the safety of Li-ion cells during their usage as the main energy source of EVs.
The thesis is structured into several parts. The *first part* contains the introduction of EVs and their battery packs, the safety measures of those battery packs, and the known safety issues of Li-ion cells in automotive context. To tackle the challenges of Li-ion battery safety our group carried out several funded research projects. The first part of the thesis ends with an overview of the safety relevant projects and test facilities where the author was involved.
The *second part* consists of four peer reviewed articles from the author. The articles are chronologically ordered. The first two articles contain results from abuse tests with smaller cells. The third article introduces the automotive Li-ion technology in more detail and compares the safety behaviour of large Li-ion cells, Ni-MH cells and sealed lead-acid batteries. The last article contains results from a first test series with large automotive cells.
The *third part* and *fourth part* consist of two unpublished project reports by the author. The subject of the first report was to extract safety relevant parameters from worst case scenarios and use the parameter to derive safety recommendations for testing laboratories. In the second report the same cell type was subject to a test series with the goal to measure resilience of the cell towards localized heating and internal short circuits.
The thesis ends with the *fifth and sixth part*, a summary of the previous work and an outlook to future research on yet unresolved safety issues.

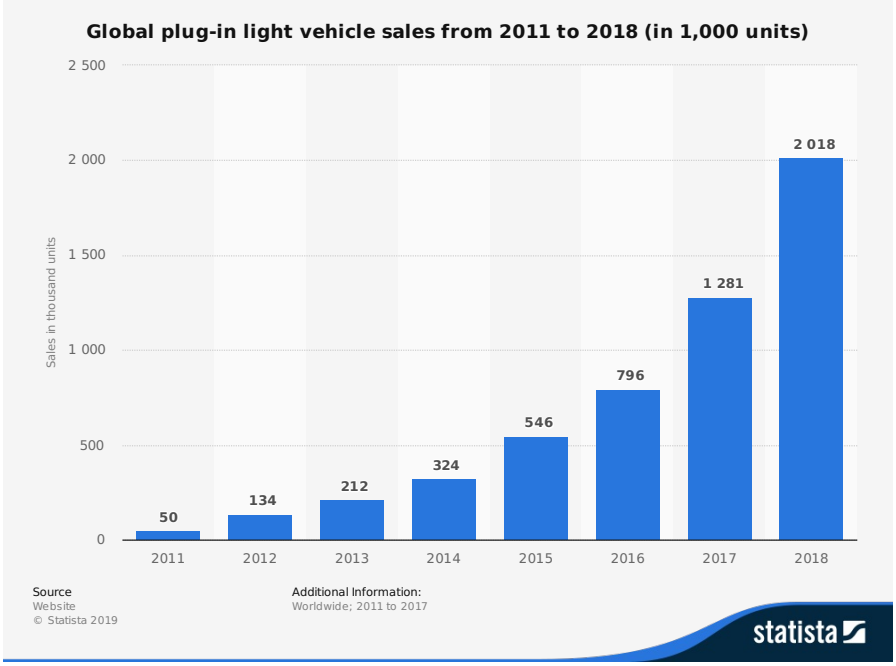

Figure 1.1: Pure EV and plug in hybrid vehicles sales[1].

1.2 Market Share of Electric Vehicles

It is important to understand the safety issues of battery packs of EVs because they are becoming increasingly common on our streets. Pure electric and plug-in hybrid light passenger vehicles annual sales rose from 50,000 in 2011 to 2000,000 in 2018 with an average annual sales growth of 73% (fig. 1.1). Forecasts show further market share increase in the next decades (fig. 1.2). The statistics and forecast show that EVs will have a significant role in future transport of people and goods.

1.3 Introduction to Li-Ion Battery Packs for EVs

This work focuses on the safety of large battery packs for long range, pure EVs such as the passenger vehicles from TESLA or the Nissan Leaf fig. 1.3. Their main energy storage for propulsion is a large battery mounted at the underside of the car chassis. This battery is sometimes called battery pack, high-voltage battery or electrochemical storage device. For example, the battery specifications of a typical

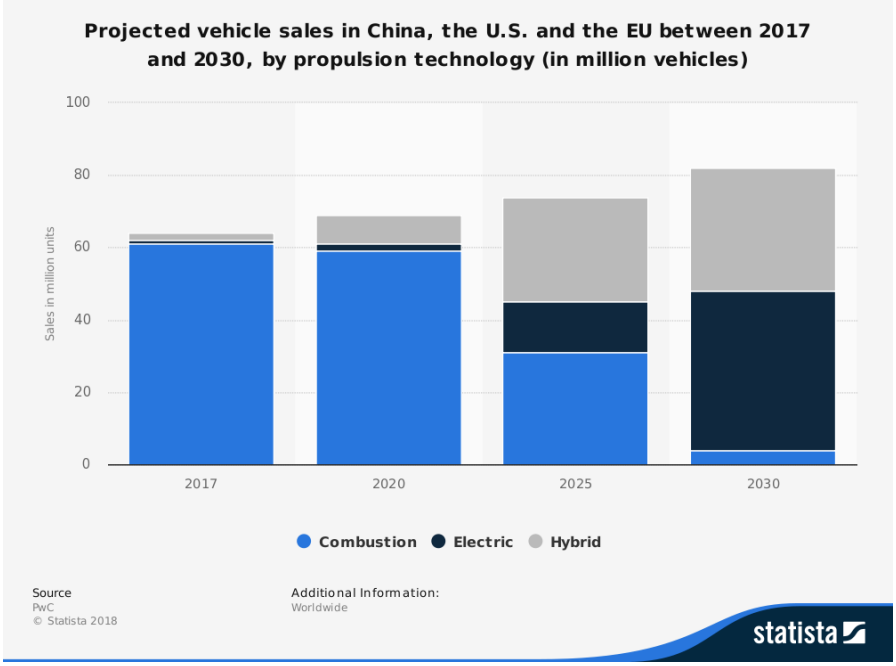

Figure 1.2: Forecast of light passenger vehicles sales [2].

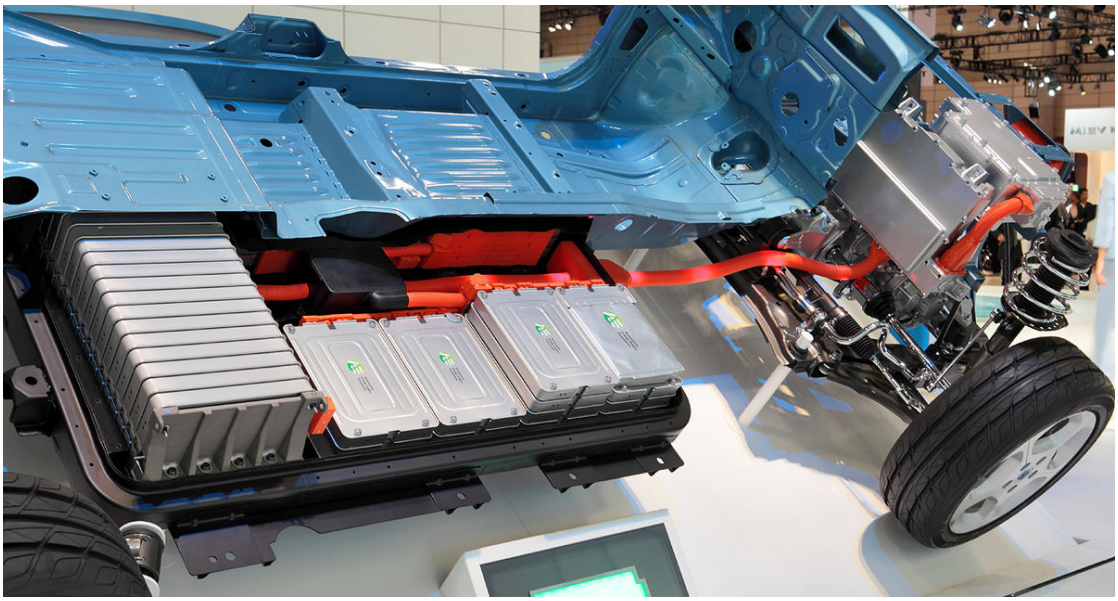

Figure 1.3: Battery pack of the Nissan Leaf. ©H. Kashioka / Wikimedia Commons / CC-BY-SA-3.0

EV - the Nissan Leaf 2018 [3] - are: maximal terminal voltage 420 V, stored energy 42 kWh, dimensions: (1547 x 1188 x 264 mm), weight of 305 kg.

A typical battery pack (fig. 1.4) consists of a case which houses a number of components. A brief overview of the components includes:

The battery case itself is often made from two parts; the lower casing which takes all other battery components during the assembly and the upper casing which is attached to the lower part at the final step of battery assembly. The next section (section 1.4) goes into detail of this important component.

Li-ion cells are the galvanic cells which store the electrochemical energy in a battery pack. As of 2019 all modern EVs with significant market share use batteries based on Li-ion technology[4]. Li-ion cells can have different form-factors and casing and electrodes as described in section 2.3.

Battery modules are mechanical sub-assemblies of several Li-ion cells which are electrically interconnected. E.g. a Nissan Leaf module consists of 6 Li-ion cells.

Thermal conditioning components are needed to keep the battery pack in a temperature range between 10°C and 60°C. The cooling/heating can be realized with preconditioned liquid coolant and a separate cooling circuit in the car or with preconditioned air from the passenger cabin, which is reused to cool or heat the battery pack.

The battery disconnect unit (BDU) is electric interface of the battery and the vehicle. It consists of the main contactors, the precharge circuit and the fuse in the main current path.

The battery management unit (BMU) or battery management system (BMS) is the main electronic control unit of the battery. The BMU monitors the status of the battery, in controls the BMU and it communicates with the vehicle [5].

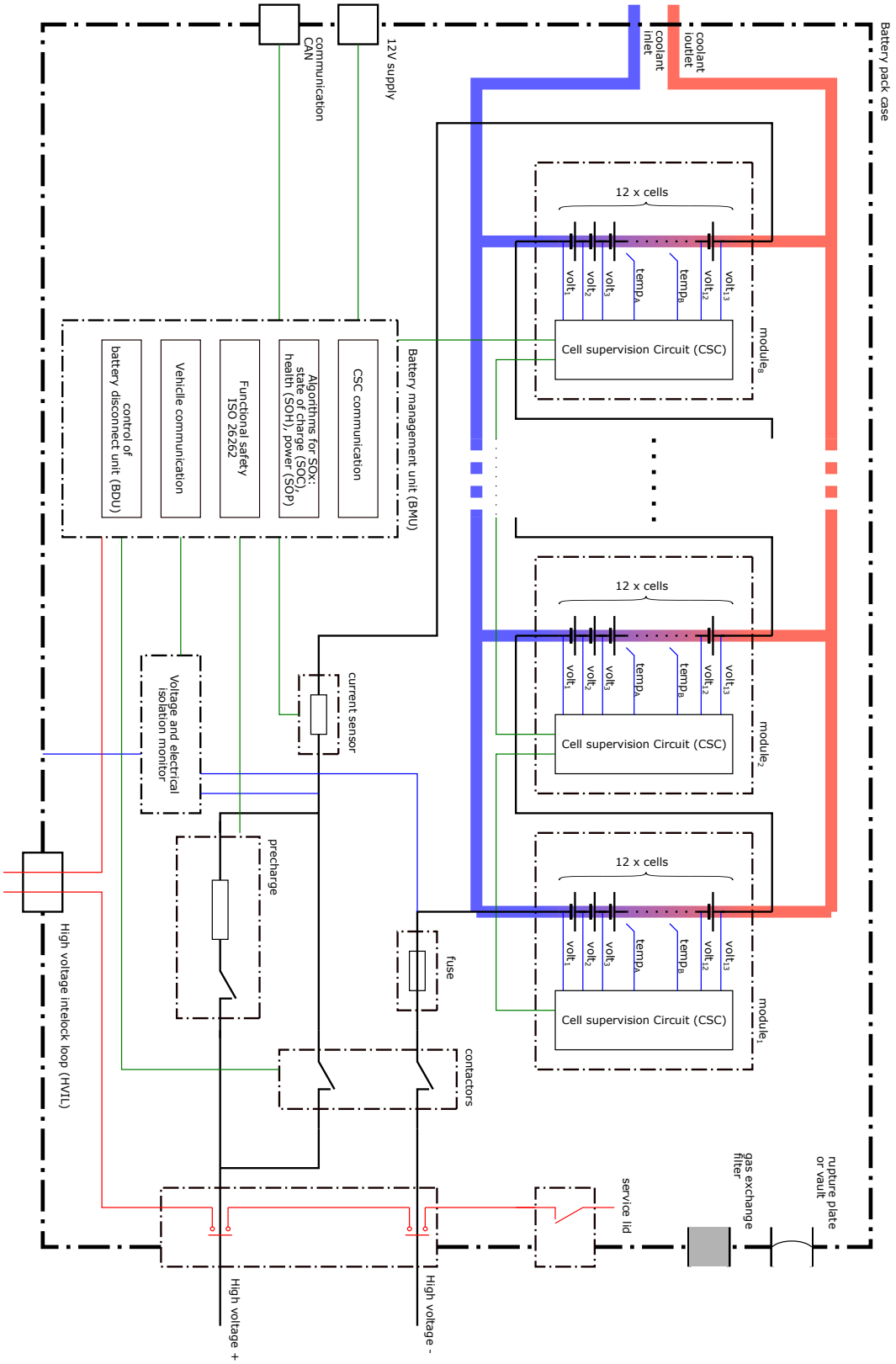

Figure 1.4: Typical layout of a battery pack.

1.4 Casing of the Battery Pack

The casing is the main structural part of the battery pack. It is one of the essential components to ensure battery pack safety, therefore it is described in more detail. In many EVs it consists of the lower part and the upper part which are screwed together. The lower part is often made in the form of a shell by injection moulding of aluminium or deep draw of steel sheets. Lower parts of big EV batteries are sometimes too large to be made from one main component. They can be made from welded steel sheets or from multiple connected battery trays. The lower part is the main structural element of the battery pack. It must withstand the mechanical load during normal operation and needs to have sufficient crash worthiness [6].
Suitable materials for the upper part can be a deep drawn steel or aluminium, or moulded fibre reinforced plastic. The upper part can be omitted, if the lower part of the battery is tightly attached to the underside of the passenger cabin which is usually made from steel or aluminium sheet metal. The casing has to meet safety related requirements *viz.*: crash and crush worthiness, water tightness, resistance to pressure changes, limited thermal protection against fuel fire, resistance to hot gases from failed cells.
Large battery packs are installed outside of the front and rear crush (crumple) zone but they are inside intrusion space of side impact and lateral pole crash tests [7]. The casings include crumple zones on the sides of the pack which absorb mechanical energy and have optimized load paths (*e.g.* cross members) for force distribution. Other concepts rely on airbags on the sided of the battery casing to distribute the side impact force [8]. As the battery pack is located below the passenger cell, a stiff battery case also improves the occupant safety. The need to protect the battery led to an excellent safety rating of large EV like the Tesla model S[9].
The case must be watertight to withstand wading through salt water as specified by the vehicle manufacturer and it must withstand cleaning with high pressure water jets (Water Exposure Test, IP Code Rating, UL 2271). At the same time the casing must withstand gas pressure changes during normal operation. Pressure changes can be caused by temperature change inside and outside of the pack. Temperature change can be caused by internal heating of the cells during fast charge and by internal cooling. It can be caused by external effects like entering a place with different temperature (e.g. tunnel or garage), by the day and night cycle or by

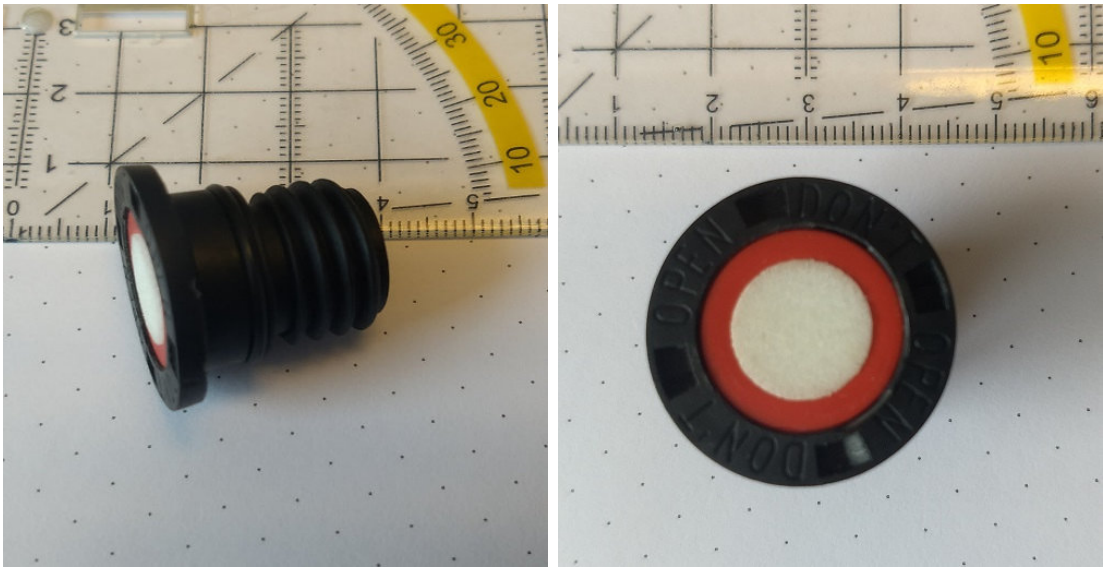

Figure 1.5: Pressure equalization element.

coming into contact with cold water during wading. Pressure change can also be caused by elevation change or by dynamic effects e.g. entering a rail tunnel during transportation.
Although the casings are designed to withstand some overpressure, e.g. 200 mbar they need some pressure equalisation for normal operation and vent-gas valves or burst plates with high cross sections for failure situations. In normal operation valves with waterproof membranes (e.g. microporous Polytetrafluoroethylene (PTFE)) with protection against water jets are used for pressure equilibration fig. 1.5.

The membranes are not sufficient for gas exchange in severe failure situations like thermal runaway. In addition to the membranes, burst-plates or valves are build in to vent excess overpressure to the outside of the pack. The burst-plates may have diameters >20 mm and can vent directly to the outside of the pack (in underfloor mounting of the pack) or through a hose to the outside of the cabin (for packs that which are mounted in the trunk). In some solutions, both the membrane and the overpressure valve are combined into one assembly [10].

Item		M ($\mathrm{g\,mol^{-1}}$)	ρ (kilogram/$\mathrm{m^3}$)	T_b (°C)	T_m (°C)	T_f (°C)
PC	$C_4H_6O_3$	102.09	1.20	242	-49	132
EC	$C_3H_4O_3$	88.06	1.40	238	37	157
DMC	$C_3H_6O_3$	90.08	1.06	90	3	18
DEC	$C_5H_{10}O_3$	118.13	0.97	126	-43	33

Table 1.1: Basic data for the usual species of electrolytes. Data taken from Wang *et al.* [18]. Here M is the molecular mass, ρ is the density at 25 °C, T_b is the boiling temperature, T_m is the melting temperature and T_f is the flash temperature.

1.5 Failure-Cases in Battery Packs

A charged battery-pack is vulnerable to many failure cases all of which [11, 12] can not be covered here. Instead, this section focuses on failure cases which are caused by a TR of one cell. The TR itself is described in detail in the included articles inside this work sections 2.1, 2.2 and 2.4 and in recent literature [13–17]. The TR causes further secondary risks such as combustion of the cell material and gas release, risks of intoxication and risks of electric short circuits in the battery pack.

1.5.1 Electrolyte combustion

The TR of a cell may cause release of combustible electrolyte vapour. Two scenarios must be considered: the electrolyte vapour can either burn at the point where it is released from the cell and where it comes into contact with fresh air or the unburnt electrolyte vapour can escape into the ambient air until some ignition source causes a deflagration of the flammable vapour-air mixture [19].
Basic data for alkyl carbonate solutions that are used as electrolytes are summarized in 1.1. Enthalpies of combustion ($\Delta_c H_j$) of some electrolyte components are shown below: Combustion of ethylene carbonate (EC) (Vogdanis *et al.* [20])

$$\mathrm{C_3H_4O_3} + 2.5\mathrm{O_2} \xrightarrow{\Delta \mathrm{H} = \text{-}1161.4\ \mathrm{kJmol}} 3\,\mathrm{CO_2} + 2\,\mathrm{H_2O} \tag{1.1}$$

Combustion of diethyl carbonate (DEC) (Mansson [21])

$$C_5H_{10}O_3 + 6\,O_2 \xrightarrow{\Delta H = \text{-2715.2 kJmol}} 5\,CO_2 + 5\,H_2O \tag{1.2}$$

and ethyl methyl carbonate (EMC)

$$C_3H_8O_3 + 4.5O_2 \longrightarrow 3\,CO_2 + 4\,H_2O \tag{1.3}$$

As MacNeil and Dahn [22, 23] point out, measured and calculated reaction heat values may not agree. In their experiments, the measured heat produced during accelerated rate calorimetry (ARC) tests with Li-ion cells (with $C/Li_xMn_2O_4$) and C/Li_xCoO_2 based cells) accounted for only 25 % to 50 % of the theoretical value.

1.5.2 Deflagration of vent-gas or electrolyte vapour

In the case of a TR of Li-Ion cell, vent-gas will escape from the cell into the casing of the battery pack. The vent-gas consists of electrolyte vapour and other highly combustible gases with high percentages of H_2, CO, and CH_4 (sections 2.1, 2.2 and 2.4).
There is a high chance of deflagration of the burnable gases with the available oxygen since an ignition source may easily be available (sparks are visible in recordings of thermal runaway experiments). A standard for deflagration protection is available for industry applications and this work proposes to adopt this standard for the design of the venting system for a battery system casing [24]. The key parameters from a deflagration experiment are the volume of the vessel $V(m^3)$, the maximal pressure P_{max}(bar) and the maximal pressure-rise rate dP/dt(bar s^{-1}). Using these parameters, the (gas) deflagration index K_G(bar m/s) can be calculated

$$K_G = \left|\frac{dP}{dt}\right|_{max} V^{1/3}, \tag{1.4}$$

and the required venting area A_v(m) for the battery housing can be estimated

$$A_v = \left[(0.127\,log_{10}(K_G) - 0.0567)\,P_{red}^{-0.582}\right] V^{2/3} + \left[0.175\,P_{red}^{-0.572}(P_{stat} - 0.1)\right] V^{2/3}, \tag{1.5}$$

where $P_{red}(\text{bar}_{\text{gauge}})$ is the maximal allowed pressure during deflagration in the battery-pack casing (e.g. the maximal pressure which the casing can withstand

without rupture), $P_{stat}(\mathrm{bar_{gauge}})$ is the pressure that activates the venting system and $V(\mathrm{m^3})$ is the free volume inside the battery-back. The equation is valid for $K_G < 550\,\mathrm{bar\,m\,s^{-1}}$, $P_{stat} + 0.05\,\mathrm{bar} < P_{red} < 2\,\mathrm{bar}$, $P_{stat} < 0.5\,\mathrm{bar}$. As an example, if $K_G = 55\,\mathrm{bar\,m\,s^{-1}}$ as for Methane, $P_{red} = 0.3\,\mathrm{bar}$, $P_{stat} = 0.1\,\mathrm{bar}$ and $V = 0.04\,\mathrm{m}$ than $A_v = 0.038\,\mathrm{m}$ and the burst disc diameter is then $d = 0.2\,\mathrm{m}$; quite a high value.
An example calculation of explosion limits and recommendations to reduce deflagration risk for a specific Li-ion cell are given in section 3.8.2. Recent literature on the deflagration risk of vent gas includes work from Said et al.[25], Chen et al. [26] and Baird et al.[27].

1.5.3 Overpressure by released gas

Even without deflagration, high amount of released gas may cause overpressure inside the battery pack. To prevent damage, battery-pack casings should be equipped with an overpressure venting device. The minimal requirements can be derived from thermal runaway experiments as shown in section 2.4 and in section 3.8.3.

1.5.4 Production of toxic substances

The main contribution to toxicity of the vent-gas is the high share of CO. Further, sources of toxic gas are HF and fluoro-organics an electrolyte vapour. The toxicity of those components is described in section 3.8.4.
Hammami *et al.* [28] report the formation of toxic fluoro-organics from heated Li-ion electrolytes such as EC and DMC. In the presence of a cathode material bis-(2-fluoroethyl)-ether was formed at elevated temperature of 240°C from the electrolyte by the proposed reaction:

$$2\,\mathrm{EC} + \mathrm{LiPF_6} \longrightarrow (\mathrm{FCH_2CH_2})_2\mathrm{O} + \mathrm{LiF} + \mathrm{POF_3}\uparrow \tag{1.6}$$

the $\mathrm{LD_{50}}$ for this compound is $4mg/kg$ as measured by Bergmann *et al.* [29]. $\mathrm{POF_3}$ is a toxic gas with a boiling point of -39.7°C.
During TR the cells release vent-gas at high rates and the flow of the vent-gas

Figure 1.6: Cell holder covered with particles which were released by the cell during the venting and during thermal runaway. Particle samples were taken, where white spots are seen.

tend to carry away high amounts of solid particles from the anode and cathode material. Cells may release >40 % of their mass as gas and particles as shown in table 3.3. The particles [30] settle on the surfaces near the cell (fig. 1.6). They were sampled after the TR and the size distribution and composition of those particles was analysed in the diploma thesis of Eva Gasser [31]. Her work showed that the particles may be carcinogenic and small enough to be absorbed through the lung (section 3.8.6).

1.5.5 Ejection of Electrically conducting parts

During TR Li-ion cells may not only release small particles but also eject larger pieces of electrically conductive material [32]. Such material may be parts of the current collector foil of the anode which is made from copper. Pieces of copper foil may cause electrical short circuits and electric arcing inside the battery pack, when they accidentally connect electric components with different electric potential such as busbars or terminals of the cells. Thus, a cell may cause additional secondary failures inside the pack due to ejection of material.

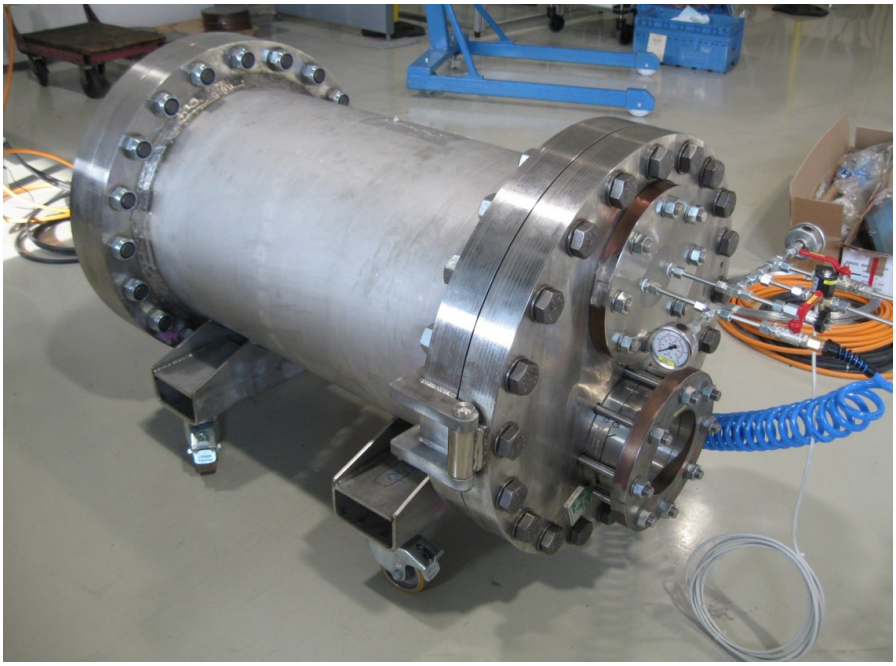

Figure 1.7: Reactor that was used for TR testing at Magna Steyr in 2009. (Volume 200 L, design pressure 40 bar)

1.6 Battery Safety Projects

The author was involved during the work or initiation of the projects and directly supported the diploma and bachelor thesis that are shown in fig. 1.8.
The work on battery safety started already in the company Magna Steyr Battery Systems in 2009. The advanced development group at Magna Steyr commissioned of a heavy duty reactor for TR testing (fig. 1.7). Here the first experiments were done with larger cells. Ideas for a further testing were born. The need to understand the TR behaviour of Li-ion batteries resulted in a first funded K2 Project Li-Ion Battery Safety in Automotive Environment (LISAE). The purpose of this initial project was to generate first test results by overheating and overcharging smaller cells with capacities up to 5 Ah (mainly with the geometrical format: cylindrical 18650). For this experiments a small test stand was build in the laboratory for fuel cells at the CEET. David Fuchs and Sebastian Scheikl finished their masters thesis at the end of this project [33, 34]. Two articles were published with the results of LISAE [35, 36]. They are included as part of this dissertation (sections 2.1 and 2.2).

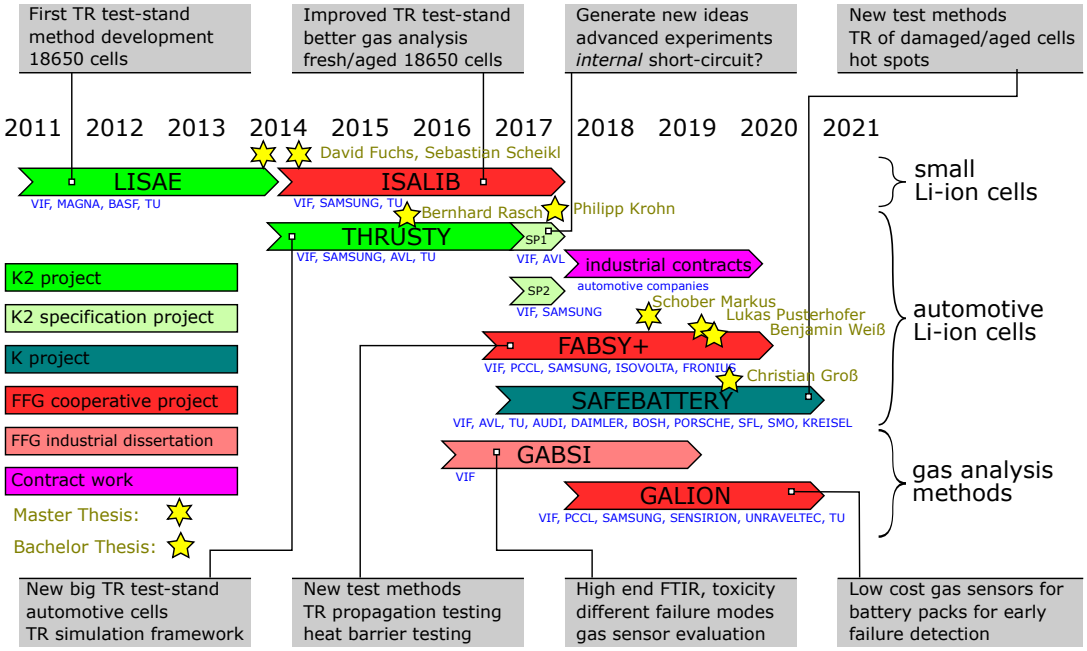

Figure 1.8: Battery safety related projects at the Virtual Vehicle (ViF) where the author participated.

LISAE was followed by Intrinsic Safety and Risk of Automotive Li-Ion Batteries (ISALIB) which focused on aged small format cells. The cells were aged at VVR and TR tests were done at CEET. In a parallel follow up project Thermal Runaway Safety (THRUSTY) a much bigger test stand for large automotive Li-Ion batteries was designed and installed in a new battery test-laboratory at VVR. Bernhard Rasch was involved in the design of the gas management and gas analysis part of the stand and Philipp Krohn did a series of TR experiments with large cells with a capacity of 50 Ah. Both students used the material from THRUSTY to write their thesis [37, 38]. Two articles were published [39, 40] which are also part of this dissertation (sections 2.3 and 2.4).

Later work focused on large automotive cells and on gas analysis. THRUSTY was followed by two small specification projects where localized heating and hot-spots was used to trigger a TR (SP1) and where thermocouples were inserted into the cell to measure the internal temperature during TR (SP2). Then, starting with 2017, the test stand at VVR was being used in different industrial contracts and in the projects Failsafe Battery System Plus (FABSY+) and SafeBattery.

The goal of FABSY+ was to develop thin cost-effective spacer-foils between cells in a module to prevent or to slow down thermal runaway propagation (TP) from cell to cell as well as to reduce the risk of battery fire by using thermal insulation. In their bachelor thesis Lukas Pusterhofer designed a test stand to characterise the thermal conductivity and mechanical properties of the spacer [41] and Benjamin Weiß did principal validation measurements [42].
SafeBattery is a large project with many partners. It focuses on safety of aged and mechanically preloaded automotive batteries (vibration and small accidents). Some of the tasks of VVR is to compare the TR characteristics of aged and fresh batteries, to understand the TR when it is started by a hot spot, and to find new ways to predict battery failure. Two large reports from SafeBattery are part of this thesis (chapters 3 and 4). Markus Schober created a first open modellica based simulation framework of TP [43] and Christian Groß is doing follow up work to simplify the model and to port it to the Dymola simulation framework. Both students worked on their thesis in SafeBattery.
In 2016 Christiane Essl started her dissertation with the topic of gas analysis in different battery failure cases with her industrial dissertation project Gas-Analysis for Battery Safety (GABSI). A high end fourier-transform infrared spectroscopy (FTIR) was purchased. It increased the number of detectable gas components (including HF) which were released by the cells. An additional laboratory with a large fume hood was opened to test the gas sensors. The project was significantly enlarged by the project Gassensorik für Li-IONen Batteriesyteme (GALION) with the target to get gas sensors into the battery packs.

1.7 Literature Review: Thermal-Runaway Characteristics

Li-ion cells and packs can have different sizes spanning from small batteries for bluetooth airbuds such as single cells from Varta Microbatteries with stored energies starting at 160 mWh [44] up to batteries for EVs such as VW ID.3. with 77 kWh [45] and even larger batteries for grid-connected energy storage such as the Hornsdale Power Reserve with 129 MWh [46]. Commercially available Li-ion cells can be based

in different chemistries for the electrodes such as $LiFePO_4$ or different metal oxides as the cathode and Li-titanate or graphite as the anode (section 2.3).
The diversity of Li-ion batteries gives rise to a broad field of safety research on batteries for the different applications. This chapter focuses on the state of the art of battery safety research that is relevant for EV applications. This includes TR characteristics of small cylindrical cells, similar to those used by Tesla and the TR characteristics of larger cells which are used by other car manufacturer.

1.7.1 Thermal runaway of small cylindrical cells

The included publications (sections 2.1 and 2.2) already cover the literature review on TR of small cells (<5 Ah, mainly 18650 format) up to the year 2015. In the meantime (between 2015 and 2020) new research articles were released, therefore it is time to update the review and to compare the new results with papers from 2014 and 2015.

The SANDIA REPORT SAND2016-0486 [47] contains over temperature characteristics of $Li(NiCoAl)O_2$ (NCA) and $LiFePO_4$ (LFP) cells in a closed reactor similar to the test setups of this thesis. For LFP cells, they measure low max. cell temperature with 325 °C and H_2 as the main gas component. In contrast to this thesis and to other publications no CO and CO_2 was detected. The cell produced a total of 2.1 L_{STP}/Ah. The results fo a NCA cell were 400 °C releasing 2.5 L_{STP}/Ah with the main components CO, CO_2 followed by H_2.
Waldmann and Wohlfahrt-Mehrens [48] did ARC tests with 18650 cells (NCA cathodes and a capacity of 3.25 Ah). They created Li-plating on the anode of the cells, by cycling at a low temperate (0 °C) and tested thermal stability after different waiting time. They showed that Li-plating decreases the onset and increases the ferocity of the TR. If Li-plated cells were allowed to rest for eight days, the metallic Li intercalated and effects of Li-plating were reduced. Our second publication (section 2.2) also shows that cells with Li-plating (which was created by slow overcharge) have a lower onset temperature and more violent reaction than cells at 100% SOC. Overcharge can lead to Li-plating, because the anode is almost fully lithiated at 100% state of charge (SOC) and can not intercalate further Li-ions

when the cell is charged beyond 100%. When excess Li can not intercalate into the graphite, it is forced to form Li-plating on the surface of the graphite particles. Both publications conclude that Li-plating decreases the safety of Li-ion cells.
In a follow up publication Waldmann *et al.* [49] show a linear correlation of SOC and the ferocity of the TR. Our publication (section 2.2) also show a correlation of gas release, gas composition and maximal cell temperature to the SOC of the cell. Liu *et al.* [50] also show a positive correlation of SOC and the maximal temperature during TR. They also notice a decrease of onset temperature when the cell is charged with >3 C. The decrease may be caused by Li-plating at higher charge currents.
Lei *et al.* [51] performed unique measurement of the pressure inside a cylindrical 18650 cell and compared different heating methods and the TR characteristics of cells with different cathodes. Heating with the heat-wait-search (HWS) method needs about 1800 min until TR and results in a maximal temperature of 580 °C. Heating with a simple temperature ramp reduces the time until TR to only 60 min and results in a slightly higher maximal temperature of 610 °C. This shows that the heating duration has a small impact on the TR characteristics. A very long heating duration may causes some early degradation of the cell, so that less energy is left for the final violent part of the TR reaction. In an limit case with extremely long heating time the cell could completely self-discharge before an TR could happen. In our measurements we always used the simple heat ramp with moderate heating durations from 30 min to 160 min. TR results for cells with different cathodes show similar trends to (section 2.1). In both, the publication of Lei and our publication the LFP cell was followed by $LiMn_2O_4$ (LMO) and $Li(NiMnCo)O_2$ (NMC) cell when arranged by the maximal cell temperature and released heat. In addition, they show that the internal cell pressure increases when the cell is heated until the burst plate of the cell opens at 12.5 bar and 130 °C. In our publications (sections 2.1 and 2.2) we also observed an opening of the burst plate between 130 °C to 180 °C.
Kvasha *et al.* [52], Perea *et al.* [53], Barkholtz *et al.* [54], and Nguyen *et al.* [55] all report a correlation of SOC and the severity of the TR and the superior stability of LFP compared to LMO, NMC and NCA cells. Similar findings were presented in our papers.
Liao *et al.* [56] tested 111-NMC cells with 2.4 Ah at different SOC. Their findings are in line with the other mentioned publications; positive correlation of maximal

temperature and SOC and negative correlation of the onset temperature and SOC. Their analysis of the vent-gas composition (qualitative with gas chromatography – mass spectrometry (GC-MS)) shows increased amount of gas species at higher SOC. They used a chemical test kit to detect HF and found indications that HF concentration increases with higher SOC. They measured the composition of released particles with scanning electron microscope (SEM)-energy-dispersive X-ray spectroscopy (EDS) and X-ray powder diffraction (XRD) and found oxidized electrode material and LiF.

Zhao *et al.* [57] tested a 523-NMC cell with 2.0 Ah at different SOC and ageing. They measure a positive correlation between the SOC and the parameter viz.: mass loss of the cell, maximal pressure in the test chamber to SOC, maximal cell temperature. They measure a negative correlation to temperature when the burst disc of the cell ruptures, and the temperature when the TR starts. Our publication in (section 2.2) also shows similar correlations of maximal temperature and gas release. Tests of Zhao *et al.* with cycled cells indicate that aged cells have higher mass loss, lower temperature of burst plate opening, lower start temperature of TR and lower maximal cell temperature.

Lammer *et al.* [58] tested different 18650 cells in our cooperative research project ISALIB (section 1.6). They describe a unique setup to measure the amount of released gas using a fluid displacement tube and sampling for taking several gas samples at specified times. Gas composition was quantified with gas chromatography (GC) (Agilent micro-GC 3000A). They measured gas composition after opening of the burst plate and after TR. The cells released mainly CO_2 before TR (the GC was not set-up to detect electrolyte vapours which would also occur) and CO, H_2 and CO_2 during TR.

In a follow up publication Lammer *et al.* [59] found that cells which were *aged by storing* at 60°C – compared to fresh cells – had an increased share of C_2H_2 in the gas before TR and released less heat during TR. One of the tested cells (ICR18650HE4) even could not be brought into TR.

Cell which were *aged by cycling* also showed less heat release but otherwise similar TR parameter. The exception was again the cell ICR18650HE4 which was designed for high power applications. It showed the highest change of TR parameters due to ageing. It had only a mild TR reaction. Its maximal temperature reduced from 690 °C to 373 °C and the volume of released gas changed from 3.3 l to 0.4 l.

1.7.2 Thermal runaway of large prismatic metal can and pouch cells

The included publication (section 2.4) contains a review on TR of large Li-ion cells up to the year 2018. This section covers the literature on TR of cells with capacities >20 Ah after 2018 and compares is to our publication in 2018 (section 2.4). Correlations from those publications are summarised in table 1.2.

Koch *et al.* [60] tested different methods to detect the TR of large batteries. EVs need early detection of battery failure to warn the passengers and to prevent further damage to the car. They found that all test sensor types *viz.*: voltage, gas, smoke, creep distance, temperature, pressure, force are able to detect the TR. They conclude that depending on battery design two or three sensor technologies should be combined in a series product.
In Koch *et al.* [61] summarizes their large test campaign consisting of 51 cells with capacities ranging from 20 Ah to 81 Ah with pouch and metal-can cases. All cells had NMC based cathodes. Their main findings were: correlation of released amount of gas and cell capacity with a linear approximation of $1.96\,\mathrm{l\,A^{-1}\,h}$, correlation of gaseous mass loss and total mass loss, no correlation between gas composition and amount of gas, higher energy densities lead to more severe TR. In our publication (section 2.4) the 50 A h cells released 3.2 mol of gas which translates to $79.32\,\mathrm{l_{STP}}$ and $1.58\,\mathrm{l_{STP}/Ah}$. The main gas components were the same as in the work of Koch *et al.*
In another large publication Feng *et al.* [15] presents a large database of cells with capacities from 1 Ah to 50 Ah (thermal analysis database of the Tsinghua University). The publication includes correlation graphs between various parameters which are relevant to TR. Notably are statistics of the lowest temperature of detected self heating $T1$ and the onset temperature of the TR $T2$ and the maximal cell temperature $T3$. The $T1$ depends on state of health (SOH) and the conditions during ageing: cycling at high temperatures increases $T1$, whereas cycling at low temperatures lowers $T1$. The linear correlation of SOC and $T3$ is known for small cells. Feng *et al.* show that it also holds for larger cells with >20 A h. Increasing energy density also strongly correlates to higher $T3$.

Table 1.2: Correlations between cell conditions and TR results for cells >20 Ah

Source	correlation	cell condition	TR parameter
Koch *et al.* [61]	positive, $1.96\,\mathrm{l\,A^{-1}\,h^{-1}}$	capacity	released gas
Koch *et al.* [61]	positive	energy density	severity of TR
Feng *et al.* [15]	positive	cycling at high temperature	$T1$
Feng *et al.* [15]	negative	cycling at low temperature	$T1$
Feng *et al.* [15]	positive, linear	SOC	$T3$
Feng *et al.* [15]	positive	energy density	max. dT/dt

Test results of (section 2.4) with 50 Ah and $109\,\mathrm{W\,h\,kg^{-1}}$ (only group A2) adopting the nomenclature of Feng *et al.* are $T2 = 230\,^{\circ}\mathrm{C}$, $T3 = 594\,^{\circ}\mathrm{C}$, $dT/dt = 1 \times 10^{3}\,\mathrm{K\,min^{-1}}$. The results fit into the graphs (fig. 6) of Feng *et al.* [15]. In (section 2.4) early internal short circuit (ISC) (group B1) did not generate significant additional heat or different $T3$. This is inline with Feng *et al.* who tested the influence of the ISC on the TR and estimated that the ISC is responsible for only 9% of total heat generation during TR.

2 Published Work

2.1 Thermal Runaway Experiments on Consumer Li-ion Batteries with Metal-oxide and Olivin-type Cathodes

The following journal article was published in RSC Advances in 2014. It summarizes our first results on the thermal runaway of small cylindrical cells in the format 18650.

In this work Andrey Golubkov wrote the text of the article, designed and build the TR test-stand, performed the TR experiments analysed the TR data. David Fuchs participated in making the TR experiments and building the test stand. Julian Wagner did the Energy-dispersive X-ray spectroscopy (EDX) and Helmar Wiltsche the Inductively coupled plasma (ICP)-Optical Emission Spectroscopy (OES) analysis of the electrodes. Christoph Stangl and Gisela Fauler measured the electrolyte composition. Gernot Voitic helped to make the GC measurements of the vent-gas. Alexander Thaler and Viktor Hacker supervised the work.

RSC Advances

PAPER

View Article Online
View Journal | View Issue

Cite this: *RSC Adv.*, 2014, **4**, 3633

Thermal-runaway experiments on consumer Li-ion batteries with metal-oxide and olivin-type cathodes

Andrey W. Golubkov,*[a] David Fuchs,[a] Julian Wagner,[b] Helmar Wiltsche,[c] Christoph Stangl,[d] Gisela Fauler,[d] Gernot Voitic,[e] Alexander Thaler[a] and Viktor Hacker[e]

Received 11th October 2013
Accepted 26th November 2013

DOI: 10.1039/c3ra45748f

www.rsc.org/advances

Li-ion batteries play an ever-increasing role in our daily life. Therefore, it is important to understand the potential risks involved with these devices. In this work we demonstrate the thermal runaway characteristics of three types of commercially available Li-ion batteries with the format 18650. The Li-ion batteries were deliberately driven into thermal runaway by overheating under controlled conditions. Cell temperatures up to 850 °C and a gas release of up to 0.27 mol were measured. The main gas components were quantified with gas-chromatography. The safety of Li-ion batteries is determined by their composition, size, energy content, design and quality. This work investigated the influence of different cathode-material chemistry on the safety of commercial graphite-based 18650 cells. The active cathode materials of the three tested cell types were (a) $LiFePO_4$, (b) $Li(Ni_{0.45}Mn_{0.45}Co_{0.10})O_2$ and (c) a blend of $LiCoO_2$ and $Li(Ni_{0.50}Mn_{0.25}Co_{0.25})O_2$.

1 Introduction

Li-ion batteries have been commercially available since 1991.[1] As of 2013, Li-ion batteries are in wide use for portable electronics, such as cell phones and notebook computers. They are also gaining traction as a power source in electrified vehicles. Li-ion batteries have a high specific energy and favourable ageing characteristics compared to NiMH and lead acid batteries. However, there are concerns regarding the safety of Li-ion batteries. Abuse conditions such as overcharge, over-discharge and internal short-circuits can lead to battery temperatures far beyond the manufacturer ratings. At a critical temperature, a chain of exothermic reactions can be triggered. The reactions lead to a further temperature increase, which in turn accelerates the reaction kinetics. This catastrophic self-accelerated degradation of the Li-ion battery is called thermal runaway.[2]

During thermal runaway, temperatures as high as 900 °C can be reached,[3] and the battery can release a significant amount of burnable and (if inhaled in high concentrations) toxic gas.[4] To quantify possible hazards of exothermic Li-ion battery over-temperature reactions, tests with complete batteries should be performed. Such experiments were undertaken with commercial Li-ion batteries produced for consumer electronics[3–11] and with Li-ion batteries fabricated in the laboratory.[12–16]

This work investigated the thermal stability of three types of commercially available Li-ion batteries for consumer electronics. Particular attention was given to (1) the dynamics of the thermal responses of the cells, (2) the maximum temperatures reached, (3) the amount of gases produced and (4) to the production rates of the gases. To further assess the hazard potential of the released gases, samples were taken and analysed with a gas chromatography system.

2 Experimental

2.1 Brief description of the test rig

To carry out unrestricted thermal-runaway experiments, a custom-designed test stand was built (Fig. 1). The main component of the test rig is a heatable reactor with electric feedthroughs for the temperature measurement and the inner sample heating. The reactor has gas feedthroughs that connect it to an inert gas flask, to a gas sampling station and to a cold trap with an attached vacuum pump. The pressure inside the reactor is recorded by a pressure transmitter. The whole structure is hosted inside a fume hood to prevent any escaping of gases and electrolyte vapours.

A removable sample holder is placed inside the reactor. The sample holder consists of a metal structure, which houses a

[a]*VIRTUAL VEHICLE Research Center, Inffeldgasse 21a, 8010 Graz, Austria. E-mail: andrej.golubkov@alumni.tugraz.at; Fax: +43-316-873-9002; Tel: +43-316-873-9639*
[b]*Graz Centre for Electron Microscopy, Steyrergasse 17, 8010 Graz, Austria*
[c]*Institute of Analytical Chemistry and Food Chemistry, Graz University of Technology, Stremayrgasse 9/III, 8010 Graz, Austria*
[d]*Varta Micro Innovation GmbH, Stremayrgasse 9, 8010 Graz, Austria*
[e]*Institute of Chemical Engineering and Environmental Technology, Graz University of Technology, Inffeldgasse 25/C/II, 8010 Graz, Austria*

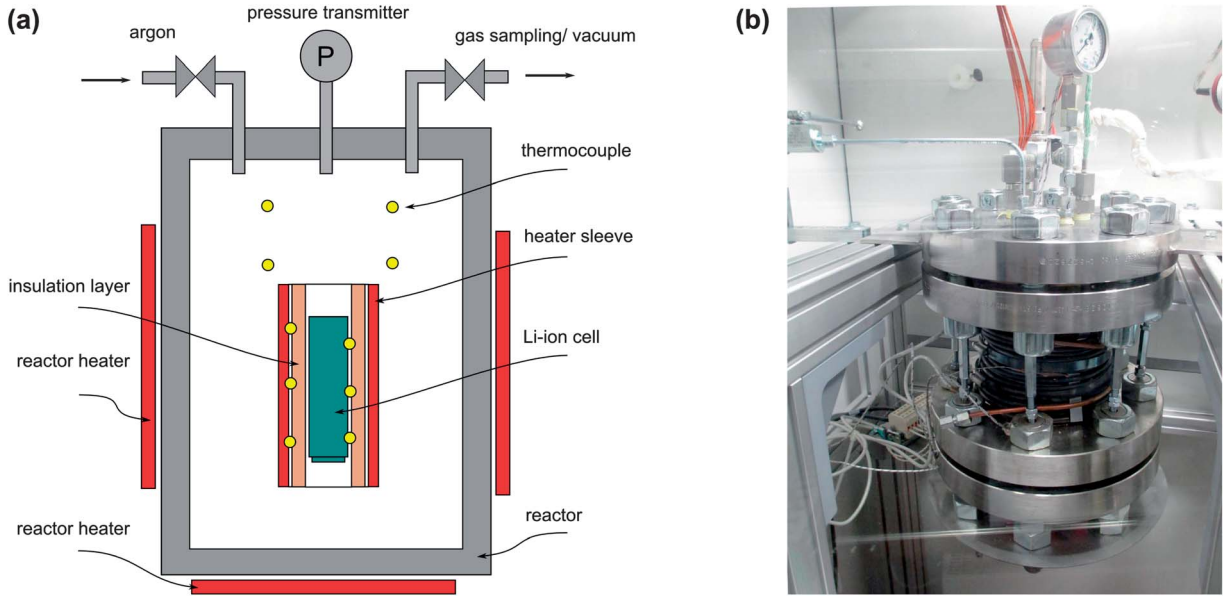

Fig. 1 (a) The reactor and its principal elements. (b) The reactor is the main component of the test stand.

heating sleeve and the thermocouples. A Li-ion battery with the dimensions 18650 (cylindrical geometry with $d = 18$ mm and $l = 65$ mm) can be fitted into the centre of the heating sleeve. The inside wall of the heating sleeve is thermally insulated. The role of the thermal insulation layer is to provide the thermal connection between the heating sleeve and the sample. Due to the low thermal conductivity of the insulation layer, a thermal runaway reaction can proceed in adiabatic-like conditions. Ten thermocouples measure the temperature at different positions inside the reactor: three thermocouples are directly attached to the sample housing, three thermocouples are attached to the heating sleeve and four thermocouples measure the gas temperature inside the reactor.

2.2 Testing method

Initially, the sample battery is CC/CV charged to the respective cut-off voltage. Then, the plastic envelope is removed from the cell and the cell mass and cell voltage are recorded. Three thermocouples are welded to the cell housing, and the whole package is inserted into the heating sleeve of the sample holder. The sample holder is placed inside the reactor. The reactor is evacuated and flushed with argon gas twice. The heaters are set to constant power, and the pressure and temperature signals are recorded. In order to trace fast temperature and pressure changes, each signal is recorded with a high sampling rate of 5000 samples per second.

When a critical temperature is reached, the cell goes into rapid thermal runaway: it produces gas and heat. During the thermal runaway, the temperature of the cell increases by several hundred degree Celsius in a few seconds. After the thermal-runaway event, the cell cools down slowly. Gas samples are taken and analysed with the gas chromatograph. In the next step, the vacuum pump is switched on, and the cooling trap is filled with liquid nitrogen. The gas is carefully released through the cooling trap and the vacuum-pump into the fume hood. The reactor and the gas tubes between the reactor and the cooling trap are heated above 130 °C to avoid gas condensation.

By following this procedure, most liquid residue in the reactor is passed from the reactor to the cooling trap. The liquid residue can be easily removed from the cooling trap before the next experiment run.

2.3 Gas analysis

The compositions of the sampled gases were analysed using a gas chromatograph (GC, Agilent Technologies 3000 Micro GC, two columns, Mol Sieve and PLOTU). A thermal conductivity detector (TCD) was used to detect permanent gases. The GC was calibrated for H_2, O_2, N_2, CO, CO_2, CH_4, C_2H_2, C_2H_4 and C_2H_6. Ar and He were used as carrier gases.

Note, that the current test set-up cannot detect HF, which can be a major source of toxicity of gas released by Li-ion batteries during thermal runaway.[4]

2.4 Cell-components identification

In order to identify the components of each cell species, several cells were disassembled: the cells were discharged to 2.0 V, and the cell casings were then carefully removed without causing short circuits. The exposed jelly rolls were subject to several tests.

For electrolyte identification, the jelly rolls were immersed in flasks with CH_2Cl_2 solution immediately after casing removal. The solutions were then analysed using a gas-chromatography-mass spectrometry system (GC-MS: Agilent 7890 & MS 5975MSD) with the ChemStation software and the NIST spectrum library. To analyse the solid materials of the cells, the extracted jelly rolls were separated into the anode, cathode and separator layers. After drying in a chemical fume hood, anode

and cathode-foil samples were taken for identification of the electrochemically active materials. Microwave-assisted sample digestion followed by inductively coupled plasma optical emission spectrometry (ICP-OES, Ciros Vision EOP, Spectro, Germany) was used to obtain the gross atomic compositions of the cathode active masses. A scanning-electron microscope with energy-dispersive X-ray spectroscopy (SEM/EDX: Zeiss Ultra55 & EDAX Pegasus EDX) was used to confirm the ICP-OES results for the compositions of the cathodes and to validate the anode materials.

For the mass-split calculation, the following procedure was followed for each cell type: positive and negative electrode samples were extracted from the jelly roll. The samples were rinsed with diethyl carbonate (DEC) and then dried again, in order to remove the remaining electrolyte residues from the active materials. The samples were weighed, and the geometries of the electrode foils were recorded, so that the mass split could be calculated. The amount of electrolyte was estimated as the mass difference between the initial cell mass and the calculated dry mass for each cell. The thickness of the active material layers on the electrode substrates was extracted from SEM images. The thicknesses of the aluminium and copper substrates were calculated from the measured area density. The thickness of the separator foils was measured with a micrometer.

2.5 Li-ion cells

18650 consumer cells with three types of chemistry were purchased for the experiments. The cells were produced by three well-known companies. For simplicity, the samples will be referred to as LFP, NMC and LCO/NMC cells, in order to reflect their respective cathode material. Despite the simple naming scheme, please note that the cells do not differ in the types of their cathode material alone. Naturally, they also have different layer geometries (Table 2) and different ratios of their component masses (Fig. 2), and there are differences in the composition of the active masses as well (Table 1).

• The LCO/NMC cell had a blended cathode with two types of electrochemically active particles $LiCoO_2$ and $Li(Ni_{0.50}Mn_{0.25}Co_{0.25})O_2$. A clean cut through the sample was done with a focused ion beam (FIB). Subsequently, EDX measurements of the bulk materials of individual cathode particles were performed. The ratio of LCO and NMC layered oxide particles was estimated by comparing the SEM-EDX and ICP-OES results. The resulting ratio of LCO and NMC was LCO : NMC = (66 : 34) with 5% uncertainty. The cells with LCO/NMC blended cathodes are a compromise to achieve high rate capability of LCO material and to maintain acceptable safety and high capacity of the NMC material.[17] The average voltage of this cell was ~3.8 V.

• The NMC cell had a $Li(Ni_{0.45}Mn_{0.45}Co_{0.10})O_2$ layered oxide cathode. The properties of the NMC mixed oxide cathodes depended on the ratios of nickel, manganese and cobalt material. In general, NMC cells have an average voltage of ~3.8 V and high specific capacity.[18]

• The LFP cell had a $LiFePO_4$ cathode with olivine structure. This cathode type is known for featuring good safety characteristics. Commercial $LiFePO_4$ cathode material for high power Li-ion batteries consists of carbon-coated $LiFePO_4$ nano-scale particles. The cathode material is readily available and non-hazardous. Commercially available LFP cells have a lower operating voltage (~3.3 V) than cells with LCO and NMC cathodes.[18]

The active anode materials consisted only of carbonaceous material for all cells, as verified by SEM/EDX. The exact types of graphite materials could not be identified.

2.6 Electrical characterisation

An electrical characterisation of the cells was done with a BaSyTec CTS cell test system. In the first step, the cells were discharged to their respective minimum voltage. In the second step, the cells were charged using a pulse-pause protocol, until the voltage of the cells stayed above their respective maximum voltage during a pause. The current pulses were set to 100 mA and 30 s. The duration of the pauses was set to 50 s. The open-circuit voltage (OCV) at the end of each pause and the charge capacity were recorded (Fig. 3). For the NMC cell, the cell

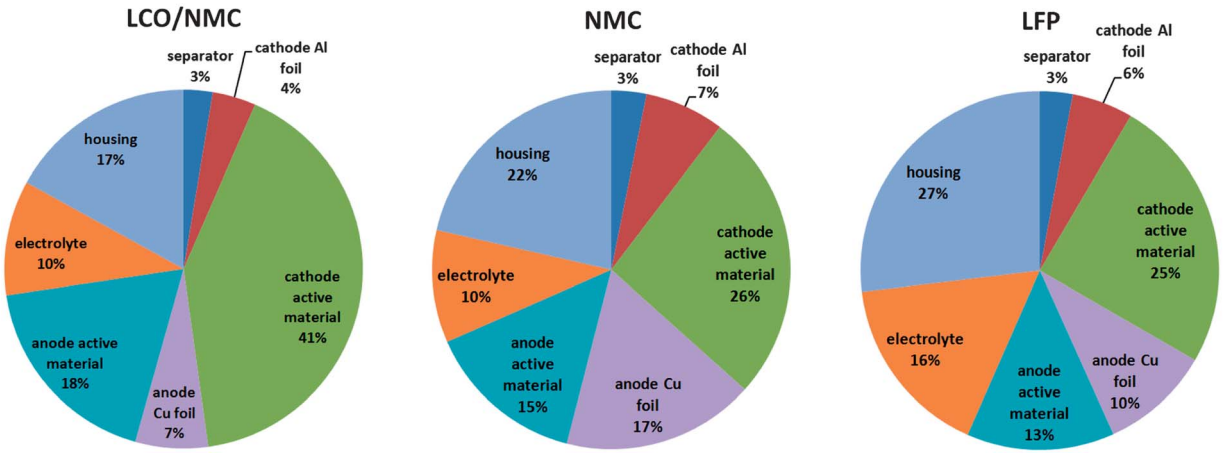

Fig. 2 Mass split (*m*%) of the main components of the three cell species.

Table 1 Overview of the three cells species used in the experiments. All ratios in this table are given as mol ratios. The electrolyte solvents are dimethyl carbonate (DMC), ethyl methyl carbonate (EMC), ethylene carbonate (EC) and propylene carbonate (PC)

		LCO/NMC	NMC	LFP
Cell mass	g	44.3	43.0	38.8
Capacity	A h	2.6	1.5	1.1
Minimum voltage	V	3.0	3.0	2.5
Maximum voltage	V	4.2	4.1	3.5
Electrolyte solvents		DMC : EMC : EC (6 : 2 : 1)	DMC : EMC : EC : PC (7 : 1 : 1 : 1)	DMC : EMC : EC : PC (4 : 2 : 3 : 1)
Cathode material		$LiCoO_2$: Li $(Ni_{0.50}Mn_{0.25}Co_{0.25})O_2$ (2 : 1)	$Li(Ni_{0.45}Mn_{0.45}Co_{0.10})O_2$	$LiFePO_4$
Anode material		Graphite	Graphite	Graphite

manufacturer did not provide the voltage ratings. For safety reasons, 4.1 V was selected as the maximum voltage.

3 Results and discussion

3.1 Typical course of a thermal runaway experiment

In order to illustrate the events during the heat-up process and the thermal runaway itself, one experiment with a NMC cell is described here in detail:

The NMC sample cell was prepared as described above. At the start of the test, the cell heater sleeve was set to constant heating power. The sample was slowly heated, starting at 25 °C, with a heat-rate of ~2 °C min^{-1}. After reaching 220 °C, the cell went into rapid thermal runaway. The cell temperature rose from 220 °C to 687 °C in a few seconds. When the exothermic reaction ended, the cell cooled down slowly (Fig. 4a).

The amount of gas produced inside the pressure vessel was calculated by applying the ideal gas law:

$$n = \frac{pV}{R\theta_{gas}} - n_0 \quad (1)$$

where p is the recorded pressure in the reactor, $V = 0.0027$ m^3 is the reactor volume, R is the gas constant, θ_{gas} is the recorded gas temperature in the reactor (in K), and n_0 is the initial amount of gas in the reactor at the start of the experiment.

At 160 °C, the safety vent device of the battery housing opened, and 0.02 mol of gas were released by the cell. The cell cooled down by 10 °C during the release process because of the Joule–Thomson effect. The vent opening was then probably clogged until, at 230 °C, concurrent with the rapid thermal runaway, the cell vented for a second time. The second venting was the major venting: an additional 0.15 mol of vent gas were produced (Fig. 4b).

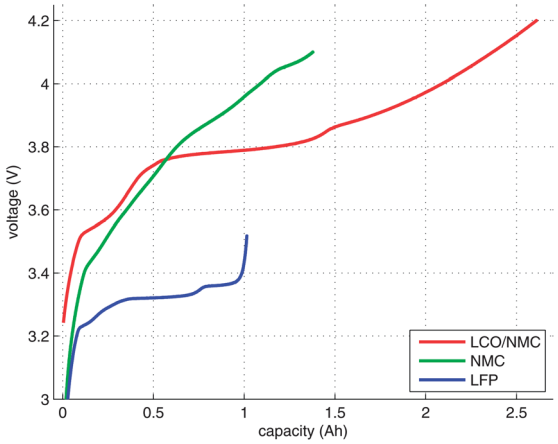

Fig. 3 OCV profiles of the three cell species.

Note that the amount of gas in the reactor decreased shortly after venting. This effect can be explained by the condensation of gas at the reactor walls. Since the reactor walls had a lower temperature (~150 °C) than the cell in full thermal runaway (up to 687 °C), the walls could act as a gas sink.

Table 2 Mass (m), area (A), thickness (d) and volume (V) of the main components of the three cell species. The geometrical volume of a standard 18650 cell is 16.5 cm^3

	LCO/NMC				NMC				LFP			
	m (g)	A (cm^2)	d (μm)	V (cm^3)	m (g)	A (cm^2)	d (μm)	V (cm^3)	m (g)	A (cm^2)	d (μm)	V (cm^3)
Separator	1.2	942	19	1.8	1.4	944	23	2.2	1.2	940	20	1.9
Cathode Al foil	1.7	403	16	0.6	3.1	389	30	1.1	2.1	396	19	0.7
Cathode active material	18.3	715	91	6.5	11.3	654	67	4.4	9.7	793	70	5.5
Anode Cu foil	2.9	402	8	0.3	7.5	418	20	0.8	3.9	396	17	0.7
Anode active material	8.1	739	81	6.0	6.2	695	60	4.2	5.2	793	50	4.0
Electrolyte	4.6				4.4				6.4			
Housing	7.5				9.2				10.5			
Sum	44.3			15.2	43.1			12.7	39.0			12.8

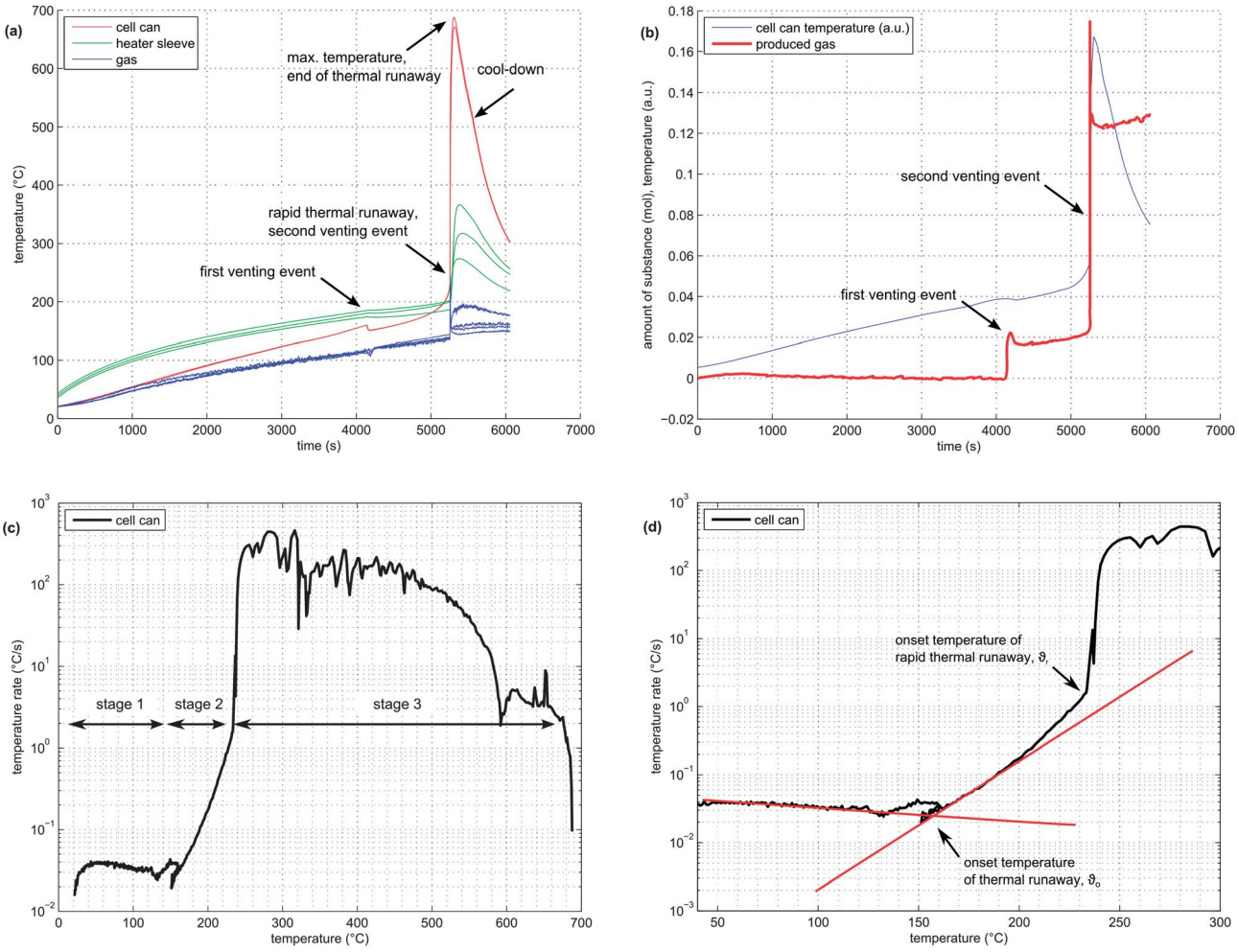

Fig. 4 (a) Temperature *versus* time plot of all temperature sensors in the pressure vessel. The whole duration of the experiment is shown. (b) Amount of produced gas *versus* time plot. Cell temperature is shown in arbitrary units. (c) Temperature rate of the cell *versus* cell temperature. Overview of a whole experiment duration. (d) Temperature rate of the cell *versus* cell temperature. The straight lines are fitted to the heat-up stage and to the quasi-exponential stage. The intersection of the two lines marks the onset point θ_o of the thermal runaway reaction. A sharp increase in the temperature rate marks the onset of the rapid thermal runaway θ_r.

In order to visualise subtle changes in thermal behaviour of the cell during the experiment, rate diagrams are utilized. Contrary to a common temperature *versus* time diagram (θ *vs.* t), the temperature rate is plotted *versus* temperature ($d\theta/dt$ *vs.* θ) in a rate diagram. This type of diagram is often used to visualise accelerating rate calorimetry (ARC) results as well. Three distinct experiment stages can be seen in the rate diagram for the NMC cell (Fig. 4c):

(1) Heat-up stage ($\theta < \theta_o$): In the temperature range from room temperature to θ_o at ~170 °C, the cell generated no heat. The heater sleeve was the only heat source in this phase. The negative peak at 130 °C is associated with endothermic separator melting. (It is analogous to a negative endothermic peek in a differential scanning calorimetry (DSC) diagram during the phase change of a sample). The temperature θ_o at which a cell starts to generate heat is commonly called the onset temperature of the thermal runaway.

(2) Quasi-exponential heating stage ($\theta_o < \theta < \theta_r$): At temperatures higher than θ_o, the battery became a heat source. Between 170 °C and 220 °C, the temperature rate increase followed a nearly straight line in the logarithmic plot (Fig. 4d). At 220 °C, a sharp increase in temperature rate marked the end of the quasi-exponential heating stage.

(3) Rapid thermal runaway stage ($\theta_r < \theta < \theta_m$): At 220 °C, θ/dt increased sharply and initiated the rapid thermal runaway. The transition to thermal runaway was accompanied by a venting event. The thermal runaway ended when all reactants had been consumed. At this point, the maximum temperature $\theta_m = 687$ °C was reached.

It is difficult to pinpoint the exact transition between stage 1 and 2. Several endothermic events often occurred near the onset temperature θ_o: the separator melt temperature was 130 °C, the cell safety vent usually opened at 160 °C and some material was released from the cell, causing a slight cool-down due to the Joule–Thomson effect. Thus, the exact value of θ_o can be obscured by the intermediate cell cool-down.

To keep it simple, θ_o was defined as the point at which the heating-rate curve switches from constant to quasi-exponential

rising. One line is fitted to the heat-up part and one line to the quasi-exponential part of the rate curve in the logarithmic rate plot. The onset temperature θ_o can be further defined as the temperature at which the two lines cross (Fig. 4d).

3.2 Thermal-runaway experiments

At least 3 thermal-runaway experiments were conducted with each of the three cell species. A temperature profile overview of all experiments is shown in Fig. 5a. Each species had its unique thermal-runaway characteristics. The high capacity, cobalt rich LCO/NMC cells reached the highest θ_m at (853 ± 24)°C during thermal runaway. The cobalt poor NMC cells had a lower θ_m of (678 ± 13)°C. The LFP cells showed a less pronounced thermal runaway and reached a moderate θ_m of (404 ± 23)°C. The temperature curves showed small variations from sample to sample. It is likely that the variations were caused by different burst times of the rupture plates, which, together with subtle effects of venting, Joule–Thomson cool-down and clogging of the vent openings, influence the thermal-runaway reaction-pathways.

For the sake of completeness, two additional LFP experiments with different heater-sleeve heating-rates (1.5 and 3.5 °C min^{-1}) were also included in the analysis (Fig. 5a). The thermal runaway characteristics of the LFP cell (θ_r, θ_m and n) did not depend on the heater-sleeve heating rate in the given heat-rate range. The two additional experiments contributed to the mean values in table 3 and Fig. 6

For clarity, only one representative curve for each cell species is shown in the following graphs.

Each cell species had distinctive kinetic thermal-runaway characteristics (Table 3 and Fig. 5b). Of the three specimen, the LCO/NMC cell showed the lowest θ_o and θ_r, hence the LCO/NMC cell was the cell most vulnerable to over-heating conditions. For the NMC cell, θ_o and θ_r were shifted to higher temperatures. Transition temperatures of the LFP specimen were noticeably higher than those of both metal/oxide cells (LCO/NMC and NMC). The LFP cell was able to withstand the highest temperature before going into thermal runaway.

Table 3 Characteristic temperatures and venting parameters in the thermal-runaway experiments. Here, θ_o is the onset temperature, θ_r is the transition temperature into rapid thermal runaway, θ_m is the maximum recorded temperature, n is the total amount of gas produced as measured in the reactor at a reactor temperature of 150 °C, and Δt is the typical venting duration

		LCO/NMC	NMC	LFP
θ_o	°C	149 ± 2	168 ± 1	195 ± 8
θ_r	°C	208 ± 2	223 ± 3	—
θ_m	°C	853 ± 24	678 ± 13	404 ± 23
n	mmol	265 ± 44	149 ± 24	50 ± 4
Δt	s	0.8	0.2	30.0

Both metal oxide cells showed the three stages described above (heat-up, quasi exponential heating, rapid thermal runaway). In contrast, the thermal runaway profile of the LFP cell lacked a distinct quasi-exponential stage. For the LFP cell, it was difficult to find a clear distinction between θ_o and θ_r. Therefore, θ_r is not given for the LFP species.

During the thermal runaway, the cells produced a significant amount of gas (Table 3). The amount of gas strongly depended on the cell type. The highest amount of gas was released by the LCO/NMC cell, followed by the NMC cell. The LFP cell yielded the least amount of gas.

Two successive gas production events were evident in all experiments (Fig. 7):

1 In the first venting event, prior to rapid thermal runaway, the burst plate of the battery opened, and ~20 mmol were released by all three cell types.

2 In the second venting event, at the start of rapid thermal runaway, both metal-oxide cells released a high amount of additional gas at a high rate (Fig. 8). In contrast, the LFP cell released only a small amount of additional gas at a low production rate. In the case of the metal-oxide cells the gas was released in very short time. The NMC cell produced the main

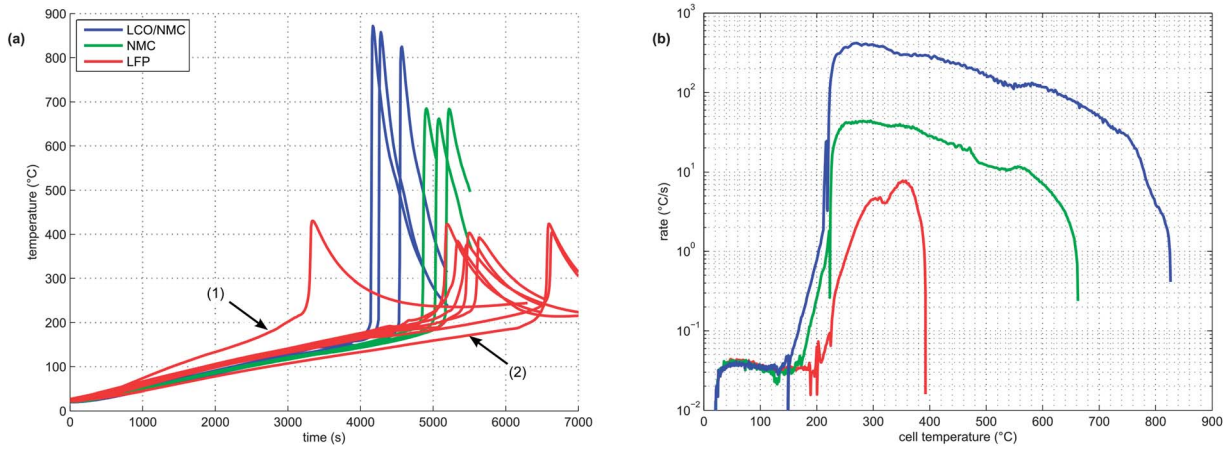

Fig. 5 (a) Overview of the time–temperature profiles for the cells tested. Data for the whole experiment durations and for the whole experiment sets is shown. For the sake of completeness, one LFP test with a higher (1) and one with a lower (2) heating rate of the heater sleeve are included. (b) Temperature rates from three representative experiments.

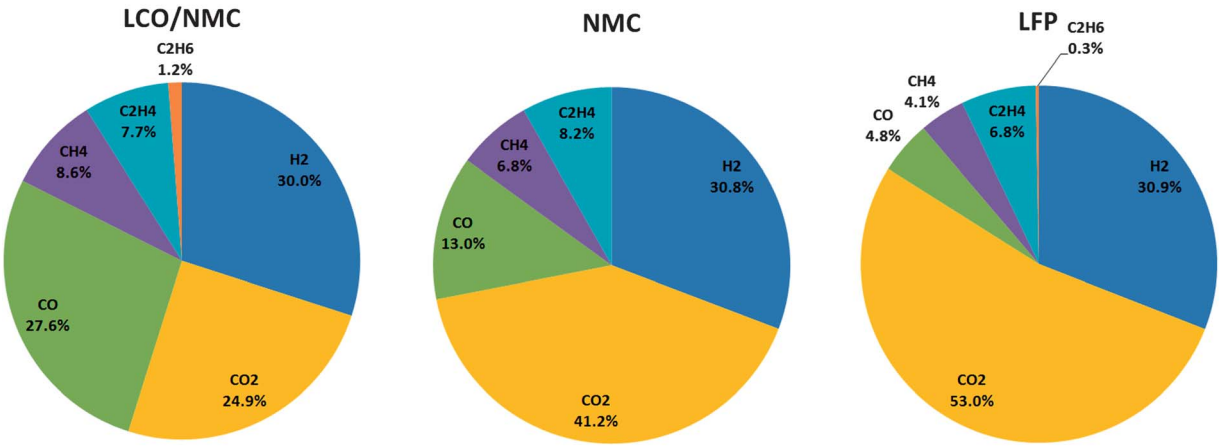

Fig. 6 Detected components of the produced gases (mol%).

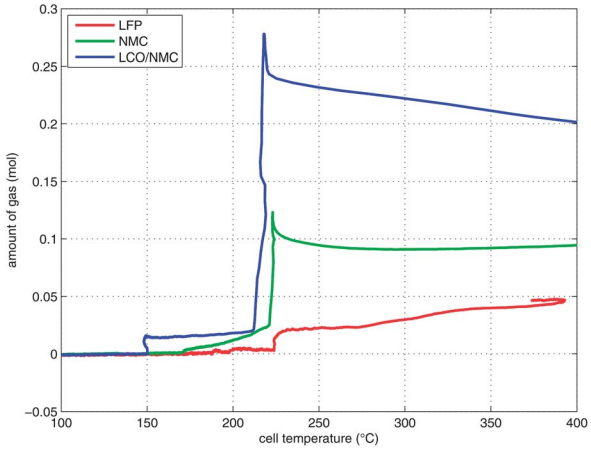

Fig. 7 Temperature-vent gas profiles. Note that the *x*-axis is limited to the relevant temperature range.

amount of gas in just 0.2 s, and the LCO/NMC in 0.8 s. After release, the hot gas was not in thermal equilibrium with the cooler walls of the reactor, and therefore the amount of gas decreased, as the released gas came into contact with the walls and condensed. In contrast, the gas production duration of the second venting for the LFP cell was ~30 s. Because of the gradual release, the gases of the LFP cell were in better temperature equilibrium with the reactor walls and the gas condensation effect was not noticeable.

3.3 Gas analysis

At least one gas analysis was performed for each cell species. Each cell type showed a unique gas composition footprint (Fig. 6). The main components were H_2 and CO_2. Both metal-oxide cells produced a significant amount of CO. Additionally, smaller fractions of CH_4, C_2H_4, and C_2H_6 were identified. As mentioned before, HF was not measured.

Most components of the gases are flammable. The gases can be toxic due to the presence of CO.

3.4 Gas producing reactions

During the thermal runaway gases are released by thermally and electrochemically driven reactions of the electrode active

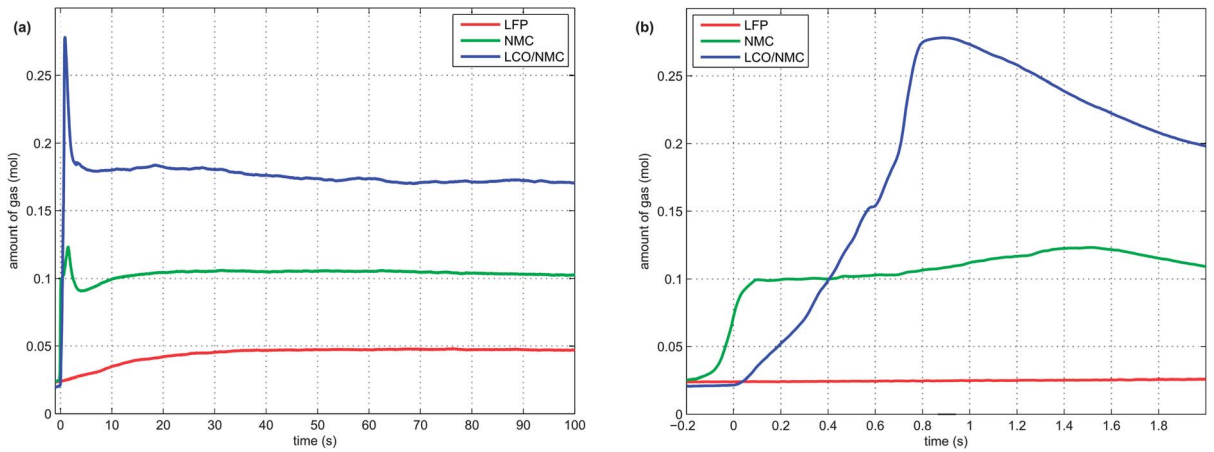

Fig. 8 Time-vent gas profiles. Note: to make the curves comparable, each curve was moved on the time axis, so that the second venting event starts at time zero. (a) The first 100 seconds and (b) the first 2 seconds of the second venting event are shown.

materials, the intercalated lithium, the binder, the solid electrolyte interface (SEI), the electrolyte and the separator.

Evolution of H_2. One possible source of hydrogen is the reaction of the binder with Li^0. Common binder materials are polyvinylidene fluoride (PVdF) and carboxymethyl cellulose (CMC).[19] At temperatures above 230 °C graphite particles of the anode defoliate and Li is exposed to the surrounding electrolyte and binder.[20] Above 260 °C PVdF may react with Li at the anode and release H_2:[21]

$$\text{-CH}_2\text{-CF}_2\text{-} + \text{Li} \xrightarrow{\Delta H} \text{LiF} + \text{-CH=CF-} + \frac{1}{2}\text{H}_2 \quad (2)$$

A similar reaction of CMC and Li may take place above 250 °C:[22]

$$\text{CMC-OH} + \text{Li} \xrightarrow{\Delta H} \text{CMC-OLi} + \frac{1}{2}\text{H}_2 \quad (3)$$

Evolution of CO_2. Many SEI and electrolyte mechanisms can lead to carbon dioxide generation. The SEI can decompose in thermally driven reactions,[23,24]

$$(\text{CH}_2\text{OCO}_2\text{Li})_2 \xrightarrow{\Delta H} \text{Li}_2\text{CO}_3 + \text{C}_2\text{H}_4 + \text{CO}_2 + \frac{1}{2}\text{O}_2 \quad (4)$$

or by reactions with traces of water or HF[25,26,26–29]

$$\text{ROCO}_2\text{Li} + \text{HF} \rightarrow \text{ROH} + \text{CO}_2 + \text{LiF} \quad (5)$$

$$2\text{ROCO}_2\text{Li} + \text{H}_2\text{O} \rightarrow 2\text{ROH} + \text{Li}_2\text{CO}_3 + \text{CO}_2 \quad (6)$$

Li_2CO_3 may be present in the cathode[30] and/or can be produced by two-electron reduction of EC at the anode.[31] Li_2CO_3 reacts with traces of HF with CO_2 evolution:[24,30]

$$\text{Li}_2\text{CO}_3 + 2\text{HF} \xrightarrow{\Delta H} 2\text{LiF} + \text{CO}_2 + \text{H}_2\text{O} \quad (7)$$

EC solvent reduction through SEI (re)formation at the carbon surface of the anode can release CO_2.[32,33] Above 263 °C pure EC can thermally decompose and produce CO_2.[34] Linear carbonate solvents can decompose with CO_2 release in the presence of CH_3OLi.[31]

In the presence of impurities $LiPF_6$ may react to POF_3 that in turn reacts with the electrolyte in a decarboxylation reaction with CO_2 release:[31,35–38]

$$\text{LiPF}_6 \rightarrow \text{LiF} + \text{PF}_5 \quad (8)$$

$$\text{PF}_5 + \text{ROH} \rightarrow \text{HF} + \text{RF} + \text{POF}_3 \quad (9)$$

$$\text{POF}_3 + \text{solvent} \rightarrow \text{CO}_2 + \text{phosphate} \quad (10)$$

In the presence of oxygen, combustion of the carbonate based electrolyte solvents takes place,[28,34,39] *e.g.*

$$\frac{5}{2}\text{O}_2 + \text{C}_3\text{H}_4\text{O}_3(\text{EC}) \xrightarrow{\Delta H} 3\text{CO}_2 + 2\text{H}_2\text{O} \quad (11)$$

A plausible source of oxygen is the structural breakdown of delithiated metal oxide cathodes of the LCO/NMC and NMC cell.[40] It was shown, that CO_2 is mainly produced on the cathode side of an overcharged LCO cell.[41] Therefore the electrolyte oxidation with O_2 freed from the cathode may be the dominant CO_2 producing reaction for the LCO/NMC and NMC cell. The cathode material of the LFP cell is thermally more stable and does not release oxygen.[42]

Evolution of CO. One possible mechanism of carbon monoxide is the reduction of CO2 with intercalated Li at the anode:[26,43,44]

$$2\text{CO}_2 + 2\text{Li}^+ + 2\text{e}^- \rightarrow \text{Li}_2\text{CO}_3 + \text{CO} \quad (12)$$

On the other hand, as shown in the case of an overcharged LCO cell, the main contribution of CO gas may come from the cathode side and not from the anode side.[41] We suggest, that another source of CO may be incomplete combustion of carbon containing material with a limited amount of O_2 that is freed from the cathode.

Evolution of CH_4. In the presence of H_2 methane can be produced by reduction of the electrolyte to lithium carbonate[45–47] *e.g.*

$$\text{C}_3\text{H}_6\text{O}_3(\text{DMC}) + 2\text{Li}^+ + 2\text{e}^- + \text{H}_2 \rightarrow \text{Li}_2\text{CO}_3 + 2\text{CH}_4 \quad (13)$$

Evolution of C_2H_4. Ethylene can be produced by the reduction of EC at the lithiated anode[31,39,47]

$$2\text{Li} + \text{C}_3\text{H}_4\text{O}_3(\text{EC}) \rightarrow \text{Li}_2\text{CO}_3 + \text{C}_2\text{H}_4 \quad (14)$$

and[24,48,49]

$$2\text{Li} + 2\text{C}_3\text{H}_4\text{O}_3(\text{EC}) \rightarrow (\text{CH}_2\text{OCO}_2\text{Li})_2 + \text{C}_2\text{H}_4 \quad (15)$$

or by SEI decomposition[23]

$$2\text{Li} + (\text{CH}_2\text{OCO}_2\text{Li})_2 \rightarrow 2\text{Li}_2\text{CO}_3 + 2\text{C}_2\text{H}_4 \quad (16)$$

Evolution of C_2H_6. In an analogous reaction ethane can be produced by the reduction of DMC at the lithiated anode:[31,39,48]

$$2\text{Li} + \text{C}_3\text{H}_6\text{O}_3(\text{DMC}) \rightarrow \text{Li}_2\text{CO}_3 + \text{C}_2\text{H}_6 \quad (17)$$

4 Conclusion and outlook

Three types of consumer Li-ion batteries with the format 18650 with different cathode materials were evaluated in thermal runaway tests. The cells were brought into thermal runaway by external heating. All tests were performed in a pressure-tight reactor in an argon atmosphere. In agreement with literature,[5] the cell containing LFP showed the best safety characteristics. The LFP cell had the highest onset temperature (~195 °C), the smallest temperature increase during the thermal runaway (~210 °C), the lowest amount of produced gas (~50 mmol) and the lowest percentage of toxic CO in the gas (~4%). Unfortunately, it was also the cell with the lowest working voltage (3.3 V) and the lowest energy content (3.5 W h).

Batteries with higher energy content (5.7 W h and 9.9 W h) performed worse in safety tests. The onset temperature shifted

down to ~170 °C and ~150 °C, the temperature increase during thermal runaway rose to ~500 °C and ~700 °C, the amount of gas released was ~150 mmol and ~270 mmol, and significant percentages of CO (13% and 28%) were found for the NMC and NMC/LCO cells, respectively.

All cells released high amounts of H_2 and hydrocarbons. These gases are highly flammable. Even though the gas could not burn in the inert atmosphere inside the reactor, the surface of the high-energy cells reached temperatures of up to 850 °C during the experiments.

Modern devices are equipped with battery temperature and voltage monitoring. If a state beyond specification is detected, the devices shut down automatically to prevent battery abuse.[18] If system shut-down can not prevent a thermal runaway in all cases, data in this work may be a valuable source for the specification of a robust energy-storage system which can withstand conceivable abuse events.

To reduce possible damage from thermal-runaway events in consumer devices, we suggest the following design optimization targets: (1) increase the temperature endurance and heat absorption capability of used materials; (2) minimize heat propagation to neighbouring burnable elements; (3) minimize gas ignition probability (*e.g.* mechanical separation of electric components from the gas release position).

This work has shown that the kinetics of the thermal-runaway process strongly depend on the energy content of the Li-ion battery. Future work will focus on the thermal runaway triggered by over-heating at different states of charge (SOC) and the thermal runaway caused by overcharge. Emphasis will be given to assessment of HF gas evolution, to gas analysis with GC-MS, and to the analysis of the liquid residues that are collected in the cooling trap.

Acknowledgements

The present work was conducted in the K2 project "New Component Simulation Models for HEVs" in the task "Li-Ion Battery Safety in Automotive Environment (LISAE)". The authors would like to acknowledge the financial support of the "COMET K2 – Competence Centres for Excellent Technologies Programme" of the Austrian Federal Ministry for Transport, Innovation and Technology (BMVIT), the Austrian Federal Ministry of Economy, Family and Youth (BMWFJ), the Austrian Research Promotion Agency (FFG), the Province of Styria and the Styrian Business Promotion Agency (SFG). We would furthermore like to express our thanks to our supporting scientific project partners, namely Graz Centre for Electron Microscopy, Varta Micro Innovation GmbH and the Graz University of Technology. This work was made possible by the principal industrial project partners BASF SE and MAGNA STEYR Battery Systems GmbH & Co OG.

References

1 T. Nagaura and K. Tozawa, *Prog. Batteries Sol. Cells*, 1990, **9**, 209.
2 J. Wen, Y. Yu and C. Chen, *Mater. Express*, 2012, **2**, 197–212.
3 C.-Y. Jhu, Y.-W. Wang, C.-M. Shu, J.-C. Chang and H.-C. Wu, *J. Hazard. Mater.*, 2011, **192**, 99–107.
4 P. Ribière, S. Grugeon, M. Morcrette, S. Boyanov, S. Laruelle and G. Marlair, *Energy Environ. Sci.*, 2012, **5**, 5271.
5 D. Doughty and E. P. Roth, *Electrochem. Soc. Interface*, 2012, **21**, 37–44.
6 C.-Y. Jhu, Y.-W. Wang, C.-Y. Wen and C.-M. Shu, *Appl. Energy*, 2012, **100**, 127–131.
7 S.-I. Tobishima and J.-I. Yamaki, *J. Power Sources*, 1999, **81–82**, 882–886.
8 D. Belov and M.-H. Yang, *Solid State Ionics*, 2008, **179**, 1816–1821.
9 H. Maleki, G. Deng, A. Anani and J. Howard, *J. Electrochem. Soc.*, 1999, **146**, 3224.
10 C.-Y. Jhu, Y.-W. Wang, C.-Y. Wen, C.-C. Chiang and C.-M. Shu, *J. Therm. Anal. Calorim.*, 2011, **106**, 159–163.
11 C.-Y. Wen, C.-Y. Jhu, Y.-W. Wang, C.-C. Chiang and C.-M. Shu, *J. Therm. Anal. Calorim.*, 2012, **109**, 1297–1302.
12 E. P. Roth and C. J. Orendorff, *Electrochem. Soc. Interface*, 2012, **21**, 45–49.
13 D. Abraham, E. P. Roth, R. Kostecki, K. McCarthy, S. MacLaren and D. Doughty, *J. Power Sources*, 2006, **161**, 648–657.
14 Z. Chen, Y. Qin, Y. Ren, W. Lu, C. Orendorff, E. P. Roth and K. Amine, *Energy Environ. Sci.*, 2011, **4**, 4023.
15 D. H. Doughty, E. P. Roth, C. C. Crafts, G. Nagasubramanian, G. Henriksen and K. Amine, *J. Power Sources*, 2005, **146**, 116–120.
16 G. Nagasubramanian and C. J. Orendorff, *J. Power Sources*, 2011, **196**, 8604–8609.
17 K.-S. Lee, S.-T. Myung, D.-W. Kim and Y.-K. Sun, *J. Power Sources*, 2011, **196**, 6974–6977.
18 Z. J. Zhang and P. Ramadass, *Encyclopedia of Sustainability Science and Technology*, Springer, New York, 2012.
19 J.-H. Lee, U. Paik, V. a. Hackley and Y.-M. Choi, *J. Electrochem. Soc.*, 2005, **152**, A1763.
20 O. Haik, S. Ganin, G. Gershinsky, E. Zinigrad, B. Markovsky, D. Aurbach and I. Halalay, *J. Electrochem. Soc.*, 2011, **158**, A913.
21 A. D. Pasquier, *J. Electrochem. Soc.*, 1998, **145**, 472.
22 W. Haiyan, A. Tang and W. Kelong, *Chin. J. Chem.*, 2011, **29**, 27–32.
23 M. N. Richard and J. Dahn, *J. Electrochem. Soc.*, 1999, **146**, 2068.
24 M. Onuki, S. Kinoshita, Y. Sakata, M. Yanagidate, Y. Otake, M. Ue and M. Deguchi, *J. Electrochem. Soc.*, 2008, **155**, A794.
25 J.-S. Hong, H. Maleki, S. A. Hallaj, L. Redey and J. R. Selman, *J. Electrochem. Soc.*, 1998, **145**, 1489.
26 D. Aurbach, A. Zaban, Y. Gofer, Y. E. Ely, I. Weissman, O. Chusid and O. Abramson, *J. Power Sources*, 1995, **54**, 76–84.
27 D. Aurbach, *J. Electrochem. Soc.*, 1995, **142**, 2882.
28 W. Kong, H. Li, X. Huang and L. Chen, *J. Power Sources*, 2005, **142**, 285–291.
29 D. Aurbach, *J. Electrochem. Soc.*, 1991, **138**, 3529.

30 C. Doh, D. Kim, J. Lee, D. Lee, B. Jin, H. Kim, S. Moon, Y. Hwang and A. Veluchamy, *Bull. Korean Chem. Soc.*, 2009, **30**, 783.
31 G. Gachot, P. Ribière, D. Mathiron, S. Grugeon, M. Armand, J.-B. Leriche, S. Pilard and S. Laruelle, *Anal. Chem.*, 2011, **83**, 478–485.
32 C. Yang, Y. Wang and C. Wan, *J. Power Sources*, 1998, **72**, 66–70.
33 S. Mori, H. Asahina, H. Suzuki, A. Yonei and K. Yokoto, *J. Power Sources*, 1997, **68**, 59–64.
34 G. G. Botte and T. J. Bauer, *J. Power Sources*, 2003, **119–121**, 815–820.
35 A. Hammami, N. Raymond and M. Armand, *Nature*, 2003, **424**, 635–636.
36 C. L. Campion, W. Li and B. L. Lucht, *J. Electrochem. Soc.*, 2005, **152**, A2327.
37 C. L. Campion, W. Li, W. B. Euler, B. L. Lucht, B. Ravdel, J. F. DiCarlo, R. Gitzendanner and K. M. Abraham, *Electrochem. Solid-State Lett.*, 2004, **7**, A194.
38 T. Kawamura, A. Kimura, M. Egashira, S. Okada and J.-I. Yamaki, *J. Power Sources*, 2002, **104**, 260–264.
39 R. Spotnitz and J. Franklin, *J. Power Sources*, 2003, **113**, 81–100.
40 I. Belharouak, W. Lu, D. Vissers and K. Amine, *Electrochem. Commun.*, 2006, **8**, 329–335.
41 T. Ohsaki, T. Kishi, T. Kuboki, N. Takami, N. Shimura, Y. Sato, M. Sekino and A. Satoh, *J. Power Sources*, 2005, **146**, 97–100.
42 A. K. Padhi, *J. Electrochem. Soc.*, 1997, **144**, 1188.
43 A. D. Pasquier, F. Disma and T. Bowmer, *J. Electrochem. Soc.*, 1998, **145**, 472.
44 S. E. Sloop, J. B. Kerr and K. Kinoshita, *J. Power Sources*, 2003, **119–121**, 330–337.
45 K. Kumai, *J. Power Sources*, 1999, **81–82**, 715–719.
46 J.-S. Shin, C.-H. Han, U.-H. Jung, S.-I. Lee, H.-J. Kim and K. Kim, *J. Power Sources*, 2002, **109**, 47–52.
47 H. Yoshida, T. Fukunaga, T. Hazama, M. Terasaki, M. Mizutani and M. Yamachi, *J. PowerSources*, 1997, **68**, 311–315.
48 G. Gachot, S. Grugeon, G. G. Eshetu, D. Mathiron, P. Ribière, M. Armand and S. Laruelle, *Electrochim. Acta*, 2012, **83**, 402–409.
49 D. Aurbach, A. Zaban, Y. Ein-Eli, I. Weissman, O. Chusid, B. Markovsky, M. Levi, E. Levi, A. Schechter and E. Granot, *J. Power Sources*, 1997, **68**, 91–98.

2.2 Thermal Runaway of Commercial 18650 Li-ion Batteries with LFP and NCA Cathodes – Impact of State of Charge and Overcharge

The following journal article was published in RSC Advances in 2015. This was our second article. Again we tested commercial 18650 cells. This time we focused on the dependency of the TR on the SOC.
In this work Andrey Golubkov wrote the text of the article, did the TR experiments and analysed the TR data. Sebastian Scheikl and René Planteu participated in making the TR experiments and updating the test stand. Helmar Wiltsche used ICP-OES to measure the composition of the cathode. Gisela Fauler measured the electrolyte composition and Christoph Stangl and provided industry insight to make a realistic cell mass-split. Gernot Voitic helped to make the GC measurements of the vent-gas. Alexander Thaler and Viktor Hacker supervised the work.

RSC Advances

PAPER

View Article Online
View Journal | View Issue

Cite this: *RSC Adv.*, 2015, **5**, 57171

Thermal runaway of commercial 18650 Li-ion batteries with LFP and NCA cathodes – impact of state of charge and overcharge

Andrey W. Golubkov,*[a] Sebastian Scheikl,[a] René Planteu,[a] Gernot Voitic,[b] Helmar Wiltsche,[c] Christoph Stangl,[d] Gisela Fauler,[d] Alexander Thaler[a] and Viktor Hacker[b]

Received 2nd April 2015
Accepted 22nd June 2015

DOI: 10.1039/c5ra05897j

www.rsc.org/advances

Thermal runaway characteristics of two types of commercially available 18650 cells, based on Li_xFePO_4 and $Li_x(Ni_{0.80}Co_{0.15}Al_{0.05})O_2$ were investigated in detail. The cells were preconditioned to state of charge (SOC) values in the range of 0% to 143%; this ensured that the working SOC window as well as overcharge conditions were covered in the experiments. Subsequently a series of temperature-ramp tests was performed with the preconditioned cells. Charged cells went into a thermal runaway, when heated above a critical temperature. The following thermal runaway parameters are provided for each experiment with the two cell types: temperature of a first detected exothermic reaction, maximum cell temperature, amount of produced ventgas and the composition of the ventgas. The dependence of those parameters with respect to the SOC is presented and a model of the major reactions during the thermal runaway is made.

1 Introduction

Li-ion batteries[1,2] excel in energy density and cycle life. Unfortunately those benefits come with a price: when Li-ion batteries are mistreated with high over-temperature or strong overcharge, they can transit into a so-called thermal runaway. During the thermal runaway, the battery temperature increases due to exothermic reactions. In turn, the increased temperature accelerates those degradation reactions and the system destabilizes. At the end of the thermal runaway, battery temperatures higher than 1000 °C can be reached and high amounts of burnable and harmful gases can be released.

Because Li-ion batteries are widely used, the possible hazards of Li-ion batteries are a key issue for automotive, aerospace and consumer electronics industries. The safety characteristics of Li-ion battery systems depend (a) on the used cell type (geometry, materials), (b) on the initial conditions before misuse (state of charge, ageing effects), (c) on the type of misuse (over-temperature, over-charge) and (d) on external measures (built-in safety devices, forced cooling, confinement).[3–5]

In the past, accelerated rate calorimetry (ARC) tests with limited maximum temperature[6–12] and without limitation[13] as well as fire experiments and mechanical abuse[14–17] with complete Li-ion cells were done. Recently over-temperature and over-charge tests with large format cells (which may be used for automotive applications) were published.[18–20] It is known that the severity of the thermal runaway event in over-temperature experiments increases with increasing SOC.[4,21–27] It is also known, that a thermal runaway can be triggered by strong overcharge beyond safe voltage limits of the cell.[28–34] Even if the overcharge condition does not trigger a thermal runaway, safety may be compromised by Li-plating on the anode.[35]

In our previous publication[36] the safety characteristics of three different commercial Li-ion batteries charged to 100% SOC were investigated. It was demonstrated, that cells with cathodes based on iron-phosphate as well as on metal-oxide material exhibit a thermal runaway in thermal-ramp experiments. The severity of the thermal runaway showed a strong dependence on the material composition of the cells.

In this publication two cell types are introduced and the mass inventory of the cells is calculated based on tear down results. The thermal runaway testing method is explained and the outcomes of experiments with discharged, partially charged, fully charged and over-charged cells are presented. Possible chemical reactions are listed and quantitative calculations of ventgas generation are made for two cases.

[a]*Kompetenzzentrum – Das Virtuelle Fahrzeug Forschungsgesellschaft mbH, Inffeldgasse 21a, A-8010 Graz, Austria. E-mail: andrej.golubkov@alumni.tugraz.at*
[b]*Institute of Chemical Engineering and Environmental Technology, Graz University of Technology, Inffeldgasse 25/C/II, 8010 Graz, Austria*
[c]*Institute of Analytical Chemistry and Food Chemistry, Graz University of Technology, Stremayrgasse 9/III, 8010 Graz, Austria*
[d]*Varta Micro Innovation GmbH, Stremayrgasse 9, 8010 Graz, Austria*

2 Samples

The two types of commercially available Li-ion batteries, with the geometrical format 18650, were purchased from two well known manufacturers. The first cell, rated to a nominal capacity of $C^{nom} = 1.1$ A h is based on a Li_xFePO_4 (LFP) cathode. The LFP material is considered as relatively safe. Unfortunately commercial LFP-based cells have lower capacity and nominal voltage compared to metal-oxide based cells. According to the datasheet the LFP cell is designed for a maximum discharge current of 30 A and has a cycle life of >1000 full discharge cycles.

The second cell has a much higher nominal capacity $C^{nom} = 3.35$ A h and is based on a $Li_x(Ni_{0.80}Co_{0.15}Al_{0.05})O_2$ (NCA) cathode. To our knowledge, this mass produced cell has the highest energy density which is commercially available as of 2013. It is specified to a maximum discharge current of 6.7 A h and its cycle life is >300 cycles.

In the following, the two cell types will be denoted as LFP and NCA for easy reading.

2.1 Cell composition, methods

For the interpretation of the misuse experiment results it is beneficial to know the mass split of the cell components. Unfortunately information regarding detailed cell composition is kept confidential by the manufacturers. We had to make a tear down and an analysis of the cell components for both cell species by ourselves. The following parameters were measured directly using the same methods and equipment as in ref. 36:

• Mass of the anode and cathode coating, the electrolyte, the current collector foils, the separator and the housing material.

• The solvent mass-ratios of the electrolyte. Detected solvents were dimethyl carbonate (DMC), ethyl methyl carbonate (EMC), ethylene carbonate (EC), propylene carbonate (PC) and methyl phenyl carbonate (MPC).

• The mole-ratios of the different transition metals and phosphor in the cathode coating.

Additionally, separator foils were examined with differential scanning calorimetry coupled with thermal gravimetric analysis (DSC-TGA, NETZSCH STA 449 C). Separator samples were rinsed with diethyl carbonate and dried in a desiccator for 12 hours. During the test the DSC-TGA was flushed with and the heat ramp was set to 10 K min^{-1}.

2.2 Cell composition, results and discussion

It is not in the scope of this work to compile an exhaustive material inventory of the two commercial cell types. Nevertheless, to obtain some insight into chemical reactions taking place during cell misuse, it is helpful to make at least rough estimations for cell components that were not accessible to direct measurements (Table 1). Estimations for the amount and composition of active material, particle coating, binder, carbon black and the SEI in the electrode coatings as well as for the amount of salt, additives and soluble SEI in the electrolyte were discussed with our project partners. Effects of cell formation were considered. The compositions of the separators were estimated from DSC measurements.

2.2.1 Binder and conducting agent. The mass ratio of binder material and conducting agents in the electrode coatings was not measured. We assume that sodium carboxymethylcellulose (CMC) with a degree of carboxymethyl substitution (DS) of 0.7 is used as the anode binder[37] and polyvinylidene fluoride (PVDF) is used as the cathode binder.[38] CMC is a cost effective binder material in the anode, but can not be used in the cathode. We suppose that 5% of anode coating and 2.5% (NCA) or 5% (LFP) of cathode coating is binder material.

Additionally a conducting agent is needed to improve the electrical conductivity between the cathode particles and cathode substrate-foil. We suppose that 2.5% (NCA) or 5% (LFP) of cathode coating consists of carbon black. We justify the increased amount of binder and conducting agent of the LFP cell with its higher power capability.

2.2.2 LFP particle coating. The active cathode material of the LFP cell consists of Li_xFePO_4. The Li_xFePO_4 particles need to be nano structured and carbon coated to achieve good diffusion of Li-ions and good inter-particle electrical conductivity.[39] It is hard to tell which amount of carbon coating was actually used in the tested commercial battery. Optimum values of carbon coating found in the literature vary from 1.5% to 15%.[40] We assume that 10% of the LFP cathode consists of carbon coating. Please note, that this might be the upper estimate. One of the reviewers suggested, that the carbon coating of a commercial battery is probably in the range of 1% to 2%.

2.2.3 Electrolyte and SEI. The amount of salt in the electrolyte could not be measured as well, it is supposed that both cells use the traditional salt $LiPF_6$ with a concentration of 1.1 mol L^{-1}. The density of the electrolytes is estimated with 1.21 kg L^{-1}.

Vinylene carbonate (VC) is a common solid electrolyte interface (SEI) improving additive.[41] We assume that 2% of VC was added to the electrolyte.[42] During initial charging VC and EC undergo reduction reactions and form the SEI at the surface of the graphite particles of the anode. A fully developed SEI prevents further reduction of the electrolyte solvents.[43] The SEI composition and formation reactions can be complicated[41,44,45] and lie beyond the scope of this work. Instead, for further calculations, we treat the SEI as being made of only four components:

(1) The polymerization product of VC[41,46]

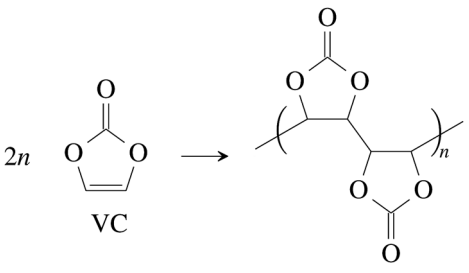

polymer organic SEI (1)

(2) The organic Li-carbonate from EC reduction[47–49]

$$2C_3H_4O_3\ (EC) + 2Li^+ + 2e^- \rightarrow (CH_2OCO_2Li)_2 + C_2H_4 \quad (2)$$

Table 1 Mass split of the discharged NCA and LFP cell. Please note, that the mass ratios for the binder, carbon black, the SEI and the salt were not measured; instead rough estimates are given. The chemical formulas for the SEI are taken from literature. The composition of the separator is deduced from DSC-TGA scans. For known or estimated materials the molar mass M and the amount of material n in the cell is given. For polymers M and n of the monomers is given. In the case of CMC the average number of atoms per monomer is used. The Li fractions in the molecular formulas of the electrodes were calculated for discharged cells with consideration of the irreversible capacity loss n_{Li}^{irr} and the residual capacity n_{Li}^{res}. In addition, the maximum theoretical capacity of intercalated Li in the electrodes was calculated using Faraday's laws of electrolysis

	NCA cell						LFP cell					
Component	Mass ratio	Mass (g)	Formula	M (g mol^{-1})	n (mmol)	Li-capacity (A h)	Mass ratio	Mass (g)	Formula	M (g mol^{-1})	n (mmol)	Li-capacity (A h)
Cathode coating:												
Active material	95.0%	17.04	$Li_{0.925}(Ni_{0.80}Co_{0.15}Al_{0.05})O_2$	95.6	178.2	4.78	80.0%	7.73	$Li_{0.882}FePO_4$	156.9	49.2	1.32
Particle coating	—	—	—	—	—		10.0%	0.97	C	12.0	80.5	
Carbon black	2.5%	0.45	C	12.0	37.4		5.0%	0.48	C	12.0	40.2	
Binder (PVDF)	2.5%	0.45	$(C_2H_2F_2)_n$	64.0	7.0		5.0%	0.48	$(C_2H_2F_2)n$	64.0	7.5	
Sum	100%	17.93					100%	9.66				
Anode coating:												
Graphite	93.5%	10.92	$Li_{0.008}C_6$	72.1	151.5	4.06	93.5%	4.84	$Li_{0.006}C_6$	72.1	67.2	1.80
Binder (CMC)	5.0%	0.58	$(C_{7.4}H_{10.7}O_{6.4})_n$	202.1	2.9		5.0%	0.26	$(C_{7.4}H_{10.7}O_{6.4})_n$	202.1	1.3	
SEI, lithium fluoride	0.4%	0.04	LiF	25.9	1.7		0.4%	0.02	LiF	25.9	0.8	
SEI, lithium carbonate	1.1%	0.13	Li_2CO_3	73.9	1.7		1.1%	0.06	Li_2CO_3	73.9	0.8	
Sum	100.0%	11.67					100.0%	5.18				
Separator:												
PP	—	—	—	—	—		66%	0.76	$(C_3H_6)_n$	42.1	18.0	
PE	—	—	—	—	—		34%	0.39	$(C_2H_4)_n$	28.1	13.9	
UHMWPE	100%	0.70	$(C_2H_4)_n$	28.1	25.0		—	—	—	—	—	
Sum	100%	0.70					100%	1.15				
Electrolyte:												
SEI, polymer organic	2.0%	0.09	$(C_6H_4O_6)_n$	86.1	1.0		2.0%	0.13	$(C_6H_4O_6)_n$	172.1	0.7	
SEI, organic	12.7%	0.56	$(CH_2OCO_2Li)_2$	162.0	3.5		3.9%	0.25	$(CH_2OCO_2Li)_2$	162.0	1.5	
EC	17.1%	0.75	$C_3H_4O_3$	88.1	8.5		24.8%	1.59	$C_3H_4O_3$	88.1	18.1	
DMC	49.7%	2.19	$C_3H_6O_3$	90.1	24.3		33.0%	2.12	$C_3H_6O_3$	90.1	23.5	
EMC	5.3%	0.23	$C_4H_8O_3$	104.1	2.2		16.5%	1.06	$C_4H_8O_3$	104.1	10.2	
PC	—	—	—	—	—		8.3%	0.53	$C_4H_6O_3$	102.1	5.2	
MPC	2.7%	0.12	$C_8H_8O_3$	196.1	0.6		—	—	—	—	—	
Salt	10.6%	0.46	$LiPF_6$	151.9	3.1		11.5%	0.74	$LiPF_6$	151.9	4.9	
Sum	100.0%	4.41					100.0%	6.41				
Inactive components:												
Housing (metal can)		5.71						10.45				
Cathode Al foil		1.20						2.14				
Anode Cu foil		2.72						3.86				
Other components		1.05						—				
Sum		10.69						16.46				
Total sum		45.40						38.87				

(3) The inorganic Li-carbonate Li_2CO_3 from EC reduction[50–52]

$$C_3H_4O_3\ (EC) + 2Li^+ + 2e^- \rightarrow Li_2CO_3 + C_2H_4 \quad (3)$$

(4) And LiF which can be produced from decomposition of the salt and the Li-carbonate[53]

$$\begin{aligned} &LiPF_6 \rightarrow LiF + PF_5 \\ &PF_5 + ROH \rightarrow HF + RF + POF_3 \\ &Li_2CO_3 + 2HF \rightarrow 2LiF + CO_2 + H_2O \end{aligned} \quad (4)$$

We assume that all VC (2% of electrolyte) goes into polymerization (1) and that the additional SEI components $(CH_2OCO_2Li)_2 : Li_2CO_3 : LiF$ are in the ratio 1/2 : 1/4 : 1/4.[44] The components of the SEI are listed (Table 1) as a part of either anode or electrolyte depending on their solubility in the electrolyte solvent.[54] To calculate the actual amounts of lithium containing SEI we need to take the irreversible capacity loss into account.

2.2.4 Irreversible capacity loss. We think that the most economical anode material for both manufacturers is surface treated natural graphite. During cell assembly the graphite is in delithiated state and the cathode is in fully lithiated state. At the first charging (cell formation) an amount of lithium n_{Li}^{irr} that is equivalent to ~8% of the maximum anode-Li-capacity is trapped.[2] The associated charge C^{irr} is called irreversible capacity loss:

$$n_{Li}^{irr} = 0.08 n_{C_6}^{a} \quad (5)$$

$$C^{irr} = F n_{Li}^{irr} \quad (6)$$

here F is the Faraday constant and $n_{C_6}^{a}$ is the amount of graphite units C_6 in the anode (in mol). We assumed that all trapped lithium is integrated and immobilized in the SEI according to the chemical reactions (2)–(4). The calculated values for the NCA and LFP cell are $n_{Li}^{irr}(NCA) = 12.1$ mmol and $n_{Li}^{irr}(LFP) = 5.4$ mmol respectively. As a consequence, after formation, the cathode can never again be fully lithiated. Even when the cell is fully discharged, n_{Li}^{irr} is missing, and the amount of Li per stoichiometric formula in the cathode is <1. The effect of the missing lithium n_{Li}^{irr} (proportional to C_{irr}) in the cathode is taken into account in further stoichiometric calculations.

2.2.5 Residual capacity. Commercial Li-ion cells must not be discharged beyond their rated minimal operation voltage ($V_{min}(NCA) = 2.5$ V and $V_{min}(LFP) = 2.0$ V) during normal cycling. If cells are discharged to voltages lower than V_{min} dissolution of the copper foil may occur,[55] because the anode potential may reach the oxidation potential[56] of Cu. Anodes of cells that are discharged to V_{min} are not fully delithiated, instead a small amount of Li stays in the anodes and acts as a safety margin to keep the anode potentials below the copper dissolution potential. We assume that the residual capacity C^{res} (which is proportional to the amount of residual Li n_{Li}^{res}) equals to 1% of the nominal cell capacity:

$$C^{res} = 0.01 C^{nom} \quad (7)$$

$$n_{Li}^{res} = 1/F C^{res} \quad (8)$$

The amount of residual lithium is considered in further calculation of the lithiation states of both electrodes.

2.3 Available capacities in the electrodes

With identified amount of active cathode material n_{cat}^{a} and with known C^{irr} and C^{res} the theoretically usable capacity of the cathode after cell formation can be calculated

$$C_{cat}^{u} = F n_{cat}^{a} - C^{irr} - C^{res} \quad (9)$$

and compared to the nominal capacity as given in the data sheet.

In the case of LFP cell $C_{cat}^{u} = 1.16$ A h. In theory, LFP material can be fully delithiated, and C_{cat}^{u} should be equal to C^{nom}. In our work, the calculated C_{cat}^{u} exceeded C^{nom}. According to the data sheet the LFP cell is rated to $C^{nom} = 1.1$ A h and the measured capacities in the allowed voltage range were even smaller (Fig. 1). The discrepancy may be caused by incomplete utilization of the LFP material of a real cell or by ageing effects of the cathode.

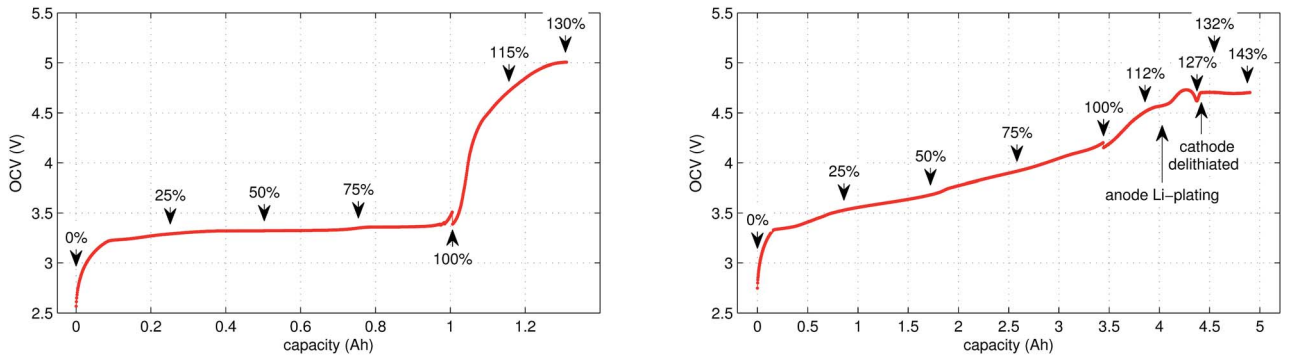

Fig. 1 OCV characteristics of the (left) LFP and (right) NCA cells. Measured values in the allowed voltage range and additionally in the overcharge region are given. SOC points, at which temperature-ramp experiments were done, are marked. Rough estimates, where Li-plating and complete cathode delithiation may occur, are indicated for the NCA cell. The discontinuities at 100% are caused by relaxations during the time-gaps between cycling and the overcharge experiments.

It is noteworthy that the available capacity of the LFP anode

$$C^{u}_{and} = Fn^{a}_{C_6} \quad (10)$$

exceeds the C^{u}_{cat} by 50%. In other words, the anode of the LFP cell is overbalanced. This makes sense for a high power cell, as it allows high charging currents with reduced risk of Li-plating.

In contrast to LFP, the NCA cathodes should not be fully delithiated during normal operation. Correspondingly, the theoretically available capacity of the NCA cell of 4.42 A h was higher than the nominal capacity 3.35 A h. The calculated capacity of the active material in the anode was 4.06 A h. That means the NCA anode was slightly overbalanced by 21%.

2.3.1 Separator. The composition of the separator materials was deduced from DSC-TGA measurements. The separator of the LFP cells showed endothermic (melting) peaks at 132 °C and 159 °C which are typical for a 3-layered laminate with a polyethylene (PE) core between two polypropylene (PP) skin layers (PP/PE/PP). We assume that the LFP separator consists of 2/3PP and 1/3PE.

The separator of the NCA cell showed only one indistinct endothermic peak at ~130 °C. We assume that the NCA separator consists of ultra-high molecular weight polyethylene (UHMWPE) membrane.[57,58]

3 Experimental

In this work a total of 23 thermal ramp experiments with the two cell types were done at different SOC. Each experiment consisted of the following steps; the cell underwent a open circuit voltage (OCV) check, was charged to the selected SOC and inserted into the sample holder. The sample holder was attached inside a sealed reactor and the thermal ramp experiment was started (the test-rig and thermal ramp method is described in ref. 36). After the thermal ramp experiment gas samples were taken and analysed.

3.1 Initial OCV check

We applied the same OCV measurement procedure as in ref. 36. Each sample was fully discharged to 0% SOC (2.5 V) and then fully charged to 100% SOC (LFP: 3.5 V, NCA: 4.2 V). The health status of the cells was checked by comparing the measured capacities with the nominal capacity from the manufacturer. Typical OCV profiles are given in Fig. 1. BaSyTec CTS cell test system and Heiden Power DC-source-load were used for battery cycling.

3.2 Sample preparation

After the OCV check the insulation foil was stripped from the cell and the sample was weighed. Three K-type thermocouples were spot-welded to the cell housing. Then the sample was wrapped in a thermal insulation layer and inserted into the heating sleeve of the sample holder. Finally, the sample holder was installed inside the reactor, the electrical connections were made and the reactor was sealed.

3.3 SOC set-point

The cell was brought to the desired SOC by charging or discharging, starting from 100% SOC. The coulomb counting method was used for SOC calculation and the charge/discharge was stopped when the required SOC was reached. For experiments with SOC < 100% the cell was discharged outside of the reactor. For SOC > 100% the cell was overcharged inside the reactor, for safety reasons. In order to prevent cell heating, the overcharge current was set to very low values. The SOC set-points of all experiments are marked in Fig. 1.

3.4 Thermal-ramp experiment

The sealed reactor was evacuated and flushed with inert gas. The heaters were turned on. The sample inside the reactor was heated slowly with a rate of 2 °C min^{-1} (NCA) or 4 °C min^{-1} (LFP). Cell temperatures, gas temperatures and the pressure in the sealed reactor were recorded. At some point the cell transited into thermal runaway and ventgas was released in the reactor. The amount of gas inside the reactor n^{ideal}_{sum} was calculated using the ideal gas law

$$n^{ideal}_{sum} = \frac{pV}{R\theta_{gas}} - n_0. \quad (11)$$

Here p denotes the pressure in the reactor, $V = 0.0027$ m^3 is the reactor volume, R is the gas constant, θ_{gas} is the gas temperature in the reactor (in K) and n_0 is the initial amount of gas in the reactor at the start of the experiment.

The eqn (11) is only valid, when θ_{gas} is equal to the mean gas temperature in the reactor. During the thermal runaway a violent cell venting may take place and hot gases are released into the pressure vessel. In the first seconds after venting, when the gas temperature inside the reactor is not homogeneous, n^{ideal}_{sum} may be over or underestimated. Thus, given n^{ideal}_{sum} values were calculated when the gas temperature was in equilibrium.

3.5 Ventgas analysis

Gas samples were taken after the thermal runaway reaction. If no thermal runaway occurred, then the gas samples were taken after the cell temperature exceeded 250 °C. The gas was analysed with a gas chromatograph system (GC, Agilent Technologies 3000 Micro GC, two columns, Mol Sieve and PLOTU). A thermal conductivity detector (TCD) was used to detect permanent gases. The GC was calibrated for H_2, O_2, N_2, CO, CO_2, CH_4, C_2H_2, C_2H_4 and C_2H_6. The GC used Ar and He as carrier gases.

3.6 Role of the inert gas

Before each experiment, the reactor was filled with inert gas to prevent reactions of the vent-gas with the reactor atmosphere. We used either N_2 or Ar as inert gas. Both gases have advantages and disadvantages.

• Advantages of using Ar as inert gas: in this case N_2 is not present in the reactor. There are no reactions which can produce N_2 during thermal runaway. The only possible source

of N_2 in a ventgas sample is leakage from ambient air. Therefore, the presence of N_2 (accompanied by O_2) in the GC results indicates gas leakage. The amount of Ar in the samples could not be quantified, because it was used as a carrier gas in the GC setup.

• Advantages of using N_2 as inert gas: in this case N_2 fulfils two functions. It serves as inert gas and also as an internal standard. Since the amount of N_2 in the reactor is known ($V_{N_2} = 0.0027\ m^3$), absolute amounts of other detected gas components can be derived from their relative GC results r_i^{GC}

$$n_i^{GC} = \frac{n_{N_2}}{r_{N_2}^{GC}} r_i^{GC} \quad (12)$$

The absolute amount of vent-gas n_{sum}^{GC} can be calculated from the GC results.

$$n_{sum}^{GC} = \sum_{i \neq N_2} n_i^{GC} \quad (13)$$

The amount of ventgas calculated with the ideal gas eqn (11) can be compared with the total amount of gas from GC results (13). If $n_{sum}^{ideal} = n_{sum}^{GC}$ than it is likely, that all formed gases were detected by the GC.

However, there is also one strong disadvantage of using N_2. If leaks from ambient air occur, leaked N_2 falsifies the internal standard. Therefore, for the most experiments we used Ar as inert gas in the reactor and detected N_2 indicated gas leaks. Only in the last three experiments, after enough experience was gained, we were confident to use N_2 as the inert gas.

4 Results

We did 23 thermal-ramp experiments with NCA and LFP cells set to different SOC. The results are summarized in Tables 2 and 3. Typical experiment runs are shown in Fig. 2 and 4. The dependence of the thermal runaway parameters on the SOC is visualised in Fig. 3 and 5.

4.1 NCA cells

We tested the thermal stabilities of discharged as well as partially charged, fully charged and over charged NCA cells.

Discharged NCA cells (Experiment 1–5) showed no pronounced thermal runaway characteristics. Only small unremarkable exothermic peaks were observed between 150 °C and 300 °C. The amount of gas depended on the timespan which the cells spend at increased temperature: after the initial burst plate opening of the cell housing the vent-gas was released from the cell into the reactor with an uniform rate. There was no sudden gas liberation and no violent chemical reaction. CO_2 was the major identified component of the vent-gas. Interestingly, the mass loss of the discharged cells of 4.4 g equalled to the mass of electrolyte in the cells (Table 1).

In Experiment 1 we used N_2 as internal standard. The GC detected $n_{sum}^{GC} = 23.2$ mmol of produced gas (Table 3). In

Table 2 Results of thermal ramp experiments with NCA and LFP cells. Here SOC is the state of charge, θ_o is the onset temperature, θ_m is the maximum cell temperature during the experiment, Δm is the mass loss of the cell, n_{sum}^{ideal} is the measured amount of produced vent-gas (11) and the chemical components are those species that were detected by the GC system. Missing values could not be measured or detected. The ratios of the detected gases are given in mol%

No.	Cell	SOC (%)	θ_R (°C)	θ_m (°C)	Δm (g)	n_{sum}^{ideal} (mmol)	H_2 (%)	CO_2 (%)	CO (%)	CH_4 (%)	C_2H_4 (%)	C_2H_6 (%)
1	NCA	0	—	302	—	65	1.7	94.6	1.6	1.6	0.3	—
2	NCA	0	160	316	4.4	52	1.8	94.7	1.9	1.2	0.4	—
3	NCA	0	160	315	4.5	55	1.2	96	1.5	1.1	0.2	—
4	NCA	0	161	214	4.4	39	0.9	96.2	1.1	1.4	0.3	—
5	NCA	0	150	243	4.4	59	0.8	96.6	1	1.3	0.3	—
6	NCA	25	150	739	5.9	67	15.5	62.7	5.5	8.7	7.5	—
7	NCA	50	140	970	8.5	157	17.5	33.8	39.9	5.2	3.2	0.4
8	NCA	75	140	955	—	217	24.2	20.8	43.7	7.5	3.3	0.5
9	NCA	100	144	904	—	273	22.6	19.7	48.9	6.6	2.4	—
10	NCA	100	138	896	20.5	314	26.1	17.5	44	8.9	2.7	0.9
11	NCA	100	136	933	20.9	244	28.5	22.7	41.5	5.9	1.3	0.3
12	NCA	112	144	—	19.2	252	25.1	18.8	48.1	5.9	2.1	—
13	NCA	120	80	929	—	281	23.5	20.8	48.7	5.4	1.6	—
14	NCA	127	80	983	—	317	28.8	16.2	46.6	6.4	1.3	0.3
15	NCA	132	80	943	17	262	25.8	18.9	49.2	4.7	1.4	—
16	NCA	143	65	1075	20.1	303	26.2	22	43.4	6.9	1.5	—
17	LFP	0	—	251	6.1	55	2.7	93.5	1.8	0.7	0.7	0.7
18	LFP	25	195	231	6.1	31	7.1	85.3	3.1	1.2	3.1	0.2
19	LFP	50	130	283	6.1	32	20.8	66.2	4.8	1.6	6.6	—
20	LFP	75	149	362	6.3	41	21.8	62.6	6.4	1.9	6.3	1
21	LFP	100	140	440	7.1	32	29.4	48.3	9.1	5.4	7.2	0.5
22	LFP	115	155	395	6.2	61	34	52.2	6.4	2.6	4.7	0.1
23	LFP	130	80	448	—	58	30.1	55.8	7.7	6.4	—	—

Table 3 Thermal runaway parameters of experiments with NCA cells. Experiments with N_2 as internal standard were selected and the amounts of measured gases are given in absolute units (12). The amount of vent-gas n_{sum}^{ideal} and n_{sum}^{GC} was calculated with ideal gas eqn (11) and with results of the GC (13) respectively

No.	SOC (%)	n_{sum}^{ideal} (mmol)	n_{sum}^{GC} (mmol)	H_2 (mmol)	CO_2 (mmol)	CO (mmol)	CH_4 (mmol)	C_2H_4 (mmol)
1	0	65.4	23.2	0.4	21.9	0.4	0.4	0.1
13	120	281.3	279.1	65.5	57.9	136	15.1	4.6
14	127	317	317.1	91.6	51.6	148.6	20.2	4.1

contrast, the amount of ventgas inside the reactor (11) was much higher $n_{sum}^{ideal} = 65.4$ mmol. We conclude that the GC could not identify the missing 42.2 mmol of gas, because its setup was optimized for a limited set of permanent gases.

The cells with SOC $\geq$ 25% displayed an unmistakable thermal runaway behaviour. When (partially) charged NCA cells were heated beyond a critical temperature, self accelerating exothermic reactions started and the cell temperatures suddenly increased up to maximum values in the range of 739 °C and 1075 °C.

The onsets of the exothermic reactions were obtained from the rate plot: the temperature, where a first clear deviation towards increased temperature rate was detected, was defined as the onset temperature θ_o. For NCA cells with SOC $\leq$ 100% θ_o was in the range between 136 °C and 160 °C. Overcharged NCA cells (SOC > 100%) showed much lower onset temperatures between 65 °C and 80 °C. It is an important finding, that overcharged NCA cells can proceed straight into thermal runaway when heated above 65 °C.

The thermal runaway reactions were accompanied by abrupt vent-gas releases. Cells with higher SOC produced more vent-gas. Up to 317 mmol of gas were recorded. The gas composition depended on the SOC as well: the fractions of CO_2 decreased and the fractions of CO and H_2 increased with rising SOC. A clear trend for other detected gases (CH_4, C_2H_4 and C_2H_6) was not observed.

We used N_2 as inert gas in the Experiments 13 and 14 (overcharged NCA) in the same way as in Experiment 1. The calculated amounts of gas n_{sum}^{ideal} and n_{sum}^{GC} were in good agreement, indicating that all produced gases were detected by the GC. In other words, it is likely that the quantitative GC results (Table 3) represent the major vent-gas components for over-charged cells and that only smaller amounts of gas may be missing.

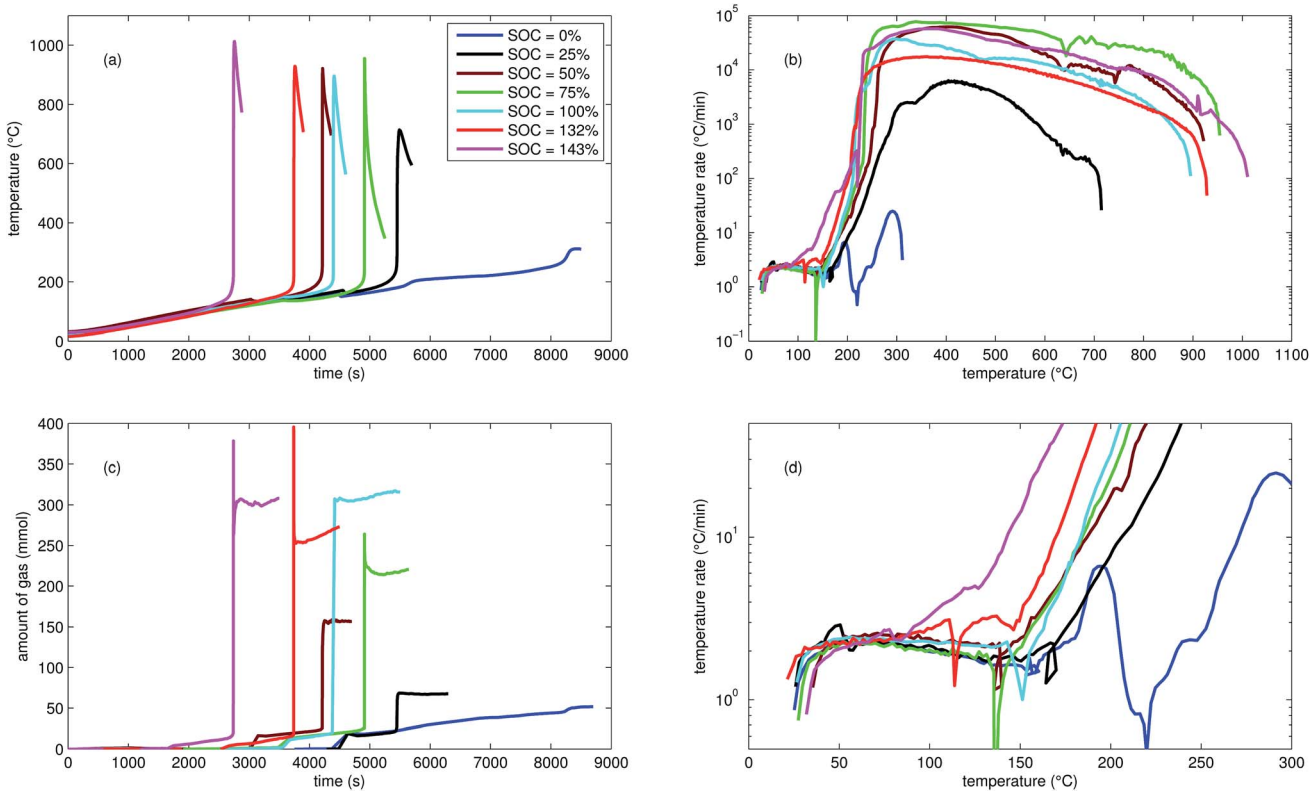

Fig. 2 Typical thermal ramp experiments with NCA cells. (a) Cell temperature profiles. (c) Amount of produced vent-gas. The overshoot peaks are artefacts of the calculation (11) caused by inhomogeneous gas temperature. (b) Cell temperature rate $d\theta/dt$ *vs.* cell temperature θ, full temperature range. (d) Close up view of the cell temperature rate.

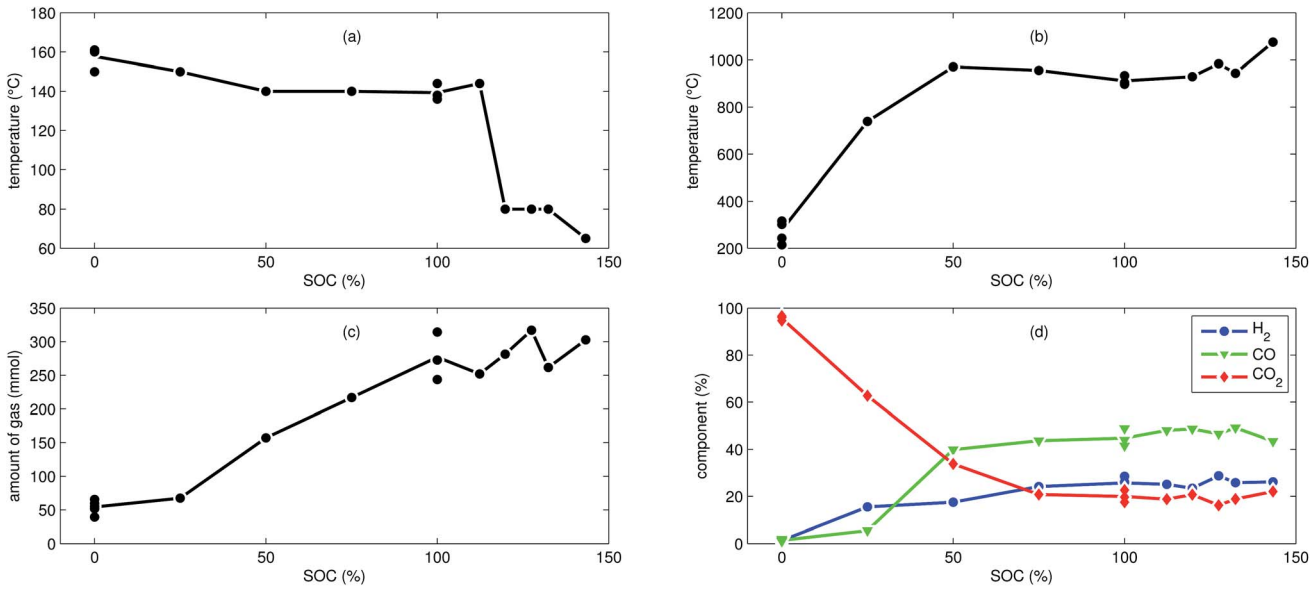

Fig. 3 Characteristic thermal runaway parameters from all NCA experiments. (a) Onset cell temperature θ_o. (b) Maximum cell temperature θ_m. (c) Amount of produced gas n_{sum}^{ideal}. (d) Main detected gas components r_i^{GC}.

4.2 LFP cells

In addition to the experiments with NCA cells, we did 7 thermal-ramp experiments with LFP cells at different SOC (Table 2).

The discharged LFP cell (Experiment 17) showed a behaviour similar to discharged NCA cells. Exothermic reactions could not be detected. After the initial burst plate opening of the cell housing, the amount of gas increased evenly over time as the cell

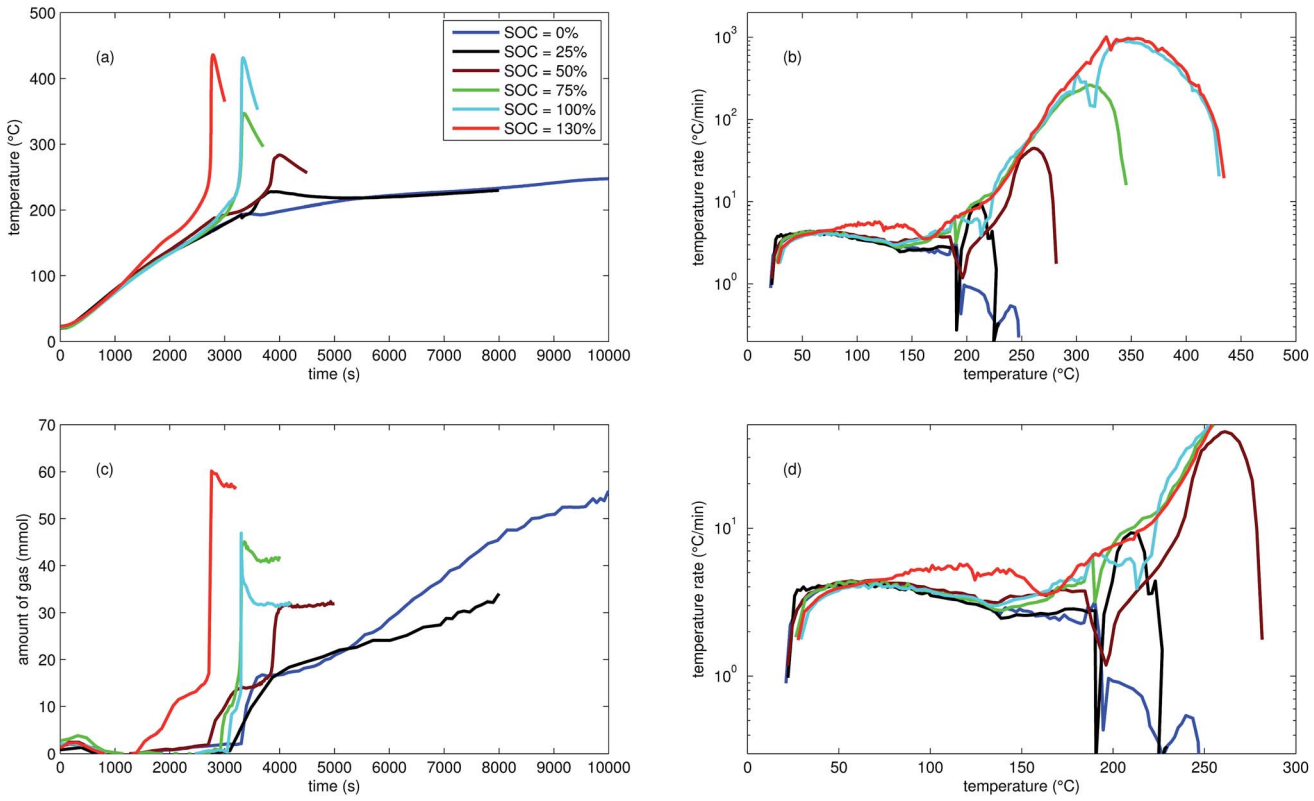

Fig. 4 Typical experiments with LFP cells: (a) cell temperature profiles. (c) Amount of produced vent-gas. (b) Cell temperature rate $d\theta/dt$ *vs.* cell temperature θ, full temperature range. (d) Close up view of the cell temperature rate.

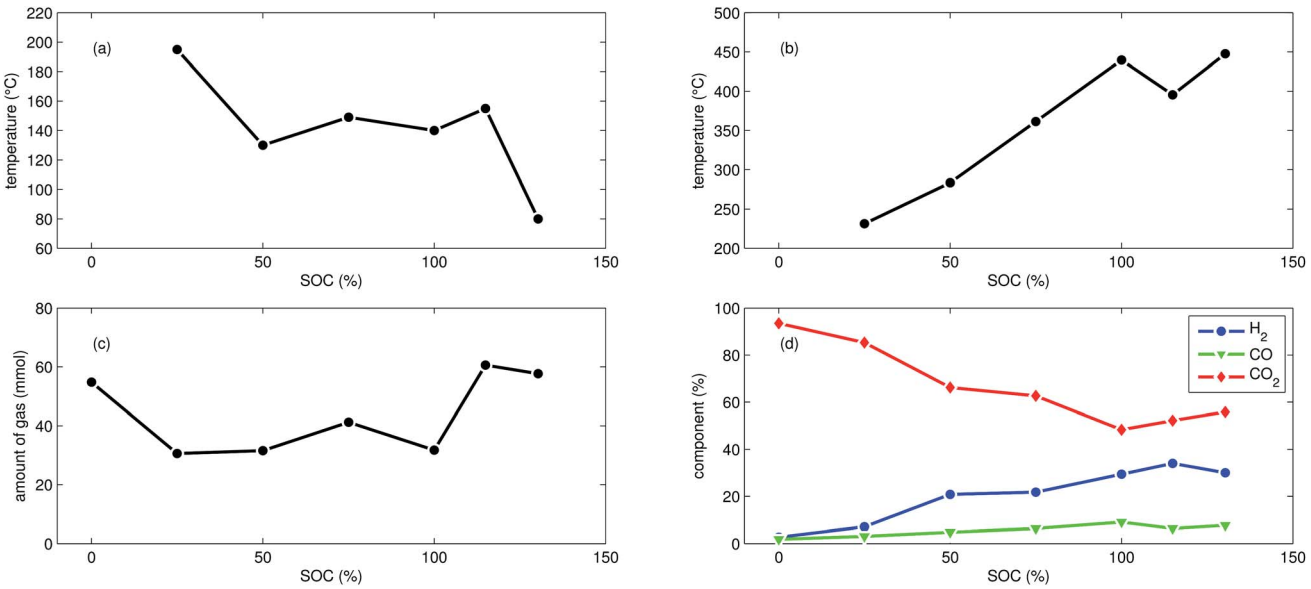

Fig. 5 Summary of all experiments with LFP cells at different SOC: (a) onset cell temperature θ_o. (b) Maximum cell temperature θ_m. (c) Amount of produced gas n_{sum}^{ideal}. (d) Main detected gas components r_i^{GC}.

was heated. For the discharged cell, the GC registered essentially only CO_2. We suspect that the GC could not detect all gas components that were produced by the discharged cell: similar to Experiment 1 with a discharged NCA cell, significant amounts of gas may be missing in the GC results, simply because the used GC equipment was not capable of detecting them.

First mild exothermic reactions were seen for a cell that was charged to 25% SOC. The reactions were not strong enough to evolve into a distinct thermal runaway. Vent gas was produced continuously with time, likewise to the experiments with discharged cells.

LFP cells charged to SOC $\geq$ 50% showed pronounced thermal runaway reactions. Increasing SOC caused increasing maximum temperatures during thermal runaway. The maximum temperatures θ_m ranged from 283 °C to 448 °C.

The onset temperature θ_o was ~140 °C for cells between 50% SOC and 100% SOC. The cell overcharged to 130% SOC showed a exothermic reaction already at 80 °C. In contrast to overcharged NCA cells, the initial exothermic reaction of the overcharged LFP cell could not sustain a full thermal runaway. The overcharged LFP cell proceeded into thermal runaway only after it was heated by the heating sleeve beyond 140 °C.

The amount of gas n_{sum}^{ideal} ranged between 31 mmol and 61 mmol and showed no clear dependence on the SOC. With increasing SOC the relative composition of the detected gases changed to lower CO_2 and higher H_2 fractions. The fractions of CO (max. 9.1%) were lower than for NCA cells.

The mass loss of the LFP cells ranged from 6.1 g to 7.1 g and is comparable to the amount of electrolyte (6.5 g) in this cells.

5 Discussion

It is tempting to pinpoint the main contributors of heat and gas release during the thermal runaway reactions. Can the amount of produced gas and its components be explained with a set of chemical equations?

Material n_j^a that is available for the reaction system is listed in Table 1. In addition lithium $n_{O_2}^a$ and oxygen n_{Li}^a may be released in heated cells. Part of the material is consumed (by becoming a reactant n_j^r of the reaction system).

$$0 \leq n_j^r \leq n_j^a \tag{14}$$

The reaction products may consist of gases, fluids and solids. A measurable subset of the resulting gaseous products n_i^{GC} and the sum of ventgas n_{sum}^{ideal} is given in Table 3. The challenge is to find the right set A of equations and to find the utilisation number b for each equation (how often is each equation applied) so that the calculated amounts of products n_i^p match the measured values:

$$\text{minimize } (n_i^{GC} - n_i^p) > 0 \tag{15}$$

and

$$\text{minimize}\left(n_{sum}^{ideal} - \sum_{i=\text{gaseous}} n_i^p\right) > 0 \tag{16}$$

In other words, the difference of calculated and measured amounts of products is defined as the cost function and the system is restricted by the amounts of reactants and products. The algorithm should minimise the cost function and respect the restrictions.

The mathematical problem was solved using the LIPSOL linear programming toolbox in Matlab. The set of chemical equations and two explicit calculations (discharged NCA cell, Experiment 1 and over-charged NCA cell, Experiment 13) are disclosed in the next subsections:

5.1 Oxygen release from cathode material

At elevated temperatures cathode materials of Li-ion batteries can release oxygen. It is believed, that the exothermic reaction of oxygen with electrolyte is the main contributor to the extent of the thermal runway effect.[4] The amount of released oxygen depends on the lithiation state of the cathode.

In ref. 59–62 it is shown, that delithiated $Li_x(Ni_{0.80}Co_{0.15}Al_{0.05})O_2$ cathode material undergoes complex phase transitions accompanied by formation of O_2 in the temperature range from 175 °C to 600 °C. In a simplified scheme, heated NCA transits from layered to rock salt structure with O_2 release, depending on the lithiation state:

$$Li_x(Ni_{0.80}Co_{0.15}Al_{0.05})O_2 \rightarrow Li_x(Ni_{0.80}Co_{0.15}Al_{0.05})O_{1+x} + \frac{1}{2}(1-x)O_2 \quad (17)$$

The lithiation state x can be calculated using

$$x = 1 - \frac{n_{Li}^{irr} + n_{Li}^{res} + 1/F\ SOC\ C^{nom}}{n_{NCA}^{a}} \quad (18)$$

The amount of liberated O_2 is

$$n_{O_2}^{a} = \frac{1-x}{2} n_{NCA}^{a}. \quad (19)$$

This calculation gives $n_{O_2}^{a}(SOC = 100\%) = 69.2$ mmol for a fully charged NCA cell and $n_{O_2}^{a}(SOC = 0\%) = 6.7$ mmol for a fully discharged NCA cell.

LFP cathodes have better thermal stability than layered metal oxide cathodes such as $Li_x(Ni_{0.80}Co_{0.15}Al_{0.05})O_2$, because of the strong covalent bonds of the phosphate groups of Li_xFePO_4.[63] Nevertheless a phase transition with O_2 release of heated $FePO_4$ can be detected by XRD experiments.[64,65] If assumed that the partly lithiated LFP cathode in a Li-ion battery consists of a mix of lithiated ($LiFePO_4$) and delithiated ($FePO_4$) particles[66] then the oxygen release of a partially charged cathode is given by:

$$(1-x)LiFePO_4 + xFePO_4 \rightarrow (1-x)LiFePO_4 + x\frac{1}{2}Fe_2P_2O_7 + \frac{1}{4}O_2 \quad (20)$$

The absolute amount of O_2 from the LFP cell can be calculated with equations similar to (18) and (19).

Both cathodes materials NCA and LFP can contribute O_2 (Fig. 6) which in turn can take part in further exothermic degradation reactions. The amount of O_2 is higher for delithiated cathodes (battery is charged). Note, that because of the irreversible capacity loss during formation of actual cells, the cathode can not be fully lithiated by discharge of the cell: even at 0% SOC (battery is discharged) the lithiation factor $x < 1$ and a small amount of O_2 may be released.

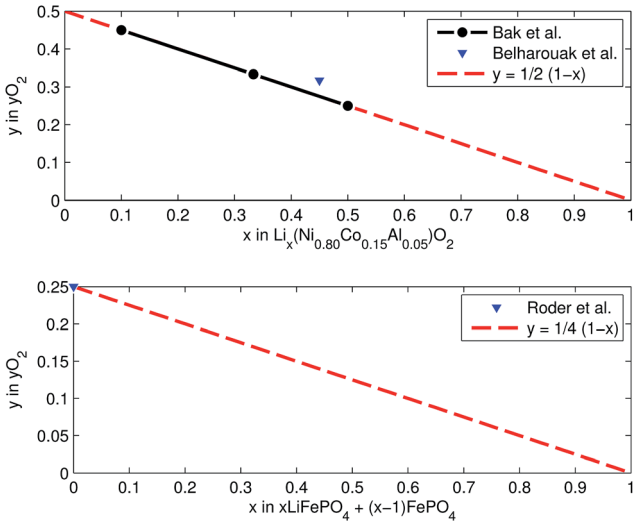

Fig. 6 Oxygen release at different lithiation states: (a) NCA powder upon heating up to 600 °C (from ref. 59 and 61) and (b) LFP powder in electrolyte upon heating to 350 °C (from ref. 64).

5.2 Exposure of lithium by the anode

On the anode side graphite particles can defoliate and expose intercalated Li at temperatures above 230 °C.[67,68] The amount of released Li depends on SOC of the battery:

$$n_{Li}^{a} = 1/F\ SOC\ C^{nom} + n_{Li}^{res} \quad (21)$$

The NCA cell can release $n_{Li}^{a}(SOC = 100\%) = 126.2$ mmol in the fully charged state and $n_{Li}^{a}(SOC = 0\%) = 1.24$ mmol in discharged state.

5.3 Typical chemical reactions

In this section we compile a list of probable degradation reactions which may take place during thermal runaway. The most significant chemical reactions may be reactions with O_2 and Li: partially delithiated cathodes release O_2 and partially lithiated anodes release Li at elevated temperatures (17), (20) and (21). Both released materials are highly reactive and promote a number of reactions that are summarized in a previous publication.[36] Additionally, following reactions are considered:

Combustion of the carbon black (conducting additive) or anode graphite

$$C + \frac{1}{2}O_2 \rightarrow CO \quad (22)$$

the water–gas shift reaction

$$CO + H_2O \rightarrow CO_2 + H_2 \quad (23)$$

oxidation of exposed Li with water

$$2Li + H_2O \rightarrow H_2 + Li_2O \quad (24)$$

endothermic decomposition of liquid lithium carbonate (at high temperatures, $\theta_{melt} = 720$ °C) with carbon black[69]

$$Li_2CO_3 + C \rightarrow Li_2O_2 + 2CO \quad (25)$$

hydrolysis of the hexafluorophosphate salt[70,71]

$$LiPF_6 + H_2O \rightarrow 2HF + LiF + POF_3 \quad (26)$$

$$POF_3 + 2H_2O \rightarrow POF(OH)_2 + 2HF \quad (27)$$

5.4 Alternative CO_2 producing reactions

CO_2 was the main gaseous product that was identified in the ventgas of discharged cells. Little O_2 is available in cells at 0% SOC and it is questionable if combustion alone can account for all CO_2. Therefore effort was made to find further alternative reactions with CO_2 evolution without oxygen involvement. Following reactions were found in the literature:

Ring-opening and polymerisation of EC and PC[72–74] *e.g.*:

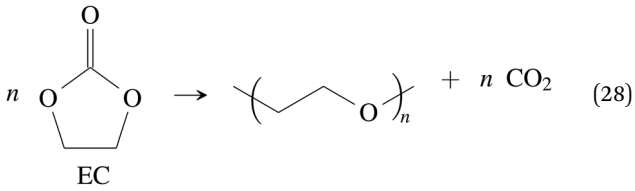

(28)

thermal decomposition of the carbonate esters[50,75,76] *e.g.*:

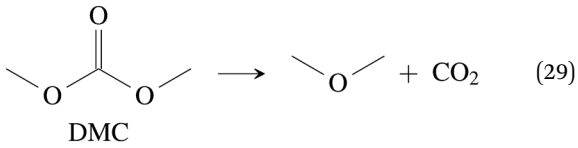

(29)

or

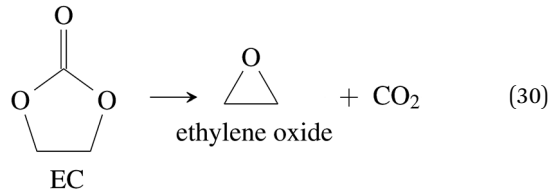

(30)

Gnanaraj *et al.* notes[75] that the electrolyte salt decomposes

$$LiPF_6 \leftrightarrow LiF + PF_5 \quad (31)$$

and the resulting strong Lewis base PF_5 lowers the onset-temperatures of solvent decomposition reactions by acid–base catalysis. The onset temperature for DEC and DMC decomposition lies at 170 °C (ref. 75) and 190 °C (ref. 77) respectively. This values are well below the maximal temperatures reached in our thermal-ramp experiments. Electrolyte decomposition with CO_2 release was also observed in other research.[5,78]

The maximum amount of CO_2 generated from purely thermal decomposition of the electrolyte solvents (28)–(30) is only limited by the amount of available electrolyte.

Further CO_2 may be produced from the SEI degradation: The organic SEI produced by EC reduction (2) can decompose in thermally driven reactions,[79]

$$(CH_2OCO_2Li)_2 \rightarrow Li_2CO_3 + C_2H_4 + CO_2 + \frac{1}{2}O_2 \quad (32)$$

or react with HF analogous to[80]

$$C_2H_5OCO_2Li + HF \rightarrow C_2H_5OH + LiF + CO_2 \quad (33)$$

with the proposed scheme

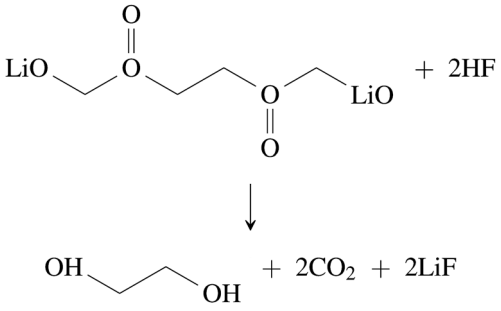

(34)

Inorganic SEI can react with HF as well.[48,53]

$$Li_2CO_3 + 2HF \rightarrow 2LiF + CO_2 + H_2O \quad (35)$$

In the presence of impurities such as trace water $LiPF_6$ may react to POF_3 that in turn reacts with the electrolyte in a decarboxylation reaction with CO_2 release:[50,77,81–83]

$$\begin{aligned} &LiPF_6 \rightarrow LiF + PF_5 \\ &PF_5 + ROH \rightarrow HF + RF + POF_3 \\ &POF_3 + \text{solvent} \rightarrow CO_2 + \text{phosphate} \end{aligned} \quad (36)$$

What is the most significant CO_2 production mechanisms in oxygen depleted environment? In the case of the NCA cell (Table 1) decomposition of all electrolyte solvent (28)–(30) may translate to 35.0 mmol CO_2. The amount of SEI is lower than the amount of electrolyte solvents and therefore only 8.7 mmol of CO_2 can be produced with eqn (34) and (35). The reactions involving HF (33)–(36) may be further suppressed by the limited amount of trace ROH and $LiPF_6$.

5.5 Gas release of a discharged NCA cell

In the Experiment 1 a discharged NCA cell was subject to a thermal-ramp test and absolute amounts of produced gas

Table 4 Model reaction system for the Experiment 1 (discharged NCA cell)

Reaction l	Utilization b_l (mmol)
$DMC_{liq} \rightarrow DMC_{gas}$	11.6
$EC_{liq} \rightarrow EC_{gas}$	8.5
$MPC_{liq} \rightarrow MPC_{gas}$	0.6
$(CH_2OCO_2Li)_2 \rightarrow Li_2CO_3 + C_2H_4 + CO_2 + 0.5O_2$	0.1
$CMC + 3.175O_2 \rightarrow 7.4CO + 5.35H_2O$	1
$PVDF + Li \rightarrow (CH{=}CF) + 0.5H_2 + LiF$	0.9
$0.5O_2 + H_2 \rightarrow H_2O$	7
$CO + H_2O \rightarrow CO_2 + H_2$	7.2
$DMC \rightarrow CO_2 + CH_3OCH_3$	12.5
$EMC \rightarrow CO_2 + CH_3OC_2H_5$	2.2
$DMC + 2Li + H_2 \rightarrow Li_2CO_3 + 2CH_4$	0.2

Table 5 Initially available material in the cell as well as material that is consumed as a reactant according to the proposed reaction system in Table 4 for the Experiment 1 (discharged NCA cell)

Compound j	Availibility n_j^a (mmol)	Consumption n_j^r (mmol)
PE	25	0
O_2	6.7	6.7
C	946.4	0
CMC	2.9	1
PVDF	7	0.9
DMC_{liq}	24.3	24.3
EMC_{liq}	2.2	2.2
EC_{liq}	8.5	8.5
MPC_{liq}	0.6	0.6
$LiPF_6$	3.1	0
$(CH_2OCO_2Li)_2$	3.5	0.1
$C_6H_4O_6$	1	0
Li	1.3	1.3
Li_2CO_3	1.7	0
LiF	1.7	0

components were measured (Table 3). Gas analysis with GC gave 23.2 mmol of CO_2 and small amounts of H_2, CO and hydrocarbons. The overall amount of produced gas n_{sum}^{ideal} inside the heated reactor was 65.4 mmol. This means that the GC system was unable to detect 42.2 mmol of unknown gas components.

What is the source of CO_2 and what is the nature of the not identified gas components? The cathode material of a discharged cell is not fully lithiated and may release a small amount of O_2 (19). The released O_2 can participate in a combustion reaction, but the amount of released O_2 is not sufficient to produce all measured CO_2 ($n_{O_2}^a = 6.7$ mmol *vs.* $n_{CO_2}^{GC} = 21.9$ mmol). We needed to consider alternative reactions in order to account for the measured amounts of gases.

Table 6 Produced material in the Experiment 1 (discharged NCA cell): calculated values of the model reaction system according to Table 4, values quantified by the GC system and the overall measured amount of produced gas inside the reactor

Compound i	Calculated n_i^p (mmol)	From GC n_i^{GC} (mmol)	n_{sum}^{ideal} (mmol)
O_2	0	0.1	—
–[*CH*=*CF*]–	0.9	—	—
Li_2CO_3	0.3	—	—
DMC_{gas}	11.6	—	—
EC_{gas}	8.5	—	—
MPC_{gas}	0.6	—	—
CH_3OCH_3	12.5	—	—
$CH_3OC_2H_5$	2.2	—	—
H_2O	5.3	—	—
CO	0.4	0.4	—
CO_2	21.9	21.9	—
H_2	0.4	0.4	—
CH_4	0.4	0.4	—
C_2H_2	0.1	0.1	—
Sum of gaseous products	63.9	23.2	65.4

Table 4 was calculated with the linear optimisation algorithm. It gives one possible set of reactions to reproduce the measured value of CO_2 and the overall amount of produced gas in the reactor. Because of the elevated temperature all liquid solvents present inside the Li-ion cell either decompose or evaporate (Table 5). The calculation gives rise to new gaseous components and the amount of those components can be compared to the actual measurements (Table 6).

In this mathematical solution, the missing 42.2 mmol of gas consist mainly of solvent decomposition products (CH_3OCH_3, $CH_3OC_2H_5$) and remaining solvents as well as water in gaseous state. Such gases can not be found by the GC system due to following reasons: (a) the sampler of the GC runs at room temperature and therefore the solvents condense and are not

Table 7 Model reaction system for the Experiment 13 (over-charged NCA cell)

Reaction l	Utilization b_l (mmol)
$DMC + 1.5O_2 \rightarrow 3CO + 3H_2O$	10.4
$DMC \rightarrow C_2H_4 + CO_2 + H_2O$	1.1
$EC + O_2 \rightarrow 3CO + 2H_2O$	8.5
$MPC_{liq} + 4.5O_2 \rightarrow 8CO + 4H_2O$	0.6
$C + 0.5O_2 \rightarrow CO$	60.9
$CO + 0.5O_2 \rightarrow CO_2$	12.3
$(CH_2OCO_2Li)_2 + 2Li \rightarrow 2Li_2CO_3 + C_2H_4$	3.5
$C_6H_4O_6 + 2O_2 \rightarrow 6CO + 2H_2O$	1
$CMC + 3.175O_2 \rightarrow 7.4CO + 5.35H_2O$	2.9
$PVDF + O_2 \rightarrow 2CO + 2HF$	7
$CO + H_2O \rightarrow CO_2 + H_2$	15.5
$2Li + H_2O \rightarrow H_2 + Li_2O$	57.5
$DMC \rightarrow CO_2 + CH_3OCH_3$	5.3
$EMC \rightarrow CO_2 + CH_3OC_2H_5$	2.2
$DMC + 2Li + H_2 \rightarrow Li_2CO_3 + 2CH_4$	7.5
$Li_2CO_3 \rightarrow Li_2O + CO_2$	3.1
$Li_2CO_3 + 2HF \rightarrow 2LiF + CO_2 + H_2O$	13.1
$LiPF_6 + H_2O \rightarrow 2HF + LiF + POF_3$	3.1
$POF_3 + 2H_2O \rightarrow POF(OH)_2 + 2HF$	3.1

Table 8 Initially available material in the cell as well as material that is consumed as a reactant according to the proposed reaction system in Table 7 for the Experiment 13 (over-charged NCA cell)

Compound j	Availibility n_j^a (mmol)	Consumption n_j^r (mmol)
PE	25	0
O_2	81.6	81.6
C	946.4	60.9
CMC	2.9	2.9
PVDF	7	7
DMC_{liq}	24.3	24.3
EMC_{liq}	2.2	2.2
EC_{liq}	8.5	8.5
MPC_{liq}	0.6	0.6
$LiPF_6$	3.1	3.1
$(CH_2OCO_2Li)_2$	3.5	3.5
$C_6H_4O_6$	1	1
Li	151	137
Li_2CO_3	1.7	1.7
LiF	1.7	0

Table 9 Produced material in the Experiment 13 (over-charged NCA cell): calculated values of the model reaction system according to Table 7, values quantified by the GC system and the overall measured amount of produced gas inside the reactor

Compound i	Calculated n_i^{p} (mmol)	From GC n_i^{GC} (mmol)	$n_{\mathrm{sum}}^{\mathrm{ideal}}$ (mmol)
LiF	29.3	—	—
$POF(OH)_2$	3.1	—	—
Li_2O	60.6	—	—
CH_3OCH_3	5.3	—	—
$CH_3OC_2H_5$	2.2	—	—
CO	136	136	—
CO_2	52.6	57.9	—
H_2	65.5	65.5	—
CH_4	15.1	15.1	—
C_2H_4	4.6	4.6	—
Sum of gaseous products	281.3	279.1	281.3

injected into the GC column and (b) the present GC setup is not designed to identify and quantify any components other than H_2, O_2, N_2, CO, CO_2, CH_4, C_2H_2, C_2H_4 and C_2H_6.

5.6 Gas release of a charged NCA cell

The situation changes when the cells in thermal ramp experiments are charged. High amounts of oxygen and lithium become available and the cells go into distinct thermal runaway. In the Experiment 13 (Table 3) an overcharged NCA cell was tested and the vent-gases were quantified by the GC system using an internal N_2 standard.

The cell in Experiment 13 was overcharged to a capacity of 4.03 A h (120% SOC). The lithiation factor of the cathode was $x_{\mathrm{Li}}^{\mathrm{cat}} = 0.08$ and the calculated oxygen release (17) was $n_{\mathrm{O_2}}^{\mathrm{a}} = 81.6$ mmol. The lithiation factor of the anode was $x_{\mathrm{Li}}^{\mathrm{and}} = 1.00$ and the amount of intercalated Li on the anode side equalled $n_{\mathrm{Li}}^{\mathrm{a}} = 151$ mmol. In other words, the anode was fully lithiated to the maximum theoretical Li capacity. The cell produced 281.3 mmol of ventgas during thermal runaway and high amounts of CO, H_2, CO_2 were detected.

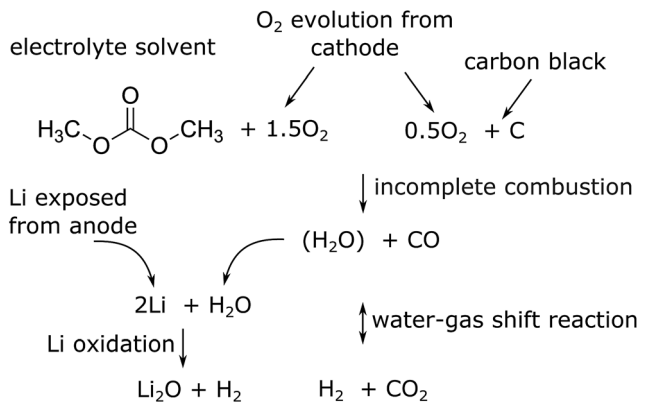

Fig. 7 Proposed main reaction system for a thermal runaway of a (partially) charged or over-charged Li-ion battery.

To find one of the possible solutions explaining the measured gas composition the equations in Table 7 were used. In this exemplary mathematical solution all electrolyte solvents, organic SEI, lithium carbonate and the released O_2 were consumed (Table 8). The major products in the calculation were the gases as measured by the GC as well as the solids LiF and Li_2O. The overall amount of measured gas $n_{\mathrm{sum}}^{\mathrm{ideal}}$ and the amounts of the individual gas components n_i^{GC} could be reproduced by the calculation (Table 9). The quantity of LiF and Li_2O was not measured and therefore not verified by the experiments.

The major reactions which were responsible for the gas and heat production during thermal runaway are summarized in a simplified picture (Fig. 7). In this scheme the released oxygen triggers a chain of exothermic reactions. Because of O_2 insufficiency incomplete combustion of organic material takes place. The resulting H_2O reacts with the exposed Li with H_2 production. Simultaneously H_2 and CO_2 are produced with the water–gas shift reaction. In the end the main gases are CO, CO_2 and H_2.

Although the calculation shows good agreement of measured and computed amounts of gas it has some flaws: (a) the full amount of CO_2 could not be reproduced (b) it is not considered, that the separator material must decompose and add additional gas volume at temperatures >900 °C and (c) in reality the reactants are not distributed homogeneously when the reactions take place, instead material is violently expelled from the cell into the reactor during thermal runaway. Further work is needed to take those effects into account.

6 Conclusions and outlook

We measured the thermal runaway characteristics of commercial Li-ion cells in destructive thermal ramp experiments in inert atmosphere. Our samples were 23 NCA and LFP based Li-ion batteries with the geometrical format 18650 charged to different SOC. The main findings of this work are:

(1) The cell material and cell design (*e.g.* high energy density *vs.* high power density) have a high influence on the maximum cell temperature and on the released gases in thermal runaway conditions (Table 10). Charged NCA cells showed a drastic thermal runaway behaviour. NCA cells could reach maximum temperatures of 1075 °C and they released up to 317 mmol of gas (equal to 7.1 L at standard conditions). Charged LFP cells exhibited a less pronounced thermal runaway: maximum cell temperatures as high as 448 °C were observed and the LFP cells released up to 61 mmol of gas.

(2) Discharged cells showed no thermal runaway upon heating up to ~250 °C. Both cell types needed to be at least partially charged in order to go into thermal runaway.

(3) The severity of the thermal runaway increased with increasing SOC.

(4) The thermal runaway reactions produced high amounts of CO, H_2 and CO_2 thus making the gas flammable and potentially toxic. The gas composition depended on the cell type and SOC. NCA cells produced more CO and H_2 than LFP

Table 10 Comparison of the two tested cell types. Cell specifications and averaged experimental results

		LFP	NCA
Voltage (50% SOC)	V	3.32	3.68
Nominal capacity	A h	1.1	3.35
Cell mass	g	38.87	45.40
Max continuous discharge	A	30	6.7
Cycle life		>1000	>300
Min. SOC for a pronounced thermal runaway	%	50	25
Onset temperature θ_o (100% SOC)	°C	140	139
Max. temperature θ_m (100% SOC)	°C	440	911
Produced gas n_{sum}^{ideal} (100% SOC)	mmol	32	277
Detected CO_2 (100% SOC)	%	48.3	20.0
Detected CO (100% SOC)	%	9.1	44.8
Detected H_2 (100% SOC)	%	29.4	25.7
Impact of overcharge		Weak	Strong

cells. Discharged cells generated mainly CO_2. Increased SOC led to increased amounts of CO and H_2.

(5) The SOC and the cell type had less effect on the onset temperature, as long as no Li plating occurred. Overcharge may cause metallic Li deposition on the anode which compromises the thermal stability. The onset temperature of overcharged cells decreased dramatically from 140 °C to values as low as 65 °C!

(6) In three experiments, the absolute amounts of gases from NCA cells were quantified. It is shown, that it is theoretically possible to explain the absolute amounts of the measured gases with a set of chemical degradation reactions and with known amounts of initial material in the cell.

(7) We think that the main reactions in charged cells are combustion of carbonous material and Li oxidation. Both are strong exothermic reactions which contribute to the energy release during the thermal runaway of a Li-ion battery. The amounts of O_2 and Li available to degradation reactions depend on the SOC as well as on the amount and type of active cathode and anode material. Higher SOC increases the O_2 release of the cathode and the amount of intercalated Li in the anode. In over-charged cells these amounts increase further and deposition of highly reactive metallic Li may occur on the anode.

(8) It is proposed that both, the cathode and anode side participate in the reaction system. Therefore experiments with only one electrode may not cover the full picture.

Many open questions concerning the safety of Li-ion batteries remain. The industry needs scaling rules to evaluate the safety of large battery systems with hundreds of cells based on results of misuse experiments with individual cells. Many test results exist for small 18650 cells but we think that more effort must be made to understand the thermal runaway behaviour of large cells with capacities as high as 60 A h. It is yet to prove, if specific amount of gas and heat are the same for small and large cells. The risks of fire and toxicity (including HF) of vent gas must be quantified for real life applications including misuse of battery packs for electric vehicles, airliners and for home storage of solar energy.

Our future work in the next three years will include (a) additional testing of 18650 cells in an improved test rig, (b) experiments with large automotive Li-ion cells in a new large test rig, (c) bottom up thermodynamic calculations of the chemical reaction systems and (d) top down FEM simulation of failure propagation and the reaction kinetics in large battery packs.

Nomenclature

Δm	Mass loss of the cell, caused by temperature ramp experiment (g)
θ	Cell temperature (°C)
θ_m	Maximum cell temperature during the temperature ramp experiment (°C)
θ_o	Onset temperature of the thermal runaway (°C)
θ_{gas}	Gas temperature inside the reactor (K)
C^{irr}	Charge associated with n_{Li}^{irr} (A h)
C^{nom}	Typical cell capacity as specified in the datasheet (A h)
C^{res}	Charge associated with n_{Li}^{res} (A h)
C_{and}^{u}	Theoretically usable capacity of the anode (A h)
C_{cat}^{u}	Theoretically usable capacity of the cathode (A h)
F	Faraday constant ($F = 96\,485$ A s mol^{-1})
n_i^a	Amount of substance i in a pristine cell, at the start of a thermal ramp experiment (mol)
n_i^p	Theoretically calculated amount of product i, which is produced by chemical reactions during the thermal runaway (mol)
n_j^a	Amount of material j in the cell, that is available for chemical reactions during the thermal runaway (mol)
n_{cat}^a	Amount of either LFP or NCA units in the cathode
n_i^{GC}	Absolute amount of gas component i in the reactor, calculated from GC results (mol)
n_{sum}^{GC}	Amount of gas produced by a cell during a temperature ramp experiment, calculated from GC results (mol)
n_{sum}^{ideal}	Amount of gas produced by a cell during a temperature ramp experiment, calculated with the ideal gas law (mol)
n_{Li}^{irr}	Amount of irreversibly trapped Li in the anode caused by initial cell formation (mol)
n_{Li}^{res}	Amount of residual Li in the anode of a cell which is discharged to V_{min} (mol)
n_j^r	Theoretically calculated amount of reagent j in the cell, which is consumed by chemical reactions during the thermal runaway (mol)
n_0	Initial amount of gas in the reactor at the start of the experiment (mol)
n_{N_2}	Actual amount of N_2 in the reactor (mol)
P	Gas pressure in the reactor (Pa)
R	Gas constant ($R = 8.314$ J mol^{-1} K^{-1})
r_i^{GC}	Result of GC measurement: fraction of gas component i in the GC sample (mol%)
T	Time (s)
V	Volume of the reactor (m^3)
V_{min}	Minimum cell voltage as specified in the datasheet (V)
x	Lithiation factor of the anode or cathode

Acknowledgements

VIRTUAL VEHICLE Research Center is funded within the COMET Competence Centers for Excellent Technologies programme by the Austrian Federal Ministry for Transport, Innovation and Technology (BMVIT), the Federal Ministry of Science, Research and Economy (BMWFW), the Austrian Research Promotion Agency (FFG), the province of Styria and the Styrian Business Promotion Agency (SFG). The COMET programme is administrated by FFG. We would furthermore like to express our thanks to our supporting scientific project partners, namely "Varta Micro Innovation GmbH" and to the Graz University of Technology. The work was made possible by the principal industrial project partners "BASF SE" and by "MAGNA STEYR Battery Systems GmbH & Co OG".

References

1 K. Xu, *Chem. Rev.*, 2004, **104**, 4303–4417.
2 Z. J. Zhang and P. Ramadass, in *Encycl. Sustain. Sci. Technol.*, Springer New York, New York, NY, 2012, pp. 319–356.
3 J. Wen, Y. Yu and C. Chen, *Mater. Express*, 2012, **2**, 197–212.
4 D. Doughty and E. P. Roth, *Electrochem. Soc. Interface*, 2012, **21**, 37–44.
5 E. P. Roth and C. J. Orendorff, *Electrochem. Soc. Interface*, 2012, **21**, 45–49.
6 D. Abraham, E. P. Roth, R. Kostecki, K. McCarthy, S. MacLaren and D. Doughty, *J. Power Sources*, 2006, **161**, 648–657.
7 Z. Chen, Y. Qin, Y. Ren, W. Lu, C. Orendorff, E. P. Roth and K. Amine, *Energy Environ. Sci.*, 2011, **4**, 4023.
8 G. Nagasubramanian and C. J. Orendorff, *J. Power Sources*, 2011, **196**, 8604–8609.
9 H. Maleki, G. Deng, A. Anani and J. Howard, *J. Electrochem. Soc.*, 1999, **146**, 3224.
10 P. Ping, Q. Wang, P. Huang, J. Sun and C. Chen, *Appl. Energy*, 2014, **129**, 261–273.
11 P. Röder, B. Stiaszny, J. C. Ziegler, N. Baba, P. Lagaly and H.-D. Wiemhöfer, *J. Power Sources*, 2014, **268**, 315–325.
12 M. Fleischhammer, T. Waldmann, G. Bisle, B.-I. Hogg and M. Wohlfahrt-Mehrens, *J. Power Sources*, 2015, **274**, 432–439.
13 D. H. Doughty, E. P. Roth, C. C. Crafts, G. Nagasubramanian, G. Henriksen and K. Amine, *J. Power Sources*, 2005, **146**, 116–120.
14 J. Lamb and C. J. Orendorff, *J. Power Sources*, 2014, **247**, 189–196.
15 G. Trattnig and W. Leitgeb, in *Automot. Batter. Technol.*, Springer, 2014, pp. 19–37.
16 X. Liu, S. I. Stoliarov, M. Denlinger, A. Masias and K. Snyder, *J. Power Sources*, 2015, **280**, 516–525.
17 P. Ping, Q. Wang, P. Huang, K. Li, J. Sun, D. Kong and C. Chen, *J. Power Sources*, 2015, **285**, 80–89.
18 X. Feng, M. Fang, X. He, M. Ouyang, L. Lu, H. Wang and M. Zhang, *J. Power Sources*, 2014, **255**, 294–301.
19 F. Larsson and B.-E. Mellander, *J. Electrochem. Soc.*, 2014, **161**, A1611–A1617.
20 P. Huang, Q. Wang, K. Li, P. Ping and J. Sun, *Sci. Rep.*, 2015, **5**, 7788.
21 H. Wang, A. Tang and K. Wang, *Chin. J. Chem.*, 2011, **29**, 27–32.
22 C.-Y. Wen, C.-Y. Jhu, Y.-W. Wang, C.-C. Chiang and C.-M. Shu, *J. Therm. Anal. Calorim.*, 2012, **109**, 1297–1302.
23 T.-Y. Lu, C.-C. Chiang, S.-H. Wu, K.-C. Chen, S.-J. Lin, C.-Y. Wen and C.-M. Shu, *J. Therm. Anal. Calorim.*, 2013, **114**, 1083–1088.
24 C.-Y. Jhu, Y.-W. Wang, C.-M. Shu, J.-C. Chang and H.-C. Wu, *J. Hazard. Mater.*, 2011, **192**, 99–107.
25 C.-Y. Jhu, Y.-W. Wang, C.-Y. Wen, C.-C. Chiang and C.-M. Shu, *J. Therm. Anal. Calorim.*, 2011, **106**, 159–163.
26 H. Ishikawa, O. Mendoza, Y. Sone and M. Umeda, *J. Power Sources*, 2012, **198**, 236–242.
27 E. P. Roth and D. H. Doughty, *J. Power Sources*, 2004, **128**, 308–318.
28 S.-i. Tobishima and J.-i. Yamaki, *A consideration of lithium cell safety*, 1999.
29 D. Belov and M.-H. Yang, *Solid State Ionics*, 2008, **179**, 1816–1821.
30 Y. Zeng, K. Wu, D. Wang, Z. Wang and L. Chen, *J. Power Sources*, 2006, **160**, 1302–1307.
31 T. Ohsaki, T. Kishi, T. Kuboki, N. Takami, N. Shimura, Y. Sato, M. Sekino and A. Satoh, *J. Power Sources*, 2005, **146**, 97–100.
32 J. Jeevarajan, in *Lithium-Ion Batter. Adv. Appl.*, Elsevier, 2014, pp. 387–407.
33 C. Orendorff, *Electrochem. Soc. Interface*, 2012, **21**, 61–65.
34 R. a. Leising, M. J. Palazzo, E. S. Takeuchi and K. J. Takeuchi, *J. Electrochem. Soc.*, 2001, **148**, A838.
35 Z. Li, J. Huang, B. Yann Liaw, V. Metzler and J. Zhang, *J. Power Sources*, 2014, **254**, 168–182.
36 A. W. Golubkov, D. Fuchs, J. Wagner, H. Wiltsche, C. Stangl, G. Fauler, G. Voitic, A. Thaler and V. Hacker, *RSC Adv.*, 2014, **4**, 3633.
37 J.-H. Lee, U. Paik, V. a. Hackley and Y.-M. Choi, *J. Electrochem. Soc.*, 2005, **152**, A1763.
38 S.-L. Chou, Y. Pan, J.-Z. Wang, H.-K. Liu and S.-X. Dou, *Phys. Chem. Chem. Phys.*, 2014, **16**, 20347–20359.
39 Z. Chen and J. R. Dahn, *Reducing Carbon in $LiFePO_4$/C Composite Electrodes to Maximize Specific Energy, Volumetric Energy, and Tap Density*, 2002.
40 J. Wang and X. Sun, *Energy Environ. Sci.*, 2012, **5**, 5163.
41 H. Ota, Y. Sakata, A. Inoue and S. Yamaguchi, *J. Electrochem. Soc.*, 2004, **151**, A1659.
42 J. C. Burns, R. Petibon, K. J. Nelson, N. N. Sinha, A. Kassam, B. M. Way and J. R. Dahn, *J. Electrochem. Soc.*, 2013, **160**, A1668–A1674.
43 S. Zhang, *J. Power Sources*, 2006, **162**, 1379–1394.
44 E. Peled, D. Golodnitsky, A. Ulus and V. Yufit, *Electrochim. Acta*, 2004, 391–395.
45 K. Ushirogata, K. Sodeyama, Y. Okuno and Y. Tateyama, *J. Am. Chem. Soc.*, 2013, **135**, 11967–11974.
46 L. El Ouatani, R. Dedryvere, C. Siret, P. Biensan, S. Reynaud, P. Iratcabal and D. Gonbeau, *J. Electrochem. Soc.*, 2009, **156**, A103.

47 G. Gachot, S. Grugeon, G. G. Eshetu, D. Mathiron, P. Ribière, M. Armand and S. Laruelle, *Electrochim. Acta*, 2012, **83**, 402–409.
48 M. Onuki, S. Kinoshita, Y. Sakata, M. Yanagidate, Y. Otake, M. Ue and M. Deguchi, *J. Electrochem. Soc.*, 2008, **155**, A794.
49 D. Aurbach, A. Zaban, Y. Ein-Eli, I. Weissman, O. Chusid, B. Markovsky, M. Levi, E. Levi, A. Schechter and E. Granot, *J. Power Sources*, 1997, **68**, 91–98.
50 G. Gachot, P. Ribière, D. Mathiron, S. Grugeon, M. Armand, J. B. Leriche, S. Pilard and S. Laruelle, *Anal. Chem.*, 2011, **83**, 478–485.
51 R. Spotnitz and J. Franklin, *J. Power Sources*, 2003, **113**, 81–100.
52 H. Yoshida, T. Fukunaga, T. Hazama, M. Terasaki, M. Mizutani and M. Yamachi, *J. Power Sources*, 1997, **68**, 311–315.
53 C. Doh, D. Kim, J. Lee, D. Lee, B. Jin, H. Kim, S. Moon, Y. Hwang and A. Veluchamy, *Bull. Korean Chem. Soc.*, 2009, **30**, 783.
54 K. Tasaki and S. J. Harris, *J. Phys. Chem. C*, 2010, **114**, 8076–8083.
55 H. Maleki and J. Howard, *J. Power Sources*, 2006, **160**, 1395–1402.
56 H. He, Y. Liu, Q. Liu, Z. Li, F. Xu, C. Dun, Y. Ren, M.-x. Wang and J. Xie, *J. Electrochem. Soc.*, 2013, **160**, A793–A804.
57 X. Huang, *J. Solid State Electrochem.*, 2010, **15**, 649–662.
58 C. T. Love, *J. Power Sources*, 2011, **196**, 2905–2912.
59 S.-m. Bak, K.-w. Nam, W. Chang, X. Yu, E. Hu, S. Hwang, E. A. Stach, K.-B. Kim, K. Y. Chung and X.-Q. Yang, *Chem. Mater.*, 2013, **25**, 337–351.
60 K.-W. Nam, S.-M. Bak, E. Hu, X. Yu, Y. Zhou, X. Wang, L. Wu, Y. Zhu, K.-Y. Chung and X.-Q. Yang, *Adv. Funct. Mater.*, 2013, **23**, 1047–1063.
61 I. Belharouak, W. Lu, D. Vissers and K. Amine, *Electrochem. Commun.*, 2006, **8**, 329–335.
62 H. J. Bang, H. Joachin, H. Yang, K. Amine and J. Prakash, *J. Electrochem. Soc.*, 2006, **153**, A731.
63 Z. Li, D. Zhang and F. Yang, *J. Mater. Sci.*, 2009, **44**, 2435–2443.
64 P. Röder, N. Baba, K. Friedrich and H.-D. Wiemhöfer, *J. Power Sources*, 2013, **236**, 151–157.
65 J. Kim, K.-Y. Park, I. Park, J.-K. Yoo, J. Hong and K. Kang, *J. Mater. Chem.*, 2012, **22**, 11964.
66 W.-J. Zhang, *J. Power Sources*, 2011, **196**, 2962–2970.
67 O. Haik, S. Ganin, G. Gershinsky, E. Zinigrad, B. Markovsky, D. Aurbach and I. Halalay, *J. Electrochem. Soc.*, 2011, **158**, A913.
68 Y. He, Z. Tang, Q. Song, H. Xie, Q. Xu, Y. Liu and G. Ling, *Thermochim. Acta*, 2008, **480**, 15–21.
69 J.-w. Kim and H.-g. Lee, *Metall. Mater. Trans. B*, 2001, **32**, 17–24.
70 R. Yazami and A. Martinent, in *Fluorinated Mater, Energy Conversion*, Elsevier Science, 1st edn, 2005, ch. Fluorinate, pp. 173–194.
71 L. Terborg, S. Weber, F. Blaske, S. Passerini, M. Winter, U. Karst and S. Nowak, *J. Power Sources*, 2013, **242**, 832–837.
72 L. Vogdanis and W. Heitz, *Makromol. Chem., Rapid Commun.*, 1986, **7**, 543–547.
73 L. Vogdanis, B. Martens, H. Uchtmann, F. Hensel and W. Heitz, *Makromol. Chem., Rapid Commun.*, 1990, **191**, 465–472.
74 S. E. Sloop, J. B. Kerr and K. Kinoshita, *J. Power Sources*, 2003, **119–121**, 330–337.
75 J. S. Gnanaraj, E. Zinigrad, L. Asraf, H. E. Gottlieb, M. Sprecher, M. Schmidt, W. Geissler and D. Aurbach, *J. Electrochem. Soc.*, 2003, **150**, A1533.
76 G. Gachot, S. Grugeon, I. Jimenez-Gordon, G. G. Eshetu, S. Boyanov, A. Lecocq, G. Marlair, S. Pilard and S. Laruelle, *Anal. Methods*, 2014, **6**, 6120.
77 T. Kawamura, A. Kimura, M. Egashira, S. Okada and J.-I. Yamaki, *J. Power Sources*, 2002, **104**, 260–264.
78 G. G. Botte and T. J. Bauer, *J. Power Sources*, 2003, **119–121**, 815–820.
79 M. N. Richard and J. Dahn, *J. Electrochem. Soc.*, 1999, **146**, 2068.
80 W. Kong, H. Li, X. Huang and L. Chen, *J. Power Sources*, 2005, **142**, 285–291.
81 A. Hammami, N. Raymond and M. Armand, *Nature*, 2003, **424**, 635–636.
82 C. L. Campion, W. Li and B. L. Lucht, *J. Electrochem. Soc.*, 2005, **152**, A2327.
83 C. L. Campion, W. Li, W. B. Euler, B. L. Lucht, B. Ravdel, J. F. DiCarlo, R. Gitzendanner and K. M. Abraham, *Electrochem. Solid-State Lett.*, 2004, **7**, A194.

2.3 Thermal Runaway and Battery Fire: Comparison of Li-ion, Ni-MH and Sealed Lead-acid Batteries

The following proceeding was presented at the conference: 7th Transport Research Arena TRA 2018 in April 16-19 2018 held in Vienna, Austria. In the proceeding we describe different battery types which are used in electrified vehicles with a focus on Li-ion technology. We show failure mechanism of the different batteries, again focusing on the Li-ion technology.
In this work Andrey Golubkov wrote the text of the article and analysed the data of TR experiments. René Planteu, Christiane Essl and Bernhard Rasch did the TR experiment with the Li-ion cell. Alexander Thaler and Viktor Hacker supervised the work.

Proceedings of 7th Transport Research Arena TRA 2018, April 16-19, 2018, Vienna, Austria

Thermal runaway and battery fire: comparison of Li-ion, Ni-MH and sealed lead-acid batteries

Andrey W. Golubkov[a]*, Rene Planteu[a], Bernhard Rasch[a], Christiane Essl[a], Alexander Thaler[a], Viktor Hacker[b]

[a] *VIRTUAL VEHICLE Research Center, Inffeldgasse 21a, 8010 Graz, Austria*
[b] *Institute of Chemical Engineering and Environmental Technology - Graz University of Technology, Inffeldgasse 25/C/II, 8010 Graz, Austria*

Abstract

Rechargeable batteries are a key component for sustainable mobility. The last years showed a significant reduction of price and increase in energy density of Li-ion batteries for electric vehicles. Unfortunately, batteries with high energy density can be source of hazard. Recently, burning Li-ion batteries of mobile-phones got a lot of negative attention in the media.
In the first part of the paper we review the hazards of conventional Ni-MH and sealed lead-acid batteries. In the second part we focus on Li-ion batteries: we introduce different cell geometries and electrode types, we show a test-stand designed to measure thermal runaway characteristics in our laboratory and finally we conclude with results of a real thermal runaway experiment.

Keywords: Li-ion batteries; thermal runaway; battery fire; battery safety; electric vehicles

* Corresponding author. Tel.: +43 (316) 873 - 9639
E-mail address: andrej.golubkov@v2c2.at

Nomenclature

AGM	absorbed glass mat battery (lead acid)
DCA	dynamic charge acceptance (of lead acid batteries)
EFB	enhanced flooded battery (lead acid)
ICE	internal combustion engine
LCO	$LiCoO_2$, cathode material for Li-ion batteries
LFP	$LiFePO_4$, cathode material for Li-ion batteries
LMO	$LiMn_2O_4$, cathode material for Li-ion batteries
LTO	$Li_4Ti_5O_{12}$, anode material for Li-ion batteries
NMC	$Li(NiMnCo)O_2$, cathode material for Li-ion batteries

1. Introduction

Electrified vehicles differ from conventional vehicles by utilizing electric energy for traction in addition or instead of an ICE engine. The electrified vehicles are categorized – with increasing battery size – in micro hybrid, 48V (mild hybrid) to full hybrids, plug-in vehicles (PHEV) and battery-electric vehicles (BEV) (Table 1). The later are fully electrified and have no ICE at all. Different type of battery technologies are utilized for different degrees of electrification. Advanced lead-acid batteries are used in micro hybrids, Ni-MH is predominantly used in full-hybrid vehicles from Toyota, and different types of Li-ion batteries are used for all ranges of electrification (Rosenkranz et al. 2016).

In this paper we discuss safety risks of those battery technologies: what can go wrong and what are the consequences. Electric shock hazard and fires risk from faulty electric connectors or electric drivetrain components are equally important but outside of the scope of this paper.

Table 1. Basic battery types for electrified vehicles (Fetcenko et al. 2015)

	Advanced lead-acid	Ni-MH	Li-ion power optimized	Li-ion energy optimized
Applications	micro hybrid	micro hybrid, full hybrid	micro hybrid, full hybrid	PHEV, BEV
Energy density, cell level, Wh/kg	40	50 - 110	50 -100	250
Power density, cell level, W/kg	450 (at -18°C)	1500	up to 4000	400

2. Lead-acid batteries

Prolonged charging at high temperatures can cause a thermal runaway of valve regulated EFB and AGM batteries. The thermal runaway is caused by reactions which accelerate each other: high temperature, water loss from electrolysis, increased exothermal oxygen recombination, further temperature increase, increase of the float current and again temperature increase (Fig. 1). Eventually the plastic casing may soften and battery temperature can reach the boiling temperature of the electrolyte. If the overpressure valve fails, the battery casing will expand under hydrogen-gas pressure and the battery will pose a significant risk of gas deflagration and spill of sulfuric acid electrolyte. To avoid chances of thermal runaway easily observable parameters like temperature, electrical resistance or voltage fluctuation due to arcing should be monitored. If an anomaly is detected, the power should be reduced (Rand et al. 1996).

Advanced lead-Acid batteries for micro hybrid systems incorporate carbon additives (Karden 2017) or carbon grid structure (McKenzie 2017) in the negative plate to improve charge kinetics. Unfortunately this increases the risk of H_2 production: there is a trade-off between improved DCA (through carbon material) and H_2 evolution during charge with high currents at high temperatures. The hydrogen may accumulate inside the battery pack where it may cause explosion hazard. Good venting or gas monitoring is needed.

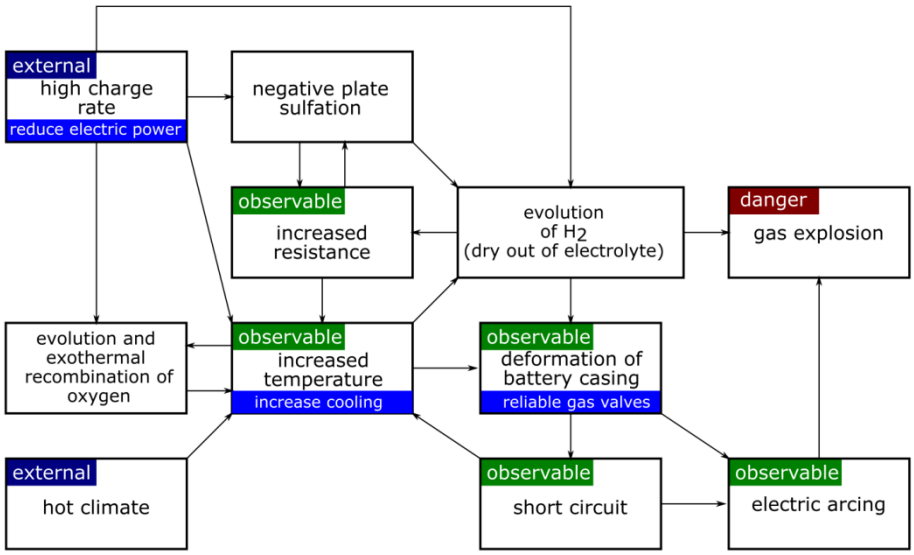

Fig. 1 Thermal runway mechanism and mitigation options of valve regulated lead acid batteries

3. Ni-MH batteries

Nickel metal-hydride (Ni-MH) batteries are being used since 1997 in hybrid cars and there is still little literature on their safety (Fetcenko et al. 2015). This indicates that there seems to be few known safety issues with this type of batteries. Similar to lead acid batteries, Ni-MH batteries can produce O_2 during overcharge and at temperatures > 40°C. An effective countermeasure is incorporation of oversized negative electrodes and LiOH additives which enable O_2 and H_2 recombination during charge and overcharge. Large cells incorporate valves to prevent excessive gas pressure build-up.

4. Li-ion batteries

Most literature on battery safety deals with Li-ion batteries. Safety risks are caused by their high energy density, the high cell voltages and the inflammable electrolyte. In Li-ion batteries a small local failure can grow to a full thermal runaway. This can be pictured like bursting of a dam which starts with a small trickle and then quickly evolves into a full breach. Unlike to the thermal-runaway of a lead acid battery, a thermal runaway of a Li-ion battery can easily cause battery fire. Before we go into detail of failure modes, we need to explain the different types of Li-ion batteries.

4.1. Types of Li-ion batteries

Li-ion battery-cells can have different casings, different sizes and different anode/cathode combinations (Zhang & Ramadass 2012). They can be either optimized for high power-density or high energy-density. Common cell-casings are small cylindrical metal cans, bigger prismatic metal cans and so called pouch cells (Fig. 2). The casings of metal cans are made by deep drawing from stainless steel or aluminium. The casings of pouch cells are made of composite aluminium-plastic foils.

Most common cylindrical cells have a diameter of 18 mm and a length of 65 mm. Their capacity ranges from 1 to 3.5 Ah. They are mostly used for consumer electronics, power tools and electric bikes. Tesla is the only car manufacturer who utilises 18650 cells in mass produced electric cars. Prismatic metal-can cells for automotive applications have capacities ranging from 5 to 120 Ah. The smaller cells are used for hybrid cars and the bigger ones are used in battery packs for pure electric vehicles. Small pouch cells are found in consumer electronics such as notebooks or mobile phones, bigger pouch cells with capacities up to 90 Ah are used in battery packs of electric vehicles. It is not yet clear if pouch cells or metal-can cells will dominate in battery packs of future electric vehicles. Pouch cells have cheaper and lighter casings but prismatic metal-can cells have better mechanical properties and are easier to cool.

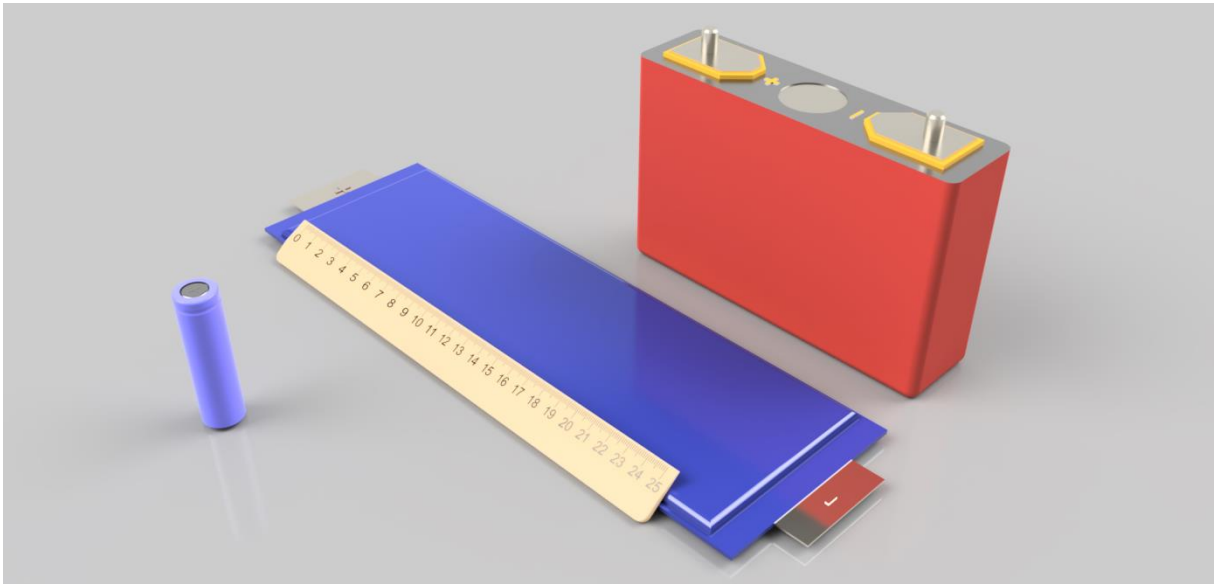

Fig. 2 Different sizes and casings of Li-ion battery-cells. From left to right: cylindrical metal-can, pouch cell, prismatic metal-can

All commercial Li-ion cells have the same basic elements inside their casings: thin metal foils which are thickly coated with electrochemically active cathode or anode material and separator layers are either stacked or rolled and soaked with Li-ion conducting electrolyte. The metallic foils are electrically connected to the outside terminals (Fig. 3).

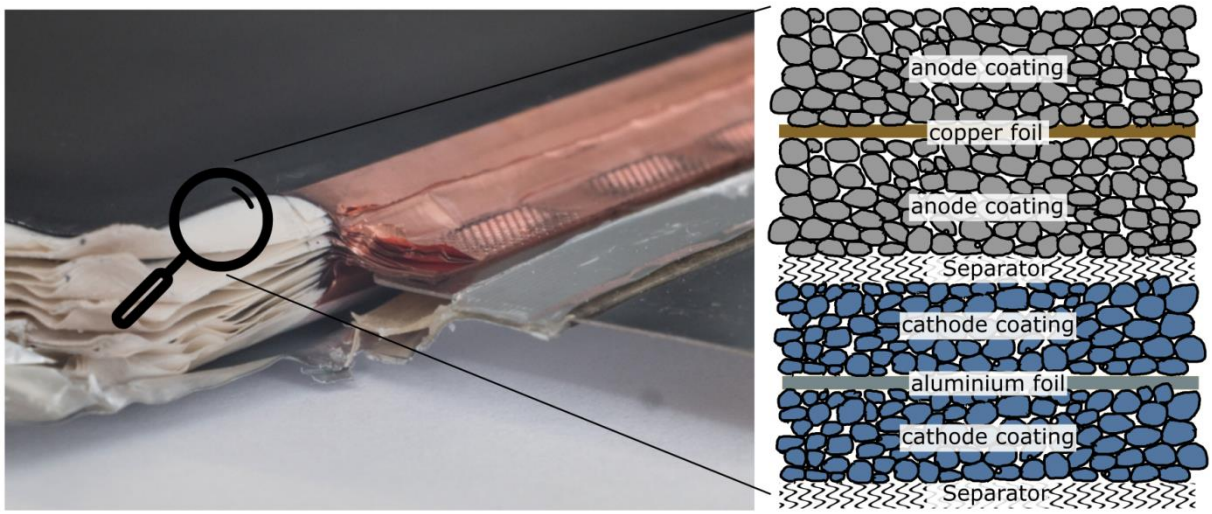

Fig. 3 (left) Photograph of a pouch cell with removed casing and revealed layer structure. Extensions of the copper foils are connected to the negative terminal. (right) Sketch of one repeating unit of the layer structure

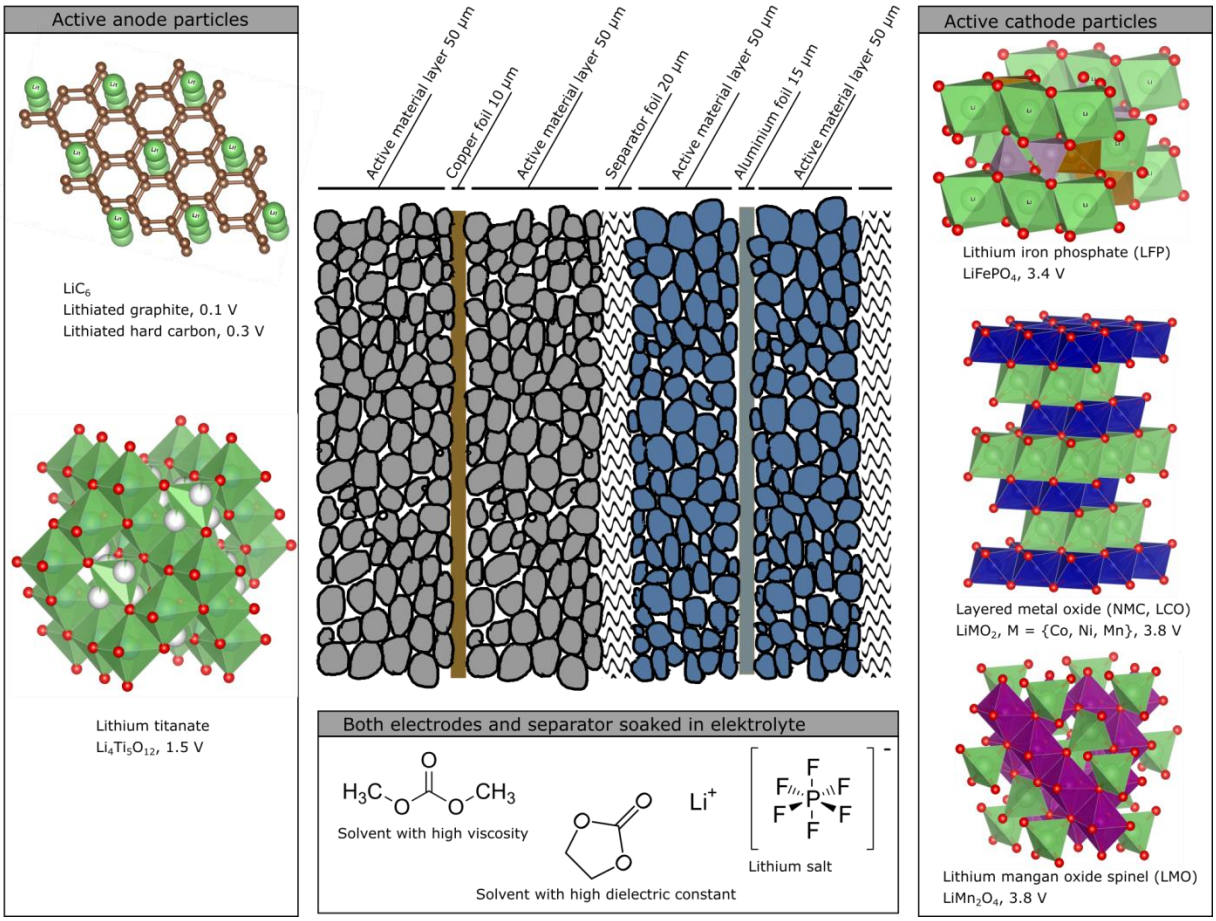

Fig. 4 (left) Typical choices for electrochemically active anode material. (centre) Typical thicknesses of the layers. (Right) Typical choices for electrochemically active cathode material. (Bottom) commercially used electrolyte components. The voltages describe the mean potential of the materials vs Li/Li^+

Typical choices of electrode material are graphite particles for the anode and layered metal oxide particles such as $Li(NiMnCo)O_2$ (NMC) for the cathode. During cell production the particles are mixed with an conducting agent and a binder in a liquid solvent to form a so called slurry. The slurry is then coated on the respective metal foil and the solvent is removed by drying. The anode slurry is coated on copper foil and the cathode slurry is coated on an aluminium foil. The separator foil is placed between the electrodes. The layers are then either rolled or stacked and placed into the cell casing. The next steps are the filling of the electrolyte, the first charging of the cell and the final sealing of the cell casing.

The open circuit voltage (OCV) of the cell is the difference of the electrochemical potential of the two electrodes. In case of graphite (0.1 V vs. Li) and NMC (3.8 vs. Li) the mean OCV is 3.7 V. Such extreme electrochemical potentials require special electrolytes with specialized components. Typical cells use $LiPF_6$ as the lithium salt because it also helps to passivate the aliminium foil of the cathode. Ethylencarbonate (EC) is used as the solvent with high dipole moment to increase Li-salt concentration and also because it builds a Li-ion conducting passivation layer on top of the graphite particles (Xu 2004). Unfortunately, EC has high viscosity and dimethylcarbonate or diethylcarbonate are added to lower viscosity and to improve Li-ion conductivity at low temperatures. The stack structure and some alternative choices for anode and cathode material are shown in figure 4.

The power to energy ratio of Li-ion cells is determined by the type of electrode material, by the electrode porosity and by the thicknesses of the electrode coatings and metal foils (Table 2). Thicker coatings and lower porosity (higher compression during manufacturing) increase the cell capacity. Unfortunately, this also increases the path length for the Li-ions on their way from one electrode particle to the other thus limiting the electric power of the cell. High power cells have thinner coatings and higher porosity to decrease ionic resistance and thicker metal foils to decrease electric resistance. High power cells also may use special anodes like lithiumtitanate (LTO) or hard-carbon to improve fast charging because their electrochemical potential vs. lithium

allows for higher dynamic polarisation and current density before unwanted metallic lithium deposition happens on the anode (Zhao et al. 2015).

Table 2. Optimization options for Li-ion batteries

	power optimized	energy optimized
Anode	LTO, hard carbon	graphite
Cathode	LFP, NMC, LMO	NMC, NCA
electrode porosity	60%	30%
thickness of electrode coatings	thin	thick
thickness of the metal foils	thick	thin

4.2. Initial causes of cell failure

The thermal runaway of a Li-ion cell is a chemical reaction, with a temperature higher than the *temperature of no return*, where the heating rate from the exothermal reaction is higher than the cooling rate by the adjacent components. A battery pack has several potential sources of unwanted initial heating (Larsson & Mellander 2014) which are able to exceed the temperature of no return:

- External sources like fire
- Bad electrical interconnectors with increased electrical resistance combined with high current
- Internal short circuits (foreign particles/objects, lithium dendrites from overcharge, copper dendrites from over-discharge)

The case of overcharge is complicated because several effects may take place simultaneously:

- Joule heating due to increased cell resistance
- Chemical destabilization of the cathode particles due to over-delithiation
- Deposition of reactive metallic lithium on the surface of the fully lithiated anode particles

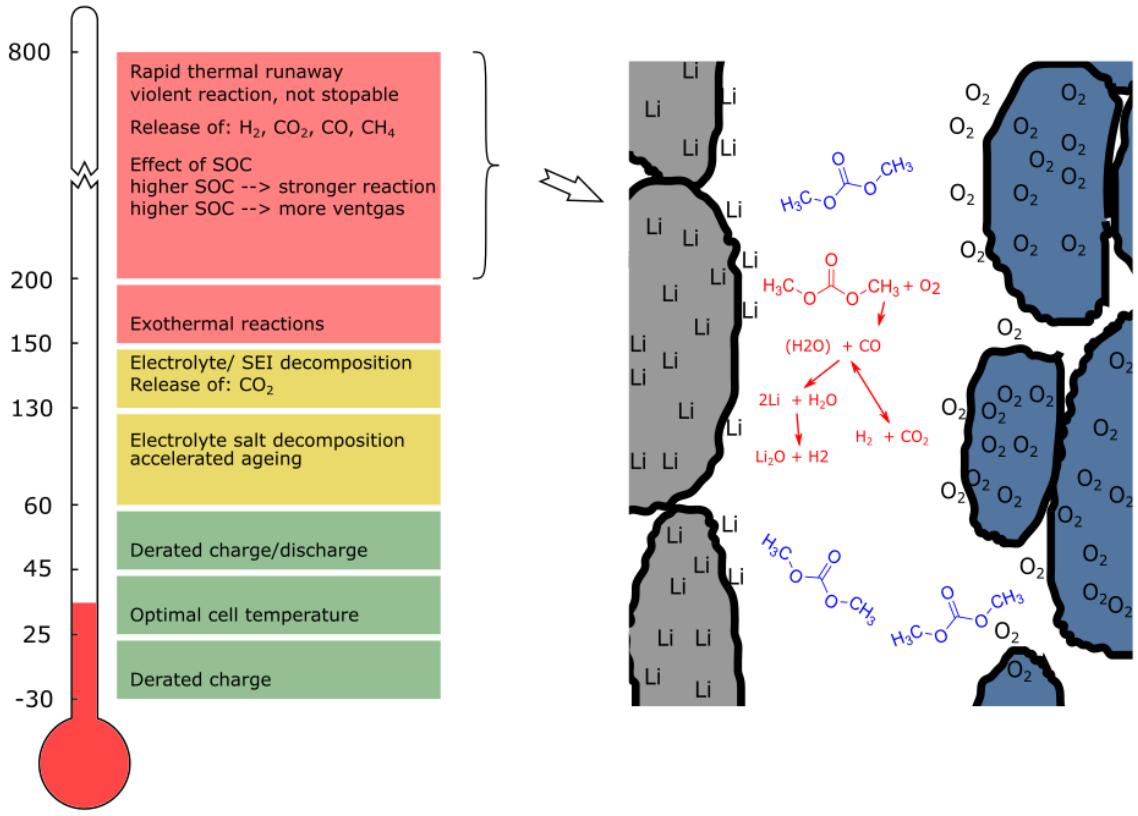

Fig. 5 (left) Sketch of thermal events for a Li-ion battery with energy density above 200 Wh/kg. (right) Main thermal runaway reactions

4.3. Single cell failure

Figure 5 shows the effects of temperature on a charged (or overcharged) Li-ion cell. Normal operating temperatures lie between -30°C and 60°C. To prevent excessive ageing, the battery management will derate the power below 10°C and above 45°C. Above 60°C the battery will be completely disconnected to prevent Li-salt decomposition. Above 130°C the SEI and electrolyte will decompose and release CO_2 (Lammer et al. 2017). Above 150°C reactions will become exothermal and the cell will go into rapid thermal runaway above 200°C.

The main thermal-runaway reactions are combustion of electrolyte with oxygen which is released by the metal-oxide cathode and oxidation of the lithium which is released by the graphite anode. The amount of both released ingredients – lithium and oxygen – is directly proportional to the stored energy of the Li-ion cell. A fully charged cell will release the complete amount of Li and O_2 while a fully discharged cell will neither release any Li nor O_2. Overcharged cells release even more Li and O_2. Similarly, a cell with high capacity will release more Li and O_2 than a cell with low capacity. Consequently, a charged cell with high energy density shows a more severe thermal runaway reaction compared to a not fully charged cell or a cell with low energy density.

The main components of released gas are CO and CO_2 from oxygen starved combustion electrolyte, binder and separator and H_2 from lithium oxidation (Golubkov et al. 2015; Golubkov et al. 2014). The ratio of CO and CO_2 depends on the reaction temperature (Boudouard reaction). Temperatures above 700°C favour CO over CO_2.

4.4. Thermal runaway propagation

In automotive battery packs cells are stacked as tight as possible to reduce pack volume. Typical numbers of cells in a battery pack range from 88 (PHEV) to 400 (BEV) in case of prismatic/pouch cells and 8000 (Teslas BEV) in case of small cylindrical cells. If one of those cells fails and transits into thermal runaway it will heat the adjacent cells. If the adjacent cells reach the critical temperature, they go into thermal runaway as well and the thermal runaway starts to propagate through the whole battery pack, eventually ending in a full battery fire. To prevent thermal runaway propagation, thermal barriers must be included between adjacent cells (Feng et al. 2015).

5. Experiment results, thermal runaway of large automotive Li-ion cells

5.1. Tested cell

We did experiments with automotive prismatic cells with graphite anodes and LMO cathodes. The cell has a mass of 1.7 kg, a capacity of 50 Ah and a mean voltage of 3.6 V. The cell designs dates from 2009 and therefore the energy density is rather low with 105 Wh/kg if compared with up-to date cells.

5.2. Test method

We developed a heavy-duty test rig to do experiments with large Li-ion cells. The test rig consists of a pressure tight reactor with a heatable sample-holder, many temperature sensors and a pressure sensor. Figure 6 shows the reactor in opened and closed state and figure 7 shows the sample holder.
In each experiment the cell is fully charged and placed into the sample holder. Subsequently the reactor is closed, evacuated and filled with nitrogen. Then the sample holder starts to heat the cell until a thermal runaway is detected. The test stand measures the cell-casing temperature, the gas temperature near the exit of the burst plate of the cell and the mean gas temperature in the reactor as well as the cell voltage and the gas pressure. The amount of released gas is calculated with the ideal gas law.

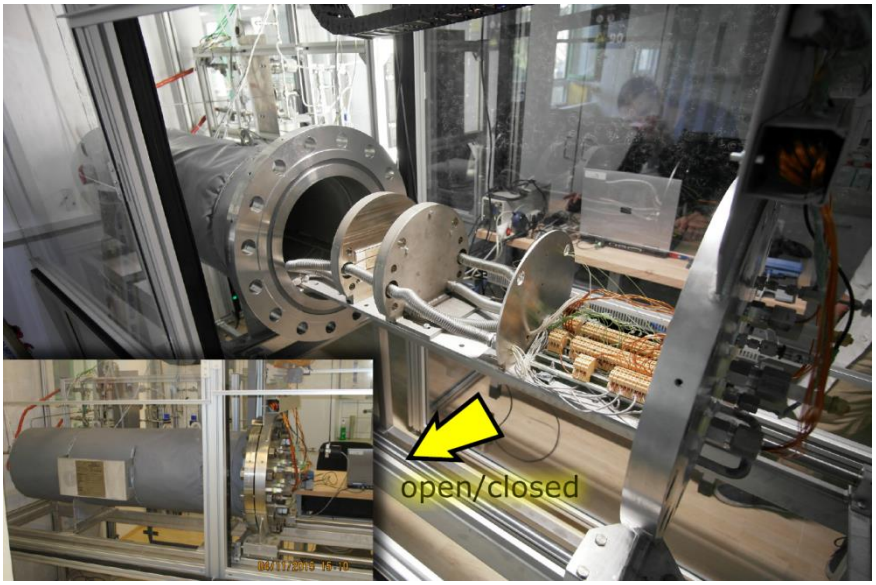

Fig. 6, Photograph of the thermal runaway test-stand. The main component is a massive gas-tight reactor, shown in opened and closed state

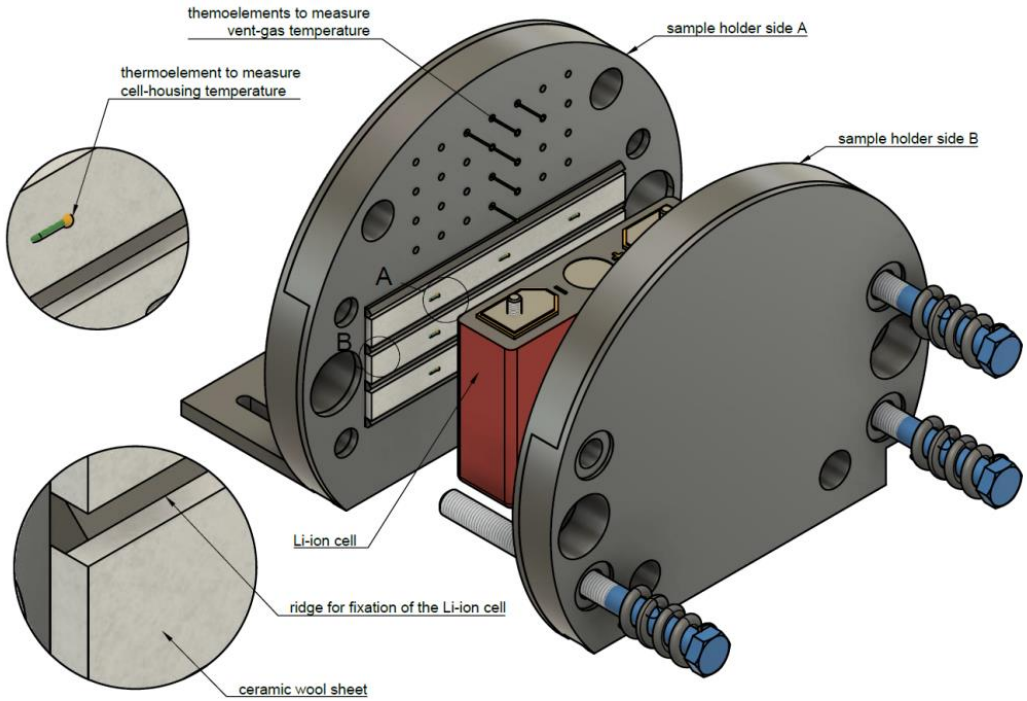

Fig. 7, Sketch of the sample holder for metal-can cells. The sample holder includes internal electric heating and a number of temperature sensors (thermocouples) to measure the cell surface temperature and the vent-gas temperature

5.3. Typical experiment outcome

The sample was heated with a constant temperature rate (2.3 °C/min). The voltage of the cell collapsed from 4.08 to 0 V at 176 °C. The burst plate of the cell opened at a cell temperature of 205°C and released 0.36 mol of gas. After further heating, up to a cell temperature of 247°C, the cell transited into a rapid thermal runaway and at the same time a second venting occurred with a gas release of additional 2.8 mol. The cell reached a maximum temperature of 532°C during thermal runaway. The maximum recorded temperature of the vent-gas was 530°C measured directly above the burst plate of the cell. After the thermal runaway the heating of the sample holder was switched off and the cell cooled down subsequently (Fig. 8). The cell lost 35% of its mass during the experiment by ejecting gas and particles through its venting plate.

It is important to know the duration of the main thermal runaway reaction and how long it takes to emit the gas. The cell emits hot vent-gas as long as the rapid thermal runaway reaction takes place. Therefore we can assume

that the duration of the reaction is the same as the duration where vent-gas temperature sensors measure high temperature. In the temperature plot, the vent-gas sensors stay above 500°C for 2.7 s and so we assume 2.7 seconds as the duration. Alternatively, we can estimate the venting duration from the pressure plot. The representative time - the time the pressure needs to increase from the pressure level before the main reaction to the maximum pressure level - is equal to 3 seconds.

Now we can calculate the release rate of the vent-gas. By taking 3 seconds as release time and 2.8 mol as the amount of released gas we arrive at 0.9 mol/s. This is equal to 22 litre/s at standard temperature and pressure. The release rate can be further used to specify the venting system of the battery pack housing so that gases are emitted to the outside of the electric vehicle.

The maximum temperature and the onset temperature can be included in thermal runaway propagation models to specify the needed heat barriers between individual cells in the battery pack.

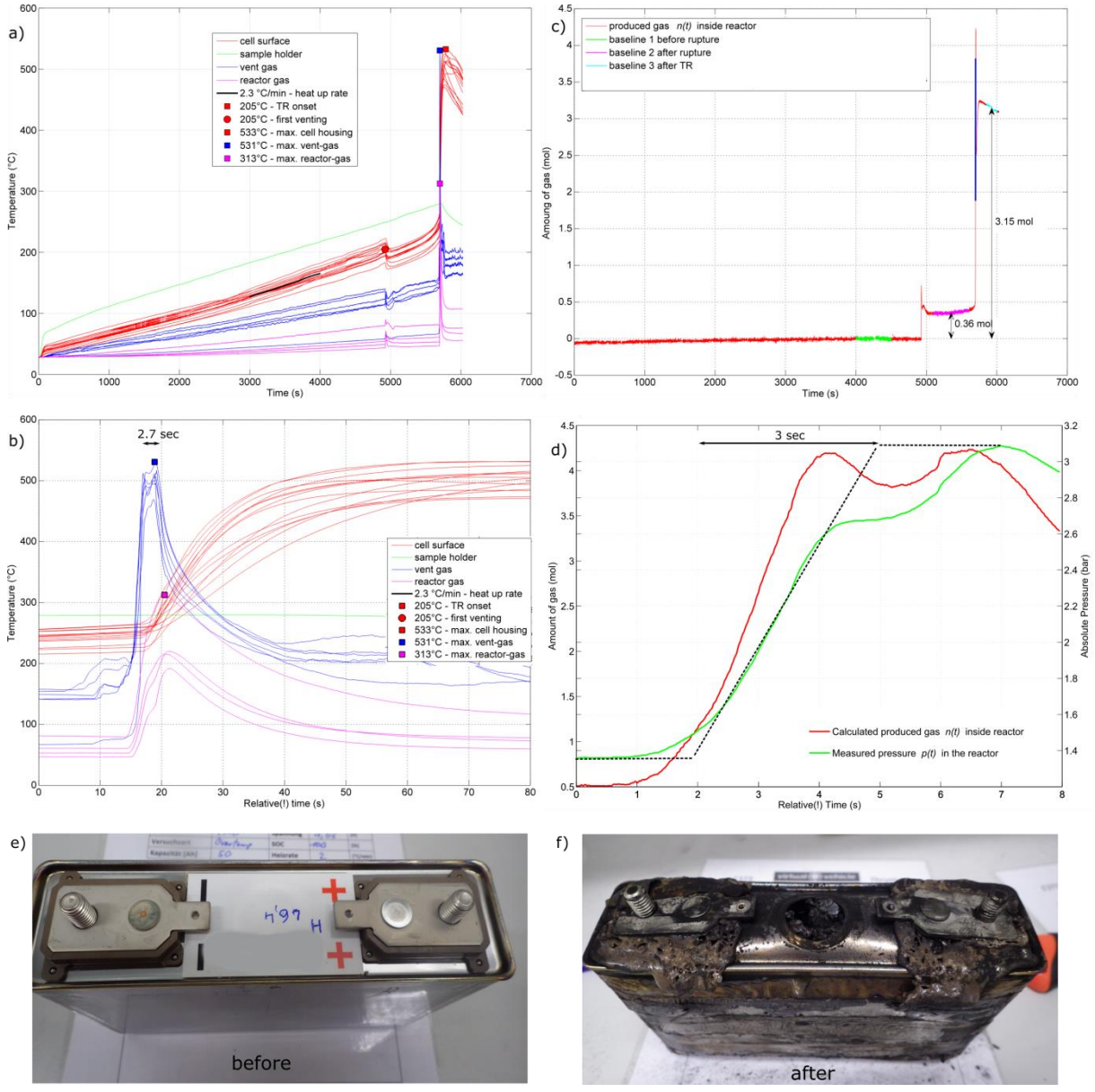

Fig. 8, (a) temperature of the cell casing, the vent-gas and the reactor-gas. Full experiment duration. (b) Detailed temperature plot showing only the main thermal runaway event. (c) Calculated amount of released gas inside the reactor. Full experiment duration. (d) Detailed pressure plot, showing only the main gas release. (e,f) Cell sample before and after the experiment.

6. Conclusion

In this paper we compared the safety of batteries for electrified vehicles. The thermal runaway of lead acid batteries batteries is driven by high charging current/voltage at high temperatures. It is easily detectable with temperature or gas sensors and can be mitigated by reducing the electric load. Ni-MH batteries show very good safety records. We could not find any literature on possible thermal runaway reactions of Ni-MH batteries.

The thermal runaway of Li-ion cells is initiated by overtemperature or overcharge. Their main thermal runaway reaction can be quite dramatic and can easily end with a battery fire. The severity of the Li-ion thermal-runaway reaction is proportional to the amount of electrochemical energy inside the cell. Cells with higher energy density reach higher maximal temperatures and release more vent-gas. Charged cells can go into thermal runaway but discharged cells show no thermal runaway reaction. In Li-ion battery packs special care must be taken to prevent hot-spots, foreign object intrusion, dendrites inside the cells and overcharge. Thermal barriers between the cells may be used to prevent thermal runaway propagation from cell to cell. Battery packs need proper gas venting (exhasut) systems so that in case of failure harmfull gases are directed to the outside of the vehicle.

7. Acknowledgements

This work was accomplished at the VIRTUAL VEHICLE Research Center in Graz, Austria. The authors would like to acknowledge the financial support of the COMET K2 - Competence Centers for Excellent Technologies Programme of the Austrian Federal Ministry for Transport, Innovation and Technology (bmvit), the Austrian Federal Ministry of Science, Research and Economy (bmwfw), the Austrian Research Promotion Agency (FFG), the Province of Styria and the Styrian Business Promotion Agency (SFG). They would furthermore like to express their thanks to their supporting industrial and scientific project partners, namely AVL List GmbH and to the Technical University Graz.

8. References

Feng, X. et al., 2015. Characterization of penetration induced thermal runaway propagation process within a large format lithium ion battery module. *Journal of Power Sources*, 275, pp.261–273. Available at: http://dx.doi.org/10.1016/j.jpowsour.2014.11.017.

Fetcenko, M., Koch, J. & Zelinsky, M., 2015. Nickel–metal hydride and nickel–zinc batteries for hybrid electric vehicles and battery electric vehicles. In *Advances in Battery Technologies for Electric Vehicles*. Elsevier, pp. 103–126. Available at: http://dx.doi.org/10.1016/B978-1-78242-377-5.00006-6.

Golubkov, A.W. et al., 2014. Thermal-runaway experiments on consumer Li-ion batteries with metal-oxide and olivin-type cathodes. *RSC Advances*, 4(7), p.3633. Available at: http://xlink.rsc.org/?DOI=c3ra45748f [Accessed December 20, 2013].

Golubkov, A.W. et al., 2015. Thermal runaway of commercial 18650 Li-ion batteries with LFP and NCA cathodes – impact of state of charge and overcharge. *RSC Adv.*, 5(70), pp.57171–57186. Available at: http://xlink.rsc.org/?DOI=C5RA05897J.

Karden, E., 2017. How Harmful Are Carbons in Enhanced Flooded Batteries for High Temperature Use Cases ? In *7th Advanced Automotive Battery Conference Europe*. Mainz, Germany: Advanced Power Supply and Energy Management Ford Research & Advanced Engineering Europe.

Lammer, M., Königseder, A. & Hacker, V., 2017. Holistic methodology for characterisation of the thermally induced failure of commercially available 18650 lithium ion cells. *RSC Adv.*, 7(39), pp.24425–24429. Available at: http://xlink.rsc.org/?DOI=C7RA02635H.

Larsson, F. & Mellander, B.-E., 2014. Abuse by External Heating, Overcharge and Short Circuiting of Commercial Lithium-Ion Battery Cells. *Journal of the Electrochemical Society*, 161(10), pp.A1611–A1617. Available at: http://jes.ecsdl.org/cgi/doi/10.1149/2.0311410jes [Accessed August 26, 2014].

McKenzie, S., 2017. High DCA and Low Water Consumption. In *7th Advanced Automotive Battery Conference Europe*.

Rand, D.A.J. et al., 1996. Valve-regulated lead/acid batteries. *Journal of Power Sources*, 59(1–2), pp.191–197. Available at: http://linkinghub.elsevier.com/retrieve/pii/0378775396023221.

Rosenkranz, C. et al., 2016. Advanced Lead-Acid for 14V Applications Johnson Controls Power Solutions FY2015. In *AABC2016 Europe*. Mainz.

Xu, K., 2004. Nonaqueous liquid electrolytes for lithium-based rechargeable batteries. *Chemical Reviews*, 104(10), pp.4303–4417. Available at: http://pubs.acs.org/doi/abs/10.1021/cr030203g [Accessed May 21, 2013].

Zhang, Z.J. & Ramadass, P., 2012. Lithium-Ion Battery Systems and Technology. In R. A. Meyers, ed. *Encyclopedia of Sustainability Science and Technology*. New York, NY: Springer New York, pp. 319–356. Available at: http://link.springer.com/10.1007/978-1-4419-0851-3 [Accessed May 22, 2013].

Zhao, B. et al., 2015. A comprehensive review of Li 4 Ti 5 O 12 -based electrodes for lithium-ion batteries : The latest advancements and future perspectives. , 98, pp.1–71.

2.4 Thermal Runaway of Large Automotive Li-ion Batteries

The following journal article was published in RSC Advances in 2018. In this work we investigated large prismatic Li-ion cells. The cells experienced different types of TR, depending on if an ISC took place or not.
In this work Andrey Golubkov wrote the text of the article and analysed the TR experiments. René Planteu, Phillip Krohn and Bernhard Rasch performed the TR experiments. Bernhard Brunnsteiner, Alexander Thaler and Viktor Hacker supervised the work.

RSC Advances

PAPER

View Article Online
View Journal | View Issue

Cite this: *RSC Adv.*, 2018, **8**, 40172

Thermal runaway of large automotive Li-ion batteries

Andrey W. Golubkov, *[ac] René Planteu,[a] Philipp Krohn,[a] Bernhard Rasch,[a] Bernhard Brunnsteiner,[b] Alexander Thaler[a] and Viktor Hacker[c]

Received 31st July 2018
Accepted 26th October 2018

DOI: 10.1039/c8ra06458j

rsc.li/rsc-advances

Damaged or heavily over-heated Li-ion batteries in electric vehicles can transit into a thermal runaway reaction with further heat and gas release. The heat may cause a battery fire and fast gas release may damage the battery-pack casing. To characterise heat and gas release of large automotive Li-ion cells, a heavy duty test bench was developed and a test series was performed.

1 Introduction

A typical application for a battery pack is a plug-in hybrid electric vehicle (PHEV): a PHEV with an electric range of 70 km needs a battery which can store 13 kW h of electric energy. Such a battery pack may consist of 96 large cells fixed inside the battery-pack casing as shown in Fig. 1. The battery pack is often fitted inside the available space in the luggage compartment of the car. Then, the only barrier between the passengers of the car and the Li-ion cells is the casing of the battery pack. The casing must protect the occupants from any gas or heat emission of the Li-ion cells.

PHEV batteries can be always energized, even when the battery pack is disconnected from the rest of the vehicle. The potential energy is a source of hazard and its uncontrolled release can easily cause battery fire.[1–7] Examples of unwanted initial energy release are:

- Short circuits inside a cell.[8]
- Short circuits between cells, busbars and other metallic components.
- Failures inside the cell supervision circuits.
- Hot spots from damaged electric connectors.

All those failures can cause local heating of adjacent Li-ion cells. Charged cells are vulnerable to elevated temperatures because heated cell components can overcome chemical activation energy and decompose in exothermic chemical reactions. In the worst case, if heated to a critical temperature, the unwanted self heating rate of the cell becomes larger than the heat dissipation rate and the cell will transit into the so called thermal runaway. In case of charged Li-ion cells with high energy density, the thermal runaway is a fast, violent, self accelerating chemical reaction of the electrodes and the electrolyte which releases high amounts of heat and gas: cell temperatures up to 1000 °C and gas release of up to 25 mol kW^{-1} h^{-1} (600 L kW^{-1} h^{-1}) were measured in previous work.[9] The main components of the gas were CO_2, CO and H_2 making it burnable[10,11] and toxic.[12–15]

In this work we address two safety topics for an automotive battery pack:

- The immediate risk of toxic gas intrusion from a vented cell into the passenger compartment and the countermeasures which consist of making a sturdy battery pack casing which can withstand some overpressure and including an appropriately sized exhaust port.
- The risk of thermal runaway propagation[16,17] from cell to cell and the countermeasure of utilizing adjacent heat capacities, heat barriers and active cooling to keep the failure localised.[18,19]

To quantify those risks a test stand was built to measure the characteristic temperatures and gas emission rates of an automotive cell during thermal runaway.

This paper describes the tested cells, the test bench for thermal runaway experiments, and the methods for calculating the main thermal runaway parameters. The used methods to initiate thermal runaway of large Li-ion cells, to quantify the gas emission (amount, production rate, gas temperature) and to measure the cell-temperature are explained and an overview of the results from a test series and some details on exemplary tests are provided. After understanding the safety behaviour of the cells, we make first estimations for the design of the vent-gas exhaust of the battery-pack casing and we assess the risk of thermal runaway propagation.

2 Tested Li-ion cells

Large automotive cells designed for EV applications[20] (Table 1) were tested. Each cell consists of a hermetically sealed prismatic casing made from stainless steel which contains the electrodes

[a]*Kompetenzzentrum – Das Virtuelle Fahrzeug Forschungsgesellschaft mbH, Inffeldgasse 21a, A-8010 Graz, Austria. E-mail: andrej.golubkov@alumni.tugraz.at*
[b]*AVL List GmbH, Hans-List Platz 1, 8020 Graz, Austria*
[c]*Institute of Chemical Engineering and Environmental Technology, Graz University of Technology, Inffeldgasse 25/C/II, 8010 Graz, Austria*

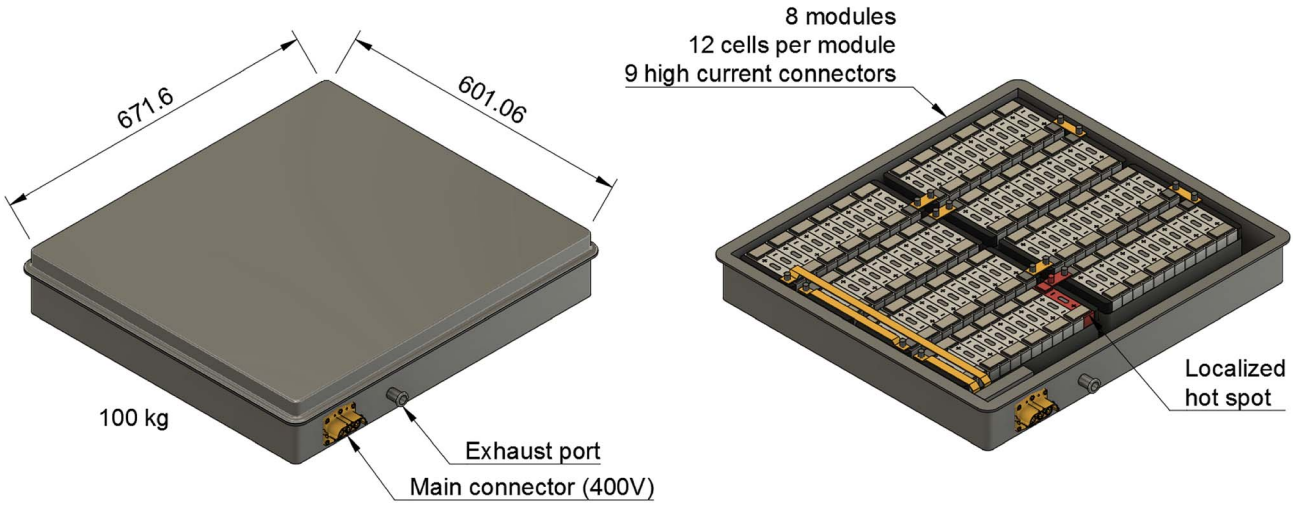

Fig. 1 Drawing of a hypothetical PHEV battery-pack to demonstrate the safety issues: (left) including complete casing, (right) with upper part of the casing removed. A possible hot spot is shown in red. Dimensions in mm.

Table 1 Specifications of the tested Li-ion cells

Cathode	$LiMn_2O_4$ (LMO)
Anode	Graphite
Mean voltage	3.7 V
Nominal capacity	50 A h
Maximal current	300 A
Dimensions	113.5 mm × 43.8 mm × 171 mm
Mass	1.7 kg
Specific energy	109 W h kg^{-1}

assembly. The positive and negative terminal and the rupture plate are integrated in the upper side of the casing (Fig. 2). The cells had been manufactured around the year 2009 and were stored until 2016. During this time their capacity decreased from 50 A h to 47 ± 2 A h due to ageing.

Compared to modern cell designs, those cells have low energy density. They use LMO cathodes whereas modern cells use mostly NMC and NCA cathodes. Test with new automotive cell-types with improved energy density (>200 W h kg^{-1}) will be shown in follow-up publications.

3 Test stand for thermal runaway experiments

The test stand for thermal runaway experiments was designed and built. The central component of the test stand is the heavy-duty gas-tight reactor with a volume of 121 l and a pressure rating of 40 bar. The reactor is limited to tests with cells and modules sized up to 1000 W h in nitrogen atmosphere. Test samples with higher energy content could possibly exceed the maximal pressure rating resulting in damaged test setup. Tests must be made in nitrogen atmosphere to avoid dealing with explosive gas mixtures. The main body of the reactor is fixed. The blind flange can be unscrewed from the main body and slid open along the rails until the attached cell holder stage is revealed outside of the reactor. Fig. 3 shows the reactor in opened and closed state. The blind flange also provides all

Fig. 2 Tested cell before and after the thermal runaway experiment. On the fresh cell, the burst-plate of the cell is hidden below the white sticker. After a thermal runaway the cell is heavily damaged: the burst plate is open, the plastic insulation of the terminals is melted and the cell casing is deformed by the pressure inside the cell.

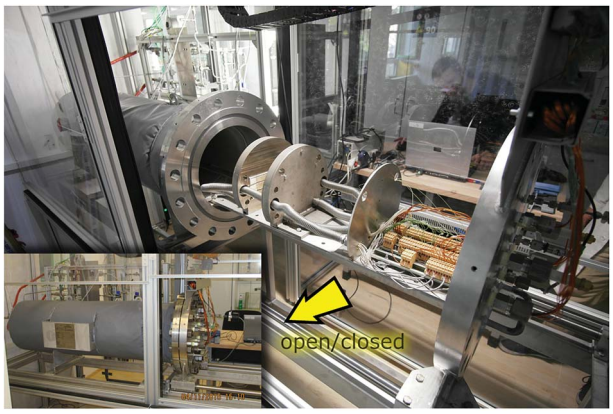

Fig. 3 Reactor in opened and closed state.

electrical feedthroughs for the sensors, the electrical heating of the cell holder and the electrical connection to the cell.

The reactor contains the cell-holder for the Li-ion cell, a screen plate with gas-temperature sensors and heat resisting wiring (Fig. 5). All components inside the reactor must withstand some abuse by the violent thermal runaway reactions of the Li-ion cells (Fig. 4)

3.1 Cell holder

The Li-ion cell is fixed inside a custom made cell holder. The cell holder and the cell sample are placed into the reactor. The geometry of the cell holder is optimised to the cylindrical shape of the reactor (Fig. 6).

The functions of the cell holder are:

1. Applying mechanical pressure on the sides of the cell to simulate the mechanical situation in a battery module.

2. Heating of the cell.

3. Sensor fixture for the measurement of the cell casing temperatures.

4. Sensor fixture for the measurement of the vent gas temperature.

The two plates with the cell sandwiched in between are pressed together by metal springs. Each plate is equipped with internal heating cartridges (maximal heating power of 1200 W). The cell holder can heat with different heating rates depending on the settings of the power controller.

At cell temperatures above a critical temperature exothermic reactions inside the cell start and the cell begins to self heat. The objective is to detect the minimal temperature, at which self heating is evident. To increase the sensitivity of exothermic-event-detection the cell holder must not interfere with the self heating of the cell: the cell should perform the exothermic reactions as adiabatic as possible. To minimise the thermal coupling of the plates and the cell we put insulation sheets made from ceramic wool in between (heat conductivity $\lambda = 0.1\ \mathrm{W\ m^{-1}\ K^{-1}}$, thickness $d = 5$ mm).

The plates also provide mechanical fixtures for temperature sensors. Each sample holder-plate has 9 positions for thermocouples. The tips of the thermocouples are positioned at equal distances along the cell-casing. They protrude through the insulation material and are pressed against the cell casing. Further thermocouples are placed in the space directly above the rupture-plate of the cell in order to measure the vent-gas temperature during the cell venting.

3.2 Screen plate

The screen plate is placed inside the reactor between the cell holder and the flange. It has two functions (1) mechanical protection of electrical wiring and connectors behind the screen and (2) fixture of four thermocouples at different heights to measure the mean gas temperature inside the reactor. The tips of the thermocouples are bare and uninsulated and they protrude through the screen plate towards the cell holder for 10 mm. This setup facilitates fast take up of temperature-change of the surrounding gas and minimizes the time delay of the temperature measurement.

3.3 Pressure sensor

Off-the-shelf pressure sensor (GEMS 3300B06B0A05E000) to measure gas pressure inside the reactor was used. The sensor is attached at the blind flange.

Fig. 4 View of the inside of the reactor, before and after a couple of thermal runaway experiments. The inside of the reactor became coated with anode and cathode particles which were vented by the cells during the experiments.

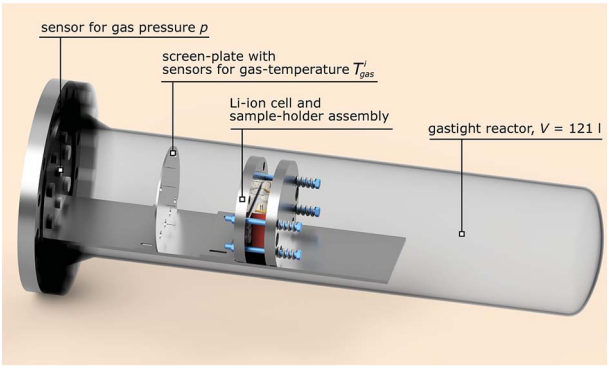

Fig. 5 Simplified sketch of the reactor in closed state, wiring not shown.

3.4 DAQ system

The DAQ system consists of standard modules in a cDAQ-9178 chassis from National Instruments. In this setup 30 channels for temperature measurements (k-type thermocouples), one channel for pressure measurement and one channel for cell voltage measurement with a sampling rate of 50 S s^{-1} for each channel were used.

In experiments for this work 18 thermocouples measured the cell surface temperature, 6 measured the vent-gas temperature near the burst-plate of the cell and 4 were attached to the screen plate to measure the gas temperature inside the reactor. The validity of the system can be checked by comparing measurements of the thermocouples to RTD sensors and by comparing the pressure signal to read-out of a manual manometer.

4 Methods and definitions

4.1 Initiation of thermal runaway

Thermal runaway of Li-ion cells can be triggered by localised or homogeneous heating and by overcharge. In the experiments we compare the thermal runaway initiated by four methods:

Heat ramp. Homogeneous heating of both large areas of the cell with constant temperature rate (both sample holder plates heat).

One-sided heating. Homogeneous heating of one single large area of the cell with constant temperature rate (only one sample-holder plate heats).

Stepwise heating. Homogeneous heating of both large areas of the cell with temperature steps (both sample-holder plates heat in steps).

Reactor heating. The whole reactor is heated from outside by the reactor heater.

4.2 Max cell temperature

The maximal cell case temperature T_{cell}^{max} is the maximum recorded value of any temperature sensor that measures the cell case temperature. In most cases the maximal cell case temperature was recorded at the centres of the two large side-areas of the cells.

4.3 Critical cell temperature

The cell transits into a rapid thermal runaway, after its hottest surface location exceeds a critical temperature. Here we define the critical temperature T_{cell}^{crit} in two steps: in the first step we

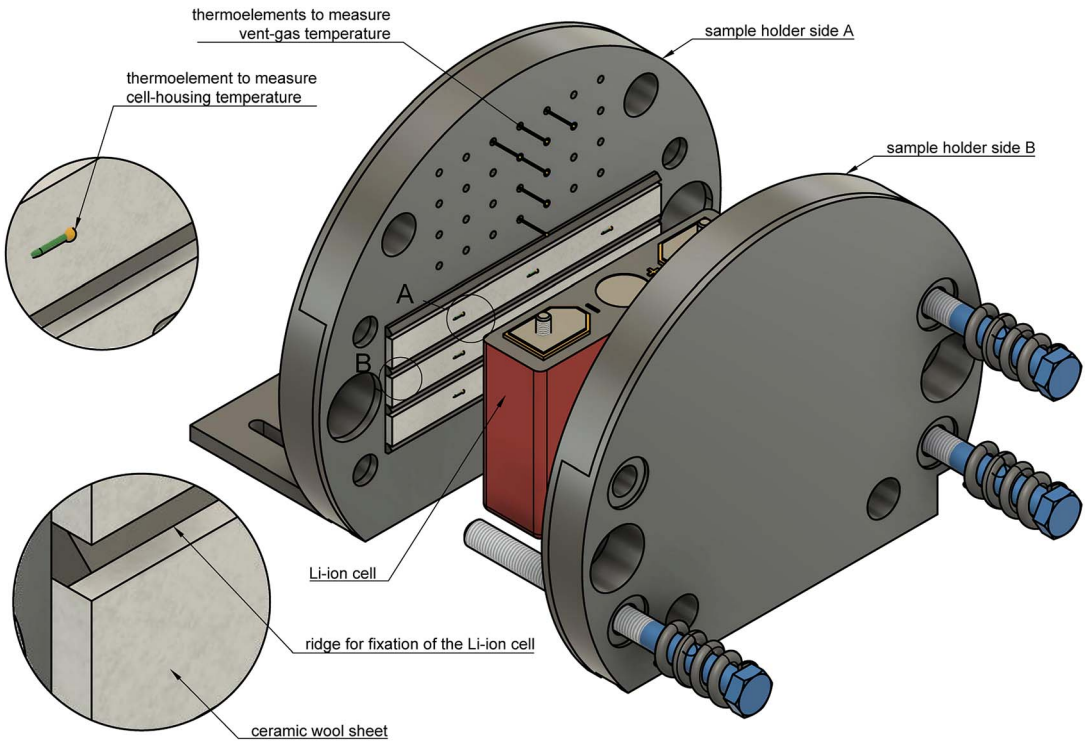

Fig. 6 Exploded view of the cell holder and the Li-ion cell.

look at the time span immediately before the main exothermic event and select the hottest temperature sensor. This is where the imminent rapid thermal runaway of the cell will originate. In the second step we define the critical temperature $T_{\text{cell}}^{\text{crit}}$ as the temperature when the temperature rate of the selected sensor $\dot{T}_{\text{cell}}$ exceeds 10 °C min^{-1}.

4.4 Fail temperature

The fail temperature T_{fail} is the average cell surface temperature when the cell fails electrically: its voltage drops to zero volt.

4.5 Venting temperatures

The first and second venting temperature T_{V1} and T_{V2} are the average cell surface temperatures at which the (first) minor and the (second) major venting occurs.

4.6 Maximal vent-gas temperature

The maximal vent-gas temperature $T_{\text{V2}}^{\max}$ is the maximum recorded temperature of the gas which was emitted by the cell through the rupture plate of the cell.

4.7 Temperature in the reactor

The temperature in the reactor T_{reactor} is the mean gas temperature in the reactor at the end of the experiment (several minutes after the thermal runaway event), when the gas temperatures come to an equilibrium. Gas species that are emitted by the cell condensate, when T_{reactor} is below their boiling point.

4.8 Amount of gas inside the reactor

During the thermal runaway of a cell, gas is released into the sealed reactor. To estimate the amount of produced vent gas and the vent gas release rate we calculate the overall amount of gas $n(t)$ inside the reactor with the ideal gas equation:

$$n(t) = \frac{p(t)V}{R\langle T_{\text{gas}}(t)\rangle} \tag{1}$$

Here, the reactor volume $V = 0.1208$ m^3, the gas constant $R = 8.314$ J mol^{-1} k^{-1}, p (in Pa) is the gas pressure in the reactor and $\langle T_{\text{gas}}\rangle$ (in K) is the average gas temperature in the reactor.

To measure the pressure is straightforward; a standard industry grade pressure sensor has sufficient resolution and fast step response. It is much more challenging to estimate the average gas temperature $\langle T_{\text{gas}}\rangle$. The exact definition of $\langle T_{\text{gas}}\rangle$ contains the 3D integral of the temperature over the volume V inside the reactor:

$$\langle T_{\text{gas}}(t)\rangle := \frac{1}{V}\iiint_V T(t)\,\mathrm{d}V \tag{2}$$

It is not possible measure the gas temperature at every point of space inside the reactor. Instead, we are limited to four temperature sensors which are fixed by the screen plate at four different heights (Z-direction) inside the reactor (Fig. 5). We approximate the volume-integral with the average of the sensors $T_{\text{gas}}^{\text{i}}$ (in °C) and apply a correction factor c_g and then convert from °C to K:

$$\langle T_{\text{gas}}(t)\rangle = 273 + c_g\frac{1}{4}\sum_{\text{i}=1}^{4} T_{\text{gas}}^{\text{i}}(t) \tag{3}$$

The factor c_g compensates the temperature deviations originating from convective flow between the heated sample holder and the not heated reactor (*vice versa* in case of experiment 10 and 11). The values of c_g typically range between 0.85 and 0.95.

The c_g was evaluated by looking at the value of n between the start of experiment and the first venting of the cell. At the beginning of the experiment the reactor and the cell are gas tight sealed. The heating ramp is started and when the temperature of the cell is high enough, its rupture disc burst and causes abrupt gas release into the reactor. The amount of gas n from the start of the heating ramp to the burst disc opening remains constant and corresponds to (1). The value of c_g is adjusted, so that the calculated n indeed stays constant between the start of experiment and first venting.

4.9 Amount of released gas

In the thermal ramp experiment the sample holder heats the cell and the cell releases gas in either only one (only major venting) or two subsequent events (minor venting followed by a major venting) (Fig. 7). The sum of the gas releases is the overall released vent-gas during the experiment:

$$n_{\text{V}} = n_{\text{V1}} + n_{\text{V2}} \tag{4}$$

Minor gas release n_{V1}. Increased cell temperature facilitates electrolyte decomposition into gaseous products. The build up of decomposition gas increases the internal cell pressure and causes deformations of the casing. High cell temperature, deformations and overpressure eventually cause the opening of the rupture disc. At the moment when the cell is no longer gas tight, it releases the surplus gas into the reactor. The gas release can be abrupt and the cell might cool down slightly (Joule–Thomson effect). The temperature of the surplus gas is below 220 °C.

Major gas release n_{V2}. Either an internal short circuit or further temperature-increase and exothermic reactions start an accelerating chain reaction (thermal runaway), resulting in a major violent gas release. The temperature of the vent-gas is comparable to the maximum cell case temperature (>400 °C). The amount of gas in the major gas release is always higher than in the minor release ($n_{\text{V2}} > n_{\text{V1}}$).

4.10 Venting-rate of the gas

The venting sub system of the battery pack casing must ensure, that the gas is safely transported to the outside of the vehicle. Therefore, the speed of the gas release during the major venting n_{V2} is crucial. We define the characteristic venting-rate $\dot{n}_{\text{ch}}$ as the 'speed' of gas release (in mol s^{-1}). This so called venting rate

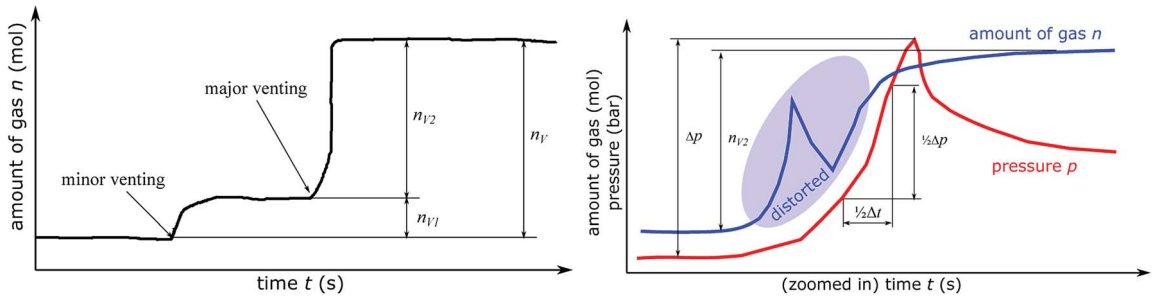

Fig. 7 (left) Sketch of the amount of gas inside the reactor during a typical thermal ramp experiment. The cell can produce gas in two venting events: the first (minor) venting and the second (major) venting. (right) The method to calculate the characteristic venting rate $\dot{n}_{ch}$. The amount of gas n can not be used directly because n is calculated from gas temperature measurement, which is distorted by violent gas flows during the main venting event. Instead, it is assumed, that 50% of n_{V2} is released during $1/2\Delta t$ and $1/2\Delta t$ is the timespan during which pressure rises by $1/2\Delta p$. The pressure based method can characterise high venting rates, because it is less affected by gas flows.

is the most important parameter needed to calculate the dimensions of the vent gas pipe of the battery pack.

A simple algorithm calculates the characteristic venting-rate by estimating the minimum time which is needed to vent 50% of n_{V2}. By choosing 50% of pressure rise, the algorithm automatically selects the main phase of fast gas release in the middle of the venting event and it excludes the slow onset and the final trailing-off of the gas emission.

The algorithm mainly depends on the pressure signal because pressure is less prone to be obfuscated even by violent venting (Fig. 7). The pressure has the value p_0 before the major venting, during major venting it reaches a maximum p_{max} and then it slowly decreases to p_1 as the released hot vent-gas cools down. We define $\Delta p = p_{max} - p_0$ as the maximal pressure change (Fig. 7). In the next step the algorithm scans the whole time-series of the p_k-signal. Here k is the index of the time series running from 1 to *e.g.* 300 000 for an experiment duration of 6000 s and a time resolution of $r = 0.02$ s. The algorithm starts at every p_k and increases the index l until

$$p_{k+l} - p_k > 1/2\Delta p \tag{5}$$

The value of l is proportional to the time which is needed to vent 50% of gas ($1/2\Delta t = rl$). The value of l is stored in $D_k = l$. After calculating D_k for every k the minimum of D_k is used to calculate the characteristic venting rate $\dot{n}_{ch}$:

$$\dot{n}_{ch} = \frac{n_{V2}}{r \min D_k} \tag{6}$$

In other words, the algorithm scans the whole length of the experiment and selects the time-span where the pressure changes by $1/2\Delta p$ in a minimum amount of time.

5 Results

5.1 Overview

The outcome of thermal-runaway experiments with different heating methods is compared: five cells were heated by a heat ramp, two cells by one-sided heating, two cells by stepwise heating and two cells by heating of the whole reactor. All experiments were done in nitrogen atmosphere. The results from the eleven experiments are compiled in Table 2 and characteristic temperatures are compared in Fig. 8. Unfortunately, the cells showed different event sequences (Fig. 9) during repeated experiments. We identified three types of event sequences and categorised them in three groups:

Group A2. Most experiments showed both venting events (minor and major) and a forerunning temperature increase immediately before the main exothermic reaction.

Group B1. In three experiments (experiment no. 3, 5, 6) the cell vented only once (only major venting during the main exothermic thermal runaway reaction) and showed no forerunning temperature increase.

Group B2. In one experiment (no. 8) we observed two venting events (as in A2) but no forerunning temperature increase.

The overall results show, that some thermal runaway characteristics depend and some do not depend on the heating method or group. The voltage of the cells broke down to 0 V at $T_{cell}^{fail} = 170 \pm 30$ °C for all groups and heating methods. Temperatures of the venting events showed more dependence on the group then on the heating method. In the group A2 the (first) minor venting occurred at an average cell casing temperature of $T_{cell}^{V1} = 200 \pm 20$ °C and the (second) major venting and thermal runaway reaction occurred at $T_{cell}^{V2} = 230 \pm 30$ °C. In the group B1, with only the major venting, venting occurred simultaneously with their thermal-runaway reaction at cell temperatures $T_{cell}^{V2} = 182 \pm 30$ °C. We suspect that – in contrast to group A2 – in group B1 the mechanical stress from cell swelling caused an internal short circuit, which, in turn, caused a very fast transition to a full thermal runaway. In other words, we suspect that in group B1 the minor venting, short circuit, thermal runaway and the major venting happened almost simultaneously so that the venting could not be resolved into a minor and major part.

The overall measured amount of released gas mainly depended on the reactor temperature (Fig. 10). In the first nine experiments (except for experiment no. 5.) with unheated reactor we measured $n_v = 3.2 \pm 0.2$ mol. In experiment no. 5 the released amount of gas exceeded the average by 40%. Unfortunately we could not come up with any explanation for this outlier. In the experiments 10 and 11 the whole reactor was heated and a reactor temperature of 250 °C prevented

Table 2 Results of all experiments. "–" means that the first (minor) venting did not take place. "n.a." means not available, because associated temperature sensors failed or – in case of experiment 4 – because we forgot to measure the cell mass after the experiment. Here type is the initiation method to start the thermal runaway, V_{cell}^{before} is the cell voltage before the experiment is started, group is the category into which the experiment result was classified, T_{cell}^{crit} is the temperature at which the hottest cell case sensor exceeds 10 °C min^{-1}, T_{cell}^{fail} is the average cell case temperature at which the cell voltage drops to zero, T_{cell}^{V1} and T_{cell}^{V2} are the average cell case temperatures at which the first and second gas release occurs, T_{cell}^{max} is the maximal cell case temperature during the thermal runaway, T_{V2}^{max} is the maximum vent-gas temperature, n_{V1} and n_{V2} are the amounts of released gas during first and second venting, n_V is the overall released amount of gas, $T_{reactor}$ is the reactor temperature when n_V is measured, $\dot{n}_{V2}^{ch}$ is the characteristic venting rate during the main venting event, M_{cell}^{before} and M_{cell}^{after} are the cell masses before and after the experiment

No	Type	V_{cell}^{before} V	Group	T_{cell}^{crit} °C	T_{cell}^{fail} °C	T_{cell}^{V1} °C	T_{cell}^{V2} °C	T_{cell}^{max} °C	T_{V2}^{max} °C	n_{V1} mol	n_{V2} mol	n_V mol	$T_{reactor}$ °C	$\dot{n}_{V2}^{ch}$ mol s^{-1}	M_{cell}^{before} g	M_{cell}^{after} g
1	Heat ramp	4.08	A2	248	176	203	247	531	530	0.4	2.8	3.2	61	0.9	1693	1092
2	Heat ramp	4.08	A2	251	206	220	270	558	n.a.	0.3	2.7	2.9	70	0.9	1695	1074
3	Heat ramp	4.06	B1	192	160	—	171	518	418	—	3.1	3.1	55	0.7	1695	1119
4	Heat ramp	4.06	A2	239	165	194	239	469	488	0.3	2.7	3.1	62	1.4	1691	n.a.
5	Heat ramp	4.10	B1	176	154	—	155	529	415	—	4.6	4.6	53	0.4	1638	1101
6	One-sided heating	4.08	B1	266	221	—	221	528	n.a.	—	3.2	3.2	58	0.6	1696	1156
7	One-sided heating	4.04	A2	281	180	180	203	500	512	0.5	2.8	3.3	43	0.6	1693	1177
8	Stepwise heating	4.08	B2	173	138	167	172	427	405	0.4	2.9	3.4	73	0.7	1696	1143
9	Stepwise heating	4.10	A2	265	154	210	248	530	483	0.3	3.3	3.6	69	0.7	1637	1063
10	Reactor heating	4.08	A2	206	140	174	200	495	411	1.1	4.5	5.6	249	1.3	1695	1115
11	Reactor heating	4.08	A2	222	155	191	221	595	n.a.	1.6	4.4	5.9	253	1.4	1696	1118

condensation of electrolyte vapour. The additional gaseous electrolyte increased the amount of gas by 80% to $n_V = 5.77 \pm 0.2$ mol.

Minor venting was only observed in the groups A2 and B2. In the experiments with unheated reactor minor venting contributed $n_{V1} = 0.4 \pm 0.1$ mol to the overall amount of gas. In the last two experiments, with heated reactor, minor venting contributed by a higher amount of gas $n_{V1} = 1.3 \pm 0.3$ mol because released electrolyte vapour stayed in gas phase.

The accumulation rate of gas in the reactor showed a high variation and no clear dependency on heating method (Fig. 10). In the first nine experiments, with unheated reactor, therefore not counting the electrolyte vapour, the cells released $\dot{n}_{V2}^{ch} = 0.8 \pm 0.3$ mol s^{-1}. In the last two experiments, with heated reactor and therefore including the electrolyte vapour the cells released $\dot{n}_{V2}^{ch} = 1.3$ mol s^{-1}.

The maximum cell temperatures and maximum vent gas temperatures showed no apparent dependency on the heating method or group. We measured $T_{cell}^{max} = 520 \pm 40$ °C and $T_{V2}^{max} = 460 \pm 50$ °C.

The cells lost significant amount of mass during the thermal runway (Fig. 10). The mass of the cells decreased from $M_{cell}^{before} = 1680 \pm 20$ g to $M_{cell}^{after} = 1120 \pm 40$ g independent of group or heating method.

5.2 Heat ramp (group A2)

Fig. 11 shows the experiment no. 1. The cell was heated with a heating ramp of 2.4 °C s^{-1}. The first minor venting occurred at 5000 s and the second main venting at 5700 s.

The combination of gas build up in the cell and the minor venting caused two effects which produced a measurable temperature drop of the cell case sensors at 5000 s. First effect:

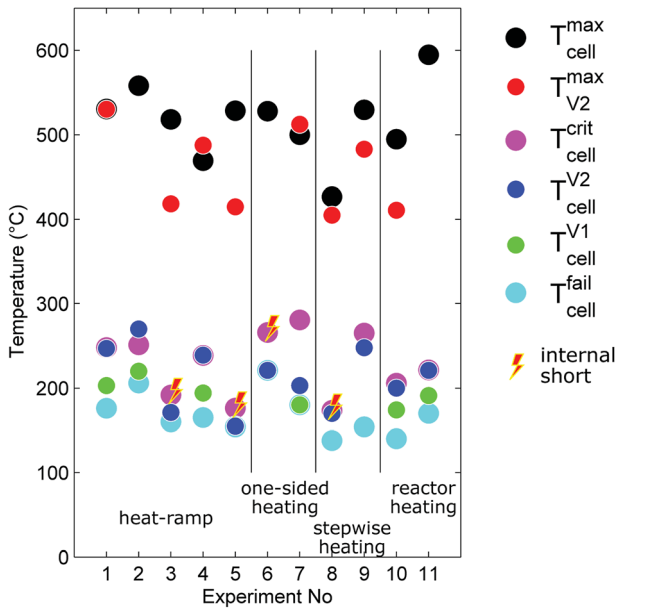

Fig. 8 Characteristic temperatures associated with the events of cell failure (voltage drop), first and second gas release, reaching the critical temperature, reaching the maximal cell temperature during thermal runaway and the maximum vent-gas temperature.

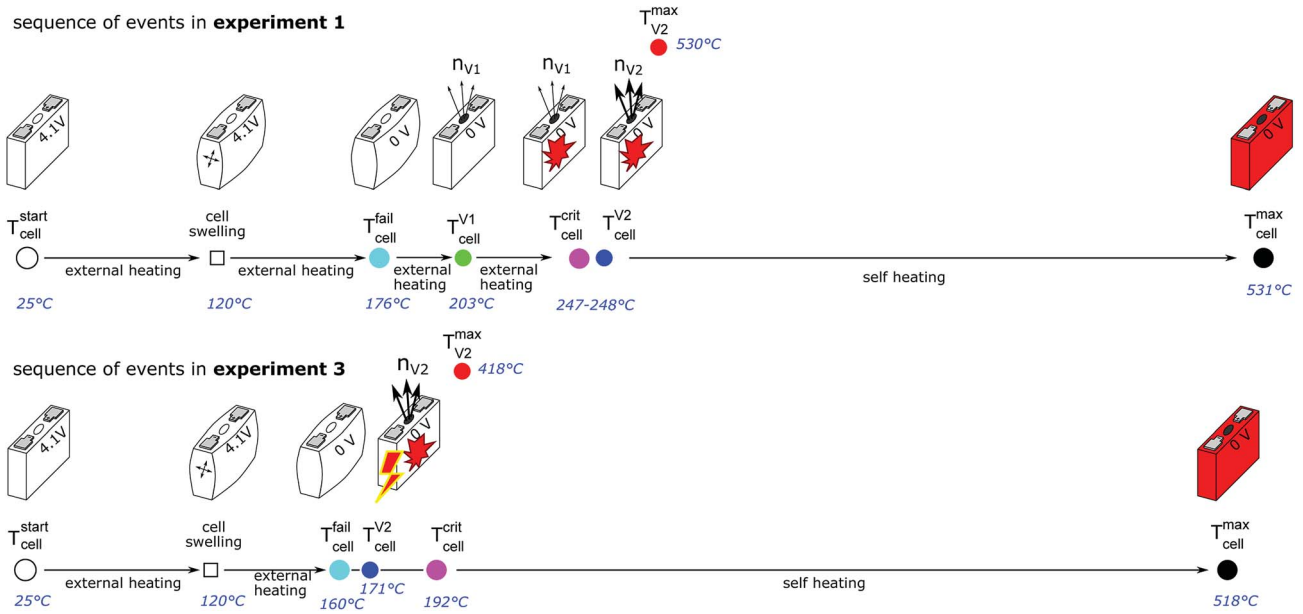

Fig. 9 Sketch of the sequence of events as the temperature of the cell increases for experiment 1 and 3. In experiment 1 cell case swelling occurs at 120 °C, the cell fails at 176 °C, the burst disc opens and releases the overpressure from the cell into the reactor and some cell swelling is reversed at 203 °C then increasingly exothermic chemical reactions slowly evolve into a thermal runaway with a critical temperature of 248 °C and second major venting at 247 °C. The cell casing reaches a maximum temperature of 531 °C. In experiment 3 the cell also starts to swell at 120 °C and the cell fails at 160 °C. Then – at an average cell temperature of 170 °C and the hottest cell case sensor showing 192 °C – an internal short circuit triggers a sudden heat release which immediately causes venting and thermal runaway. The cell casing reaches a maximum temperature of 518 °C.

the Joule–Thomson effect causes some cooling of the cell and of the vent-gas temperature-sensors as the gas expands from the cell into the reactor. Second effect: the cell case swelling effect, this is more intricate. During heating above 120 °C gas builds up inside the cell and causes a bulging of the cell casing. The bulging forces the temperature sensors on the cell casing towards the heating side plates of the sample holder. At the same time gas inside the cell builds up an insulating gas layer between the active material (jelly roll) and the heated casing of the cell. The measured temperature increases, because the place which the sensors measure is shifted towards the hot cell holder plates and away from the cooler active material in the cell. Then, during minor venting, the built-up gas is released from the cell, the bulging of the cell casing is reversed, the cell casing with the attached temperature sensors comes in thermal contact with the cooler active material inside the cell and the temperature sensors measure a sudden temperature drop. (In other words, imagine a frozen ice cream inside an inflated air balloon with temperature sensors attached to the outer balloon shell. As long as there is air inside the balloon, the temperature sensors would measure the ambient temperature, but when gas is released they would measure the temperature of the cooler melting ice.)

Note that the duration of the major gas release – and also the duration of the thermal runaway reaction which causes the

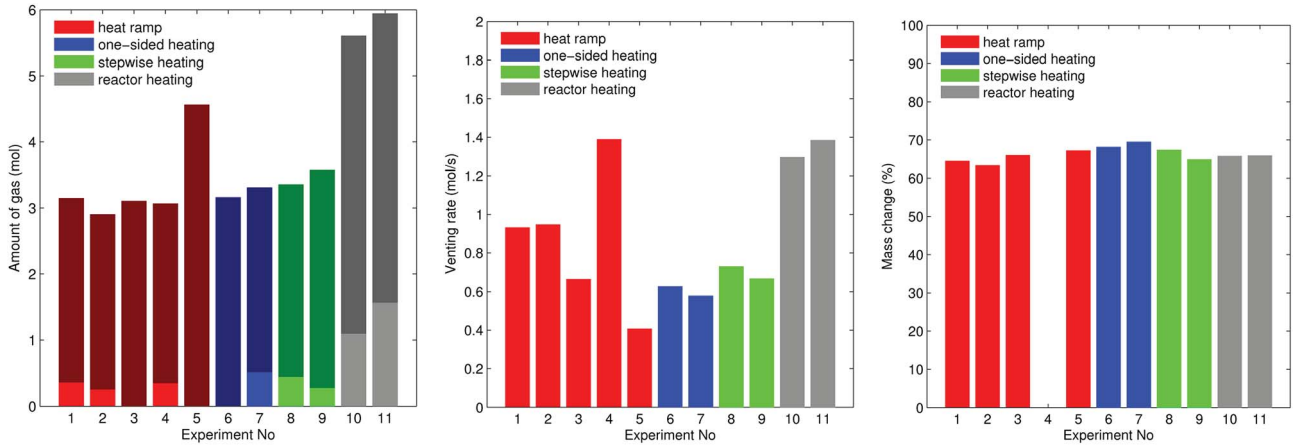

Fig. 10 (left) Gas emission. Each bar shows the minor venting n_{V1} (if present) and the major venting n_{V2} on top. (center) Rate of gas emission $\dot{n}^{ch}_{V2}$. (right) Mass of the cell after the thermal runaway experiment compared to mass of the fresh cell.

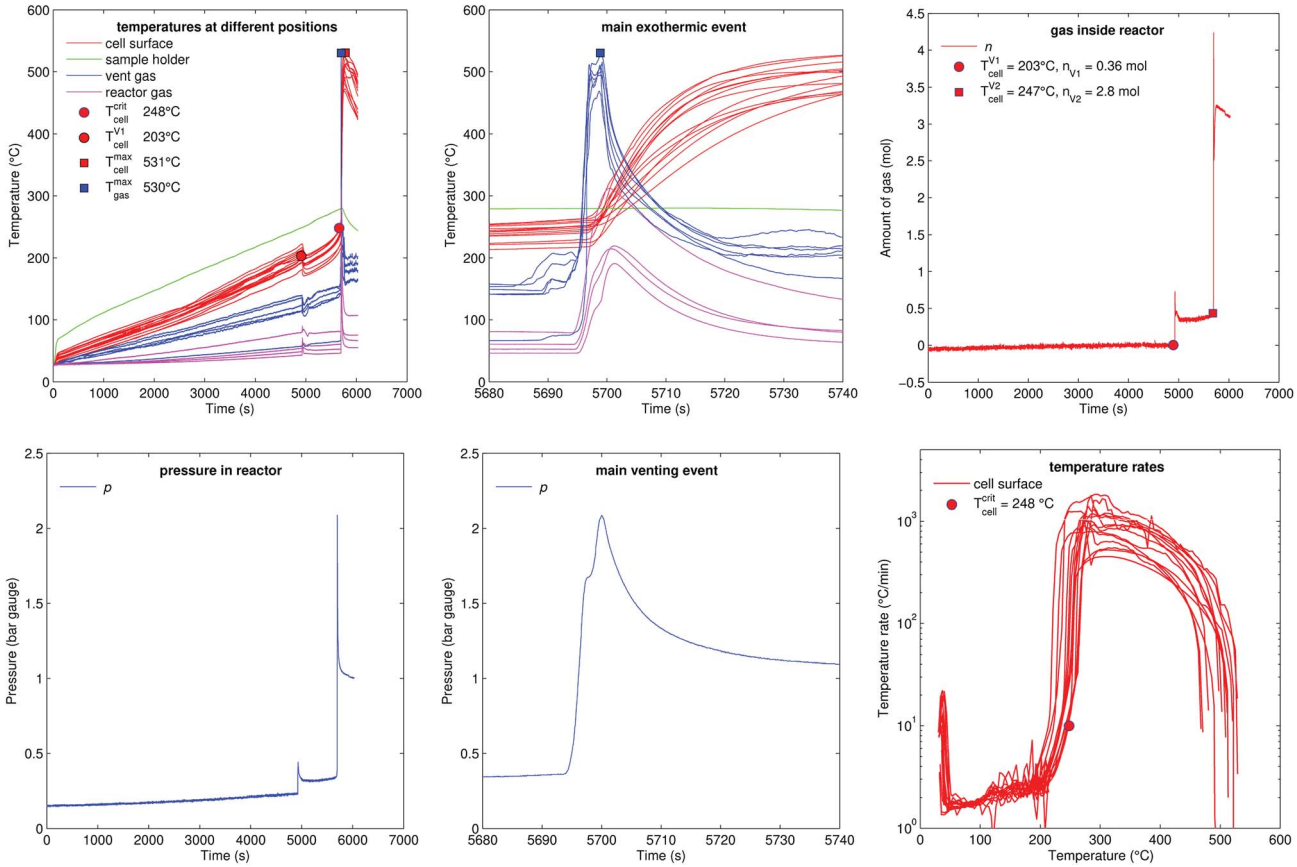

Fig. 11 Experiment no. 1 (heat ramp). (left) Temperatures and gas pressure during the whole duration of the experiment and (centre) during the main exothermic event. (right) Amount of released gas into the reactor and temperature rates of the cell case sensors.

major gas release – at 5700 s was very short (2 s). The cell casing reached the maximal temperature 40 s after the major gas release and the completion of the thermal runaway reaction inside the cell. This delay of temperature response is caused by thermal masses and finite heat conductivity from inside the cell to the sensors on the outside of the cell (high Biot number). Therefore, we believe that the gas release duration is a much better indicator to judge the duration of the main thermal runaway reaction than the outside cell case temperature.

The hot gases (530 °C) from the major venting caused a maximal pressure of 2 bar in the reactor. Then the gas cooled down (to 61 °C) and partially condensed and the pressure dropped to 1 bar.

5.3 Heat ramp (group B1)

Fig. 12 shows the experiment no. 3. The setup was the same as in the experiment no. 1: the cell was heated from both sides with a heat ramp. In contrast to experiment no. 1 (classified to group A2) the cell showed a different sequence of events, classified as group B1: this time we could observe only one venting and a simultaneous thermal event at an average cell temperature of only 171 °C at 5572 s. Another difference was that the event was not preceded by any detectable self heating: the main event happened spontaneously without any warning (compare temperature plots in Fig. 11 and 12) and resulted in a maximum temperature of 518 °C. The cell in experiment no. 5 showed similar behaviour, with the main (and only) event at 155 °C.

We conclude that the spontaneous thermal runaway event was caused by an internal short circuit inside a cell. The short circuit occurred before the minor venting would normally happen and therefore the cell experienced only one major venting during the main exothermic reaction.

5.4 One-sided heating (group A2)

Fig. 13 shows the experiment no. 7. Here the cell was heated from one side and the other side stayed unheated by the sample holder. This created a huge temperature gradient through the cell. At 10 000 s the cell vented for the first time and at 10 770 s the main exothermic event occurred. At this point the heated side of the cell was at 270 °C and the unheated side was at 120 °C. The thermal runaway caused cell temperature increase to a maximum of 500 °C.

5.5 Stepwise heating (group B2)

Fig. 14 shows the experiment no. 8. The cell was heated from both sides with subsequent temperature steps. In this experiment only two thermocouples could measure the cell case temperature. (The actual motivation for this experiment was to do Electrochemical Impedance Spectroscopy (EIS) measurements at different temperatures. The temperature steps look

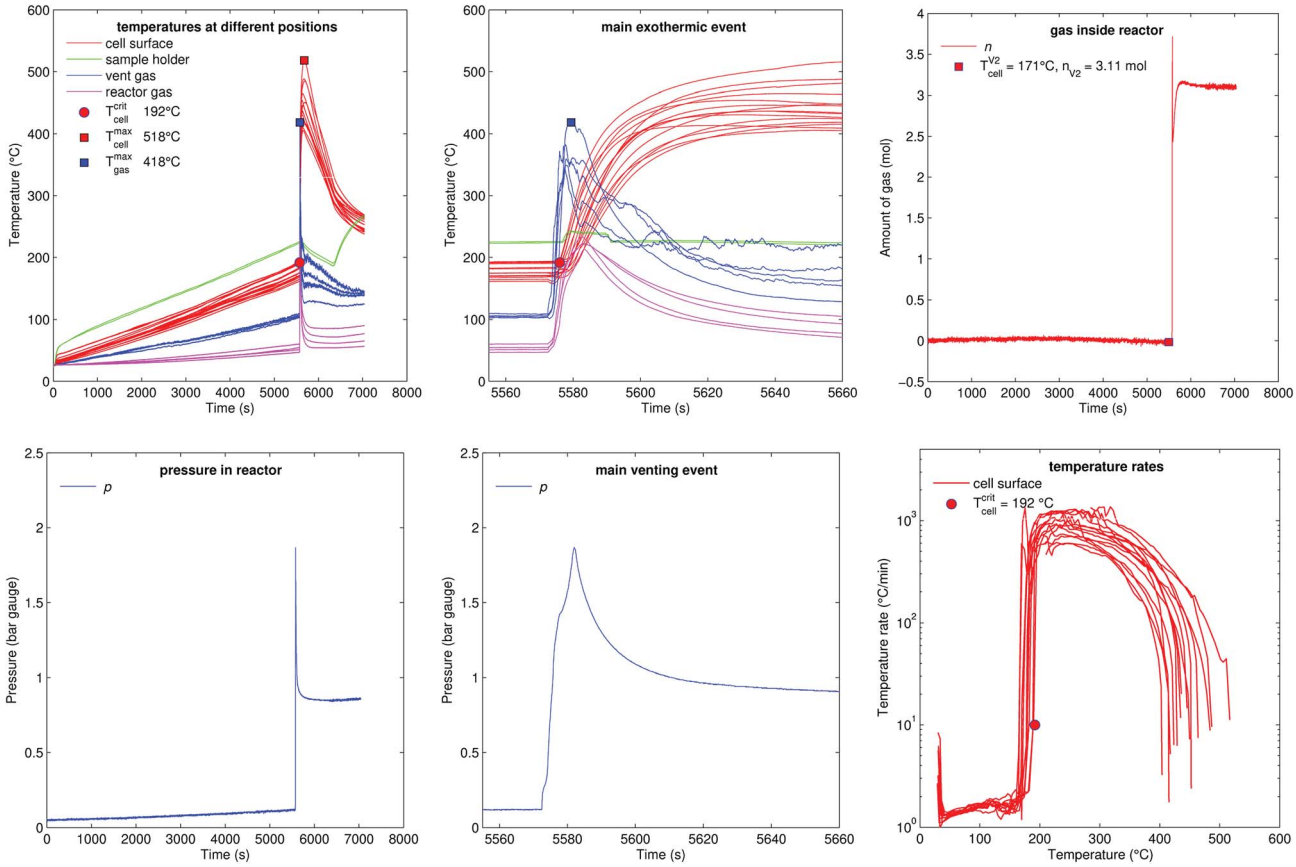

Fig. 12 Experiment no. 3 (heat ramp), with an internal short circuit occurring at 171 °C. (left) Temperatures and gas pressure during the whole duration of the experiment and (centre) during the main exothermic event. (right) Amount of released gas into the reactor and temperature rates of the cell case sensors.

sporadic, because they were set manually during the experiment. EIS results could not be included in this paper.)

The cell showed the minor venting events at 13 000 s (releasing 0.4 mol), it was heated further to 180 °C then the cell was let to cool down to 167 °C. Surprisingly – after cooling down from 180 °C to 167 °C – a short circuit occurred and caused a thermal runaway at 14 250 s. The cell released additional gas during its major venting (2.9 mol, 405 °C) and the cell reached a maximal temperature of 427 °C.

5.6 Reactor heating (A2)

Fig. 15 shows the experiment no. 10. Here not the sample holder, but the whole reactor was heated. The reactor reached a temperature above 200 °C when the cell went into thermal runaway. The main difference to the previous experiments was, that more of the released material stayed in the gas phase, because the hot walls of the reactor prevented condensation inside the vessel. After the minor venting at $t = 8280$ s the reactor contained $n_{V1} = 1.1$ mol of gas instead of 0.25–0.51 mol as in previous experiments. The additional amount of gas was likely composed of electrolyte-solvent vapours which stayed in gas phase because of high reactor temperature. A possible candidate for the additional electrolyte vapour could be ethyl methyl carbonate[21] (EMC) with a molecular mass 104 g mol^{-1} and a boiling point of 110 °C. An additional amount of 0.59–0.85 mol of EMC vapour has a mass of 61–88 g which corresponds to about 5% of the cell mass.

The minor venting was followed by the main thermal event and major gas release at $t = 8700$ s: the cell reached a surface temperature of $T_{cell}^{max} = 495$ °C and released additional $n_{V2} = 4.51$ mol of gas. The amount of gas n continued to increase after the major venting (from 5.5 mol to 7.3 mol), probably due to further thermal decomposition of the remaining solvent components on the hot reactor walls. The reactor heating was switched off at 11 500 s.

The calculated venting rate of the major event was higher than in most previous experiments $\dot{n}_{V2}^{ch} = 1.3$ mol s^{-1}. The increase in venting rate was not caused by a higher reaction rate of the cell, but by electrolyte vapour which contributed to a higher value of n_{V2}.

6 Discussion

How are the results useful for designing safe battery packs? A robust battery pack should not allow propagation of thermal runaway from cell to cell and it needs safe vent-gas management.

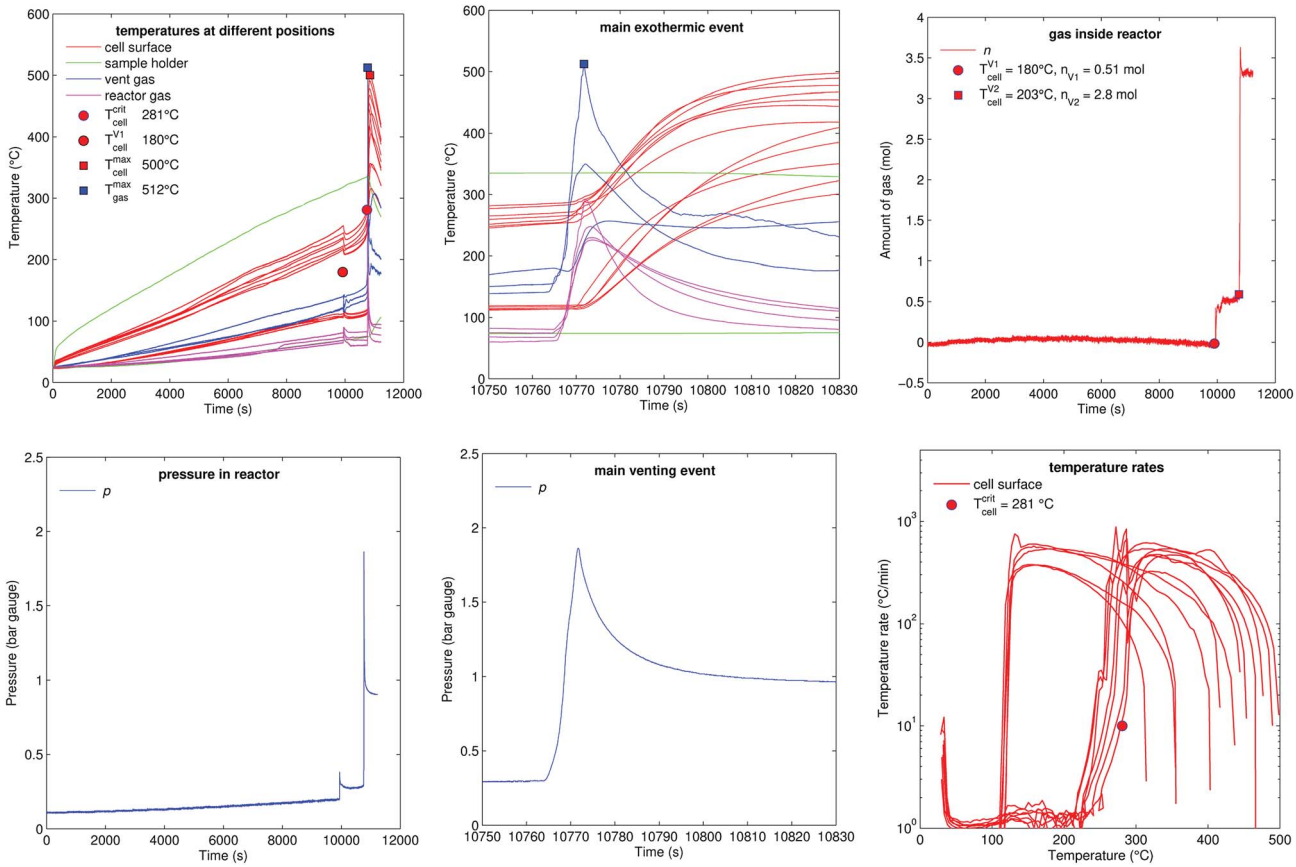

Fig. 13 Experiment no. 7 (one sided heating). (left) Temperatures and gas pressure during the whole duration of the experiment and (centre) during the main exothermic event. (right) Amount of released gas into the reactor and temperature rates of the cell case sensors. Here the one-sided heating method created a huge temperature difference between the heated and the non-heated surface of the cell. This divided the cell case temperature sensors into two groups: ones that measured the heated side of the cell and ones that measured the cooler side. Sensors of both groups reached above 400 °C during the thermal runaway of the cell. Both groups are also clearly seen in the rate plot. The thermal runaway started, when the hottest sensor on the heated side of the cell reached 281 °C. The thermal runaway propagated throughout the cell from the hot side to the cooler side. After it reached the cooler side it caused a steep temperature rate increase in the sensors which were only at 120 °C.

6.1 Thermal runaway propagation

First we focus on the thermal runaway propagation: a chain reaction which occurs when a failed cell heats its adjacent cells to a point, where they transit into thermal runaway as well, they in turn infecting the next row of adjacent cells, ultimately ending in a full battery fire. The propagation progresses by heat transfer from one cell to the next. For stacked metal-can cells (arranged as in Fig. 1) the main thermal interfaces for heat exchange are the large areas on the sides of the cells.

We have shown that thermal runaway of the initial cell can be caused by heating or a combination of heating and internal short circuit. Without internal short circuit, if the cell is heated uniformly, the cell will transit into rapid thermal runaway when its hottest point exceeds 246 °C. In a subsequent thermal runaway reaction the first failed cell may reach a temperature of up to 595 °C. The failed cell will then transfer the majority of the produced heat to one or two of its adjacent cells: each adjacent cell will be heated from one side.

In our experiments we compared uniform and one sided heating. One sided heating creates a huge temperature gradient from heated to non-heated cell side. In our experiments non-uniform heated cells transited into rapid thermal runaway when their hottest point exceeded 281 °C (while the opposite site was only at 120 °C). This is in contrast to uniform heating, where the critical temperature is already at 246 °C.

Such results can be used to develop and to validate thermal runaway models. Such models can further be used to determine if – in a certain scenario – thermal runaway propagation is possible or not. For example; the outcome of the propagation study may depend on the position of the failed cell in the cell stack.

In a first scenario: consider that the failed cell sits in the middle of the cell stack. For some reason it goes into thermal runaway and instantly reaches 595 °C, while the rest of the cells stays at ambient temperature at 25 °C. Next, the major amount of heat will be transported from the failed cell to its left and its right neighbour. If local temperatures inside the neighbours would reach some critical temperature, they would transit into thermal runaway as well, and the fault propagation would start.

In a second scenario: consider that the failed cell is the outermost cell in a cell stack. In contrast to the first scenario the failed cell has only one adjacent cell with which it will share

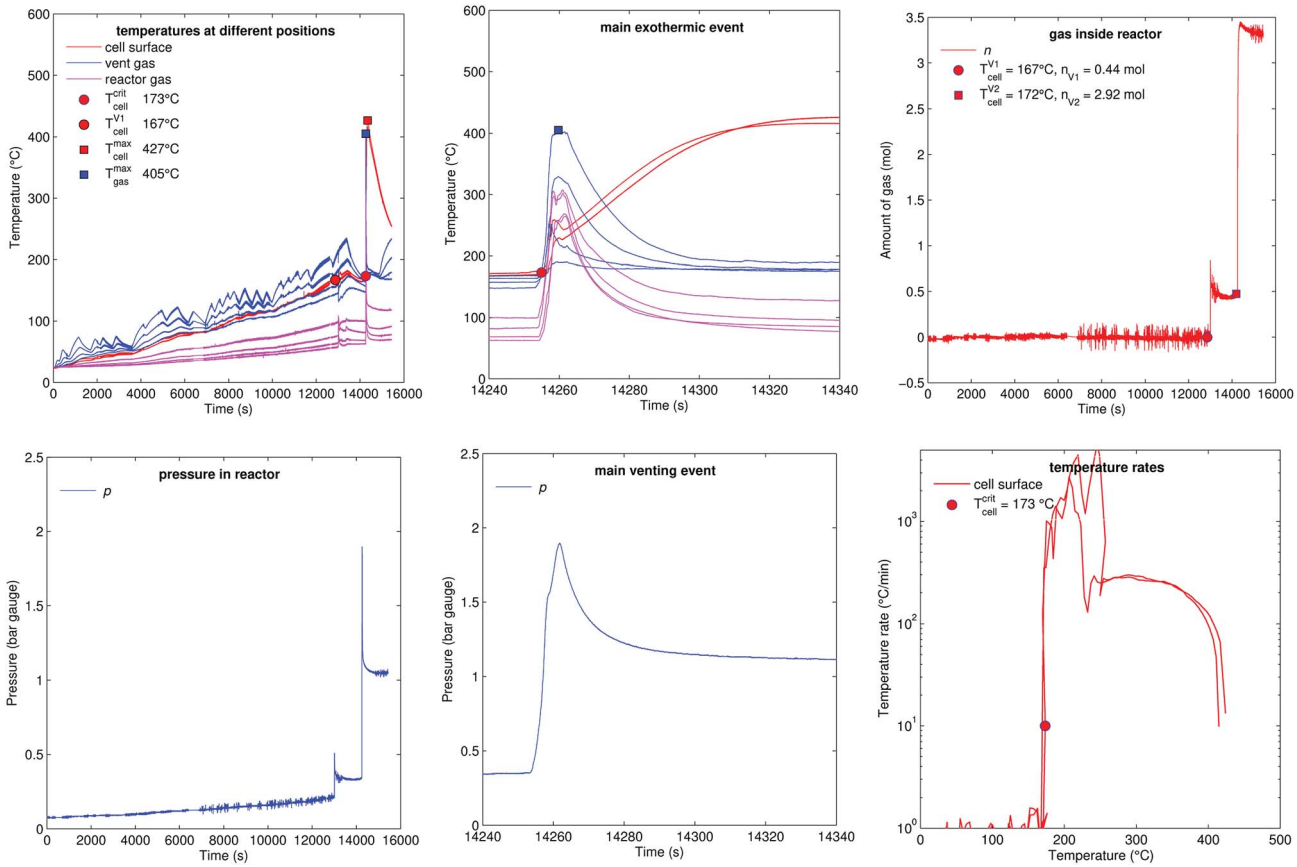

Fig. 14 Experiment no. 8 (stepwise heating), unfortunately only two cell temperature sensors remained intact in this experiment. (left) Temperatures and gas pressure during the whole duration of the experiment and (centre) during the main exothermic event. (right) Amount of released gas into the reactor and temperature rates of the cell case sensors.

most of the generated heat. If no other heat sinks are provided then propagation is more likely to happen then in the first scenario.

In general, to prevent the propagation, the heat from the failed cell must be distributed to as many cells (or other components with thermal capacities) as possible, while keeping the local temperatures of all non failed cells below their critical temperature. If the recipient of all heat is only one adjacent cell, propagation is very likely. With several heat recipients, propagation is less likely.

6.2 Vent gas management

A robust battery pack also needs a vent-gas management which consist of a battery pack enclosure which can withstand some overpressure and a venting duct which can guide the vent-gas to the outside. The main parameters for the design of those venting elements are the gas release rate, gas temperature and the gas composition. The gas temperature and release rate were measured in our experiments and the gas composition can be estimated from our previous experiments.[9,12]

We measured the gas release rate inside unheated reactor and compared it to gas release in a heated reactor. Here the reactor simulated the environment inside a battery pack. The first failed cell would release gas into a pack with normal working temperature, and some gas components would condensate, before they exit through the venting port. If propagation occurs, the next cell would vent inside an already preheated pack, fewer gas would condensate inside the pack, and more gas would exit though the venting port. If propagation can not be excluded, venting tests should be done in a heated reactor. Our experiments showed a trend of higher venting rate for a heated reactor, but, unfortunately, also a high variation from experiment to experiment (Fig. 10).

For a first exemplary specification of the venting port we assume an isentropic flow of the vent-gas.[22] The gas is released by the failed cell, then it flows inside the battery pack and exits through the venting port to the outside of the battery pack. We assume that the main obstacle to be the venting port of the battery pack with its limiting cross section A.

For a simple estimation we further assume that the vent-gas consists of equal mole parts of H_2, CO_2 and CO. The gas has a mean mol mass $M_s = 0.02467$ kg mol^{-1} and the mean isentropic expansion factor $\gamma = 1.32$ at a temperature of $T^{V2}_{max} = 800$ K (Table 3). We further assume that the pressure inside the battery pack is $p_0 = 120$ kPa and the ambient pressure is $p_t = 100$ kPa, meaning $p_t - p_0 = 200$ mbar of overpressure caused by the failed cell during the venting event.

The flow factor Ψ is given by:

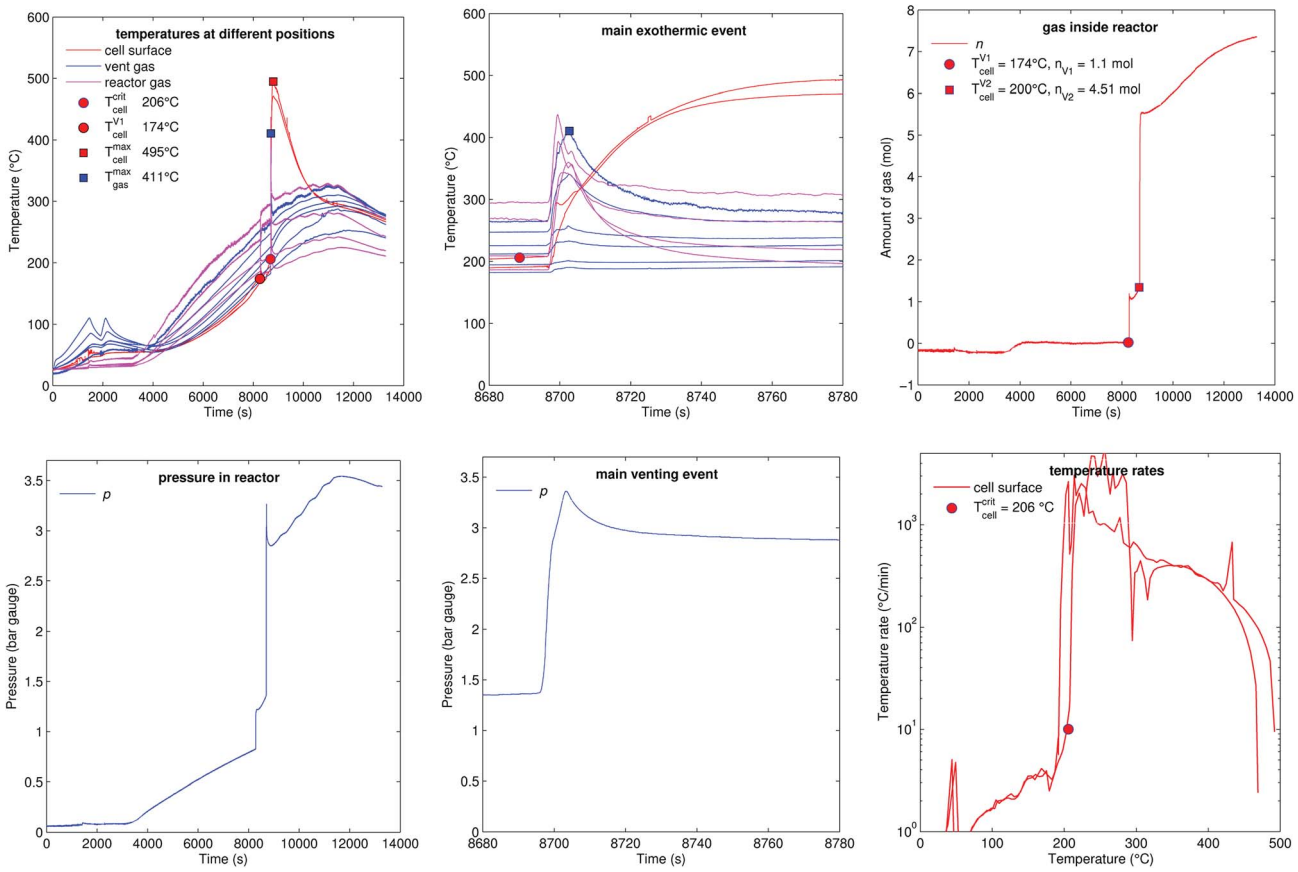

Fig. 15 Experiment no. 10 (reactor heating), unfortunately only two cell temperature sensors remained intact in this experiment. (left) Temperatures and gas pressure during the whole duration of the experiment and (centre) during the main exothermic event. (right) Amount of released gas into the reactor and temperature rates of the cell case sensors.

$$\Psi = \sqrt{\frac{2\gamma^2}{\gamma - 1}\left[\left(\frac{p_t}{p_0}\right)^{\frac{2}{\gamma}} - \left(\frac{p_t}{p_0}\right)^{\frac{\gamma+1}{\gamma}}\right]} = 0.60 \quad (7)$$

With the universal gas constant $R = 8.314$ mol J^{-1} s^{-1} and the characteristic venting rate of $\dot{n}_{V2}^{ch} = 1.39$ mol s^{-1} the mass flux equation for an isentropic flow gives the minimal cross section of the vent-port:

$$A = \frac{\dot{n}_{V2}^{ch}}{p_0 \Psi}\sqrt{\gamma R M_s T_{max}^{V2}} = 285 \text{ mm}^2 \quad (8)$$

and, finally, the diameter of the vent-port:

$$D = \sqrt{\frac{4A}{\pi}} = 19.1 \text{ mm} \quad (9)$$

This simple calculation shows the main dependencies between the vent gas temperature, composition and venting rate on the one side and the required size of the vent port on the other side. It does not account for complex geometric factors of the vent port inlet, friction effects and heat exchange between the vent gas and battery components. Some of those effects are covered in ISO 4126.

The calculation also does not account for a possible combustion of the vent gases inside the pack. Combustion (deflagration) with air volume inside the pack would cause significant pressure and temperature increase in the pack-casing.[11]

Table 3 Characteristics of typical vent-gas components at 800 K. The average is valid when the gas consists to 1/3 of each component. Retrieved from NIST Chemistry WebBook[23]

	C_p (J mol^{-1} K^{-1})	C_v (J mol^{-1} K^{-1})	γ	M (g mol^{-1})
H_2	29.65	21.34	1.39	2.02
CO	29.81	21.48	1.39	28.01
CO_2	51.46	43.13	1.19	44.00
Average			1.32	24.67

7 Conclusions

Eleven overtemperature experiments were performed with prismatic metal-can Li-ion cells with a capacity of 50 A h which were produced in 2009. The experiments were done inside a custom build gas-tight heatable reactor in nitrogen atmosphere. We used four different methods to heat the cells: temperature ramp with heating of both cell sides, temperature

ramp with heating of one side, stepwise heating and heating of the whole reactor.

With increasing temperature, the cells experience a sequence of events eventually finalizing in a exothermic thermal runaway reaction. An important finding is that sometimes the sequence of events is interrupted by an unforeseeable internal short circuit. When it occurs, the cell skips the remaining events and takes a direct route into final exothermic reaction. We suspect that the short circuits were caused by internal mechanical failures which damaged the electrical insulation inside the heated cells.

For cells with complex internal construction such as the tested metal-case cells it is important to repeat several test runs in order to capture the worst case outcome. The variability may be less an issue for cells with simpler construction such as pouch-type cells. The characteristics of the final reaction are: the final thermal runaway may start when the hottest point of the cell exceeds 206 °C, during thermal runaway the cell casing reaches a maximum temperature up to 594 °C and the cell releases an overall amount of up to 5.9 mol of vent-gas with up to 530 °C. When the vent-gas cools down to room temperature then part of it condensates and the remaining gas phase shrinks to a value between 2.9 mol and 4.6 mol.

Further findings are:

• The final thermal runaway reactions is triggered by either increasingly exothermic chemical reactions (classified into group A2) or by joule heat from internal short circuits (classified into group B1 or B2).

• Most cells belonged to group A2. They showed a preceding minor venting event (opening of burst plate and overpressure release from the cell) and – after further heating – a gradual onset of exothermic reactions and thermal runaway with a second major venting.

• In three experiments (group B1) internal short circuits occurred. The shorts triggered the final thermal runaway reaction and gas release before the first minor venting would normally happen.

• In one experiment (group B2) an internal short circuit triggered the thermal runaway after the first minor venting and further heating by the sample holder.

• For the tested cell type it is difficult to anticipate an imminent short circuit of a cell, because it can happen at temperatures as low as 155 °C and without previous venting, cell voltage drop or accelerating temperature increase of the cell casing.

• The cells release significant amounts of gas during thermal runaway: up to $n_v = 5.95$ mol (in liter at STP conditions $n_v = 133$ L).

• The gas release rate shows large variation from experiment to experiment, therefore several test are required for a reliable result. Up to 1.39 mol s^{-1} were measured.

• From the measured gas release rate we estimate a venting port with a diameter of at least 19.1 mm.

• The cell temperature measurements can be used to develop dynamic and spatially resolved thermal runaway models. Such models would be useful to determine at which conditions thermal runaway propagation occurs and to evaluate the effectiveness countermeasures against propagation.

In the next step we focus on newer cells with higher energy density and much higher maximal temperatures during thermal runaway. FTIR and GC equipment will be added to the test bench to quantify the vent gas composition.

Conflicts of interest

There are no conflicts to declare.

Acknowledgements

The publication was written at VIRTUAL VEHICLE Research Center and at Graz University of Technology in Graz, Austria. The authors would like to acknowledge the financial support of the COMET K2 – Competence Centers for Excellent Technologies Programme of the Federal Ministry for Transport, Innovation and Technology (bmvit), the Federal Ministry for Digital, Business and Enterprise (bmdw), the Austrian Research Promotion Agency (FFG), the Province of Styria and the Styrian Business Promotion Agency (SFG). The thermal runaway test stand was developed with technical and financial support by AVL List GmbH.

Notes and references

1 F. Larsson, S. Bertilsson, M. Furlani, I. Albinsson and B.-E. Mellander, *J. Power Sources*, 2018, **373**, 220–231.
2 P. Andersson, J. Anderson, F. Larsson and B.-e. Mellander, *2nd IAFSS European Symposium of Fire Safety Science*, Nicosia, 2015.
3 P. Andersson, J. Brandt and O. Willstrand, *Full scale fire-test of an electric hybrid bus*, SP Technical Research Institute of Sweden , SP Report 2016:05, 2016, ISBN 978-91-88349-12-5.
4 D. Sturk, L. Hoffmann and A. Ahlberg Tidblad, *Traffic Inj. Prev.*, 2015, **16**, S159–S164.
5 A. Lecocq, M. Bertana, B. Truchot and G. Marlair, *International Conference on Fires in Vehicles*, Boras, 2012, pp. 183–194.
6 C. Petit Boulanger, J. Thomazo, B. Azmi, O. Labadie, B. Poutrain, M. Gentilleau and H. Bazin, *24th ESV-Conference*, Gothenburg, 2015, pp. 1–7.
7 D. Struk, P. Gustafsson, H. Sundmark, R. Persson, K. Vavalidis, D. Dufault and N. Evrat, *24th ESV-Conference*, Gothenburg, 2015, pp. 1–10.
8 D. P. Finegan, E. Darcy, M. Keyser, B. Tjaden, T. M. M. Heenan, R. Jervis, J. J. Bailey, R. Malik, N. T. Vo, O. V. Magdysyuk, R. Atwood, M. Drakopoulos, M. DiMichiel, A. Rack, G. Hinds, D. J. L. Brett and P. R. Shearing, *Energy Environ. Sci.*, 2017, **10**, 1377–1388.
9 A. W. Golubkov, S. Scheikl, R. Planteu, G. Voitic, H. Wiltsche, C. Stangl, G. Fauler, A. Thaler and V. Hacker, *RSC Adv.*, 2015, **5**, 57171–57186.
10 J. Johnsplass, M. Henriksen, K. Vågsæther, J. Lundberg and D. Bjerketvedt, *Proceedings of the 58th Conference on*

Simulation and Modelling (SIMS 58), Reykjavik, 2017, pp. 157–161.

11 V. Somandepalli, K. Marr and Q. Horn, *SAE International Journal of Alternative Powertrains*, 2014, **3**(1), DOI: 10.4271/2014-01-1857.

12 A. W. Golubkov, D. Fuchs, J. Wagner, H. Wiltsche, C. Stangl, G. Fauler, G. Voitic, A. Thaler and V. Hacker, *RSC Adv.*, 2014, **4**, 3633.

13 M. Lammer, A. Königseder and V. Hacker, *RSC Adv.*, 2017, **7**, 24425–24429.

14 M. Lammer, A. Königseder, P. Gluschitz and V. Hacker, *J. Electrochem. Sci. Eng.*, 2018, **8**, 101.

15 A. Nedjalkov, J. Meyer, M. Köhring, A. Doering, M. Angelmahr, S. Dahle, A. Sander, A. Fischer and W. Schade, *Batteries*, 2016, **2**, 5.

16 C. F. Lopez, J. A. Jeevarajan and P. P. Mukherjee, *J. Electrochem. Soc.*, 2015, **162**, A1905–A1915.

17 N. S. Spinner and K. M. Hinnant, *Lithium-Ion Battery Failure: Effects of State of Charge and Packing Configuration*, 2016.

18 S. Wilke, B. Schweitzer, S. Khateeb and S. Al-Hallaj, *J. Power Sources*, 2017, **340**, 51–59.

19 X. Feng, L. Lu, M. Ouyang, J. Li and X. He, *Energy*, 2016, **115**, 194–208.

20 D. Dvorak, H. Lacher and D. Simic, *2014 IEEE Vehicle Power and Propulsion Conference (VPPC)*, 2014, pp. 1–6.

21 K. Xu, *Chem. Rev.*, 2004, **104**, 4303–4417.

22 P. Balachandran, *Gas dynamics for engineers*, PHI Learning Private Limited, Delhi, 2010, ch. Isentropic, pp. 70–71.

23 E. Lemmon, M. McLinden and D. Friend, Thermophysical Properties of Fluid Systems, in *NIST Chemistry WebBook*, National Institute of Standards and Technology, Gaithersburg MD, 2018.

3 Results From Project SafeBattery, Part 1: Safety Recommendations

3.1 Background

Batteries of EVs are safe at temperatures below ca. 80 °C. If a Li-ion cell reaches temperatures above ca. 80 °C the cells start to degenerate and when they reach a even higher temperatures they may transit into TR [35, 36, 39]. An over temperature of a cell may be caused by failures inside the cell or by the neighbourhood of the cell. The most prominent failures inside a cell are internal short circuits. They can be caused by Li-dendrites, Cu-dendrites, foreign particles and by mechanical damage to the cell. Over-temperature may be caused by failures outside of the cell: external fire, overheated or failed adjacent cells, failed electrical connectors with excessive resistance generating joule heat.

Not only normal operation of large Li-ion batteries in a vehicle but also testing of batteries in laboratories needs special safety requirements. Damaged cells may release gas, heat and particles which can be a threat to the personnel. Therefore, it was decided to measure the TR characteristics of the selected cells early in the project SafeBattery.

This chapter focuses on safety relevant characteristics of the selected cell during over-temperature experiments. Fully charged and partially charged cells were tested in the laboratory of VVR. In the next step safety critical parameters like maximal temperatures and the gas composition were derived from measured data. These parameters were used to calculate different scenarios like TR of a cell inside an enclosure. The scenarios were used to make safety recommendations for testing laboratories.

Several staff members from VVR contributed to this chapter. René Planteu, Bernhard Rasch, Oliver Korak and Thomas Humitsch did the experimental work in the laboratory. The author of this dissertation (Andrey Golubkov) was responsible for the test design, data analysis (except for the vent-gas analysis with GC and FTIR) and wrote the text of this chapter. The measurement and documentation of the vent-gas components was done by Christiane Essl.

3.2 Literature Review

3.2.1 Control of battery fire

During TR Li-ion cells reach temperatures above 900 °C as shown in the included publications (chapter 2) and the first literature review (section 1.7). High cell temperatures may start battery fire [26, 62]. Cases of large battery fires are covered by media [63–68]. Sun *et al.* [12] published a review article on case of EV-fire. They show that fires of EVs may have higher peak heat release rates (PHHRs) than fires of conventional vehicles.

Fire suppression in laboratory environment may be realized by cooling of the battery and by restricting access to O_2. Sun *et al.* [12] recommend water as the most effective coolant but warn that care must be taken when water comes into contact with high electric potentials inside the battery. Water cools the failed cells and inhibits TR-propagation to neighbouring cells. Large quantities of water may be needed, when the water is sprayed on the outside of a battery-pack (>2600 gal, >12 m^3 for a 16 kWh battery) and the firefight operation time may be as long as 50 min according to experiments by Blum and Long [69]. The cooling is most effective when water is injected directly into the battery pack [70, 71] and the amount of water can be significantly reduced (down to only 13 l [72]).

A review of battery fires in EVs and suitable extinguishing agents was compiled by Bisschop *et al.* [73]. They cite reports where different additives (F-500®, PyroCool®, FireIce®, Firesorb®) were tested. Most of those reports conclude that the additives reduce the amount of required water.

Sun *et al.* [12] and Bisschop *et al.* [73] note that distinguishing the visible flames

Table 3.1: Published explosion ranges of vent-gas - air mixtures.

LEL vol%	UEL vol%	source
6.3	30	Somandepalli *et al.* [74]
5	55	Li *et al.* [77]
5.79	–	Said *et al.* [78]
4.08	–	Chen *et al.* [26]
6.3	–	Baird *et al.* [27]

(burning of released gas) with CO_2 may not be sufficient to stop TR-propagation from cell to cell. If the fire is distinguished, but the TR-propagation is not stopped then unburned gases may escape into the surrounding of the battery. If the event happens in a closed building the unburned gases may accumulate and they may cause gas-deflagration.

3.2.2 Preventing deflagration of the vent-gas

The vent-gas of Li-ion cells contains high amounts of burnable components [27]. In fact, of all released components, only H_2O and CO_2 are not burnable. Combustion (deflagration) of the burnable released gas with air volume inside an enclosure would cause significant pressure and temperature increase in the enclosure [74]. Media reports cases where garage doors [68] or windows [75] were possibly damaged by deflagration of released gas. Mckinnon and Kerber [76] report a deflagration event during a firefighter operation in a energy storage system (ESS) container.
Mixtures of air and released vent-gas have a wide explosion window. Values for lower explosion limit (LEL) and upper explosion limit (UEL) are given in table 3.1. The LEL can be easily reached in an enclosure such as a temperature chamber. The ignition source could be the hot cell itself. Two strategies to prevent deflagration of the vent-gas are known:

- Increase the volume of the enclosure. More air lowers the concentration of the vent-gas. If the concentration stays below 50% of the LEL the enclosure must

not be treated as explosion-endangered area according to Austrian regulation §2, BGBl. II Nr. 309/2004[79].

- Decrease the amount of O_2 in the enclosure. The air in the enclosure may be either diluted or completely exchanged with a non flammable gas e.g. N_2, Ar or CO_2. The effects of dilution are published by Li *et al.* [77].

Practical measures to prevent deflagration are missing in the literature.

3.2.3 Control of overpressure inside a cell confinement

During TR the cell releases high amounts of vent-gas in short time. Even if deflagration can be prevented, it will still cause pressure increase inside a gas-tight enclosure. The enclosure may burst, when the inside pressure exceeds the design pressure. To prevent the bursting, the enclosure must be either designed to withstand high pressure (Like the reactor shown in fig. 1.7) or it must be outfitted with an overpressure valve or burst plate with sufficient cross-section A for pressure relief.
The input for the design of the overpressure-relief-device are the specifications of the confinement and the venting characteristics of the cell. These cell characteristics include the overall amount, the temperature, the composition and the release rate of the vent-gas. Literature values for the overall amount and the composition of the vent-gas are available (see section 1.7). Little literature exists on the release rate and temperature of the vent-gas. The only publication which reports temperature, amount and release-rate and which derives the necessary value for A is our own publication from 2018 (included in section 2.4).
New reports from our group which contain all four vent-gas parameter (including gas-composition) were published recently by Essl *et al.* [80] and Essl *et al.* [81].

3.2.4 Preventing intoxication by released vent gas

Many publications report the composition of the released vent-gas (see section 1.7). Fernandes *et al.* [82] included a good review in their paper. Most of the cited publications report high amounts of toxic CO, but do not recommend specific

safety measures. The other component which received a lot of attention is HF. Fluorine is contained in the electrolyte (as the salt – $LiPF_6$) and it can be contained in the binder.

Only one publication includes recommendations on how to handle released toxic gases: Diaz *et al.* [83] focused on toxic gases and identified HF, COF_2, acrolein, CO, HCL, formaldehyde and the electrolyte components with FTIR (Gasmet DX4000, with a resolution of $4\,cm^{-1}$). They conclude that up to $379\,m^3$ are contaminated by gases released from a small LFP based cell with a capacity of 1.1 A h. (This is probably the same cell type as in our publications section 2.1 and section 2.2.) According to Fernandes *et al.* [82] LFP cells release more toxic components than NMC and $LiCoO_2$ (LCO) cells and the cells release more toxic components in N_2 environment that in air environment. Sadly Diaz *et al.* skip the details on the amounts of the gas components and do not comment on the accuracy of quantification of the halogenated-gases with a FTIR which had relatively low spectral resolution.

Fernandes *et al.* [82] also measured HF in a concentration up to 10 ppm in overcharge tests. They noticed that the HF signal appeared after the main venting of the cell. The concentration of HF increased and the concentrations of all other components decreased after the TR finished. They conclude that the HF formation mechanism was decoupled from the TR reaction and offer a possible explanation: HF could be formulated when the Li-salt reacts with residual water in the reactor. Fernandes *et al.* do not report the overall amount of HF (in mol or L).

Recently Forestier *et al.* [84] published gas composition released during TR of small prototype cells (0.6 Ah). They quantify the amount of released electrolyte C_2H_4, CH_4, OCH_2, CO_2, CO, HF, POF_3 and apply ISO 13571 to asses the toxicity. Unfortunately their low maximal cell temperatures (420 °C) and the low ration of CO:CO_2 indicate that their cell reacted less violent than state-of-the-art cells (compare to section 1.7 and chapter 2).

Release of fluorinated gaseous compounds was also reported in [70, 85–90].

3.2.5 Preventing intoxication by electrolyte vapour

Little literature exist on toxicity of the electrolyte and electrolyte-vapour. Electrolyte vapour from cells with damaged casing is carcinogenic, and - at high concentrations - toxic [91]. Some electrolyte additives like 1,3-Propansulton (PS) [92, 93] are carcinogenic [94, 95].
Weber *et al.* [96] and Grützke *et al.* [97] investigate release of toxic alkyl fluorophosphates from components of discharged batteries. Grützke *et al.* state that critical lethal concentrations could be only released from large quantities of material (>290 kg).

3.2.6 Preventing inhalation of released solid particles

During TR the vent-gas jet carries high amounts of solid material from the cell to the outside. The ejected material consists of the electrode particles (graphite, metal-oxide or metal-phosphate) parts of the current collector of the anode (copper foil) and molten aluminium compounds. The material has high temperature and it may be ejected with high speed therefore it can damage neighbouring components. Zhang *et al.* [30, 32] and Patel *et al.* [98] report released particles with a broad distribution of sizes ranging from small particles with 2 µm [98] to bigger parts of the cell with 8 mm [32]. After the release the particles cool down and settle on the nearby surface. Patel *et al.* [98] report a mean particle diameter distribution of 6.5 µm. Such small particles/dust can be easily raised into the air and – since a large share of them is <4 µm – they can be inhaled deeply into the lungs [99]. Their admissible concentration in workplace atmospheres is regulated in the Technical Rules for Hazardous Substances (TRGS) [100].
In addition to the size of the particles also the elemental composition of the particles is relevant. Zhang *et al.* [30] found the following elements in settled particles released by abused Li-ion batteries: C, Ni, O, Cu, Al, Co, Mn and others in smaller quantities. Liao *et al.* [56] determined the crystal structures of the released particles with XRD. The main compounds were graphite, transition metal oxides and LiF. Essl *et al.* [80] reports particles containing Al_2O_3, $Li(M)_3O_4$ with M=Ni, Mn, Co, Mn_3O_4, and carbon with a broad size distribution ranging from 1 µm to 100 µm. Zhang *et*

al. [30, 32] note that the released material is harmful to humans and that it should be contained, but gives no specific advise for testing laboratory.

3.3 Cell Samples

To answer the above research questions a series of experiments was done with a cell type which should represent a typical automotive cell. The board of SafeBattery decided to use cells which were extracted from a Nissan Leaf. The main properties of the cell (fig. 3.1) are:

Manufacturer: Automotive Energy Supply Corporation (AESC)
Car Nissan Leaf 2016
Type pouch
Size of the electrode stack 189 mm x 228 mm x 8.3 mm
Mass 870 g
Nominal capacity: 42 Ah
Nominal voltage: 3.65 V
Energy density: 176 $\mathrm{W\,h\,kg^{-1}}$

The cell composition is described in detail in the publication of Kovachev *et al.* [101]. The open circuit voltage (OCV) curve of the cell is given in fig. 3.2.

If the tested cell is similar to other cell types, then the main findings from experiment results can also be applied to other cell types.
The focus of this work lies on TR characteristics. The specific energy which is released by the TR mainly depends on the chemical composition of the cathode. The energy release causes temperature increase and the propagation of the TR inside the cell. Those effects depend on the specific heat capacity C_p ([102, 103]) and heat conductivity λ ([104–106]) of the electrode stack. In turn, those quantities depend on the layer thicknesses and composition inside the stack.
Electrode stack composition for the tested cell and references from literature are compiled in table 3.2. Lain *et al.* [107] measured the layer thicknesses of nine commercial cylindrical Li-ion cells. From his publication four high energy density

Figure 3.1: Foto of one of the cells used in experiments described in this report.

cells with capacities >3.0 A h were selected. Loges *et al.* [104] published electrode thicknesses of commercial automotive Li-ion cells for EV/plug-in hybrid electric vehicle (EV) applications. From his publication data of the prismatic hard case (metal-can) cell and a pouch cell were selected. The comparison shows, that the layer thicknesses of the tested cell fall into the range of other commercial cells.
Another important quantities are the temperature-rate profile (or the onset temperature) during TR and the heat release of the TR. The TR characteristics of different cell types are compared in [51] and in section 2.2. Those publications show that the tested cell with its NMC/LMO cathode has a TR profile which is similar to other cells with NMC and NCA cathodes.
Based on the comparison to literature values it can be concluded that the general findings of the two final parts of this work with the selected cell can be transferred to other automotive Li-ion cells.

Table 3.2: Thicknesses (µm) and composition of the layers in the electrode stacks of commercial Li-ion batteries. Comparison of the tested cell to other commercial cells.

		selected cell			
		Kovachev [101]	Lain [107]	Loges [104]	
		pouch	cylindrical	prismatic	pouch
Capacity A h		42	3.0 to 4.8	60	50
Energy density W h kg^{-1}		176	245 to 263	n.a.	n.a.
Anode	coating	65	45 to 85	57.2	72.8
	copper foil	10	10 to 14	9.7	14.2
	type	graphite	graphite	graphite	graphite
Separator	polymer	17	7 to 10	n.a.	n.a.
	Al_2O_3 coating	3	n.a.	n.a.	n.a.
Cathode	coating	75	44 to 71	65	56.7
	aluminum foil	20	10 to 14	15.2	23.7
	type	NMC/LMO	NMC or NCA	NMC	NMC

3.4 Test-Stand

3.4.1 Cell sample holder

An already existing sample holder for pouch cells was adopted for the first five experiments in this part of the thesis. The experiments were done with the cell sandwiched inside a sample holder which consisted of several layers. The stack consisted of the following elements, beginning with the lowest layer: stainless steel plate (10 mm), thermal insulation, thermocouples, cell, thermocouples, thermal insulation, stainless steel plate.

The stiff outer steel plates were compressed by four springs. The plates applied a uniform force to the layers and to the cell between them. The cell was compressed with a force of 3 kN in all experiments (this is equivalent to a mechanical pressure of 70 kPa on the cell surface). The steel plates were equipped with large heaters (2 x 500 W for each plate). The large heaters were activated to heat the whole sample-holder up to maximal 400 °C.

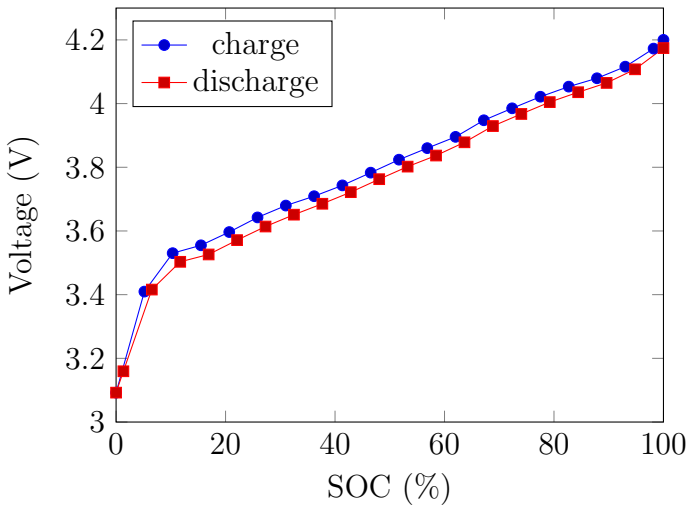

Figure 3.2: Charge and discharge OCV of the tested cell.

The function of the thermal insulation sheets was to prevent large heat flow between the compression plates and the cell: At cell temperatures above a critical temperature, exothermic reactions inside the cell start and the cell begins to self heat. To characterize the TR of the cell, the sample holder should not interfere with the self heating of the sample. The sample should perform the exothermic reactions as adiabatic as possible therefore insulation layers were put between the cell and the pressure plates. The thermal insulation sheets also provided channels for the thermocouple wires.

In the first experiments compressible mineral wool paper (Schuba BFP 120) with a thickness of 5 mm (uncompressed) and a thermal conductivity of $\lambda = 0.1 \cdots 0.22\ \mathrm{W\,m^{-1}\,K^{-1}}$ (uncompressed) was used. In later experiments the compressible mineral paper was replaced with incompressible mica sheets from RS Pro with a thickness of 1.5 mm and ($\lambda = 0.23\ \mathrm{W\,m^{-1}\,K^{-1}}$). Material data sheets for both materials are in the appendix: chapter 6.

In the experiments the cell was uniformly heated on its both large areas by the two steel plates (fig. 3.3). The cell was heated with a steady temperature ramp set to about $30\,^{\circ}\mathrm{C\,h^{-1}}$. With a uniform temperature the spatial effects play a lesser role. This makes it possible to identify average cell temperatures when different temperature depending events like venting, resistance increase or onset of TR occur. Steady increase of temperature while maintaining small temperature gradient along

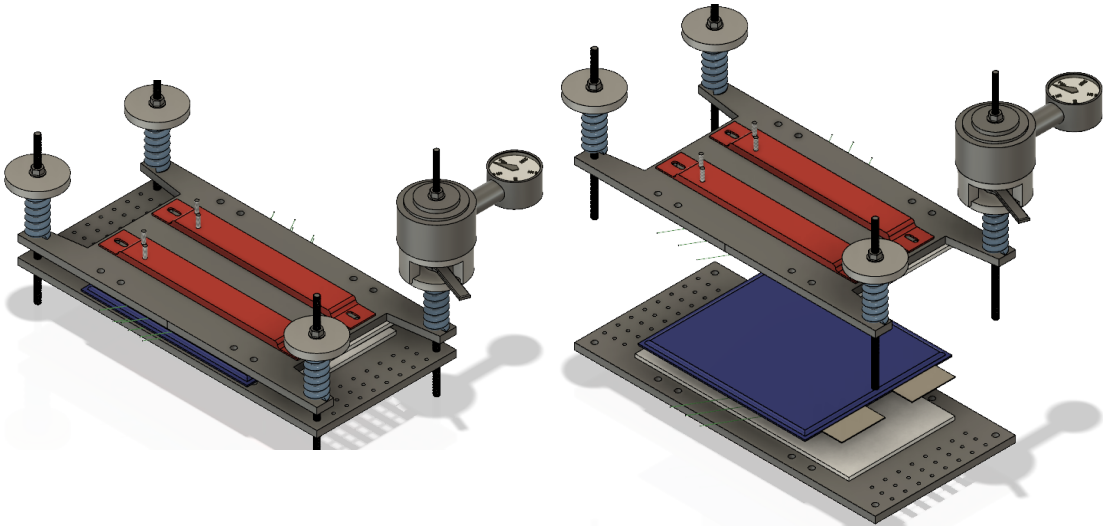

Figure 3.3: Sample holder used for uniform overtemperature experiments. The electric strip heater are coloured in red/brown.

the cell also make it possible to extract the self heating profile of the cell. The profile is essential input to TR modelling.

Type: OT-1205 HT S 240V1P 500W129760 from *Chromalox* https://www.chromalox.com/
Heated plate area: $A_P = 4 \times (38.1\ \text{mm} \times 305\ \text{mm}) = 116\ \text{cm}$
Rated power: $P_R = 4 \times 500\ \text{W} = 2000\ \text{W}$ at 240 V
Max temperature: 400°C

Cell case temperature was measured with K-type thermocouples. In most experiments 18 thermocouples were arranged in 3x3 grid on the lower and upper surface of the cell. Thermocouples were made from IEC Glassfibre Insulated Flat Pair Thermocouple Cable. Type: KX. Manufacturer RS-PRO, RS Best.-Nr. 236-3836. Class 2 $\pm 100\,\text{V}$ ($\pm 2.5\,°\text{C}$). The temperature sensing points were made by wire twisting: fig. 3.4.

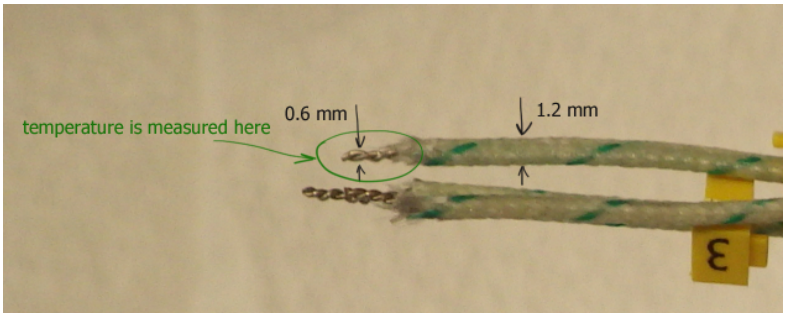

Figure 3.4: Picture of three thermocouple tips, including dimensions.

3.4.2 Reactor

The same reactor setup as for the work in sections 2.3 and 2.4 was used. The reactor was made from stainless steel. It has an volume of 120.8 l and is rated for 40 bar at 200°C. The main body of the reactor is fixed. The gas lines are connected to the back-side of the reactor. The blind-flange on one side can be opened. A sample holder stage is attached to the blind-flange. After the blind-flange is unscrewed from the main body it can be slid open along the rails until sample holder stage is completely outside of the reactor. The blind flange also provides all electrical feedthroughs for the sensors, the electrical heating of the sample holder and the electrical connection to the sample. The main body of the reactor can be heated to 200°C and the flange can be heated to 100°C. Figure 3.5 shows the reactor in opened and closed state.
At least four thermocouples measured the gas temperature in the reactor at different heights. Gas-pressure is measured by an industrial pressure sensor: GEMS 3300B06B0A05E000 (range of 0 $\mathrm{bar_{absolut}}$ to 6 $\mathrm{bar_{absolut}}$).

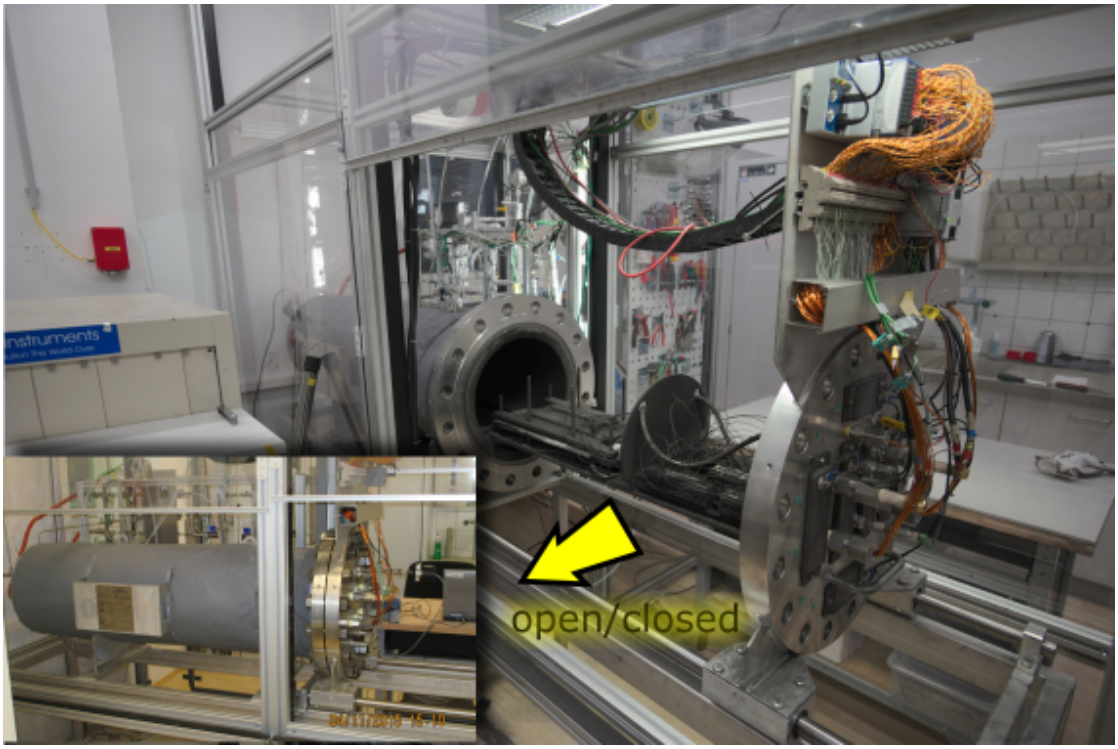

Figure 3.5: Reactor in opened and closed state.

Specifications

Performance	
Long Term Drift	0.2% FS/YR (non-cumulative)
Accuracy	0.25% FS
Thermal Error	±1% max./80°C (176°F)
Compensated Temperatures	-20°C to +100°C (-4°F to +212°F)
Operating Temperatures	-40°C to +125°C (-40°F to +257°F)
Zero Tolerance	±0.5% of span, max.
Span Tolerance	±1% of span, max.
Fatigue Life	Designed for more than 100 M cycles

Figure 3.6: Specs. of 3300B06B0A05E000 gas-pressure sensor.

3.4.3 Plumbing

Outgoing gas-lines connect the reactor to different equipment: fig. 3.7. Gas lines to the gas analysis and to the vacuum pump are heated to prevent condensation. Cooling traps and washing flasks are used to collect the condensate.

3.4.4 Gas analysis

The gas composition is quantified with two complementary methods. FTIR is used to measure all infrared (IR) active gases and GC is used to measure all permanent gases. The results of the two methods are combined into one table (fig. 3.8). Depending on expected gas components and their concentration range the measured results of a method, either FTIR or GC, can be chosen. FTIR results were compared to the test gas concentrations with the accuracy analysis result of at least four percent of the measured concentration value (for permanent gases). With the FTIR it is possible to quantify HF and H_2O. GC is calibrated with test gas at different concentrations and has its benefits at large concentrations of permanent gases, especially H_2, N_2 and O_2.
Details of our gas-measurement setup and accuracy analysis can be found in the recent publication by Essl *et al.* [80].

FTIR

For gas analysis with FTIR we use a Bruker MATRIX-MG01 with a resolution of $0.5\,\mathrm{cm}^{-1}$ and a gas-measurement chamber at a temperature of 190 °C. The upstream gas connection to the reactor is heated to 170 °C. Therefore, all IR active gases that have a condensation temperature below 170 °C will stay in gas phase and will be detected by the FTIR.

GC

For gas analysis with GC we use Agilent microGC 3000 with three columns and thermal conductivity detector (TCD) detectors: Molsieve (10m x 320µm x 12µm),

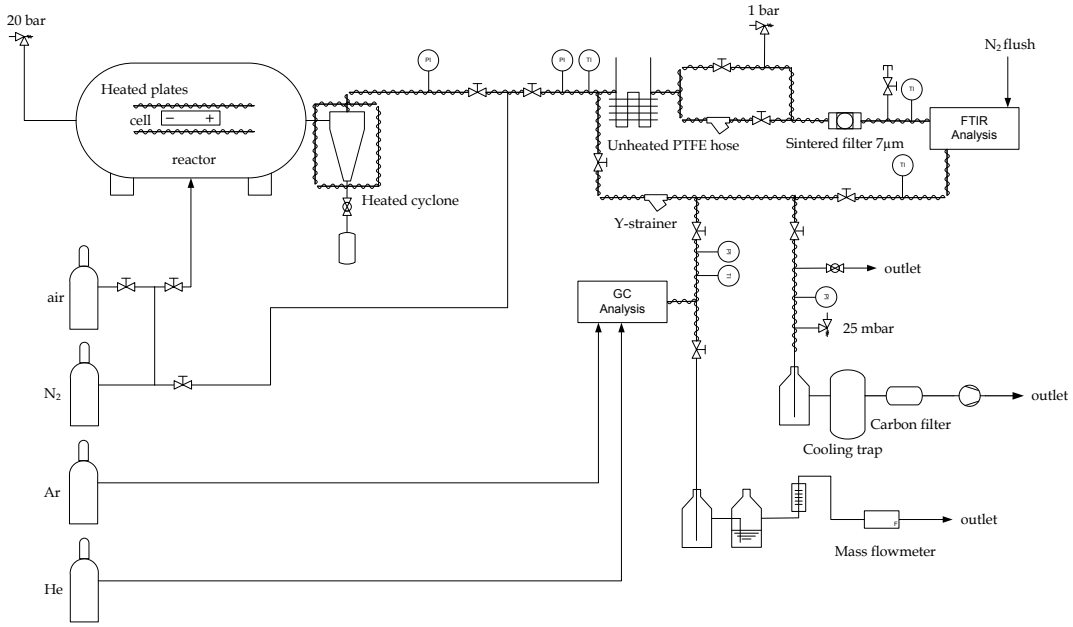

Figure 3.7: Simplified sketch of the whole test stand.

	Gases	Comment	GC	FTIR
Hydrogen	**H_2**	highly flammable	yes	
Nitrogen	N_2		yes	
Oxygen	O_2		yes	
Ethin	**C_2H_2**	flammable	yes	yes
Ethan	**C_2H_4**	flammable	yes	yes
Ethen	**C_2H_6**	flammable	yes	yes
Methan	**CH_4**	flammable	yes	yes
Carbon monoxid	**CO**	toxic, flammable	yes	yes
Carbon dioxid	CO_2		yes	yes
Diethylcarbonat	DEC			yes
Dimethylcarbonat	DMC			yes
Ethylencarbonat	EC			yes
Ethylmethylcarbonat	EMC			yes
Hydrogen dioxide	H_2O			yes
Hexane	C_6H_{14}		yes	yes
Hydrogen fluoride	**HF**	toxic, corrosive		yes
Butane	C_4H_{10}	flammable	yes	yes
Phosphoryl fluoride	POF3			yes
Phosphorus pentafluoride	PF5	toxic, corrosive		yes
Sulfur dioxide	SO2			yes
Sulfur trioxide	SO3			yes

Expected, safety-relevant and measureable gases:
conventional gas chromatography (GC)
versus FTIR spectrometer (FTIR)

GC and FTIR applied parallel

→ best combination to characterise battery failure cases

Figure 3.8: Comparison of used GC and FTIR to measure the composition of the ventgas.

Plot U (8m x 320µm x 30 µm) and OV1 (8m x 150µm x 2,0µm). The GC is calibrated for: H_2, O_2, N_2, CH_4, CO, CO_2, C_2H_6, C_2H_4 and C_2H_2.

3.4.5 DAQ system

The data aquisition (DAQ) system is fixed on a mounting plate on top of the blind flange (fig. 3.5). The short distance between the DAQ system and the electrical feedthrougs in the blind flange assures good signal quality. The DAQ system consists of several components from National Instruments. The sampling rate was set to 60 S/s for each channel.

NI cDAQ-9178 8-slot chassis for different I/O Modules. USB 2.0 connection to the PC with LabView Software.

4 x NI 9212 8 channels for temperature measurements (k-type thermocouples), build in cold junction compensation, Maximum sampling rate 95 S/s, accuracy 0.29°C

NI 9208 16 channels for ±20 mA signals, 24 bit resolution, maximum sampling rate 500 S/s. Used for readout of pressure sensors.

NI 9206 16 differential channels, voltage measurement, Maximum sampling rate 8 kS/s. Used to measure the cell voltage and the voltage of the current-shunt.

NI 9217 4 channels, PT100 RTD or strain gauge analog Input. Measures the PT100 temperatures. Maximum sampling rate 50 S/s.

3.5 Experiment Sequence

All TR experiments were carried out in a heavy duty test rig (section 3.4). The experiments were executed with the following base-line steps:

1. Cell is put into the sample holder and mechanically pressurized with 3 kN
2. Sample holder is fixed inside the reactor
3. Reactor is closed
4. Reactor is evacuated
5. Reactor is filled with inert gas (N_2) until ambient pressure reached

6. Gas analysis, check for air leaks with GC
7. All gas-valves are closed. (The reactor is hermetically sealed.)
8. Sample is charged/discharged to either 0%, 30% or 100% SOC (in case of 100% SOC the CC-CV method is used)
9. The data acquisition system is started
10. The cell is heated by the sample holder
11. The heating is manually switched off, when TR of the cell starts. If TR can not occur (because cell is discharged) then the cell is heated further above 200 °C and the hater is switched off between 250 °C to 300 °C
12. The cell reaches maximal temperature, either by external heating or by self-heating due to the TR
13. After the heating and TR finishes: wait for 5 min
14. Gas analysis with GC and FTIR

After the experiment the whole reactor is heated from 100 °C to 200 °C and evacuated to 100 mbar to extract the vent-gas and condensate. The removed gas is guided though a cooling trap and an active carbon filter and exits the vacuum pump into the fume-hood. The condensate is collected in the cooling trap and removed after every experiment.

3.6 Analysis Methods

3.6.1 Amount of gas inside the reactor

During the thermal runaway of a cell, gas is released into the sealed reactor. The amount of produced vent gas is estimated similar to the method described in section 2.4.

As described in section 2.4 the amount of produced vent gas is calculated with the ideal gas law

$$n(t) = \frac{p(t)V}{R\,\langle T_{gas}(t)\rangle} \tag{3.1}$$

The required pressure is measured with the pressure sensor. The estimation of the $\langle T_{gas}(t) \rangle$ differs slightly from section 2.4: the correction factor c_g only corrects the measured values above 25 °C.

$$\langle T_{gas}(t) \rangle = 273.15 + 25 + c_g \, (\frac{1}{4} \sum_{i=1}^{4} T_{gas}^{i}(t) - 25) \tag{3.2}$$

The factor c_g compensates the temperature deviations originating from convective flow between the heated sample holder and the not heated reactor. It is assumed that the reactor has a temperature of 25°C. The values of c_g typically range between 0.3 for hot-spot experiments with small heaters and 0.8 for heating of the whole sample holder.
The c_g was evaluated for each experiment individually. It is done by observing the value of n between the start of experiment and the first venting of the cell. At the beginning of the experiment the reactor and the cell are gas tight sealed. The heating ramp is started and when the temperature of the cell is high enough, its seals fail and the cell starts to release gas into the reactor. The amount of gas n from the start of the heating ramp to the failing of the seals remains constant and corresponds to (3.1). The value of c_g is adjusted, so that the calculated n indeed stays constant between the start of experiment and the start of gas release.

3.6.2 Amount of released gas

In the thermal runaway experiment the sample holder heats the cell and the cell releases gas before and after the TR. The sum of the gas releases is the overall released vent-gas during the experiment:

$$n_V = n_{V1} + n_{V2} \tag{3.3}$$

3.6.3 Venting-rate of the gas

The venting rate, or speed of gas release was estimated with the same algorithm as in section 2.4.

3.7 Experiments

3.7.1 Experiment T0139

In this experiment the cell was (actually unintentionally) discharged to 0 % SOC and the heating experiment started with a cell voltage of 3.12 V. The cell was placed in a sample holder fig. 3.12 and heated with a temperature ramp as described in section 3.5. The cell was heated for 10 h and up to a maximal cell temperature of 242 °C. Successive current pulses of ±1 A with a duration of 1 s were used to observe the internal resistance of the cell.

0 s Start of heating ramp
15000 s Average cell temperature 128 °C, cell starts to release gas
30000 s Average cell temperature 180 °C to 200 °C. Cell resistance starts to increase up to 170 mΩ.
35700 s Experiment is stopped (to prevent damage to the heater elements)

Discussion: An exothermic reaction was not observed. The electrical resistance increased by three magnitudes. The resistance increase can be explained by different propositions: (1) evaporation of all electrolyte, thus preventing the ionic transport or (2) damage to the separator, preventing ionic transport through the separator. The voltage of the cell started to decrease rapidly at 190 °C and the cell deep discharged to 0.54 V eventually (fig. 3.11).
The cell released 0.41 mol of gas. The cell would probably release additional gas, if heated further, but the laboratory crew had to stop the experiment because of late time and concerns about the high temperature of the strip heaters. The gas composition was measured with the GC (the FTIR was not available) therefore electrolyte vapour was not quantified.
Visually the cell showed only minor damage (fig. 3.13), but its mass changed by −15.3 %. The mass reduction was probably caused by evaporation of electrolyte. The mass fraction is comparable to the amount of electrolyte used for Li-ion cells (an electrolyte mass fraction of 10% to 16% was found for 18650 cells described in section 2.1).

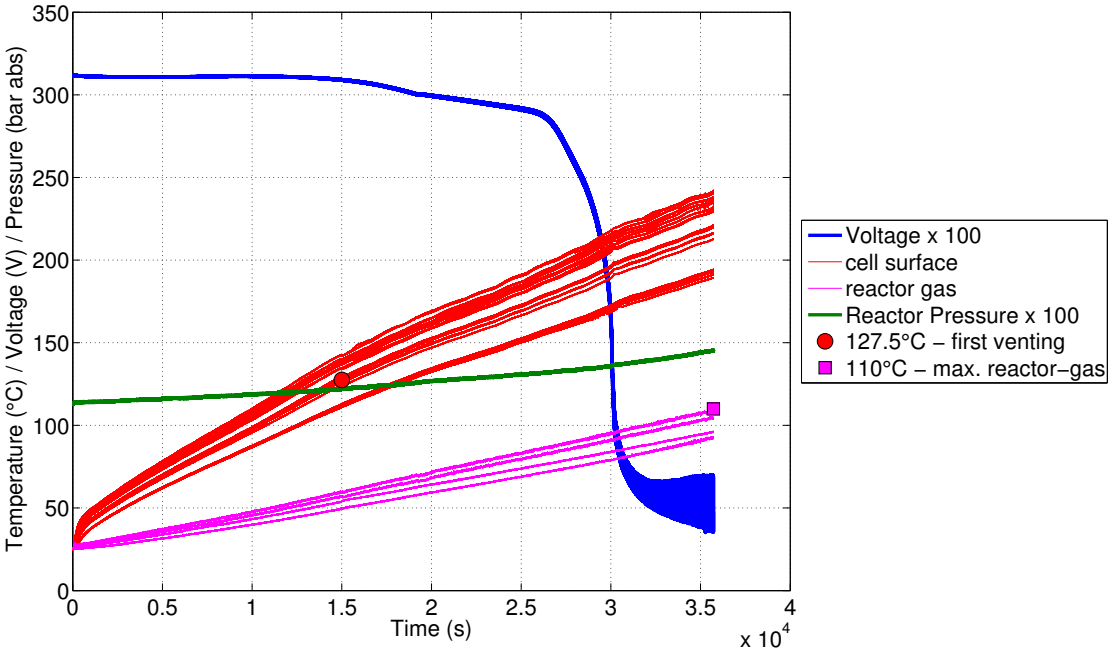

Figure 3.9: Experiment T0139. Plot of all sensor values. The blue curve represents the cell voltage. The envelope of the cell voltage is proportional to the resistance increase of the cell as it is cycled with ±1 A pulses. The green line is the *absolute* gas pressure in the reactor.

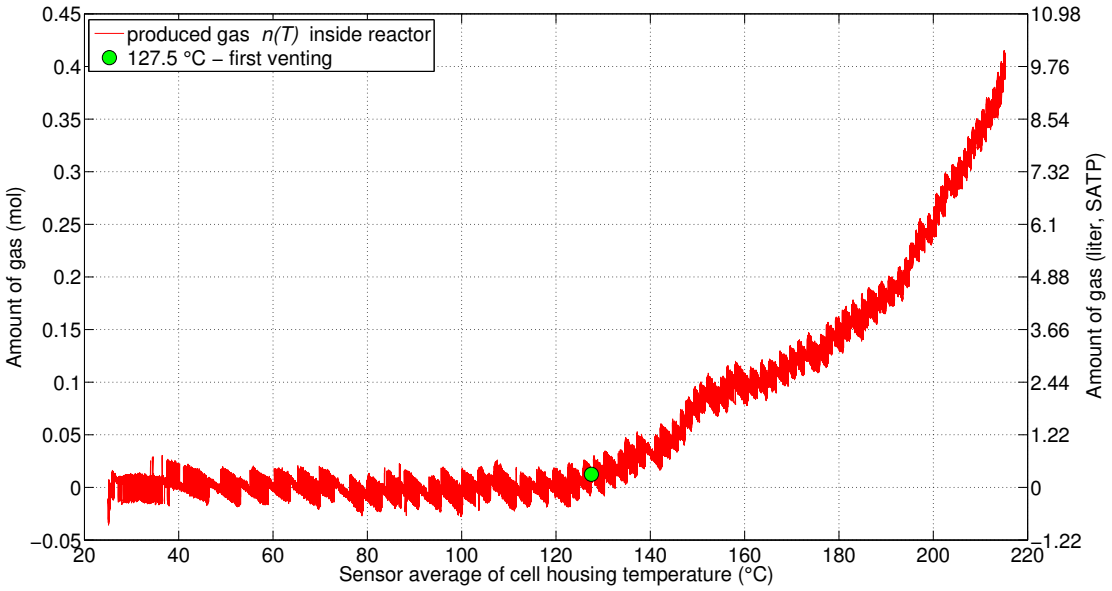

Figure 3.10: Experiment T0139. Released gas plotted vs. the average cell case temperature.

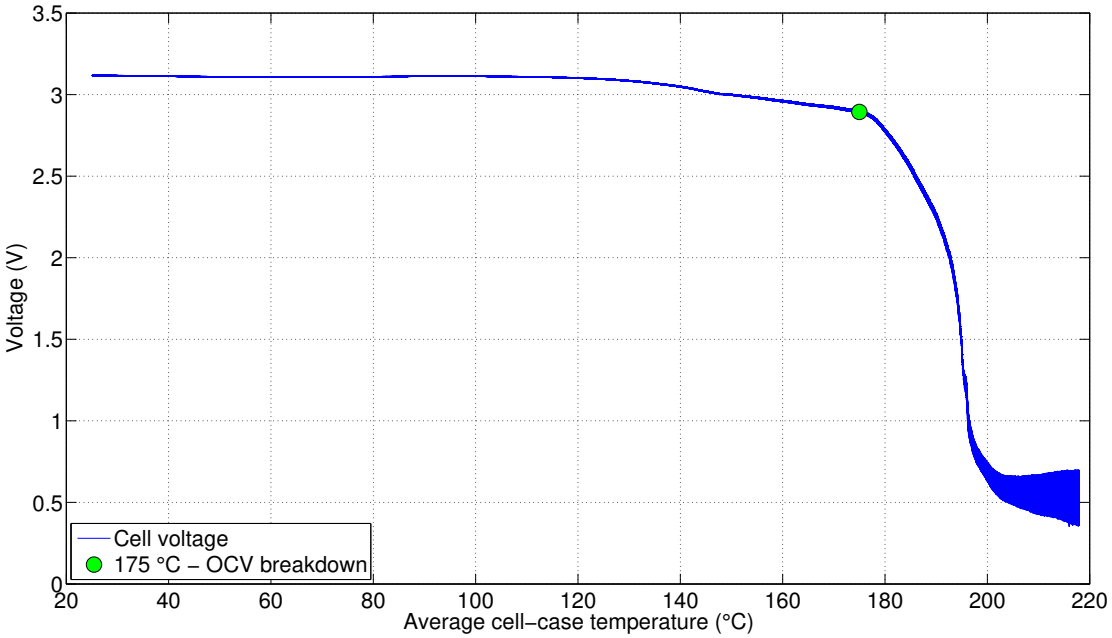

Figure 3.11: Experiment T0139. Cell voltage vs. average cell temperature.

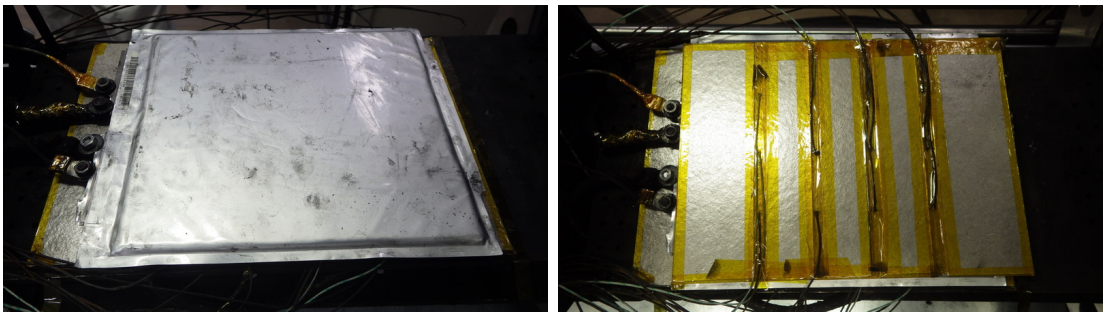

Figure 3.12: T0139. (left) Cell placed on the lower part of the sample holder. (right) Cell covered with a thermal insulation made from mica sheet. Note the protrusions in the mica sheet for the thermocouples to measure the cell case temperatures at different positions in a grid pattern.

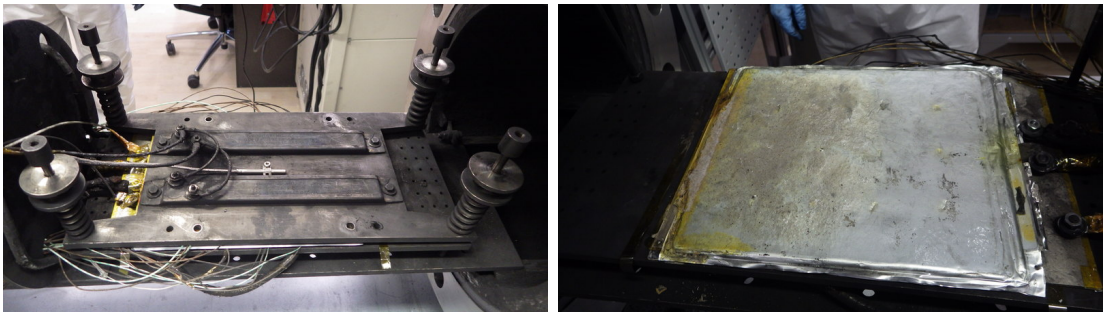

Figure 3.13: T0139. (left) Complete test setup. (right) Cell after the experiment.

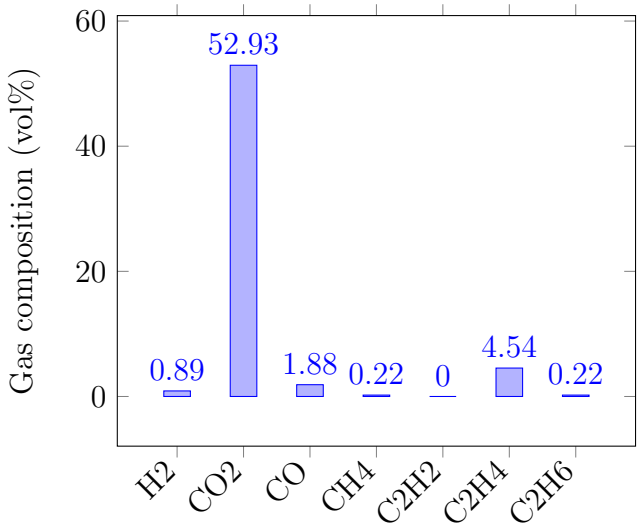

Figure 3.14: Experiment T0139. Detected gas components which were released by the cell. Gas composition was measured only by the GC.

3.7.2 Experiment T0141

The next experiment was almost a repetition of the previously described T0139. The difference was, that the cell was properly charged to 30% SOC resulting in a terminal voltage of 3.67 V at the start of the experiment. The cell was placed in a sample holder fig. 3.18 and heated with a temperature ramp as described in section 3.5. Near the end of the experiment at 38 100 s the heater power was increased to reach higher maximal temperature. The cell was heated for 11 h and up to a maximal cell temperature of 309 °C. As in T0139, current pulses of ±1 A with a duration of 1 s were used to observe the internal resistance of the cell.

0 s Start of heating ramp
13500 s Average cell temperature 127 °C, cell starts to release gas
27000 s Average cell temperature 200 °C. Cell resistance starts to increase up to 50 mΩ.
38100 s Increase of heater power to reach higher temperatures
39200 s Experiment is stopped

Discussion: The result of the experiment was very similar to the previous experiment T0139 with the completely discharged cell. Again, an exothermic reaction was not observed. The cell showed a slightly different voltage profile upon heating. The voltage decreased with inflection points at 100 °C and 190 °C. The voltage stabilised above 230 °C at 3.04 V(fig. 3.17). Again, the electrical resistance increased by several magnitudes.
The cell released 0.53 mol of gas (fig. 3.16). Again, the cell would probably release additional gas, if heated further, but unfortunately the crew had to stop the experiment because of late time. The gas composition was measured with the GC and FTIR. The amount of electrolyte vapour in the reactor could be measured (fig. 3.20).
Visually the cell showed only minor damage fig. 3.19, again similar to T0139. The mass change was not recorded.

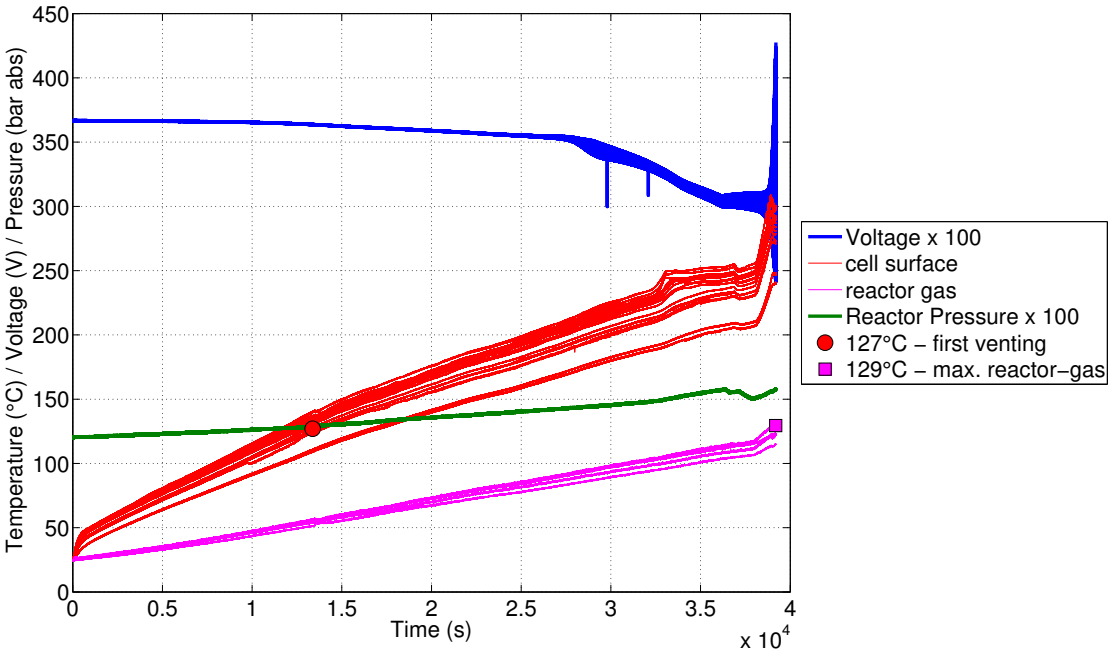

Figure 3.15: Experiment T0141. Plot of all sensor values. The blue curve represents the cell voltage. The envelope of the cell voltage is proportional to the resistance increase of the cell as it is cycled with ±1 A pulses. The green line is the *absolute* gas pressure in the reactor.

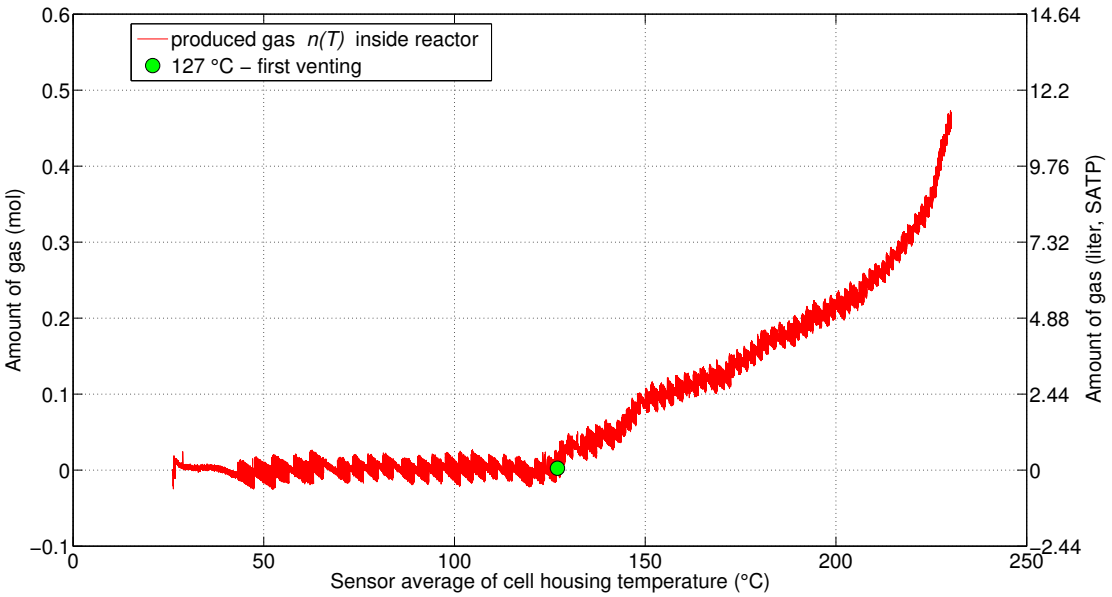

Figure 3.16: Experiment T0141. Overall gas release during the TR.

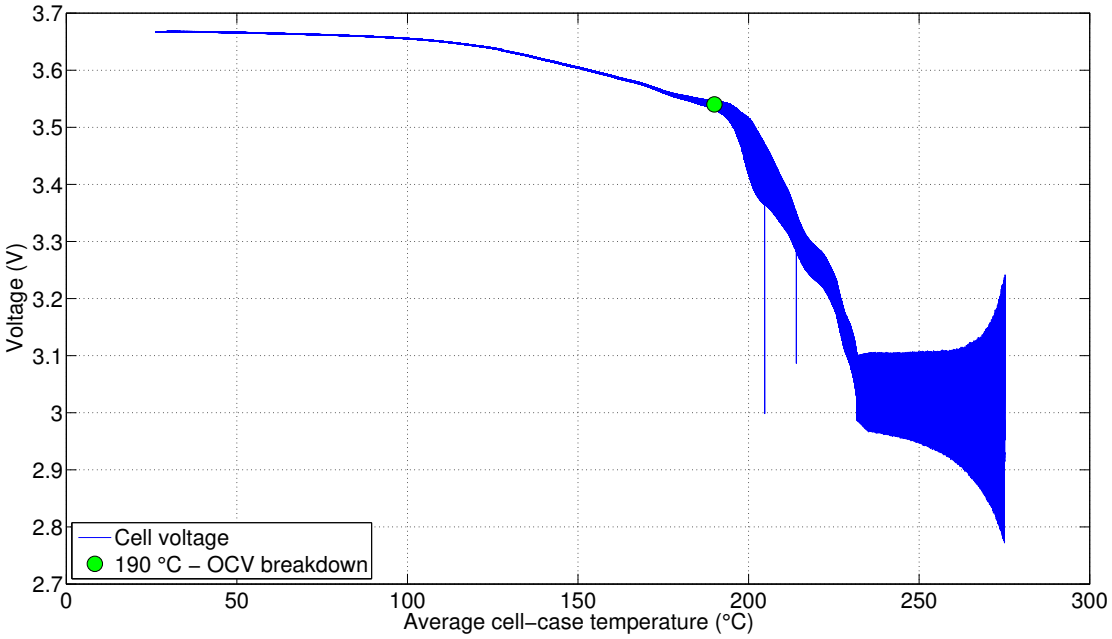

Figure 3.17: Experiment T0141. Cell voltage vs. average cell temperature.

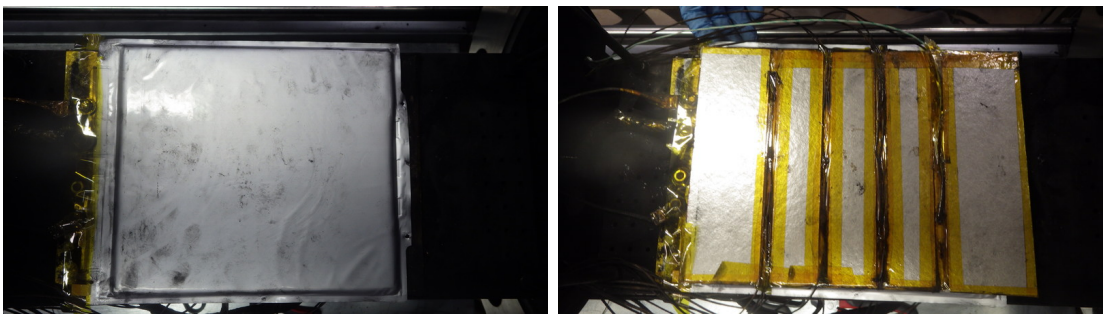

Figure 3.18: T0141. (left) Cell placed on the lower part of the sample holder. (right) Cell covered with a thermal insulation made from mica sheet.

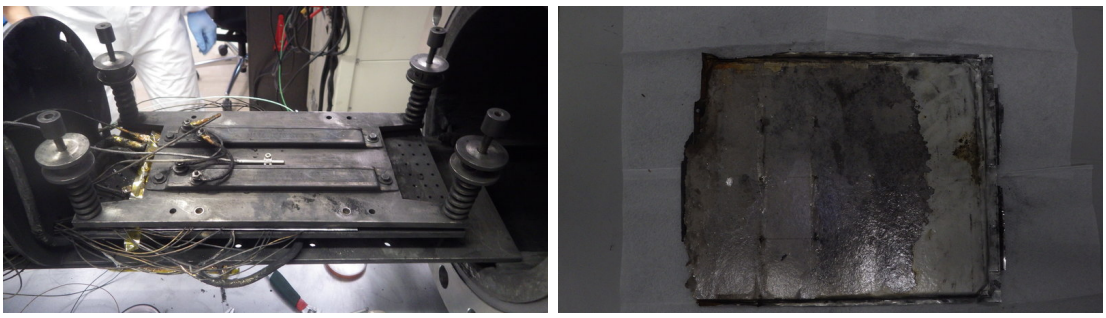

Figure 3.19: T0141. (left) Complete test setup. (right) Cell after the experiment.

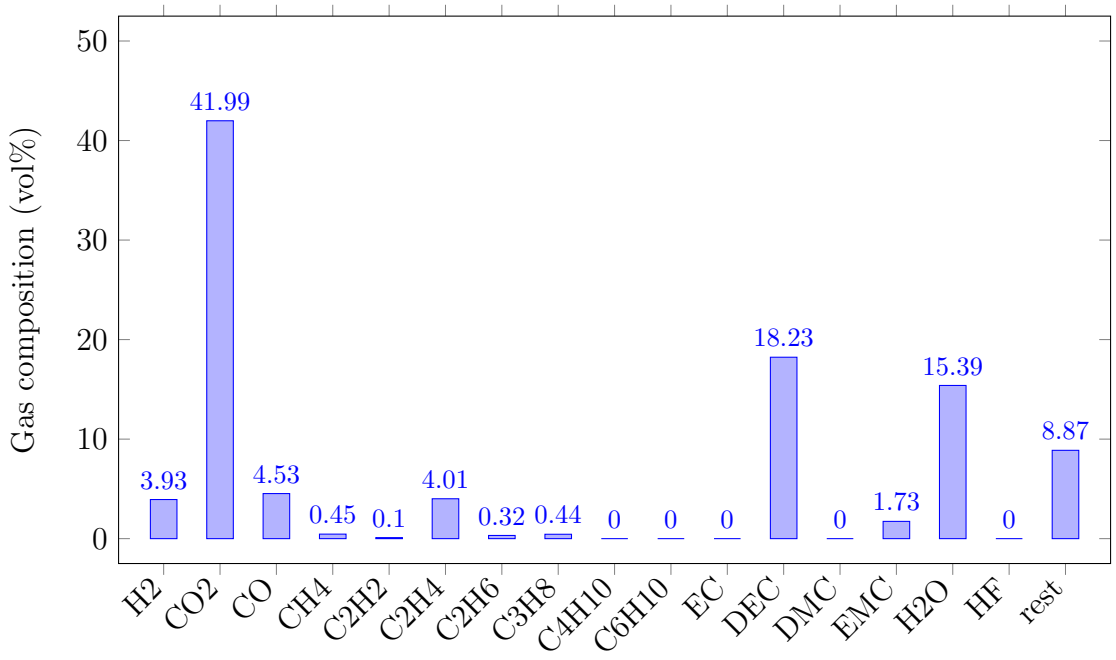

Figure 3.20: Experiment T0141. Detected gas components which were released by the cell. Gas composition was measured by GC and FTIR.

3.7.3 Experiment T0131

The experiment T0131 was the first experiment with a fully charged cell at 100% SOC and a cell voltage of 4.13 V at the start of the experiment. The cell was placed in a sample holder fig. 3.27 and heated with a temperature ramp as described in section 3.5. In contrast to most other experiments ceramic wool was used as a thermal insulator instead of mica plates. The cell was heated until a TR occurred after 6.6 h and the cell reached a max cell temperature of 754 °C. Again successive current pulses of ±1 A with a duration of 1 s were applied. Near 18 000 s some fault currents occurred and the heaters were restarted, causing a slight temperature drop.

0 s Start of heating ramp
10500 s Average cell temperature 114 °C, cell starts to release gas
18000 s Restart of the heaters
23000 s Average cell temperature 200 °C. Cell resistance increases up to 1 Ω.
23500 s Cell voltage drops to 1 V (internal short circuit?)

23638 s Cell voltage drops to 0 V. Pressure starts to rise. Gas temperatures start to rise. The TR starts.
23640 s Temperature of first cell surface sensor starts to rise rapidly
23643 s Maximal pressure (2.36 bar) and gas temperature (346 °C) in the reactor
23644 s The last temperature sensor on the cell surface starts to increase
23660 s Cell surface temperature reaches maximum at 754 °C

Discussion: In this experiment the TR of the cell was measured for the first time in the project SafeBattery. The DAQ and gas analysis could measure the cell surface temperatures at different locations, the voltage/resistance characteristics, the gas production and the gas composition (fig. 3.21).
The critical temperature, where the temperature rate of the hottest sensor exceeded 10 °C min^{-1}, immediately before the full TR, was at 239 °C (fig. 3.23). By the end of the TR the cell casing reached locally up to 754 °C. Cell case temperature sensors show that the TR propagated through the cell in 7.92 s (fig. 3.22).
The cell voltage dropped and the resistance of the cell increased throughout the experiment. The resistance of the cell increased sharply before the TR, then the voltage dropped to 1 V indicating a possible short circuit, before dropping to 0 V immediately before the TR (fig. 3.26). The cell started to release gas above a cell case temperature of 114 °C and released 0.12 mol before the TR. During the TR the cell released additional 1.92 mol of gas starting at an average cell case temperature of 225 °C with an rate of 0.9 mol s^{-1} (22.9 l_{SATP}/s) (figs. 3.24 and 3.25).
The composition of the overall release of gas (2.04 mol) was analysed with GC and FTIR (fig. 3.29).
Visually the cell showed a high degree of damage: fig. 3.28.

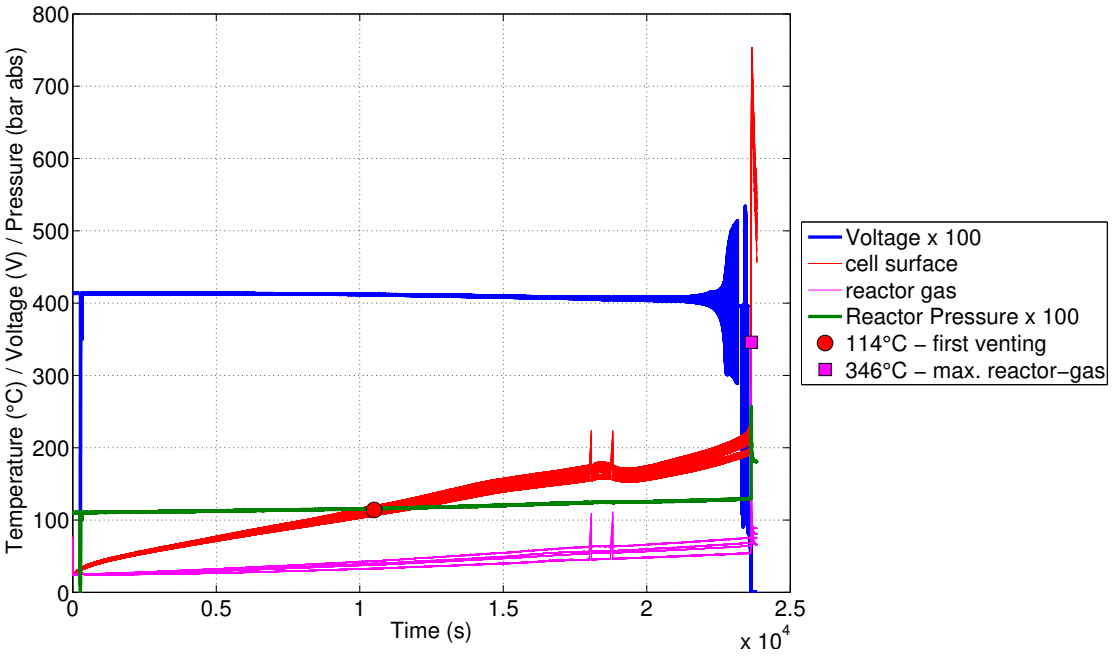

Figure 3.21: Experiment T0131. Plot of all sensor values. The blue curve represents the cell voltage. The envelope of the cell voltage is proportional to the resistance increase of the cell as it is cycled with ±1 A pulses. The green line is the *absolute* gas pressure in the reactor.

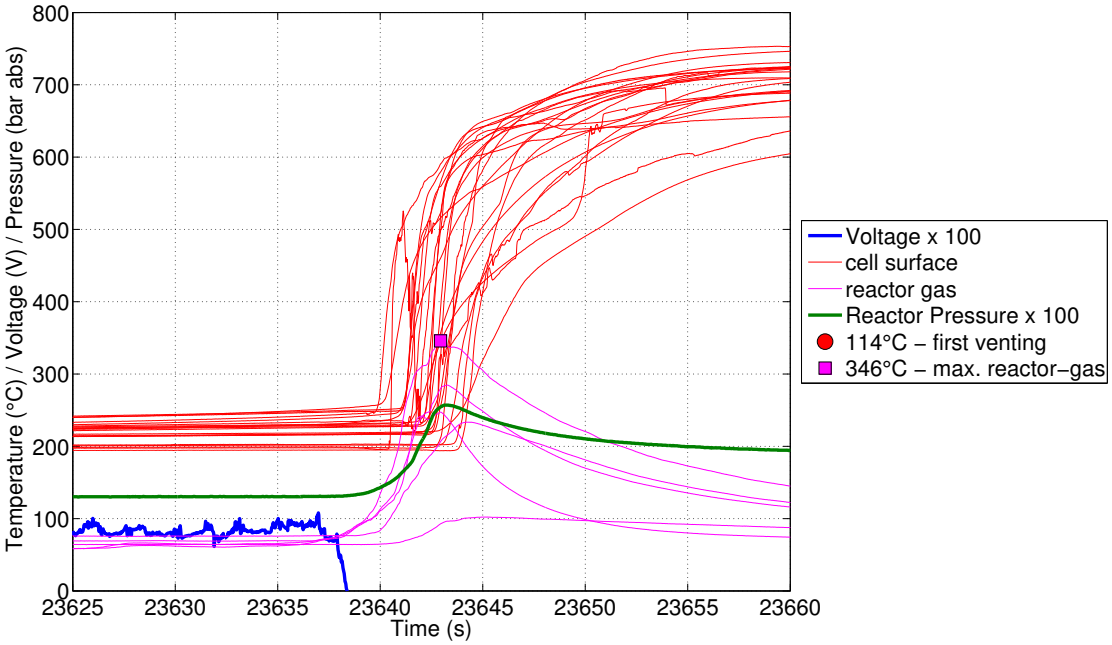

Figure 3.22: Same as fig. 3.21, but showing the timespan of the TR

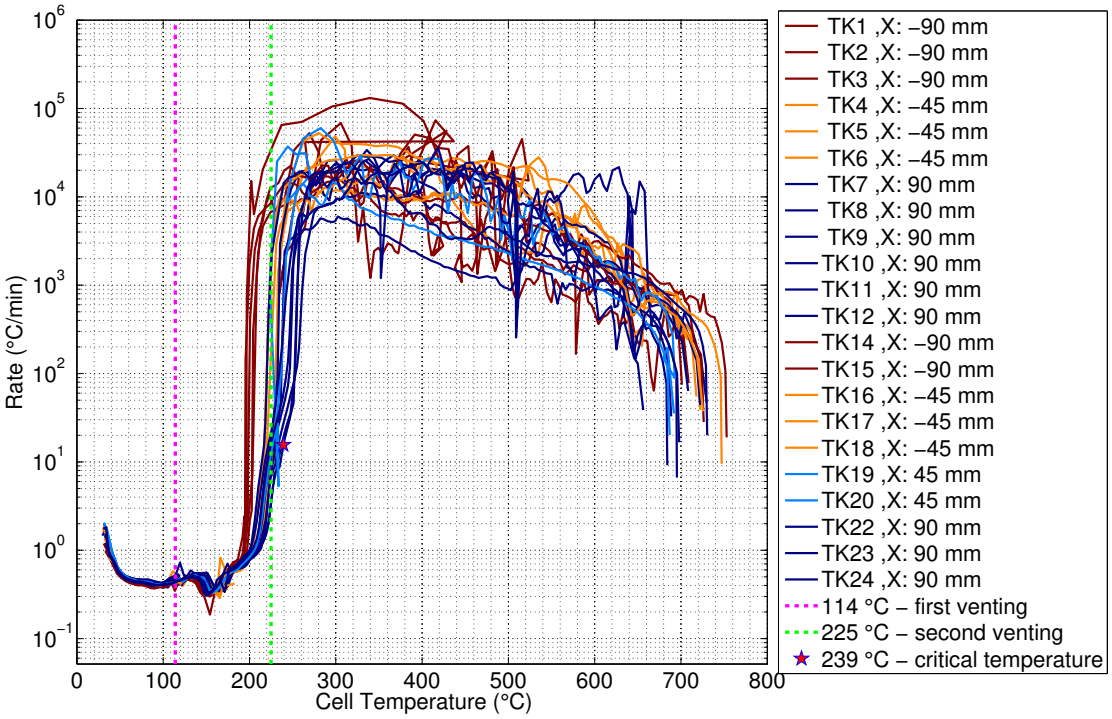

Figure 3.23: Experiment T0131. Temperature rate plot of the cell cases temperature sensors.

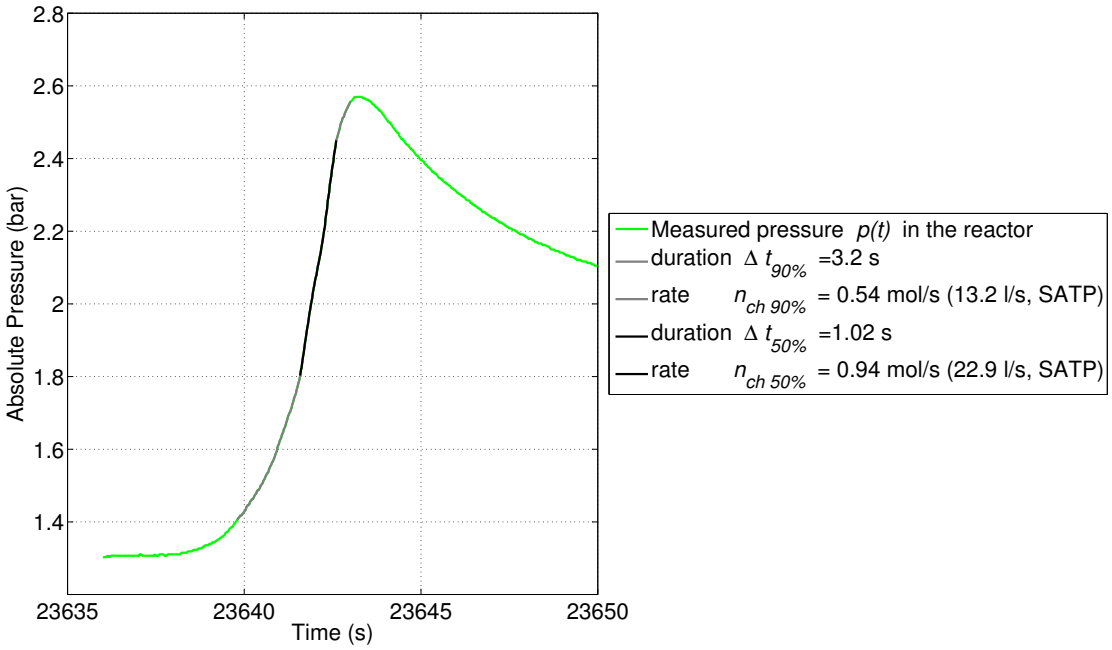

Figure 3.24: Experiment T0131. Gas release during the TR.

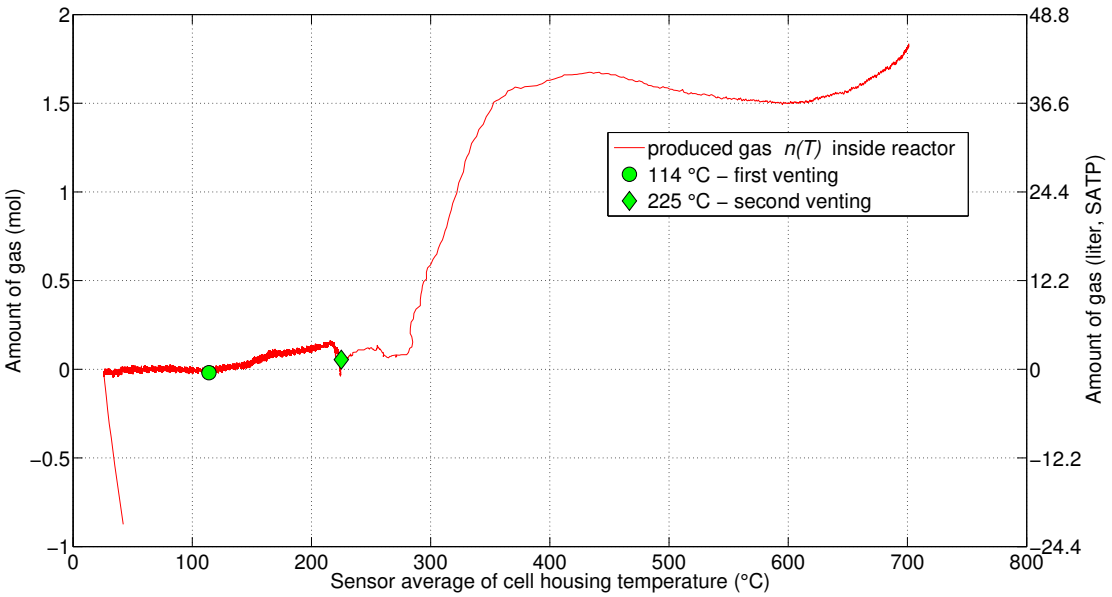

Figure 3.25: Experiment T0131. Amount of gas vs. average cell case temperature.

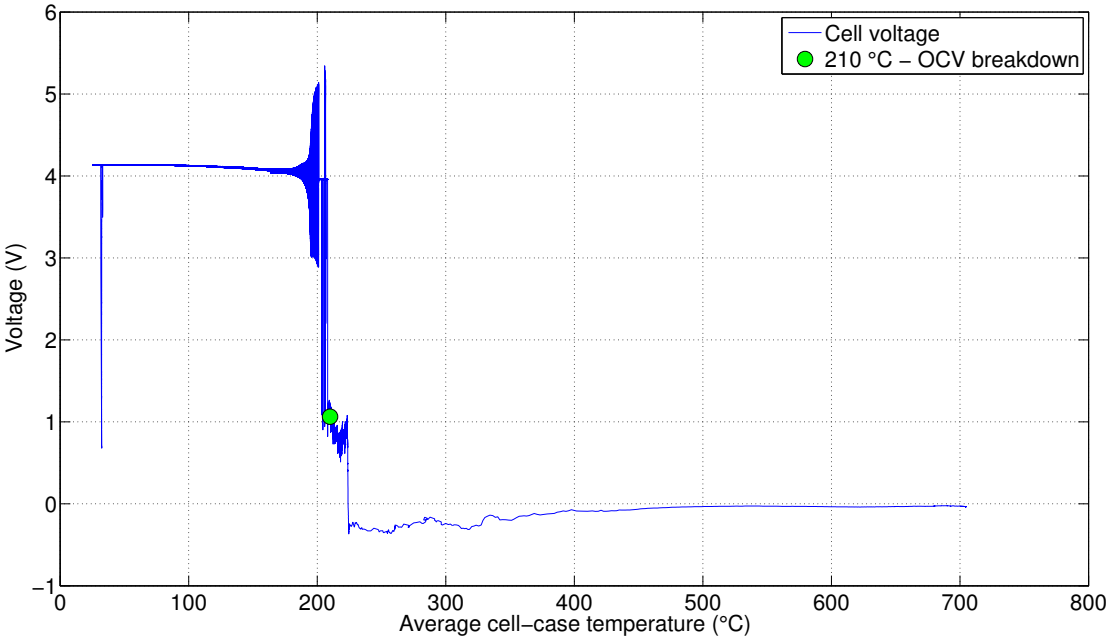

Figure 3.26: Experiment T0131. Cell voltage vs. average cell case temperature.

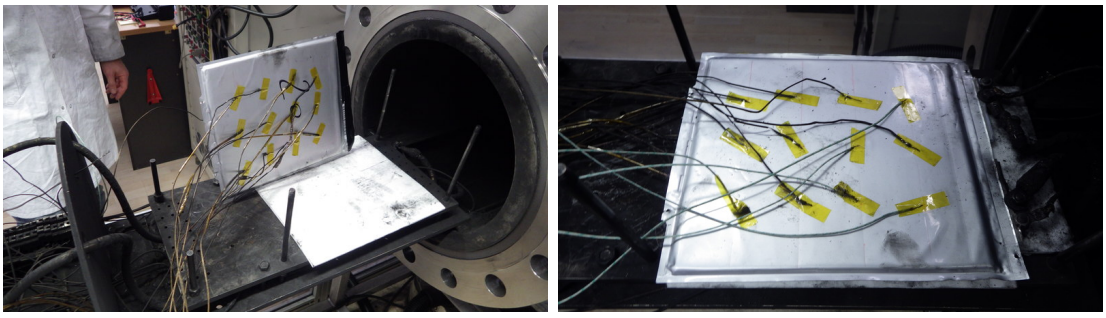

Figure 3.27: T0131. Thermocouple positions on the lower and upper side of the cell.

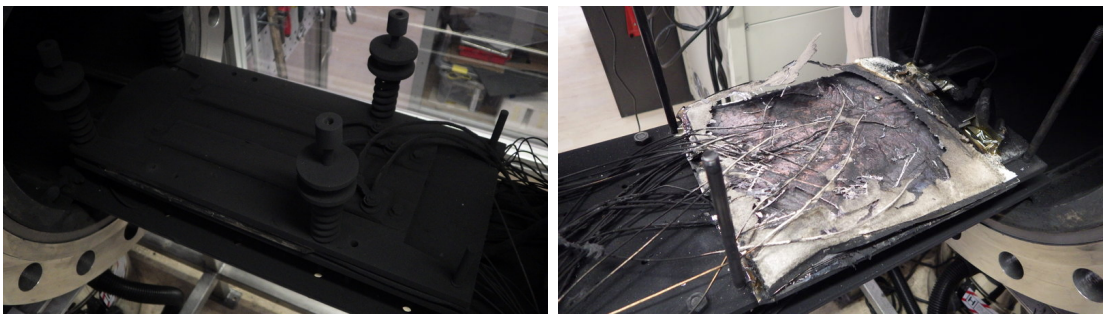

Figure 3.28: T0131. (left) Complete test setup, after the experiment. The sample holder is covered with particles which were released by the cell during the TR. (right) Damaged cell after the experiment.

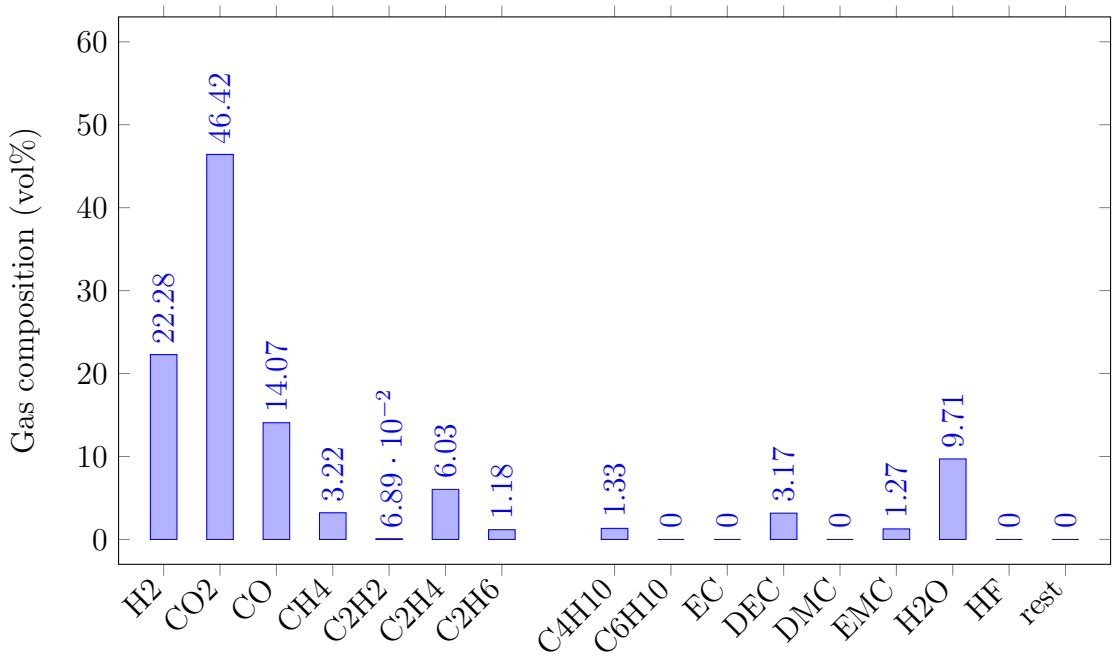

Figure 3.29: Experiment T0131. Detected gas components which were released by the cell. Gas composition was measured by both GC and FTIR.

3.7.4 Experiment T0133

T0133 was the second experiment with a fully charged cell: 100% SOC and a cell voltage of 4.18 V at the start of the experiment. The target of the experiment was to reproduce the previous experiment T0131. The cell setup was placed in a sample holder fig. 3.36 and heated with a temperature ramp as described in section 3.5. As in the previous experiment ceramic wool was used as a thermal insulator instead of mica plates. The cell was heated until a TR occured after 5.1 h and the cell reached a max cell temperature of 715 °C. Again successive current pulses of ±1 A were used.

0 s Start of heating ramp
10300 s Average cell temperature 130 °C, cell starts to release gas
18000 s Average cell temperature 180 °C. Cell resistance increases up to 150 mΩ.
19310 s Cell voltage drops from 4.0 V to 0.6 V (internal short circuit?) One of the temperature sensors measures an excursion by 30 °C for 20 s.
19380 s Cell voltage recovers to 3.6 V.
19397 s Cell voltage drops to 0 V. Gas pressure start to rise. Gas temperature sensors register start of gas temperature increase. The TR starts.
19400 s Temperature of the first cell case sensors starts to increase
19402 s Maximal pressure (2.6 bar) and gas temperature (487 °C) in the reactor
19404 s The last temperature sensor on the cell surface starts to increase
19425 s Cell surface temperature reaches maximum at 715 °C

Discussion: In this experiment the TR of a SafeBattery cell was measured for the second time. The equipment could measure the cell surface temperatures at different locations, the voltage/resistance characteristics, the gas production and the gas composition (fig. 3.30).
The critical temperature was at 231 °C (fig. 3.32). By the end of the TR the cell casing reached up to 715 °C. Cell case temperature sensors show that the TR propagated through the cell in 4.28 s (fig. 3.31).
The cell voltage dropped and the resistance of the cell increased throughout the experiment. In contrast to the previous experiment T0131 the resistance of the cell did not exceed 150 mΩ, even immediately before the TR. Seconds before the TR an internal short circuit with voltage drop to 0.6 V was observed. The short circuit

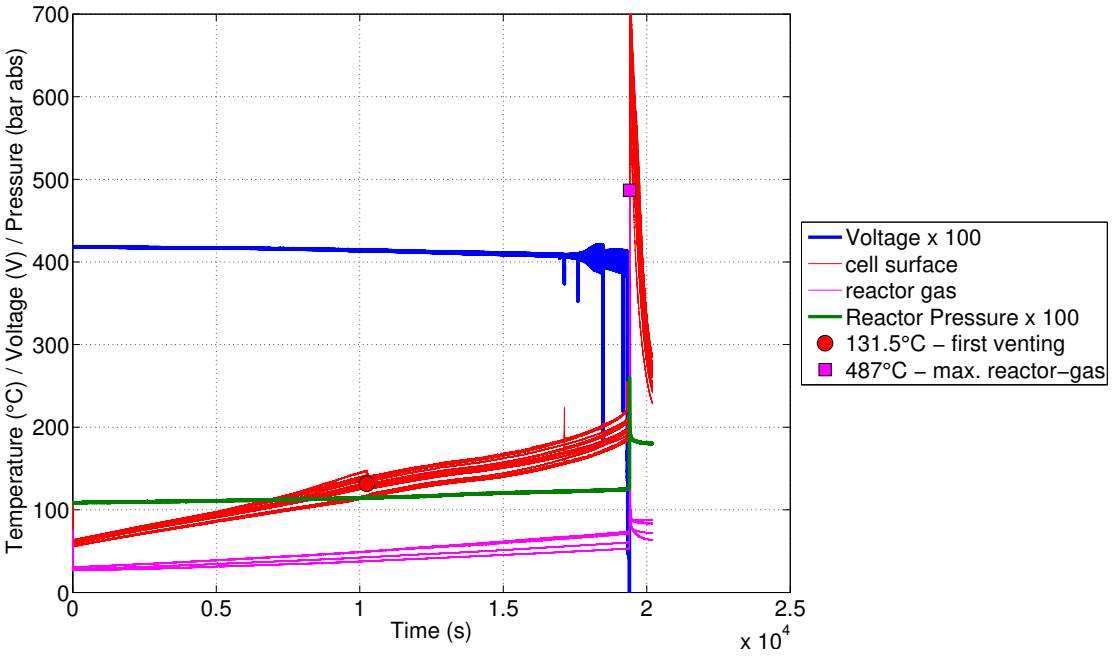

Figure 3.30: Experiment T0133. Plot of all sensor values. The blue curve represents the cell voltage. The envelope of the cell voltage is proportional to the resistance increase of the cell as it is cycled with ±1 A pulses. The green line is the *absolute* gas pressure in the reactor.

duration was 70 s and the cell voltage decreased from 4.0 V before the short circuit to 3.6 V after the short circuit. The short circuit was accompanied by a noticeable temperature excursion by two temperature sensors. Shortly after recovering the cell went into a full TR and the voltage dropped to 0 V (fig. 3.35).
The cell started to release gas above a cell case temperature of 130 °C and released 0.14 mol before the TR. During the TR the cell released additional 2.17 mol of gas starting at an average cell case temperature of 212 °C with an rate of 0.8 mol s^{-1} (18.4 l_{SATP}/s) (figs. 3.33 and 3.34). The composition of the overall release of gas (2.31 mol) was analysed with GC and FTIR (fig. 3.38).
Visually the cell showed a high degree of damage: fig. 3.37, and its mass reduced by −43.4 %.

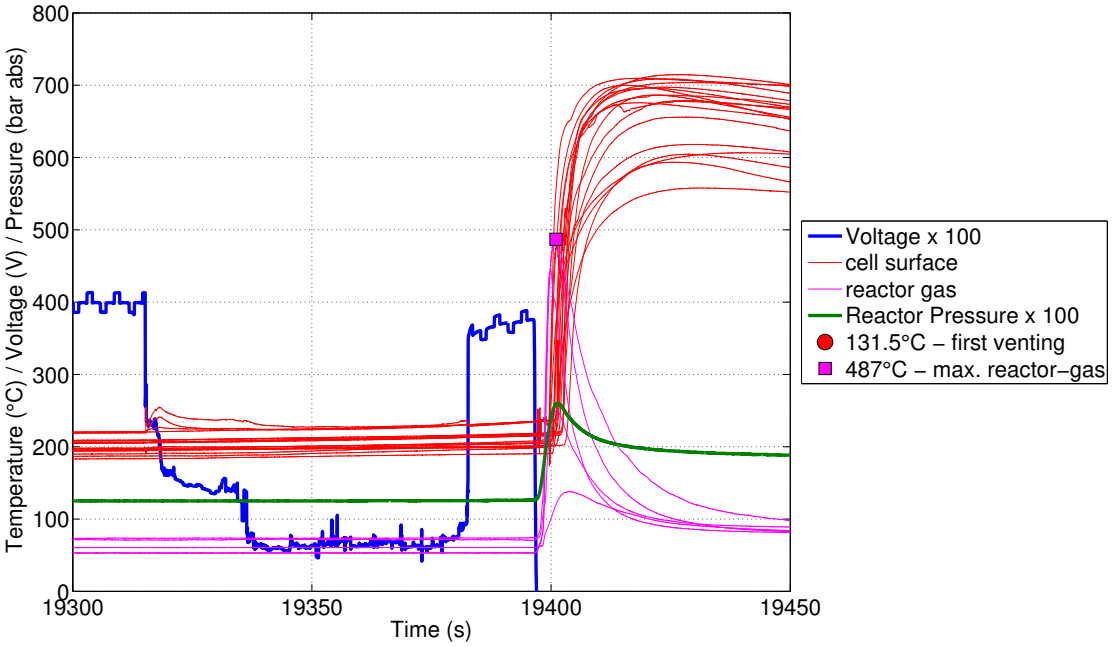

Figure 3.31: Same as fig. 3.30, but showing the timespan of the TR. Note the voltage drop before the TR, which might have been caused by a short circuit.

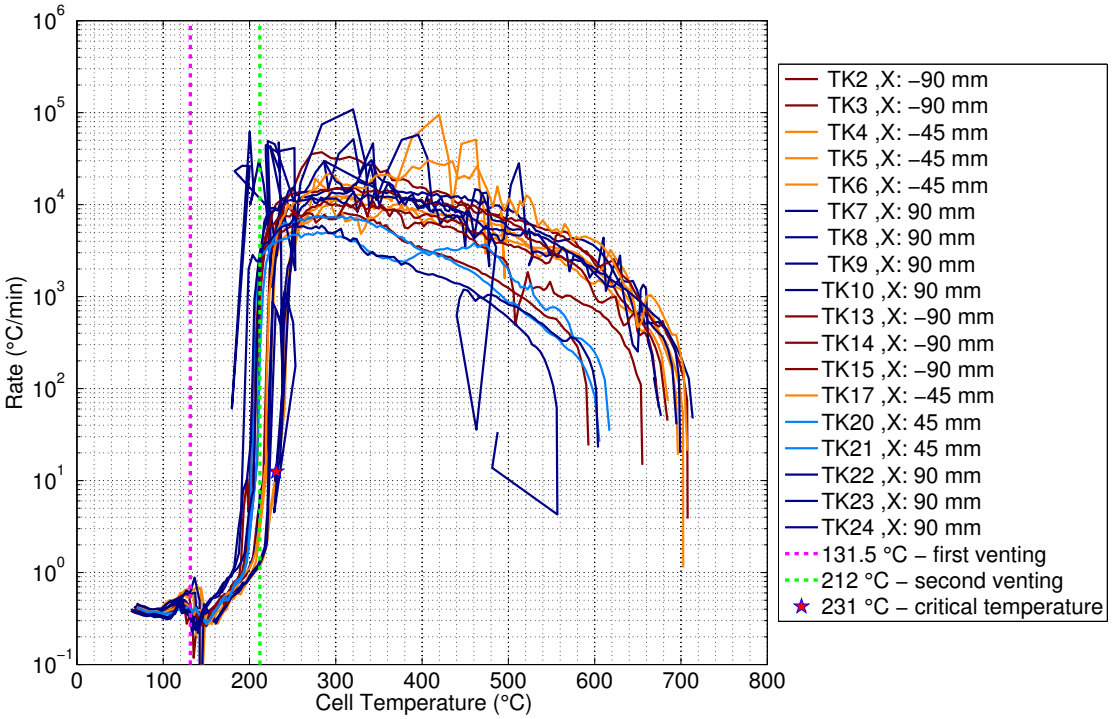

Figure 3.32: Experiment T0133. Temperature rate plot of the cell cases temperature sensors.

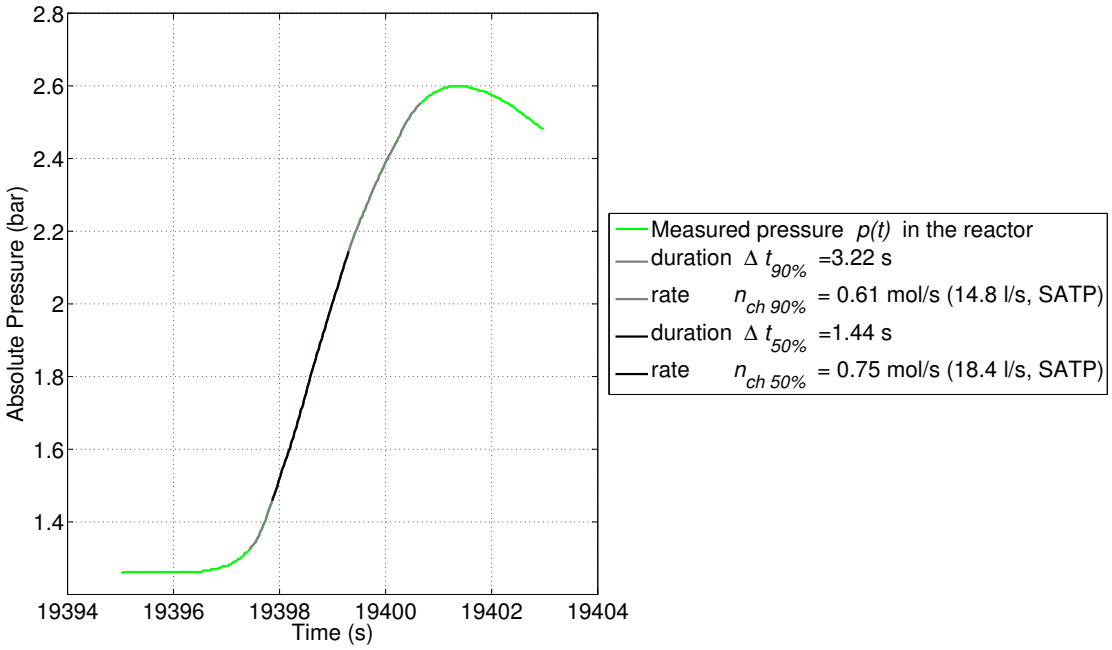

Figure 3.33: Experiment T0133. Main gas release event during the TR.

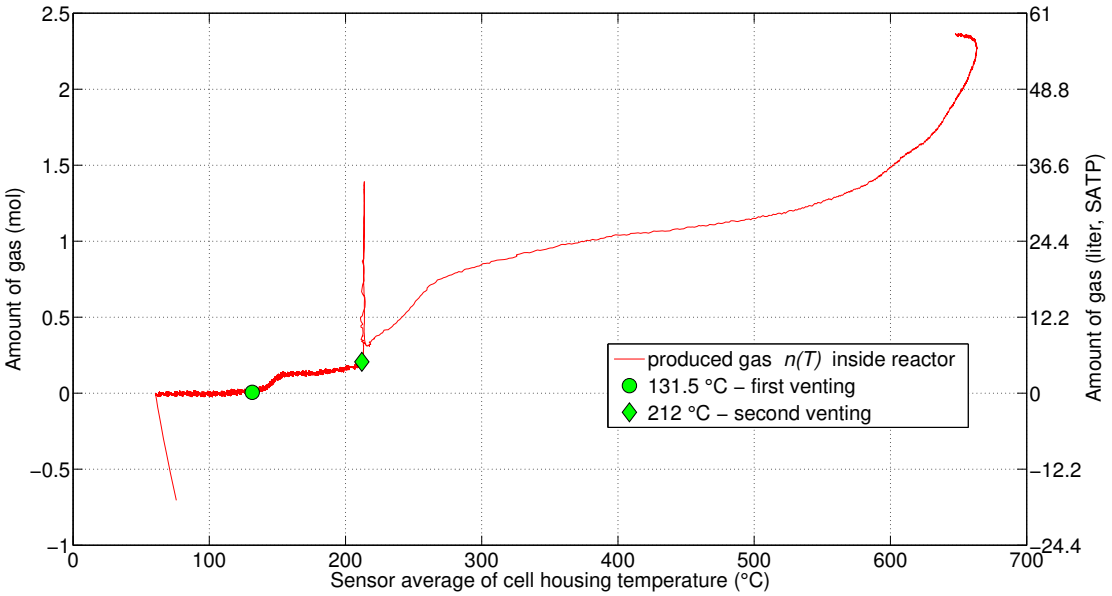

Figure 3.34: Experiment T0133. Gas release vs. average cell temperature.

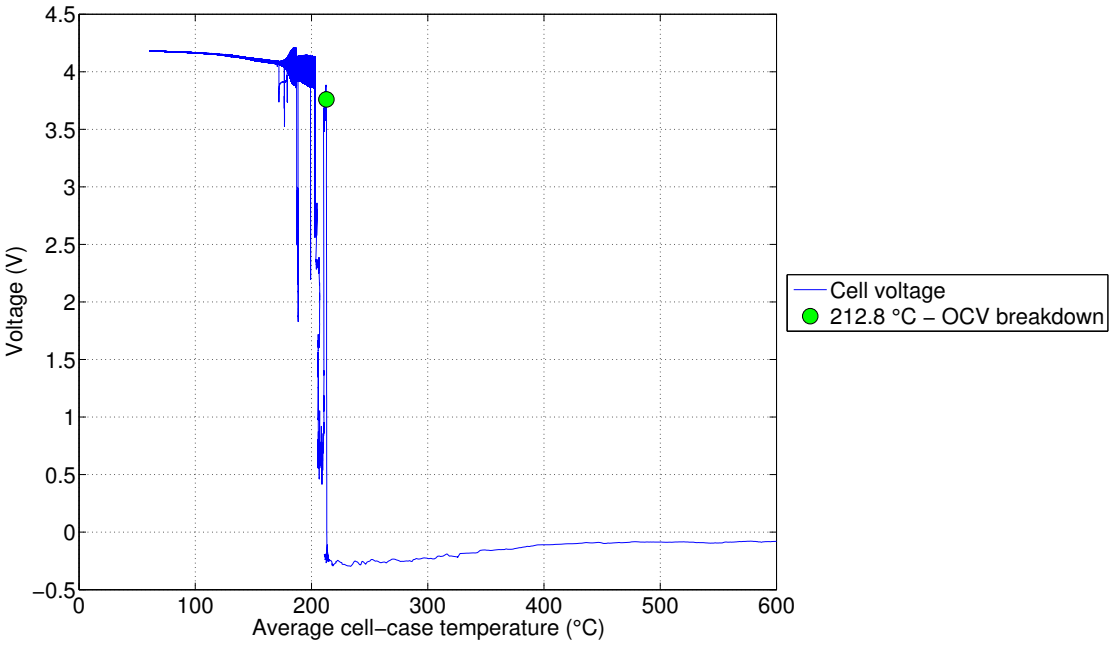

Figure 3.35: Experiment T0133. Cell voltage vs. average cell temperature.

Figure 3.36: T0133. Tested cell and the thermocouple positions on the and upper side of the cell.

Figure 3.37: T0133. (left) Complete test setup, after the experiment. The sample holder is covered with particles which were released by the cell during the TR. (right) Damaged cell after the experiment.

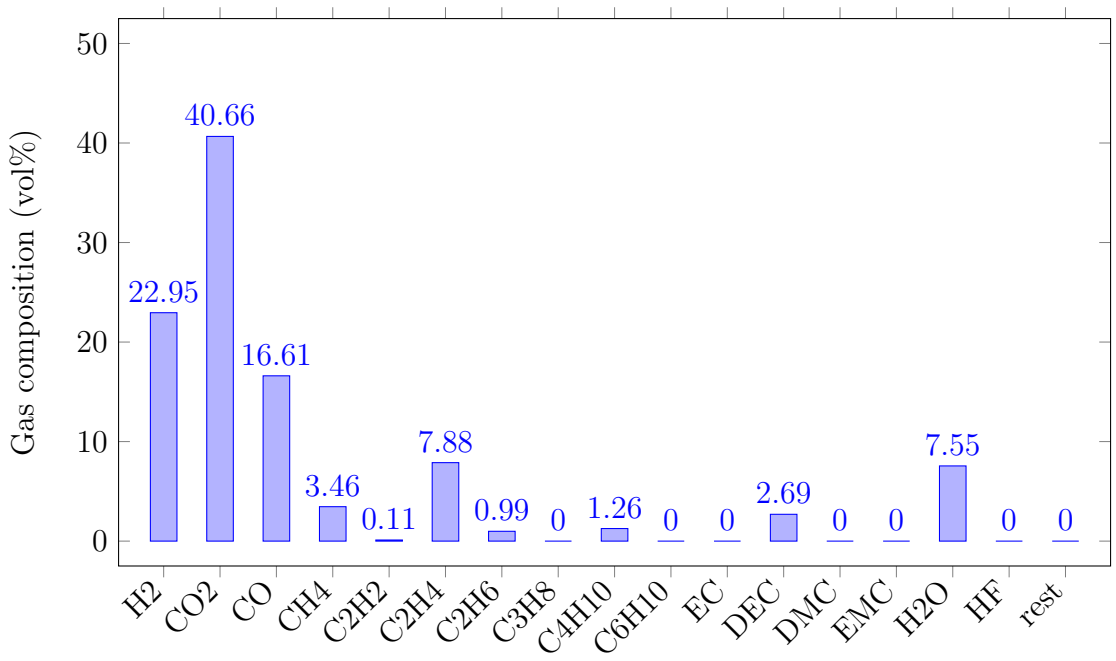

Figure 3.38: Experiment T0133. Detected gas components which were released by the cell. Gas composition was measured by both GC and FTIR.

3.7.5 Experiment T0140

The intention in T0140 was to measure the *temperature inside of the electrode stack* and not only on the outside cell case temperature during TR. Three thermocouples were prepared: their thick glas-fibre insulation was removed and replaced with thin Kapton® (Polyimide) tape. The tape was needed to prevent cell internal short circuit and to prevent leakage current through the thermocouple wire which would obscure the temperature measurement. Kapton® was chosen because of its excellent high temperature endurance. It retains reasonable mechanical stability even when it is heated to 900 °C in Ar [108].
The cell was discharged to 0 V and cut open on the sealed seam on the edges of the cell. Three thermocouples were inserted into the cell stack below the first anode layer with a distance of 115 mm to each other (fig. 3.39). A few drops of fresh electrolyte were put into the cell and then the cell was sealed with Kapton® tape (fig. 3.40). The cell was then put into the reactor and charged to 100% resulting in a cell voltage of 4.15 V. A temperature ramp was used to bring the cell into TR. Current pulses of ±1 A were used to observe the internal resistance of the cell.

0 s Start of heating ramp
12000 s Restart of DAQ software.
25000 s Average cell temperature 190 °C. Cell resistance starts to increase to 15 mΩ.
26670 s Onset of TR with a temperature rate 12.1 °C min^{-1} near the sensor TK11 at a sensor temperature of 239 °C
26780 s Start of fast TR, temperature increase near adjacent sensors, Average cell temperature: 214 °C, Cell resistance starts to increase to 76 mΩ, voltage drops to 0 V
26786 s Temperature near the latest sensor starts to rise, gas pressure near maximum. TR has propagated throughout the cell.

Discussion: In this experiment the TR of a fully charged SafeBattery cell was measured for the third time. The equipment could measure the cell surface temperatures at different locations, the temperature inside the stack at three positions, the voltage/resistance characteristics, the gas production and the amounts of main gas components (fig. 3.30).

The critical temperature, where the temperature rate of the hottest sensor exceeded $10\,°C\,min^{-1}$, immediately before the full TR, was at 239 °C (fig. 3.45). By the end of the TR the cell casing reached up to 654 °C. Cell case temperature sensors show that the TR propagated through the cell in 4.2 s (fig. 3.31).
The cell voltage dropped and the resistance of the cell increased throughout the experiment. In contrast to all previous experiments the resistance of the cell did not exceed 50 mΩ, even immediately before the TR. During the TR the voltage dropped to 0 V without intermediate voltage plateau as in the T0133 or T0131 which indicated an internal short circuit (fig. 3.47).
The cell started to release gas above a cell case temperature of 100 °C and released 0.25 mol before the TR. Note that the cell was manipulated, by cutting open and by adding foreign electrolyte, therefore the values of first gas release (electrolyte vapour and decomposition) deviated from previous experiments. During the TR the cell released additional 1.68 mol of gas starting at an average cell case temperature of 214 °C with an rate of $0.6\,mol\,s^{-1}$ ($13.8\,l_{SATP}/s$) (figs. 3.44 and 3.46). The composition of the overall release of gas (1.92 mol) was analysed with GC (fig. 3.48).
The experiment shows that inserted thermocouples can be used to measure the inside temperature during TR. The maximum temperature inside the cell stack with 821 °C was higher than the maximum cell case temperature with 654 °C. The TR started near the centre of the cell and propagated to the edges of the cell. The difference of the onset times of the inserted sensors are used to calculate the TR-front propagation speed. The differences were $\Delta T = 2.0\,s, 2.5\,s$ with the distance of 115 mm between the sensors the propagation results in $c_{\parallel} = 51\,mm\,s^{-1}$ in a preheated cell. Note that the TR started, when the average cell temperature already reached 214 °C. The propagation speed inside such a preheated cell is faster than in a cell at room temperature, because the material needs less additional heat to start the local TR reaction.
Visually the cell showed a little less damage than in T0131 and T0133: fig. 3.41, and its mass reduced by −31.1 %.

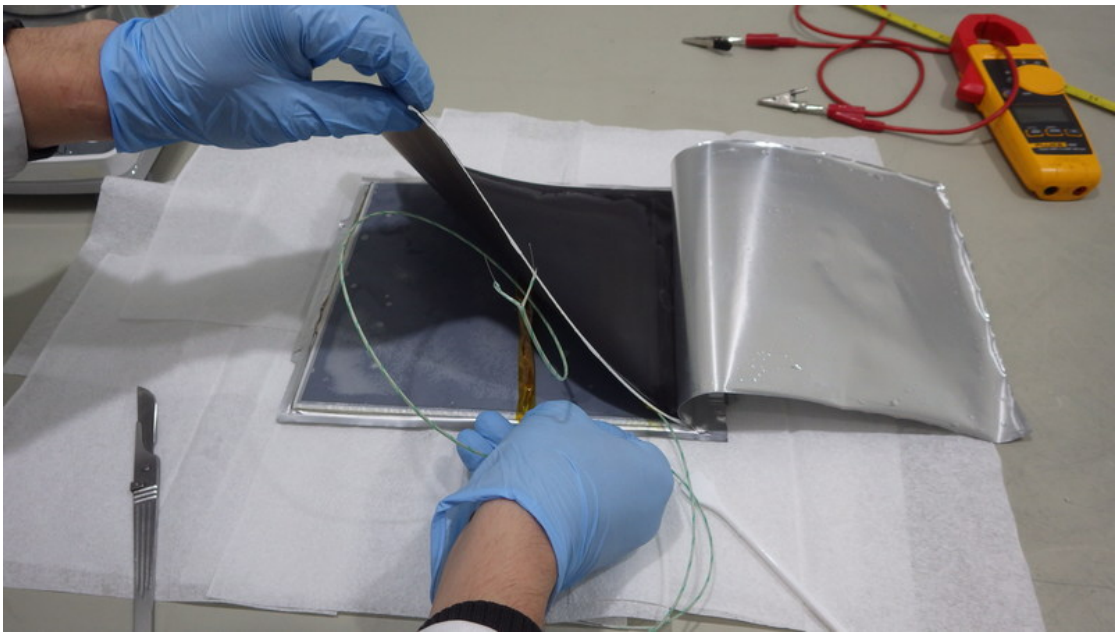

Figure 3.39: Experiment T0140. Cell prepared with internal thermocouples.

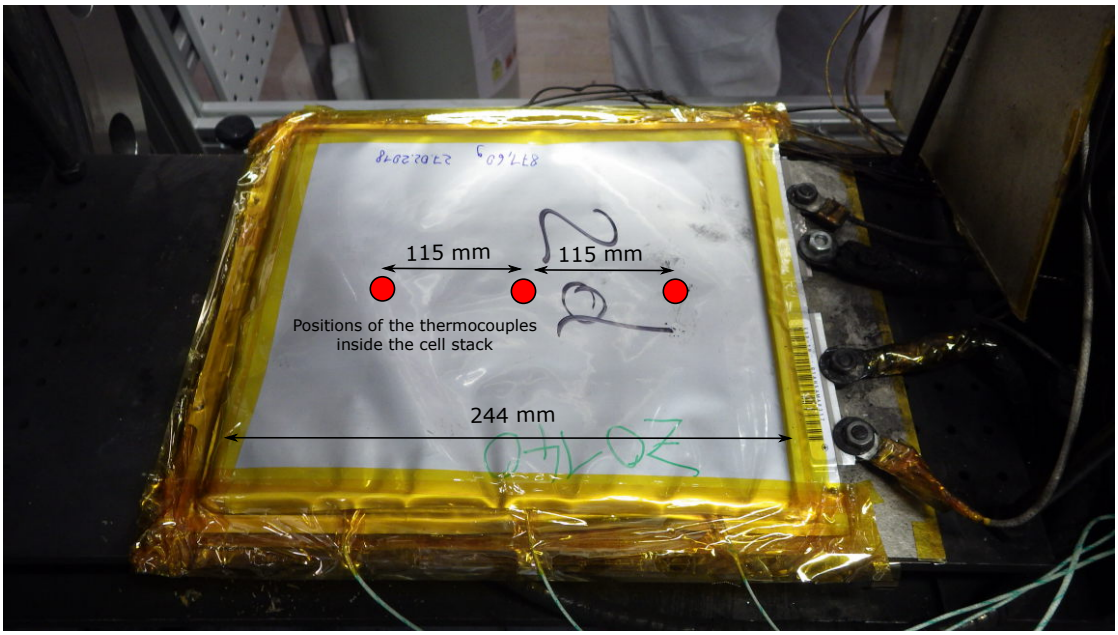

Figure 3.40: Experiment T0140. Sample holder and the cell after the experiment.

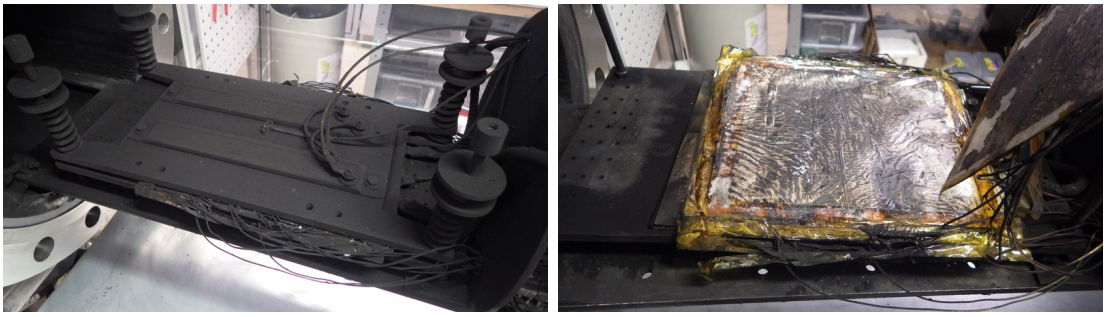

Figure 3.41: T0140. Cell prepared with internal thermocouples.

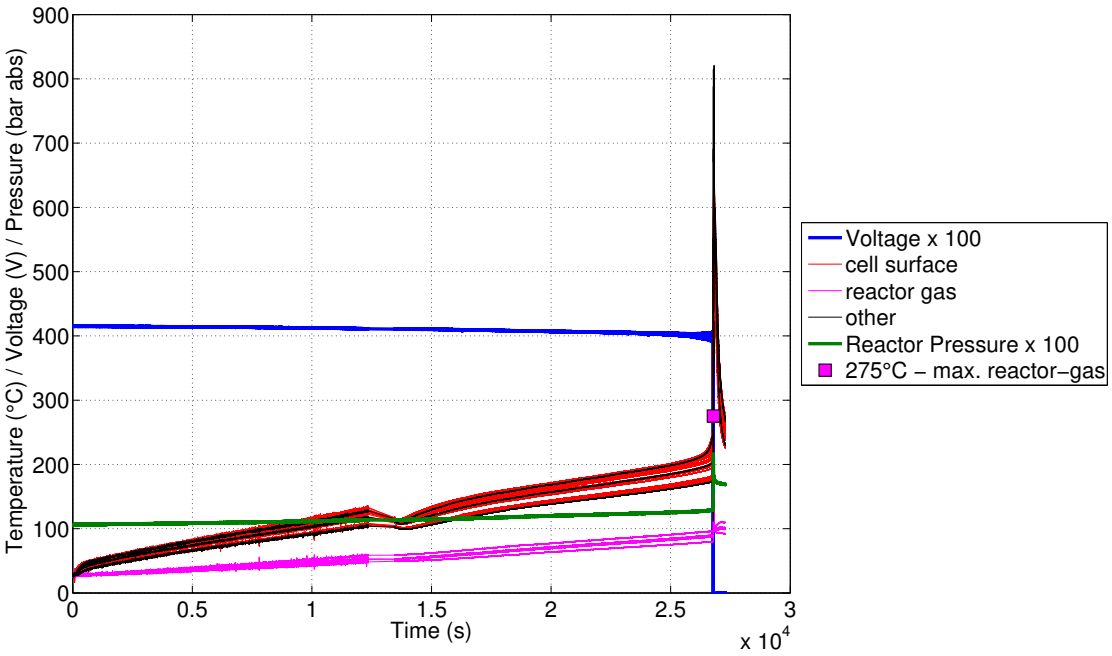

Figure 3.42: Experiment T0140. Plot of all sensor values. The blue curve represents the cell voltage. The envelope of the cell voltage is proportional to the resistance increase of the cell as it is cycled with ±1A pulses. The green line is the *absolute* gas pressure in the reactor. *Other:* temperature sensors inside the cell.

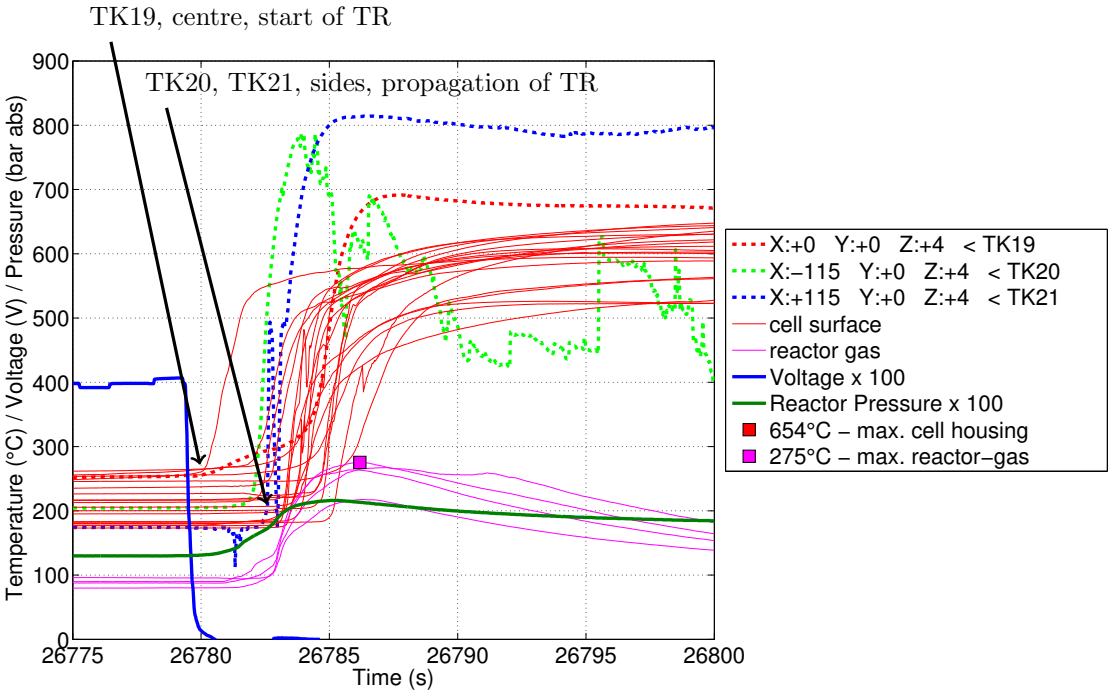

Figure 3.43: Experiment T0140. Same as fig. 3.42, but showing the timespan of the TR. Dotted: inserted temperature sensors. Note that the inserted thermocouple TK20 measured error-nous values after reaching its peak temperature, probably due insulation damage.

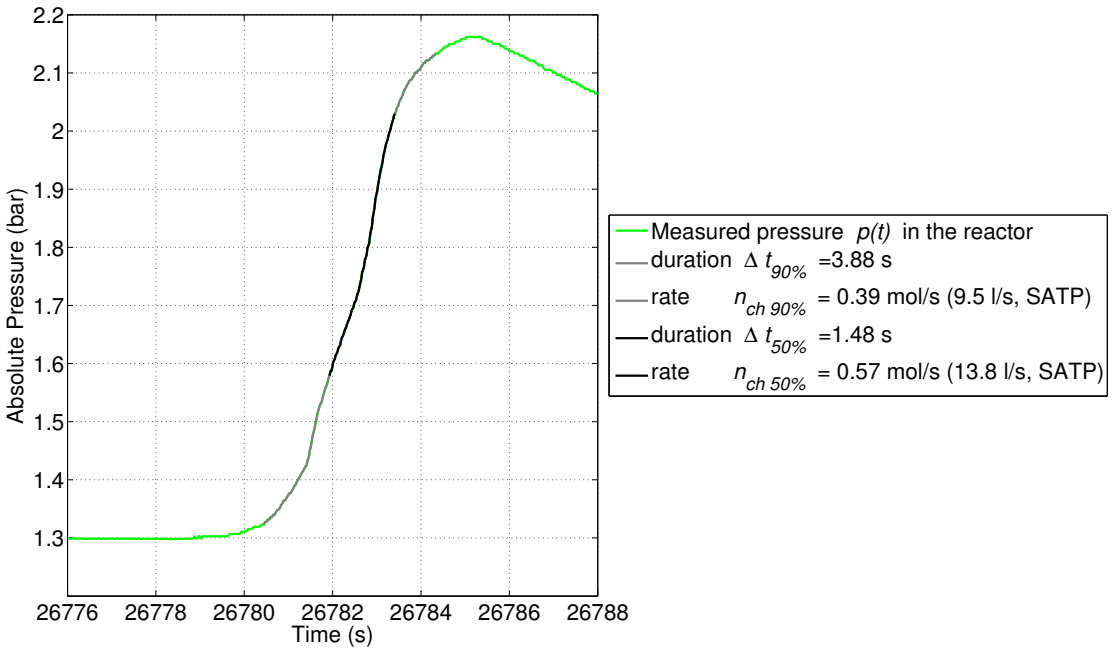

Figure 3.44: Experiment T0140. Main gas release event during the TR.

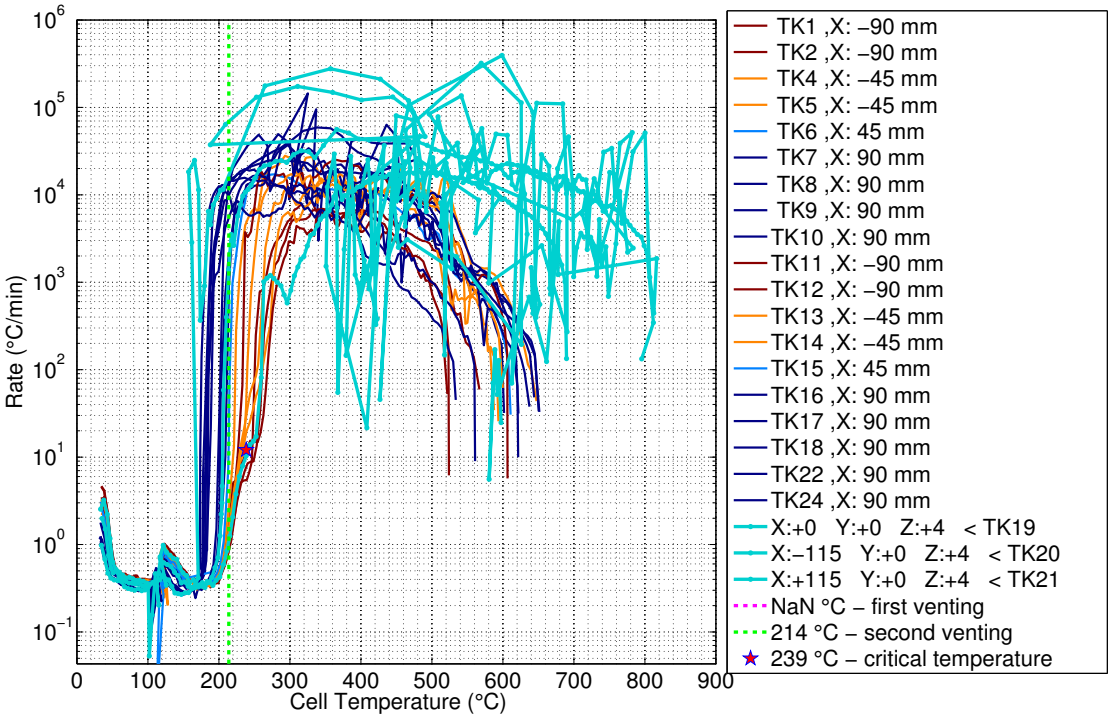

Figure 3.45: Experiment T0140. Temperature rate plot of the cell cases temperature sensors.

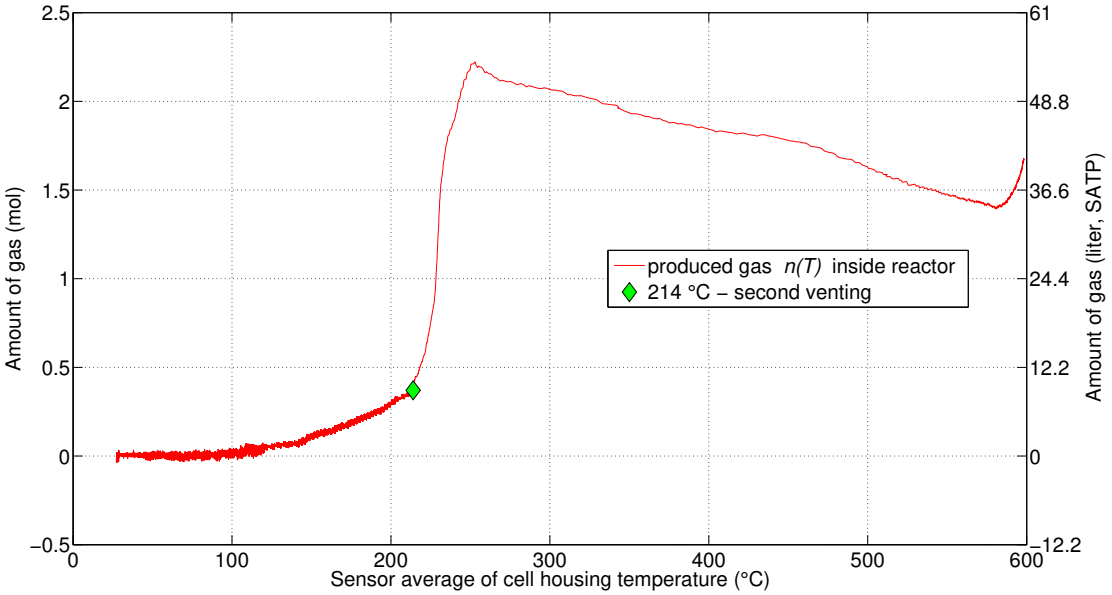

Figure 3.46: Experiment T0140. Gas release vs. average cell case temperature.

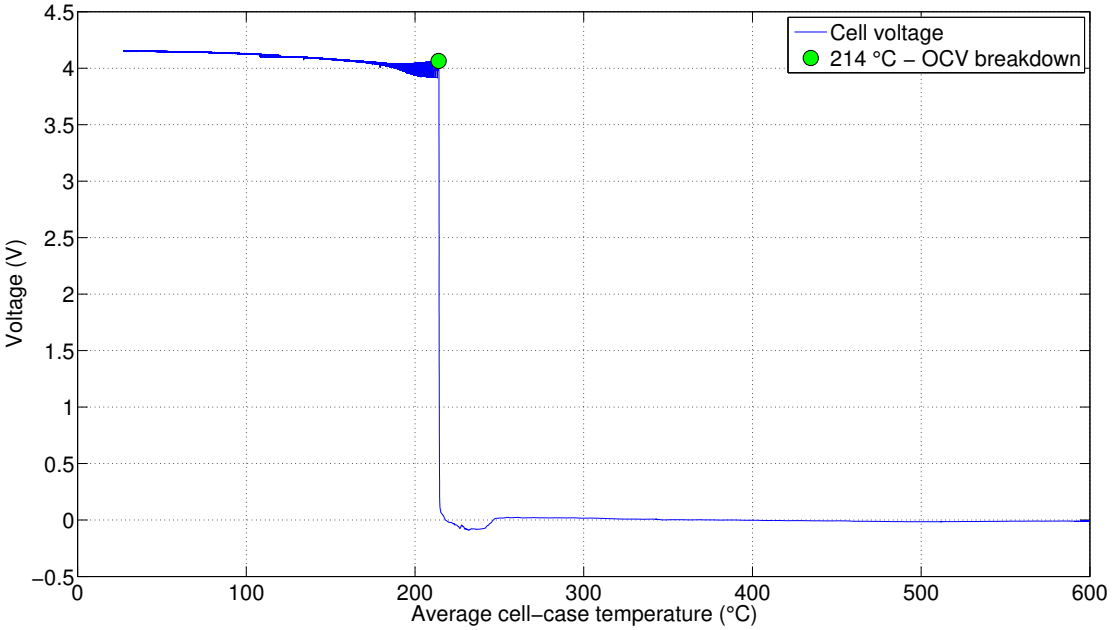

Figure 3.47: Experiment T0140. Voltage vs. average cell case temperature.

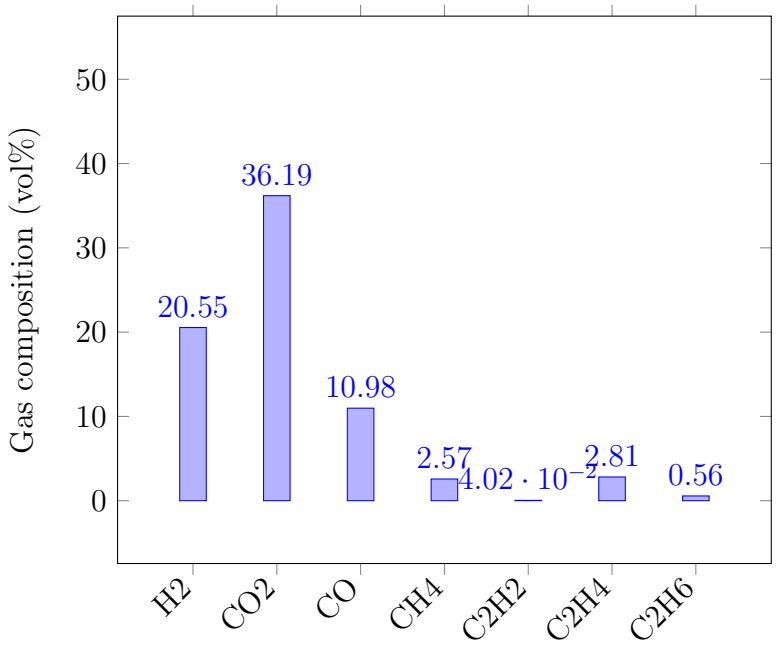

Figure 3.48: Experiment T0140. Detected gas components which were released by the cell. Gas composition was measured only by GC (FTIR was not available).

3.7.6 Summary

Results from the five thermal runaway experiments which were described in section 3.7 are compared in several tables (table 3.3, table 3.4, table 3.5). From this overview the worst case parameters are selected and used as an input for the workplace safety recommendations in section 3.8. The worst case parameter for fully charged cells are marked in red and worst case parameter for cells at ≤30 % SOC are marked in green inside the tables.
The worst case parameter were: the highest cell temperature, the highest amount of released gas, the lowest temperature when a reaction happened, the highest amount of released material and highest amounts of toxic/burnable CO and H_2.
Note, that the cell in the last experiment (T0140) was treated differently than cells in previous experiments (opening of the casing, inserted thermocouples, resealing with polyimide tape). This could have caused less gas release n_V and lower maximal temperature T_{max} during its TR in T0140.

Table 3.3: Test conditions and main results. Here SOC^* is the state of charge, V^* is the cell voltage at the start of the experiment and V_{TR} immediately before the TR (or at the end of the heating doe T0139 and T0141), TR is yes when a TR occurred, T_{crit} is the temperature of the sensor which was the first to exceed $10\,°C\,min^{-1}$, T_{max} is the maximal recorded cell surface temperature during the experiment, m^* and $m^\dagger$ are the cell masses before and after the experiment.

Experiment	SOC^*	V^*	V_{TR}	TR	T_{crit}	T_{max}	m^*	$m^\dagger$
	%	V	V		°C	°C	g	g
T0139	0	3.12	0.54	no	—	242	789	668
T0141	30	3.67	3.04	no	—	309	871	—
T0131	100	4.13	3.96	yes	239	754	—	—
T0133	100	4.18	3.99	yes	231	715	868	491
T0140	100	4.15	3.98	yes	239	654	871	600

Table 3.4: Venting results. Test conditions are same as in table 3.3. Here T_{V1} is the average cell case temperature when first outgasing becomes noticeable, and T_{V2} the average cell case temperature when TR-reactions start to produce n_{V2}. n_{v1} is the gas release before TR, n_{v2} is the gas release during TR and n_v is the overall released gas. $\dot{n}_{V2}$ is the characteristic release rate of the gas during the TR.

Experiment	SOC^*	TR	T_{V1}	n_{V1}	T_{V2}	n_{V2}	n_V	$\dot{n}_{V2}$
	%		°C	mol	°C	mol	mol	$mol\,s^{-1}$
T0139	0	no	128	0.41	—	—	0.41	—
T0141	30	no	127	0.53	—	—	0.53	—
T0131	100	yes	114	0.12	225	1.92	2.04	0.9
T0133	100	yes	130	0.14	212	2.17	2.31	0.8
T0140	100	yes	—	0.25	214	1.68	1.92	0.6

Table 3.5: Measured gas composition at the end of each experiment. Test conditions are same as in table 3.3. The gas composition is given in vol%.

Exp.	TR	H_2	CO_2	CO	CH_4	H_2O	C_2H_2	C_2H_4	C_2H_6	C_4H_{10}	DEC	EMC
T0139	no	0.9	52.9	1.9	0.2	—	0	4.5	0.2	—	—	—
T0141	no	3.9	42	4.5	0.5	15.4	0.1	4	0.3	0	18.2	1.7
T0131	yes	22.3	46.4	14.1	3.2	9.7	0.1	6	1.2	1.3	3.2	1.3
T0133	yes	22.9	40.7	16.6	3.5	7.6	0.1	7.9	1	1.3	2.7	0
T0140	yes	20.5	36.2	11	2.6	—	0.04	2.8	0.6	—	—	—

Worst case characteristics for the fully charged cells

- critical temperature $T_{crit} = 231\,°C$
- maximal cell case temperature $T_{max} = 754\,°C$
- released cell mass $\Delta m = 377\,g$
- average cell case temperature when main venting starts $T_{V2} = 212\,°C$
- overall released amount of gas $n_V = 2.31\,mol$
- characteristic gas release rate $\dot{n}_{V2} = 0.9\,mol\,s^{-1}$
- gas composition: as in experiment T0133 with $C_{CO} = 16.6\,\%$ and $C_{H_2} = 22.9\,\%$
- maximal temperature *inside* the cell $T_{max} = 821\,°C$
- HF could not be detected

Worst case characteristics for cells with SOC $\leq$30 %

- no exothermic reactions
- average cell case temperature when cell starts to release gas $T_{V1} = 114\,°C$
- amount of produce gas if heated up to 309 °C: $n_V = 0.53\,mol$
- gas composition: as in experiment T0141 with $C_{CO} = 4.5\,\%$ and $C_{H_2} = 3.9\,\%$ and high concentration of electrolyte solvents
- HF could not be detected

3.8 Safety Recommendations

This section discusses the safety recommendations based on the five experiments and on literature.

3.8.1 Battery fire

Tested cells with SOC ≤30 % show no exothermic reaction when heated up to 309 °C. Still, even at 0% SOC the cell has a voltage >0 V and can generate high short circuit currents which can start a fire. It is recommended to use insulated tools and to use fuses to prevent external short circuits to the cell.
Fully charged cells experience a TR (exothermic reaction) when overheated. The cell case reaches temperatures up to 754 °C. The cell releases gas (2.31 mol) and particles with an overall mass of up to 377 g. The released material has a temperature of up to 821 °C (as measured by the inserted thermocouples in T0140). It is likely that the released heat will ignite nearby burnable material.
Safety measures depend on the size of the device under test (DUT).

- A single cell shows a fast TR reaction: in the presented experiments it took <8 s to destroy the whole cell and to release the thermal energy. It appears to be impossible to stop the destruction of the whole cell in the short time window. Instead, it is recommended to prevent fire spreading from the cell to neighbouring equipment. Either incombustible material near the cell is used or tests are done in N_2 or Ar atmosphere. Alternatively, hot remains of the cell and nearby equipment may be cooled by moderate amount of water or water mist [72].
- Modules with multiple cells need additional attention to safety because the released heat will accumulate with each cell going into TR. If the initial TR in the module is caused by overheating of one of the cells, then TR-propagation from each failed cell to the adjacent cells may occur. The propagation may be stopped by direct cooling with water [72]. The effectivity of water based coolants may be increased with surfactants [109].

The run-off water should be treated carefully, especially if only small amounts were used, because it could contain hydrofluoric acid [110]. Ideally the water should be neutralised with alkali materials (e.g. with Calcium hydroxide) and the guidelines from material safety data sheet (MSDS) of HF-solutions should be followed.

3.8.2 Deflagration of released gas

If the cell releases burnable gas inside an enclosure, LEL may be reached and deflagration becomes possible. The concentration of vent gas c_v inside an enclosure can be easily calculated with

$$c_v = \frac{n_v}{n_e + n_v} \tag{3.4}$$

here n_v is the amount of released gas and n_e is the amount of gas in the enclosure before the TR.

Example: The SafeBattery cell is cycled inside a pressure-tight temperature chamber with a volume of 360 l at a temperature of 45 °C. The chamber is filled with air. The cell suffers an internal short circuit, transits into a TR and releases the vent-gas into the chamber ($n_V = 2.31\,\text{mol}$). Will the resulting gas mixture exceed the LEL?
The amount of gas inside the chamber before the TR is

$$n_e = \frac{p\ V}{R\ T} = \frac{100\,\text{kPa}\ 0.36\,\text{m}^3}{8.314\,\text{J}\,\text{mol}^{-1}\,\text{K}^{-1}\ (273\,\text{K} + 45\,\text{K})} = 13.6\,\text{mol}. \tag{3.5}$$

Then the concentration of vent gas inside the chamber after the TR equals to

$$c_v = \frac{n_v}{n_e + n_v} = \frac{2.31\,\text{mol}}{13.6\,\text{mol} + 2.31\,\text{mol}} = 7.4\% \tag{3.6}$$

and the resulting c_v is slightly above the LEL in table 3.1 and deflagration is possible.

Three measures to prevent deflagration are recommended:

Use enclosures with high volume so that even if all cells inside the enclosure go into TR the LEL inside the enclosure is not reached by a safety factor of two [79].

Fill the enclosure with inert gas such as N_2 or Ar to prevent vent-gas combustion. Monitor the O_2 level with an O_2-sensor to detect air leaks. Here care must be taken, if a door is opened and fresh O_2 gets access to the potentially fuel

rich gas inside the enclosure. It is better to flush the enclosure with inert gas, before opening a door.

Ventilation with high air throughput so that the c_v is reduced during the main exothermic reaction of the cell. To reduce the c_v by 50%, the ventilation throughput needs to be the same as the venting rate of the cell. The cell used in SafeBattery released up to $\dot{n}_{V2} = 0.9\,\mathrm{mol\,s^{-1}}$. This is equivalent to a ventilation throughput of $22.9\,\mathrm{l_{SATP}/s}$ or $83\,\mathrm{m^3\,h^{-1}}$.

3.8.3 Overpressure by released gas

If hot gas is released from a cell during a TR into a gas tight confinement (e.g. closed climate chamber), it will create an overpressure which can damage the equipment and cause injuries to the personnel (e.g. doors being pushed open by overpressure).

Example: the cell used in SafeBattery is cycled inside a pressure-tight temperature chamber with a volume of $V = 360\,\mathrm{l}$ at a temperature of $T_1 = 25\,^\circ\mathrm{C}$ (298 K). The chamber is filled with N_2 to prevent combustion with O_2 and is at absolute pressure of $p_1 = 100\,\mathrm{kPa}$ (in other words, room temperature and room pressure). The cell suffers an internal short circuit, transits into a TR and releases hot vent-gas into the chamber ($n_V = 2.31\,\mathrm{mol}$, $T_V = 821\,^\circ\mathrm{C}$ (1094 K), as in the experiment T0133). What is the maximal gas pressure inside the chamber, immediately after venting? (For simplicity, additional heat transfer from the cell and released particles is not considered.)

The amount of gas inside the chamber before the TR is

$$n_1 = \frac{p_1\ V}{R\ T} = \frac{100\,\mathrm{kPa}\ 0.36\,\mathrm{m^3}}{8.314\,\mathrm{J\,mol^{-1}\,K^{-1}}\ 298\,\mathrm{K}} = 14.5\,\mathrm{mol}, \tag{3.7}$$

at a temperature of $T_1 = 298\,\mathrm{K}$. Then the amount of gas inside the chamber after the TR equals to the sum of gas before the TR and the released gas by the cell

$$n_2 = n_1 + n_V = 14.5\,\mathrm{mol} + 2.31\,\mathrm{mol} = 16.8\,\mathrm{mol}. \tag{3.8}$$

To simplify the calculation we assume that no heat exchange to the outside happens, and calculate the mean gas temperature after TR with

$$T_2 = \frac{n_1\ T_1 + n_V\ T_V}{n_2} = \frac{14.5\,\mathrm{mol}\ 298\,\mathrm{K} + 2.31\,\mathrm{mol}\ 1094\,\mathrm{K}}{16.8\,\mathrm{mol}} = 408\,\mathrm{K}, \tag{3.9}$$

Table 3.6: Characteristics of the gas in the enclosure at 400 K and 120 kPa_{abs}. Gas properties retrieved from NIST Chemistry WebBook [112]. Average calculation is weighted with $n/\sum n$.

	n (mol)	C_p ($J\,mol^{-1}\,K^{-1}$)	C_v ($J\,mol^{-1}\,K^{-1}$)	γ	M ($g\,mol^{-1}$)
H_2	0.52	29.189	20.873	1.39	2.02
CO_2	0.94	41.468	33.057	1.19	44.00
CO	0.38	29.369	21.028	1.39	28.01
CH_4	0.08	40.661	32.301	1.26	16.04
H_2O	0.18	36.595	27.440	1.33	18.02
C_2H_4	0.18	53.130	44.705	1.18	28.05
N_2	14.5	29.277	20.940	1.40	28.00
weighted average				1.38	27.93

resulting in a gas pressure inside the chamber of

$$p_2 = \frac{n_2\ R\ T_2}{V} = \frac{16.8\,\text{mol}\ 8.314\,\text{J}\,\text{mol}^{-1}\,\text{K}^{-1}\ 408\,\text{K}}{0.36\,\text{m}^3} = 158\,\text{kPa}. \tag{3.10}$$

This is equal to an overpressure of $\Delta P = 58\,\text{kPa}$ or 0.58% above normal air pressure. It is likely, that a sealed temperature chamber would not withstand such an overpressure, and the door would fly open.

It is strongly recommended: **Confinements need a venting port to prevent bursting**. The example calculation of the venting port is based on section 2.4. For a simple specification of the venting port we assume an isentropic flow of the vent-gas [111]. The gas is released by the failed cell, it mixes with N_2 in the enclosure, then the gas-mix exits through the venting port to the outside of the enclosure, ideally into a gas extraction pipe. It is assumed that the main obstacle is the venting port of the battery pack with its limiting cross section A.
To further simplify the estimation only vent-gas components with more than 5 vol% are considered and it is assumed that the gas mixture in the enclosure has a temperature of $T_{mix} = 800\,\text{K}$. The gas-mix has a mean molmass $M_s = 27.93\,\text{g}\,\text{mol}^{-1}$ and the mean isentropic expansion factor $\gamma = 1.38$ at a gas-mix temperature inside the enclosure of $T_{mix} = 400\,\text{K}$ (table 3.6). It is assumed that the (absolut)

burst pressure of the confinement is $p_0 = 120\,\mathrm{kPa_{abs}}$ and the ambient pressure is $p_t = 100\,\mathrm{kPa_{abs}}$, meaning $p_t - p_0 = 20\,\mathrm{kPa}$ of allowed overpressure caused by the failed cell during the venting event.
The flow factor Ψ is given by:

$$\Psi = \sqrt{\frac{2\gamma^2}{\gamma - 1}\left[\left(\frac{p_t}{p_0}\right)^{\frac{2}{\gamma}} - \left(\frac{p_t}{p_0}\right)^{\frac{\gamma+1}{\gamma}}\right]} = 0.61 \tag{3.11}$$

With the universal gas constant $R = 8.314\,\mathrm{mol\,J^{-1}\,s^{-1}}$ and the characteristic venting rate of $\dot{n}_{V2}^{ch} = 0.9\,\mathrm{mol\,s^{-1}}$ the mass flux equation for an isentropic flow gives the minimal cross section of the vent-port:

$$A = \frac{\dot{n}_{V2}^{ch}}{p_0\ \Psi}\ \sqrt{\gamma\ R\ M_s\ T_{mix}} = 139\,\mathrm{mm^2} \tag{3.12}$$

and, finally, the diameter of the vent-port:

$$D = \sqrt{\frac{4\ A}{\pi}} = 13.3\,\mathrm{mm} \tag{3.13}$$

This simple calculation shows the main dependencies between the vent-gas temperature, composition and venting rate on the one side and the required size of the vent port on the other side. For the enclosure configuration of this example it is recommended to use a venting port with a diameter of at least 13.3 mm. Venting port diameter for other enclosures with other maximal pressures p_0 and volumes V can be calculated using the equations above. More details for designing overpressure vents can be found in ISO 4126.
The venting port should lead into the fume hood to reduce hazards of intoxication and fire. The ventilation system should be Directives for equipment intended for use in EXplosive ATmospheres (ATEX) certified to prevent deflagration inside the ventilation.

3.8.4 Toxicity of released vent gas

The gas which is released during overheating and by the TR has toxic components. In particular released fluorinated gases and CO-gas can be a danger to the personnel. HF was not detected in the first five experiments (section 3.7) and only

minimal amounts were detected in the next part (section 4.5). In contrast to HF, CO was detected in high concentrations by the test-setup. The threshold limit value (Maximale Arbeitsplatz-Konzentration) (MAK) and LEL values of the main gas components are summarized in table 3.7. The main risk of intoxication is caused by CO because of its low MAK and because of its high concentration in the vent-gas. The MAK value of CO is 30 ppm. The lethal exposure values (taken from the Gestis database:http://gestis-en.itrust.de/) are 40 000 ppm x 2 min (4 vol% x 2 min), 16 000 ppm x 5 min, 8000 ppm x 10 min, 3000 ppm x 30 min, 1500 ppm x 60 min.

Example: the fully charged cell used in SafeBattery is stored in the laboratory. The cell suffers an internal short circuit, transits into a TR and releases the vent-gas into the laboratory ($n_V = 2.31\,\text{mol}$, $C_{CO} = 16.6\,\%$). The laboratory has a room volume of $40\,\text{m}^2$ x 4 m. Will the CO release exceed the MAK levels in the laboratory? The amount of gas inside the laboratory before the TR is

$$n = \frac{p\ V}{R\ T} = \frac{100\,\text{kPa}\ 160\,\text{m}^3}{8.314\,\text{J}\,\text{mol}^{-1}\,\text{K}^{-1}\ (25\,\text{K} + 273\,\text{K})} = 6458\,\text{mol}. \tag{3.14}$$

The cell releases CO into the room

$$n_{CO} = C_{CO}\ n_V = 16.6\,\%\ 2.31\,\text{mol} = 0.37\,\text{mol}. \tag{3.15}$$

The concentration of the CO in the room is the quotient

$$C_{roomCO} = \frac{n_{CO}}{n} = 57\,\text{ppm}. \tag{3.16}$$

Here it is assumed that the CO is distributed homogeneously in the available room-volume. Even so the CO concentration in the room is well above the MAK value!

It is recommended to **use fixed and wearable gas monitoring and warning devices**. In laboratory of VVR the personnel uses wearable gas monitoring devices *Tango TX1-1* and fixed CO monitoring and alarm system from the company *ExTox*. The volume of the room or laboratory should be considered. A bigger laboratory with a higher room volume dilutes the escaped vent-gas and minimizes the risk of intoxication. A good laboratory ventilation system with an air exchange rate

Table 3.7: Electrolyte components and link to Gestis database `http://gestis.itrust.de/` or the MSDS

component	MAK ppm	LEL vol%	CAS number
CO	30	11.3	630-08-0
CO_2	5000	–	124-38-9
H_2	–	4.0	1333-74-0
CH_4	–	4.4	74-82-8
C_2H_4	carcinogenic	2.4	74-85-1
C_4H_{10}	1000	1.4	106-97-8
C_2H_6	–	2.4	74-84-0

of at least 10 times the room volume per hour to extract any harmful gases is recommended.
In SafeBattery cells with ≤30 % SOC released far less CO than charged cells. We measured max. $C_{CO} = 4.5\,\%$ in the vent-gas $n_V = 0.53\,\text{mol}$ of a discharged cell that was heated to 309 °C. This would result in a $C_{CO}^{room} = 3.6\,\text{ppm}$ in a room with $160\,\text{m}^3$, which is below the MAK value.

3.8.5 Toxicity of electrolyte and electrolyte vapour

When it is necessary to work with leaking cells, it is recommended to either use respirators which filter organic vapours (e.g. filter 6099 from 3M™) or to work inside a fume hood. Eye protection should be used, because on contact electrolyte components cause serious damage to eyes [87]. Protective gloves should be used, as described in the MSDS. Additional advises can be found in the publication from Lebedeva and Boon-Brett [91] and in the MSDS of the electrolyte components (table 3.8).

Table 3.8: Electrolyte components and link to Gestis database `http://gestis.itrust.de/` or the MSDS

short	long	usage	CAS
EC	ethylene carbonate	solvent	96-49-1
PC	propylene carbonate	solvent	108-32-7
DEC	diethyl carbonate	solvent	105-58-8
DMC	dimethyl carbonate	solvent	616-38-6
EMC	ethyl methyl carbonate	solvent	623-53-0
PS	1,3-Propansulton	additive if PC is used	1120-71-4
DTD	1,3,2-Dioxathiolane 2,2-dioxide	additive if PC is used	1072-53-3
FEC	fluoroethylene carbonate	additive	114435-02-8
VC	vinylene carbonate	additive	872-36-6

3.8.6 Inhalation of released particles

The tested cells in SafeBattery loose up to $\Delta m = 377\,\mathrm{g}$ of material during TR. A high share of this material consist of electrode particles which are ejected from the cell to the outside.

As a part of her masterthessis in SafeBattery Gasser [31] analysed the particle size distribution and the composition of the particles with SEM-EDS. She identified the following classes of particles Al_xO_w, $Ni_xCo_yMn_zO_w$, Mn_xO_w and C_xO_w. Most of the particles had a diameter $<10\,\mu\mathrm{m}$ and more than the half of the particles were $<2\,\mu\mathrm{m}$. Particles with $<4\,\mu\mathrm{m}$ are treated as alveolene penetrant fraction which can enter deep into the lungs according to TRGS 900 [100]. Maximal exposure limits for this size of particles are summarised in table 3.9.

Due the particle content and size, it is highly recommended to use suitable workplace safety equipment during the work with damaged batteries. It is recommended to use reusable **half face mask with special filters** (Respiratory protection: Particle filter, at least P2, colour code white). The personnel at VVR uses the product *7502 from 3M* with a *multi-filter 6099 from 3M* (Protection type: A2B2E2K2P3). In addition, one way overalls are used to prevent contamination of clothes by the particles. Sticky mats are used to remove particles from the soles of the shoes.

The reactor can be cleaned with an ATEX certified industrial vacuum cleaner with class H filters. Additionally, it is recommended to feed the exhaust of the vacuum

Table 3.9: Particle composition taken from Gasser [31] and Liao *et al.* [56] and links to Gestis database `http://gestis.itrust.de/` including the German occupational exposure limit (TRGS 900) values for the alveolene penetrant fraction

formula	source	CAS	TRGS 900 ($\mathrm{mg\,m^{-3}}$)
Al_2O_3	cathode current collector	1344-28-1	1.25
NiO_2	cathode active material	12035-36-8	1.25
MnO	cathode active material	1344-43-0	0.02
MnO_2	cathode active material	1313-13-9	0.02
Mn_3O_4	cathode active material	1317-35-7	0.02
Co_3O_4	cathode active material	215-157-2	–
LiF	electrolyte salt	7789-24-4	0.2
C	anode, conducting black	7782-42-5	1.25

cleaner directly into the ventilation exhaust of the laboratory. The laboratory can be cleaned with moist cloth.

4 Results from Project SafeBattery, Part 2: Hot-Spot Experiments

4.1 Background

Typical Li-ion batteries of electric vehicles (EVs) have a maximal operation temperature of 60 °C [113] and specialised Li-ion batteries can be used at 80 °C [114]. If a Li-ion cell reaches temperatures above ca. 80 °C the cells start to degenerate and when it reaches an even higher temperature it may transit into thermal runaway (TR) [35, 36]. An over-temperature of the cell may be caused by failures inside the cell or by the neighbourhood of the cell. The most prominent failures inside a cell are internal short circuits. They can be caused by Li-dendrites, Cu-dendrites, foreign particles and by mechanical damage to the cell. Over-temperature may be caused by failures outside of the cell: external fire, overheated or failed adjacent cells, failed electrical connectors with excessive resistance generating joule heat.
Failing cells release high amounts of heat which in turn may trigger the TR of adjacent cells [40]. The adjacent cells will generate further heat in their TR-reaction causing a domino effect of failing cells in an cell stack, the so called thermal runaway propagation (TP).
Different standards for battery-safety testing are published [115]. To test the resilience of battery packs against TP the Global Technical Regulation on Electric Vehicle Safety (GTR-EVS) is discussed[1] at the United Nations Economic Commission for Europe (UNECE) World Forum for Harmonization of Vehicle Regulations (WP.29). It contains the testing of TP characteristics and proposes a 5 min warning time between detection of TR and risk to the car passengers. One central point of

[1] https://wiki.unece.org/pages/viewpage.action?pageId=3178628

	Initiation of TR in the first cell			
	Small heating device	Overcharge	Thermally activated (60°C) internal short circuit device	Nail penetration
Unwanted preheat of adjacent cells	o	++	o	++
Unwanted additional energy	o	--	o	++
Suitable for cells in parallel?	++	-	++	++
Need for pack or cell manipulation?	+	+	--	++
Reproducibility	?	++	?	o
Flexibility (initial cell, SOC, starting temperature)	+	-	-	-
Evaluation of Ventgasmanagement	++	++	++	o

Figure 4.1: Advantages and disadvantages of different trigger methods. Adapted from [117].

TP testing is the initiation method to trigger the TR of the initial cell which starts the TP. A similar test standard was recently published by the People's Republic of China: GB 38031-2020, Electric vehicles traction battery safety requirements. Both standard mention different methods to trigger the first cell: by overcharge, by nail penetration and by overtemperature [116]. Each method has its advantages and disadvantages such as the need to manipulate the casing of the battery pack or adding of additional thermal or electrochemical energy to the initial cell or to the adjacent cells (fig. 4.1).

In this experimental work we focus on triggering the thermal runaway with a hot spot. The results of the work may be useful in two ways: (first) they can be used to evaluate the hot-spot method as a standardised trigger method for TP testing and (second) they may be used to judge if a certain failure mode which creates a hot-spot is critical to cell safety. Following questions are to be answered: what are the circumstances (local temperature, heat flow, duration) which trigger a TR? What are the critical parameter? Does a TR triggered by a hot spot differ from TR caused with other methods such as overcharge and overheating of the whole cell?

As in the previous chapter several staff members from Virtual Vehicle Research GmbH (VVR) contributed to this work. René Planteu, Bernhard Rasch, Oliver Korak and Thomas Humitsch did the experimental work in the laboratory. The author of this dissertation (Andrey Golubkov) was responsible for the test design, data analysis (except for the vent-gas analysis with gas chromatography (GC) and fourier-transform infrared spectroscopy (FTIR)) and wrote the text of this chapter.

The measurements and documentation of the vent-gas components were done by Christiane Essl.

4.2 Literature Review

4.2.1 Thermal Runaway Propagation Speed

The TR propagation speed c is the speed of the TR reaction front through a singe cell or through a stack of cells. If the front moves with a higher speed c, then the cell is destroyed faster and the heat and gas is released in shorter time. In a closely stacked module the propagation speed depends on the cells and on the material which is placed between the cells. Thermally insulating sheets can be used to prevent or to slow down TR propagation from cell to cell [118].
The measured speed parameter are valuable because they can be used to validate numerical TR-models. Good TR-models should reproduce the TR-front propagation inside a cell. There is very little literature on the propagation speed c inside a Li-ion cell.
Finegan *et al.* [119] extracted c from *in-situ* radiographs of a cylindrical 18650-cell during TR which was caused by an internal short circuit (ISC). The article from Finegan *et al.* is the only one which includes both, the in plane speed of $c_{\parallel}$ and the out of plane speed of $c_{\perp}$ of TR propagation inside a cell. The estimated $c_{\parallel}$ ranged from $200\,\mathrm{mm\,s^{-1}}$ to $400\,\mathrm{mm\,s^{-1}}$ and $c_{\perp}$ ranged from $6\,\mathrm{mm\,s^{-1}}$ to $8\,\mathrm{mm\,s^{-1}}$.
Archibald *et al.* [120] measured TR propagation in a compressed stack of 5 pouch cells. In their setup the outermost cell was heated until it vent into TR and the TR propagation to the other side of the cell stack was observed. The whole setup was in inert atmosphere to prevent effects of fire. Strictly speaking, they measured the TR propagation of a 5-cell module, but because there were no heat barriers between the pouch cells and because the casing of poch-cell is only a thin laminate of plastic and Al-foil, the whole stack can be viewed as one very thick pouch cell. They found a propagation speed $c_{\perp}$ of $0.78\,\mathrm{mm\,s^{-1}}$ to $0.8\,\mathrm{mm\,s^{-1}}$. The $c_{\parallel}$ could not be estimated with such setup.
The huge anisotropy between $c_{\parallel}$ and $c_{\perp}$ in [119] may be caused by two reasons (1)

by the anisotropy of the heat conductivity in the wound electrode layers of the cylindrical cell (jelly-roll) and (2) by the preferred path of the hot-gasses as they escape from the reaction front inside the cell to the opening (burst plate) of the cell casing.

The anisotropic heat conductivities λ in a Li-ion cell emerge from the layered structure of the electrodes. The active electrode material is coated on thin current collector foils made from aluminum or copper. The metallic foils have a much higher heat conductivity than the active electrode material, thus λ is much higher along the plane of the current collectors (in-plane, parallel to the layers, $\lambda_{\parallel}$) in contrast to through the planes (out-of-plane, perpendicular to the layers, $\lambda_{\perp}$) [102, 121]. Published heat conductivities of Li-ion cells are summarized in table 4.1. The high $\lambda_{\parallel}$ increases the heat transfer (*via* heat conduction) and promotes the TR propagation along the electrode stack.

The heat can also be transferred by convection inside the cell. A localized TR inside a cell will generate hot gases which will flow from the point of generation to the opening in the cell case. On its way to the opening the gases will exchange heat with adjacent material. The gas generation and venting can be fast and violent [119] and the heat exchange along the gas-path may be very effective. The hot gases may cause very fast TR propagation along the gas-path in the cell.

More literature [13, 122, 123] is available for TR propagation on module level with metal can cells. Those results are very relevant for EV-applications, but can not be used to directly estimate c inside a cell (the metallic casing and complicated internal structure of metal-can cells prevents simplifying a stack of cells as one large thick cell).

No studies are available on detailed - temporally and spatially resolved - propagation of the TR-front inside a large Li-ion cells. Experimental data on front-propagation are important to evaluate numerical TR-models.

4.2.2 Required Heating Conditions for Local Start of a Thermal Runaway

In many failure cases a cell is subjected to non-uniform over-temperature, such as by the heating of an adjacent failed cell, by failed electric contacts, by electric

Table 4.1: Published heat conductivities in Li-ion cells.

$\lambda_{\parallel}$ $\mathrm{W\,m^{-1}\,K}$	$\lambda_{\perp}$ $\mathrm{W\,m^{-1}\,K}$	source
25.6	0.77	Aiello *et al.* [121]
–	0.24(3)	Gaitonde and Nimmagadda, Amulya Marconnet [106]
–	0.74 to 0.82	Oswald [124]
24.1	1.1	Suresh and Stringfellow [125]

Table 4.2: Published heat TR propagation speeds in Li-ion cells.

$c_{\parallel}$ $\mathrm{mm\,s^{-1}}$	$c_{\perp}$ $\mathrm{mm\,s^{-1}}$	level	source
200 - 400	6 - 8	cylindrical cell	Finegan *et al.* [119]
–	0.78 to 0.8	pouch module	Archibald *et al.* [120]

arcing or by internal short circuit. Some literature is available for side heating of a cell (in other words, one flat surface of the cell is uniformly heated).
When the side of the cell is heated slowly ($<3\,^{\circ}\mathrm{C\,min^{-1}}$), then the difference between side-heating and heating the whole cell can be measured. In our publication (section 2.4) we report experiments, where a 50 Ah metalcan graphite/$LiMn_2O_4$ (LMO) cell was heated on one or two sides with a temperature ramp. In one-side heating experiments the cell started to self heat $>10\,^{\circ}\mathrm{C\,min^{-1}}$, when the externally heated side exceeded 281 °C. When both sides were heated, the critical temperature was lower at $T_{crit} = 246(6)\,^{\circ}\mathrm{C}$. (Only group A2 experiment taken into account)
When one side of the cell is brought to high temperature in seconds, then the time which the cell can sustain at such conditions can be measured. Gao *et al.* [122] tested TR-propagation in a stack of prismatic metal-can cells with graphite/$Li(NiMnCo)O_2$ (NMC) electrodes and a capacity of 37 Ah. In [122, fig. 7] after each subsequent TR the temperature between each failed cell and its yet fresh adjacent cell reached an intermediate plateau of $T_{mid} = 400\,^{\circ}\mathrm{C}$ to 500 °C. The duration of the intermediate plateaus was $t_{mid} = 141\,\mathrm{s}$ to 376 s. At the end of each plateau the fresh cell would go into TR as well. Their experiment shows that a fresh cell can sustain a high side temperature of T_{mid} for some time Δt before it transits

Table 4.3: Sustain capability of high side temperature of Li-ion cells. Here C is the capacity and E/m the energy density of the cells. T_{mid} is the intermediate temperature plateau of one side of a fresh cell in a TR-propagation experiment. t_{mid} is the duration which a fresh cell can sustain one side at T_{mid}. The TR starts at T_{crit} when the cell is heated slowly from both sides.

Electrodes	casing	E/m	T_{mid}	t_{mid}	T_{crit}	T_{crit}-method	src.
–	–	$\mathrm{W\,h\,kg^{-1}}$	°C	°C	°C		
graph./NMC	metalcan	165	400 - 500	141 - 376	215	ARC	[122]
graph./LCO	pouch	177	400	3 - 10	196	$5\,\mathrm{°C\,min^{-1}}$	[120]

into rapid TR. The same cell type transits into TR at only $T_{crit} = 215\,\mathrm{°C}$ when it is slowly heated from all sides in accelerated rate calorimetry (ARC) experiments. Archibald *et al.* [120] performed a similar TR propagation experiment with a stack of pouch cells (instead of metal-can cells) with graphite/$LiCoO_2$ (LCO) electrodes and a capacity of 10 Ah. In [120, fig. 10] they recorded a similar intermediate plateau at $T_{mid} = 400\,\mathrm{°C}$ but with a shorter duration of 5 s. In single cell experiments, when both cell sides were heated with $5\,\mathrm{°C\,min^{-1}}$, the TR occurred already at 185 °C to 196 °C.

Both results are compared in table 4.3. The temperatures T_{mid} and T_{crit} are similar, but the t_{mid} is more than 20 times higher for the metal-can cell. This could be explained by the thicker thermal insulation and heat spreading of the metallic case compared to the very thin laminated case of a pouch cell.

Some failure cases do not cause over-temperature of a whole cell side but a small hot-spot on the cell surface (e.g. overheting electric connections, electric arcing). No studies could be found, which would cover controlled localized heating and TR of a large Li-ion battery (>10 Ah). Only Zhang *et al.* [126] briefly mention that a local temperature of >300 °C is required to trigger TR. In many publications the TR is triggered by nail-penetration or internal short circuit, but then the local heat generation can not be controlled.

4.2.3 Gas release from locally overheated cells

Literature review on gas release of Li-ion cells at different state of charge (SOC) during TR is already included in section 1.7.1. No reports could be found on gas emission of locally overheated cells. As will be shown later, cells can be locally overheated without starting a TR, but still causing some gas release of the cell. No reports could be found on the composition of such gas. A mapping between a gas-fingerprint and the associated heating type (one side, both sides, local) is also missing in the literature.
The released gas could serve as early warning of a local overtemperature. If the gas is detected in a battery pack, the vehicle could switch to an emergency mode and warn the passenger. It is therefore important to know the gas-fingerprint of different failure types.

4.2.4 Internal short circuit

Santhanagopalan *et al.* [127] describe different types of ISC: shorts may occur inside the stack or at the edges of the stack between electrode active material or the current collector foils. The outcome of an appearing ISC depends on its resistance. An ISC with high resistance will only cause limited local heating and continuous self discharge of the cell while an ISC with low resistance may cause excessive local heating and may start an TR of the cell [126].
Feng *et al.* [15] measured temperature response of fresh and dried cell at 100% SOC in ARC experiments. The dried cell had very low ionic conductivity which prevented high current (and heating) during ISC. The fresh cell contained electrolyte and high-power-ISC was possible. They compared the temperature rate plots and calculated that the ISC releases (through joule-heating) 9% of the overall energy during a TR. Feng *et al.* state that those 9% are critical, because they are released in an early stage of heating and lift the temperature into a range where highly exothermic anode-cathode redox reactions take over and quickly destroy the cell.
Despite the importance of the ISC, only one work was found, where the ISC-current was actually measured: Koch *et al.* [128] build a stack of 24 large cells with 43Ah

each and installed sensors to measure the balancing current between parallel connected cells and initiated a TR on the outermost cell. Up to 80 A of inrush current into a cell during TR were measured in a 12p2s[2] configuration and Koch *et al.* calculated internal short circuit resistances of R_{ISC} in the range of 20 mΩ to 180 mΩ.

4.3 Experiment Setup

The second experiment series used the same cell type (section 3.3), the same test stand (section 3.4) and the same experiment sequence (section 3.5).

4.3.1 Updated sample holder

A new sample holder was designed specifically for the size of the tested cell (fig. 4.2). As before, it consisted of several layers with the addition of an aluminium layer for better heat spreading. The stack consisted of the following elements, beginning with the lowest layer: stainless steel plate (10 mm), aluminium plate (10 mm), mica sheet (1 mm), thermocouples, cell, thermocouples, mica sheet (1 mm), aluminium plate (10 mm), stainless steel plate (10 mm). The geometry and the dimensions of the used components are shown the Appendix (page 274).
Another new design element was a hole in the top layers of the sample holder, so that a hot-spot heater could access the cell surface. The hole could be closed with a fitting element for experiments without a hot-spot heater.
The stiff outer steel plates were compressed by four springs in order to apply a uniform force to the layers and to the cell between them. The steel plates were equipped with large heaters (1000 W for each plate). If necessary, the large heaters could be activated to heat the whole sample-holder up to max 400 °C. The large heaters were necessary when the cell had to be heated by other means because of failed hot-spot generator. The role of the aluminium plates was to distribute any heat from the large heaters to prevent uneven heating.

[2] 12 cells connected in parallel and 2 of the 12-cell-compounds connected in series

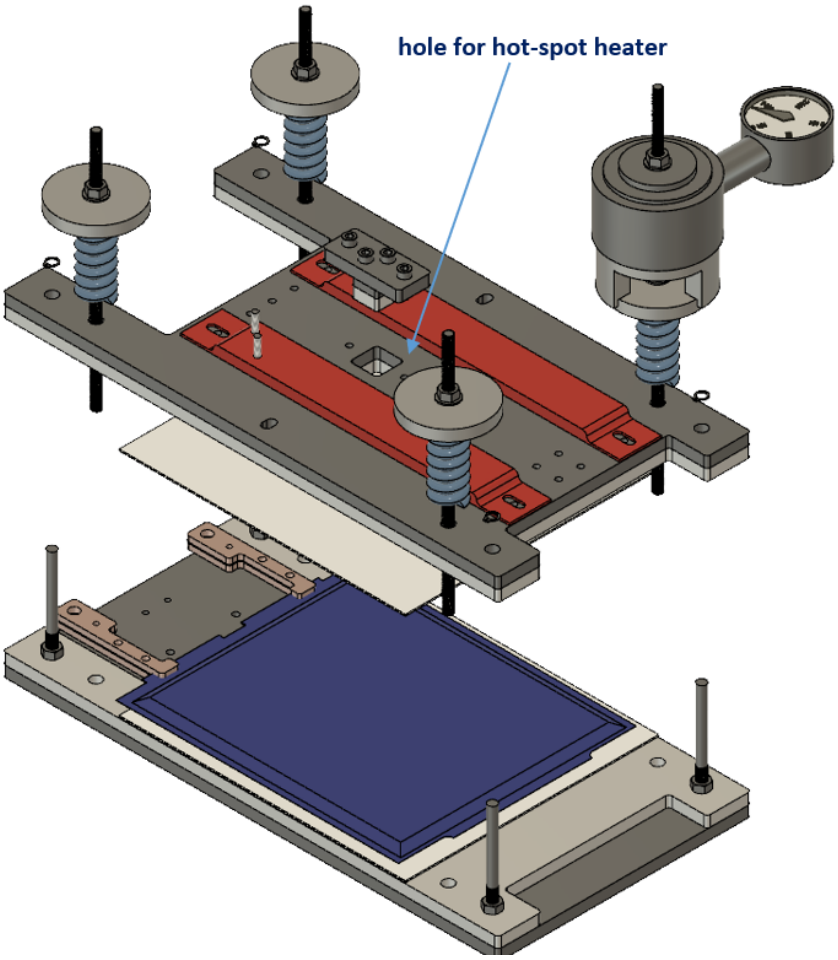

Figure 4.2: Updated sample holder.

The function of the mica sheets was to provide some thermal insulation between the aluminium plates and the cell: At cell temperatures above a critical temperature exothermic reactions inside the cell start and the cell begins to self heat. Since the interest in the further development of those exothermic reaction the sample holder should not act as a heat sink and the exothermic reactions should develop as adiabatic as possible. To minimise the thermal coupling between the aluminium plates and the cell an insulation made from mica sheets ($\lambda = 0.23\,\mathrm{W\,m^{-1}\,K^{-1}}$) with 1 mm was placed between them. The mica sheets also provided channels for the thermocouple wires which measured the cell surface temperature at different positions.

4.4 Analysis Methods

Methods to calculate the amount of gas and venting rate were already introduced in section 3.6 and in section 2.4. In this chapter a new method to characterise the ISC is added.

4.4.1 Internal short circuit current

The current of an ISC inside the cell I_{ISC} can not be measured directly. It can only be measured indirectly by observing its effects on the cell. We use two different methods to calculate the I_{ISC} using a simplified equivalent circuit of the cell: fig. 4.3. Here U_T is the terminal voltage, which can be measured between the positive and negative tab of the cell, U_{OCV} is the open circuit voltage, which depends on the SOC of the cell (The dependence is shown in the SOC-open circuit voltage (OCV) curve, fig. 3.2), R_i is the internal resistance of the cell. In case of an ISC an additional resistance R_{ISC} exists and an internal short circuit current I_{ISC} discharges the cell. For the cell used in Safe Lithium-Based Traction Batteries (SafeBattery), the U_{OCV} ranges from 3 V to 4.2 V and the R_i at room temperature is assumed with $R_i = 1\,\mathrm{m\Omega}$.

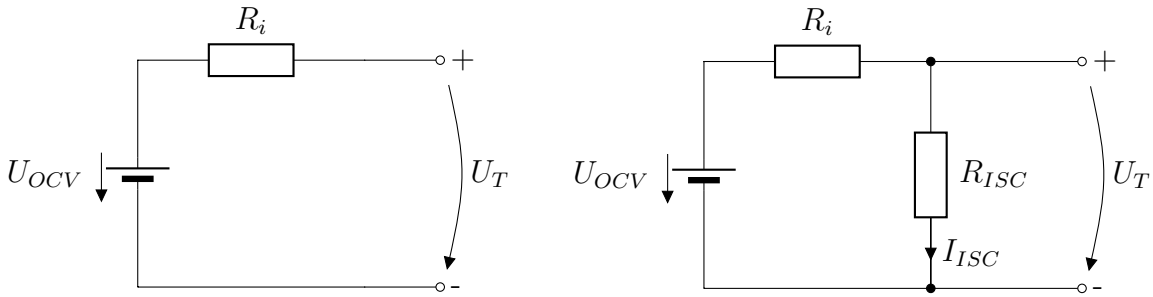

Figure 4.3: Electric model of a cell. (left) in normal operation, without an internal short circuit. (right) with an internal short circuit.

Delta SOC method

This method derives the I_{ISC} from the change of the cell voltage U_T. It ignores the voltage drop caused by the internal resistance of the cell R_i, which can be justified for small I_{ISC}.
In our experiments we record the cell voltage U_T, then use it to interpolate the SOC of the cell from a previously measured SOC-OCV curve (fig. 3.2) (the voltage drop $R_i \times I_{ISC}$ is ignored). The current is derived from the time derivative of the SOC:

$$I_{ISC} = (3600\,C)\frac{d}{dt}SOC(t) \tag{4.1}$$

Here C is the nominal cell capacity (42 A h). Additionally, a moving average filter with a time window of 100 s or piecewise linear fitting is applied to the SOC time-series, to reduce the signal noise before the time derivative is made.

Ri method

For hard ISC with high current I_{ISC} the voltage drop $R_i \times I_{ISC}$ can not be ignored and U_T can not be used to calculate the SOC. Instead, the current is calculated directly

$$I_{ISC} = \frac{U_{OCV} - U_T}{R_i} \tag{4.2}$$

This method is better suitable for ISC with short duration and small SOC change.

4.5 Experiments

An overview of the experiments is given in fig. 4.5. The goal of the experiment series was to determine the critical amount of heat that is needed to start the TR when the cell is locally heated at different positions fig. 4.4. The focus was laid on the following hot-spot positions:

Centre of the cell: in other words, localized heating of the middle of one of the two large faces of the cell. Here the localized heating represents a failure case where an internal short circuit would create excessive self-discharge and

locally restricted joule-heat which could initiate a TR of the whole cell. The location was chosen because of its approximate rotational symmetry in respect the Z axis. The symmetry simplifies the interpretation of the experiments.

Negative/ positive tab of the cell: localized heating of one of the two terminals (tabs) of the cell. Such heating represents a failing electrical connection of the cell or an error in during the welding of the terminal. In both cases excessive heat may be injected into the cell via the metallic terminal of the cell.

In addition to the hot-spot heating, one or both pressure plates of the sample holder could be heated. This was done in some cases, when hot-spot heating failed to trigger the thermal runaway.

It was found that significantly more local heat input was needed to trigger a TR than expected: First experiments with the small μ-heater (<200 W) failed to produce a TR in the centre of the cell (T0146a, T0147a). Instead of TR the μ-heater created soft internal short circuits, which caused a self discharge of the cells. A subsequent uniform heating of the discharged cells (T0146, T0147) produced no TR either. This confirmed the results from previous chapter (chapter 3), showing again that (fresh, not aged) discharged cells do not exhibit a TR.

It was decided to proceed with tab-heater experiments which used a heater with higher power (>400 W). Heating the positive tab (electrode) resulted in a TR (Experiment T0149). Surprisingly, with the same setup, heating the negative tab failed to start a TR of the whole cell (Experiment T0151).

In the mean time the new medium-heater with higher heating power (>500 W) was designed. It replaced the underpowered μ-heater. The medium-heater achieved to start the TR after prolonged heating (T0160) and with assistance of the bottom heater (T0161). It was decided to increase the electrical power to 900 W (starting with T0177) and to improve the thermal insulation of the heat conductor to reduce the heating time (starting with T0178). First TR with short heating time could be created (T0178). Some technical problems (T0179) with ground fail current had to be solved. In the final two experiments (T0180 and T0181) the TR could be started after short heating period and the cells with reproducible results.

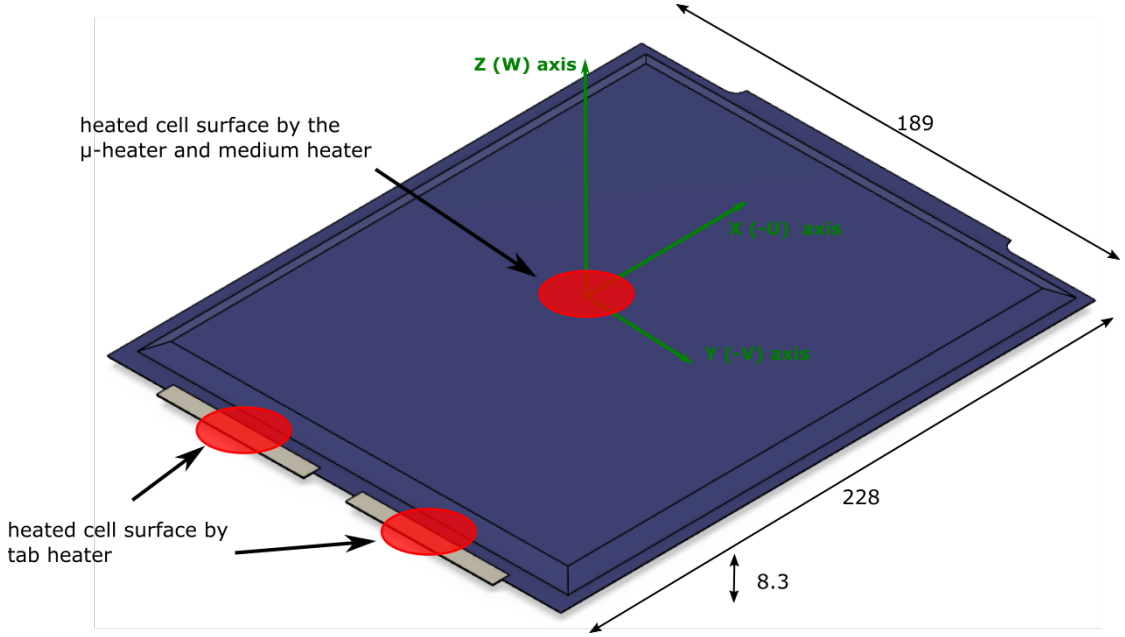

Figure 4.4: Dimensions of the cell and the positions of the heated surfaces in hot-spot tests.

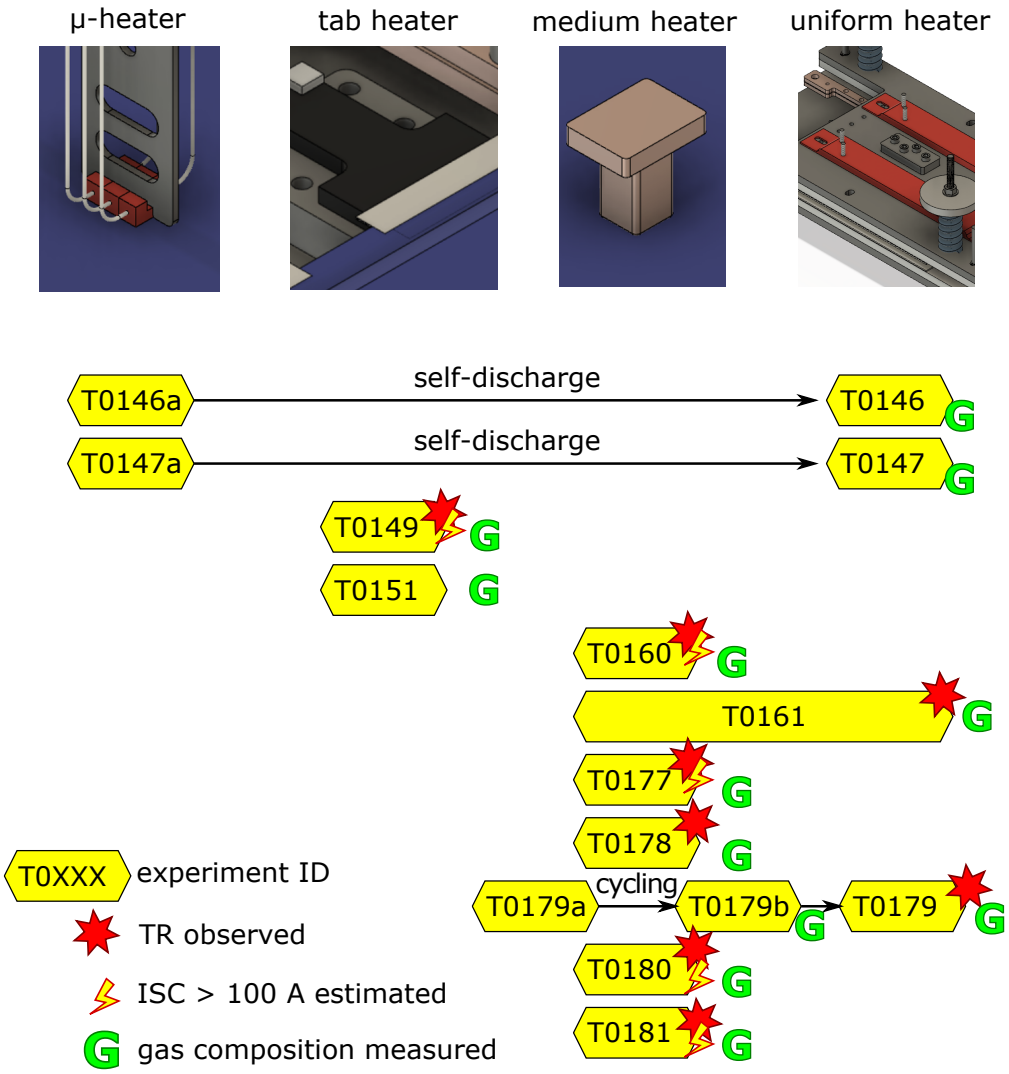

Figure 4.5: Overview of experiments in this chapter. Here each number (e.g. T0151) represents a cell ID. Each yellow hexagon represents an experiment. With some cells several subsequent experiments were done (e.g. T0146a → T0146). Four different heating methods were used (μ-heater ... uniform heater), the methods are described in the next sections. Some of the experiments ended with the TR of the cell. Sometimes the TR was accompanied by an ISC. After most experiments the composition of released gas was measured.

4.5.1 Uniform heater

Experiment Setup

The experiment setup is similar to uniform heating explained in the previous test series (section 3.4). The only difference was that a custom sized sample holder with additional aluminium layers was used (fig. 4.2). Here, the uniform heating was activated as follow-up experiment, when a TR could not be triggered by a hot-spot. The cell was heated uniformly from both sides with four heater strips:

Type: OT-1205 HT S 240V1P 500W129760 from *Chromalox* https://www.chromalox.com/
Heated cell area: $A_P = 2 \times (228\,\text{mm} \times 189\,\text{mm}) = 862\,\text{cm}^2$
Rated power: $P_R = 4 \times 500\,\text{W} = 2000\,\text{W}$ at 240 V
Max temperature: 400 °C

Here the thermocouple setup of the preceding micro-heater experiments was reused: 22 thermocouples were used on the top and bottom surface of the cell (fig. 4.25). The hot-spot thermocouples (TK13, TK24) were not reused.

Experiment T0146

This is a follow up to the experiment T0146a (section 4.5.3). In T0146a the TR could not be started by the hot spot, instead the cell started to discharge slowly. The self-discharge was caused by the damage from by the micro-heater. The cell already discharged to 2.85 V when the cell heating was started. During heating it discharged further. Interestingly the cell voltage recovered to a plateau at 2.5 V above 80 °C. A small exothermic reaction could be seen at 19 000 s when the voltage dropped from 2 V to 0.5 V (fig. 4.8). A strong exothermic reaction could not be detected during the uniform heating up to 256 °C (fig. 4.6).
Conclusion: The hot-spot attempt created an internal short-circuit with relatively high resistance. The joule heat from the ISC could not start a TR. Instead the cell discharged as explained in section 4.5.3. The experiment also shows that at least

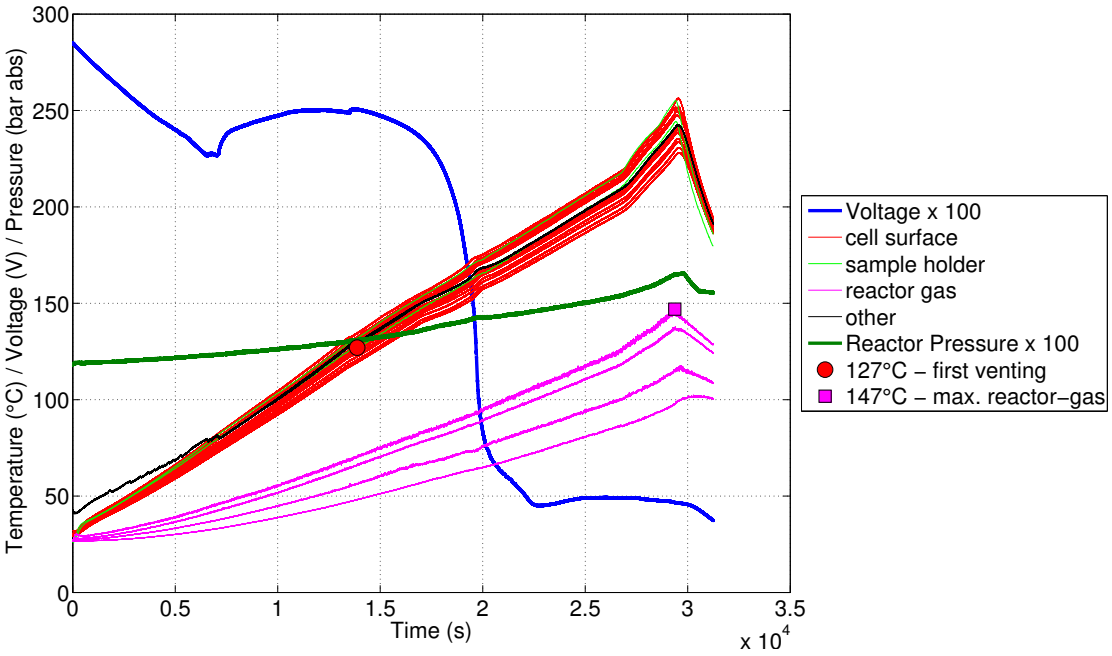

Figure 4.6: Experiment T0146. Full duration of the experiment.

up to 256 °C a TR of the discharged cell does not occur.
The cell released 0.44 mol during the experiment (fig. 4.7). The gas composition was measured with FTIR and GC: fig. 4.9.

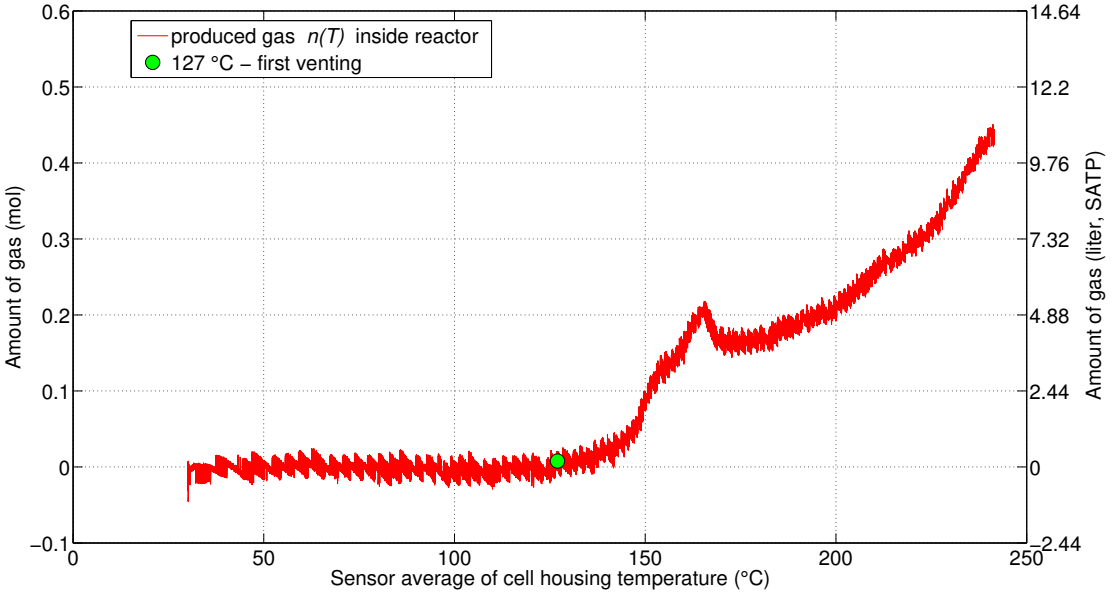

Figure 4.7: Experiment T0146. Gas release by the cell vs. average cell temperature.

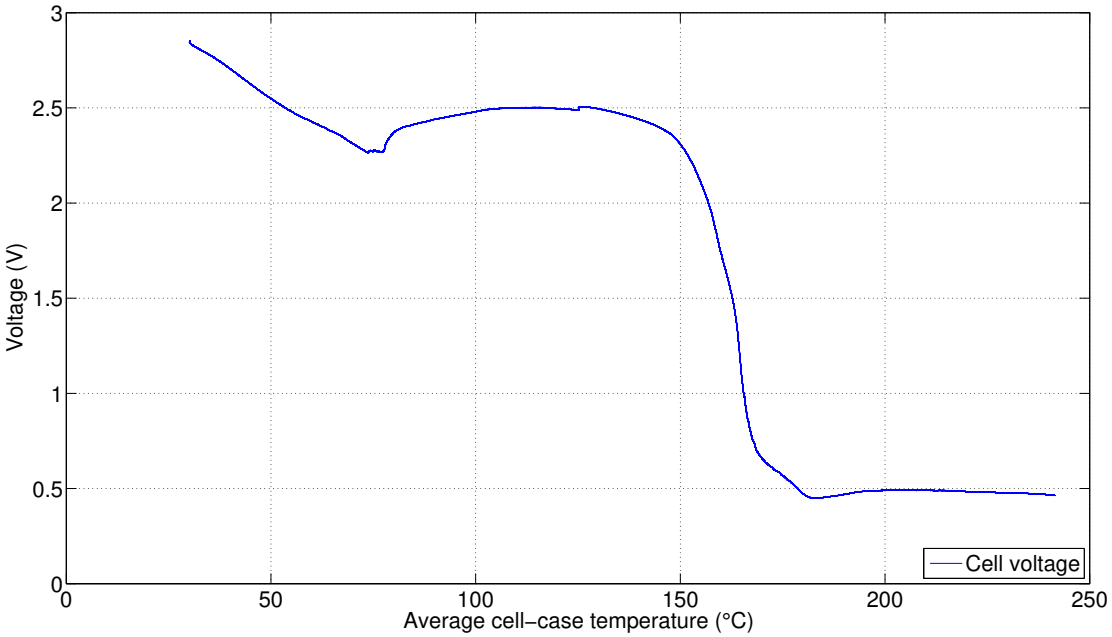

Figure 4.8: Experiment T0146. Voltage of the cell vs. average cell temperature.

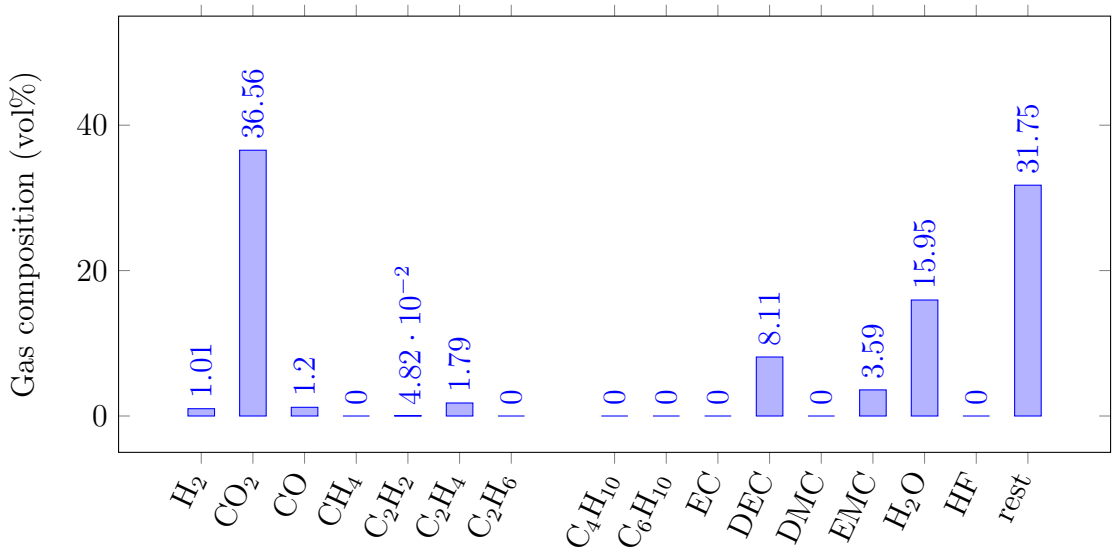

Figure 4.9: Experiment T0146. Detected gas components which were released by the cell. Gas composition was measured by FTIR and GC.

Experiment T0147

This is again a follow up, this time to experiment T0147a (section 4.5.3). Again, a TR could not be started by the micro hot spot. After T0147a the cell discharged in the course of 5 days to a value of 3.18 V. Then the experiment T0147 started and the cell was heated uniformly. During heating the cell voltage stayed above 3 V until 170 °C. Then, the voltage started to drop and stabilized at 0.7 V above 210 °C. Above 260 °C the voltage dropped to 0 V (fig. 4.12).
Small exothermic reaction were seen when the voltage dropped from 3 V to 0.7 V at 19 000 s and from 0.7 V to 0 V at 24 000 s. Temperature was held constant after the cell reached a maximum temperature of 278 °C (fig. 4.10). *Conclusion:* Again, heating up to 278 °C of a discharged cell did not start a TR. The experiment also shows a voltage plateau with 0.7 V between 170 °C and 260 °C. Only above 260 °C some effect caused a complete discharge to 0 V. One such effect could be melting of the separator at 260 °C.
The cell released 0.81 mol during the experiment (fig. 4.11). The gas composition was measured with FTIR and GC: fig. 4.13.

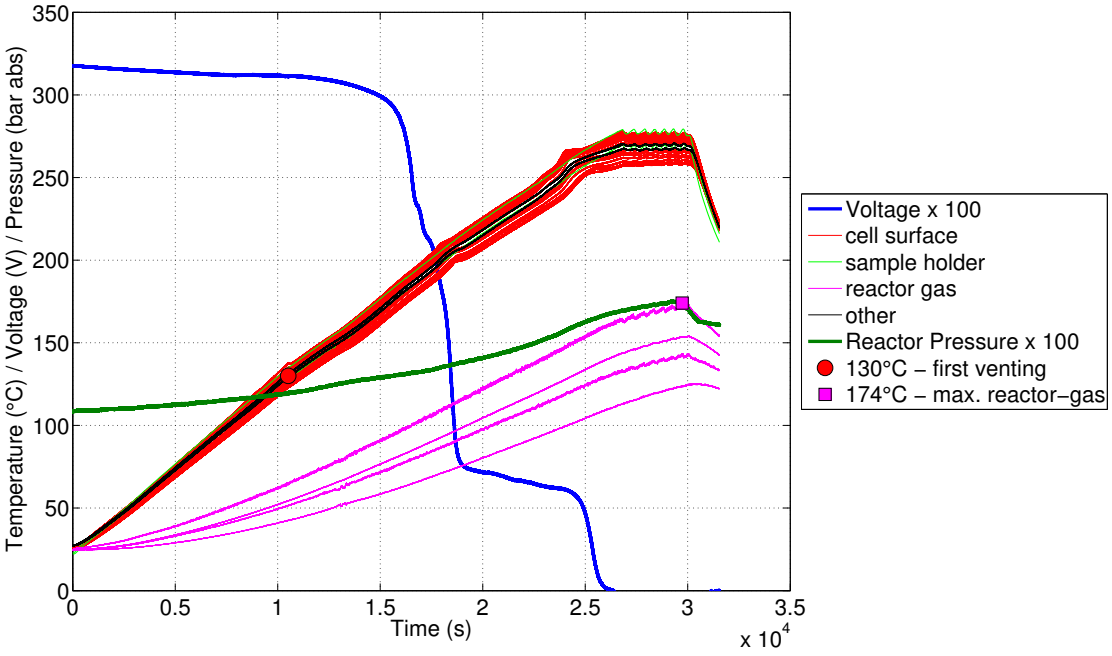

Figure 4.10: Experiment T0147. Full duration of the experiment.

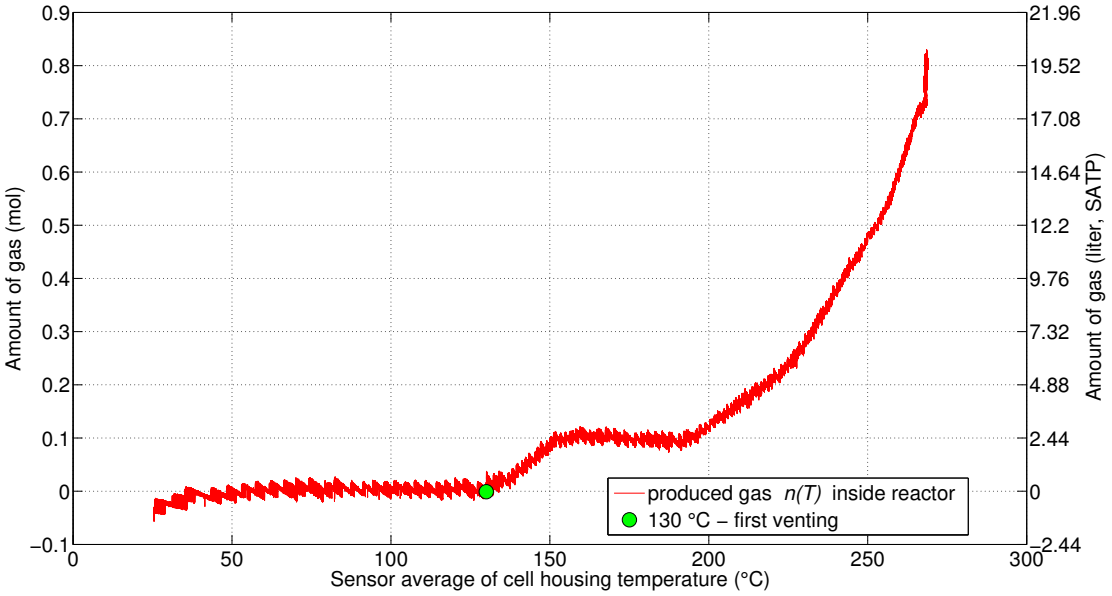

Figure 4.11: Experiment T0147. Gas release by the cell vs. average cell temperature.

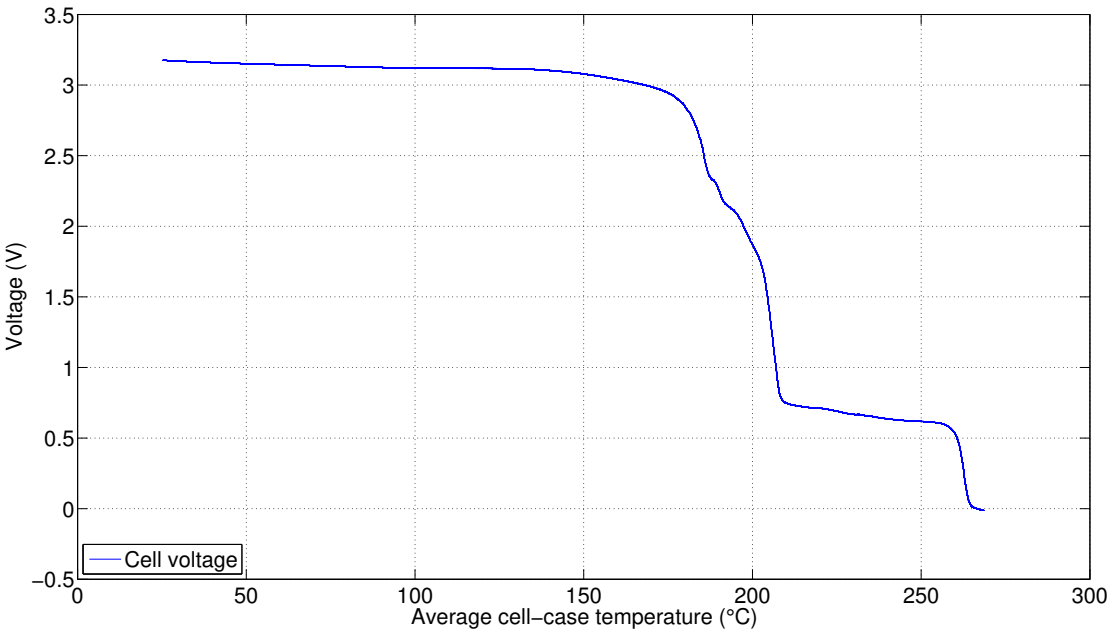

Figure 4.12: Experiment T0147. Voltage of the cell vs. average cell temperature.

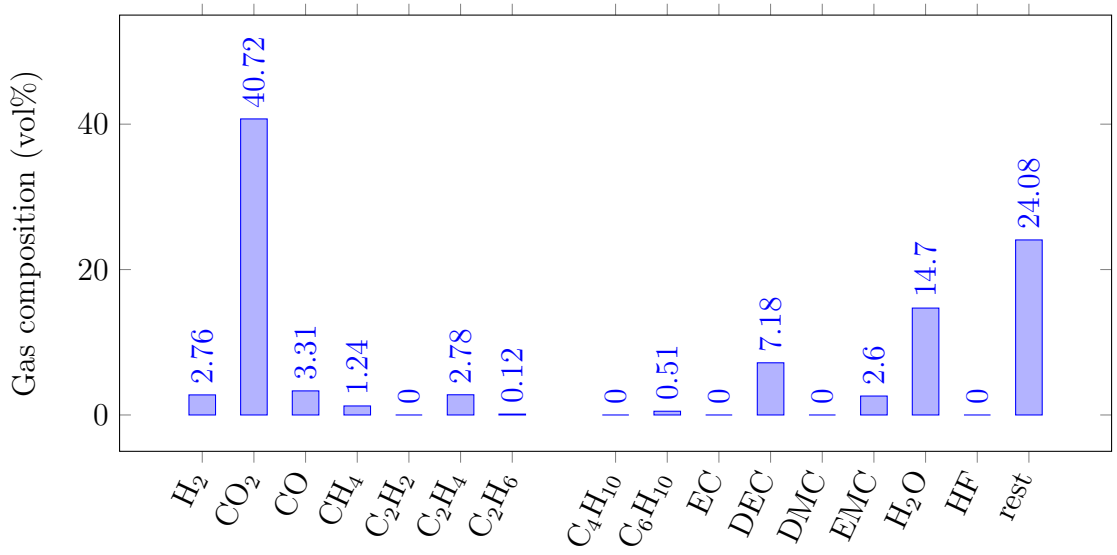

Figure 4.13: Experiment T0147. Detected gas components which were released by the cell. Gas composition was measured by FTIR and GC.

4.5.2 One sided heater

Experiment Setup

The experiment setup is the same as in uniform heating explained in the previous section (section 4.5.1) with the difference that not both **but only the bottom plate of the stack was heated**. One-sided heating with the bottom plate was used, when the TR could not be started with a hot-spot heater and when attaching the heater strips to the top plate was not possible.

Type: OT-1205 HT S 240V1P 500W129760 from *Chromalox* https://www.chromalox.com/
Heated cell area: $A_P = (228\,\text{mm} \times 189\,\text{mm}) = 431\,\text{cm}^2$
Rated power: $P_R = 2 \times 500\,\text{W} = 1000\,\text{W}$ at $240\,\text{V}$
Max temperature: $400\,°\text{C}$

Experiment T0179

This is a follow up to the experiment T0179b (section 4.5.5) which itself is a follow up to T0179a (section 4.5.5). In the two preceding experiments the TR could not be started by the hot spot, although some damage was done to the cell. In T0179, to finally trigger the TR of the previously tormented cell, it was decided to heat the whole lower pressure plate. It was also decided not to wait for the next day but to start immediately after the hot-spot experiment T0179b failed to trigger the TR; therefore the cell could not self-discharge in the meantime.
Pulses ($\pm 1\,\text{A}$) were applied to measure the internal resistance of the cell. Temperatures on the bottom and top side of the cell surface were measured (fig. 4.14). The heating of the bottom side could start a TR (fig. 4.21).
Discussion: Since the cell was already damaged by the previous attempts to start a TR this results are not fully representative for a pristine cell. The cell was heated from below. Immediately before the start of the TR the bottom surface of the cell had a temperature from $231\,°\text{C}$ to $257\,°\text{C}$ while the upper (unheated) surface had a lower temperature ranging from $189\,°\text{C}$ to $216\,°\text{C}$. Surprisingly, although the lower

surface was heated and had a higher temperature, the start of TR was detected on the upper unheated surface, at the outermost temperature sensor TK10. The TR then propagated on the top layer from the outside to the inside in 3 s and subsequently from the top layer to the bottom layer in 6 s (fig. 4.16). By the end of the TR the cell casing reached up to 561 °C.

It is unclear why the TR started on the cooler upper side and away from the hot-spot. One possible explanation is that the upper side was damaged by the previous hot-spot attempt (T0179a) and that subsequent discharge and charge of the cell (done between the experiments T0179a and T0179b) produced Li-plating in this area. Li-plating could have lowered the onset temperature (>11.3 °C min^{-1}) to 214 °C.

Another explanation would be a short circuit in the upper layer, but it is unlikely that a short circuit triggered the TR on the top side: the cell resistance grew to $R_i > 500\,\mathrm{m\Omega}$ before the TR, therefore even if the resistance of the short circuit point would have an optimal value of $R_{isc} = 0.5\,\Omega$ the overall current would be $I_{isc} = 4\,\mathrm{A}$ and the joule heat at the point of short circuit would be only $P_{sc} = 8\,\mathrm{W}$. Such small additional heat is insignificant compared to 1000 W from the bottom heater.

During heating of the bottom side, the cell started to release gas above an average cell case temperature of 120 °C and released 0.25 mol before the TR. During the TR the cell released additional 1.41 mol of gas starting at an average cell case temperature of 220 °C with a characteristic rate of 0.5 mol s^{-1} (11.3 l_{SATP}/s) (figs. 4.18 and 4.19). The vent-gas composition was measured after the TR (fig. 4.20). Note that in this experiment a small amount of HF with a concentration of 40 ppm was detected.

0 s Start of heating

10000 s Avg. cell temperature 167 °C, cell resistance starts to increase (envelope of the cell voltage starts to expand)

10900 s Avg. cell temperature 180 °C, cell resistance increases beyond 0.5 Ω. Cycler is switched off because maximal voltage limit is reached during a charge pulse.

13565 s Avg. cell temperature 220 °C, voltage drops from 3.8 V to 0 V.

13566 s Outermost sensors (TK10, TK9) on the *top side of the cell*, starting at temperatures between 203 °C and 223 °C start to increase rapidly. TR starts.

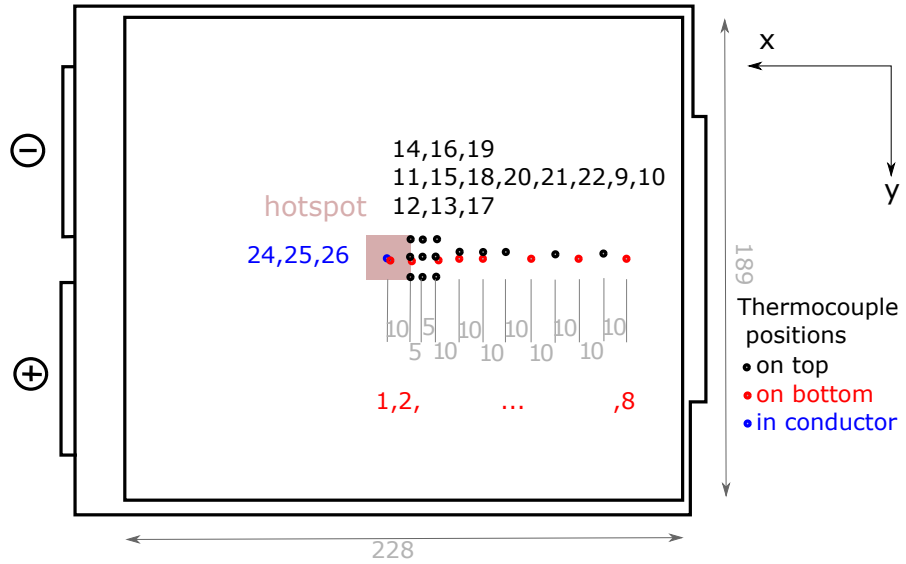

Figure 4.14: T0179. Positions of the thermocouples on the cell surface. The hot spot was not switched on here.

13567 s TR has propagated through the upper layer.

13573 s TR has propagated from the top layer to the bottom layer. Pressure and gas-temperature in the reactor reach their maximum values.

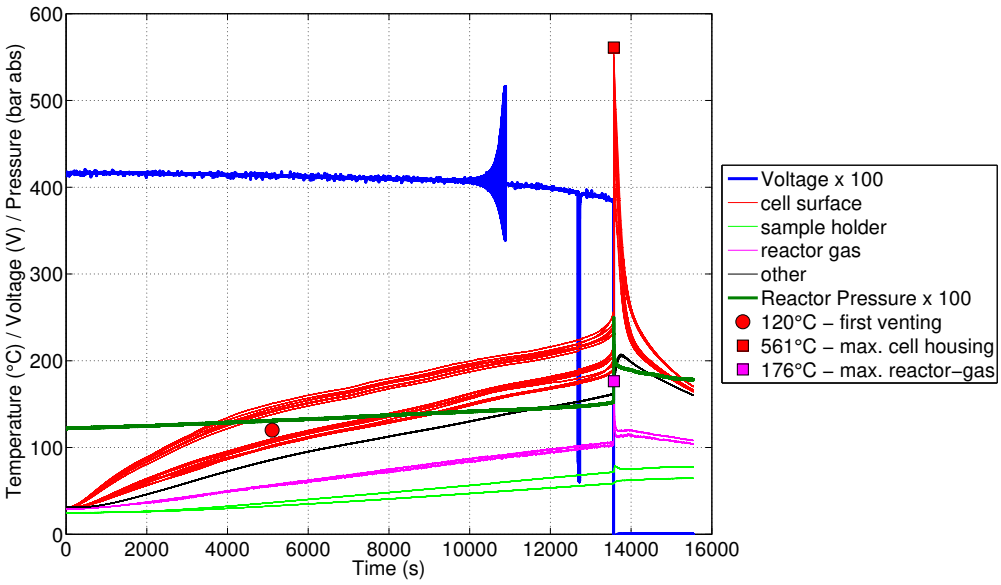

Figure 4.15: T0179. Full duration of the experiment. Note the two distinct temperature strains for the lower (heated) and upper (not heated) cell surface. *Other:* temperature inside the heat conductor of the hot-spot (not activated).

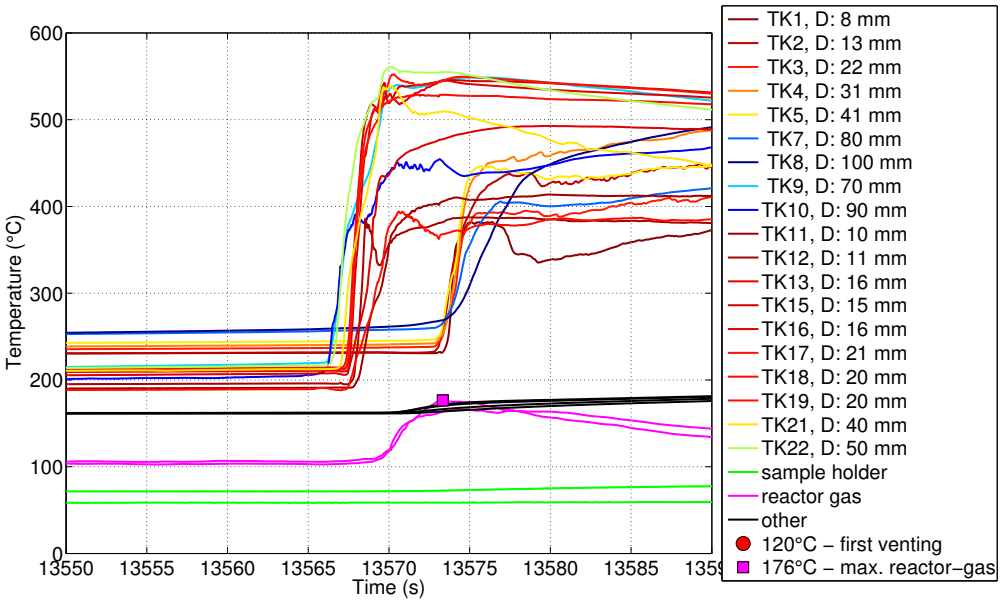

Figure 4.16: T0179. Time span of the TR. Temperatures are colour-coded according to distance from the centre of the cell. The two strains belong to the the lower (heated) and upper (not heated) cell surface. *Other:* temperature inside the heat conductor of the hot-spot (not activated).

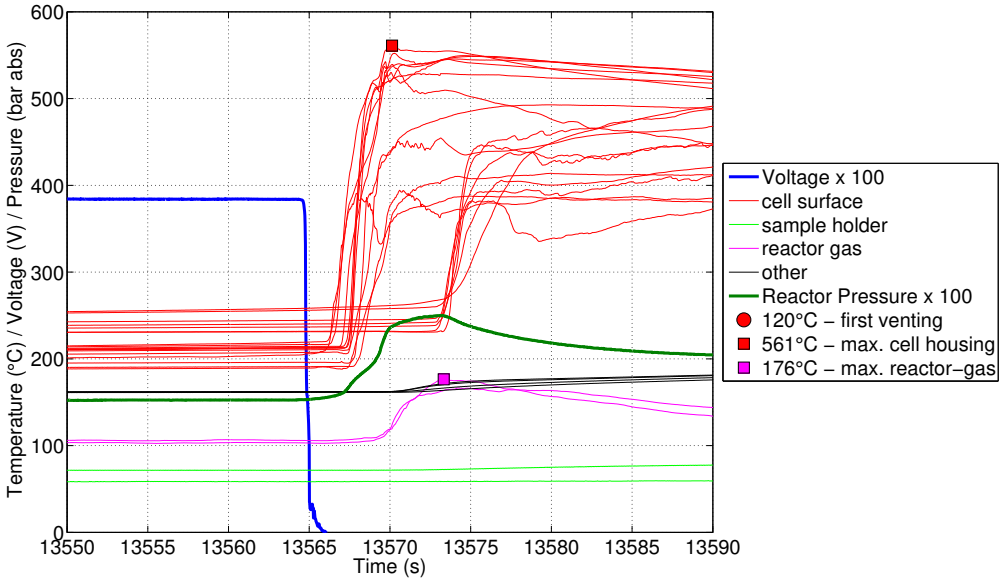

Figure 4.17: Experiment T0179, time duration of TR.

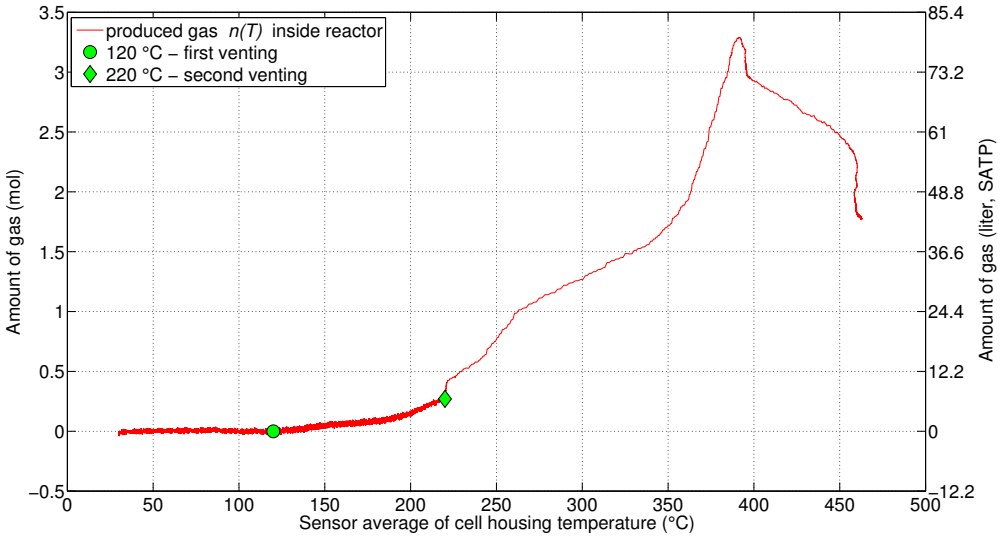

Figure 4.18: Experiment T0179, Gas release by the cell vs. average cell case temperature.

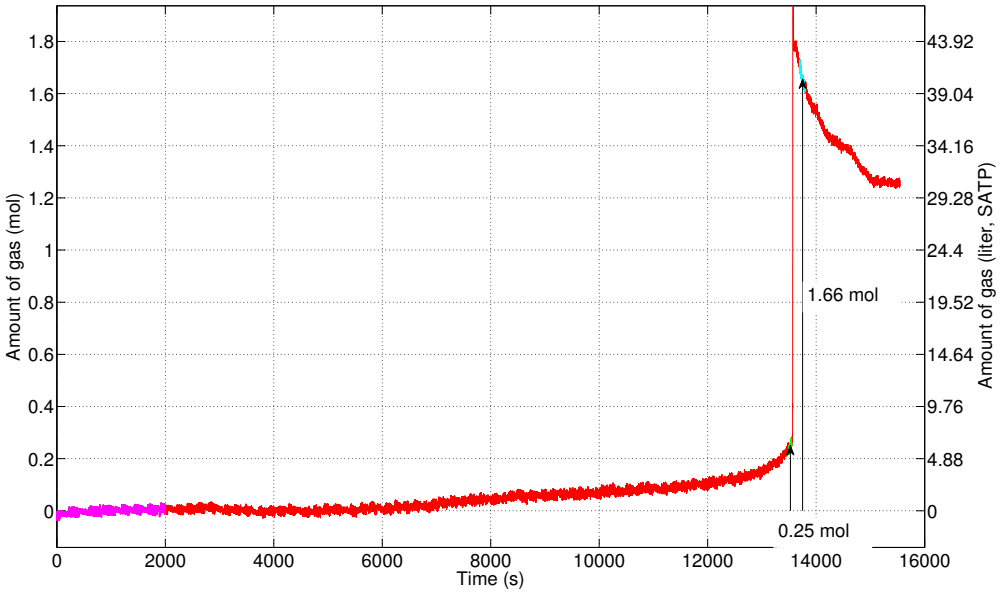

Figure 4.19: Experiment T0179, Gas release by the cell vs. time.

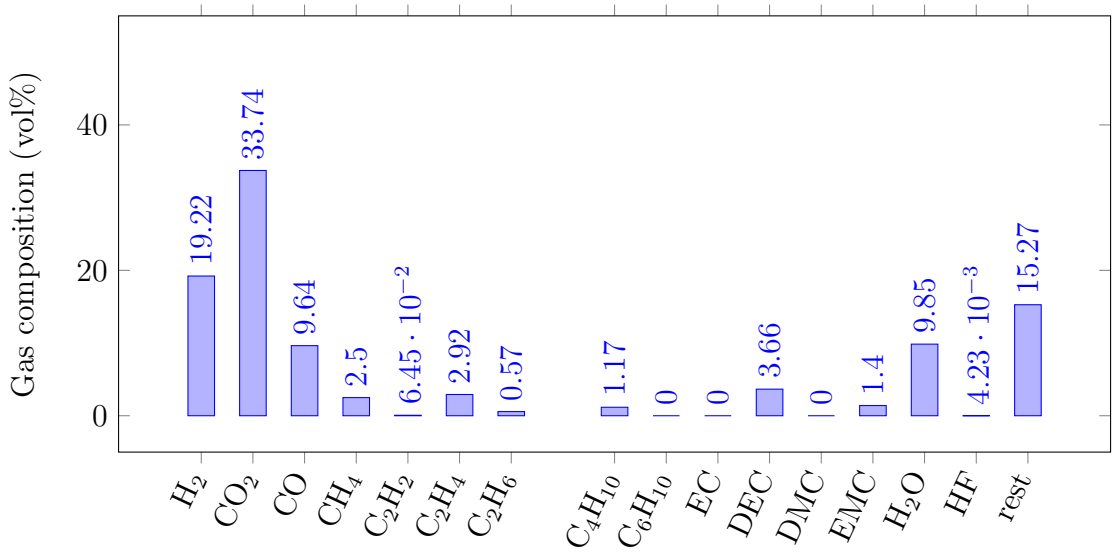

Figure 4.20: Experiment T0179. Detected gas components which were released by the cell. Gas composition was measured by FTIR and GC.

Figure 4.21: Experiment T0179, cell after TR experiment.

4.5.3 Hot spot, micro heater

Experiment Setup

In this setup the cell was heated by a small hot-spot located in the centre of the large upper surface of the cell. To access this area the upper steel plate, aluminium plate and mica sheet had an opening (25 mm × 25 mm) made so that the micro heaters had access to the cell surface. The micro-heater elements were attached to a lever and the lever was pressed to the surface of the cell by small springs (figs. 4.22 to 4.24).
The heater consisted of three micro-heater elements which were electrically connected in parallel. Heater parameter are:

Type: FLE 100 576 from *Bach RC* https://www.bachrc.de/
Heated cell area: $A_H = 3 \times (3\,\text{mm} \times 7\,\text{mm}) = 27\,\text{mm}^2$
Rated power: $P_R = 3 \times 30.8\,\text{W} = 92.4\,\text{W}$ at 24 V
Max temperature: 500°C

An overall number of 24 thermocouples were used on the top and bottom surface of the cell and two thermocouples (TK13, TK24) were placed between the heater and the cell (fig. 4.25).

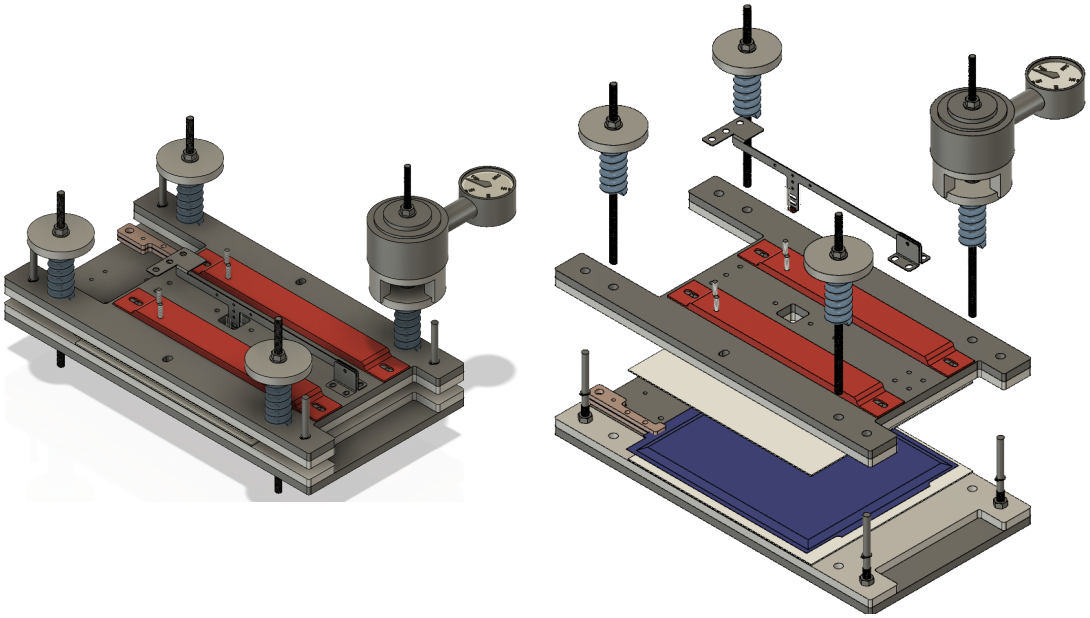

Figure 4.22: Fully assembled sample holder used for hot-spot micro-heater experiments. Cell in blue. Aluminium plates in light grey, steel plates in dark gray.

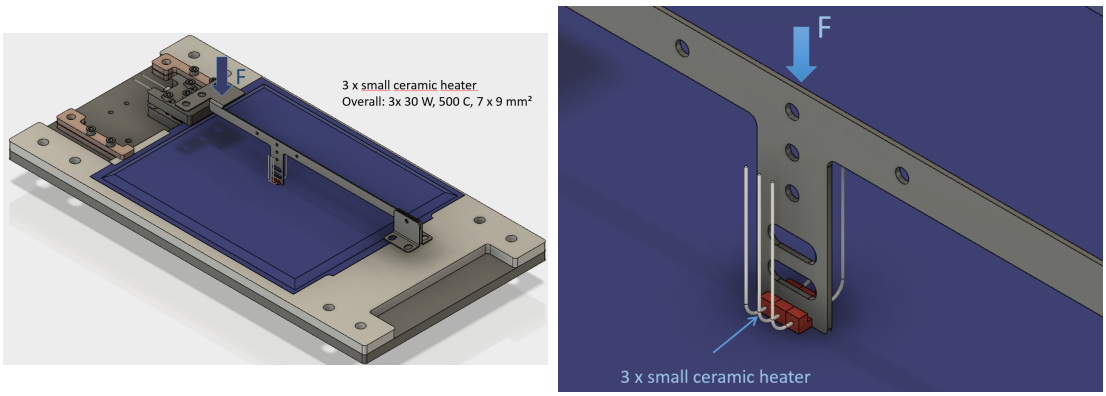

Figure 4.23: Details of the micro-heater elements.

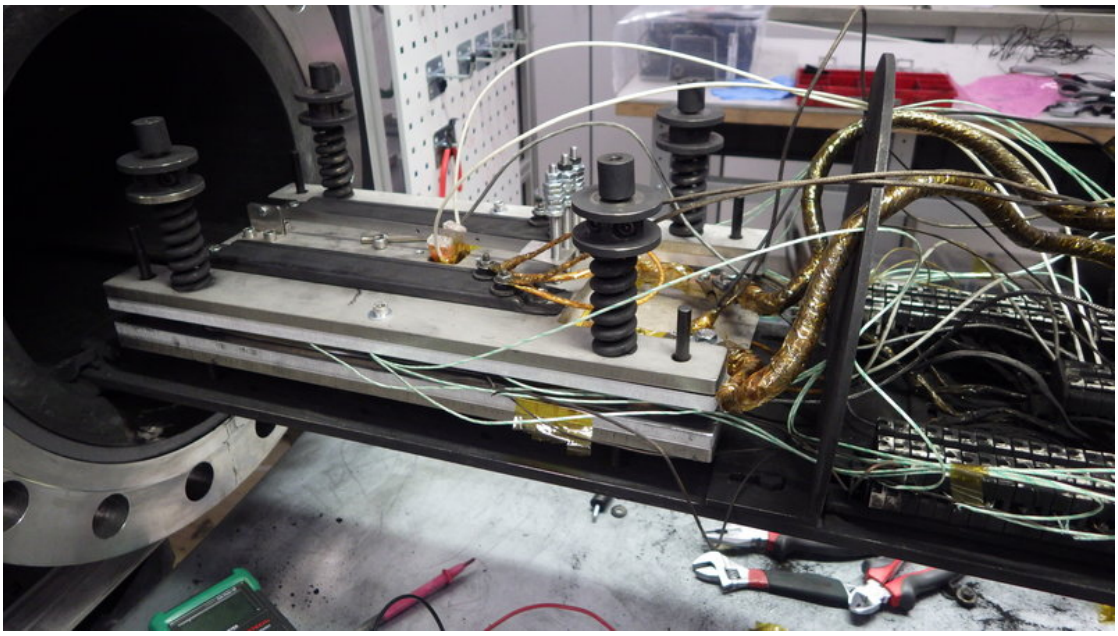

Figure 4.24: Foto of a typical test setup with the hot-spot micro-heater.

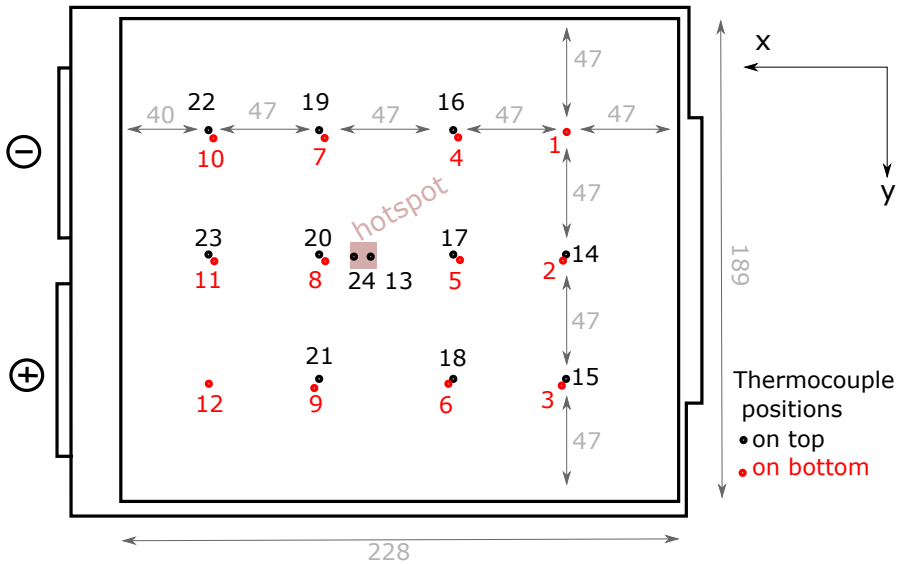

Figure 4.25: Positions of the thermocouples and the hot-spot on the cell surface used in micro-heater experiments.

Experiment T0146a

In T0146a a hot-spot experiment was done but the local heating of the cell did not trigger a TR. The surrounding cell material was heated to a maximum temperature of 84 °C (figs. 4.26 and 4.27). One working thermocouple (TK13) measured the temperature directly between the heater and the cell but the measured values fluctuated and were not reliable (probably because voltage from the heater was picked up by the thermocouple). The cell surface temperature directly below the heater (at 1800 s) is estimated as 550 °C (fig. 4.28). The direct power measurement of the hot spot heater failed, instead measurements with a multimeter were taken in even intervals. From the multimeter measurements the mean heater-power was estimated as 50 W. After a heating duration of 1525 s the heater failed and the experiment was stopped.
Discussion: The cell released a small amount of gas, 0.02 mol during the experiment (fig. 4.29). The gas composition was not measured.
Examination of the cell after the experiment revealed a hole in the cell that was caused by the heater. At least three electrode layers were damaged (fig. 4.32). The damage resulted in a slow self discharge of the cell: after the experiment the voltage decreased from 4.17 V to 2.8 V in 18 hours. During the actual hot-spot experiment the voltage dropped to 4.07 V (fig. 4.30). The derived average self discharge current was $I_{SC} = 4\,\mathrm{A}$ (fig. 4.31) and a resistance of the short circuit of $R_{SC} = \frac{U}{I_{SC}} = 1.02\,\Omega$. Such a short circuit generates Joule-heat with $P_{SC} = 16\,\mathrm{W}$.
The experiment shows that event strong (fig. 4.33) damage to the cell does not necessarily trigger a TR or a hard ISC.

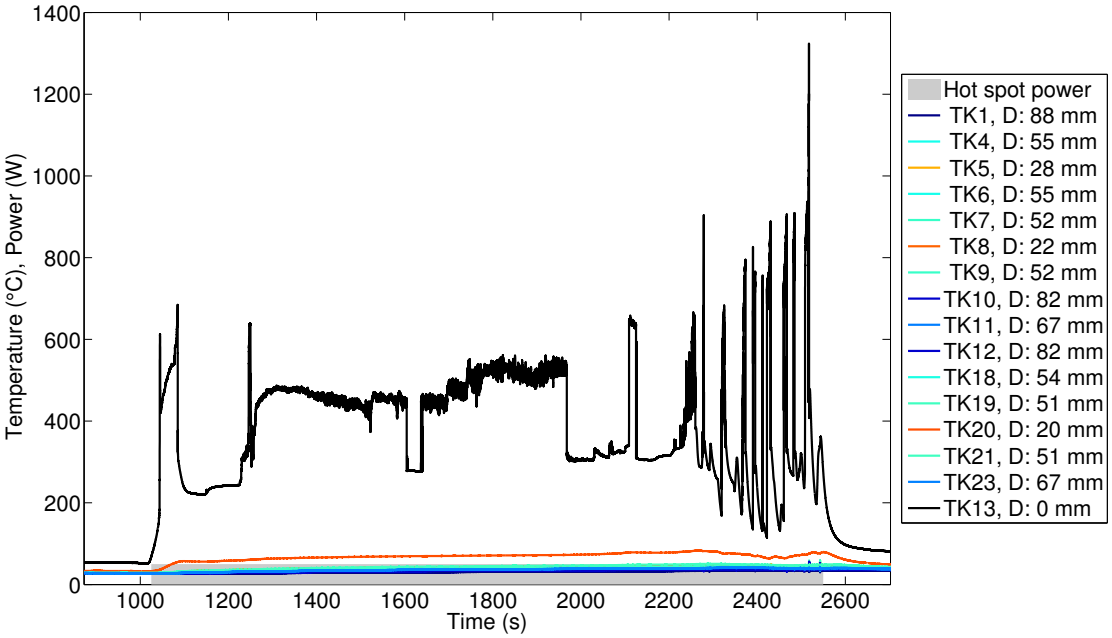

Figure 4.26: T0146a. Power of the heater element and temperatures on the cell surface. Temperatures are color-coded according to the distance from the hot spot.

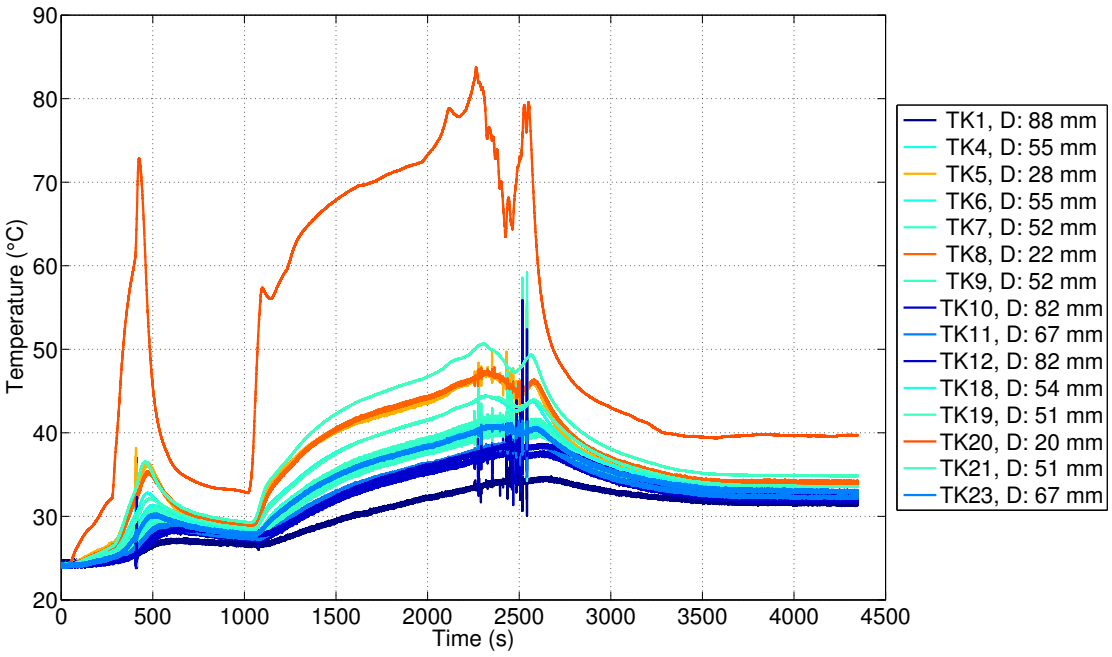

Figure 4.27: T0146a. Cell case temperatures adjacent to the heater. Colorcoded according to distance to the hot spot.

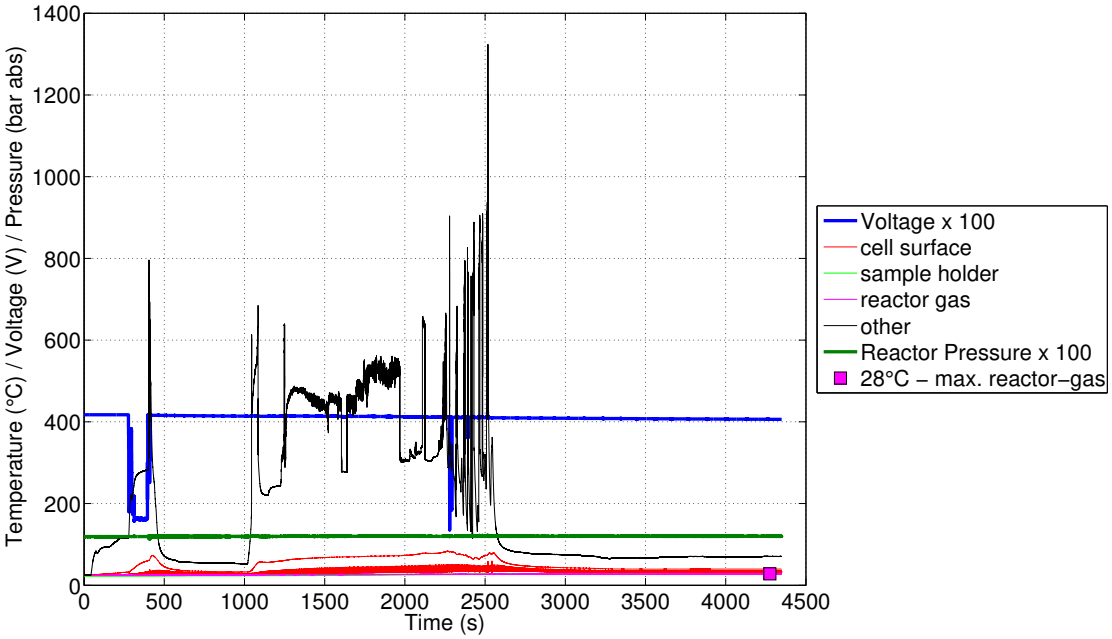

Figure 4.28: T0146a, all sensors. *Other:* temperature measurement of the thermocouple TK13 which was sandwiched between the micro-heater and the cell surface.

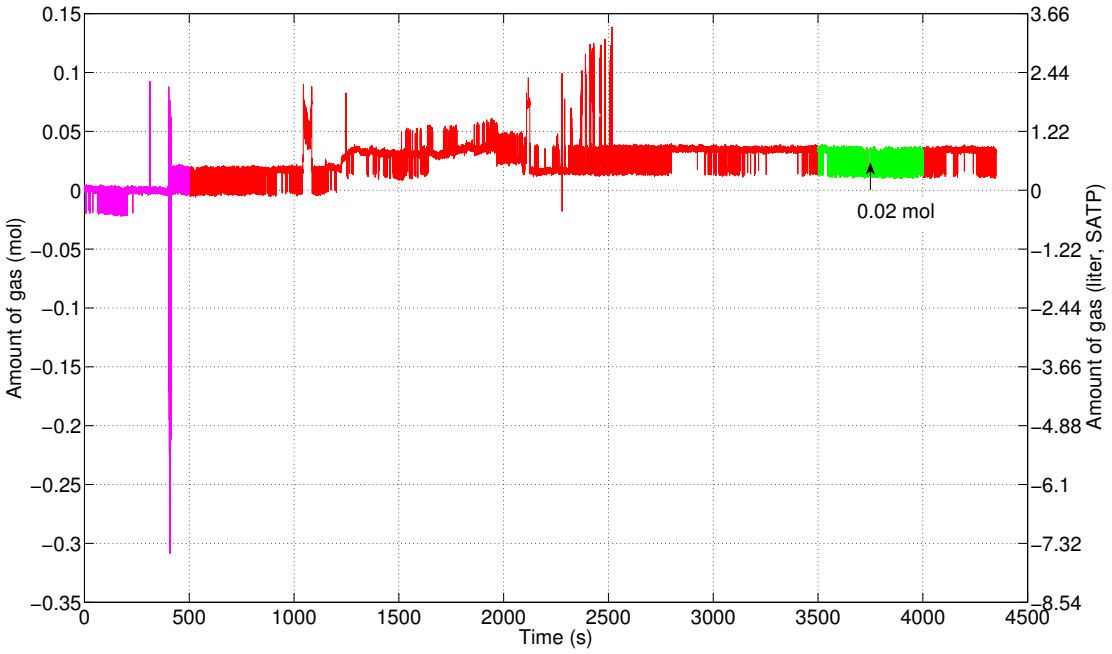

Figure 4.29: T0146a, gas release by the cell during the micro hot-spot experiment

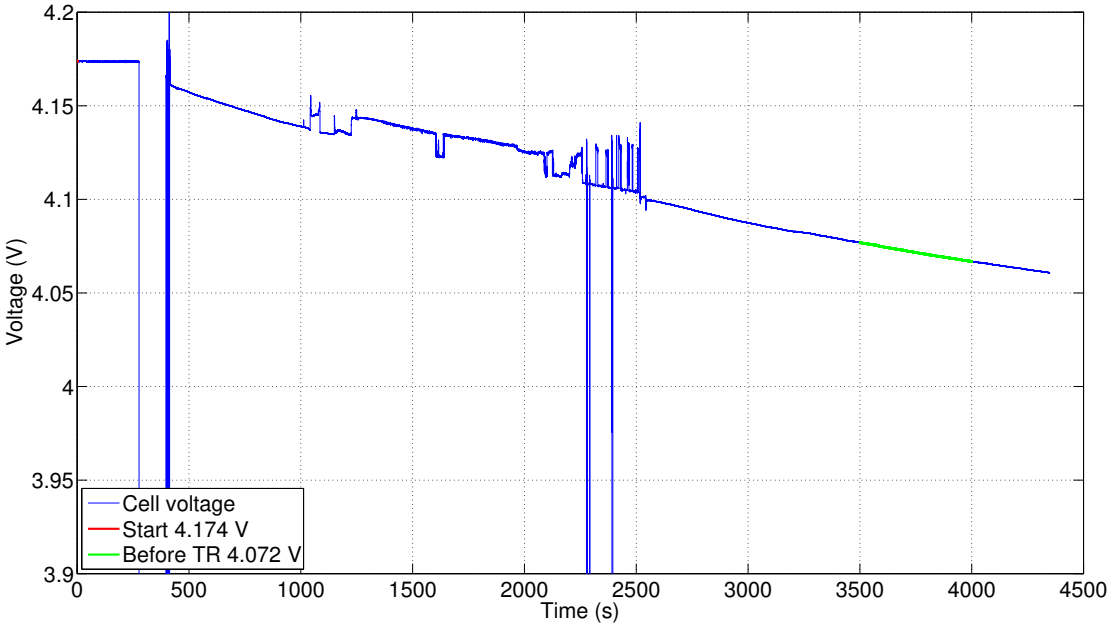

Figure 4.30: T0146a, voltage of the cell during the micro hot-spot experiment. Note that the damage causes a self discharge of the cell and a voltage drop from 4.17 V to 4.07 V in 4000 s. The voltage spikes were caused by measurement errors.

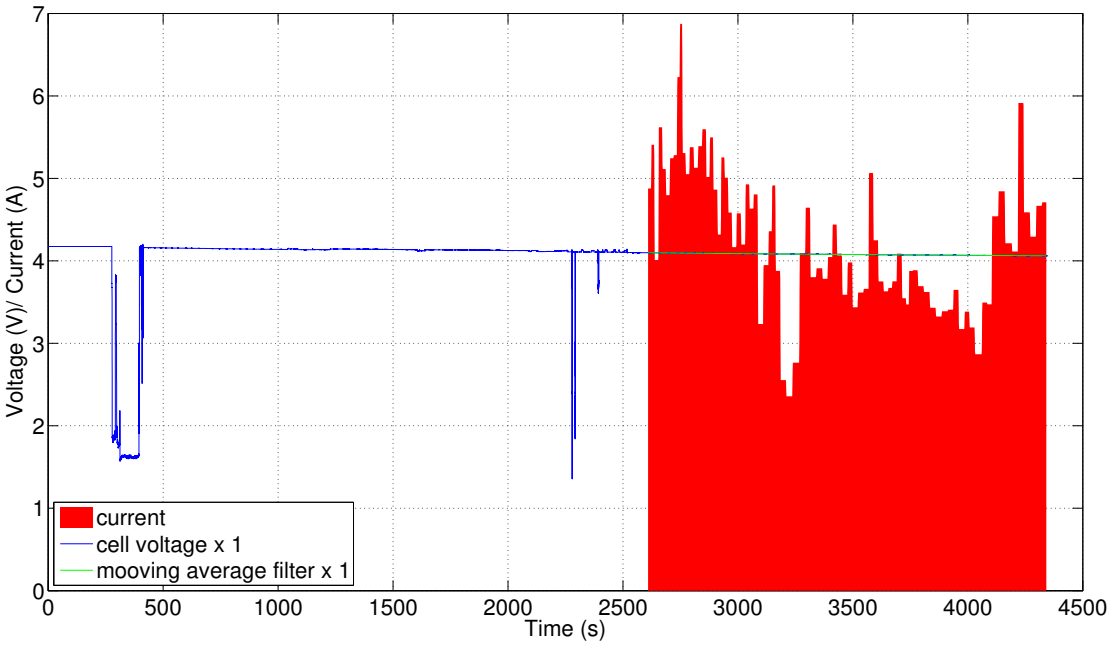

Figure 4.31: T0146a, Voltage and the derived self discharge current of the cell. The current is calculated for the later part of the experiment, where the voltage measurement had no fluctuations.

Figure 4.32: T0146a, cell sample after the failed attempt to trigger a TR with the micro heater. The heating caused a hole of the upper layers and the self-discharge of the cell.

Figure 4.33: T0146a. The upper cell layers after the hot-spot experiment. The heater melted a hole through the first cathode layer (Cu current collector foil) and through the first anode layer (Al current-collector foil). Note the circular feature of the following less damaged layers.

Experiment T0147a

In experiment T0147a the same setup as in T0146a was used. More Kapton tape was put around the micro-heater to prevent failing of the device and to minimize the influence to the thermocouples. The micro-heater was ramped up slowly, then - after it became evident that the TR could not be started event with the maximal rated power of the heater - the heater was intentionally overloaded and kept at high power with 200 W at average. At the heated point, directly below the heater device the cell surface reached temperatures up to 550 °C for a short time. During the experiment the hot-spot reached an equilibrium temperature of 460 °C (figs. 4.34 and 4.35). Other cell surface temperatures in the vicinity of the hot-spot increased very slowly up to 140 °C with a temperature ramp of approximately 10 °C h^{-1}. The temperature distribution of the cell slowly converged to a steady state with a balance of injected heat-flow by the micro-heater and the heat drain to the cooler sample holder and reactor components without any incline to transit into a TR.
Discussion: the cell was heated with a higher power than T0146a and therefore released a higher amount of gas (0.26 mol) during the experiment (fig. 4.36). The gas composition was not measured.
Examination of the cell after the experiment revealed a very pronounced hole that was caused by the heater. The cell was perforated up to the first anode layer exposing the copper foil (anode current collector). It is possible that further three layers below the heater were damaged. (fig. 4.38). Again, the damage resulted in a slow self discharge of the cell: the voltage decreased from 4.01 V to 3.17 V in 5 days. During the actual hot-spot experiment the voltage dropped from 4.17 V to 4.01 V (fig. 4.37). A discharge current of $I_{ISC} = 3$ A (fig. 4.39) and a resistance of the short circuit of $R_{ISC} = \frac{U_{OCV}}{I_{ISC}} = 1.34\,\Omega$ was calculated. Such a short circuit generates Joule heat with $P_{SC} = 12$ W.
The experiment shows again that even strong damage to the cell does not necessarily trigger a TR or a hard ISC. The cell temperature at the hot spot reached values that should start an exothermic TR reaction, but the size and heating power of the small heated area were apparently not sufficient to spread the chemical reaction beyond the perimeter of the hot-spot.

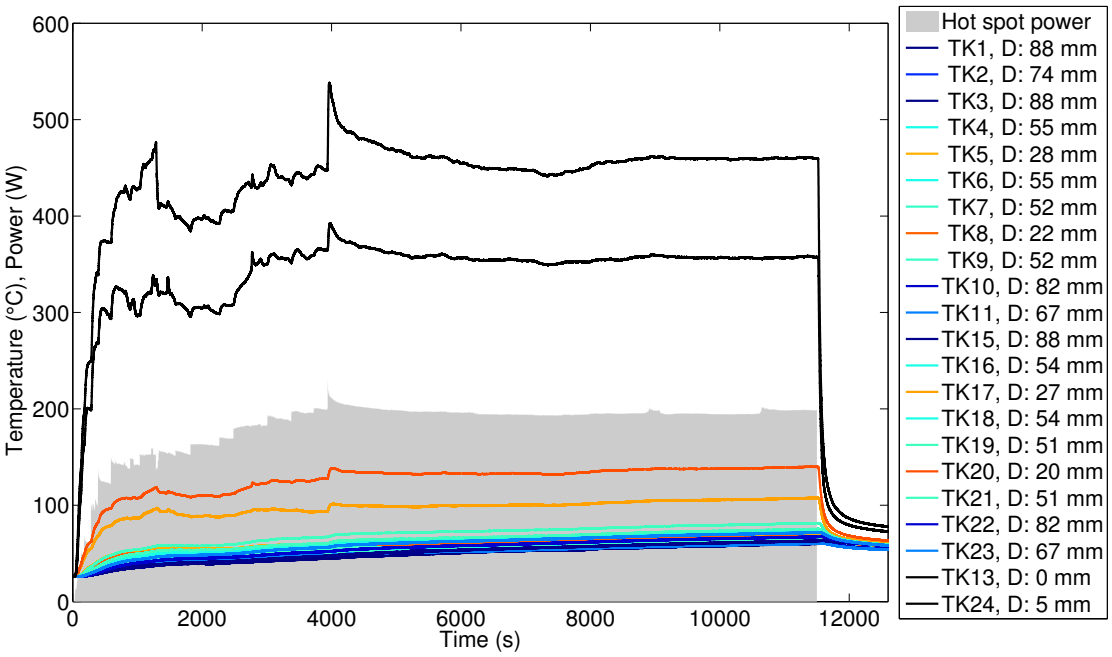

Figure 4.34: T0147a. Power of the heater element and temperatures on the cell surface at different distances to the hot-spot. Highest temperatures were measured by TK13 and TK24 which were located between the micro heater and the cell surface. Second highest temperatures were measured by TK20 and TK17.

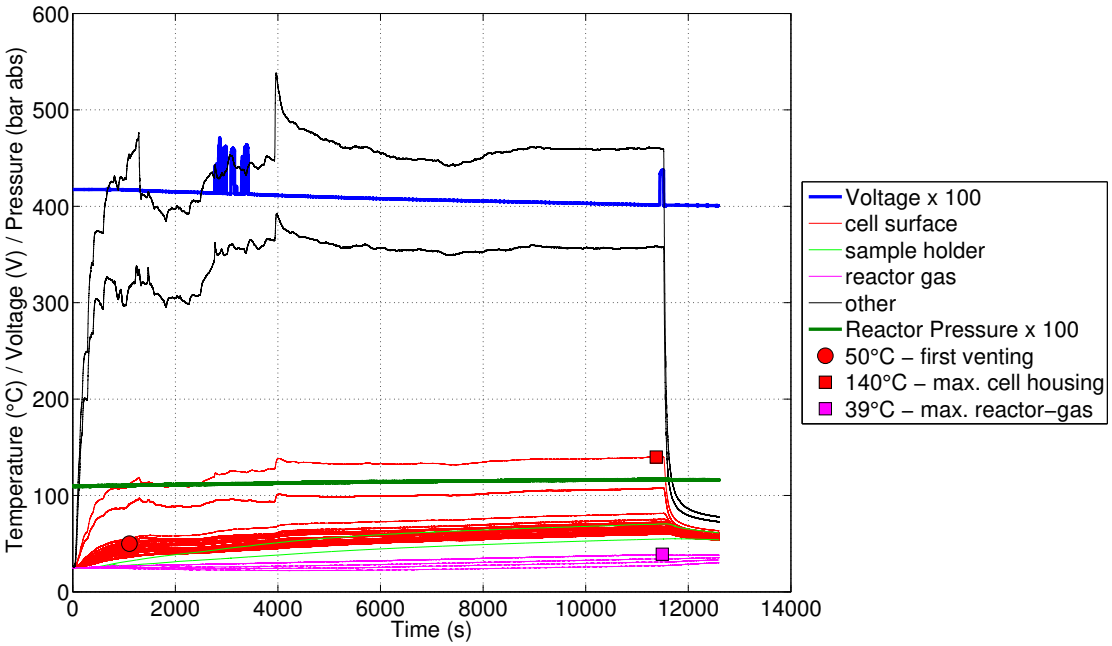

Figure 4.35: T0147a, all sensors. *Other:* temperature measurements of the thermocouples which were sandwiched between the micro-heater and the cell surface (TK13 and TK24).

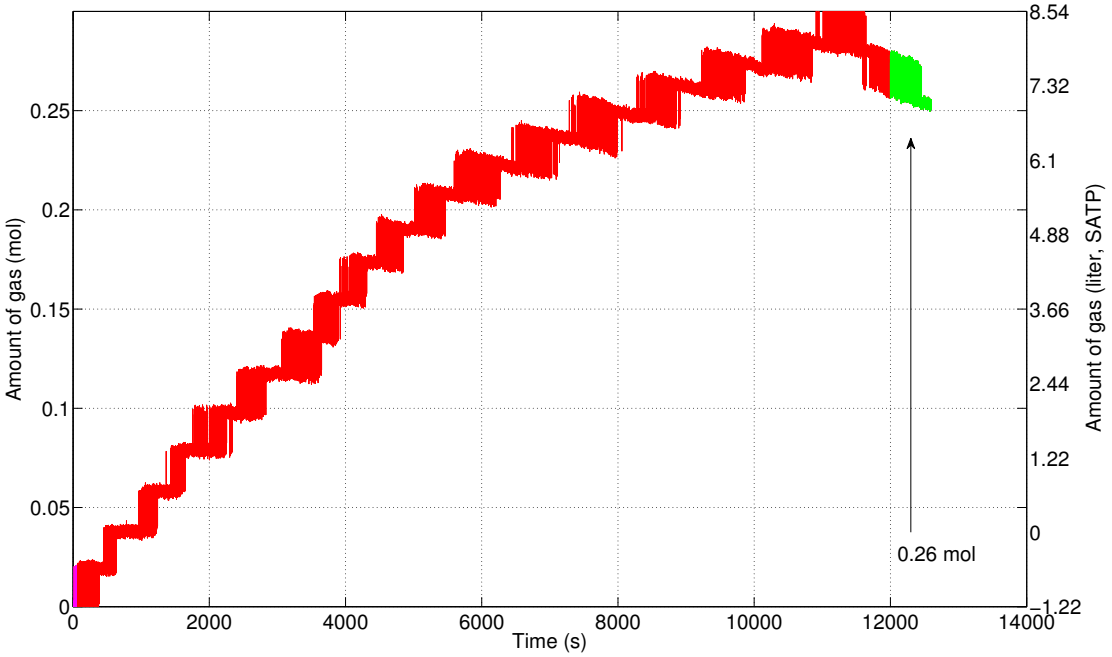

Figure 4.36: T0147a, gas release of the cell during the micro hot-spot experiment.

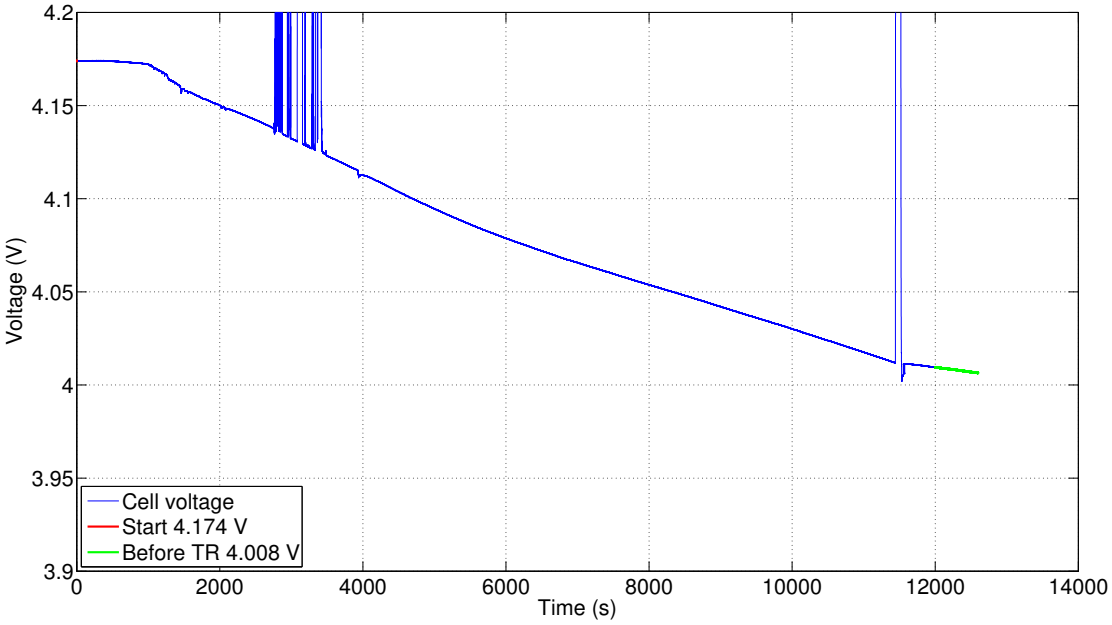

Figure 4.37: T0147a, voltage of the cell during the micro hot-spot experiment. Note that the damage causes a self discharge of the cell and a voltage drop from 4.17 V to 4.01 V in 12 000 s. The outliers were caused by measurement errors.

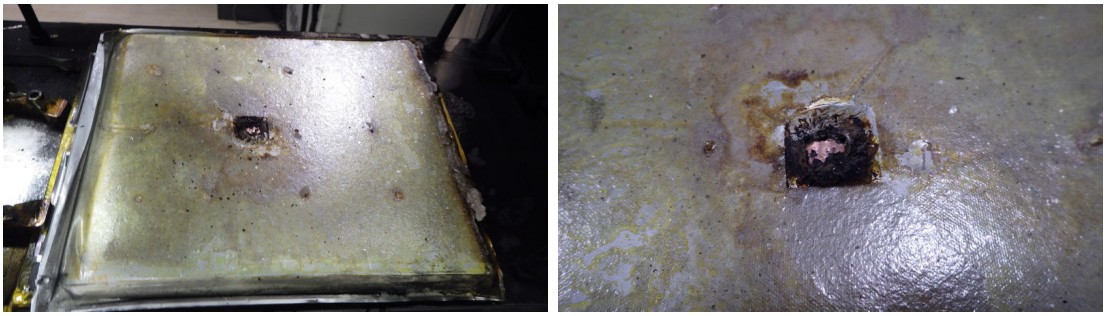

Figure 4.38: T0146a, cell sample after the failed attempt to trigger a TR with the micro heater. The heating resulted in a hole of the upper layers of the cell and in self discharge of the cell.

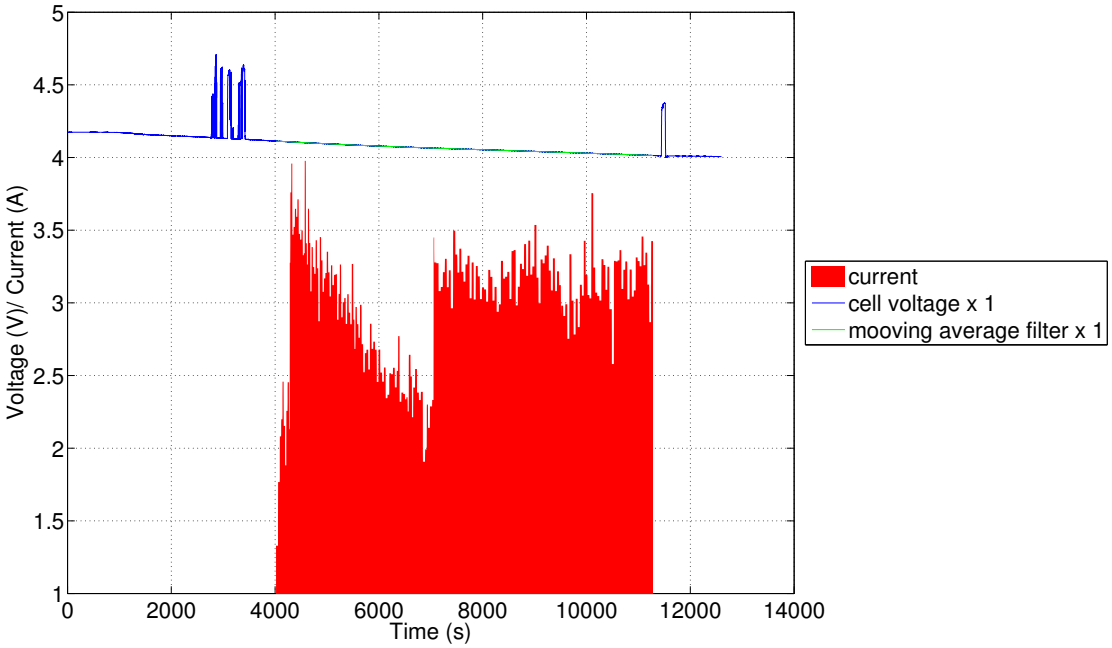

Figure 4.39: T0147a, Voltage and the derived self discharge current of the cell. The current is calculated for the part of the experiment where voltage had no fluctuations.

4.5.4 Hot spot, tab heater

Experiment Setup

Here the cell was sandwiched inside the stack as described above. The opening (25 mm × 25 mm) was closed with a fitting part and the cell was heated at one of the tabs. The tabs are the terminals, which are used as the high current electrical connections of the cell (fig. 4.40). The motivation of this test was to simulate a faulty electrical connection with high resistance, which would heat the cell through the tab (fig. 4.41).

The tab was clamped together with a heating element (and a copper plate for improved lateral heat transfer) between two small insulated steel plates. The heater injected heat into the attached tab and into adjacent region of the cell stack (fig. 4.42). Either the positive tab or the negative tab could be connected to the heater.

The tabs (terminals) of the cell were very short, with a length of approximately

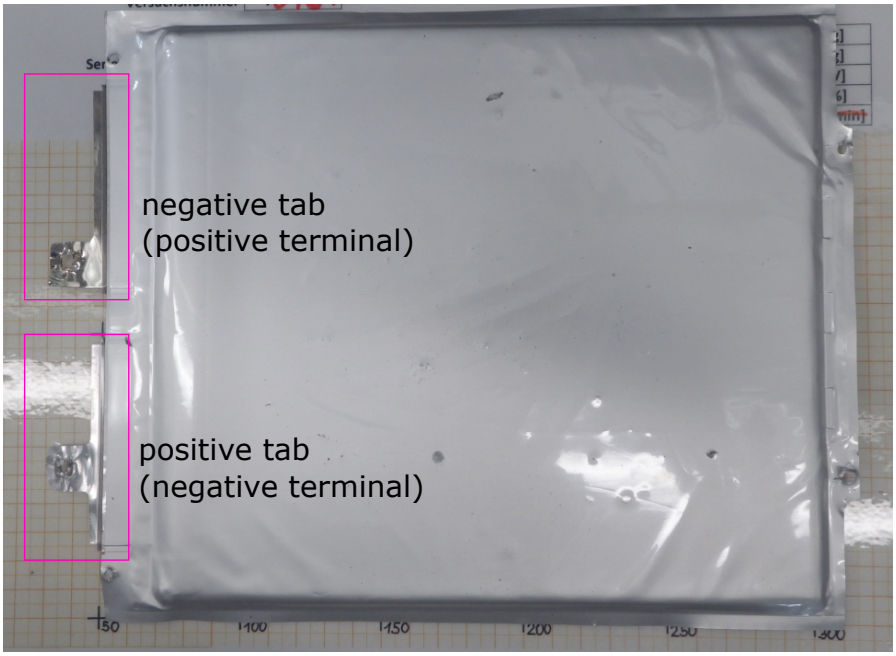

Figure 4.40: Cell with highlighted tab areas which could be heated.

only 5 mm. This decreased the contact area to about 175 mm^2. Heater parameter were:

Type: FLE 100 638 from *Bach RC* https://www.bachrc.de/
Heated tab area: $A_H = (5\,\mathrm{mm} \times 35\,\mathrm{mm}) = 175\,\mathrm{mm}^2$
Rated power: $P_R = 900\,\mathrm{W}$ at $230\,\mathrm{V}$
Max temperature: 1000 °C (for the heated part) 500 °C for electrical connectors

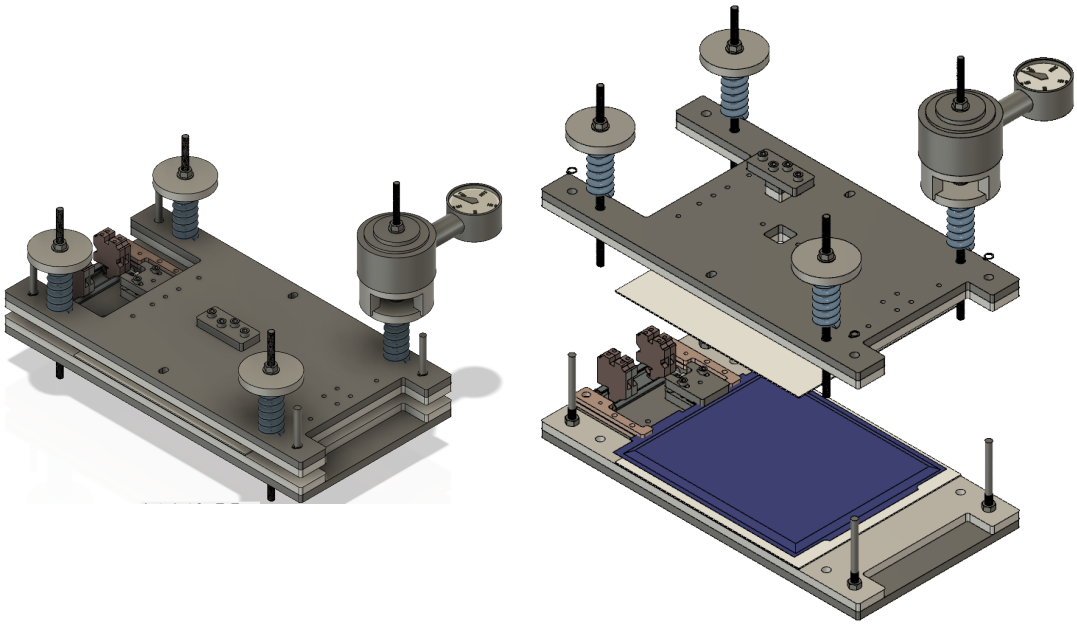

Figure 4.41: Sample holder used for tab heating experiments.

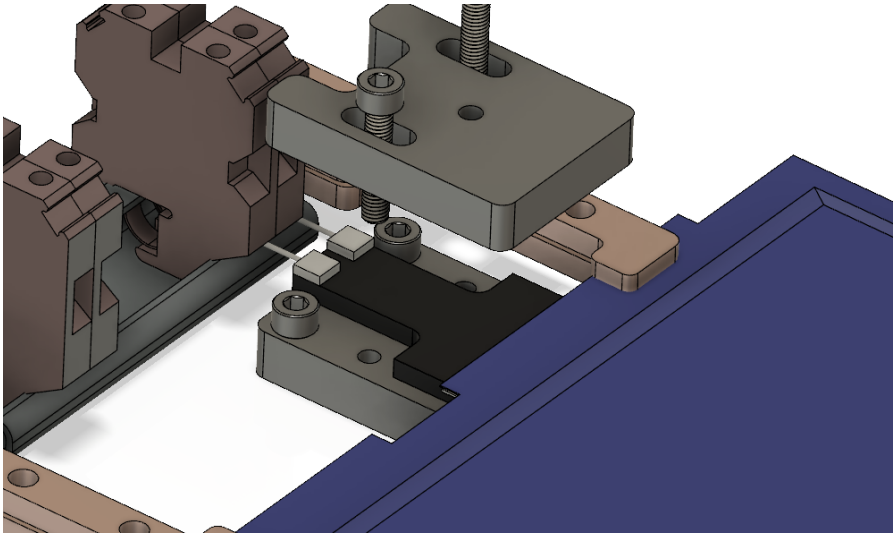

Figure 4.42: Detail of the tab heater. The black part is the heat generating ceramic element. The blue part is the cell.

Experiment T0149

In T0149 the *positive tab* of the cell was heated. Temperatures were measured on cell surface and at the heated tab (fig. 4.43). The cell transited into a TR after it was heated for 186 s with a heating power of 448 W (fig. 4.44). The heater injected a heat of 83 kJ into the tab. This is equivalent to 23 W h or to 15% of the stored cell energy. Two thermocouples (TK23, TK24) were clamped between the heater and the tab and could measure the tab temperature throughput the experiment. The TR originated directly at the positive tab and propagated throughout the cell in 14.5 s (fig. 4.52). The cell released 2.39 mol with an rate of 0.3 mol s^{-1} (6.4 l_{SATP}/s) during the experiment (fig. 4.49). The vent-gas composition was measured after the TR: fig. 4.51. Following events could be identified (fig. 4.45):

491 s Start of the tab heating.

630 s Maximum tab temperature at 432 °C caused by heating by the hot-spot device. Cell voltage starts to decrease, probably because of an ISC. The voltage decreases from 4.16 V to about 3.6 V.

635 s Maximum tab temperature at 453 °C caused by combined heating by the hot-spot device and the joule heat from ISC. Cell voltage recovers by 23 mV. Gas pressure and gas temperature in the reactor starts to rise because the cell starts to release hot gas into the reactor. Cell case temperatures at the measurement points adjacent to the positive tab start to rise. The TR starts.

651 s Tab at 453 °C. Maximum overpressure inside the reactor.Temperatures of cell case sensors at most remote locations from the positive tab starts to rise. Cell voltage is at 0 V. The TR has propagated throughout the cell.

Discussion: The TR can be initiated by tab heating. It is surprising, that - immediately before the start of TR - the temperature gradient between the heated tab at 430 °C and the adjacent cell case temperature-sensor (TK20) at 44 °C is very high with ΔT of 385 °C. Although the sensor was quite close (66 mm) to the hot spot, it could not detect an out-of-specification over-temperature and it could not sense the imminent start of the TR (fig. 4.48). In a real battery pack it would mean that a hot spot can only be detected when a temperature sensor happens to be placed directly in its vicinity. It would be unpractical to place temperature sensors all over the battery pack, at each point of a potential hot-spot. Therefore, hot spots

should be detected by other means than by individual temperature sensors.
It is also surprising, that the highest cell case temperature 658 °C was not reached near the position of the hot-spot, but further away on the other side of the cell (by TK13).
An ISC before the rapid TR started at 630 s was unlikely, because the voltage did not change from the start of experiment (4.1684 V) to the point immediately before TR (4.1662 V). On the other hand, from 630 s to 635 s the measured voltage dropped from 4.16 V to 3.6 V and the temperature of the tabs increased from 432 °C to 455 °C. The voltage drop and the temperature increase in this 5 s-interval could be caused by an ISC. The current of the ISC can be estimated from the voltage decrease. The *Delta SOC method* (section 4.4.1) gives an unrealistically high current of more than 20 kA. Instead, the *Ri method* is used (section 4.4.1). The ISC current is calculated with $I_{ISC} = \Delta U / R_i = 560\,\mathrm{A}$ which seem more reasonable (fig. 4.50). The associated heat release at the point of the ISC is

$$E_{ISC} = \Delta t\, I_{ISC} U_T = 5\,\mathrm{s} \times 560\,\mathrm{A} \times 3.6\,\mathrm{V} = 10\,\mathrm{kJ} \tag{4.3}$$

If we further assume that this energy was released in the vicinity of the tab (30% of the cell), the local temperature increase can be calculated with

$$\Delta T = \frac{E_{ISC}}{30\,\%\, M\, C_p} = 38\,^{\circ}\mathrm{C} \tag{4.4}$$

using the cell mass $M = 0.87\,\mathrm{kg}$ and the specific heat capacity which is assumed as $C_p = 1000\,\mathrm{J\,kg^{-1}}$. The resulting $\Delta T = 38\,^{\circ}\mathrm{C}$ is comparable to the measured temperature increase of the tab between 630 s to 635 s with $\Delta T_{tab} = 455\,^{\circ}\mathrm{C} - 432\,^{\circ}\mathrm{C} = 23\,^{\circ}\mathrm{C}$. The temperature calculation justifies the overall assumptions and the ISC current of approximately $I_{ISC} = 560\,\mathrm{A}$.
The additional temperature input of $\Delta T = 38\,^{\circ}\mathrm{C}$ may have triggered the rapid TR at 635 s.
The cell released 0.02 mol before the TR and additional 2.38 mol of gas during the TR with a rate of $0.3\,\mathrm{mol\,s^{-1}}$ ($6.4\,\mathrm{l_{SATP}/s}$) (fig. 4.49). The vent-gas composition was measured with the GC and FTIR (fig. 4.51).

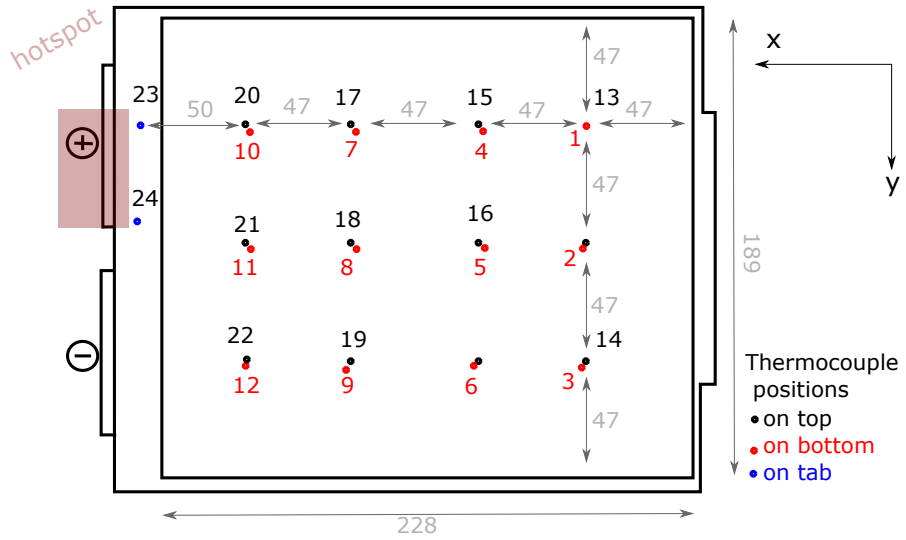

Figure 4.43: T0149. Positions of the thermocouples.

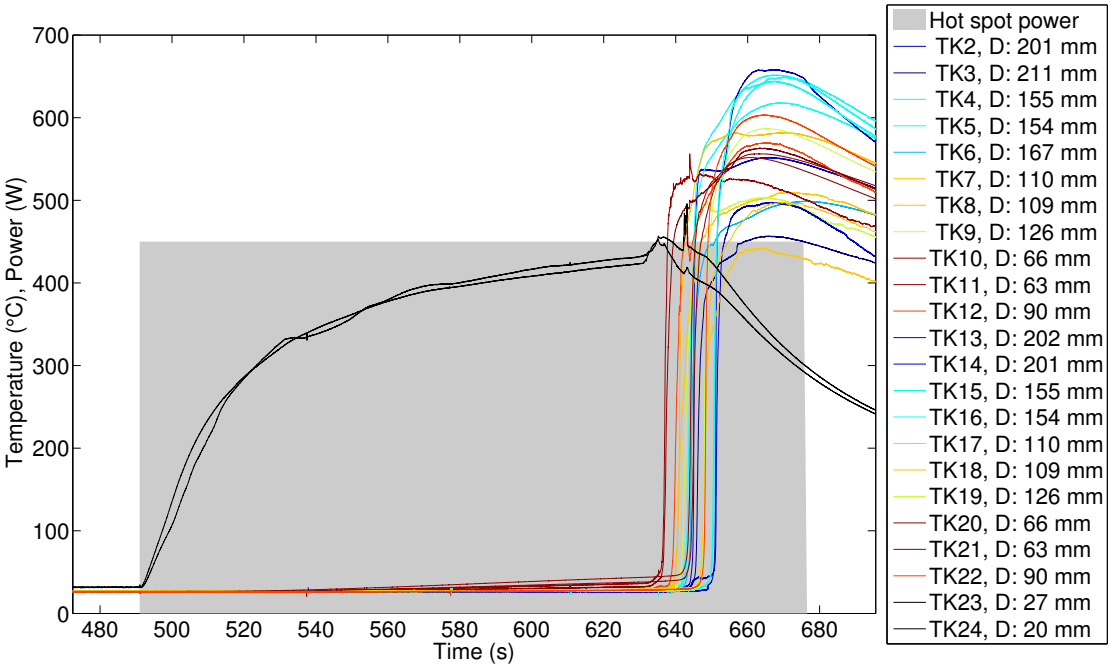

Figure 4.44: T0149. Power of the heater element and temperatures on the cell surface at different distances to the positive tab. Temperatures are color-coded according to the distance from the hot spot.

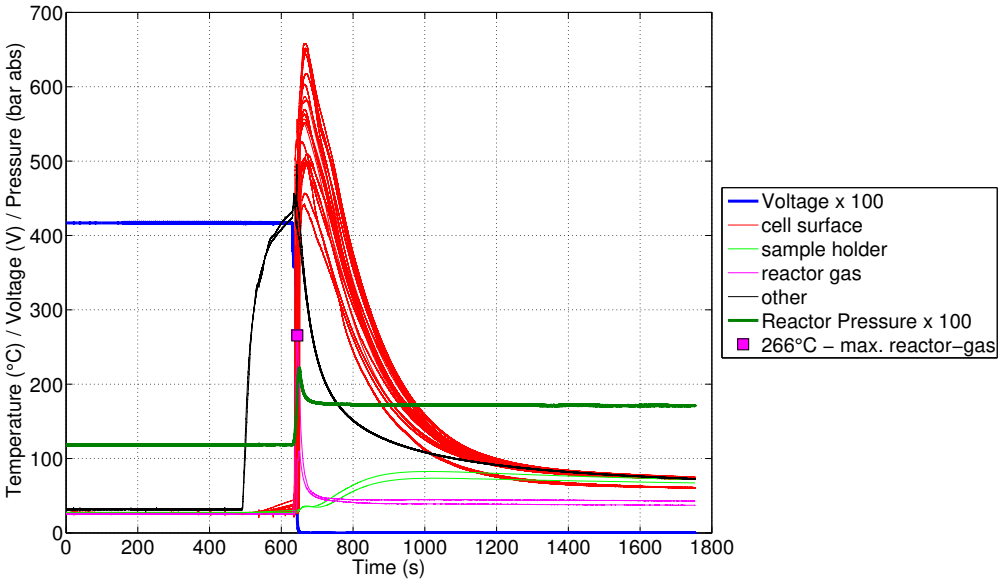

Figure 4.45: T0149. All sensors values. Whole experiment duration. *Other* are the two temperature sensors (TK23, TK24) clamped between the heater and the positive cell tab.

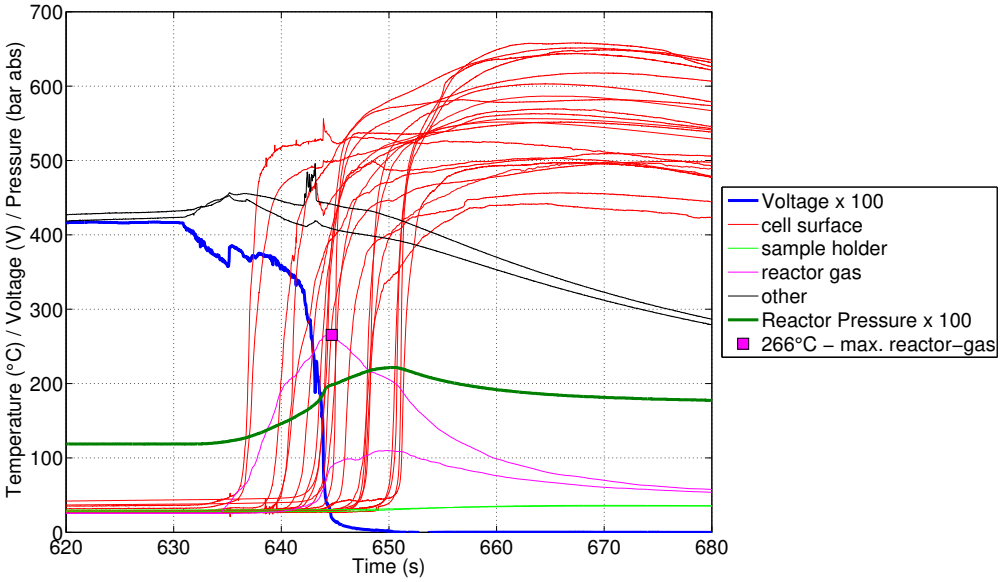

Figure 4.46: T0149. All sensors values. Time span of the TR. *Other* are the two temperature sensors (TK23, TK24) clamped between the heater and the positive cell tab.

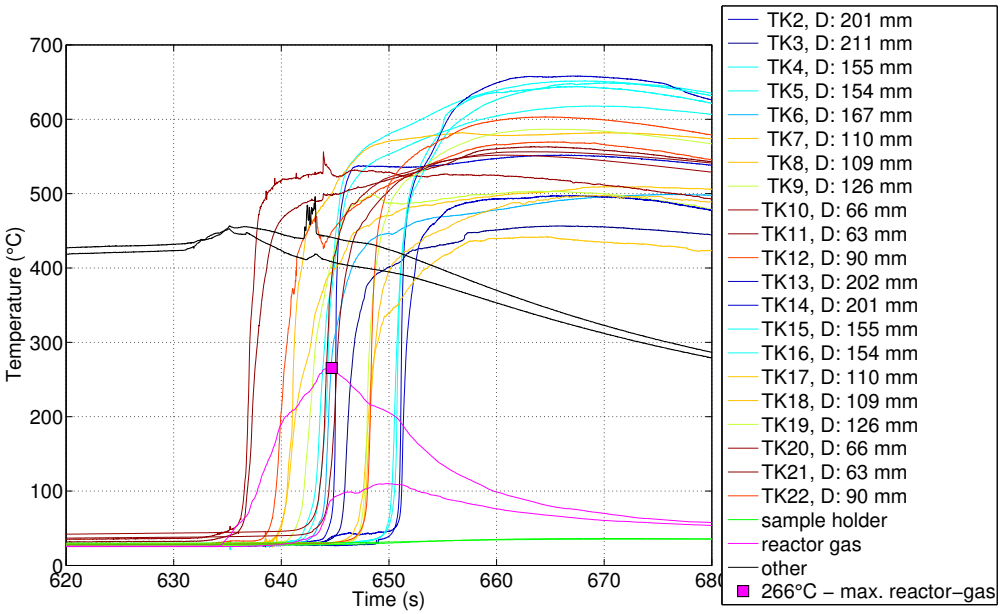

Figure 4.47: T0149. All temperatures, color-coded according to the distance from the positive tab. Time span of the TR. *Other* are the two temperature sensors (TK23, TK24) clamped between the heater and the positive cell tab.

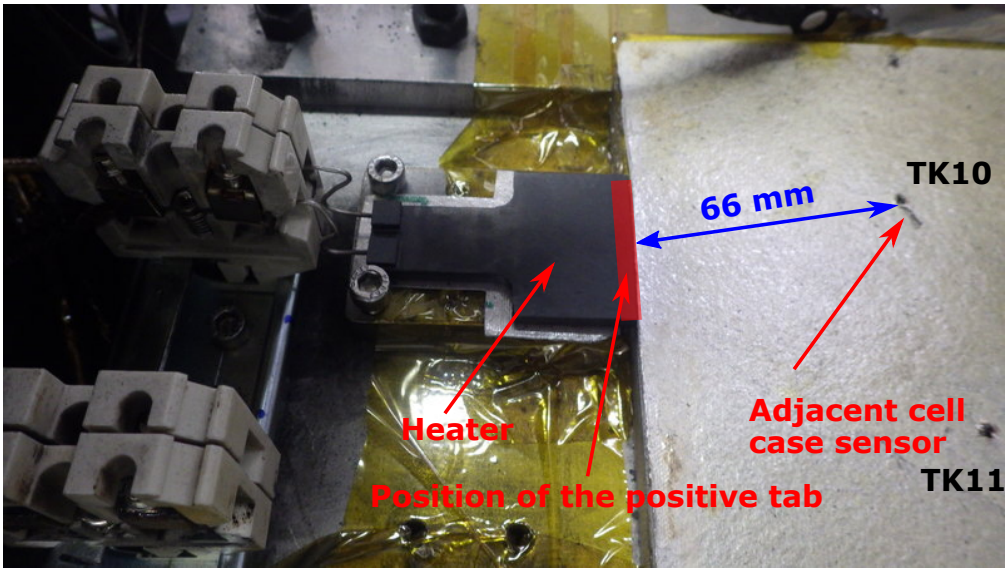

Figure 4.48: T0149. Placement of the ceramic heater (black part) and the adjacent cell case sensors. The two nearest cell case sensors (TK10 and TK11) were placed 66 mm away from the heated area. The cell itself is not shown here, it is placed later on top of the shown components.

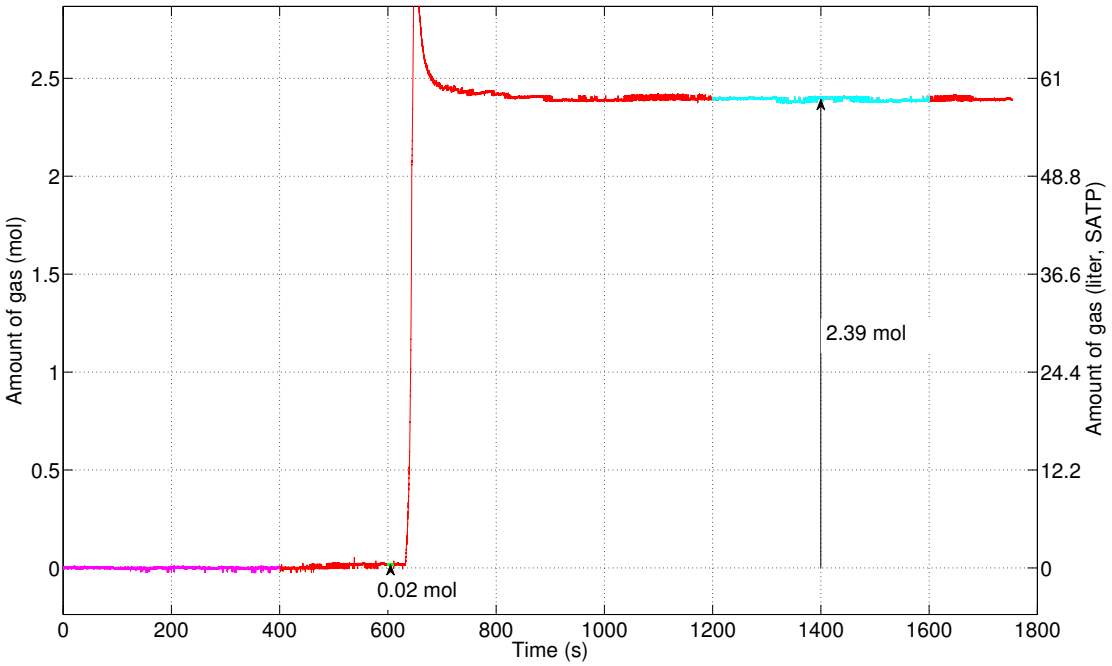

Figure 4.49: T0149. Gas release by the cell.

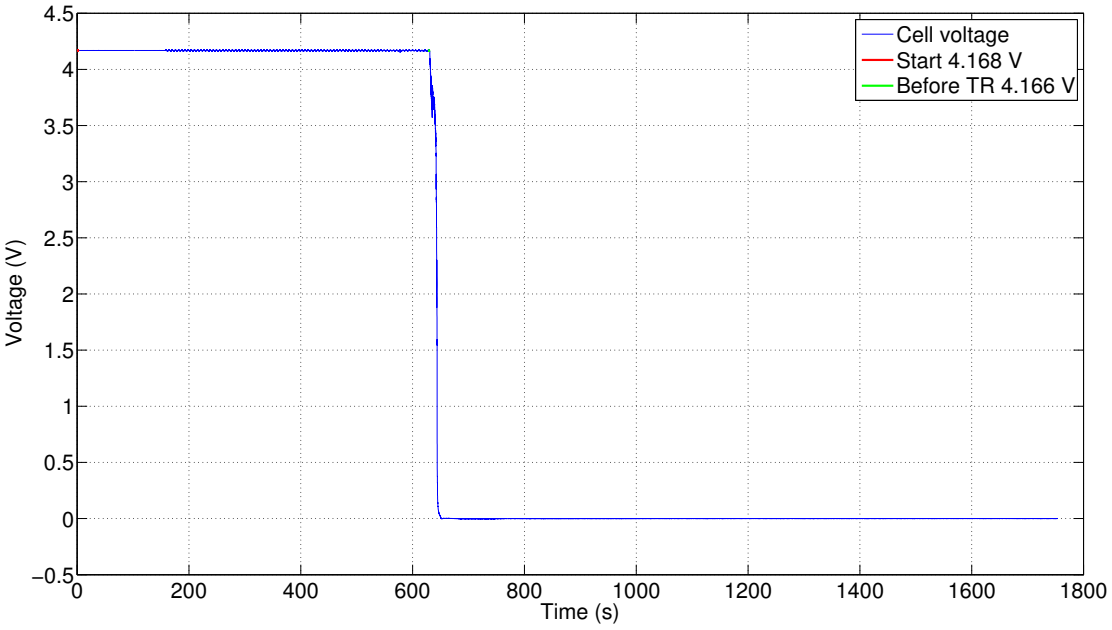

Figure 4.50: T0149. Voltage of the cell and ISC of the cell.

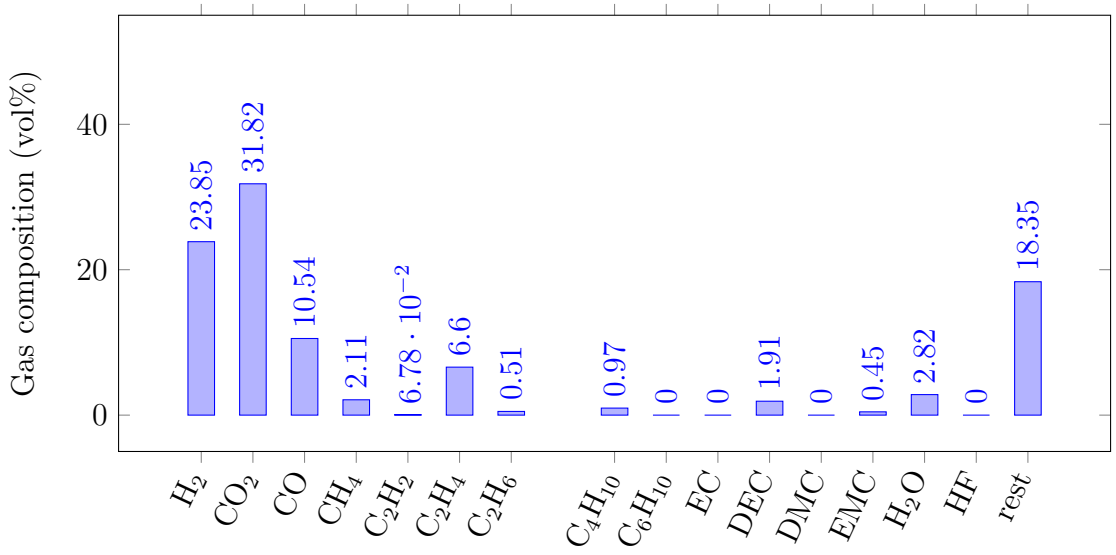

Figure 4.51: Experiment T0149. Detected gas components which were released by the cell. Gas composition was measured by FTIR and GC.

Figure 4.52: T0149. The cell after TR. Note the wrinkles that originate at the hot spot device on the tab. Note also that the cell reached its highest temperature on the remote side further away from the hot-spot. The square in the middle is only an impression from the imperfect filling of the hole for the central heater.

Experiment T0151

In T0151 the *negative tab* of the cell was heated (fig. 4.43). Unfortunately there were several issues with this experiment. After discharge, the cell could only be charged to 18.2 A h instead of to the full capacity of 42 A h (figs. 4.54 and 4.55) although the voltage of 4.2 V was set correctly in the constant-voltage phase. During the TR experiment setting the heater above 80% of power caused several electric faults which triggered the circuit breaker of the supply. The negative tab was heated up to 750 °C in a period of 6 hours without causing a TR (fig. 4.57). The adjacent cell case temperatures (at TK10, TK20) reached a maximum of 199 °C. The average heating power was 567 W (fig. 4.57). The cell voltage started at 4.17 V and slowly discharged to 4.08 V (fig. 4.59).
Conclusion: It is unclear, why the cell could not be fully charged. Temperatures of the tab were nominal during the charging process.
The TR could not be triggered. Possible causes for failing to trigger the TR are: the cell was degraded and stored only 42% of nominal capacity, or the interface between heater and tab was not sufficient, or the material in the vicinity of the tab was degraded during the extended heating and could not perform the exothermic TR-reaction.
The cell released 0.7 mol of vent-gas during the experiment (fig. 4.58). The vent-gas composition was measured with the GC (fig. 4.62). The gas-composition fingerprint has a higher resemblance to the vent-gas released by a TR (e.g. to fig. 4.51) than to the gas released from a completely discharged cell (e.g. to fig. 4.9). Therefore, the gas producing chemical reactions must have been similar to the reaction in full TR, but only a fraction of the cell was affected, as only 0.7 mol was released (in contrast, a full TR of a cell e.g. T0149 produced 2.39 mol).
Pulses with ±1 A were applied and the measured resistance R_i of the cell increased from 1 mΩ to 2.5 mΩ by the end of the experiment. The voltage of the cell decreased and the associated average self discharge of the cell was estimated with *Delta SOC method* (section 4.4.1) to $I_{ISC} = 0.5$ A (fig. 4.60).
After the experiment the cell was deep discharged, dismantled and the heated area at the negative tab was inspected. The cell showed heavy damage with a radius of about 70 mm around the heated spot (fig. 4.61).

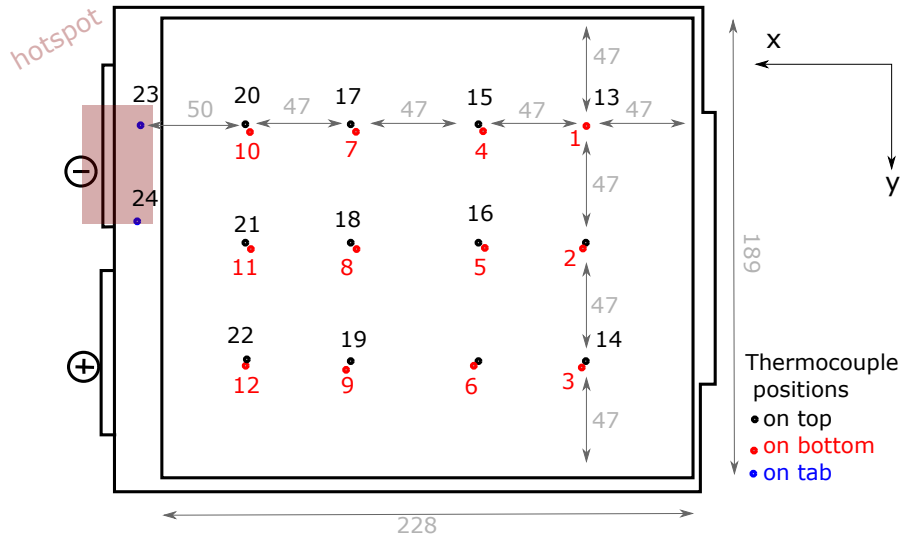

Figure 4.53: T0149. Positions of the thermocouples.

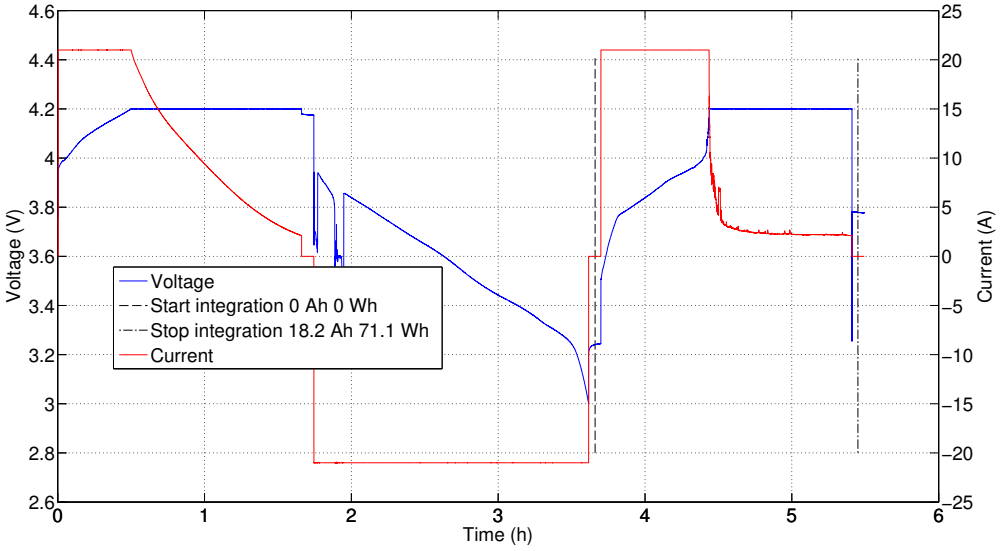

Figure 4.54: T0151. Charge, discharge and subsequent charge of the cell.

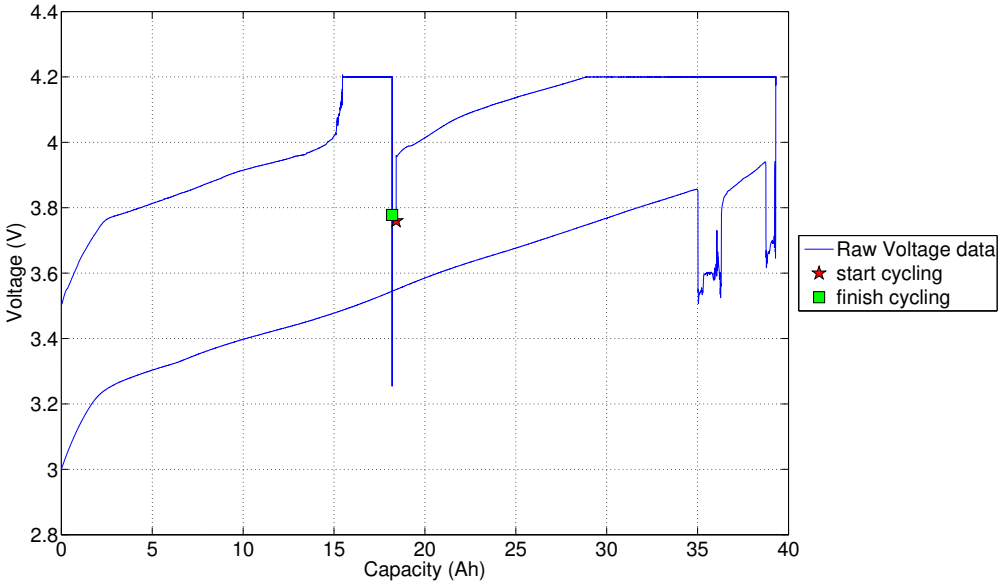

Figure 4.55: T0151. Charge, discharge and subsequent charge of the cell. Note that the cell could not be charged to full capacity.

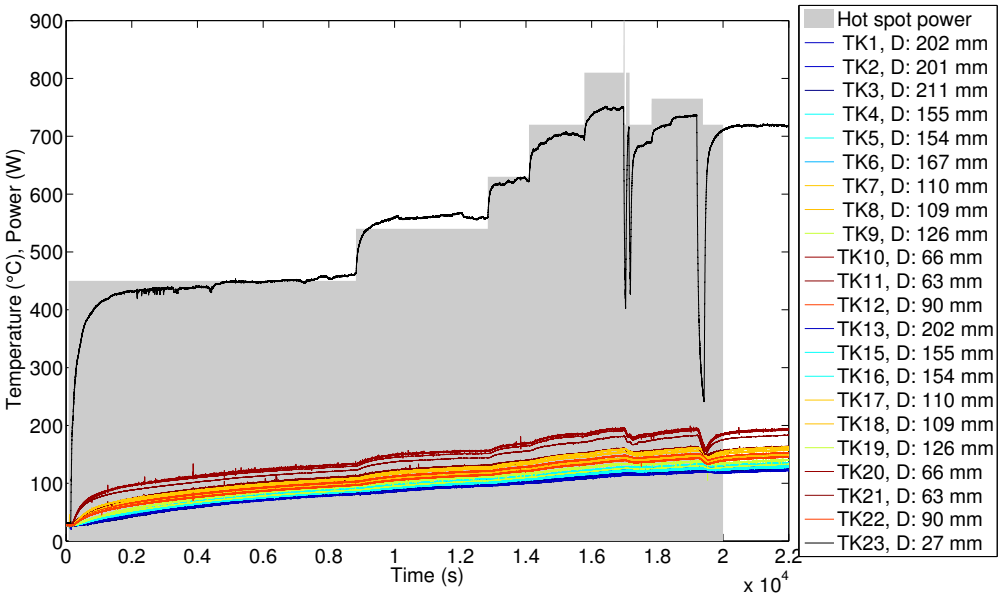

Figure 4.56: T0151. Power of the heater element and temperatures on the cell surface at different distances to the hot spot. Temperatures are colour-coded according to the distance from the hot spot.

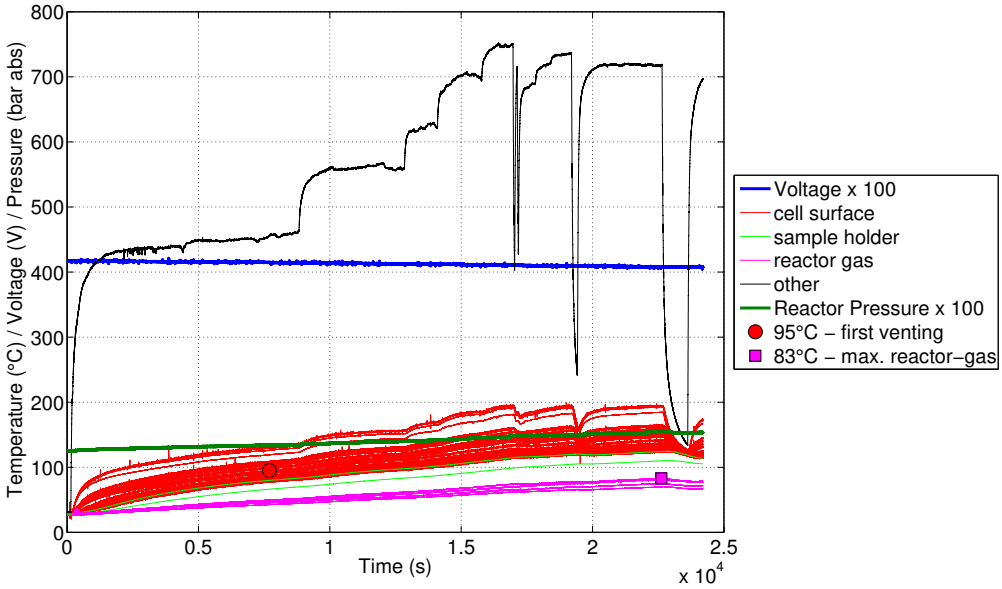

Figure 4.57: T0151. All sensors values. Whole experiment duration. *Other* is the one working temperature sensor TK23, which was clamped between the heater and the positive cell tab.

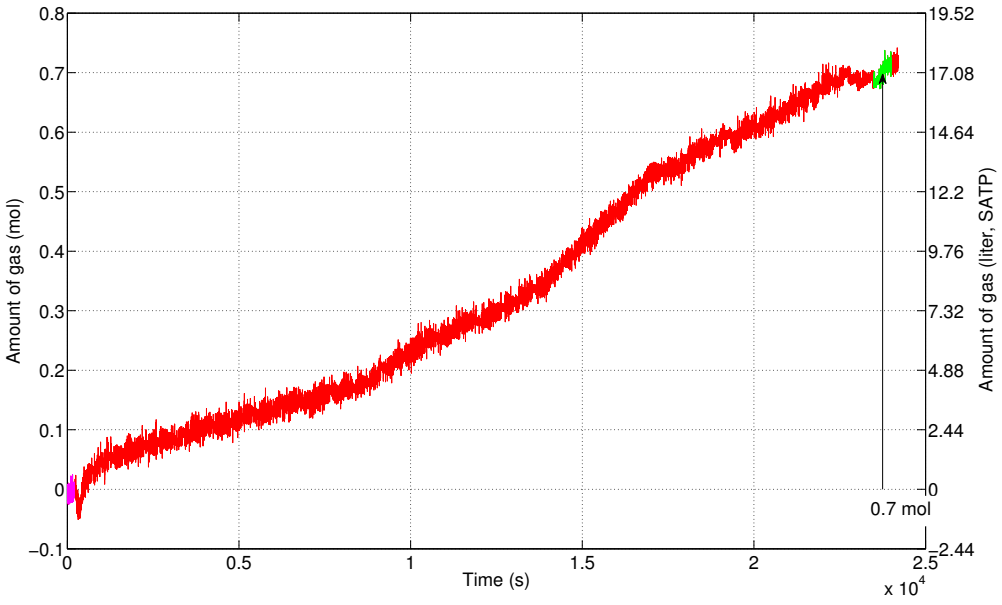

Figure 4.58: T0151. Gas release by the cell.

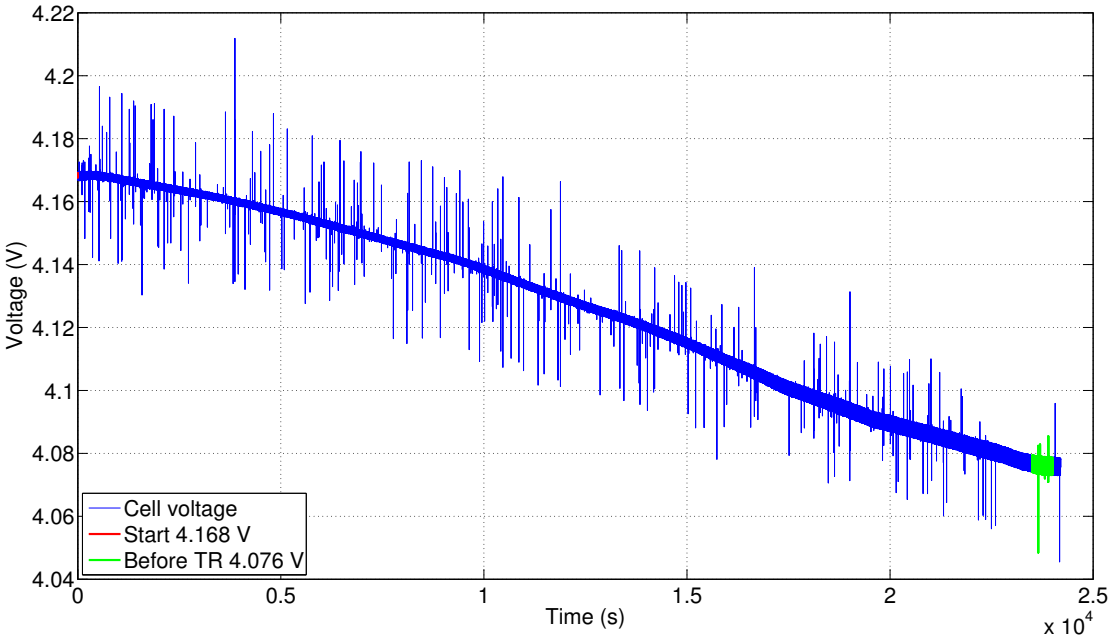

Figure 4.59: T0151. Voltage of the cell.

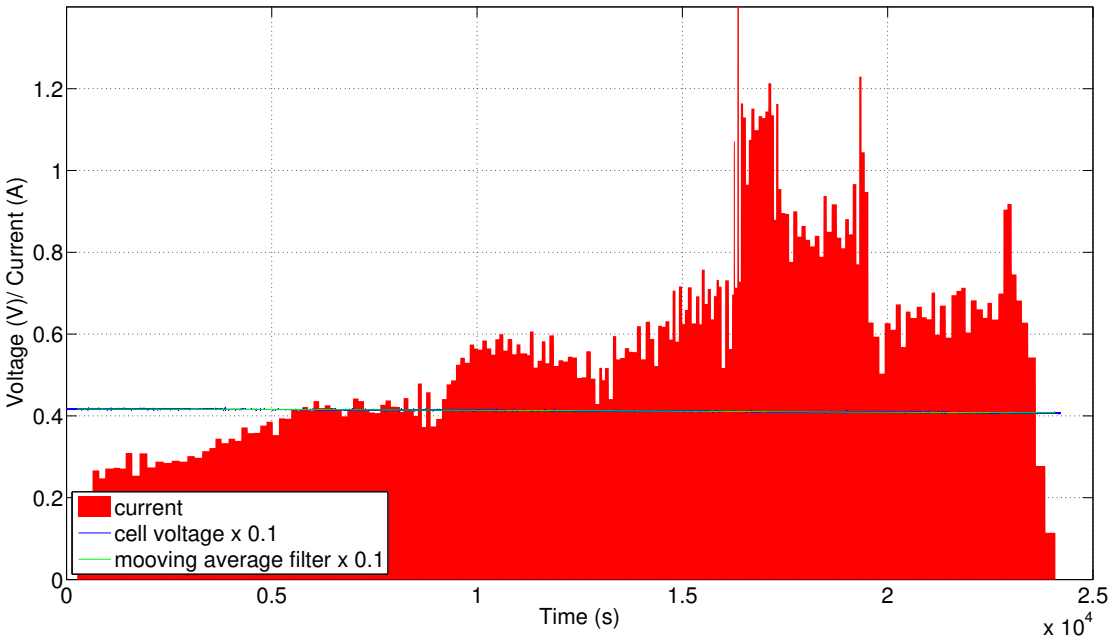

Figure 4.60: T0151. Voltage and the internal short circuit current I_{ISC} of the cell.

Figure 4.61: T0151. (left) Cell after the experiment. (right) details of the area near the heated tab in the dismantled cell.

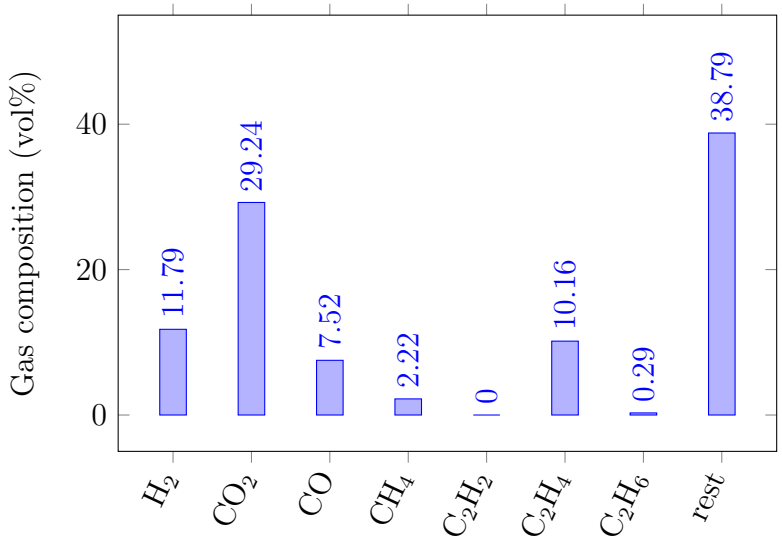

Figure 4.62: Experiment T0151. Detected gas components which were released by the cell. Gas composition was measured by GC.

4.5.5 Hot spot, medium heater

Experiment Setup

This setup is comparable to the micro-heater setup described in a previous section (section 4.5.3). As above, the cell is sandwiched inside the sample holder stack and the centre of the cell is accessed though a cut-out in the upper plates. In contrast to the micro-heater setup the medium-heater has a much higher power. Since the larger heater does not fit into the cut-out, a heat conductor transfers the heat from the ceramic heater to the surface of the cell (fig. 4.63). The contact area between the heat conductor and the cell is $A_H = 19\,\mathrm{mm} \times 19\,\mathrm{mm} = 361\,\mathrm{mm}^2$. Copper (99%, E-Cu, 2.0060) was chosen as the material for the heat conductor, because of its superior heat conductivity ($388\,\mathrm{W\,m^{-1}\,K^{-1}}$ at $20\,^\circ\mathrm{C}$). In later experiments the sides of the conductor and the upper side of the heater were covered with mica sheets to prevent heat loss to the ambient.
Thermocouples were put into the heat conductor in known positions with the intention to calculate the heat flow inside the conductor from ΔT of the thermocouples (fig. 4.64). The heat flow could not be calculated, because the thermocouples were not sufficiently accurate and because ΔT was to small.
Heater parameter are:

Type: FLE 100 638 from *Bach RC* https://www.bachrc.de/
Heated cell area: $A_H = (19\,\mathrm{mm} \times 19\,\mathrm{mm}) = 361\,\mathrm{mm}^2$
Rated power: $P_R = 900\,\mathrm{W}$ at $230\,\mathrm{V}$
Max temperature: $1000\,^\circ\mathrm{C}$ (for the heated part) $500\,^\circ\mathrm{C}$ for electrical connectors

Later the single heater was changed to three smaller with heaters which were connected in parallel:

Type: GLZ 100 058 from *Bach RC* https://www.bachrc.de/
Heated cell area: $A_H = (19\,\mathrm{mm} \times 19\,\mathrm{mm}) = 361\,\mathrm{mm}^2$
Rated power: $P_R = 3 \times 270\,\mathrm{W} \cdots 330\,\mathrm{W} = 810\,\mathrm{W} \cdots 990\,\mathrm{W}$ at $230\,\mathrm{V}$
Max temperature: $1000\,^\circ\mathrm{C}$ (for the heated part) $500\,^\circ\mathrm{C}$ for electrical connectors

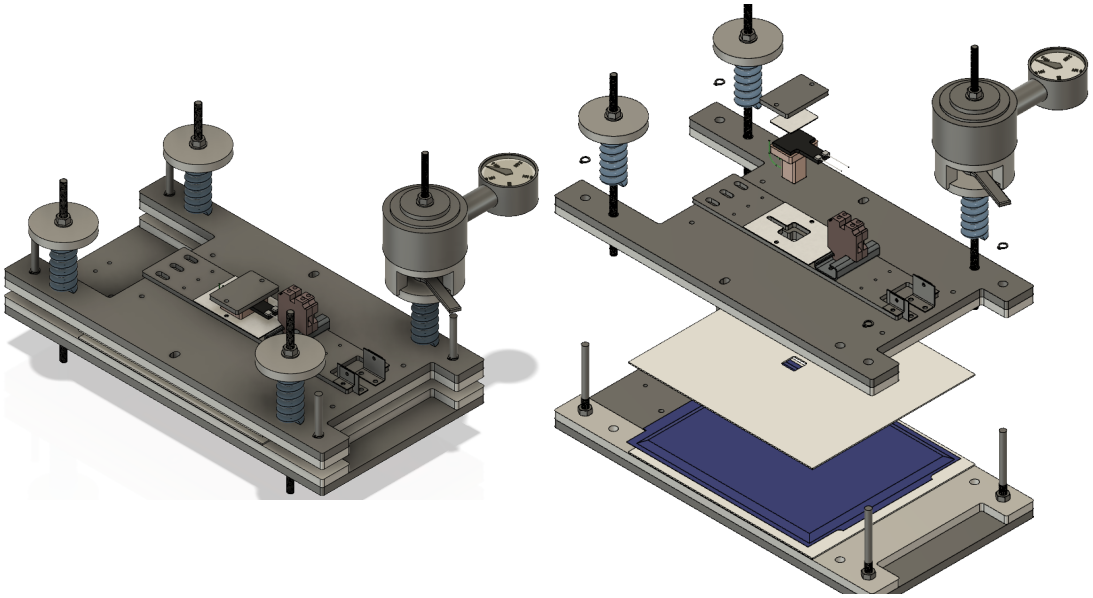

Figure 4.63: Sample holder used for hot-spot medium-heater experiments.

In the experiments with the medium-heater setup different thermocouple arrangements on the top and bottom of the cell were used. The positions are described in the descriptions of the individual experiments.

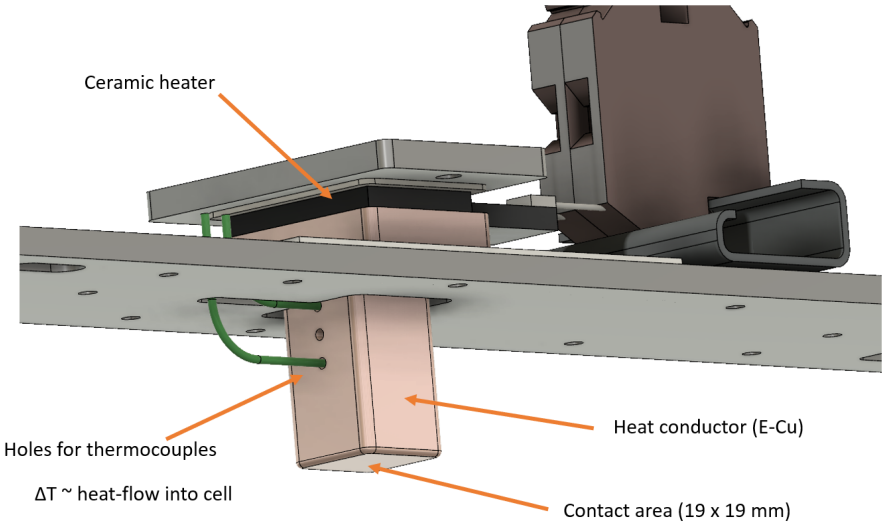

Figure 4.64: Detail of heat conductor.

Experiment T0160

In this experiment the thermocouples were distributed in a grid pattern with two extra thermocouples on the cell surface near the hot spot (fig. 4.65). The heating with the medium heater produced a TR of the cell. This experiment had two phases.
In the first phase the heater was set to 70% power. The heat conductor reached 600 °C and the cell case temperature adjacent to the hot spot reached a maximum of 250 °C and did not increase further. Then the heater was switched off and the cell was let to cool down (fig. 4.67).
In the second phase the heater was set to full power (electric consumption of the heater element: 561 W) and caused a TR after a heating duration of 4030 s and reaching a heat conductor temperature of 763 °C (fig. 4.66). The cell reached a maximum cell case temperature of 675 °C. During the TR the heat conductor perforated several layers of the cell (fig. 4.75). Following events could be identified in the second phase (fig. 4.67, fig. 4.68 and fig. 4.70) at the timestamps:

6880 s Heater set to 100% power

7500 s Heater temperature reaches a plateau at 763 °C. Cell voltage starts to decrease with 25 mV min^{-1}.

8000 s Most adjacent cell case temperature sensors (TK24, TK25) to the hot spot reach 300 °C. Some temperature fluctuation of unknown origin. Further temperature increase with 1 °C min^{-1}.

10650 s More temperature fluctuations near the hot spot.

10807 s Cell temperatures near the hot spot (TK24) reach 400 °C. Start of TR in a circle with a radius of 55 mm around the heater on the upper layer of the cell. Venting of the cell starts (increase of gas pressure and gas temperature inside the reactor)

10810 s TR has propagated through the upper layer of the cell. (All sensors on the upper side of the cell case above 400 °C)

10818 s TR has propagated from the upper layer to the lower layer of the cell. (All sensors on the lower side of the cell case above 400 °C) Maximum of gas pressure and gas temperature in the reactor.

Discussion: The experiment finally shows that the TR can be started by sufficient heating of small area on a cell surface. The high amount of temperature sensors made it possible to track the propagation of the TR throughout the cell. The cell was heated at the centre of its top side on the large face. The heat spread through the cell from the heat injection (interface to the heat-conductor) to the heat sinks. The heat sinks were the upper and the lower pressure plate with their high heat capacities and their high areas accessible to convective cooling. The heat flow created temperature gradients along the cell. The most intriguing temperature gradient spanned in two dimensions along the top layer of the cell. Before the TR it was governed by a combined effect of heat spread in-plane (in the x-y plane) along the layers of the pouch cell and the cooling by the pressure plates. During the TR, exothermic reactions in the cell freed significant amount of additional heat.

To simplify the discussion from now on it is assumed that the temperature is rotationally invariant to the out-of-plane axis (z axis), with the axis origin at the hot spot.

The evolution of the temperature gradient in the upper layer of the cell is shown in a rainbow plot: fig. 4.70. Immediately before the TR the temperature has a maximum near the heater at 380 °C and falls of to 120 °C with increasing distance to the heater. The whole bottom layer of the cell has a homogeneous temperature of only 90 °C.

When the TR starts the first exothermic reaction happens in the area directly adjacent to the heater (fig. 4.69). It releases a small amount of heat causing a temperature increase by 25 °C every second. This relatively small heat release seems to trigger the main exothermic reaction which surprisingly starts at some distance from the heater. The main reaction starts on the upper layer of the cell along a ring with a radius of 55 mm centred at the heat conductor. Along this starting ring the temperature increases with up to 200 °C s^{-1}. The TR propagates further inside the upper layer from the ring to the edges of the cell and then through the electrode layers from top to bottom throughout the cell. The duration of the out-of plane propagation from top to bottom throughout the cell is 8 s.
At the end of the TR - before the cell starts to cool down - the upper layer reaches a maximum of 553 °C near the centre and 648 °C along the ring. The bottom layer reaches a more uniform temperature between 500 °C to 600 °C.
Near the heater the main exothermic TR reaction caused a temperature increase by only 173 K and by a much more significant 528 K along the ring (55 mm away from the heater) as shown in (fig. 4.70). This means that the material located inside the ring in the upper layers released less heat. The volume in the circle in the upper layers is therefore named *inert zone*.
The photo fig. 4.75 of the upper side of the cell after TR shows the highest damage outside of the ring and less damage near the heater. It confirms that the TR caused a maximum surface temperature far from the heater.
Pulses with ±1 A were applied to measure the internal resistance R_i. Probably due to bad electric contacts a high resistance was measured with $R_i = 5.5\,\mathrm{m\Omega}$ at the start of experiment. Before the TR the measured resistance decreased to $R_i = 3.5\,\mathrm{m\Omega}$. The self discharge of the cell was estimated with *Delta SOC method* (section 4.4.1). Immediately before TR the self discharge transformed to a short circuit current with approximately $I_{ISC} = 100\,\mathrm{A}$ (fig. 4.72).
The cell released 2.72 mol with a rate of 0.5 mol s^{-1} (11.4 $\mathrm{l_{SATP}/s}$) during the experiment (fig. 4.71). The vent-gas composition was measured after the TR (fig. 4.73). The composition was similar to gas release from uniformly heated cells (e.g. T0133: section 3.7.4). This means that the exothermic TR reactions caused by hot-spot heating and uniform heating were similar.

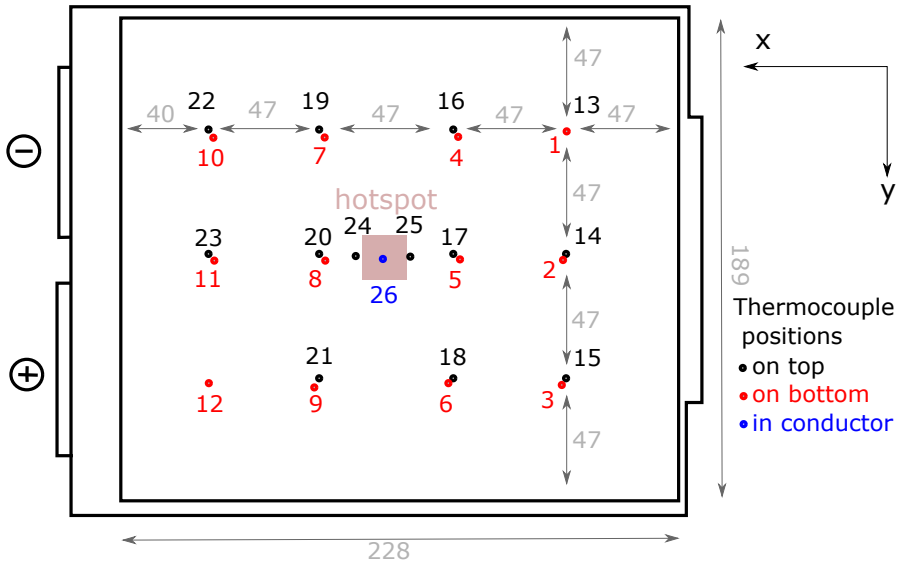

Figure 4.65: T0160. Positions of the thermocouples and the hot-spot on the cell surface.

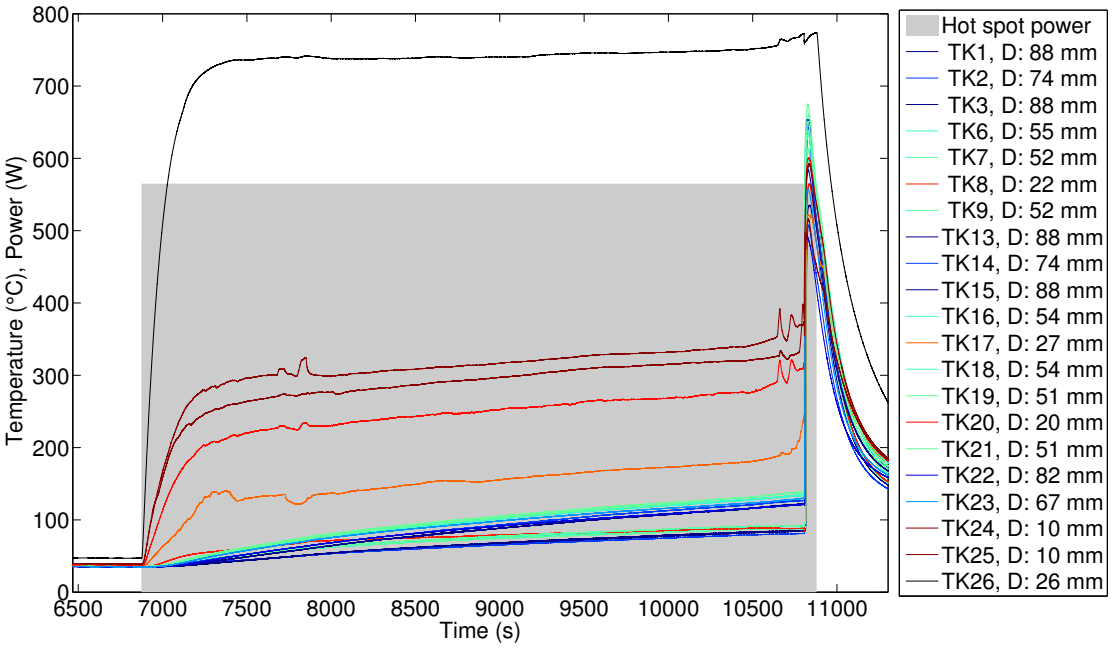

Figure 4.66: T0160. Power of the heater element and temperatures on the cell surface at different distances to the hot spot. Temperatures are color-coded according to the distance from the hot spot.

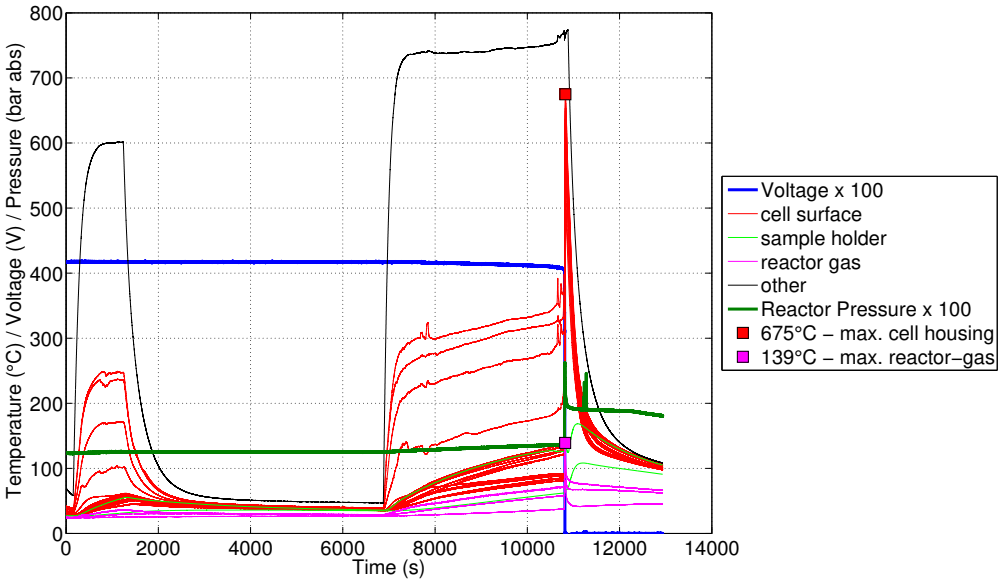

Figure 4.67: T0160. All sensors values. Whole experiment duration. *Other* is temperature sensor inside the heat conductor.

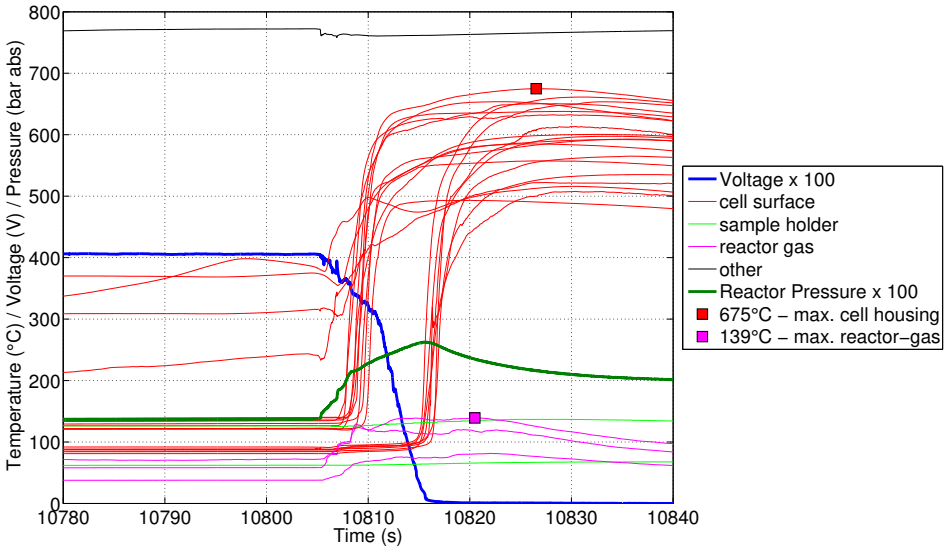

Figure 4.68: T0160. All sensors values. Time span of the TR. Two cell surface groups are distinguishable. The sensors belonging to the upper surface react first. The sensors of the bottom surface follow with 8 s delay. *Other* is temperature sensor inside the heat conductor.

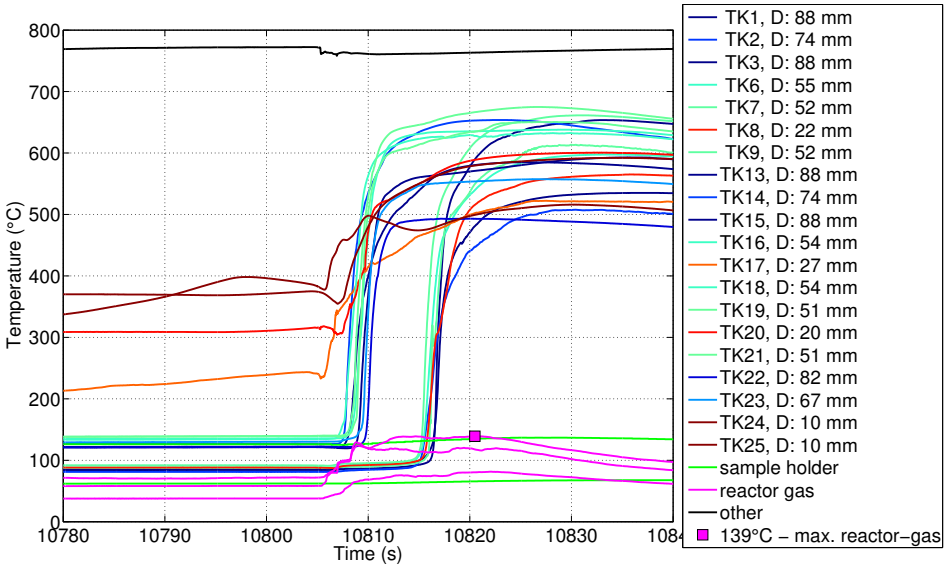

Figure 4.69: T0160. All temperature values. Colour-coding according to distance from hot-spot. Time span of the TR. Two cell surface sensor groups are distinguishable: top (start at >100 °C) and bottom (start at <100 °C). *Other* is the temperature sensor inside the heat conductor.

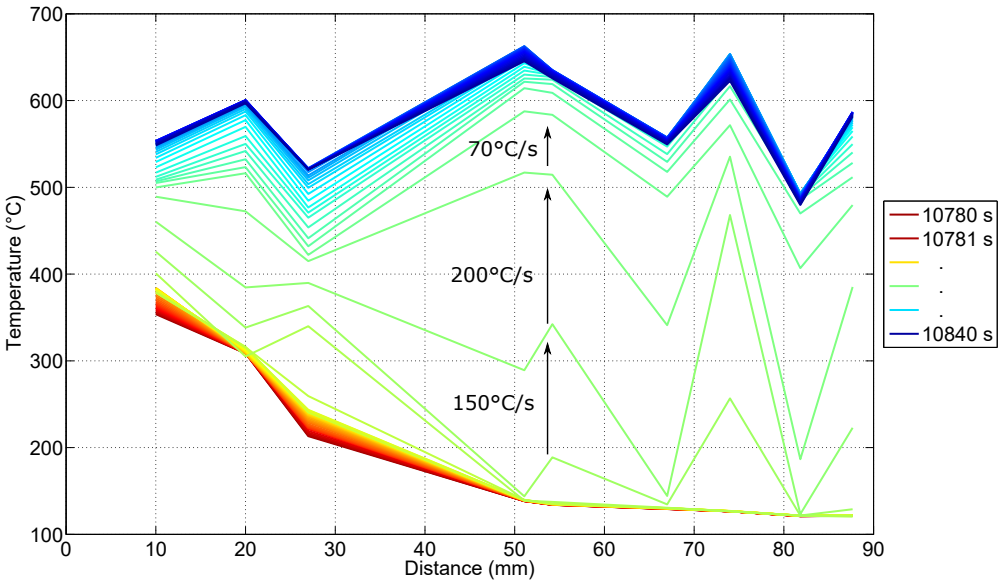

Figure 4.70: T0160. Rainbow plot showing the temperature on the upper layer of the cell. The distance is measured from the hot-spot in the middle of the upper layer. Time span of the TR.

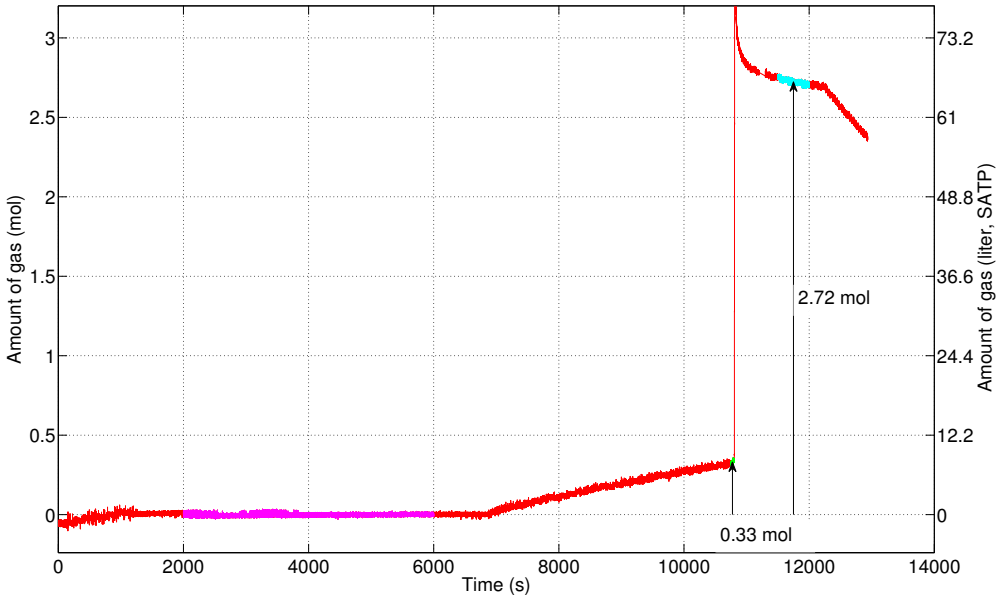

Figure 4.71: T0160. Gas release of the cell.

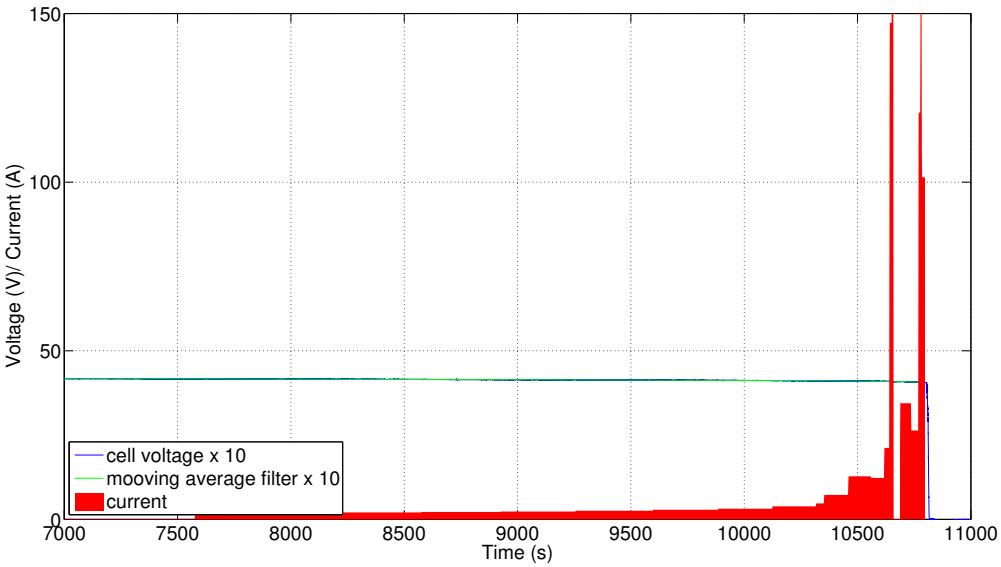

Figure 4.72: T0160. Voltage and self-discharge current / ISC-current of the cell.

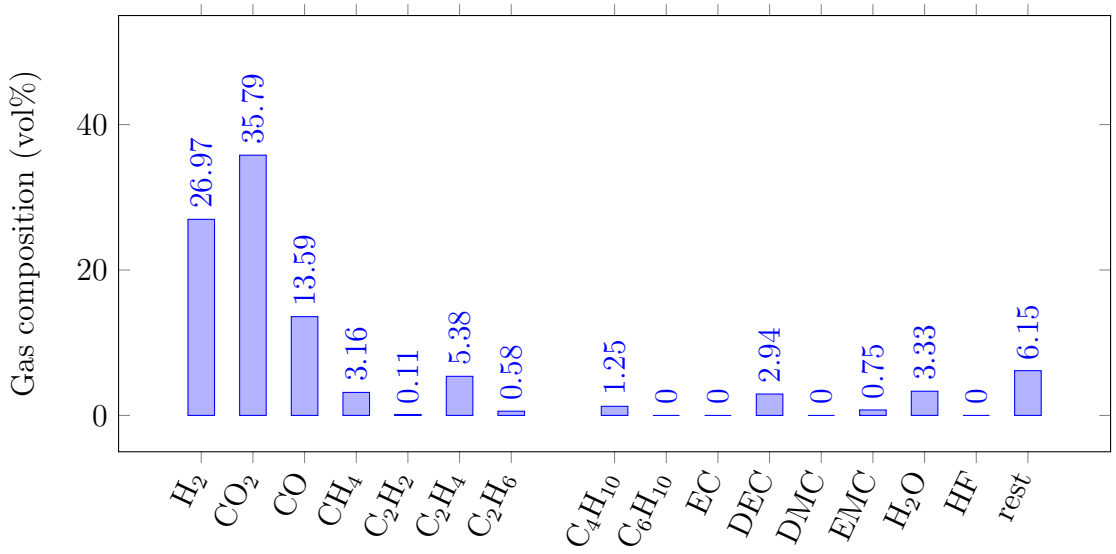

Figure 4.73: Experiment T0160. Detected gas components which were released by the cell. Gas composition was measured by FTIR and GC.

Figure 4.74: T0160. Cell after the TR experiment. The heat conductor perforated several layers of the cell during the TR experiment.

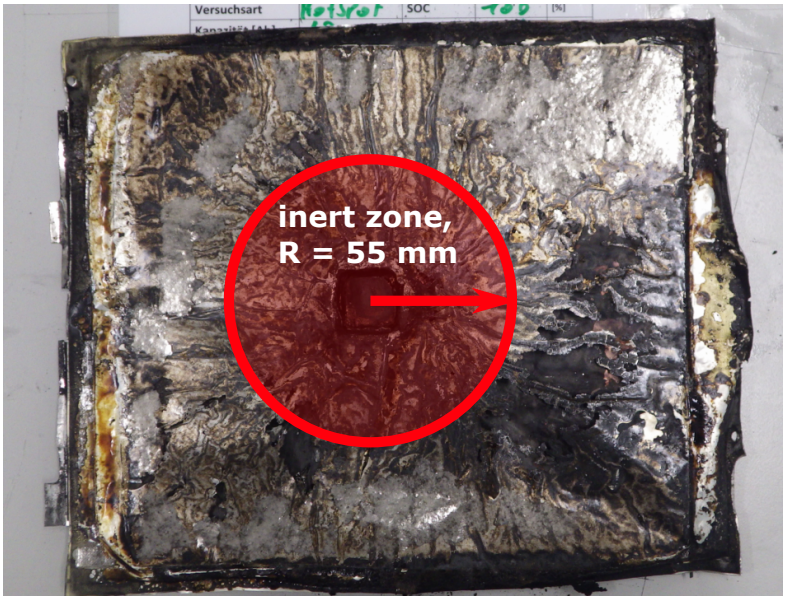

Figure 4.75: T0160. Upper side of the cell after the TR experiment. The annotation marks the starting ring where the rapid TR originated.

Experiment T0161

The experiment setup was almost the same as in T0160. Different from T0160, all cell temperature sensors were placed on the upper surface, in a line pattern, instead of a grid pattern, in order to get a better spatial resolution of the inertisation effects inside the starting ring (fig. 4.76). The cell was heated with a centre heater with a power of 407 W (72% of rated power) for over 5 hours, but a TR could not be started. The center-heater could not be set to higher than 72% because of issues with ground-fault current. To start the TR it was decided to switch on additional flat heaters which heated the lower pressure plate. From this moment the cell was not only heated by the hot spot on the upper surface of the cell, but also by the lower pressure plate, which heated the whole lower surface of the cell. The combined hating could start the TR after 6 hours.
Unfortunately the first two hours of experiment data were lost.

-7200 s Center-heater set to 72% power

4308 s Measured average cell case temperature drops from 162 °C to 152 °C. This may be caused by the bursting of the presumably bloated cell. The effect is

described in section 2.4 .

11400 s Heat conductor temperature reaches a plateau at 630 °C. Cell surface sensor near hot spot (TK2) stagnates at 280 °C. Cell voltage down to 4.0 V. Decision to switch on additional flat heaters with 1 kW on the lower pressure plate.

14000 s Increase of R_i by a factor of approximately 100. Average cell temperature 208 °C.

14900 s Cell voltage drops from 3 V to 0.25 V.

15015 s Start of fast gas release, therefore probably start of rapid TR. Before that, the cell has already released 1.03 mol of gas. Cell surface sensor near hot spot (TK2) at 337 °C. Average cell temperature 250 °C.

15019 s Temperature sensor on the top surface at a distance of 80 mm from the centre starts to increase sharply. Other sensors follow.

15029 s All cell surface sensors are above 400 °C. (TR has propagated through the upper layer of the cell.)

Discussion: In comparison to the previous experiment (T0160) the center-heater had to be operated at a lower power of 407 W instead of 561 W. The TR could not be triggered with the lower power. Therefore, the required power to start the TR must lie between the two power values. In T0161 TR could only be achieved by additional heating with the flat heaters, which rose the overall cell temperature by 50 °C to 70 °C. The unsuccessful centre-heater created an inert zone with the radius of 80 mm before the TR could happen as seen in the rainbow plot (fig. 4.81) and in the fotos of the cell after TR (fig. 4.86).

The self discharge of the cell was estimated with *Delta SOC method* (section 4.4.1). Before 14 000 s the cell showed a self discharge of up to 7 A. After 14 000 s the internal resistance of the cell increased to $R_i > 800\,\mathrm{m\Omega}$, thus preventing further increase of self-discharge current. The subsequent voltage drops were probably caused by chemical degradation of the cell (figs. 4.84 and 4.85). The small ISC probably did not contribute significant heat to start the TR.

The cell released 1.03 mol before the TR and additional 1.77 mol of gas during the TR with a rate of $0.5\,\mathrm{mol\,s^{-1}}$ ($11.6\,\mathrm{l_{SATP}/s}$) (figs. 4.82 and 4.83). The vent-gas composition was measured with the GC (fig. 4.87).

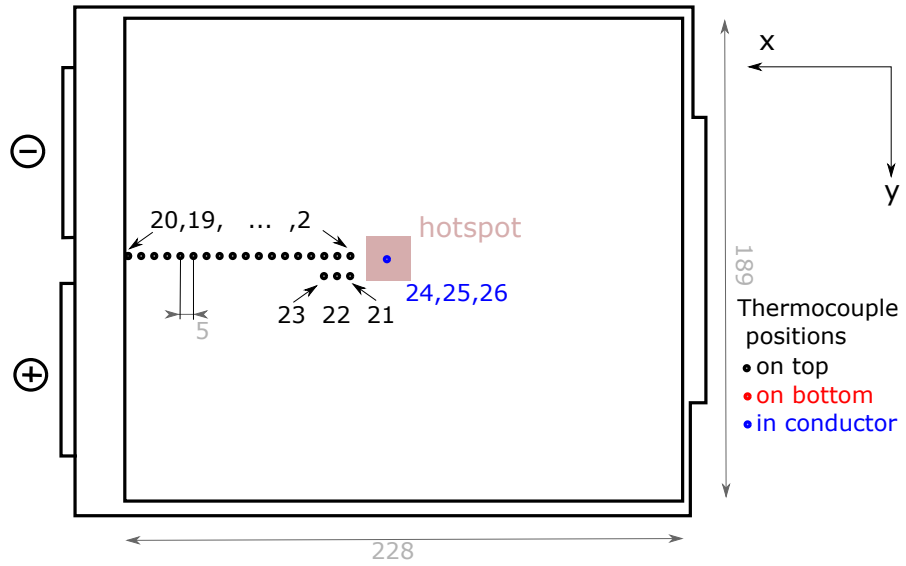

Figure 4.76: T0161. Positions of the thermocouples and the hot-spot on the cell surface.

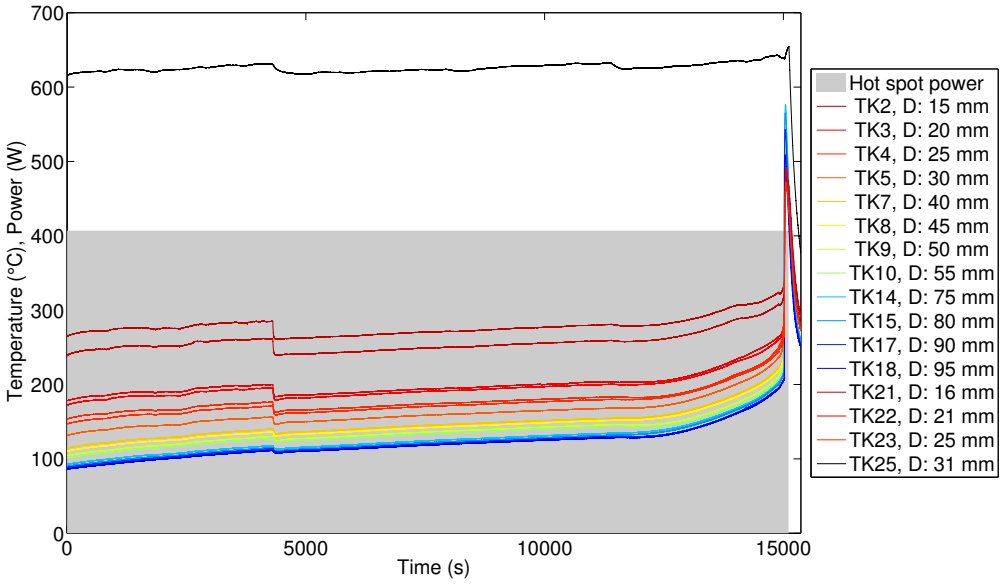

Figure 4.77: T0161. Power of the heater element and temperatures on the cell surface at different distances to the hot spot. Temperatures are color-coded according to the distance from the hot spot.

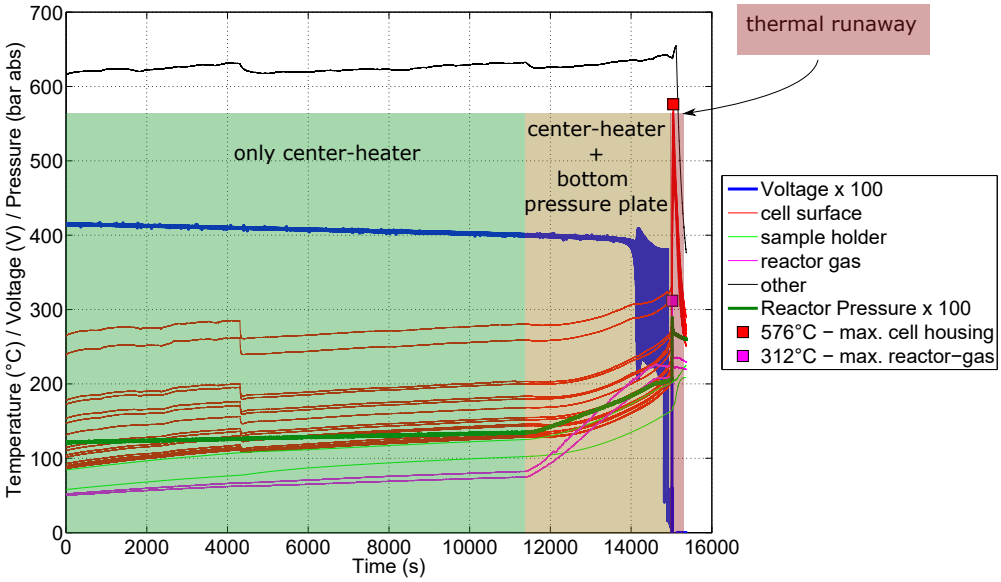

Figure 4.78: T0161. All sensors values. Whole experiment duration. *Other* is the temperature sensor inside the heat conductor.

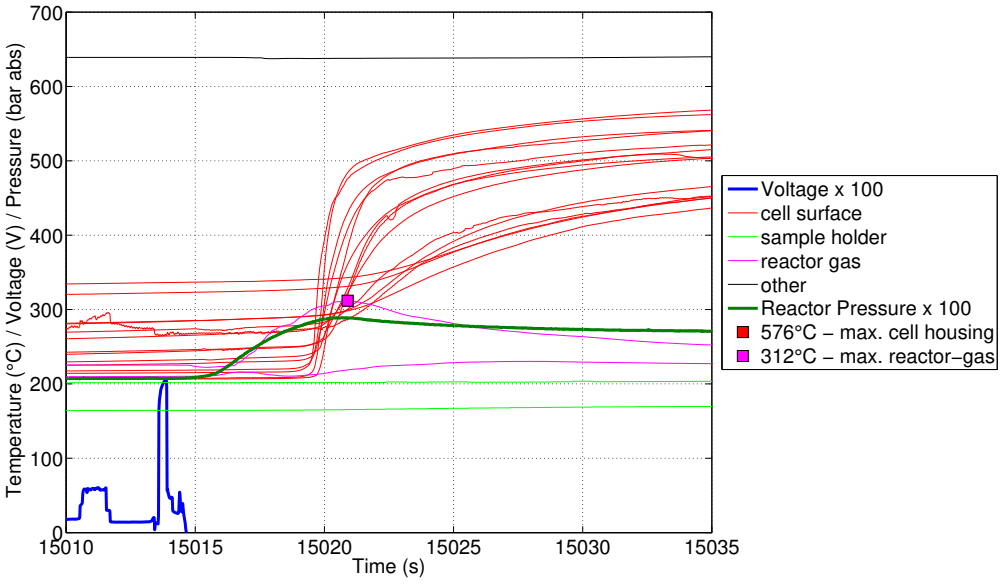

Figure 4.79: T0161. All sensors values. Time span of the TR. *Other* is the temperature sensor inside the heat conductor.

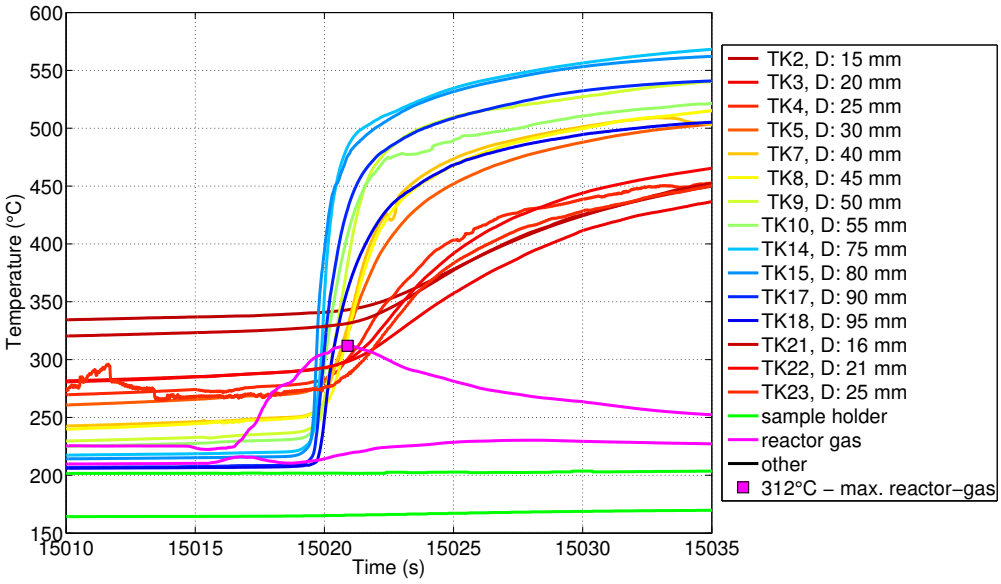

Figure 4.80: T0161. All temperature values. Colour-coding according to distance from hot-spot. Time span of the TR.

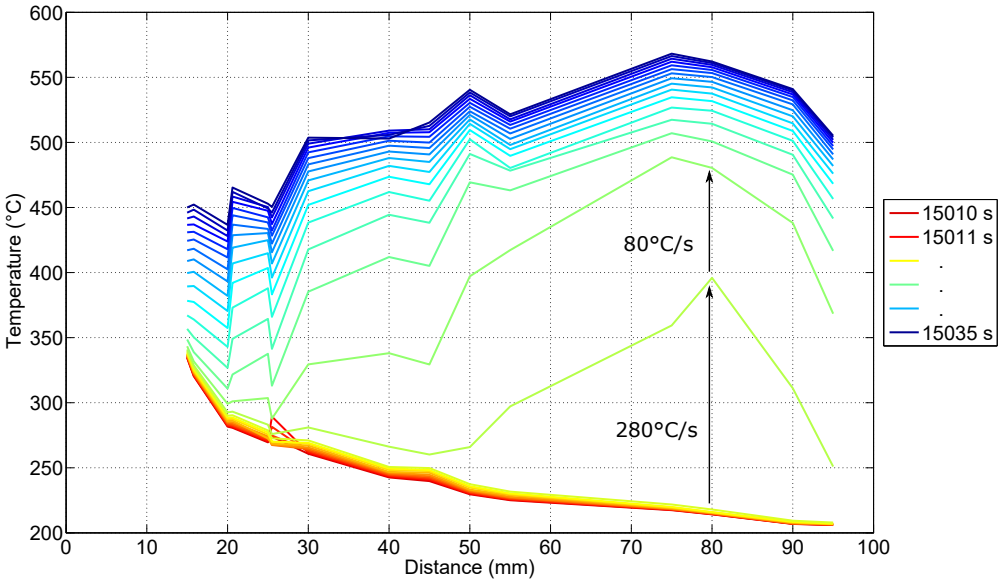

Figure 4.81: T0161. Rainbow plot showing the temperature on the upper layer. Time span of the TR.

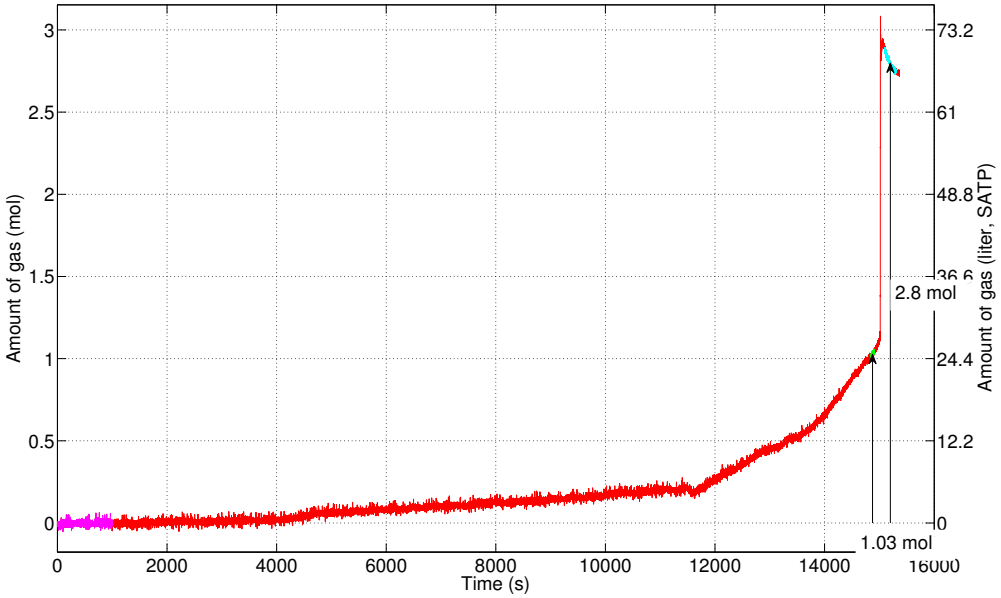

Figure 4.82: T0161. Gas release by the cell.

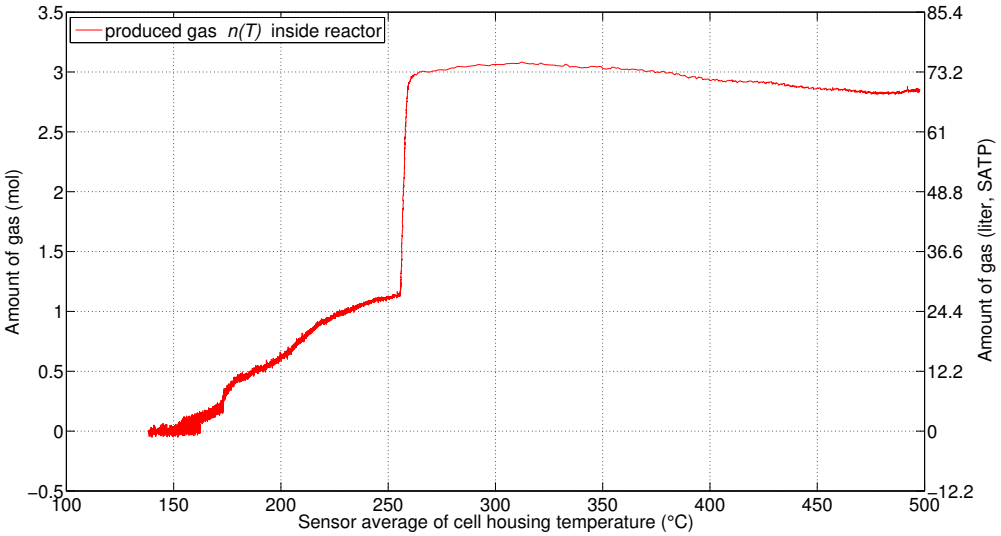

Figure 4.83: T0161. Gas release by the cell vs. average cell-surface temperature.

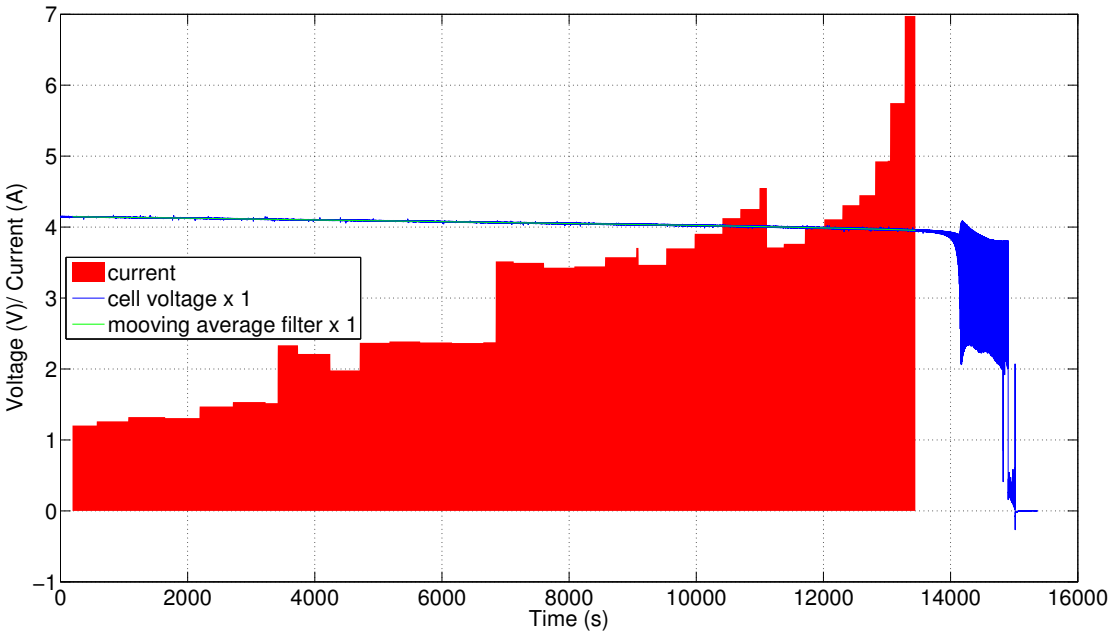

Figure 4.84: T0161. Self discharge current of the cell.

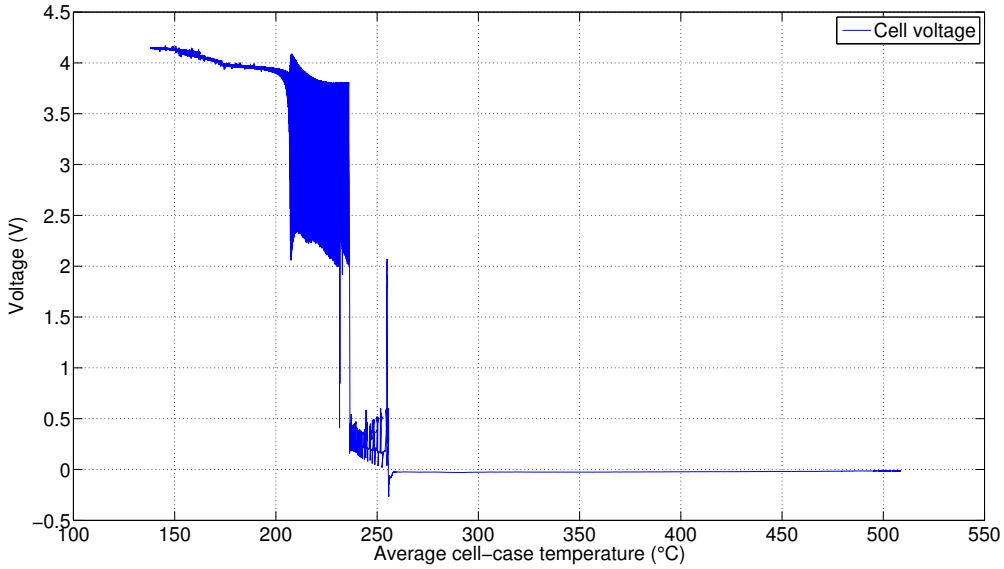

Figure 4.85: T0161. Cell voltage vs. average cell-surface temperature.

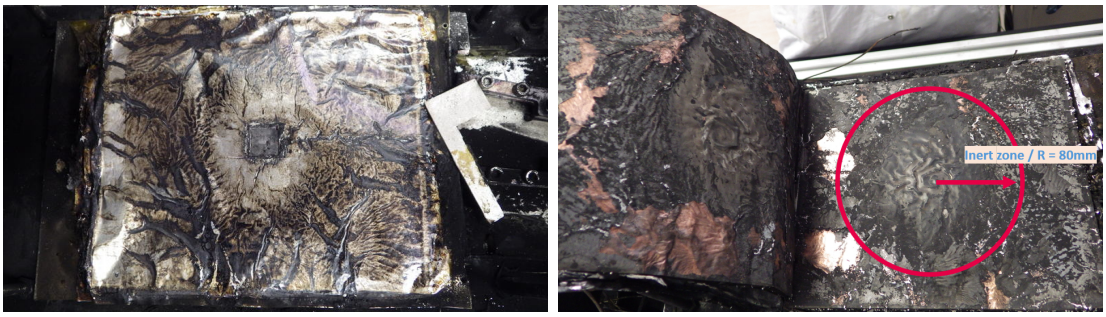

Figure 4.86: T0161. Cell after the TR experiment. In the opened cell a inert zone can be seen in the first upper layers.

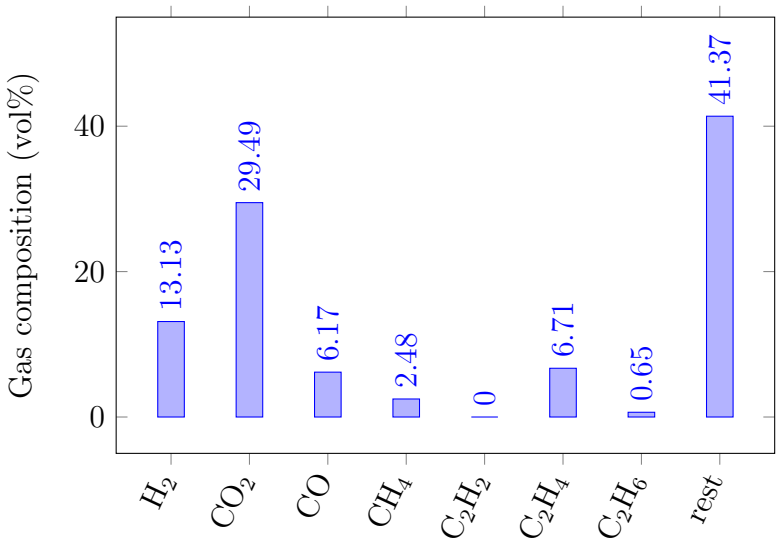

Figure 4.87: Experiment T0161. Detected gas components which were released by the cell. Gas composition was measured by GC.

Experiment T0177

Starting at experiment T0177 an isolating transformer was installed to prevent ground fault currents of the heater elements. The center-heater could be continuously operated with 900 W. The power was sufficient to start a TR after less than a hour of heating. Temperature sensors were applied on the upper and lower surface of the cell positioned equidistantly along a line from the hot spot to the cell edge (fig. 4.88).

19 s Center-heater set to 100% power

200 s - 1600 s Sporadic thermal excursions of the most adjacent cell case temperature sensor on upper surface (TK22) starting at 180 °C, 220 °C, 240 °C and 260 °C

500 s Cell voltage starts to decrease slowly

700 s Heat conductor reaches a steady state temperature of 800 °C

3026 s Most adjacent sensor on the upper side, TK22, measures 322 °C, voltage has dropped to 3.93 V. Start of rapid TR: Voltage start to drop rapidly, reactor pressure starts to increase, temperature sensors in a range of 30 mm to 70 mm on upper surface start to increase first, followed by the other sensors.

3033 s The TR has propagated through the upper layer of the cell.

3037 s Maximum pressure in the reactor

3041 s The TR has propagated from the upper layer to the lower layer of the cell. Cell voltage arrives at 0 V.

Discussion: Here the TR could be started by the center-heater alone and in shorter time than in previous experiments. The TR started again at the ring, on the upper surface of the cell (fig. 4.93). Because of the shorter time, the radius of the starting ring was 30 mm, which is smaller than in previous experiments. The TR reaction propagated to the lower surface of the cell in 7 s, appearing first again at a distance of 30 mm to the centre (fig. 4.94).
The self discharge current of the cell was calculated with the *delta SOC method* (section 4.4.1). The cell showed continuous self discharge between 10 A to 20 A with four distinct short-circuit spikes with 60 A, 100 A, 100 A and 215 A with durations about 50 s (fig. 4.96). The short circuit spikes correlated with the temperature excursions measured by the temperature sensor adjacent to the heating device

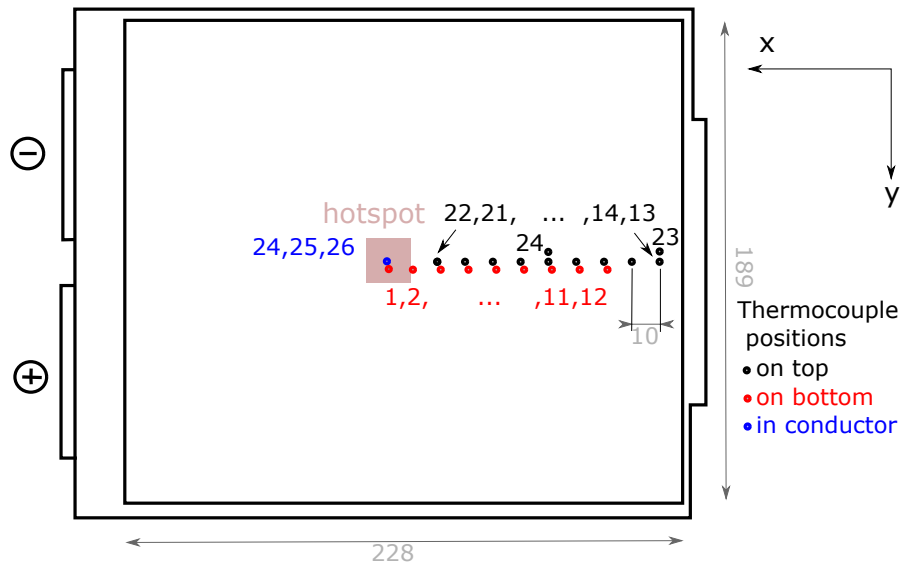

Figure 4.88: T0177. Positions of the thermocouples and the hot-spot on the cell surface.

(TK22). The last spike had the highest magnitude with $I_{ISC} = 250\,\mathrm{A}$ and appeared 10 s before the TR. It could have triggered the TR reaction.

The appearance and extinction of the short circuit spikes can be explained in two steps. In a *first* step an initial damage to the material allows higher short circuit current to flow. In a *second* step the short circuit damages (burns off) the current collectors near the fault and the short circuit dies off. This process is repeated several times as the damaged zone increases around the heater, until the final short circuit exceeds a critical heat input and triggers the full TR of the cell.

The cell released 0.3 mol before the TR and additional 2.06 mol of gas during the TR with an rate of $0.4\,\mathrm{mol\,s^{-1}}$ ($8.9\,\mathrm{l_{SATP}/s}$) (fig. 4.95). The vent-gas composition was measured with GC and FTIR (fig. 4.97).

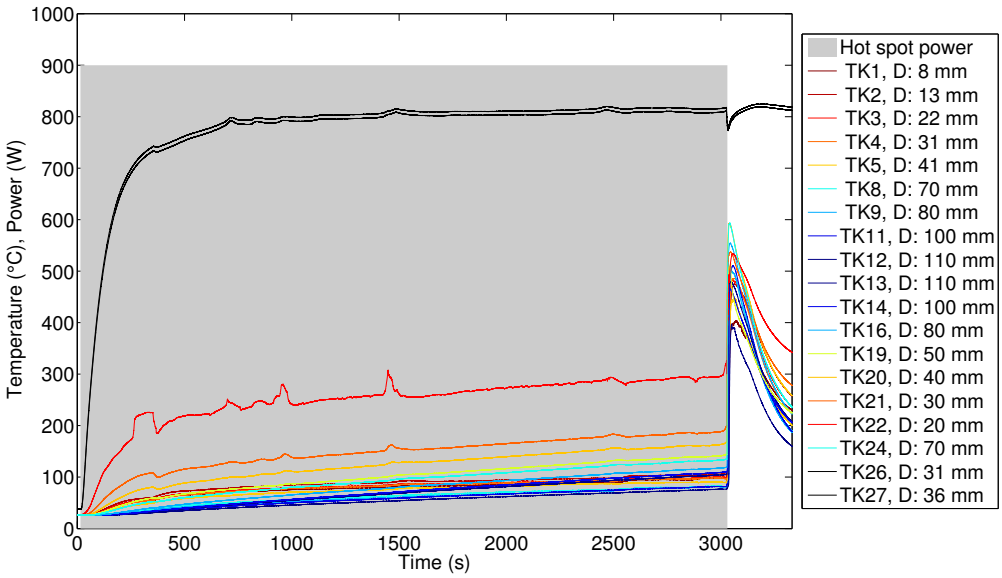

Figure 4.89: T0177. Power of the heater element and temperatures on the cell surface at different distances to the hot spot. Temperatures are color-coded according to the distance from the hot spot.

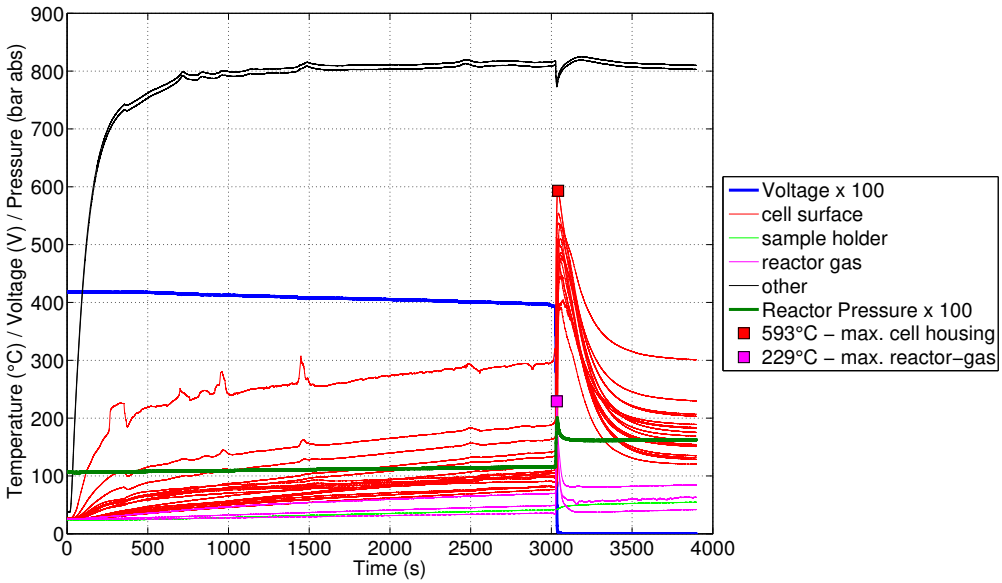

Figure 4.90: T0177. All sensors values. Whole experiment duration. *Other* is temperature sensor inside the heat conductor.

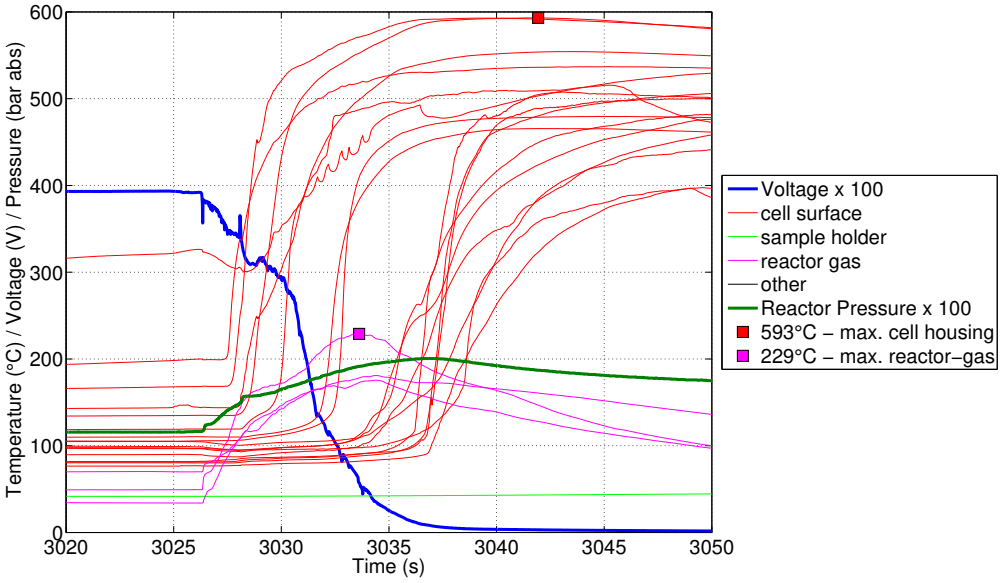

Figure 4.91: T0177. All sensors values. Time span of the TR.

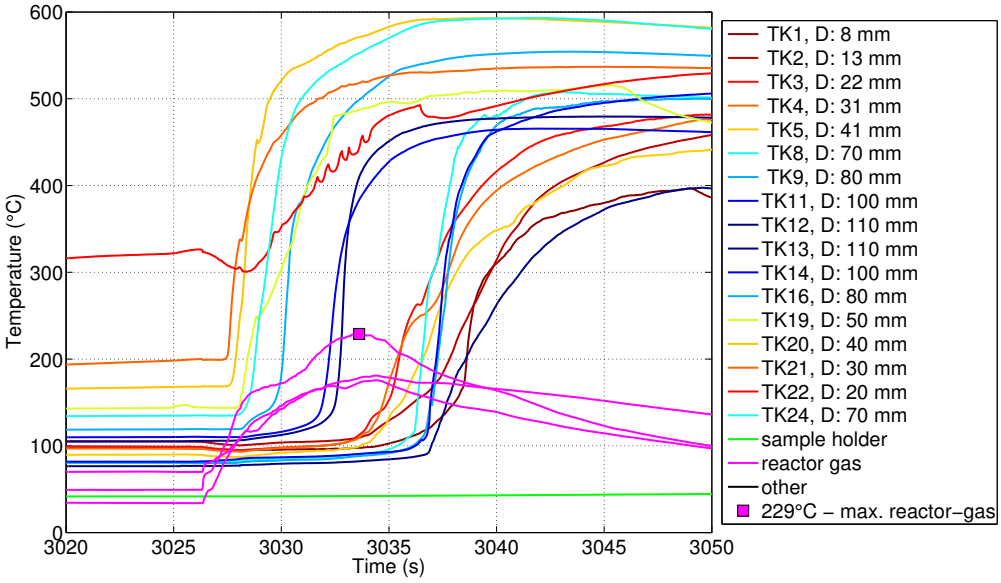

Figure 4.92: T0177. All temperature values. Colour-coding according to distance from hot-spot. Time span of the TR. The two cell surface sensor groups are distinguishable: top (start at >105 °C) and bottom (start at <105 °C).

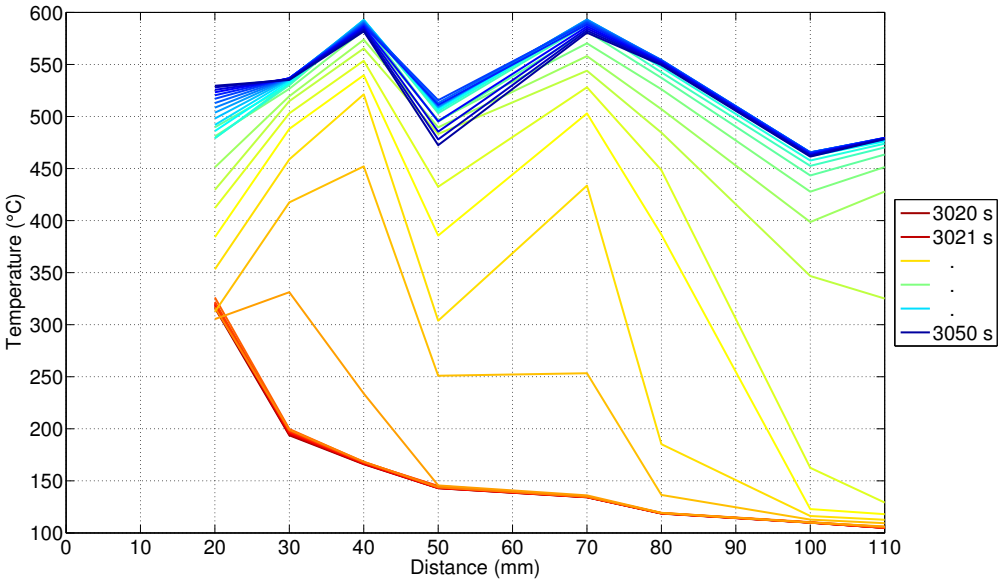

Figure 4.93: T0177. Rainbow plot showing the temperatures on the top side. Time span of the TR.

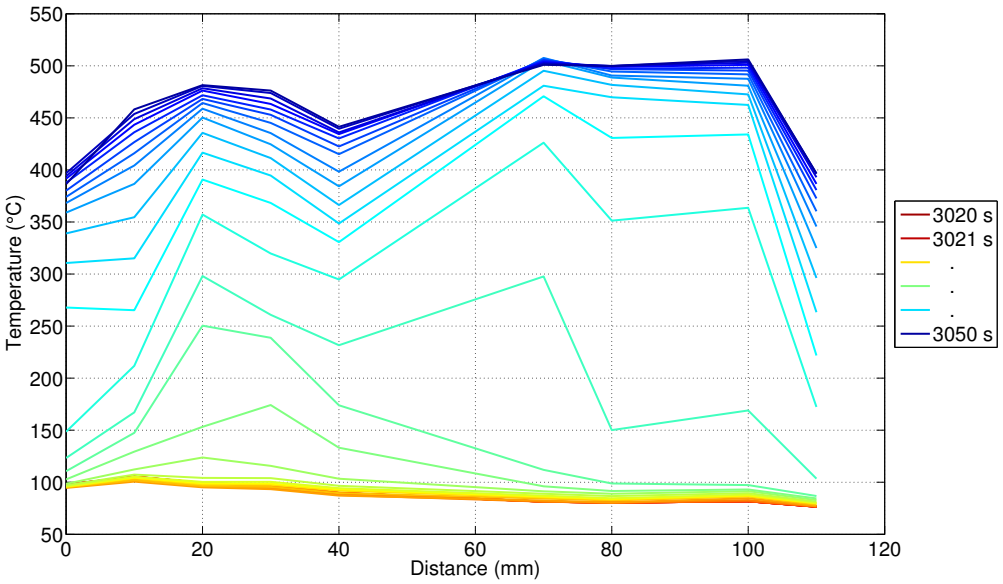

Figure 4.94: T0177. Rainbow plot showing the temperatures on the bottom side. Time span of the TR.

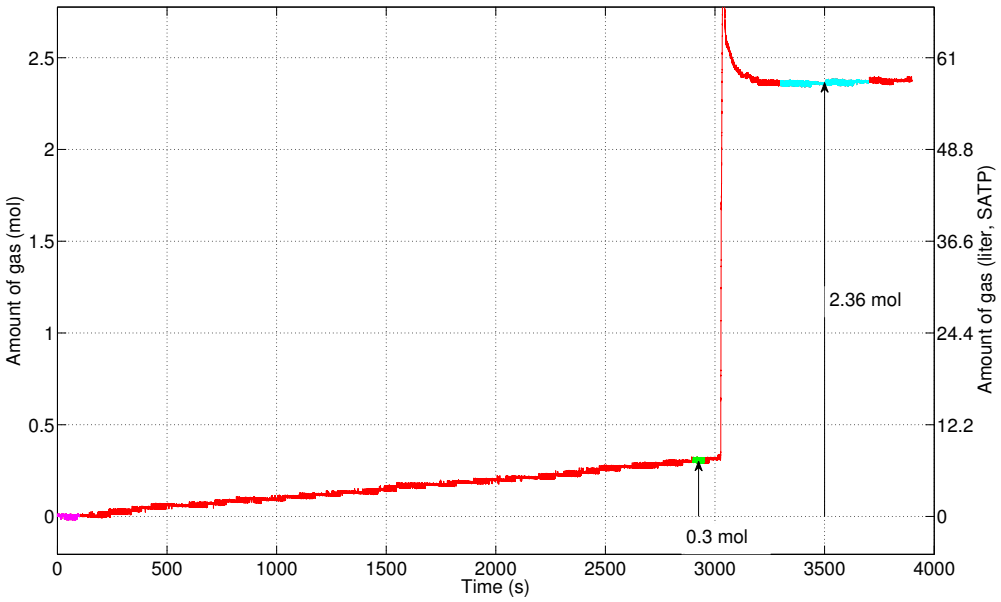

Figure 4.95: T0177. Gas release by the cell.

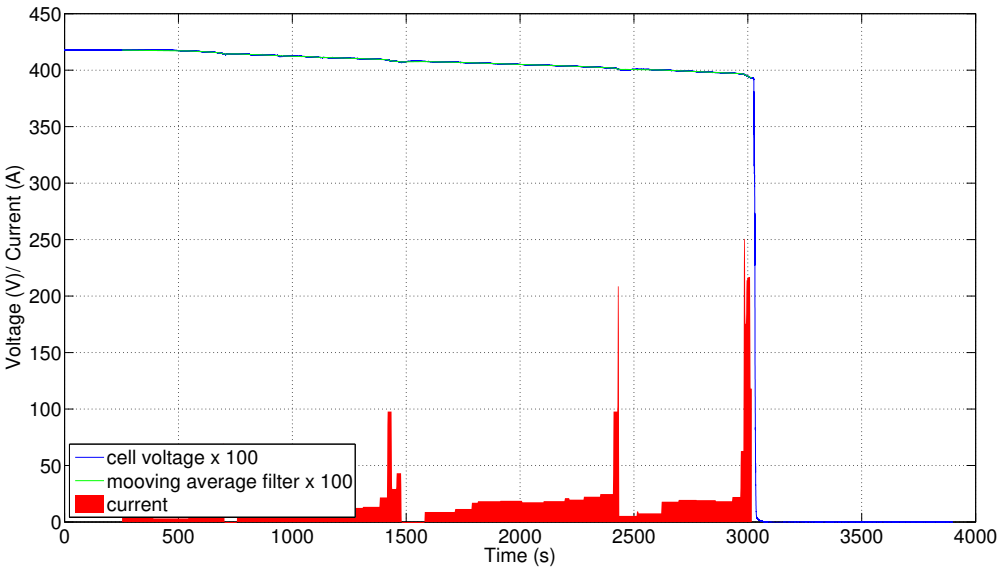

Figure 4.96: T0177. Voltage and self discharge/short circuit current of the cell.

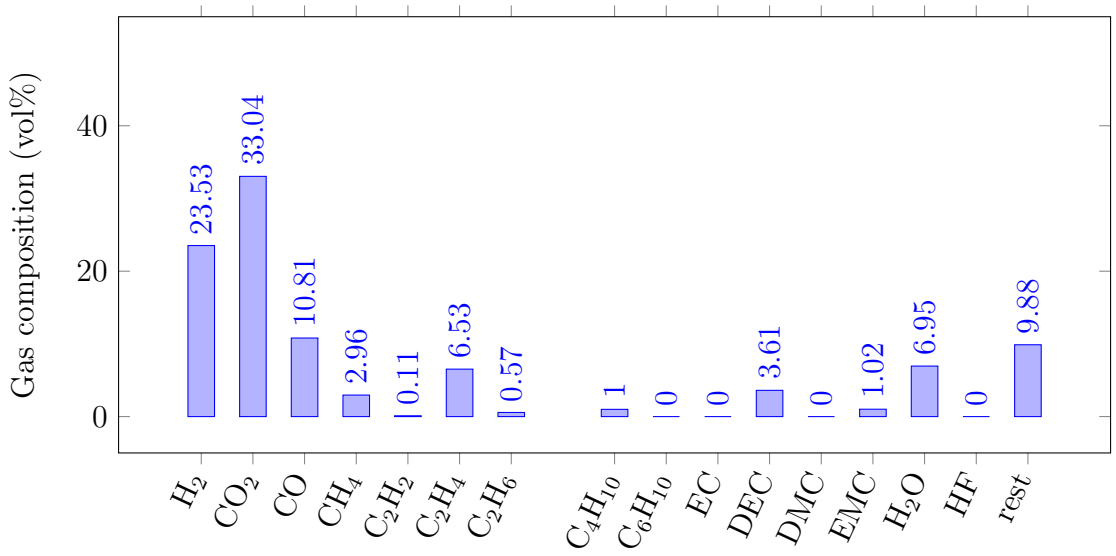

Figure 4.97: Experiment T0177. Detected gas components which were released by the cell. Gas composition was measured by FTIR and GC.

Figure 4.98: T0177. Cell after the TR experiment. In the opened cell a inert zone can is annotated in the first upper layers.

Experiment T0178

This experiment was similar to the previously described T0177. Temperature sensors were applied on the upper and lower surface of the cell (fig. 4.99). The main difference was to add 1 mm of mica-sheet as insulator to the heat conductor on all surfaces except for the interfaces to the ceramic heater and the cell. The goal of this modification was to minimize heat loss and to increase the heat flow into the cell. With this final modification the TR could be started in a short time after 175 s of heating by the medium heater.

134 s Center-heater set to 100% power

285 s Temperature fluctuations start to appear near the adjacent sensor TK23. Adjacent cell case sensor at 300 °C.

300 s Voltage drops from 4.17 V to 4.16 V. Max cell case temperature at 370 °C. Temperature rise in adjacent sensors accelerates.

306 s Gas pressure starts to increase, adjacent temperatures are above 400 °C, voltages starts to decrease, heat conductor temperature at 630 °C. Rapid TR starts near the hot spot.

312 s TR has propagated through the upper layer of the cell.

320 s TR has propagated to through the cell all the way down to the lower layer. Pressure reaches a maximum.

Discussion: Here the TR could finally be achieved after short heating time. In contrast to previous experiments, where a longer heating period was needed, an inert zone could not be detected. The TR originated directly at the hot-spot on the top layer of the cell. The TR spread along the top layer with initially $5\,\mathrm{mm\,s^{-1}}$ and accelerated to above $20\,\mathrm{mm\,s^{-1}}$ (fig. 4.104).
The TR-front arrived at the bottom layer of the cell on the whole bottom area at the same time. One puzzling feature appeared with no explanation yet: on the bottom layer the maximal temperature at the centre - directly below the hot-spot - was only 400 °C, whereas the rest of the cell reached temperatures above 500 °C.
The cell released 0.02 mol before the TR and additional 2.26 mol of gas during the TR with an rate of $0.4\,\mathrm{mol\,s^{-1}}$ ($9.8\,\mathrm{l_{SATP}/s}$) (fig. 4.106). The initial gas release with 0.02 mol was smaller than in previous experiments. This can be explained by the shorter heating time and by the smaller area which was at elevated temperature,

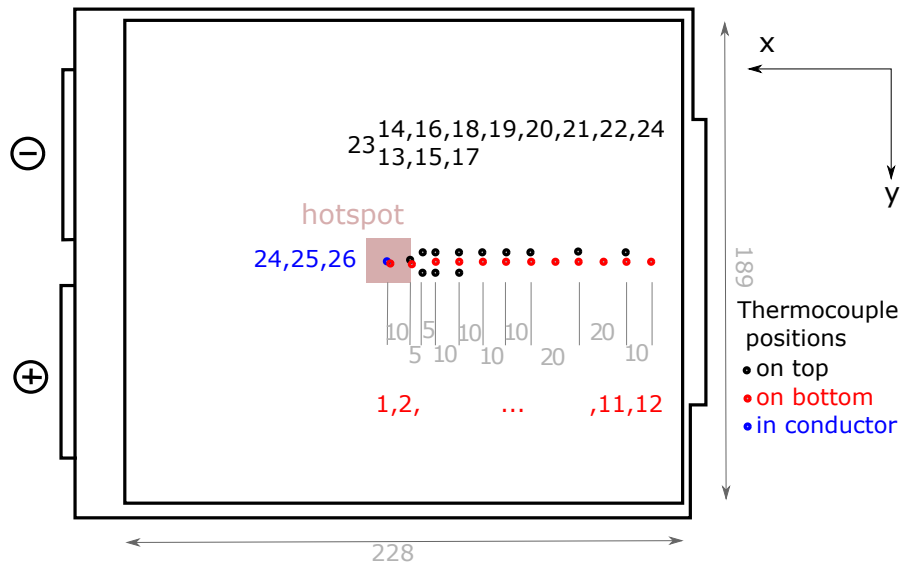

Figure 4.99: T0178. Positions of the thermocouples and the hot-spot on the cell surface.

before the TR started.

The vent-gas composition was measured with GC and FTIR (fig. 4.108). In this experiment a small amount of HF was measured with a HF-concentration in the vent-gas of $c_{\mathrm{HF}} = 53\,\mathrm{ppm}$.

The cell resistance was measured by applying $\pm 1\,\mathrm{A}$ pulses. From start to immediately before TR the cell had the nominal resistance of $R_i = 1\,\mathrm{m\Omega}$. At 295 s to 320 s the cell voltage U_T dropped from 4.1767 V to 4.163 V (fig. 4.107) and an associated internal short circuit current could be calculated using the *Ri method* (4.4.1): $I_{ISC} = 13.7\,\mathrm{A}$.

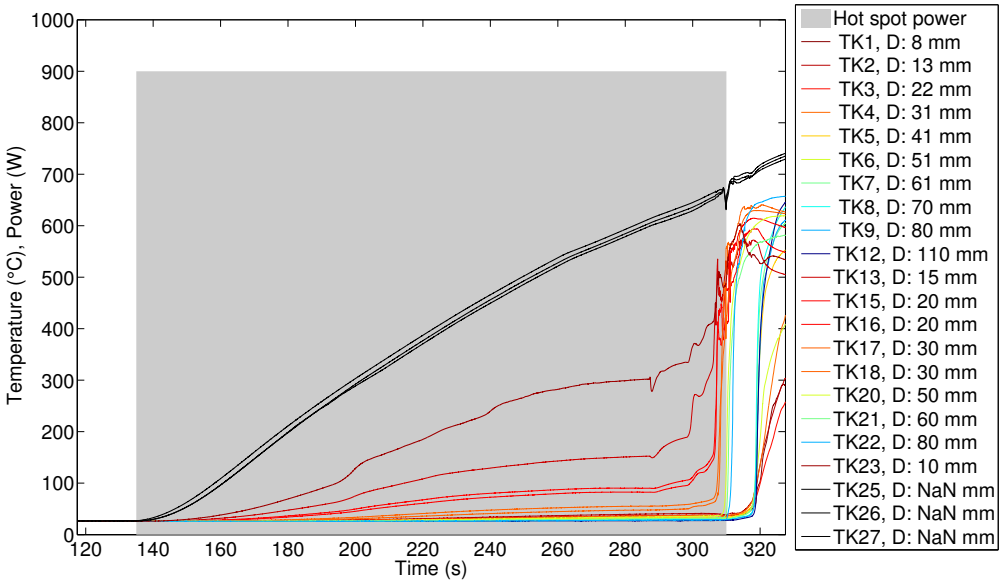

Figure 4.100: T0178. Power of the heater element and temperatures on the cell surface at different distances to the hot spot.

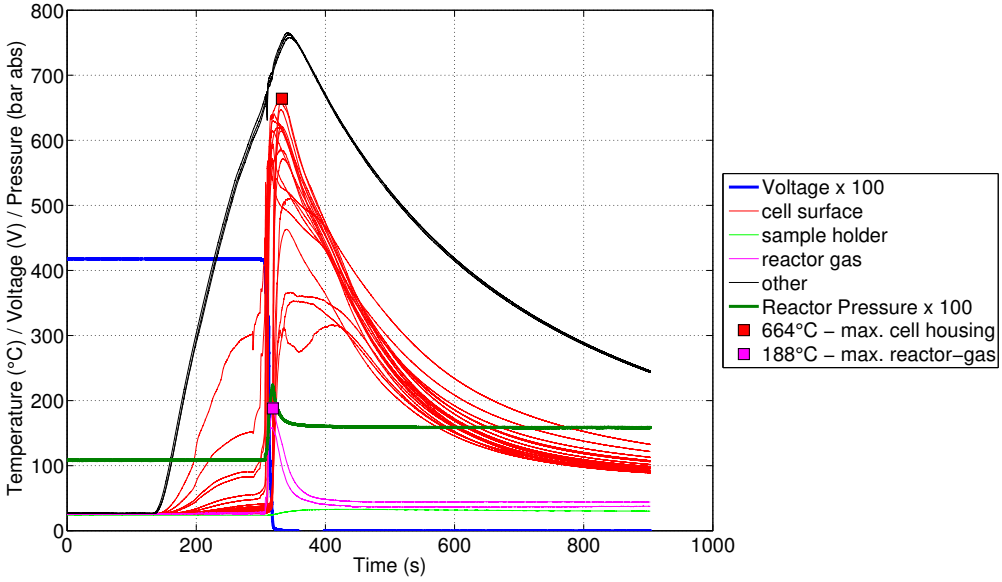

Figure 4.101: T0178. All sensors values. Whole experiment duration. *Other* is temperature sensors inside the heat conductor.

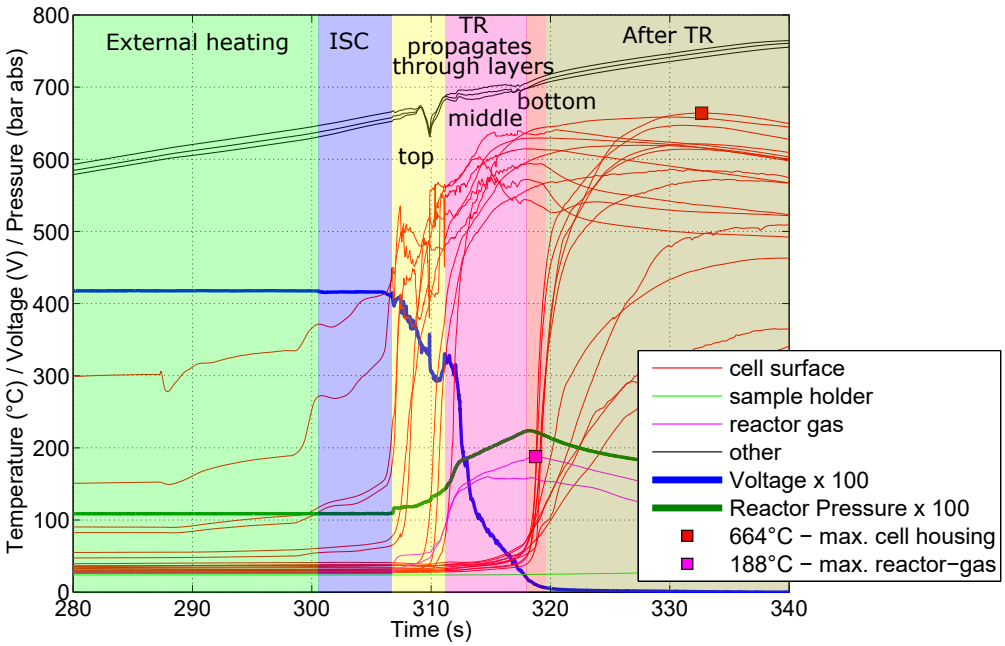

Figure 4.102: T0178. All sensors values. Time span of the TR. *Other* is temperature sensor inside the heat conductor. Different stages of the TR are annotated.

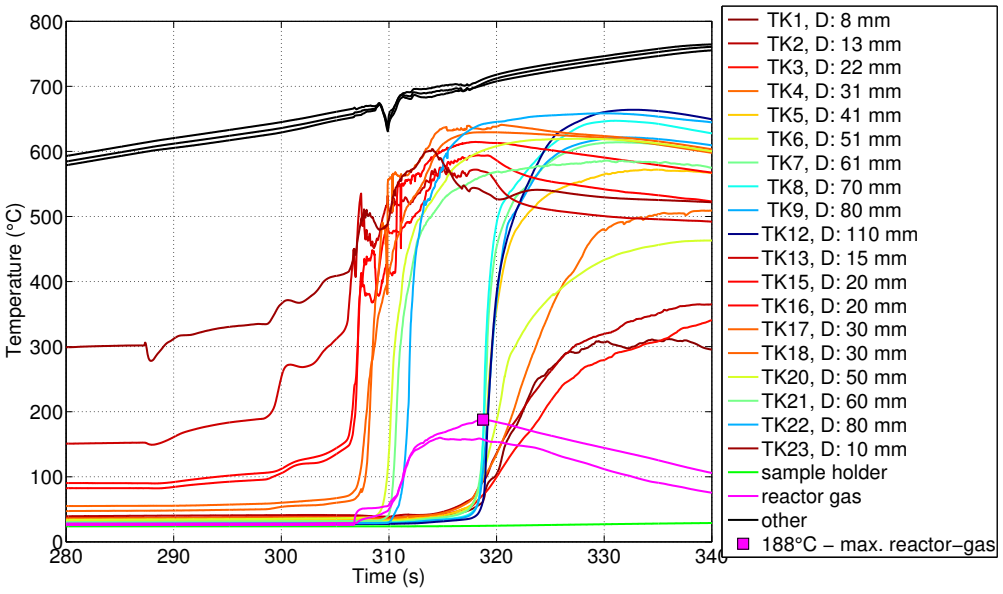

Figure 4.103: T0178. All temperature values. Colour-coding according to distance from hot-spot. Time span of the TR. The two cell surface sensor groups are distinguishable: temperatures on the top size rise first, temperatures on bottom side follow with a 10 s-delay.

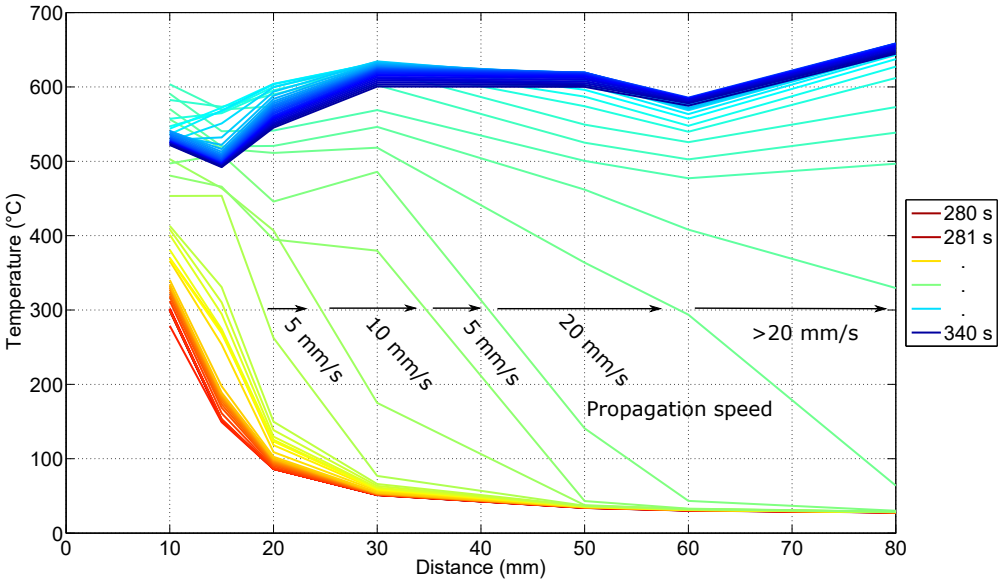

Figure 4.104: T0178. Rainbow plot showing the temperatures on the top side. Time span of the TR. The propagation speed along the top side is annotated.

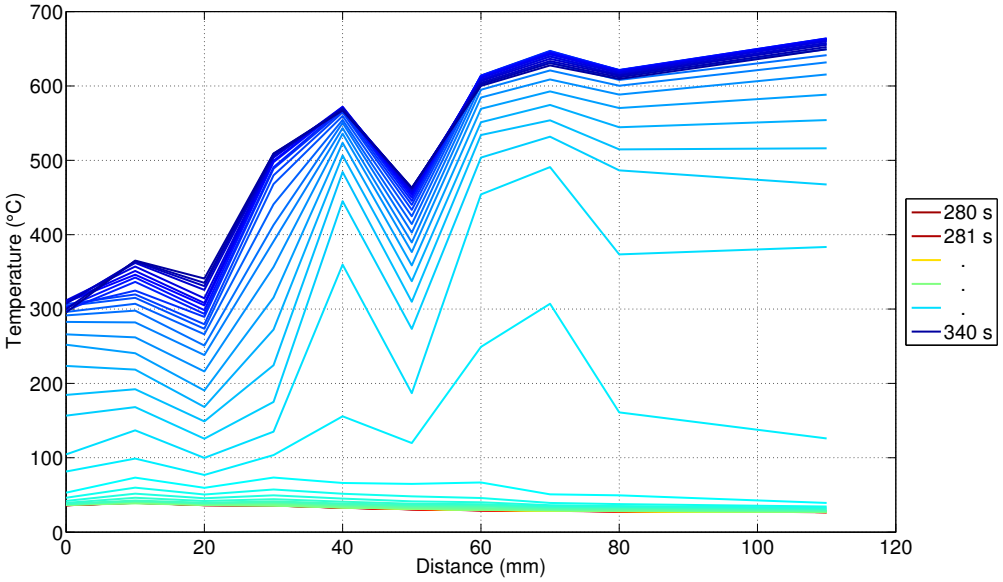

Figure 4.105: T0178. Rainbow plot showing the temperatures on the bottom side. Time span of the TR.

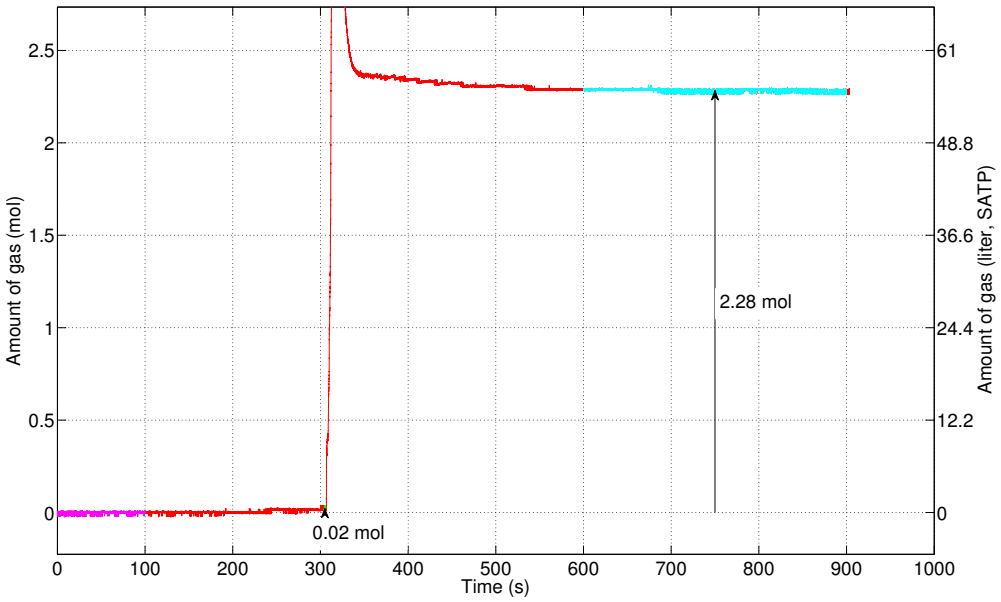

Figure 4.106: T0178. Gas release by the cell.

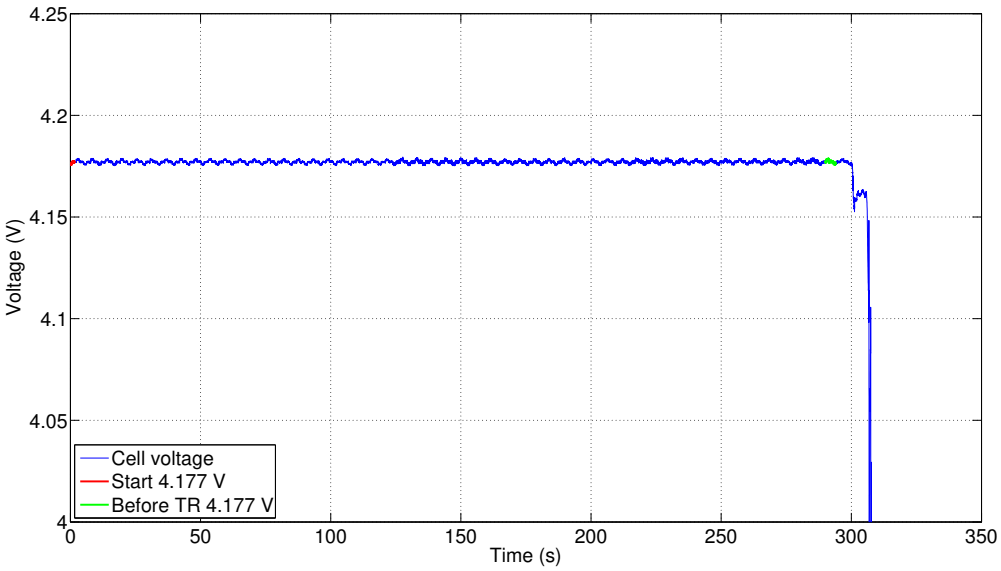

Figure 4.107: T0178. Voltage of the cell.

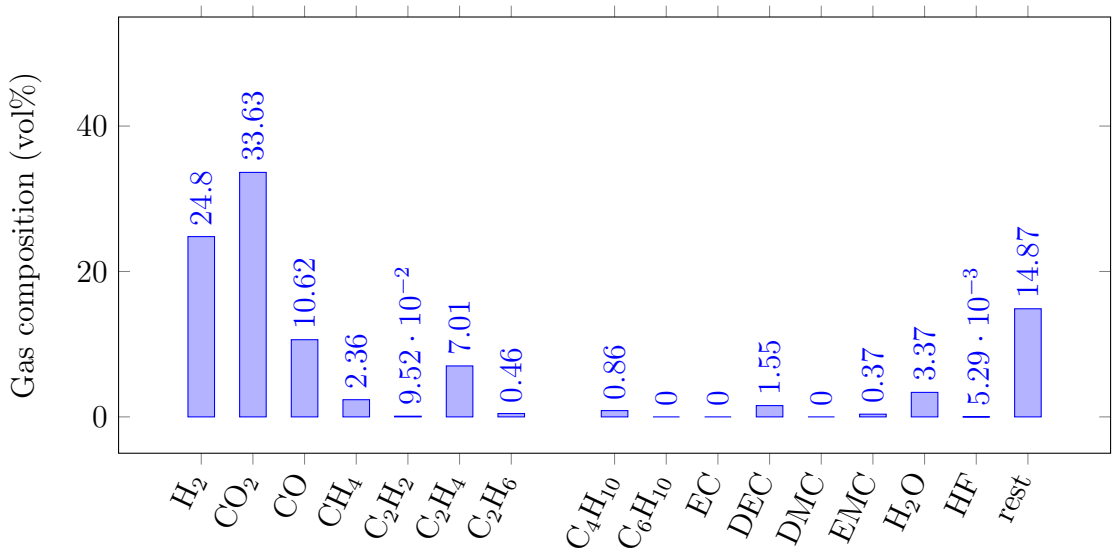

Figure 4.108: Experiment T0178. Detected gas components which were released by the cell. Gas composition was measured by FTIR and GC.

Figure 4.109: T0178. Cell after the TR experiment.

Experiment T0179a

In T0179a the setup as in Experiment T0178 was used. The intention was to reproduce T0178. The ceramic heater failed due to overheating, before a TR could be triggered. The cell reached a maximal temperature of 114 °C and cooled down subsequently (fig. 4.110). The cell was discharged and the reactor was opened. Damage to the heater was observed. The heater was repaired and the cell was then reused in the next hot-spot experiment T0179b.
The cell released a small amount of gas: 0.02 mol during heating. The cell voltage and cell resistance stayed constant at $U_T = 4.18\,\mathrm{V}$ and $R_i = 1\,\mathrm{m\Omega}$.

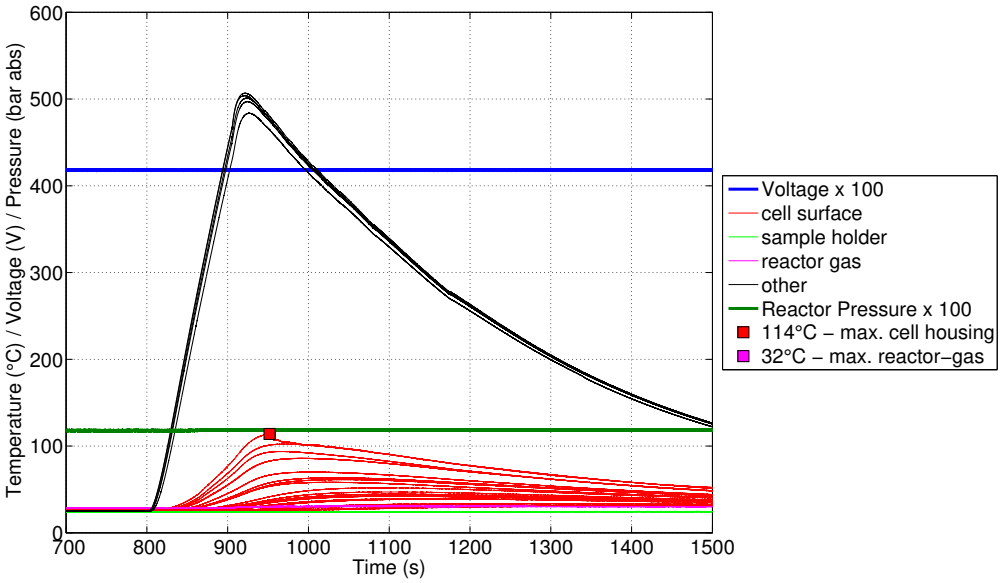

Figure 4.110: T0179. All sensors values. *Other* are temperature sensors inside the heat conductor.

Experiment T0179b

Same setup and the same cell as in Experiment T0179a was used. The cell was recharged before the experiment. Unfortunately the heater failed again due to overheating, before a TR could be triggered. The cell reached a maximal temperature of 90 °C and cooled down subsequently (fig. 4.111). The cell released again a small amount of gas: 0.03 mol during heating. Gas samples ware taken and the composition was measured. Because only small amount of gas was released, the concentration of the cell-gas in the reactor was very low with only 0.4 %, therefore the measured concentration values were unreliable. High shares of H_2, CO_2, CO, CH_4, H_2O (fig. 4.113) were identified. This was the second composition measurement of gas which was released by a local hot-spot before TR. In comparison to gas release of T0151 (section 4.5.4)), higher relative amounts of H_2 seemed to have been released.

The cell discharge was calculated with the *Delta SOC method* (section 4.4.1). The cell experienced a slight self discharge with $I_{ISC} = 0.3\,\mathrm{A}$.

Subsequently, it was decided to give up the hot-spot heating and to heat the bottom plate instead. The results of this are covered in the experiment T0179 (section 4.5.2).

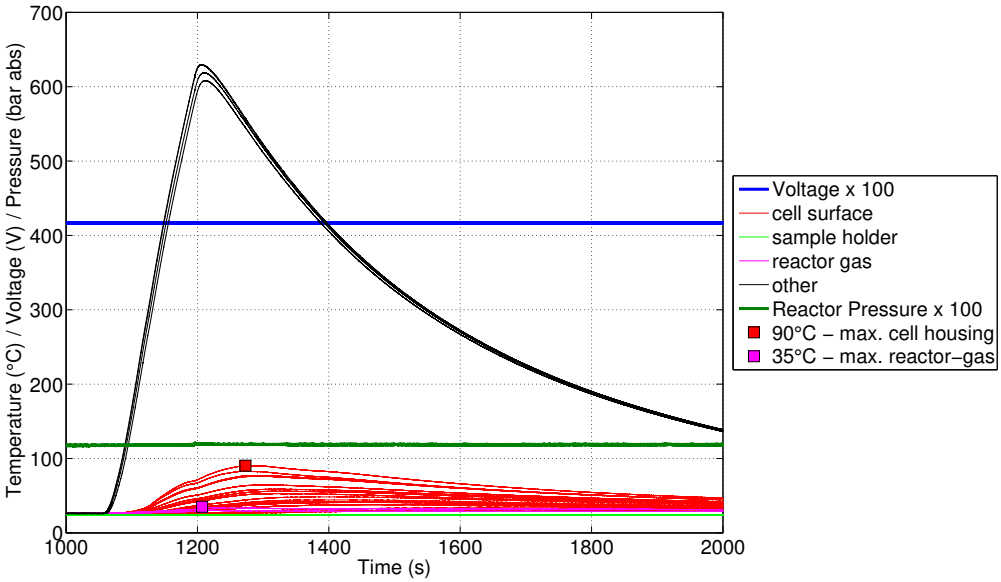

Figure 4.111: T0179b. All sensors values. *Other* are temperature sensors inside the heat conductor.

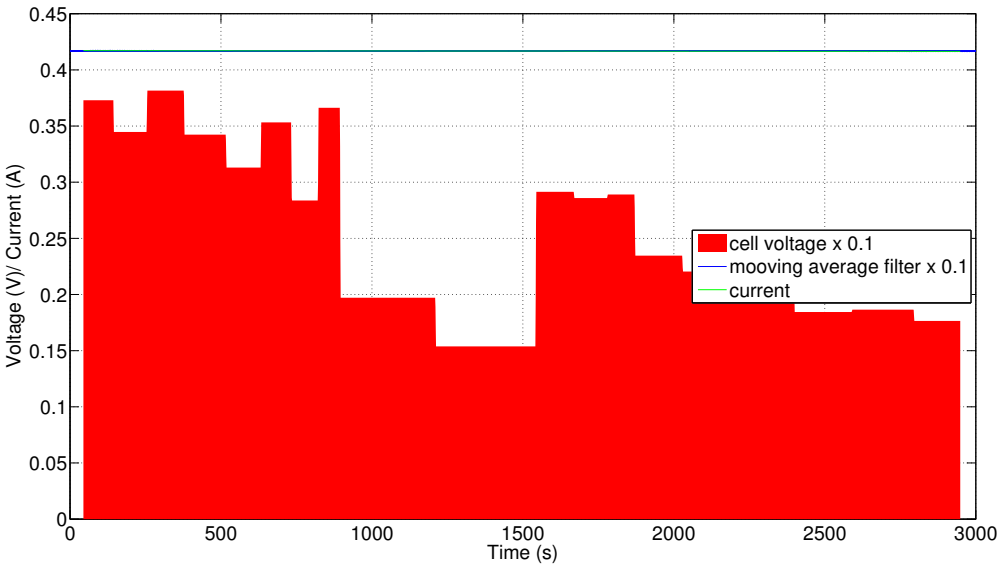

Figure 4.112: T0179b. Voltage U_T and self discharge current I_{ISC} of the cell.

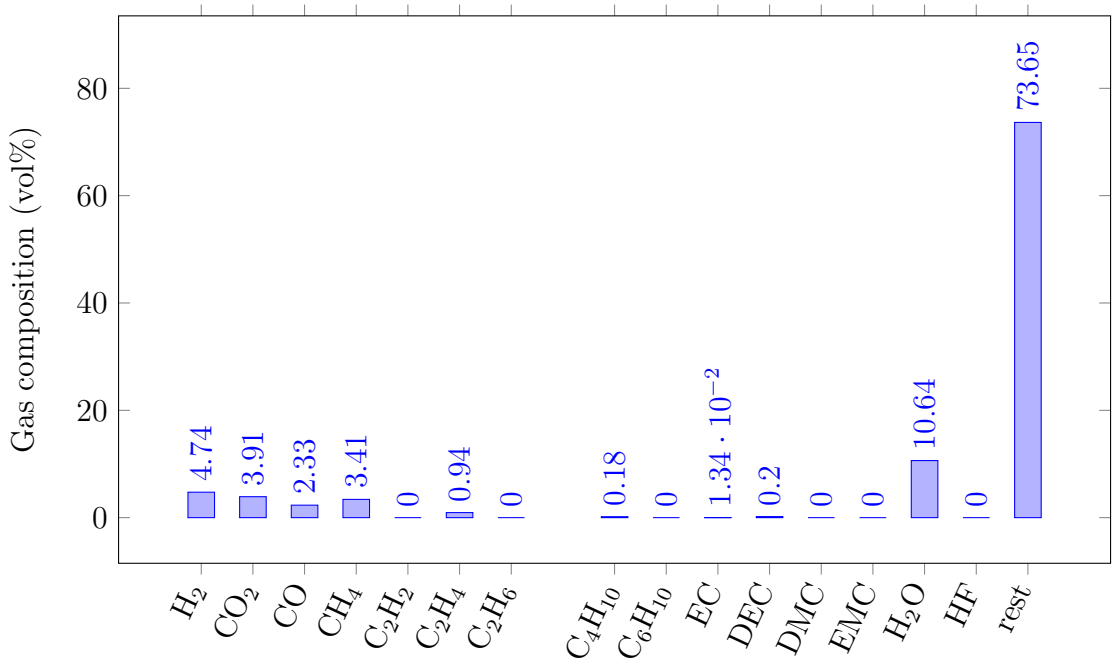

Figure 4.113: Experiment T0179b. Detected gas components which were released by the cell. Gas composition was measured by FTIR and GC. Only 0.03 mol were released by the cell therefore the concentration of vent-gas in the reactor was low (0.4 %) and - in comparison - the amount of not identified *rest* gas relatively high. Most probably too low N_2 concentration was measured by GC and the residual error of N_2-concentration was incorporated into the *rest* value.

Experiment T0180

This experiment was a repetition of the previous experiment T0179a. Same setup was used, except for removal of thermal insulation near the electric contacts of the ceramic heaters, to prevent overheating. Thermocouples were placed in a similar layout as before (fig. 4.114). The cell was cut open on the sides immediately before charging and the hot-spot experiment. This was needed to improve the temperature measurement near the hot spot. The openings were done to channel the release of vent-gas away from the hot spot. The idea was to prevent disturbance of temperature measurement from nearby flow of hot vent-gas. The TR could again be achieved in short time (405 s).

80 s Centre heater set to 100% power

460 s Voltage starts to drop slowly. Temperature fluctuations start to appear near the adjacent sensors (TK14). (TK14 measures a short temperature spike with a maximum of 168 °C.)

480 s TK14 is at 150 °C. Voltage starts to decrease with 40 mV s^{-1}. Pressure starts to increase. Begin of rapid TR.

481 s Readings of the most adjacent cell temperature sensors (TK14) start to increase sharply followed by the other sensors on the upper side of the cell.

486 s The TR has propagated through the upper side of the cell.

491 s The TR has propagated through the cell layers from top to bottom and arrives at the center of the bottom layer.

492 s Peak of the gas pressure.

493 s The TR has propagated through the whole cell. Voltage at 11 mV.

Discussion: The results of this experiment were very similar to T0177. The TR originated directly at the hot-spot and propagated through the upper layer and subsequently to the bottom layer. The propagation speed on the upper layer ranged between 10 mm s^{-1} and 20 mm s^{-1} (fig. 4.119).
The final temperature distribution at the bottom layer shows again the puzzling effect: the low maximal temperature in the centre. On the bottom-side, sensors measured a maximum temperature of 400 °C near the centre and a maximum temperature above 630 °C towards the edges.

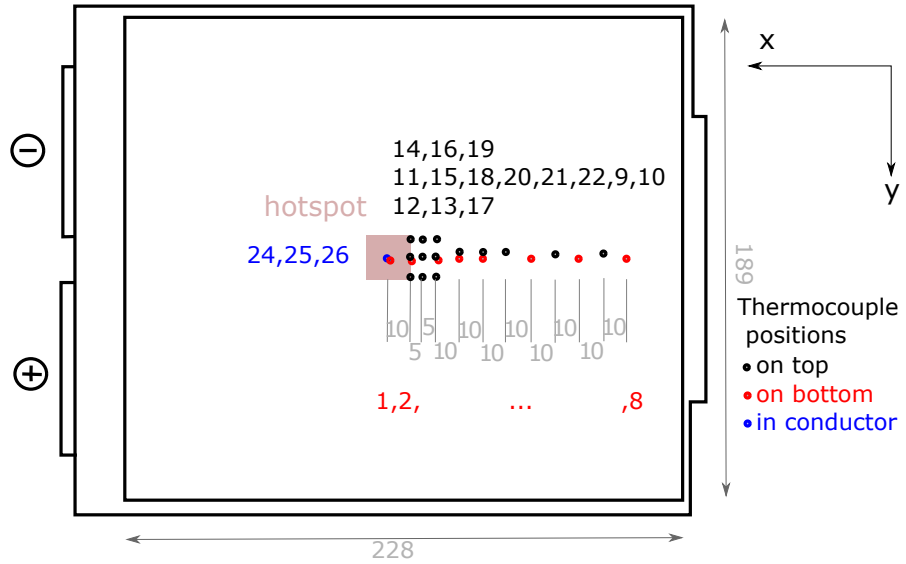

Figure 4.114: T0180 and T0181. Positions of the thermocouples and the hot-spot on the cell surface.

The cell resistance was measured by applying ±1 A pulses. From start to immediately before TR the cell had the nominal resistance of $R_i = 1.3\,\mathrm{m\Omega}$. The self discharge/short circuit current was calculated with the with *Delta SOC method* (section 4.4.1). The cell started to self-discharge at 410 s with 28 A. With time the I_{ISC} increased up to a value of 136 A 10 s before the TR (fig. 4.122).
The cell released 0.05 mol before the TR and additional 2.38 mol of gas during the TR with an rate of $0.3\,\mathrm{mol\,s^{-1}}$ ($7.3\,\mathrm{l_{SATP}/s}$) (fig. 4.121). The vent-gas composition was measured with GC and FTIR (fig. 4.123).

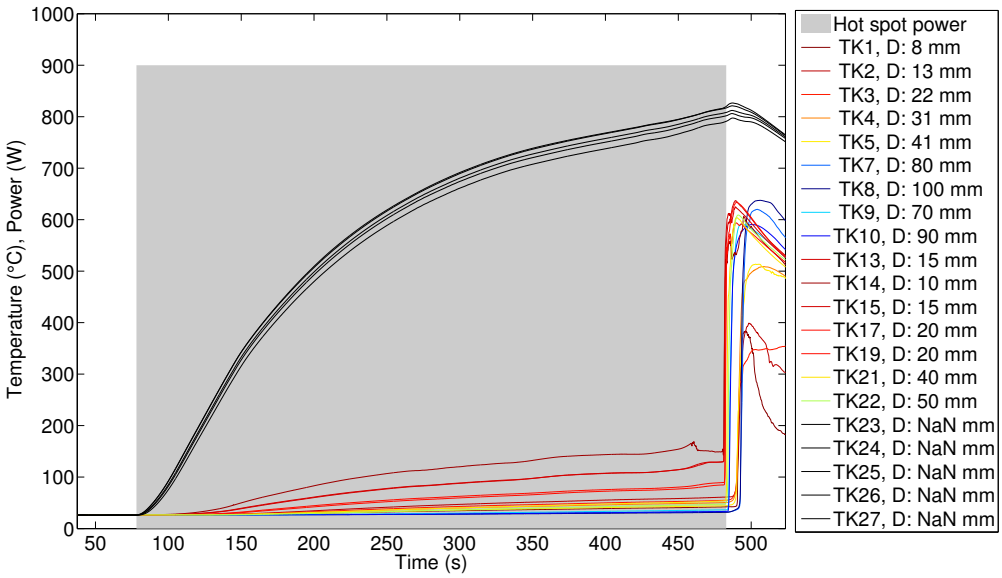

Figure 4.115: T0180. Power of the heater element and temperatures on the cell surface at different distances to the hot spot. Temperatures are color-coded according to the distance from the hot spot.

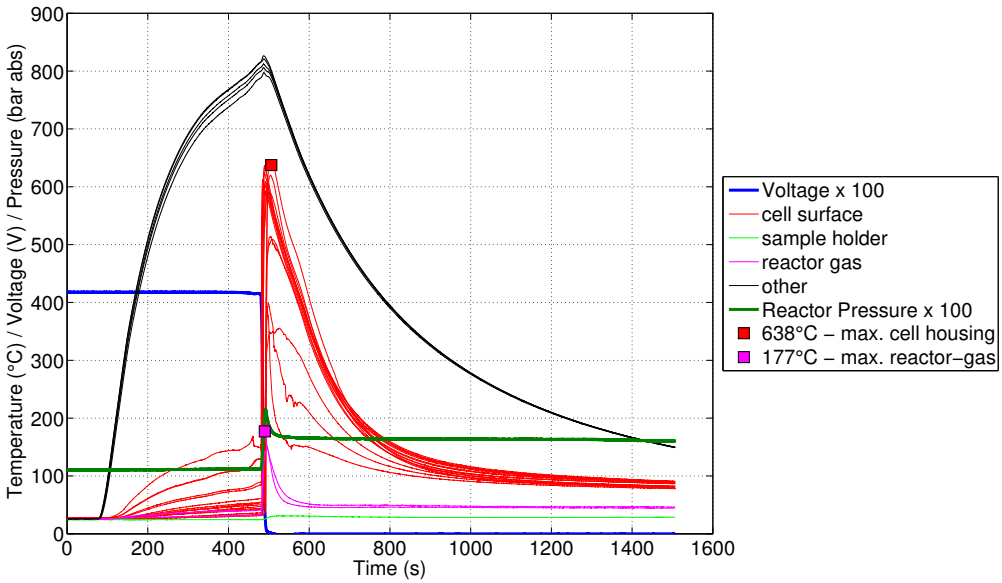

Figure 4.116: T0180. All sensors values. Whole experiment duration. *Other* are temperature sensors inside the heat conductor.

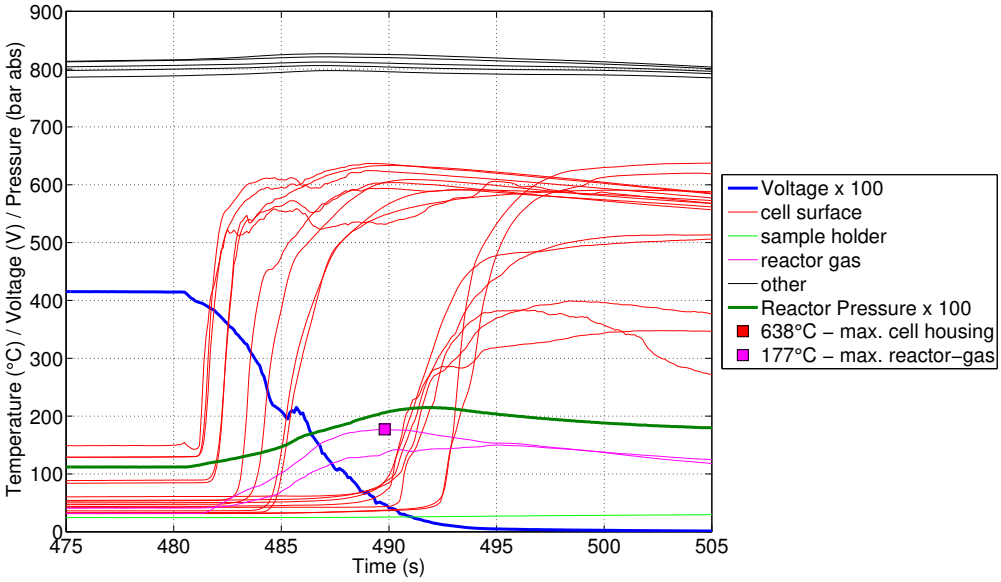

Figure 4.117: T0180. All sensors values. Time span of the TR. *Other* are temperature sensors inside the heat conductor.

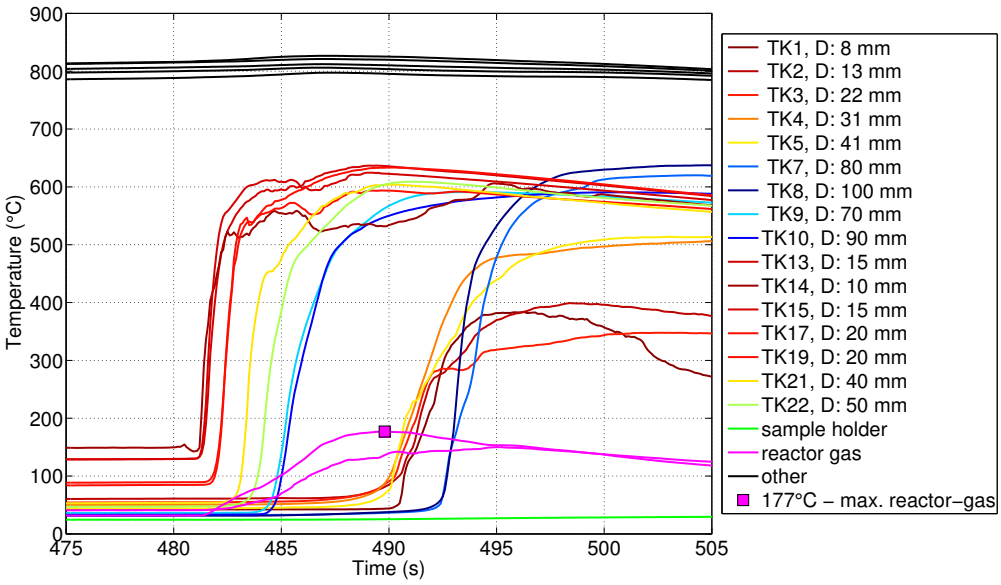

Figure 4.118: T0180. All temperature values. Colour-coding according to distance from hot-spot. Time span of the TR. The two cell surface sensor groups are distinguishable: temperatures on the top size rise first, temperatures on bottom side follow with a 5 s-delay. *Other* are temperature sensors inside the heat conductor.

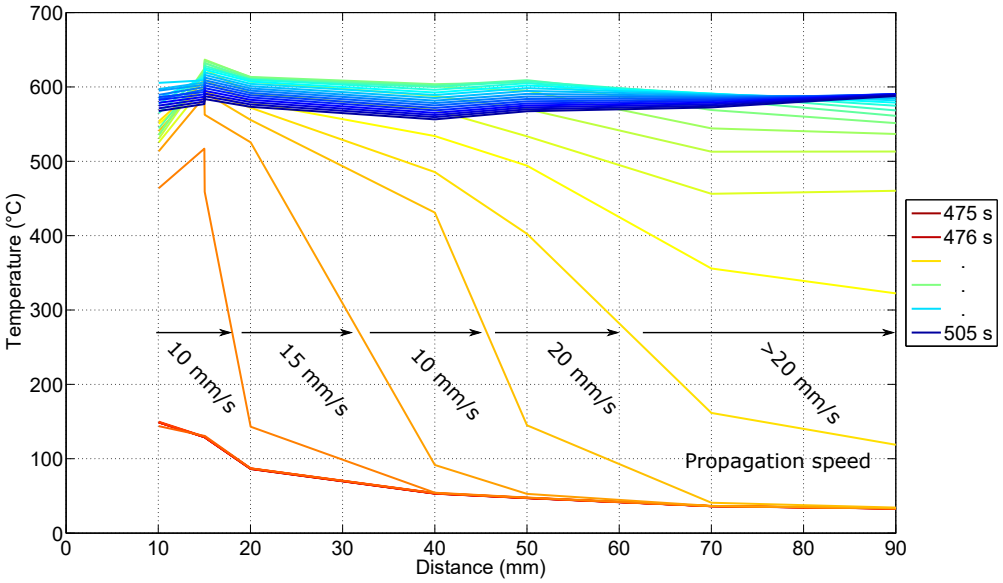

Figure 4.119: T0180. Rainbow plot showing the temperatures on the top side. Time span of the TR. The propagation speed along the top side is annotated.

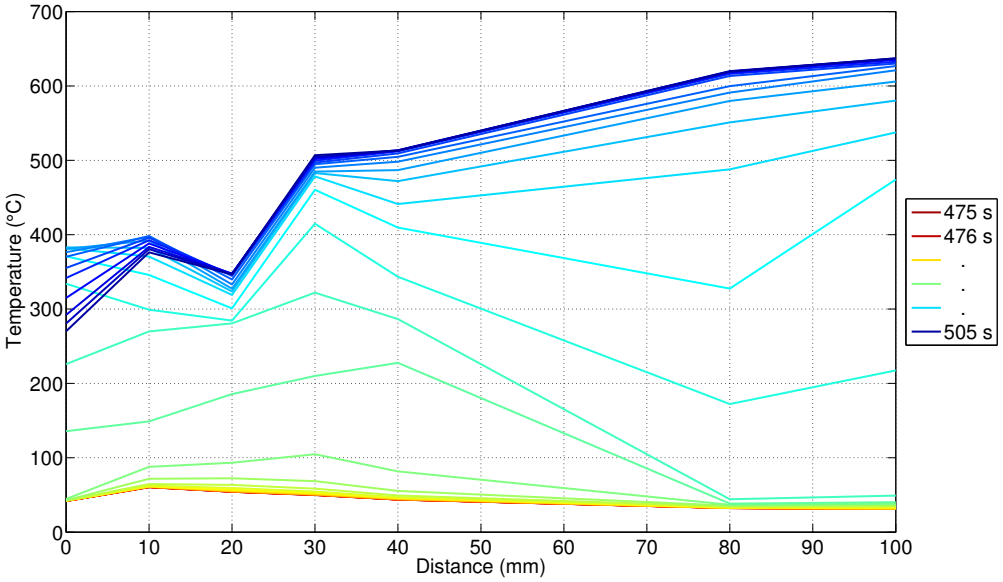

Figure 4.120: T0180. Rainbow plot showing the temperatures on the bottom side. Time span of the TR.

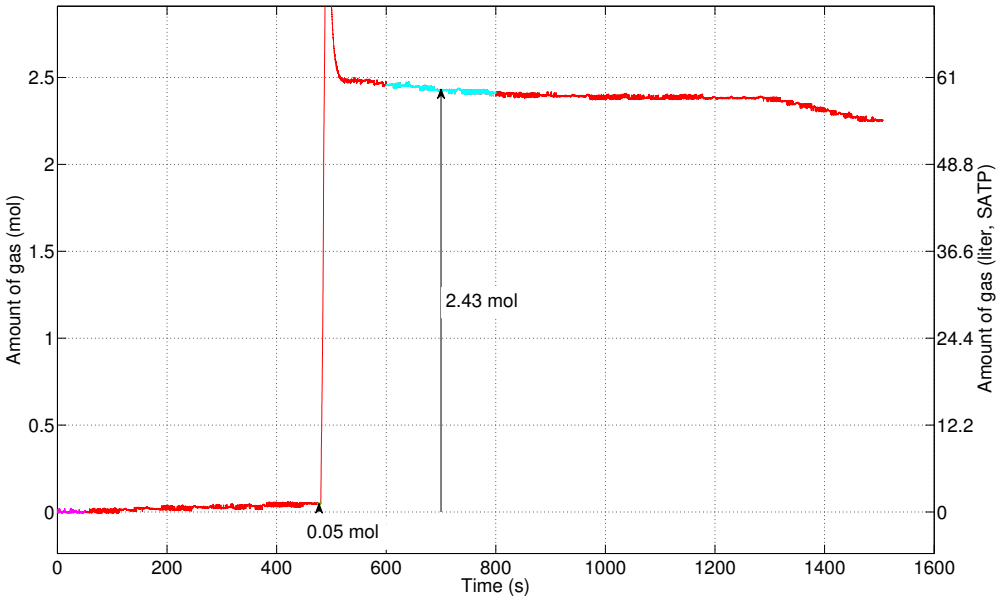

Figure 4.121: T0180. Gas release by the cell.

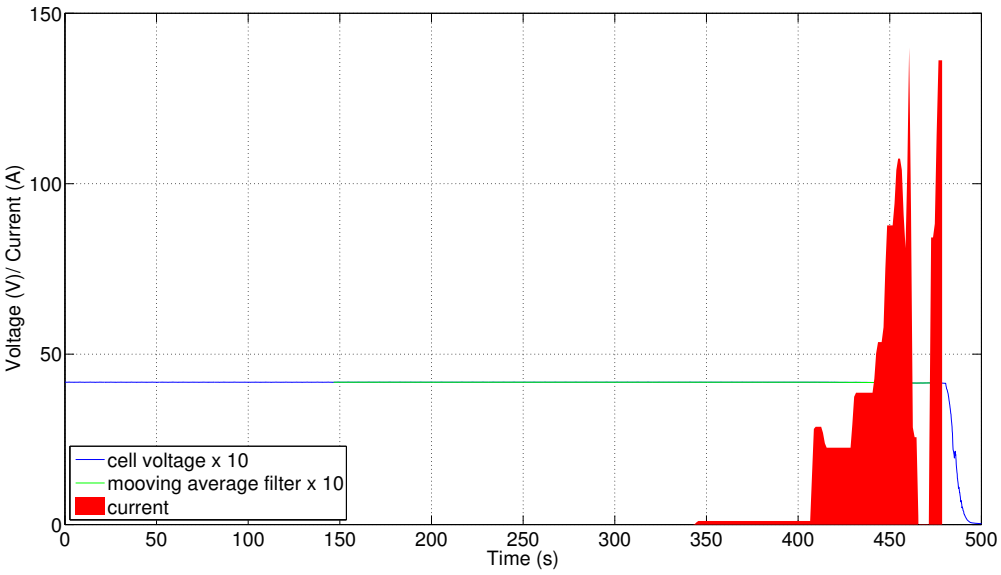

Figure 4.122: T0180. Voltage and self discharge/short circuit current of the cell.

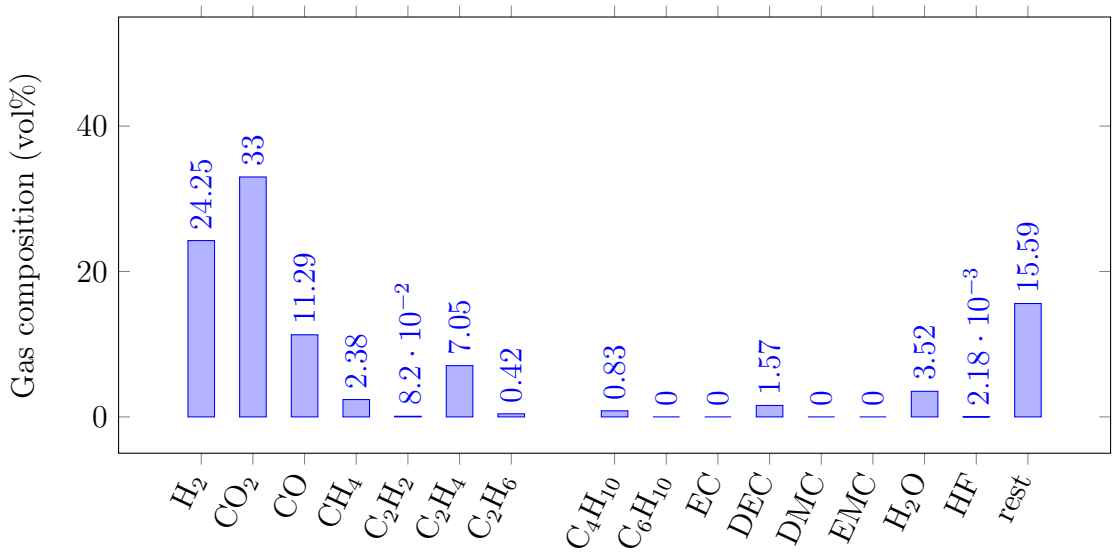

Figure 4.123: Experiment T0180. Detected gas components which were released by the cell. Gas composition was measured by FTIR and GC.

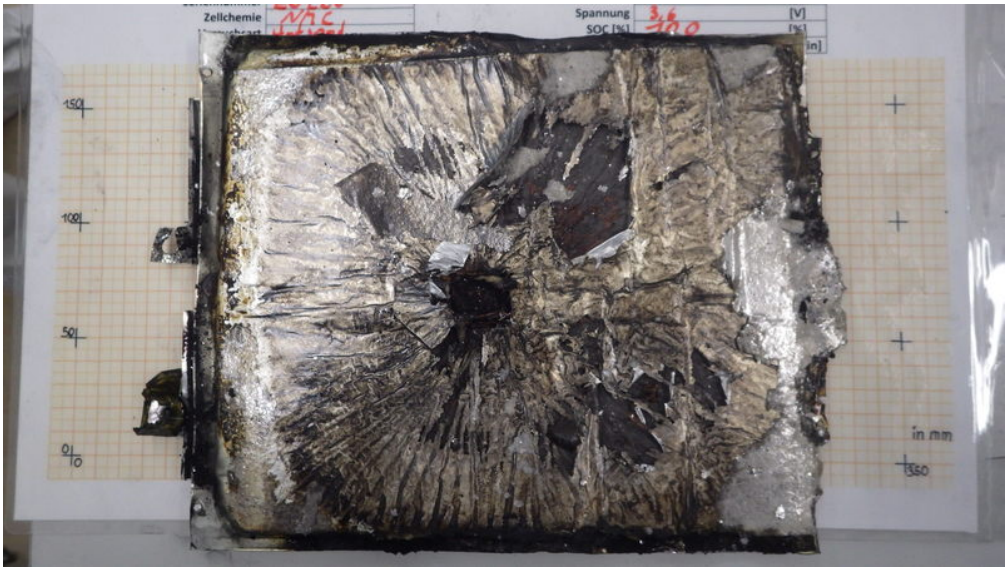

Figure 4.124: T0180. Cell after the TR experiment.

Experiment T0181

This experiment was a repetition of the previous experiment T0180. Same test-setup was used. Cell was cut open at the edges as in T0180 prior to the start of experiment (fig. 4.125). The thermocouple setup was the same as in T0180 (fig. 4.114). The TR could again be achieved in short time (396 s). The results were reproducible compared to T0180.

222 s Centre heater set to 100% power.
500 s Voltage starts to decrease with $0.2\,\mathrm{mV\,s^{-1}}$.
616 s Voltage starts to decrease with $600\,\mathrm{mV\,s^{-1}}$. Pressure starts to increase. Begin of rapid TR.
617 s Readings of the most adjacent cell temperature sensor (TK11, TK14) reach 167 °C to 189 °C and start to increase sharply followed by the other sensors on the upper side of the cell.
621 s The TR has propagated through the upper side of the cell.
624 s The TR has propagated through the cell layers from top to bottom and arrives at the centre of the bottom layer. Peak of the gas pressure.
626 s The TR has propagated through the whole cell. Voltage at 4 mV.

Discussion: In this final experiment the overall behaviour of the cell during TR was similar to T0180. Same effects could be observed. The TR started on the upper side of the cell at the heated area. The TR propagated along the upper side (fig. 4.130) and through the layers to the bottom side (fig. 4.131). Again only a comparable small temperature increase on the lower side of the cell beneath the heat conductor was observed.
The cell resistance was measured by applying ±1 A pulses. From start to immediately before TR the cell had the nominal resistance of $R_i = 1\,\mathrm{m\Omega}$. The self discharge/short circuit current was calculated with the with *Delta SOC method* (section 4.4.1). The cell started to self-discharge at 510 s with 20 A. The I_{ISC} increased up to 80 A 10 s before the TR (fig. 4.133).
The cell released 0.06 mol before the TR and additional 2.25 mol of gas during the TR with an rate of $0.4\,\mathrm{mol\,s^{-1}}$ ($8.8\,\mathrm{l_{SATP}/s}$) (fig. 4.132). The vent-gas composition was measured with GC and FTIR (fig. 4.134).

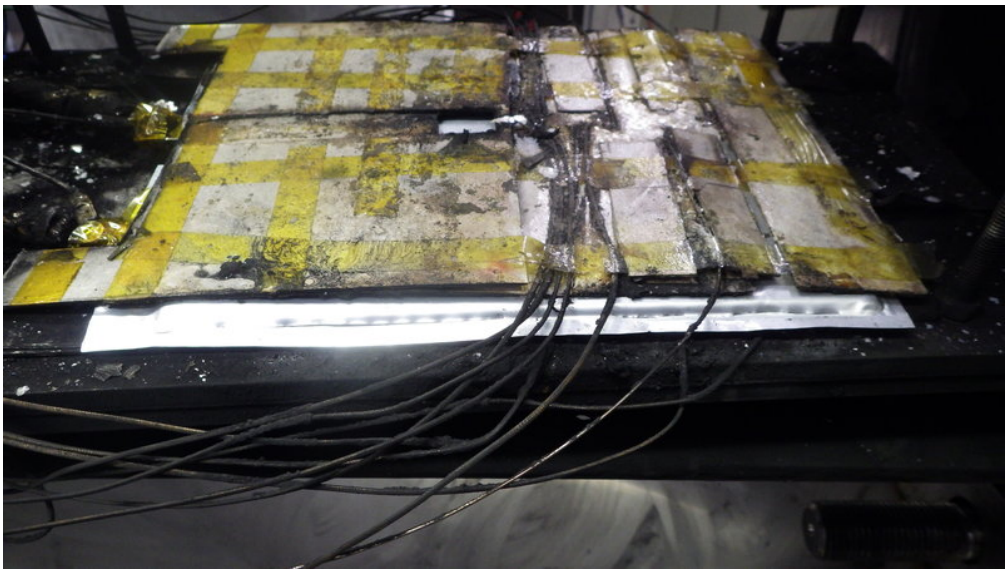

Figure 4.125: T0181. Cell before the TR experiment. Note the cut of the cell case. During TR the cell released the majority of the vent-gas through the cut. The mica sheet and temperature sensors on top of the cell were reused from experiment T0180.

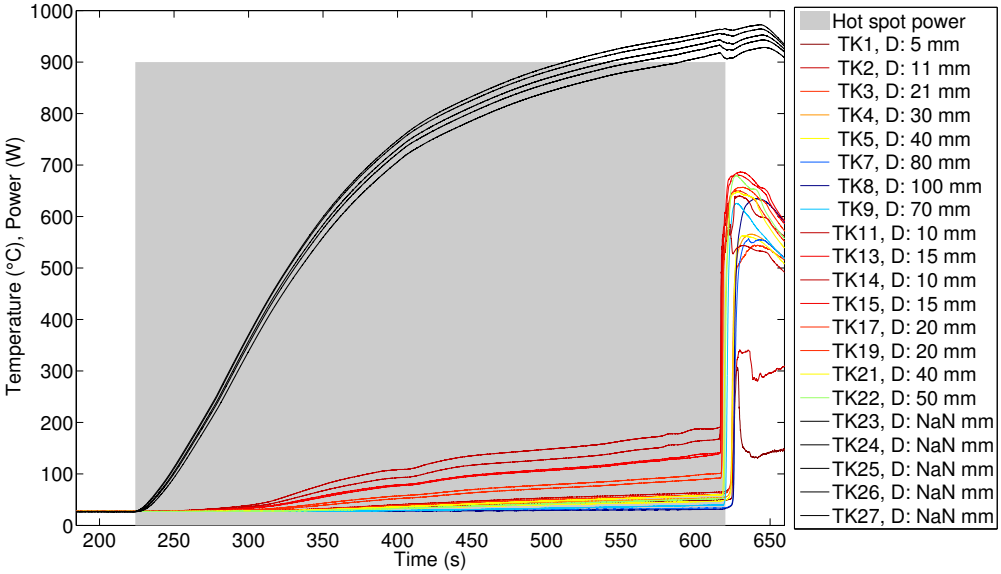

Figure 4.126: T0181. Power of the heater element and temperatures on the cell surface at different distances to the hot spot. Temperatures are colour-coded according to the distance from the hot spot. *Other* are temperature sensors inside the heat conductor.

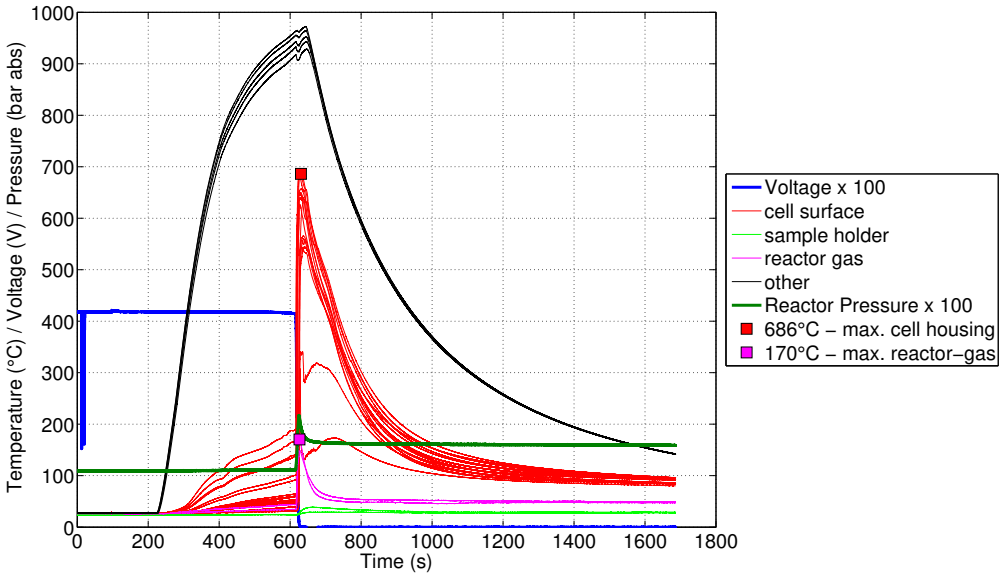

Figure 4.127: T0181. All sensors values. Whole experiment duration. *Other* is temperature sensors inside the heat conductor.

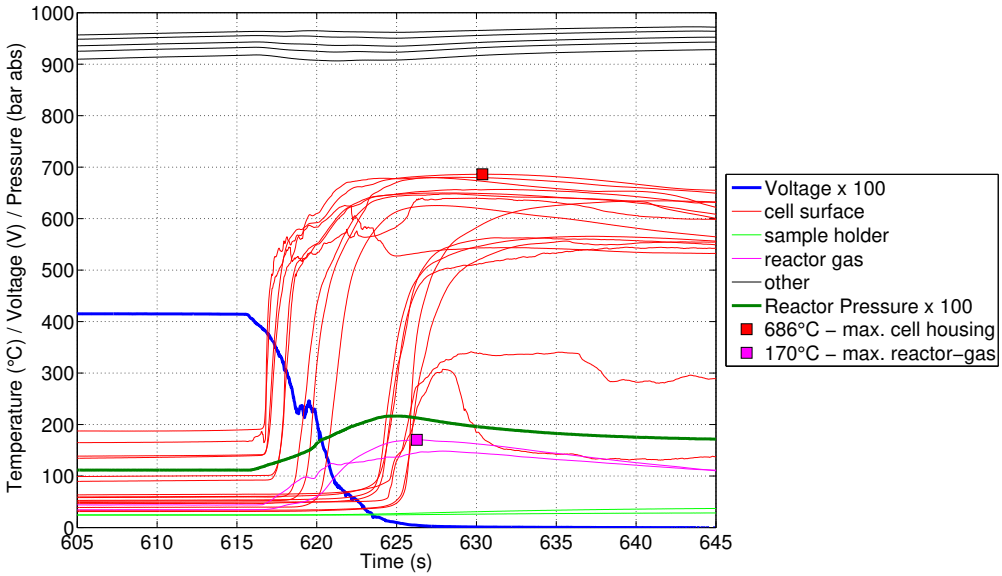

Figure 4.128: T0181. All sensors values. Time span of the TR. *Other* are temperature sensors inside the heat conductor.

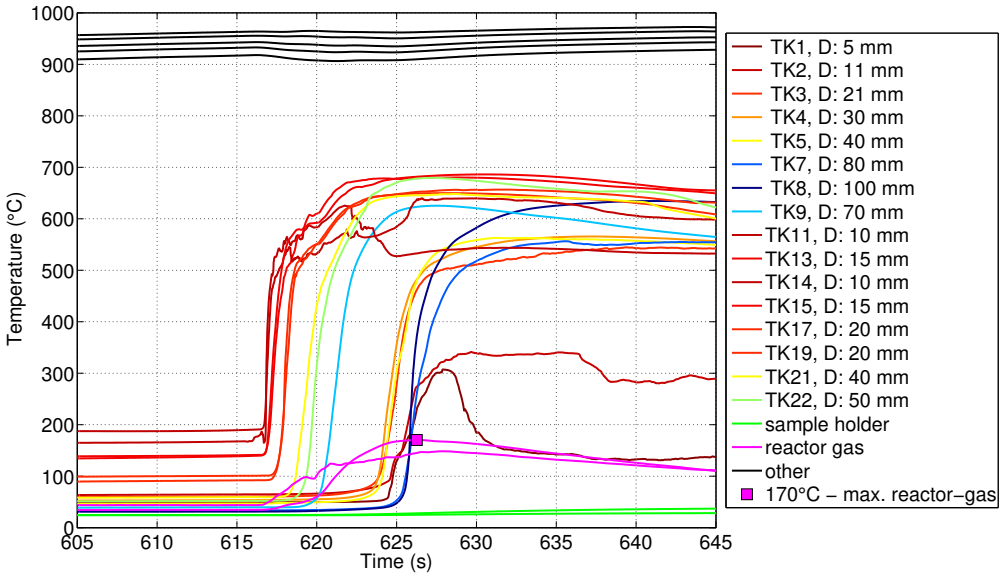

Figure 4.129: T0181. All temperature values. Colour-coding according to distance from hot-spot. Time span of the TR. The two cell surface sensor groups are distinguishable: temperatures on the top size rise first, temperatures on bottom side follow with a 4 s-delay. *Other* are temperature sensors inside the heat conductor.

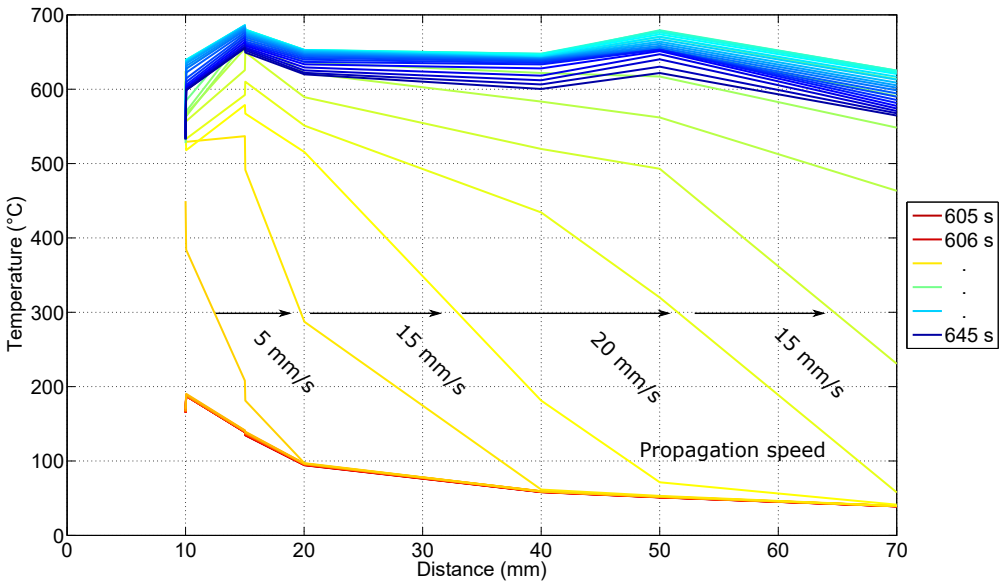

Figure 4.130: T0181. Rainbow plot showing the temperatures on the top side. Time span of the TR. The propagation speed along the top side is annotated.

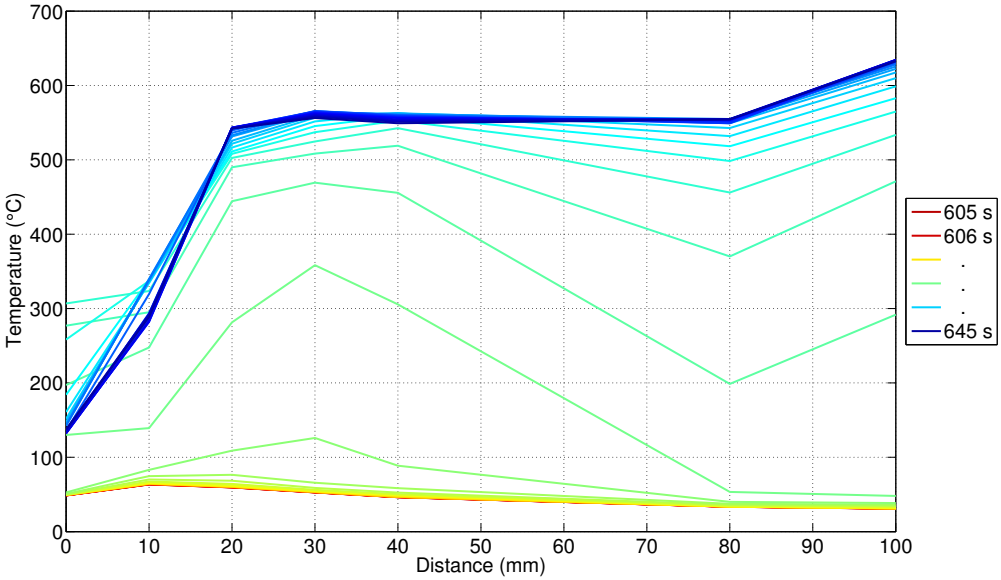

Figure 4.131: T0181. Rainbow plot showing the temperatures on the bottom side. Time span of the TR.

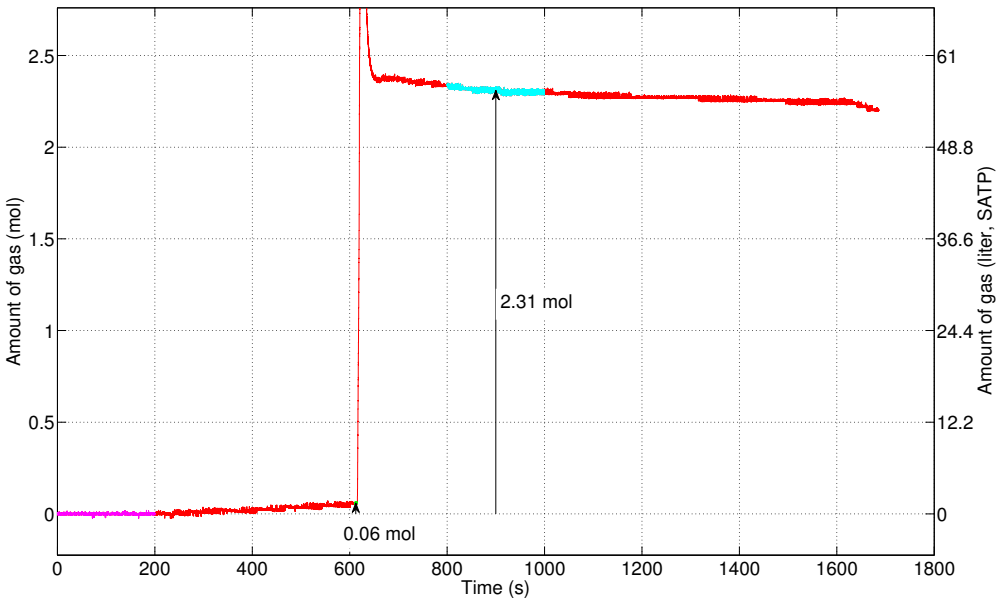

Figure 4.132: T0181. Gas release by the cell.

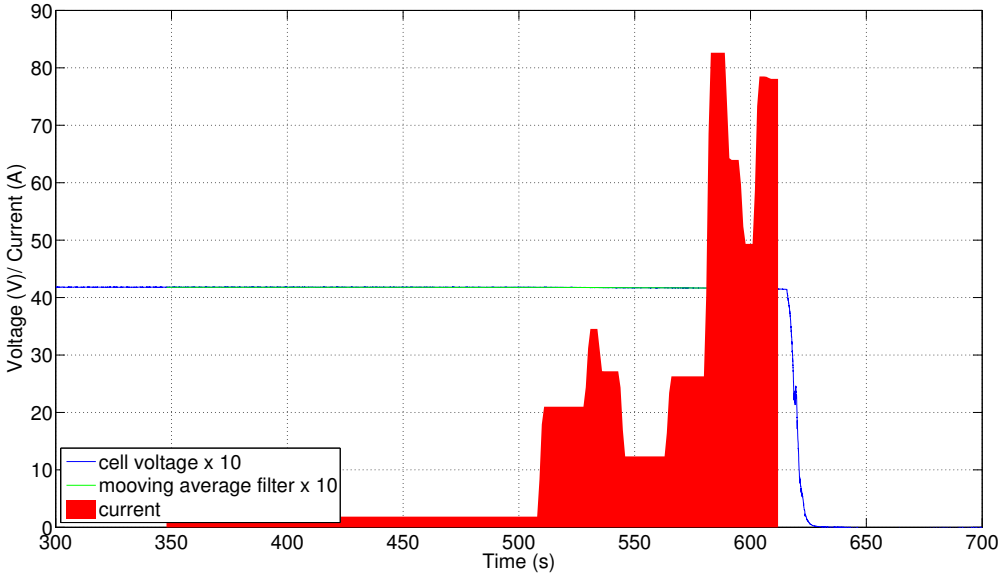

Figure 4.133: T0181. Voltage and the internal short circuit current I_{ISC} of the cell.

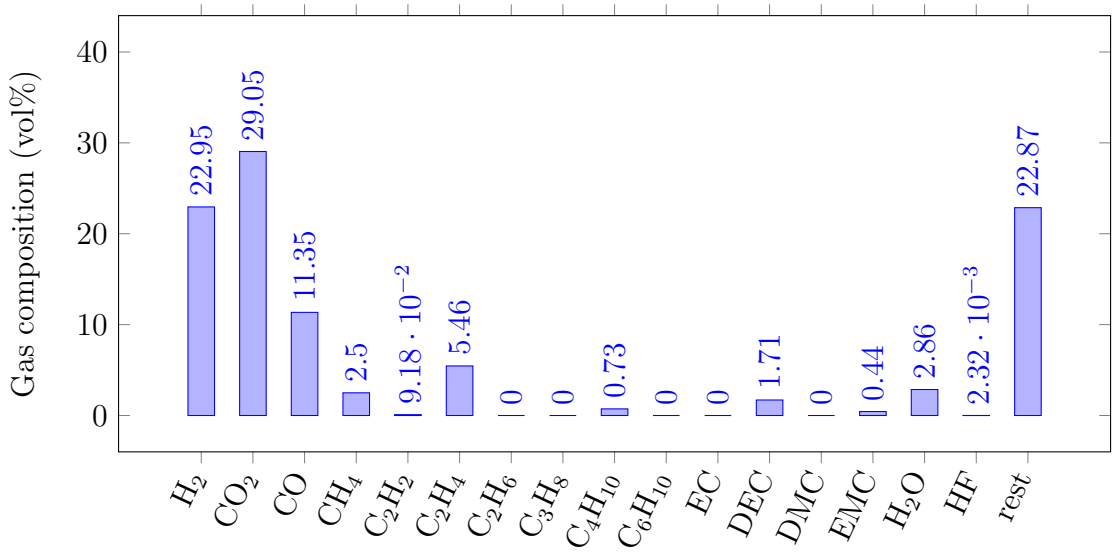

Figure 4.134: Experiment T0181. Detected gas components which were released by the cell. Gas composition was measured by FTIR and GC.

Figure 4.135: T0181. Cell after the TR experiment. Note the remaining material directly below the heat conductor. A pillar with a heights of 1 mm to 2 mm remains at the area which was directly below the heat conductor.

4.6 Discussion

4.6.1 TR propagation speed

A typical failure mode of a Li-Ion cell is a three step process: (1) an internal short circuit creates a hot-spot inside the cell (2) the hot spot starts a localized TR (3) the TR propagates through the cell until all cell material is consumed (fig. 4.136). In the experiments, step (1) was simulated by the external heater but steps (2) and (3) were the same as in a real world scenario. The results of the experiments give approximate speeds for in-plane ($c_{\parallel} = 13.8\,\mathrm{mm\,s^{-1}}$) and out-of-plane ($c_{\perp} = 0.84\,\mathrm{mm\,s^{-1}}$) propagation of the TR-front (table 4.4). The spatial speed of the TR determines the speed of consumption of a battery pack. A faster consumption speed generates higher heat release rate and higher gas release rate. The electrode stack through which the TR propagates has anisotropic heat conductivities: the in-plane conductivity ($\lambda_{\parallel} = 25.6\,\mathrm{W\,m^{-1}\,K^{-1}}$) is higher than the out-of-plane heat conductivity ($\lambda_{\perp} = 0.77\,\mathrm{W\,m^{-1}\,K^{-1}}$). The λ values of the cells used in here were provided by Aiello *et al.* [121]. The λ-anisotropy causes a faster in-plane propagation and a slower out-of-plane propagation of the TR.
The ratios of the measured λ and c (for averages of the hot-spot experiments) are of the same order of magnitude:

$$\frac{\lambda_{\parallel}}{\lambda_{\perp}} = 33.2$$

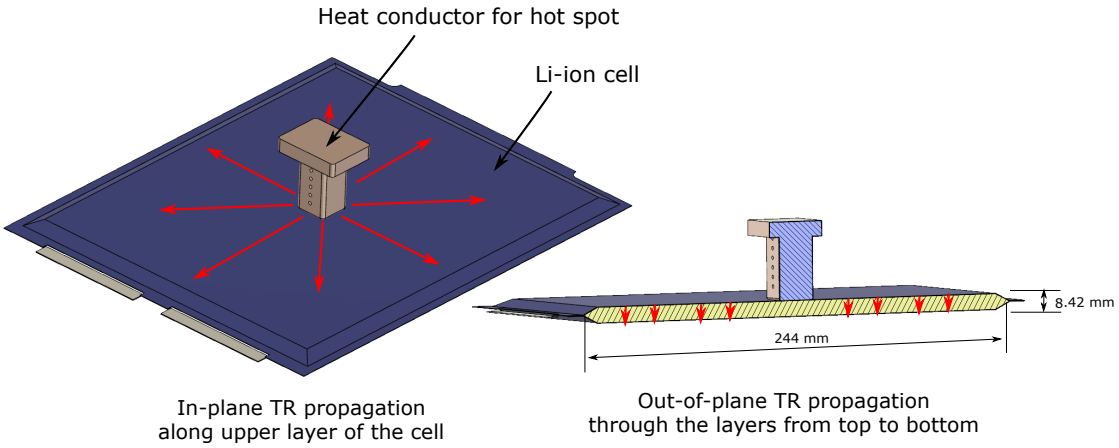

Figure 4.136: (left) TR-front propagating in-plane starting at the hot spot followed by (right) TR-front propagating out-of-plane through the layers of the electrodes from the top layer to the bottom layer of the cell.

$$\frac{c_{\parallel}}{c_{\perp}} = 16.4$$

The $c_{\perp}$ is in good agreement with measured propagation speed by Archibald *et al.* [120] because comparable cell type was used. The c differs to results from Finegan *et al.* [119], because of their different casing type (cylindrical hard case, with one burst plate on top, high gas flow inside the cell).

The out-of-plane propagation speed shows a slight dependency on the average temperature of the cell. The speed is higher in a preheated stack, because less heat is needed to start the reaction at the front (fig. 4.137).

Table 4.4: In plane ($\parallel$) and out-of-plane ($\perp$) TR propagation speed. T_{avg} is the average cell temperature immediately before the TR.

Experiment/Source	Type	T_{avg} (°C)	$c_\perp$ (mm s^{-1})	$c_\parallel$ (mm s^{-1})
T0179	temperature ramp, one side heated	220	1.40	–
T0177	hot-spot	124	0.94	15
T0178	hot-spot	98	0.70	12
T0180	hot-spot	67	0.80	13
T0181	hot-spot	83	0.90	15
Average	hot-spot		0.84	13.8
Values from literature				
Archibald *et al.* [120]	overheat pouch module	25	0.78-0.8	–
Finegan *et al.* [119]	nail-penetration, cylindrical cell	25	6 - 8	200 - 400

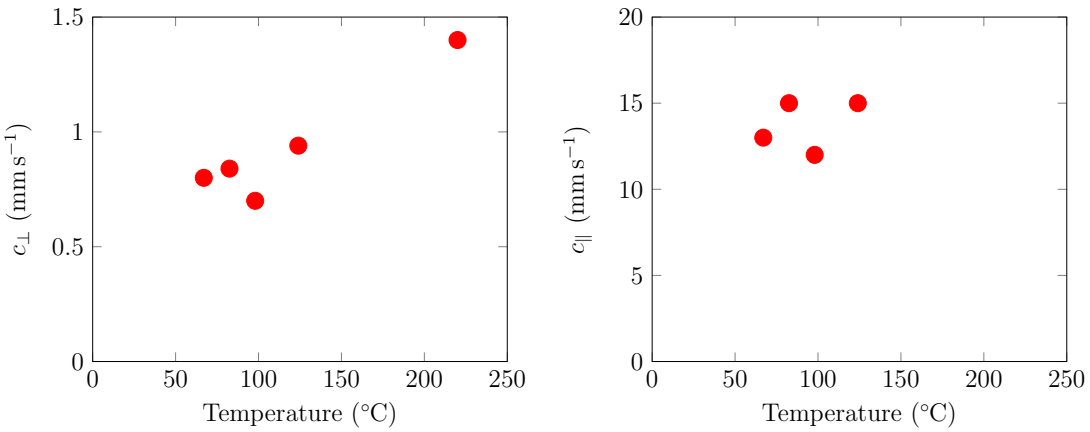

Figure 4.137: Speed of TR front vs. average cell temperature immediately before the TR.

4.6.2 Required conditions to start a TR with local heating

This section summarizes the findings on how to trigger a TR with a hot-spot. The hot-spot experiments covered a wide range of heating power and heating duration and hot-spot set-ups as shown in table 4.5.

A hot spot located in the *centre of the cell* could only trigger a TR when sufficient heating power ($P_h > 561\,\mathrm{W}$) and/or sufficient heating duration ($t_h > 175\mathrm{s}$) resulted is a hot-spot temperature of T_h above 639 °C. A plot of required heating power and temperature at the hot spot is shown in fig. 4.139. With some effort (using high power, high temperature heater with 900 W and capable of withstand up to 1000 °C, and with insulating the heat conductor to prevent heat losses) a TR could be reproducibly started in 400 s as shown in the final two experiments T0180 and T0181.

In those experiments the ceramic heater increased the temperature of the heat conductor from room temperature to 812 °C - 937 °C in only 400 s. Those high temperatures then triggered a TR which originated at the direct vicinity of the heat-conductor to Li-ion cell interface. The TR-front then propagated through the upper layer and then from the upper layer to the bottom layer, as described in the previous section.

In experiments with long heating times and lower heat flow into the cell (T0160, T0161, T0177) the heat created an inert zone with radius r_i centred at the hot spot. In those cases the TR started only after prolonged heating at the perimeter

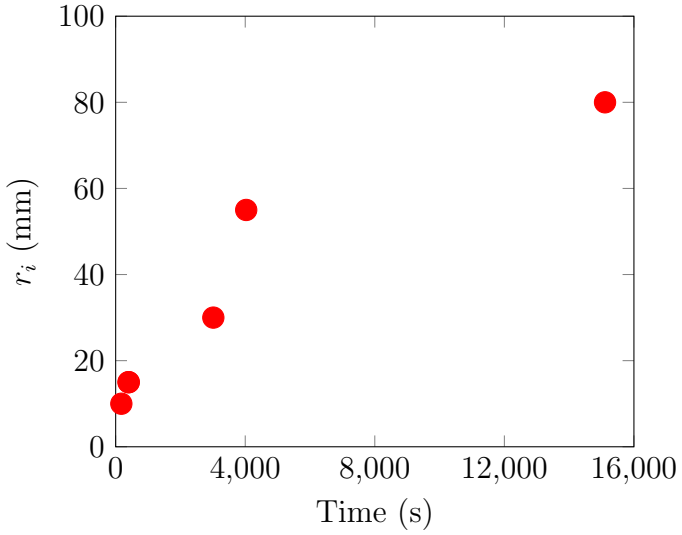

Figure 4.138: Size of the inert zone immediately before the TR compared to the necessary heating time.

of the inert zone. The TR-front then propagated from the perimeter to the outside edges of the upper layer and subsequently from the upper layer to the bottom layer. Correlation of required heating time and the final size of the inert zone are shown in fig. 4.138.

In experiments with low heating power (T146a, T147a) or insufficient heating time (T0179a, T0179b) a TR could not be started. Instead, the heater created a soft short-circuit which slowly discharged the cells.

In the experiments T0149 and T0151 the heater was attached directly to the cell tab. In the first tab-heating experiment T0149 the heater was attached to the positive tab and the TR started after short time (186 s) with a P_h of 448 W. Such low heating power would not start a TR if it was applied with a centre heater. The low power heater could start a TR on the edge of the cell because the heat could not spread as efficient as from the centre of the cell. In T0151 the results from T0149 could not be reproduced. A TR could not be started, maybe because of a failed heat interface between the ceramic heater and the negative tab or because of incomplete charge of the cell.

Unfortunately no literature exists on deliberate hot-spot heating causing a TR, therefore a comparison to published results is not possible.

Table 4.5: Hot-spot test conditions and results. Here SOC is the state of charge at the start of experiment, P_h is the electrical power of the hot spot heater (or/and the bottom heater with 1000 W), t_h is the duration of heating until the TR starts (or until the experiment is terminated, when a TR could not be started), T_h is the temperature inside the hot-spot device immediately before the TR starts (or its maximum temperature if TR does not start), V_0 is the cell voltage at the start of the experiment and V_{TR} immediately before the TR, SOC immediately before the TR calculated (from U_{OCV}/SOC curve using V_{TR}), r_i is the radius of the inert zone immediately before the TR, T_{max} is the maximal recorded cell surface temperature during the experiment. Experiments where TR happened are highlighted.

Experiment	V_0 V	SOC %	Heater setup	P_h W	t_h s	T_h °C	TR	V_{TR} V	SOC_{TR} %	r_i mm	T_{max} °C
T0146a	4.17	100	μ-heater	50	1525	305	no	—	—	—	84
T0147a	4.17	100	μ-heater	183	11 500	538	no	—	—	—	140
T0149	4.17	100	pos. tab	448	186	432	yes	4.17	99.4	30	658
T0151	4.17	100	neg. tab	567	20 000	751	no	—	—	—	199
T0160	4.18	100	medium heater	561	4030	763	yes	4.09	93	55	675
T0161	4.15	100	med. + bottom heat.	407 + 1000	15 108	639	yes	3.96	73.1	80	576
T0177	4.18	100	medium heater	900	3015	797	yes	3.97	74.4	30	593
T0178	4.18	100	med. heat. insulated	900	175	677	yes	4.18	100	10	664
T0179a	4.18	100	med. heat. insulated	900	195	497	no	—	—	—	114
T0179b	4.17	100	med. heat. insulated	820	140	620	no	—	—	—	90
T0179	4.16	100	bottom heater	0 + 1000	—	—	yes	3.85	59.7	—	561
T0180	4.18	100	med. heat. insulated	900	405	812	yes	4.18	100	15	638
T0181	4.18	100	med. heat. insulated	900	396	937	yes	4.18	100	15	686

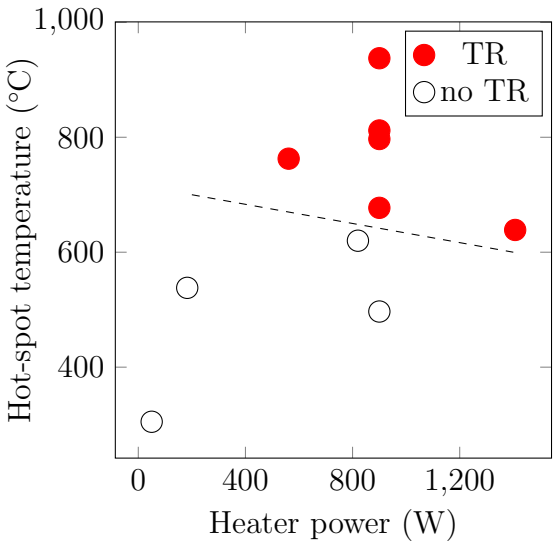

Figure 4.139: Local conditions required to start a TR in the centre of the cell. (Not including tab-heater experiments T0149 and T0151.)

4.6.3 Gas release by locally and uniformly started TR

A Li-ion cell releases different amounts of gas with different compositions in the course of an over-temperature experiment. When a TR is triggered by a overtemperature (hot-spot or uniform heating), then the gas release of the cell is divided into release before the full TR (n_{v1}) and gas release during the main TR reaction (n_{v2}). The overall released amount of gas throughout the experiment is $n_v = n_{v1} + n_{v2}$. In some experiments the composition of n_{v1} could be measured, because the the cell was not brought into TR and n_{v1} was not followed by release of n_{v2}. The source of n_{v1} depends on type of heating. In experiments where the cell was uniformly heated (one side or both side heating) low temperature reactions released n_{v1}. In hot-spot experiments medium temperature reactions released n_{v1}. When a TR could be started, then high temperature reactions released additional n_{v2}. The collected gas compositions are fingerprints of chemical reactions that take place at the different temperatures (fig. 4.140):

Low temperature gas release 25 °C to 300 °C: In one experiment (T0141) a cell at 30 % was uniformly heated up to 309 °C. It released a small amount of gas

(0.53 mol), with the main component CO_2, H_2O and electrolyte vapour. Such gas emissions are produced by electrolyte decomposition and evaporation. The cell did not went into TR.

Medium temperature gas release 300 °C to 500 °C: During hot spot experiments the hot-spot creates a localized over temperature by direct heat input or by creating a short circuit before the full TR starts. In one experiment (T0151) the negative tab was heated up to 752 °C while the nearest cell surface sensor reached 199 °C. Inbetween the sensor position and the tab cell material reached medium temperatures between those two values. The cell released 0.7 mol with the components similar to those in low temperature gas release, but with higher amounts of H_2 and CO.

Local over-temperature causes chemical reactions of the cathode and anode material in the vicinity of the hot spot as well as electrolyte evaporation and decomposition. Thus, the reactions are locally restricted, and the local cell temperatures stay below the temperatures that occur later in the actual TR. In other words, those reactions are spatially restricted *medium-temperature decomposition reactions*, whereas the reactions during the TR are spatially unrestricted *high-temperature decomposition reactions*. The medium-temperature reactions are responsible for the creation of the inert zone which is described in section 4.6.2.

High temperature gas release >500 °C may eventually occur, when the cell enters full TR. Here the gas is produced by high-temperature reactions which consume the whole cell (except for the inert zone). The gas composition shifts further to higher concentrations of H_2 and CO. The amount of released gas by the high temperature reactions is defined as n_{v2}. During TR significant amounts of n_{v2} are released in short time (e.g. 2.38 mol for experiment T0180). The gas-release rate $\dot{n}_{v2}$ is proportional to the speed with which the TR reaction consumes the cell.

An overview of released amounts of gas is shown in table 4.6 and in fig. 4.142. The gas composition of n_v is shown in table 4.7. The collected data from hot-spot experiments shows the following trends of gas release:

1. The amount of gas produced by the *medium-temperature* decomposition

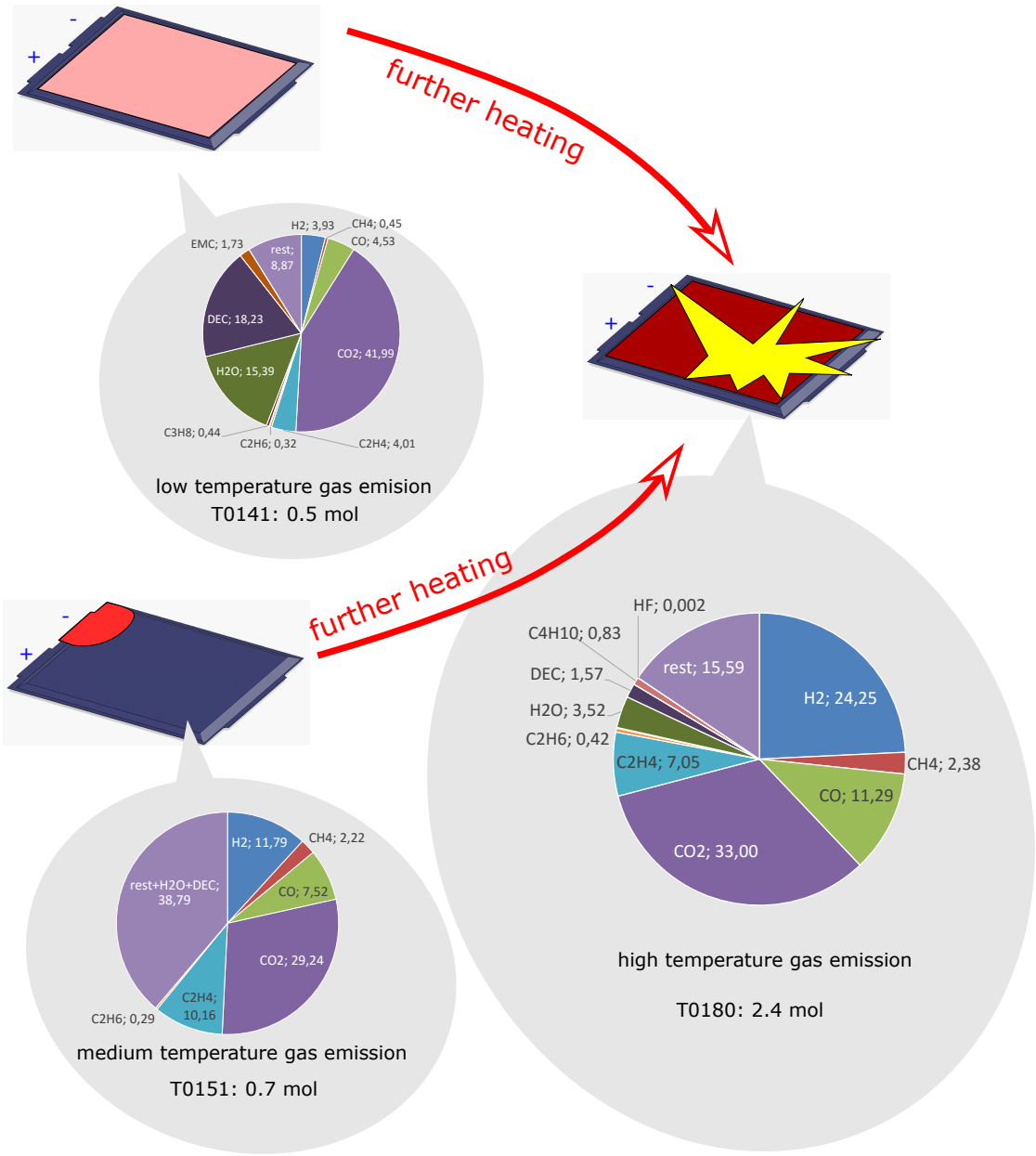

Figure 4.140: Gas compositions (mol%) released at different stages of TR.

reactions n_{v1} increases with the injected heat by the central heater. Here heat is the product of heating time and electrical heater power. The graph fig. 4.141 shows this correlation.

2. When TR happens, and when only the hot-spot heater is used to heat the cell, then the cell releases an average of $n_v = 2.38(9)$ mol gas.
3. The released gas has high concentration of H_2, CO_2 and CO. In later experiments small amounts (<50 ppm) of HF were detected.

It is not yet clear why small amounts of HF were detected in some experiments but not in others. Quantifying the amount of HF is difficult because of its low concentration, and because it may react with the particles which were ejected by the cells and with the surfaces inside the reactor and in the stainless steel pipes, as the gas is transported from the reactor to the FTIR [129].

In case of TR the overall gas release n_v shows no significant dependence on the triggering type. Both – hot-spots and uniform heating – cause release of mainly H_2, CO_2 and CO. The amount of n_v was 2.38(9) mol for hot-spot triggered cells and 2.1(2) mol for uniform heated cells. The characteristic gas release rate of $\dot{n}_{v2}$ was 0.4(1) mol s^{-1} for hot-spot triggered cells and 0.8(1) mol s^{-1} for uniform heated cells. Uniform heated cells release the gas faster, because the preheating of the cells causes higher propagation speed of the TR throughout the whole cell.

Table 4.6: Gas release in overtemperature experiments. Test conditions are the same as in table 4.5. Here n_{v1} is the gas release before TR, n_{v2} is the gas release during TR and n_v is the overall released gas. Experiments where TR happened are highlighted.

Experiment	SOC %	Heater setup	P_h W	t_h s	T_h °C	TR	n_{v1} mol	n_{v2} mol	n_v mol	$\dot{n}_{v2}$ mol s^{-1}
T0139	0	top + bottom heater	—	—	—	no	0.41	—	0.41	—
T0141	30	top + bottom heater	—	—	—	no	0.53	—	0.53	—
T0131	100	top + bottom heater	—	—	—	yes	0.12	1.92	2.04	0.9
T0133	100	top + bottom heater	—	—	—	yes	0.14	2.17	2.31	0.8
T0140	100	top + bottom heater	—	—	—	yes	0.25	1.68	1.92	0.6
T0146a	100	μ-heater	50	1525	305	no	0.02	—	0.02	—
T0146	0	bottom heater	0 + 1000	—	—	no	0.44	—	0.44	—
T0147a	100	μ-heater	183	11 500	538	no	0.26	—	0.26	—
T0147	0	bottom heater	0 + 1000	—	—	no	0.81	—	0.81	—
T0149	100	pos. tab	448	186	432	yes	0.02	2.38	2.39	0.3
T0151	100	neg. tab	567	20 000	751	no	0.7	—	0.7	—
T0160	100	medium heater	561	4030	763	yes	0.33	2.39	2.72	0.5
T0161	100	med. + bottom heat.	407 + 1000	15 108	639	yes	1.03	1.77	2.8	0.5
T0177	100	medium heater	900	3015	797	yes	0.3	2.06	2.36	0.4
T0178	100	med. heat. insulated	900	175	677	yes	0.02	2.26	2.28	0.4
T0179a	100	med. heat. insulated	900	195	497	no	0.02	—	0.02	—
T0179b	100	med. heat. insulated	820	140	620	no	0.03	—	0.03	—
T0179	100	bottom heater	0 + 1000	—	—	yes	0.25	1.41	1.66	0.5
T0180	100	med. heat. insulated	900	405	812	yes	0.05	2.38	2.43	0.3
T0181	100	med. heat. insulated	900	396	937	yes	0.06	2.25	2.31	0.4

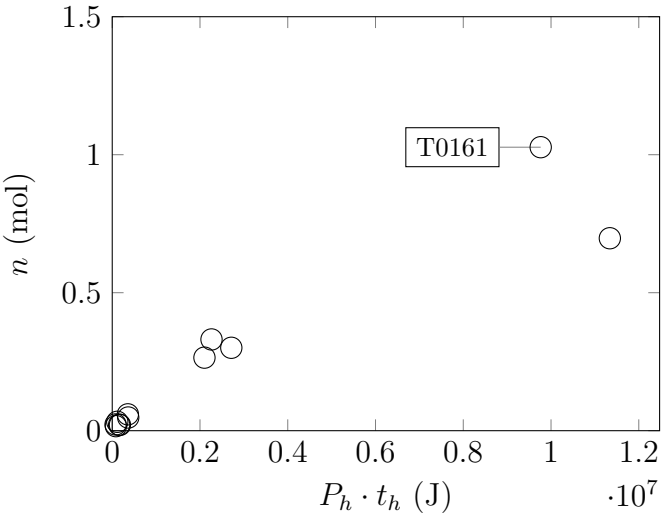

Figure 4.141: Data from hot-spot experiments. Comparing the first n_{v1} to the injected heat by the hot-spot heater $P_h \cdot t_h$. In experiment T0161 the additional heating with the flat heater caused a larger amount of n_{v1}.

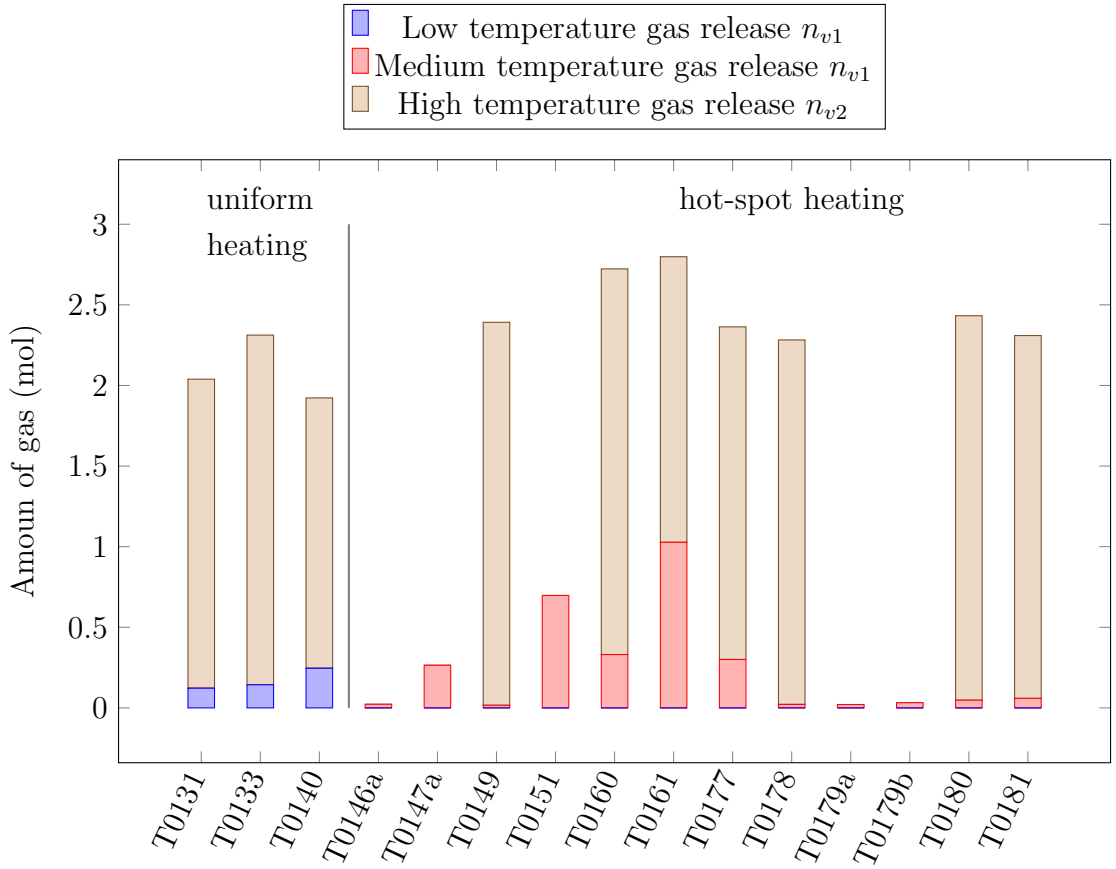

Figure 4.142: Amount of released gas in overtemperature experiments with cells at 100% SOC. First three experiments: uniform heating, both sides. Remaining experiments: hot-spot heater.

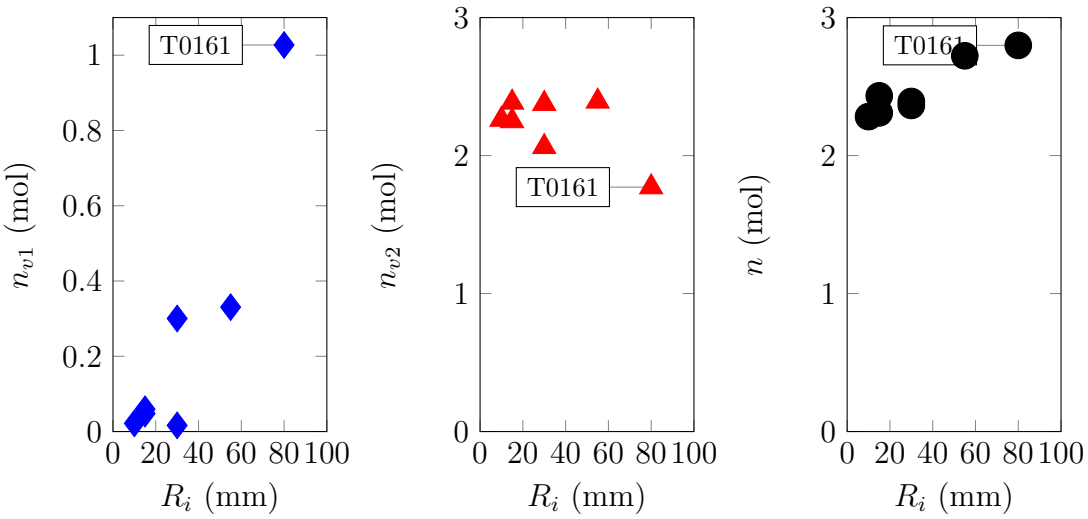

Figure 4.143: Data from experiments, where a TR could be triggered by a hot-spot. Comparing the first n_{v1} and second n_{v2} venting as well as the overall amount of released gas $n_v = n_{v1} + n_{v2}$ to the size of the inert zone r_i. In experiment T0161 the additional heating with the flat heater caused a larger amount of n_{v1}.

Table 4.7: Measured gas composition of the ventgas after the TR (or at the and of heating period, when no TR occurred). The gas composition is given in vol%. Experiments where TR happened are highlighted. A — means that the value was not measured (because the FTIR was not available in this cases).

Exp.	Heater setup	SOC	n_v	H_2	CO_2	CO	CH_4	H_2O	C_2H_2	C_2H_4	C_2H_6	C_4H_{10}	DEC	EMC	HF	rest
		%	mol							mol%						
T0139	top + bottom heater	0	0.41	0.9	52.9	1.9	0.2	—	0	4.5	0.2	—	—	—	—	—
T0141	top + bottom heater	30	0.53	3.9	42	4.5	0.5	15.4	0.1	4	0.3	0	18.2	1.7	0	8.9
T0131	top + bottom heater	100	2.04	22.3	46.4	14.1	3.2	9.7	0.1	6	1.2	1.3	3.2	1.3	0	0
T0133	top + bottom heater	100	2.31	22.9	40.7	16.6	3.5	7.6	0.1	7.9	1	1.3	2.7	0	0	0
T0140	top + bottom heater	100	1.92	20.5	36.2	11	2.6	—	0.04	2.8	0.6	—	—	—	—	—
T0147	bottom heater	0	0.81	2.8	40.7	3.3	1.2	14.7	0	2.8	0.1	0	7.2	2.6	0	24.1
T0149	pos. tab	100	2.39	23.9	31.8	10.5	2.1	2.8	0.1	6.6	0.5	1	1.9	0.5	0	18.3
T0151	neg. tab	100	0.7	11.8	29.2	7.5	2.2	—	0	10.2	0.3	—	—	—	—	38.8
T0160	medium heater	100	2.72	27	35.8	13.6	3.2	3.3	0.1	5.4	0.6	1.3	2.9	0.7	0	6.2
T0161	med. + bottom heat.	100	2.8	13.1	29.5	6.2	2.5	—	0	6.7	0.7	—	—	—	—	41.4
T0177	medium heater	100	2.36	23.5	33	10.8	3	7	0.1	6.5	0.6	1	3.6	1	0	9.9
T0178	med. heat. insulated	100	2.28	24.8	33.6	10.6	2.4	3.4	0.1	7	0.5	0.9	1.6	0.4	0.005	14.9
T0179b	med. heat. insulated	100	0.03	4.7	3.9	2.3	3.4	10.6	0	0.9	0	0.2	0.2	0	0	73.6
T0179	bottom heater	100	1.66	19.2	33.7	9.6	2.5	9.8	0.1	2.9	0.6	1.2	3.7	1.4	0.004	15.3
T0180	med. heat. insulated	100	2.43	24.2	33	11.3	2.4	3.5	0.1	7.1	0.4	0.8	1.6	0	0.002	15.6
T0181	med. heat. insulated	100	2.31	23	29.1	11.3	2.5	2.9	0.1	5.5	0	0.7	1.7	0.4	0.002	22.9

4.6.4 Internal Short Circuit

Definition and theory

Even if the temperature of local overheating is insufficient to start a TR, it can still be sufficient to create an ISC. The short circuit current can not be measured directly, but can be calculated from the voltage response of U_T as detailed in section 4.4.1: it causes self discharge of the cell resulting in observable voltage decrease.

A high-power/high-temperature hot-spot may generate, local evaporation of electrolyte, melting and possibly shrinking of the separator, chemical reactions in the anode and cathode, melting of the current collector foils, displacement of the layers if force is applied and of course it may cause a ISC. To facilitate the discussion of the measured ISC some simplifications must be made: (1) it is presumed that the thicknesses of the layers do not change and that the layers are not mechanically damaged by the hot-spot and (2) the ISC is presumed to be an electron-conductive connection between the anode and cathode coating and (3) it is presumed that the conducting area is spatially restricted to the area below the hot-spot heater. Other – less restricted – types of ISC are listed in [127].

With the above presumptions a simple electrical model which represents the ISC can be created (fig. 4.144). In this model the undamaged part of the cell acts as a voltage source with an internal resistance R_i. When an ISC occurs, the current loop is closed by the R_{ISC} and a current I_{ISC} starts to flow and the cell starts to self-discharge.

The resistance of the ISC is governed by the geometry of the ISC and by the electrical conductivity of the damaged separator and by the resistance of the cathode and anode coating (fig. 4.144) as well as the internal resistance of the cell R_i. The short circuit current depends on the cell voltage U_T, damaged area A_{ISC}, number of damaged separator layers n_{ISC} as well as the thicknesses d_j and electronic conductivities κ_j of the damaged layers.

The thicknesses of the layers in the electrode stack of the cell used in SafeBattery were published by Kovachev *et al.* [101]. The electrical conductivities are taken from literature. Only few publications could be found which report specific electrical conductivity of cathode layers κ_{cat} in Li-ion batteries. The reported values range

from $0.06\,\mathrm{S\,m^{-1}}$ to $27\,\mathrm{S\,m^{-1}}$ (table 4.8). Anode conductivities are much higher due to conductive nature of graphite and $\sigma_{and} = 0.05\,\Omega\,\mathrm{cm}$ ($\kappa_{and} = 20\,000\,\mathrm{S\,m^{-1}}$) is assumed [130]. The purpose of the separator is to electrically isolate anode and cathode, therefore a $\kappa = 0$ is assumed for a pristine cell.

It is further assumed that, when the separator is damaged by the hot spot, it will become conductive and its conductivity will increase above zero to some value X which is yet to be calculated for each experiment $\kappa^{\dagger}_{sep} = X$. The number of damaged separator layers n_{ISC} and the damaged are in a layer A_{ISC} is estimated for each experiment individually.

With the κ_j and the thickness d_j of the individual layers (anode, cathode, separator) (table 4.9) and with known n_{ISC} and A_{ISC}, the resistances of the ISC are given by:

$$R_{cat} = \frac{d_{cat}}{n_{ISC}\,A_{ISC}\,\kappa_{cat}}\,, \tag{4.5}$$

$$R_{sep} = \frac{d_{sep}}{n_{ISC}\,A_{ISC}\,\kappa_{sep}}\,, \tag{4.6}$$

$$R_{and} = \frac{d_{and}}{n_{ISC}\,A_{ISC}\,\kappa_{and}} \tag{4.7}$$

The internal short circuit current I_{ISC} can be derived from the electric circuit in fig. 4.144 with

$$I_{ISC} = \frac{U_{OCV}}{R_i + R_{cat} + R_{sep} + R_{and}}\,. \tag{4.8}$$

Under normal conditions the separator is not electrically conductive, $\kappa_{sep} = 0$ and $R_{sep} = \infty$ resulting in a zero current $I_{ISC} = 0$. In a damaged cell the separator becomes conductive ($\kappa^{\dagger}_{sep} > 0$) allowing a non-zero current $I_{ISC} > 0$.

In our experiments the I_{ISC} was estimated from the change of U_T. The estimated I_{ISC} from experiments where TR occurred ranged from 13.7 A to 560 A (table 4.11). In a different setup Koch *et al.* [128] measured short circuit currents which are in the same order of magnitude ranging from 23 A to 207 A (calculated from R_{tr} and V_{cell} in [128]).

With given I_{ISC} the resistance and specific electric conductivity of the damaged separator can be calculated with eq. (4.8) and eq. (4.6). The calculation was done for all experiments, where an $I_{ISC} > 0$ was estimated. The results are summarized in table 4.10. Following conclusions are drawn from the calculation:

- The electrical resistances of the anode and cathode coating at the damaged area as well as the internal resistance of the cell are negligible compared to the resistance of the damaged separator: $R_{and} + R_{cat} + R_i \ll R^{\dagger}_{sep}$
- In case of TR the $R^{\dagger}_{sep}$ was lower than 57 mΩ
- In case of TR the electrical conductivity of the damaged separator $\kappa^{\dagger}_{sep}$ was in the range of 0.3 mS m^{-1} to 15.8 mS m^{-1}
- The measured resistances of the ISC were much higher than the internal resistance of the cell $R_{ISC} \gg R_i$. Therefore, it will be very difficult to detect the ISC by measuring the change of the overall impedance Z of the cell. Example calculation with data from experiment T0160:

$$Z^* = R_i = 0.0035\,\Omega\,, \tag{4.9}$$

$$Z^{\dagger} = \frac{R_i\, R_{ISC}}{R_i + R_{ISC}} = 0.0032\,\Omega\,, \tag{4.10}$$

$$Z^{\dagger}/Z^* = 0.91 \tag{4.11}$$

  Here ISC reduces the impedance of the cell by only 9%. Such a small impedance change is hard to distinguish in real world environment, because the impedance Z is also influenced by temperature, SOC and current flow through the cell and because the electric sensors used to calculate Z have limited accuracy and resolution.

Although the analysis of the ISC had the shortcoming by many assumptions and the rough calculation of I_{ISC} it is still valuable in giving a first estimation for $R^{\dagger}_{sep}$ during a short circuit. The analysis is a starting point to understand the I_{ISC} as it may well contribute to the TR as shown in the next section.

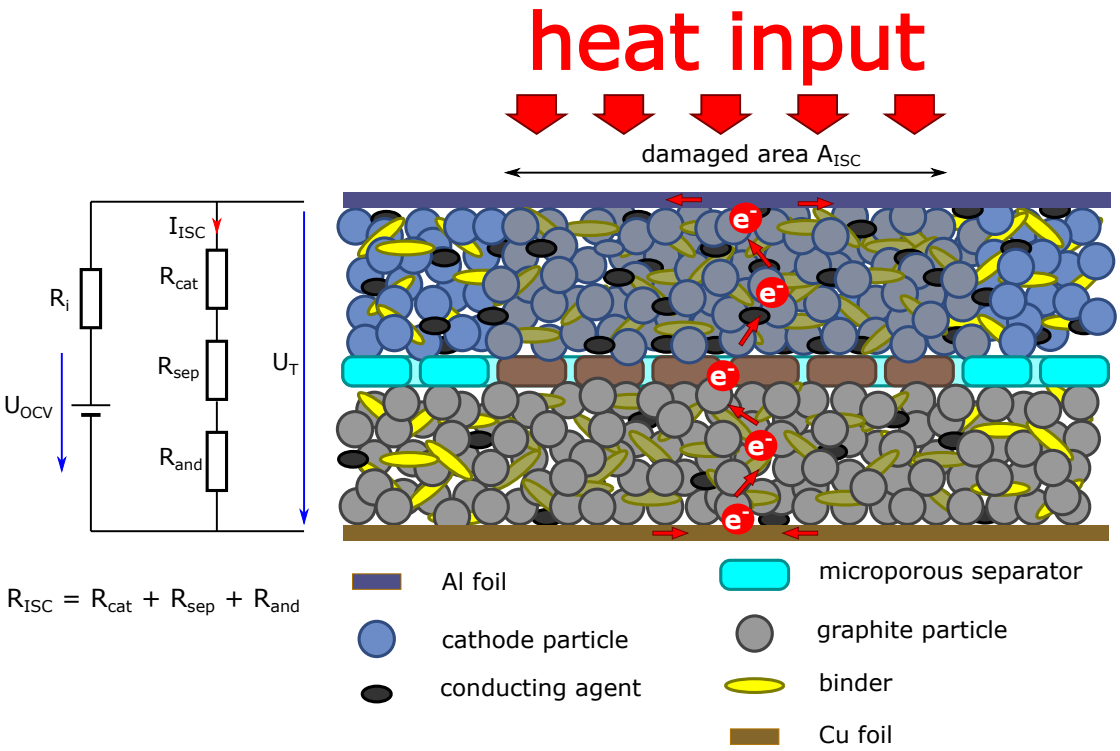

Figure 4.144: Cross section of an electrode stack (cathode, separator, anode) and an electrical model of the ISC. External heat damages the material in the hot-spot area. The damaged separator becomes electrically conductive for the electrons and a current driven by the cell voltage flows through the damaged area. The hot-spot area is not damaged mechanically.

Table 4.8: Published values for the electrical specific electrical conductivity of the cathode layers κ_{cat}. Here PVDF is polyvinylidene fluoride, LA132 is composed of polyacrylonitrile, VCF are chemical vapour deposit carbon fibres and CNTs are carbon nano tubes.

material	binder	conducting agent	κ_{cat} (S m^{-1})	source
$LiFePO_4$ (85 wt.%)	PVDF (5 wt.%)	graphite (10 wt.%)	6.4	[131]
$LiFePO_4$ (85 wt.%)	PVDF (5 wt.%)	carbon black (10 wt.%)	0.38	[131]
$LiFePO_4$ (85 wt.%)	PVDF (5 wt.%)	acetylene black (10 wt.%)	0.057	[131]
$LiCoO_2$ (94 wt.%)	LA132 (3 wt.%)	acetylene black (3 wt.%)	1.8	[132]
$LiCoO_2$ (94 wt.%)	LA132 (3 wt.%)	VCF (3 wt.%)	10	[132]
$LiCoO_2$ (94 wt.%)	LA132 (3 wt.%)	CNTs (3 wt.%)	27	[132]

Table 4.9: Thicknesses and assumed electrical conductivities of the undamaged cell layers

layer	thickness (µm)	κ (S m^{-1})
cathode	65	5
separator (undamaged)	20	0
anode	65	20000

Table 4.10: Electric parameters of the cells during the hot spot experiments. Here R_i is the cell resistance, R_{ISC} is the ISC resistance, A_{ISC} is the damaged area of one separator layer, n_{ISC} is the number of damaged separator layers, R_{cat} and R_{and} are the resistances of the cathode and anode in the short circuit path, $R^{\dagger}_{sep}$ is the resistance of the damaged separator in the short circuit path (eq. (4.8)), $\kappa^{\dagger}_{sep}$ is the calculated electrical conductivity of the damaged separator (eq. (4.6)). Experiments, where a TR occurred are highlighted.

Exper.	Heater setup	R_i mΩ	R_{ISC} Ω	A_{ISC} mm^2	n_{ISC}	R_{cat} µΩ	R_{and} µΩ	$R^{\dagger}_{sep}$ Ω	$\kappa^{\dagger}_{sep}$ mS m^{-1}
T0146a	μ-heater	—	1.02	400	5	65000	16	0.95	10.5
T0147a	μ-heater	—	1.34	400	5	65000	16	1.27	7.8
T0149	pos. tab	—	0.01	3000	42	100	0.026	0.01	15.8
T0151	neg. tab	2.5	8.15	3000	42	100	0.026	8.15	0.02
T0160	medium heater	3.5	0.04	2827	42	107	0.027	0.04	4.2
T0161	medium heater	800	0.57	2827	42	107	0.027	0.57	0.28
T0177	medium heater	—	0.02	2827	42	107	0.027	0.02	8.4
T0178	med. heat. insulated	1	0.3	2827	42	107	0.027	0.3	0.55
T0179b	med. heat. insulated	1	13.89	2827	42	107	0.027	13.89	0.014
T0180	med. heat. insulated	1.3	0.03	2827	42	107	0.027	0.03	5.6
T0181	med. heat. insulated	1	0.05	2827	42	107	0.027	0.05	3.4

Role of the internal short circuit

The measured I_{ISC} are shown in table 4.11. The experiments can be grouped into three categories depending on the test conditions and measured I_{ISC} and R_i:

(Group LH) Localized Heating, no TR: this are cases when the localized heating was not sufficient to start a TR. This was the case, when the heater power was to low (such as in T0146a and T0147a) or when the heating was interrupted before TR (such as in T0179a and T0179b). Here neither the heating nor the joule heat from the I_{ISC} could create a sustaining TR-front. In those cases moderate self discharge currents $\leq$4 A were measured. The cells showed heavy damage with several punctured layers and it was surprising, that the damage did not cause higher currents.

(Group LHT) Localized Heating, with TR: this are cases, where localized heating triggered a TR which consumed the whole cell. In those cases high I_{ISC} were calculated. Here both the heating and the joule heat from the I_{ISC} played a role in starting a local TR and in being a source of a sustaining thermal runaway front. The calculated I_{ISC} immediately before the TR varied between 13 A to 560 A. The local short circuit created heat dissipations which were in the same order of magnitude as the external heating with joule-heating powers up to 2 kW.

(Group WHT) Whole cell Heating, with TR: this are cases, where the whole surface of the cell was heated until full TR reaction. Here only small self-discharge was measured and internal short circuits were not observed. The heating damaged the electrolyte and separator *of the whole cell*, increasing the R_i of the cell by two to three magnitudes (from 1 mΩ to 5 mΩ at room temperature to 500 mΩ to 800 mΩ when heated above 180 °C) before the TR reaction. The high R_i prevented any significant current flow. In those cases the TR was caused solely by the external heat input.

Figure 4.145 compares the experiments where external heat was injected locally in the centre of the cell (by the setups μ-heater, tab-heater and medium heater). The graph visualises the contribution of the heat-release of the ISC and compares the heat release to the external heating. The comparison suggests that the heat release by the ISC should be taken into account when cells with local damage are

Table 4.11: Short circuit characteristics. Here R_i is the cell resistance, R_{ISC} is the resistance, I_{ISC} is the current and P_{ISC} the local heating power of the ISC, P_h is the power of the external heater, TR indicates if the cell went into thermal runaway, Group indicates into which group this experiment is categorized.

Experiment	Heater setup	R_i mΩ	R_{ISC} Ω	I_{ISC} A	P_{ISC} W	P_h W	Group
T0146a	μ-heater	—	1.02	4	16	50	LH
T0147a	μ-heater	—	1.34	3	12	183	LH
T0149	pos. tab	—	0.01	560	2333	448	LHT
T0151	neg. tab	2.5	8.15	0.5	2	567	LH
T0160	medium heater	3.5	0.04	100	409	561	LHT
T0161	med. + bottom heat.	800	0.57	7	28	407 + 1000	WHT
T0177	medium heater	—	0.02	250	992	900	LHT
T0178	med. heat. insulated	1	0.3	13.7	57	900	LHT
T0179a	med. heat. insulated	1	—	0	0	900	LH
T0179b	med. heat. insulated	1	13.89	0.3	1	820	LH
T0179	bottom heater	500	1.92	2	8	1000	WHT
T0180	med. heat. insulated	1.3	0.03	136	568	900	LHT
T0181	med. heat. insulated	1	0.05	80	334	900	LHT

simulated. Overall, the experiments show that *sufficient localized heating* can create significant short circuits with high local joule-heat release which contributes to the triggering of TR.

On the other hand, if the whole cell is heated, then the whole electrochemical system of the cell is damaged. The damaged system can not power high currents and ISC does not occur, even if the cell is heated until TR starts. For the tested cell in SafeBattery, uniform heating did not create an ISC. The experiment results suggest that the ISC need not be taken into account, if the whole cell is uniformly heated until TR.

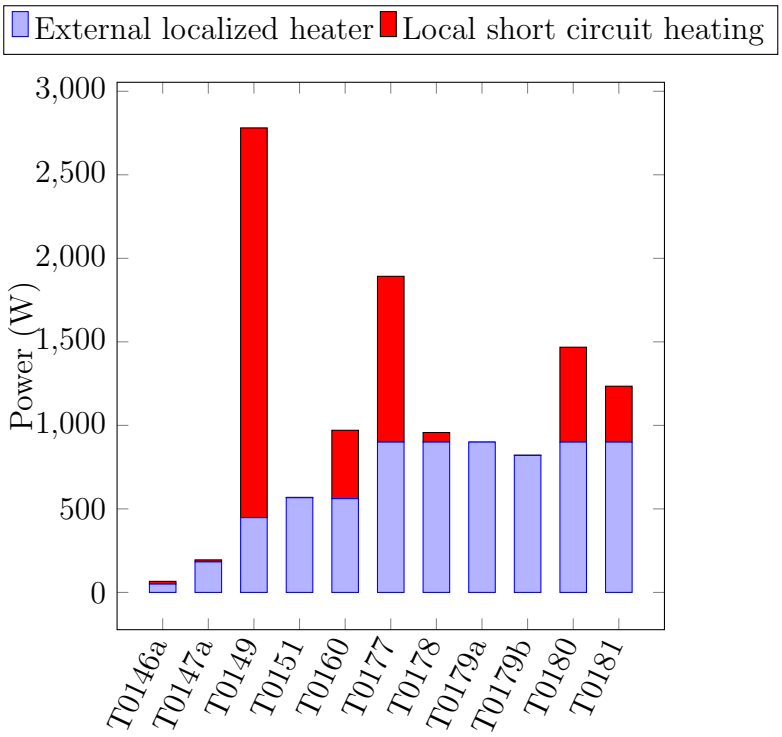

Figure 4.145: Experiments using the μ-heater, tab-heater and medium heater. Comparison of external heating and local power dissipation by the ISC.

5 Summary

This thesis describes thermal runaway (TR) tests of Li-ion batteries of different types and sizes meant for usage in mobile and automotive applications (electric cars). It includes development of test stands, experiment methods and analysis methods. The results of safety tests are presented and discussed with consideration of automotive applications.
The thesis consists of four publications and two reports. The first two papers deal with small cylindrical cells with capacities between 1.1 A h to 3.3 A h. The third and fourth papers cover a prismatic metal-can cell with a significantly larger capacity of 50 A h. The remaining two reports focus on a large pouch cell with 42 A h.

In the first publication (section 2.1) thee types of consumer Li-ion batteries with the format 18650 with different cathode materials were evaluated in TR tests. The cells were charged to 100% state of charge (SOC) and brought into TR by external heating. All tests were performed in a pressure-tight reactor in an argon atmosphere. In agreement with literature [133], the cell containing $LiFePO_4$ (LFP) showed the best safety characteristics. The LFP cell had the highest onset temperature (195 °C), the smallest temperature increase during the thermal runaway (210 °C), the lowest amount of produced gas (50 mmol) and the lowest percentage of toxic CO in the gas (4%). Unfortunately, it was also the cell with the lowest working voltage (3.3 V) and the lowest energy content (3.5 W h).
Batteries with higher energy content (5.5 W h to 9.6 W h) performed worse in safety tests. The onset temperature shifted down to 170 °C and 150 °C, the temperature increase during thermal runaway rose to 500 °C and 700 °C, the amount of gas released was 150 mmol and 270 mmol, and significant percentages of CO (13% and 28%) were found for the $Li(NiMnCo)O_2$ (NMC) and NMC/$LiCoO_2$ (LCO) cells,

respectively.
All cells released high amounts of H_2 and hydrocarbons. These gases are highly flammable. Even though the gas could not burn in the inert atmosphere inside the reactor, the surface of the high-energy cells reached temperatures of up to 850 °C during the experiments.

In the second publication (section 2.2) two types of 18650 cells, $Li(NiCoAl)O_2$ (NCA) and LFP, were charged to different SOC before being tested in over-temperature experiments. The main findings of this work were:

- The cell material and cell design (e.g. high energy density vs. high power density) have a high influence on the maximum cell temperature and on the released gases in TR conditions (table 5.1). Charged NCA cells showed a drastic TR behaviour. NCA cells could reach maximum temperatures of 1075 °C and they released up to 317 mmol of gas (equal to 7.1 L at standard conditions). Charged LFP cells exhibited a less pronounced TR: maximum cell temperatures as high as 448 °C were observed and the LFP cells released up to 61 mmol of gas.
- Discharged cells showed no TR upon heating up to 250 °C. Both cell types needed to be at least partially charged in order to go into TR.
- The severity of the TR increased with increasing SOC.
- The TR reactions produced high amounts of CO, H_2 and CO_2 thus making the gas flammable and potentially toxic. The gas composition depended on the cell type and SOC. NCA cells produced more CO and H_2 than LFP cells. Discharged cells generated mainly CO_2. Increased SOC led to increased amounts of CO and H_2.
- The SOC and the cell type had less effect on the onset temperature, as long as no Li plating occurred. Overcharge may cause metallic Li deposition on the anode which compromises the thermal stability. The onset temperature of overcharged cells decreased dramatically from 140 °C to values as low as 65 °C!
- In three experiments, the absolute amounts of gases from NCA cells were quantified. It is shown that it is theoretically possible to explain the absolute amounts of the measured gases with a set of chemical degradation reactions

Table 5.1: Comparison of the two tested cell types. Cell specifications and averaged experimental results.

		LFP	NCA
Voltage (50% SOC)	V	3.32	3.68
Nominal Capacity	A h	1.1	3.35
Cell mass	g	38.87	45.40
Max continuous discharge	A	30	6.7
Cycle life		>1000	>300
Minimal SOC for a pronounced thermal runaway	%	50	25
Onset temperature θ_o (100% SOC)	°C	140	139
Maximal temperature θ_m (100% SOC)	°C	440	911
Produced gas n_{sum}^{ideal} (100% SOC)	mmol	32	277
Detected CO_2 (100% SOC)	%	48.3	20.0
Detected CO (100% SOC)	%	9.1	44.8
Detected H_2 (100% SOC)	%	29.4	25.7
Impact of overcharge		weak	strong

and with known amounts of initial material in the cell.

- It is proposed that the main reactions in charged cells are combustion of carbonous material and Li oxidation. Both are strong exothermic reactions which contribute to the energy release during the TR of a Li-ion battery. The amounts of O_2 and Li available to degradation reactions depend on the SOC as well as on the amount and type of active cathode and anode material. Higher SOC increases the O_2 release of the cathode and the amount of intercalated Li in the anode. In over-charged cells these amounts increase further and deposition of highly reactive metallic Li may occur on the anode.
- It is proposed that both, the cathode and anode side participate in the reaction system. Therefore, experiments with only one electrode may not cover the full picture.

The third paper (section 2.3) compared the safety of different automotive battery-technologies (lead acid, nickel metal hydride (Ni-MH) and Li-ion batteries). The TR of lead acid batteries is driven by high charging current/voltage at high temper-

atures. It is easily detectable with temperature or gas sensors and can be mitigated by reducing the electric load. Ni-MH batteries show very good safety records. No literature on possible TR reactions of Ni-MH batteries could be found.
The TR of Li-ion cells is initiated by over-temperature or overcharge. Their main TR reaction can be quite dramatic and can easily end with a battery fire. The severity of the Li-ion TR reaction is proportional to the amount of electrochemical energy inside the cell. Cells with higher energy density reach higher maximal temperatures and release more vent-gas. Charged cells can go into TR but discharged cells show no TR reaction. In Li-ion battery packs special care must be taken to prevent hot-spots, foreign object intrusion, dendrites inside the cells and overcharge. Thermal barriers between the cells may be used to prevent TR propagation from cell to cell. Battery packs need proper gas venting (exhaust) systems so that in case of failure harmful gases are directed to the outside of the vehicle.

The fourth publication (section 2.4) describes an experiment series of eleven over-temperature experiments that were performed with large prismatic metal-can Li-ion cells which were charged to 100% SOC. The cells had a $LiMn_2O_4$ (LMO) cathode and graphite anode and a capacity of 50 A h. This was not the newest technology; they were produced in 2009. The experiments were done inside a large custom build gas-tight heatable reactor in nitrogen atmosphere. Four different heating methods were used: temperature ramp with heating of both cell sides, temperature ramp with heating of one side, stepwise heating and heating of the whole reactor.
With increasing temperature, the cells experienced a sequence of events eventually finalizing in an exothermic TR reaction. An important finding was that sometimes the sequence of events was interrupted by an unforeseeable internal short circuit (ISC). When it occurred, the cell skipped the remaining events and took a direct route into final exothermic reaction. It is suspected that the short circuits were caused by internal mechanical failures which damaged the electrical insulation inside the heated cells.
For cells with complex internal construction such as the tested metal-case cells it is important to repeat several test runs in order to capture the worst case outcome. The variability may be less an issue for cells with simpler construction such as pouch-type cells.

The characteristics of the final reaction were: the final TR started when the hottest point of the cell exceeded 206 °C, during TR the cell casing reached a maximum temperature up to 594 °C and the cell released an overall amount of up to 5.9 mol of vent-gas with up to 530 °C. When the vent-gas cooled down to room temperature then part of it condensed and the remaining gas phase shrunk to a value between 2.9 mol to 4.6 mol.
Further findings were:

- The final TR reactions are triggered by either increasingly exothermic chemical reactions (classified into group A2) or by joule heat from ISCs (classified into group B1 or B2).
- Most cells belonged to group A2. They showed a preceding minor venting event (opening of burst plate and overpressure release from the cell) and - after further heating - a gradual onset of exothermic reactions and TR with a second major venting.
- In three experiments (group B1) ISCs occurred. The shorts triggered the final TR reaction and gas release before the first minor venting would normally happen.
- In one experiment (group B2) an ISC triggered the thermal runaway after the first minor venting and further heating by the sample holder.
- For the tested cell type it is difficult to anticipate an imminent ISC of a cell, because it can happen at temperatures as low as 155 °C and without previous venting, cell voltage drop or accelerating temperature increase of the cell casing.
- The cells released significant amounts of gas during TR: up to $n_v = 5.95\,\mathrm{mol}$
- The gas release rate showed large variation from experiment to experiment, therefore several test were required for a reliable result. Up to $1.39\,\mathrm{mol\,s^{-1}}$ were measured.
- From the measured gas release rate a venting port with a diameter of at least 19.1 mm was estimated.
- The cell temperature measurements can be used to develop dynamic and spatially resolved TR models. Such models would be useful to determine at which conditions TR propagation occurs and to evaluate the effectiveness countermeasures against propagation.

The final parts of this work include two reports (project Safe Lithium-Based Traction Batteries (SafeBattery)) in which 20 TR-experiment were done with 42 A h pouch cells. The cells were produced in 2016 and had a graphite anode and NMC/LMO cathode.

The first report (chapter 3) focuses on workplace safety requirements for cell-abuse test laboratories. The first experiments proved that fully charged cells with SOC 100 % had a critical temperature[1] of $T_{crit} = 231\,°C$, a maximal cell temperature of $T_{max} = 754\,°C$ and a gas release of $n_V = 2.31\,mol$ with gas concentrations $C_{CO} = 16.6\,\%$ and $C_{H_2} = 22.9\,\%$. In contrast to fully charged cells, cells with SOC $\leq$30 % showed no exothermic reactions and released less gas ($n_V = 0.53\,mol$) when externally heated up to 309 °C. Their vent-gas contained less $C_{CO} = 4.5\,\%$ and $C_{H_2} = 3.9\,\%$ but high concentration of electrolyte solvents instead.

To prevent damage to laboratory equipment and hazards to personnel several measures must be taken:

- To prevent fire spreading from the cell to neighbouring equipment either incombustible material near the cell is used or tests can be done in inert atmosphere. TR propagation to neighbouring cells may be stopped by direct cooling with water/surfactants mixture.
- To prevent deflagration either the enclosure must be large enough so that the vent-gas does not reach the lower explosion limit (LEL) or the enclosure is filled with inert gas or ventilation with a throughput comparable to the gas release rate of the cell is used (e.g. $80\,m^3\,h^{-1}$).
- Confinements need a venting port to prevent bursting. An enclosure which can withstand an overpressure of 20 kPa would need a venting port with a diameter of 13.3 mm for safe gas release of the tested cell.
- To prevent intoxication personnel should wear gas monitoring and warning devices. Additional fixed CO monitoring and alarm system should be installed in the laboratory. The laboratory ventilation system should have an air exchange rate of at least 10 times the room volume per hour to extract any harmful gases.
- To prevent injuries from leaking electrolyte and electrode particles of damaged cells respirators for organic vapours and particles or a fume hood should be

[1] T_{crit} is the temperature when temperature increase becomes higher than $dT/dt > 10\,°C\,min^{-1}$

used. Eye protection and appropriate gloves should be worn.

The second report (chapter 4) focuses on triggering a TR with a hot-spot heater. Same cell type as in the first report was investigated. Fully charged cells were tested in a series of experiments with increasing heating power which was applied locally at either the centre of the cell or on the tabs. Surprisingly high power was required to initiate a localized TR (heater power $P_h > 561\,\mathrm{W}$), heating duration $t_h > 175\,\mathrm{s}$).
The main findings were:

- In experiments with low heating power or insufficient heating time a self sustaining TR could not be started. Instead, the heater created a soft short-circuit which slowly discharged the cells.
- In experiments with long heating times and lower heat flow into the cell the heat created an inert zone with radius r_i centred at the hot spot. In those cases a self sustaining TR started only after prolonged heating. The self sustaining TR front originated not at the hot spot but at the perimeter of the inert zone. A correlation of required heating time and the final size of the inert zone was found.
- In experiments with high heating power the TR could be started quickly in 400 s. In these cases the self sustaining TR originated at the hot-spot and the TR-front travelled away from the initial hot-spot and consumed the whole cell.
- The speed of the TR-front depends on the direction: it is higher along the electrode sheets and lower perpendicular to the electrode sheets. High in-plane conductivity facilitates an in-plane front speed of $c_{\parallel} = 13.8\,\mathrm{mm\,s^{-1}}$ whereas the lower out-of-plane conductivity results in lower out-of-plane speed $c_{\perp} = 0.84\,\mathrm{mm\,s^{-1}}$.
- The amount and composition of vent-gas released by a TR was the same for the triggering methods hot-spot or uniform heating.
- Gas that was released during the creation of the inert zone had a composition with higher H_2 and CO concentrations than gas from heated cells at SOC $\leq$30 % but lower H_2 and CO concentrations than gas from TR of cells at SOC 100 %.

- When local heating was not sufficient to start a self sustaining TR, an internal ISC of $\leq$4 A was estimated.
- When local heating started a TR, different ISC currents ranging from 13 A to 560 A were estimated for the different experiments.

The final conclusion is that Li-ion batteries are safe up to a critical temperature which depends on the cell type and SOC. If cells are overheated above a critical temperature self-accelerating exothermic reactions release gas, heat and particles. This work shows which temperatures and gases-releases must be expected from a failed cells and gives suggestions on how to cope with the released gas and heat in automotive and laboratory environment.

6 Outlook

Current battery packs for electric vehicles have reached the target to enable ranges >400 km. The next target is to reduce the battery pack cost below 100 $/kWh. The cost of conventional Li-ion cells can be reduced by minimizing the amount of electrolyte and by using cathodes with high capacity or high voltage cathodes with cut-off voltages above 4.3 V. Such incremental changes may have medium influence on the TR parameter of a single cell. Other promising developments include all-solid-state cells and Li/S cells.
In solid-state cells the liquid electrolyte is exchanged with a not burnable solid state matrix such as sulfide glasses or ceramics [134]. The anode is pure Li-metal while the cathode particles can be the same as in conventional Li-ion cells. Advantages of all solid state cells are higher energy density, operation at high temperature and the lack of burnable electrolyte. The lack of burnable electrolyte should improve safety performance, but the cells could theoretically still show a TR reaction. In an overheated all solid state cell the O_2 released by the cathode could come in contact with molten Li as sketched in fig. 6.1. The molten Li and O_2 could react in a highly exothermic reaction to Li_2O. Therefore the overtemperature behaviour of all solid state cells should be tested before mass market introduction.

Li/S batteries use other active materials than conventional Li-ion batteries. The anode active material, graphite (or graphite/silicon composite), is replaced with a thin Li metal layer. The cathode material (metal-oxides or metal-phosphates) is replaced with sulphur/graphite composite. An aprotic liquid electrolyte is used, e.g. 1,2-dimethoxyethane (DME) and 1,3-dioxolane (DOL) with 1M lithium bis-(trifluoromethanesulfonyl)-imide (LiTFSI) conductive salt [135].
Li/S cells have a better gravimetric energy density and do not require expensive materials such as Co or Ni for their cathodes. They could enable applications

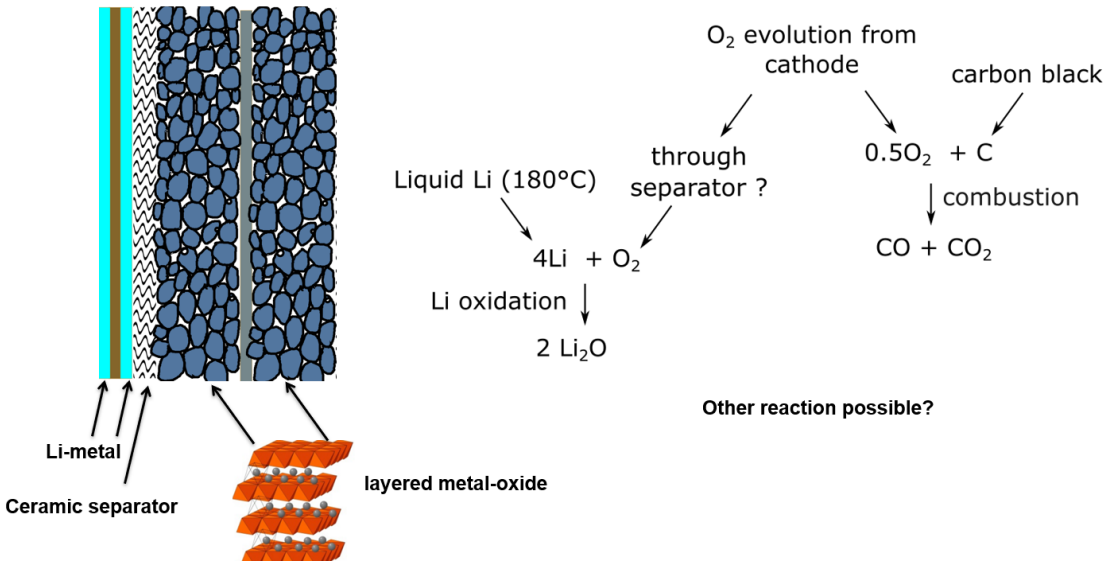

Figure 6.1: Sketch of a theoretical TR reaction in a solid state cell.

where weight is premium but volume is available such as electric planes and drones. Possible risks in case of over temperature are exothermic reactions of molten Li and molten S with ambient air and the liquid electrolyte.
In a quick survey experimental results on over temperature behaviour of all solid state cells and Li/S cells could not be found. Their safety behaviour may be fundamentally different compared to current state of the art Li-ion cells and should be addressed in future research.

The safety of the whole battery pack of an electric vehicle (EV) is one step up from the safety of a single Li-ion cell. One important failure case is the TR of one cell inside the pack. The failed cell emits heat, gas and solid material into the battery casing. The heat may start a TR-propagation from cell to cell and it can damage the electric insulation on a first location. The hot gases may cause overpressure, and a vent-gas jet may puncture the pack-casing. Ejected material may cause an insulation fault on a second location in the pack. Two insulation failures may cause a short circuit and electric arcing inside the pack. Future research topics include the interaction of the ejected debris and the electrical components, heat withstanding battery casings and cell to cell propagation of the TR.

Appendix

Thermal Insulation Materials

Feuerungs- und Schornsteinbau
Hochbau, Keramik
Günter Schulz GmbH & Co. KG
Lohweg 4 A, D-06632 Balgstädt

Produktinformation
www.schuba-shop.com

Produkt	Biolösliches Faserpapier Schuba®BFP 120, d = 5 mm				
Artikel-Nr.	126-20093 01 02				
Produkt-beschreibung	Flexibles biolösliches Faserpapier, Rollenbreite 1000 mm, Papierdicke 5 mm; erhöhte Biolöslichkeit auf Basis von Calcium-Magnesium-Silicat; ausgezeichnete thermische Stabilität in normalen, oxidierenden Atmosphären; aufgrund der hohen Biolöslichkeit erfolgt jedoch ein chemischer Angriff, besonders in feuchten Atomsphären in Verbindung mit Säuren und Laugen Besondere Merkmale: hohe Temperaturbeständigkeit, geringe Schwindung, ausgezeichnete Temperaturwechselbeständigkeit, gute mechanische Festigkeit, einfache Bearbeitung, gute Dämmeigenschaften, ohne organische Bindemittel; Gefahrstoffklassifizierung entfällt aufgrund der hohen Biolöslichkeit				
Technische Daten	Klassifikationstemperatur	1200 °C	ASTM-Gr.		/
	Abmessungen	/	1000	5	mm
	Al_2O_3-Gehalt	> 1			%
	SiO_2-Gehalt	61 - 67			%
	Fe_2O_3-Gehalt	0,6			%
	CaO	30 - 40			%
	MgO-Gehalt	30 - 40			%
	Wärmeleitfähigkeit bei	400 °C	0,10		W/mK
		600 °C	0,15		W/mK
		800 °C	0,22		W/mK
	Schwinden nach 24 h bei	1200 °C	> 4		%
	Kaltdruckfestigkeit bei	Raumtemp.*	/		N/mm²
		* bei feuerfesten Massen nach Aushärtung			
	Rohstoffart	Calcium-Magnesium-Silicat			
	Dichte / Materialbedarf	150			kg/m³
	Gewicht	0,75			kg/m²
	Bindungsart	/			
	max. Korngröße	/			mm
	Bedarf Anmachwasser	/			Liter / 100 kg
	Gebindegröße	ab 1			m²
Verarbeitungs-richtlinie	/				
	/				
	/				
	/				
Sicherheits-hinweise	**Reizungseffekte** Geringe mechanische Reizung von Haut, Augen und oberen Atemtrakt kann bei Ausgesetzt sein auftreten. Diese Wirkungen sind gewöhnlich vorübergehend. Bereits bestehende Erkrankungen von Haut und Atemwege, Dermatitis, Asthma oder chronischer Lungenerkrankungen können verschlimmert werden.				
Lagerung	Trocken lagern!				

ENGLISH

Datasheet

Rigid Mica sheet

RS Stock number 785-0827

Description
Mica is a laminate designed for providing outstanding electrical insulation at high temperatures. It is environmentally safe and non-toxic, certified by UL-94V-0 (E67143M) and conforming to IEC 371-3-3

Applications
A special low smoke and blister free grade. It fully resists the extreme high temperature cycles and can be easily cut or punched.

Availability
Various sheet sizes, 0.1 – 1.5mm thick

Storage
Unlimited shelf life in a dry place at room temperature

ENGLISH

Characterisitcs

Type		Mica	
Mica content	%	ca.90	IEC 371-2
Bond content	%	ca.90	IEC371-2
Thickness	mm	0.1-1.5	IEC 371-2
Density		2.15 ± 0.15	IEC371-2
Heat Resistance			
Continuous service	°C	500	
Intermittent service	°C	800	
Edge Strength	Kg/0.1 mm	>1.3	in house
Tensile Strength	$N.mm^{-2}$	150	ISO 527
Flexural Strength	$N.mm^{-2}$	>180	ISO178
Water absorption	%	<1	IS 62
Dielectric Strength	KV/mm	>25	IEC243
Insulation Resistance 23°C	Ω.cm	$>10_{17}$	IEC 93
Insulation resistance 550°C	Ω.cm	$>10_{12}$	IEC 93
Heat Loss at 500°C	%	<1	IEC 371-2
Thermal Expansion			
Perpendicular to Layer	$10^{-6}.K^{-1}$	100	
ǁ parallel to Layer	$10^{-6}.K^{-1}$	10	

Sample Holder used in SafeBattery, Part 2: Hot-Spot Experiments

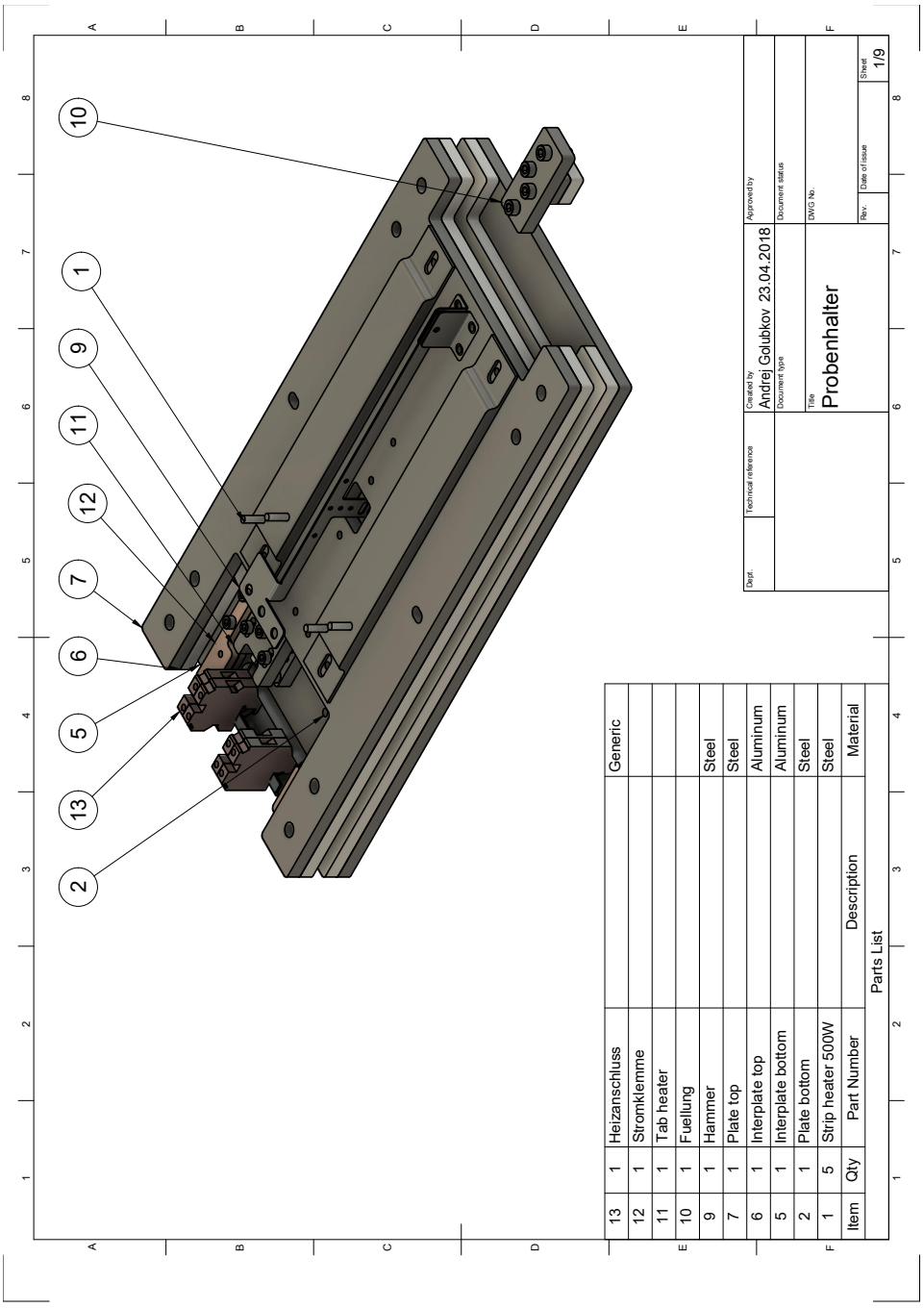

Parts List				
Item	Qty	Part Number	Description	Material
1	1	Plate bottom		Steel

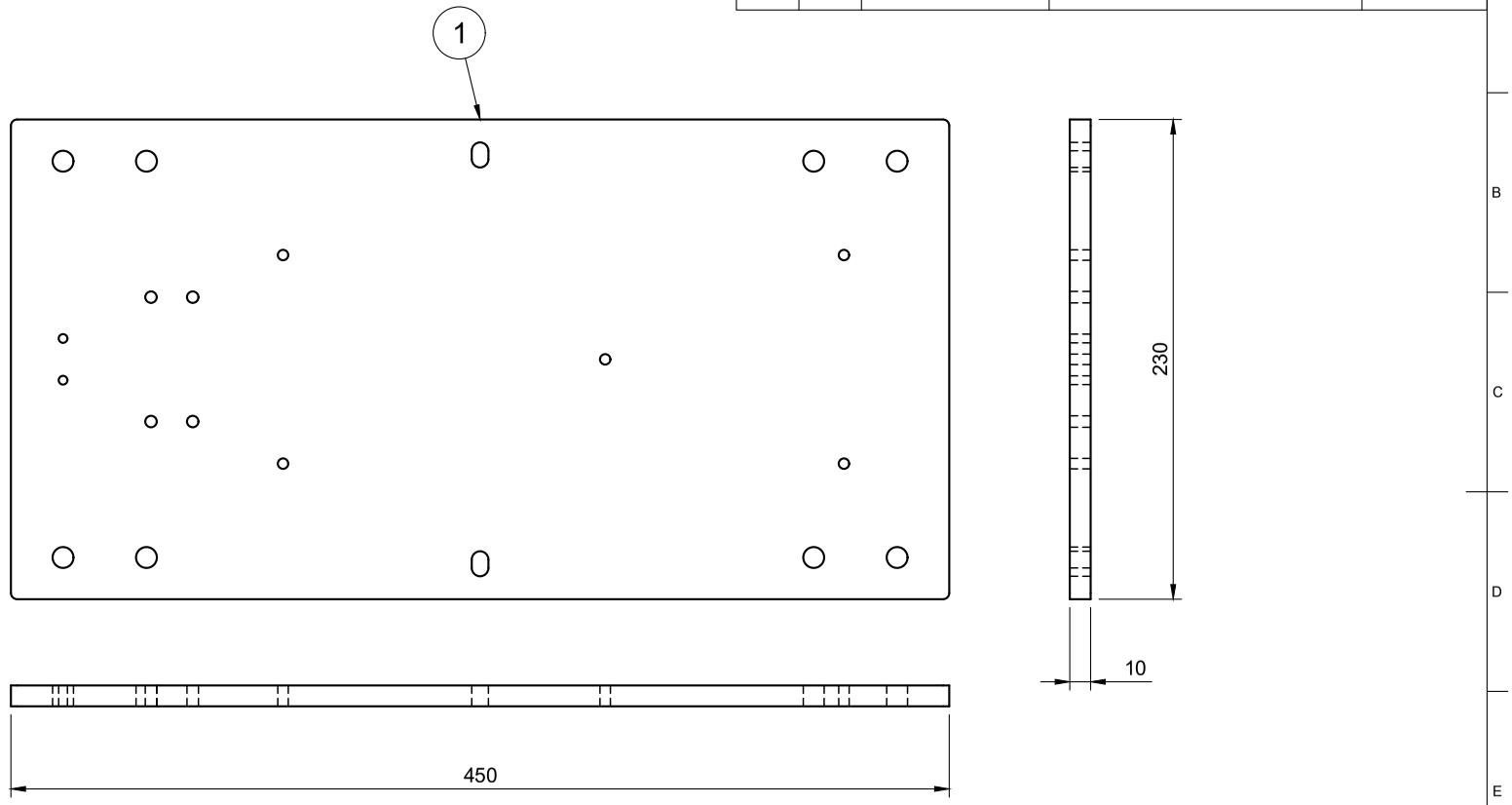

Dept.	Technical reference	Created by: Andrej Golubkov 23.04.2018	Approved by
		Document type	Document status
		Title: Probenhalter	DWG No.
			Rev. / Date of issue / Sheet: 2/9

Parts List				
Item	Qty	Part Number	Description	Material
5	1	Interplate bottom		Aluminum

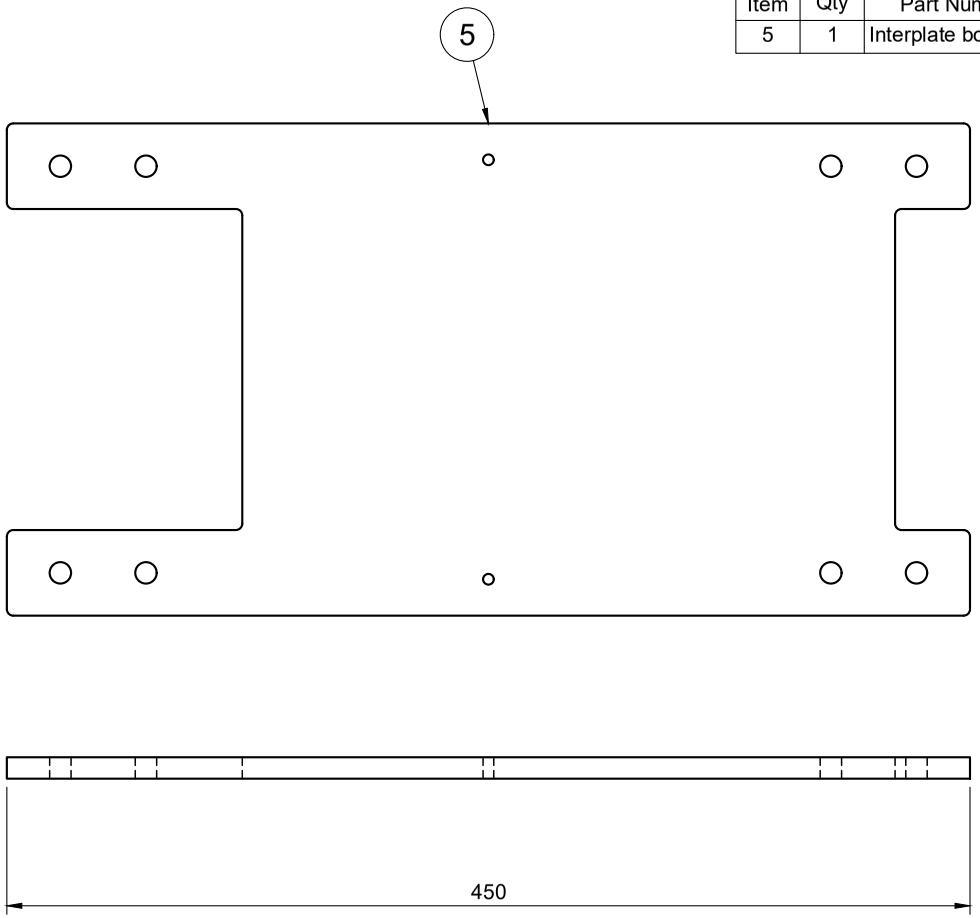

Dept.	Technical reference	Created by Andrej Golubkov 23.04.2018	Approved by
		Document type	Document status
		Title Probenhalter	DWG No.
			Rev. / Date of issue / Sheet 3/9

Parts List				
Item	Qty	Part Number	Description	Material
6	1	Interplate top		Aluminum

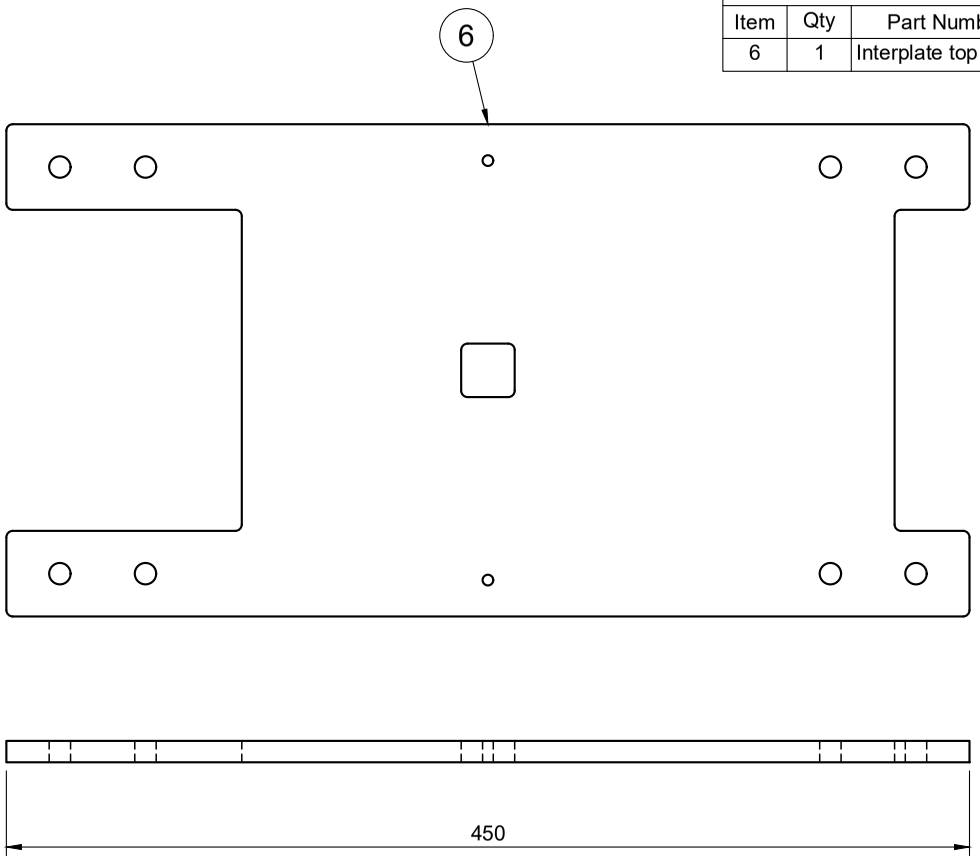

Dept.	Technical reference	Created by Andrej Golubkov 23.04.2018	Approved by
		Document type	Document status
		Title Probenhalter	DWG No.
			Rev. / Date of issue / Sheet 4/9

Parts List				
Item	Qty	Part Number	Description	Material
7	1	Plate top		Steel

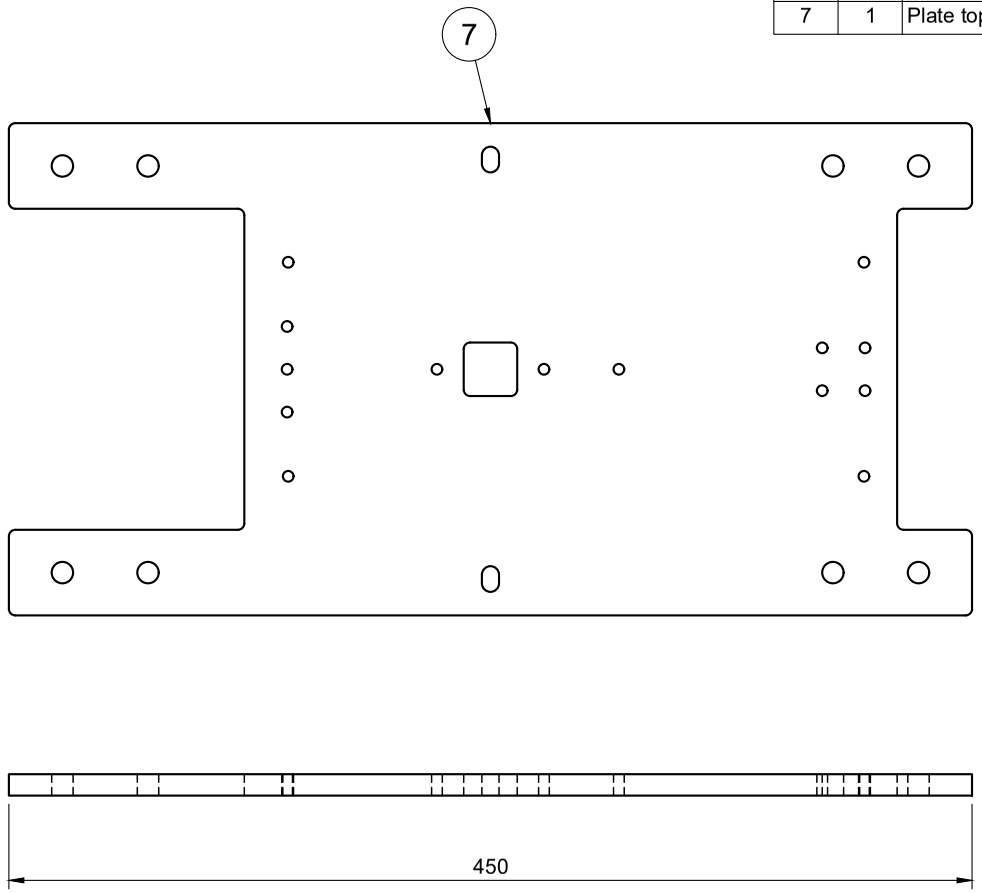

Dept.	Technical reference	Created by: Andrej Golubkov 23.04.2018	Approved by
		Document type	Document status
		Title: Probenhalter	DWG No.
			Rev. / Date of issue / Sheet: 5/9

Parts List				
Item	Qty	Part Number	Description	Material
2	1	Deckel		Steel
3	1	Stoppel mitte		Steel
4	1	Stoppel unten		Aluminum

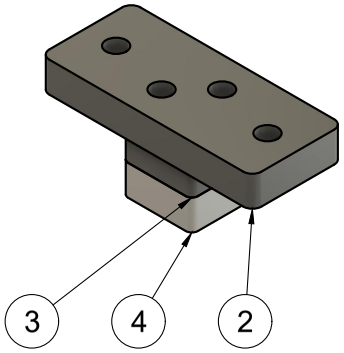

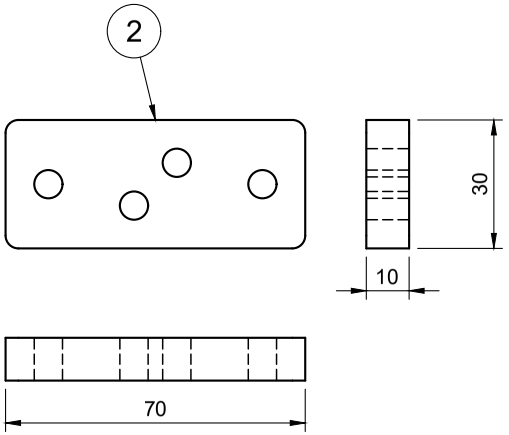

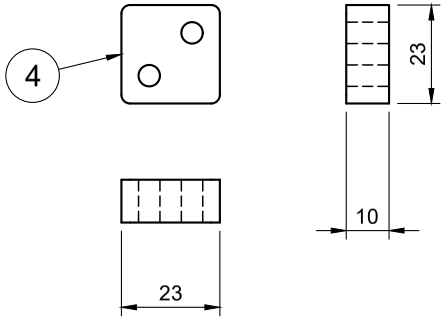

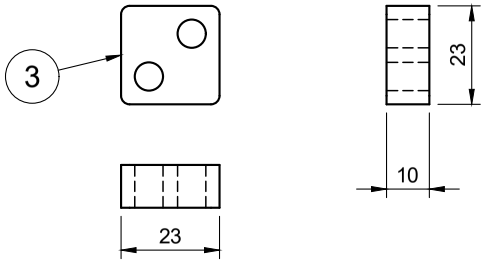

Dept. / Technical reference		Created by: Andrej Golubkov 23.04.2018	Approved by:
		Document type	Document status
		Title: Probenhalter	DWG No.
			Rev. / Date of issue / Sheet: 6/9

Parts List				
Item	Qty	Part Number	Description	Material
2	1	Table		Steel
3	1	Druckplatte		Steel

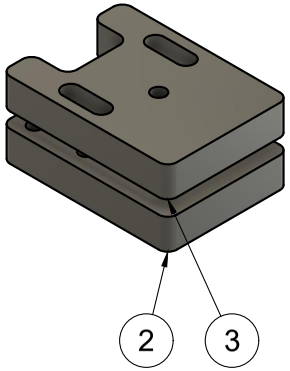

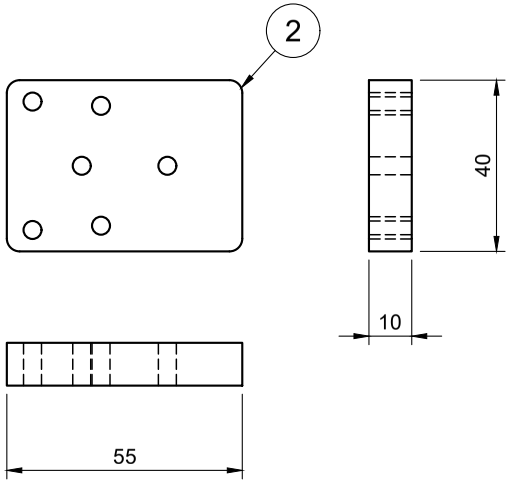

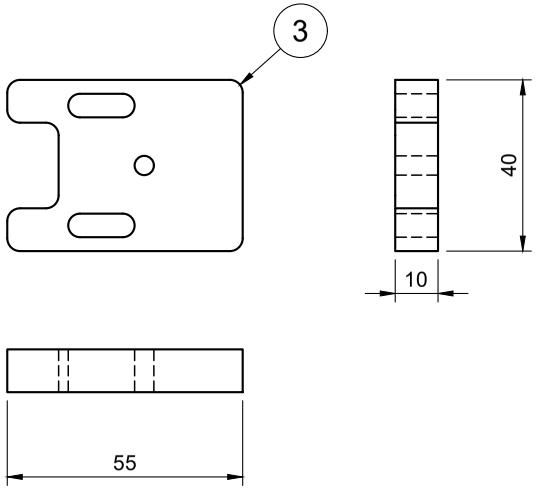

Dept. / Technical reference		Created by: Andrej Golubkov 23.04.2018	Approved by:
		Document type	Document status
		Title: Probenhalter	DWG No.
			Rev. / Date of issue / Sheet: 7/9

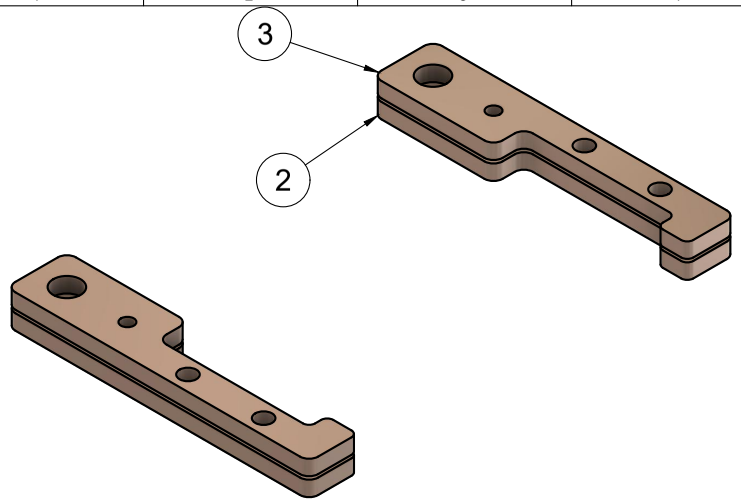

Parts List				
Item	Qty	Part Number	Description	Material
2	2	Stromklemme unten		Copper
3	2	Stromklemme oben		Copper

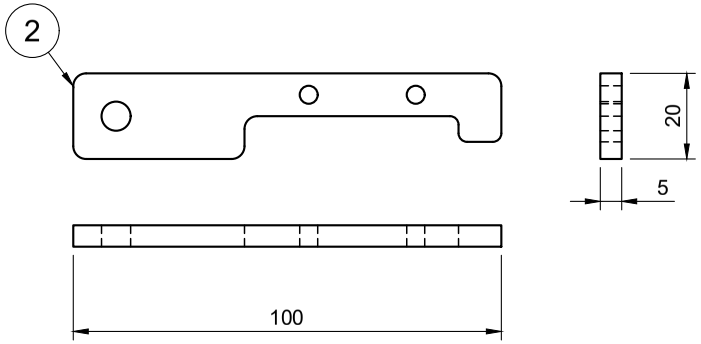

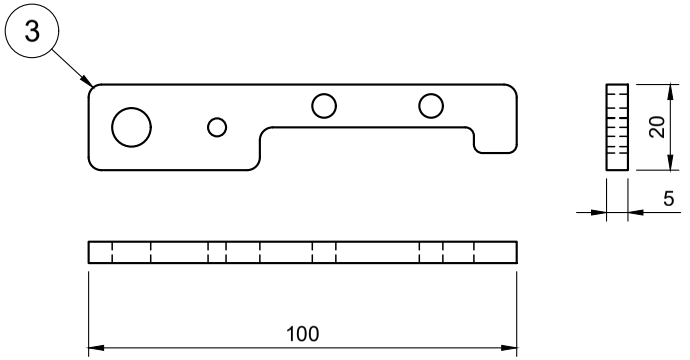

Dept. / Technical reference		Created by: Andrej Golubkov 23.04.2018	Approved by:
		Document type:	Document status:
		Title: Probenhalter	DWG No.:
			Rev. / Date of issue / Sheet: 8/9

Parts List				
Item	Qty	Part Number	Description	Material
1	1	Arm		Steel
2	2	Klammer		Steel

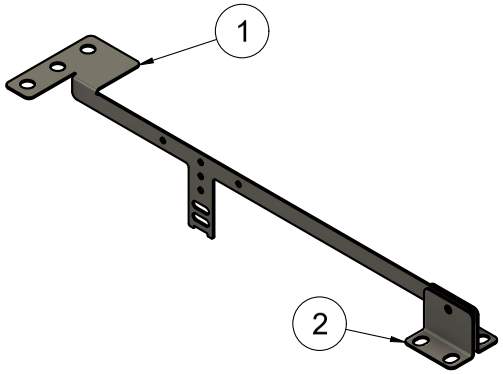

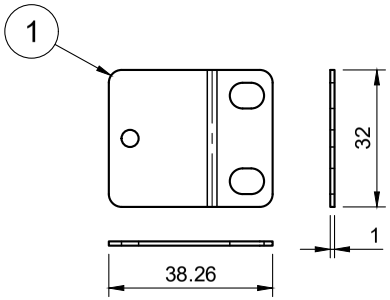

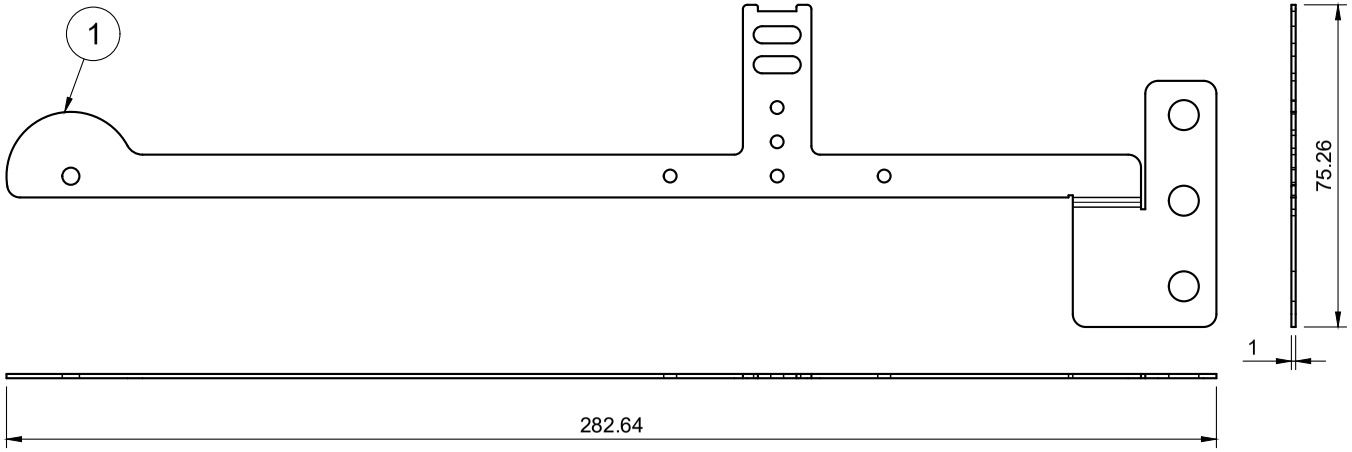

Dept.	Technical reference	Created by	Approved by
		Andrej Golubkov 23.04.2018	
		Document type	Document status
		Title: Probenhalter	DWG No.
			Rev. / Date of issue / Sheet: 9/9

Übersicht

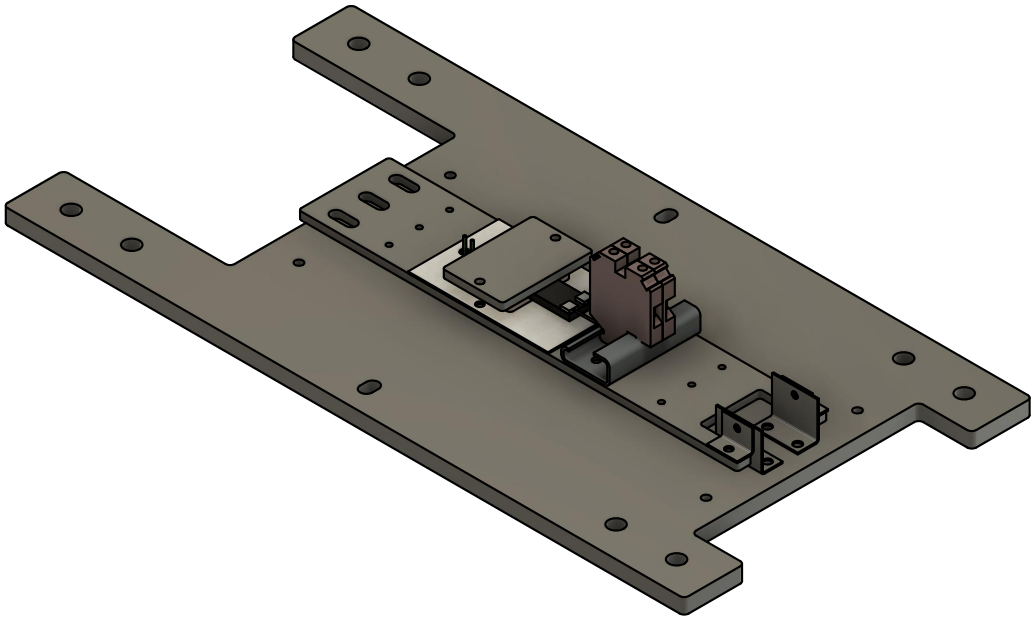

283

Dept.	Technical reference	Created by	Approved by
		Andrej Golubkov 04.07.2018	
		Document type	Document status
		Title	DWG No.
		center heater	
			Rev. / Date of issue / Sheet: 1/6

Parts List				
Item	Qty	Part Number	Description	Material
4	1	Upper pressure plate		Steel

1 x Edelstahlplatte 10mm, (Upper pressure plate)

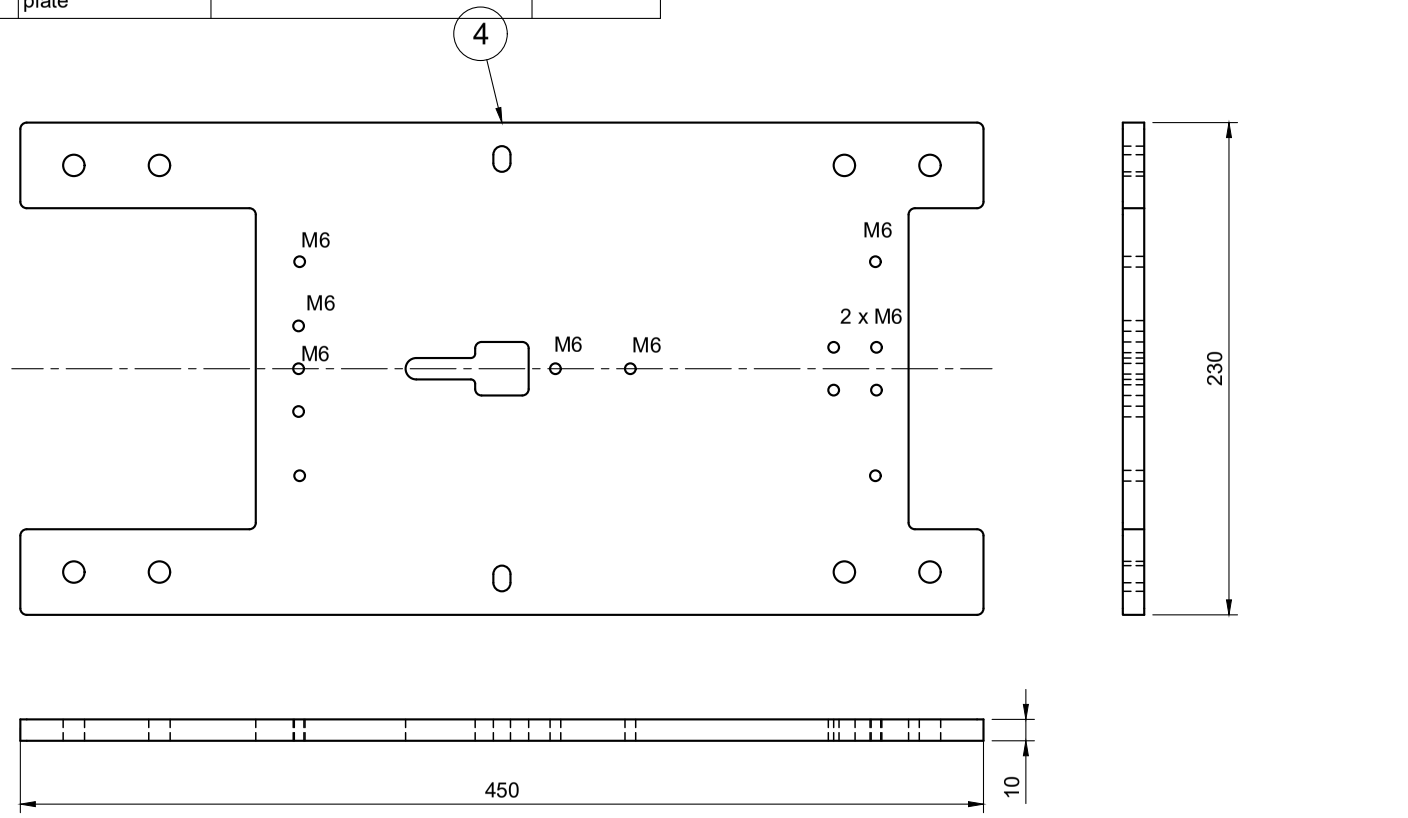

Dept.	Technical reference	Created by	Approved by
		Andrej Golubkov 04.07.2018	
		Document type	Document status
		Title: center heater	DWG No.
			Rev. / Date of issue / Sheet: 2/6

Parts List				
Item	Qty	Part Number	Description	Material
1	1	Heat conductor		Copper

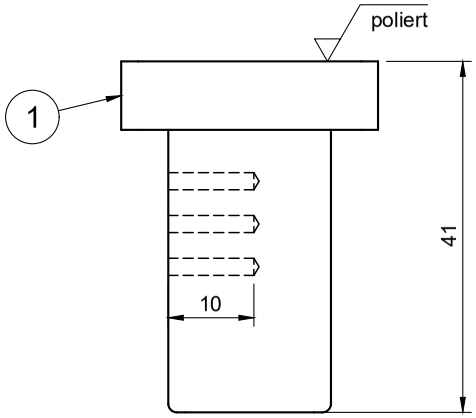

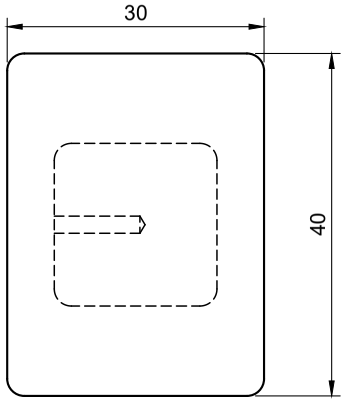

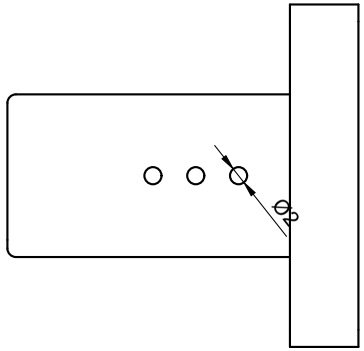

1 x Kupferteil (Heat conductor)

Sauerstofffreies Kupfer wie für Elektroanwendungen für gute Wärmeleitfähigkeit.

Oberer teil poliert, für guten Kontakt zu flachen keramischen Heizelement

Dept.	Technical reference	Created by: Andrej Golubkov 04.07.2018	Approved by
		Document type	Document status
		Title: center heater	DWG No.
			Rev. / Date of issue / Sheet: 3/6

1 x Edelstahlplatte, 5mm
(Baseplate)

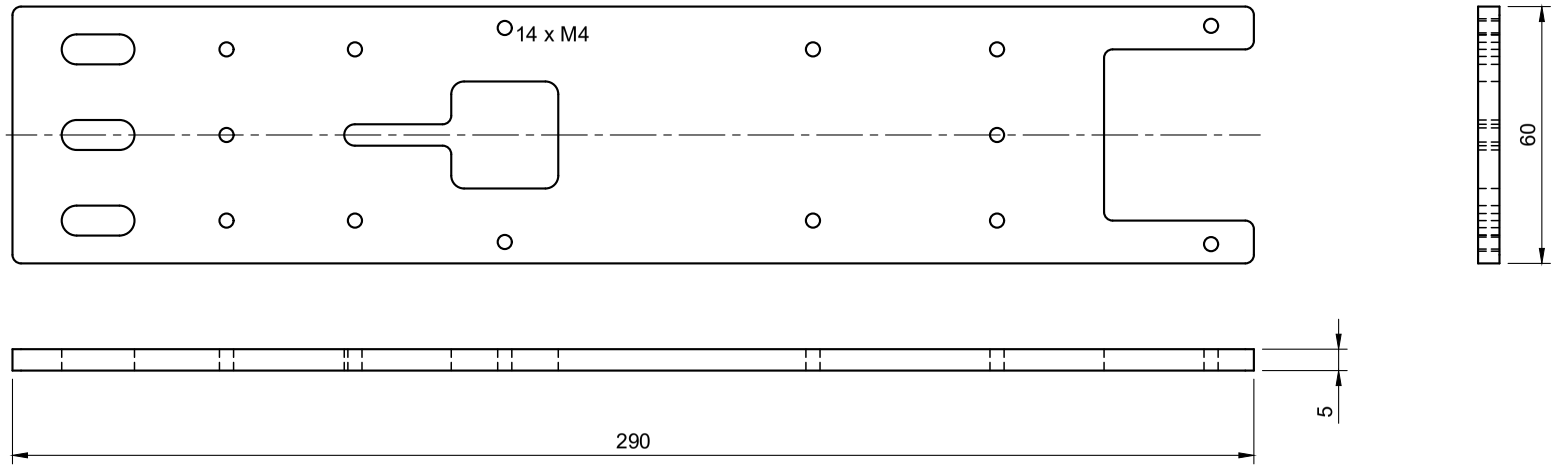

Dept.	Technical reference	Created by	Approved by
		Andrej Golubkov 04.07.2018	
		Document type	Document status
		Title: center heater	DWG No.
			Rev. / Date of issue / Sheet: 4/6

List of Figures

Acronyms

ARC accelerated rate calorimetry. 9, 15, 138, 139
ATEX Directives for equipment intended for use in EXplosive ATmospheres. 128, 131

BDU battery disconnect unit. 4
BMDW Ministry of Digital and Economic Affairs. vi
BMK Austrian Federal Ministry for Climate Action. vi
BMS battery management system. 4
BMU battery management unit. 4

CEET Institute of Chemical Engineering and Environmental Technology. iv, 12, 13
COMET Competence Centers for Excellent Technologies. vi

DAQ data aquisition. 90, 101
DEC diethyl carbonate. 9, 131
DMC dimethyl carbonate. 131
DTD 1,3,2-Dioxathiolane 2,2-dioxide. 131
DUT device under test. 124

EC ethylene carbonate. 8, 131
EDS energy-dispersive X-ray spectroscopy. 17, 131
EDX Energy-dispersive X-ray spectroscopy. 20
EMC ethyl methyl carbonate. 9, 131
ESS energy storage system. 77
EV electric vehicle. x, 1, 2, 4, 6, 14, 15, 18, 75, 76, 82, 133, 136, 269, 287

FABSY+ Failsafe Battery System Plus. 13, 14

FEC fluoroethylene carbonate. 131

FFG Austrian Research Promotion Agency. vi

FTIR fourier-transform infrared spectroscopy. 14, 76, 79, 88, 93, 97, 100, 101, 106, 108, 113, 121, 134, 148, 150, 152, 158, 176, 181, 197, 207, 214, 219, 223, 225, 230, 231, 236, 246, 251, 288–291, 294, 295, 297–299

GABSI Gas-Analysis for Battery Safety. 14

GALION Gassensorik für Li-IONen Batteriesyteme. 14

GC gas chromatography. 17, 20, 31, 76, 88, 91, 93, 97, 100, 101, 106, 108, 113, 115, 121, 134, 148, 150, 152, 158, 176, 181, 182, 187, 197, 199, 205, 207, 214, 219, 223, 225, 230, 231, 236, 288–291, 294–299

GC-MS gas chromatography – mass spectrometry. 17

GTR-EVS Global Technical Regulation on Electric Vehicle Safety. 133

HWS heat-wait-search. 16

ICP Inductively coupled plasma. 20, 31

IR infrared. 88

ISALIB Intrinsic Safety and Risk of Automotive Li-Ion Batteries. 13, 17

ISC internal short circuit. 19, 59, 135, 139, 142, 143, 146, 147, 162, 168, 175, 176, 180, 196, 199, 252–259, 263, 264, 267, 290, 294, 295, 300

LCO $LiCoO_2$. 79, 138, 260

LEL lower explosion limit. 77, 125, 129, 130, 265

LFP $LiFePO_4$. 15, 16, 79, 260–262

LISAE Li-Ion Battery Safety in Automotive Environment. 12, 13

LMO $LiMn_2O_4$. 16, 82, 137, 263, 265

MAK threshold limit value (Maximale Arbeitsplatz-Konzentration). 129, 130

MSDS material safety data sheet. 124, 130, 131

NCA $Li(NiCoAl)O_2$. 15, 16, 82, 261, 262

Ni-MH nickel metal hydride. 262, 263

NMC $Li(NiMnCo)O_2$. 16–18, 79, 82, 137, 138, 260, 265

OCV open circuit voltage. 81, 142, 143

OES Optical Emission Spectroscopy. 20, 31

PC propylene carbonate. 131
PHHR peak heat release rate. 76
PS 1,3-Propansulton. 80, 131
PTFE Polytetrafluoroethylene. 7

SafeBattery Safe Lithium-Based Traction Batteries. vi, 13, 14, 75, 81, 101, 107, 114, 125, 126, 129–131, 142, 252, 258, 265, 287
SEM scanning electron microscope. 17, 131
SFG Styrian Business Promotion Agency. vi
SOC state of charge. 15–19, 31, 121, 130, 139, 142, 143, 242, 254, 260–263, 265–267
SOH state of health. 18

TCD thermal conductivity detector. 88
THRUSTY Thermal Runaway Safety. 13
TP thermal runaway propagation. 14, 133, 134
TR thermal runaway. xii, 8–20, 31, 48, 59, 75–82, 84, 85, 90–92, 98, 100, 101, 103, 104, 106–110, 112, 114, 115, 118, 119, 121, 122, 124–126, 128, 129, 131, 133–140, 143, 144, 146–148, 150, 153–155, 157, 159, 162, 166, 168, 171, 175, 176, 178, 179, 181, 182, 190–192, 194, 195, 197–199, 201, 202, 205–207, 209, 210, 212–214, 216, 217, 219–221, 224, 225, 227, 228, 230–235, 237–247, 250–254, 256–258, 260–269, 287–300
TRGS Technical Rules for Hazardous Substances. 80, 131

UEL upper explosion limit. 77
UNECE United Nations Economic Commission for Europe. 133

VC vinylene carbonate. 131
VVR Virtual Vehicle Research GmbH. iv, vi, 13, 14, 75, 76, 129, 131, 134

XRD X-ray powder diffraction. 17, 80

Bibliography

[1] ev-volumes.com. (2018). Global plug-in light vehicle sales from 2011 to 2018 (in 1,000 units)., [Online]. Available: https://www.statista.com/statistics/665774/global-sales-of-plug-in-light-vehicles/ (visited on) (cit. on p. 2).

[2] pwc.com. (2017). Projected vehicle sales in china, the u.s. and the eu between 2017 and 2030, by propulsion technology (in million vehicles)., [Online]. Available: https://www.statista.com/statistics/264754/worldwide-vehicle-sales-by-propulsion-technology-2025/ (visited on 03/03/2019) (cit. on p. 3).

[3] NISSAN, *2018 LEAF First Responder's Guide*, 2017 (cit. on p. 4).

[4] Z. P. Cano, D. Banham, S. Ye, A. Hintennach, J. Lu, M. Fowler, and Z. Chen, "Batteries and fuel cells for emerging electric vehicle markets," *Nature Energy*, vol. 3, no. 4, pp. 279–289, Apr. 2018, ISSN: 2058-7546. DOI: 10.1038/s41560-018-0108-1. [Online]. Available: http://www.nature.com/articles/s41560-018-0108-1 (cit. on p. 4).

[5] T. Mayer and E. Donzow, "Design of Battery Packs: Strategies for High Energy Density and Range," *ATZelectronics worldwide*, vol. 14, no. 10, pp. 26–31, Oct. 2019, ISSN: 2524-8804. DOI: 10.1007/s38314-019-0095-4. [Online]. Available: http://link.springer.com/10.1007/s38314-019-0095-4 (cit. on p. 4).

[6] J. A. Turner, S. Kalnaus, H. Wang, S. Simunovic, and A. Kumar, "Crashworthiness models for automotive batteries (Report No. DOT HS 812 736)," National Highway Traffic Safety Administration, Washington, DC, Tech. Rep. May, 2019. [Online]. Available: https://rosap.ntl.bts.gov/view/dot/41005 (cit. on p. 6).

[7] R. Justen and R. Schöneburg, "Crash safety of hybrid-and battery electric vehicles," *22th ESV-Conference*, pp. 1–9, 2011. [Online]. Available: http://medcontent.metapress.com/index/A65RM03P4874243N.pdf%7B%5C%%7D5Cnhttp://www-nrd.nhtsa.dot.gov/pdf/esv/esv22/22ESV-000096.pdf (cit. on p. 6).

[8] M. Funcke, S. Lovski, S. Schafer, D. Sturk, D. Dufaut, H. Sundmark, K. Vavalidis, and P. Gustafsson, "Protection of Lithium-Ion Traction Batteries in the Electric Car," in *24th International Technical Conference on the Enhanced Safety of the Vehicles*, vol. 15-0234, U.S. DEPARTMENT OF TRANSPORTATION, 2015, pp. 1–7. [Online]. Available: http://www.nhtsa.gov/ESV (cit. on p. 6).

[9] *Euro ncap test results for tesla model s*, Euro NCAP, 2014. [Online]. Available: https://www.euroncap.com/en/results/tesla/model-s/ (visited on 03/17/2019) (cit. on p. 6).

[10] K. Peter, "Electric vehicle battery pressure-compensation element has dual functionality," *Sealing Technology*, vol. 2017, no. 11, pp. 1–14, Nov. 2017, ISSN: 13504789. DOI: 10.1016/S1350-4789(18)30001-1. [Online]. Available: https://linkinghub.elsevier.com/retrieve/pii/S1350478918300011 (cit. on p. 7).

[11] A. Masias, "Ford safety performance of rechargeable energy storage systems (Report No. DOT HS 812 756)," National Highway Traffic Safety Administration, Washington, DC, Tech. Rep. July, 2019. [Online]. Available: https://rosap.ntl.bts.gov/view/dot/40791 (cit. on p. 8).

[12] P. Sun, R. Bisschop, H. Niu, and X. Huang, "A Review of Battery Fires in Electric Vehicles," *Fire Technology*, Jan. 2020, ISSN: 0015-2684. DOI: 10.1007/s10694-019-00944-3. [Online]. Available: http://link.springer.com/10.1007/s10694-019-00944-3 (cit. on pp. 8, 76).

[13] S. Gao, X. Feng, L. Lu, M. Ouyang, N. Kamyab, R. E. White, and P. Coman, "Thermal Runaway Propagation Assessment of Different Battery Pack Designs Using the TF5 Draft as Framework," *Journal of The Electrochemical Society*, vol. 166, no. 8, A1653–A1659, May 2019, ISSN: 0013-4651. DOI:

10.1149/2.1081908jes. [Online]. Available: http://jes.ecsdl.org/lookup/doi/10.1149/2.1081908jes (cit. on pp. 8, 136).

[14] X. Feng, S. Zheng, X. He, L. Wang, Y. Wang, D. Ren, and M. Ouyang, "Time Sequence Map for Interpreting the Thermal Runaway Mechanism of Lithium-Ion Batteries With LiNixCoyMnzO2 Cathode," *Frontiers in Energy Research*, vol. 6, no. November, pp. 1–16, Nov. 2018, ISSN: 2296-598X. DOI: 10.3389/fenrg.2018.00126. [Online]. Available: https://www.frontiersin.org/article/10.3389/fenrg.2018.00126/full (cit. on p. 8).

[15] X. Feng, S. Zheng, D. Ren, X. He, L. Wang, H. Cui, X. Liu, C. Jin, F. Zhang, C. Xu, H. Hsu, S. Gao, T. Chen, Y. Li, T. Wang, H. Wang, M. Li, and M. Ouyang, "Investigating the thermal runaway mechanisms of lithium-ion batteries based on thermal analysis database," *Applied Energy*, vol. 246, no. March, pp. 53–64, Jul. 2019, ISSN: 03062619. DOI: 10.1016/j.apenergy.2019.04.009. [Online]. Available: https://doi.org/10.1016/j.apenergy.2019.04.009%20https://linkinghub.elsevier.com/retrieve/pii/S0306261919306348 (cit. on pp. 8, 18, 19, 139).

[16] D. Ren, X. Feng, L. Lu, J. Li, and M. Ouyang, "Comparison of the Overcharge Behaviors of Lithium-ion Batteries Under Different Test Conditions," *Energy Procedia*, vol. 158, no. April, pp. 4921–4926, Feb. 2019, ISSN: 18766102. DOI: 10.1016/j.egypro.2019.01.699. [Online]. Available: https://doi.org/10.1016/j.apenergy.2019.05.015%20https://linkinghub.elsevier.com/retrieve/pii/S1876610219307362 (cit. on p. 8).

[17] L. Jiang, Z. Luo, T. Wu, L. Shao, J. Sun, C. Liu, G. Li, K. Cao, and Q. Wang, "Overcharge Behavior and Early Warning Analysis of LiNi 0.5 Co 0.2 Mn 0.3 O 2 /C Lithium-Ion Battery with High Capacity," *Journal of The Electrochemical Society*, vol. 166, no. 6, A1055–A1062, Apr. 2019, ISSN: 0013-4651. DOI: 10.1149/2.0661906jes. [Online]. Available: http://jes.ecsdl.org/lookup/doi/10.1149/2.0661906jes (cit. on p. 8).

[18] Q. Wang, J. Sun, X. Yao, and C. Chen, "Micro calorimeter study on the thermal stability of lithium-ion battery electrolytes," *Journal of Loss Prevention in the Process Industries*, vol. 19, no. 6, pp. 561–569, Nov. 2006,

ISSN: 09504230. DOI: 10.1016/j.jlp.2006.02.002. [Online]. Available: http://linkinghub.elsevier.com/retrieve/pii/S0950423006000064 (cit. on p. 8).

[19] M. Henriksen, K. Vaagseather, and A. V. Gaathaug, "Laminar Burning Velocity of the Dimethyl Carbonate-Air Mixture Formed by the Li-Ion Electrolyte Solvent," *Combustion, Explosion, and Shock Waves*, vol. 56, no. 4, pp. 383–393, 2020, ISSN: 04306228. DOI: 10.15372/FGV20200402. [Online]. Available: http://sibran.ru/journals/issue.php?ID=179319%7B%5C&%7DARTICLE%7B%5C_%7DID=179322 (cit. on p. 8).

[20] L. Vogdanis, B. Martens, H. Uchtmann, F. Hensel, and W. Heitz, "Synthetic and thermodynamic investigations in the polymerization of ethylene carbonate," *Die Makromolekulare Chemie*, vol. 191, no. 3, pp. 465–472, 1990. [Online]. Available: http://onlinelibrary.wiley.com/doi/10.1002/macp.1990.021910301/abstract (cit. on p. 8).

[21] M. Mansson, "Enthalpies of combustion and formation of ethyl propionate and diethyl carbonate1," *The Journal of Chemical Thermodynamics*, vol. 4, no. 6, pp. 865–871, Nov. 1972, ISSN: 00219614. DOI: 10.1016/0021-9614(72)90008-0. [Online]. Available: http://linkinghub.elsevier.com/retrieve/pii/0021961472900080 (cit. on p. 9).

[22] D. D. MacNeil and J. Dahn, "The Reaction of Charged Cathodes with Nonaqueous Solvents and Electrolytes: II. LiMn[sub 2]O[sub 4] charged to 4.2 V," *Journal of The Electrochemical Society*, vol. 148, no. 11, A1211, 2001, ISSN: 00134651. DOI: 10.1149/1.1407246. [Online]. Available: http://link.aip.org/link/JESOAN/v148/i11/pA1211/s1%7B%5C&%7DAgg=doi (cit. on p. 9).

[23] D. D. MacNeil and J. Dahn, "The Reaction of Charged Cathodes with Nonaqueous Solvents and Electrolytes: I. Li[sub 0.5]CoO[sub 2]," *Journal of The Electrochemical Society*, vol. 148, no. 11, A1205, 2001, ISSN: 00134651. DOI: 10.1149/1.1407245. [Online]. Available: http://link.aip.org/link/JESOAN/v148/i11/pA1205/s1%7B%5C&%7DAgg=doi (cit. on p. 9).

[24] NFPA, *NFPA 68 Standard on Explosion Protection by Deflagration Venting*, 2007. [Online]. Available: http://www.nfpa.org/ (cit. on p. 9).

[25] A. O. Said, C. Lee, X. Liu, Z. Wu, and S. I. Stoliarov, "Simultaneous measurement of multiple thermal hazards associated with a failure of prismatic lithium ion battery," *Proceedings of the Combustion Institute*, vol. 37, no. 3, pp. 4173–4180, 2019, ISSN: 15407489. DOI: 10.1016/j.proci.2018.05.066. [Online]. Available: https://doi.org/10.1016/j.proci.2018.05.066 (cit. on p. 10).

[26] S. Chen, Z. Wang, J. Wang, X. Tong, and W. Yan, "Lower explosion limit of the vented gases from Li-ion batteries thermal runaway in high temperature condition," *Journal of Loss Prevention in the Process Industries*, vol. 63, no. September 2019, p. 103 992, 2020, ISSN: 09504230. DOI: 10.1016/j.jlp.2019.103992. [Online]. Available: https://doi.org/10.1016/j.jlp.2019.103992 (cit. on pp. 10, 76, 77).

[27] A. R. Baird, E. J. Archibald, K. C. Marr, and O. A. Ezekoye, "Explosion hazards from lithium-ion battery vent gas," *Journal of Power Sources*, vol. 446, no. September 2019, p. 227 257, Jan. 2020, ISSN: 03787753. DOI: 10.1016/j.jpowsour.2019.227257. [Online]. Available: https://doi.org/10.1016/j.jpowsour.2019.227257%20https://linkinghub.elsevier.com/retrieve/pii/S0378775319312509 (cit. on pp. 10, 77).

[28] A. Hammami, N. Raymond, and M. Armand, "Lithium-ion batteries: runaway risk of forming toxic compounds.," *Nature*, vol. 424, no. 6949, pp. 635–636, Aug. 2003, ISSN: 0028-0836. DOI: 10.1038/424635b. [Online]. Available: http://www.nature.com/nature/journal/v424/n6949/full/424635b.html%20http://www.ncbi.nlm.nih.gov/pubmed/12904779 (cit. on p. 10).

[29] E. D. Bergmann, S. Gitter, and I. Blank, "Organic fluorine compounds. II. Toxicology of higher alkyl fluoroacetates," *Proceedings of the Koninklijke Nederlandse Akademie van Wetenschappen, Series B: Physical Sciences*, vol. 56, pp. 427–30, 1953 (cit. on p. 10).

[30] Y. Zhang, H. Wang, W. Li, and C. Li, "Quantitative identification of emissions from abused prismatic Ni-rich lithium-ion batteries," *eTransportation*, vol. 2, p. 100 031, Nov. 2019, ISSN: 25901168. DOI: 10.1016/j.etran.2019.100031. [Online]. Available: https://doi.org/10.1016/j.etran.2019.100031%20https://linkinghub.elsevier.com/retrieve/pii/S2590116819300311 (cit. on pp. 11, 80).

[31] E. Gasser, "Characterization of Gas and Particles Released During Thermal Runaway of Li-ion Batteries," Master's Thesis, Graz Universtiy of Technology, 2019, p. 84 (cit. on pp. 11, 131, 132).

[32] Y. Zhang, H. Wang, W. Li, C. Li, and M. Ouyang, "Size distribution and elemental composition of vent particles from abused prismatic Ni-rich automotive lithium-ion batteries," *Journal of Energy Storage*, vol. 26, no. October, p. 100 991, Dec. 2019, ISSN: 2352152X. DOI: 10.1016/j.est.2019.100991. [Online]. Available: https://doi.org/10.1016/j.est.2019.100991%20https://linkinghub.elsevier.com/retrieve/pii/S2352152X19307820 (cit. on pp. 11, 80, 81).

[33] S. Scheikl, "Untersuchung der thermischen Stabilität von Sekundärzellen auf Basis der Lithium-Ionen-Technologie in Abhängigkeit von Ladezustand und Kathodenmaterial," Master's Thesis, University of Graz, 2014 (cit. on p. 12).

[34] D. Fuchs, "Thermal runaway Versuche an Lithiumionenzellen," Master's Thesis, Graz University of Technology, 2014 (cit. on p. 12).

[35] A. W. Golubkov, D. Fuchs, J. Wagner, H. Wiltsche, C. Stangl, G. Fauler, G. Voitic, A. Thaler, and V. Hacker, "Thermal-runaway experiments on consumer Li-ion batteries with metal-oxide and olivin-type cathodes," *RSC Advances*, vol. 4, no. 7, p. 3633, 2014, ISSN: 2046-2069. DOI: 10.1039/c3ra45748f. [Online]. Available: http://xlink.rsc.org/?DOI=c3ra45748f (cit. on pp. 12, 75, 133).

[36] A. W. Golubkov, S. Scheikl, R. Planteu, G. Voitic, H. Wiltsche, C. Stangl, G. Fauler, A. Thaler, and V. Hacker, "Thermal runaway of commercial 18650 Li-ion batteries with LFP and NCA cathodes – impact of state of charge and overcharge," *RSC Adv.*, vol. 5, no. 70, pp. 57 171–57 186, 2015, ISSN: 2046-2069. DOI: 10.1039/C5RA05897J. [Online]. Available: http://xlink.rsc.org/?DOI=C5RA05897J (cit. on pp. 12, 75, 133).

[37] B. Rasch, "Experimentelle Untersuchung zum thermischen Durchgehen von prismatischen Lithium-Ionen Zellen," Bachelor's Thesis, Graz University of Technology, 2015 (cit. on p. 13).

[38] P. Krohn, "Experimentelle Untersuchung des Thermal Runaway von großen Li-Ionen Akkumulatoren verursacht durch anisotropes Aufheizen," Bachelor's Thesis, Ostbayerische Technische Hochschule Regensburg, 2017 (cit. on p. 13).

[39] A. W. Golubkov, R. Planteu, B. Rasch, C. Essl, A. Thaler, and V. Hacker, "Thermal runaway and battery fire: comparison of Li-ion, Ni-MH and sealed lead-acid batteries," in *7th Transport Research Arena TRA 2018*, Vienna: zenodo, 2018. DOI: 10.5281/zenodo.1491317. [Online]. Available: https://doi.org/10.5281/zenodo.1491317 (cit. on pp. 13, 75).

[40] A. W. Golubkov, R. Planteu, P. Krohn, B. Rasch, B. Brunnsteiner, A. Thaler, and V. Hacker, "Thermal runaway of large automotive Li-ion batteries," *RSC Advances*, vol. 8, no. 70, pp. 40 172–40 186, 2018, ISSN: 2046-2069. DOI: 10.1039/C8RA06458J. [Online]. Available: http://xlink.rsc.org/?DOI=C8RA06458J (cit. on pp. 13, 133).

[41] L. Pusterhofer, "Konstruktion eines Prüfstandes zur Messung der Wärmeleitfähigkeit von Brandschutzfolien bei hohen Temperaturen und unter mechanischem Druck," Bachelor's Thesis, Graz University of Technology, 2019 (cit. on p. 14).

[42] B. Weiss, "Hochtemperaturcharakterisierung gängiger Brandschutzfolien und deren Eignung für Batteriesysteme," Bachelor's Thesis, Graz University of Technology, 2019 (cit. on p. 14).

[43] M. Schober, "Thermal Runaway Simulation - Modellierung von automotiven Zellen mittels thermischer Netzwerke mit Openmodelica," Master's Thesis, FH JOANNEUM Graz, 2018 (cit. on p. 14).

[44] *Varta MICROBATTERIES*. [Online]. Available: https://www.varta-microbattery.com/products/lithium-ionen-zellen/ (visited on 03/01/2020) (cit. on p. 14).

[45] *VW ID.3*. [Online]. Available: https://www.volkswagen.at/id3 (visited on 03/01/2020) (cit. on p. 14).

[46] *Hornsdale power reserve*, Mar. 1, 2020. [Online]. Available: https://hornsdalepowerreserve.com.au/ (cit. on p. 14).

[47] C. J. Orendorff, J. Lamb, L. A. M. Steele, S. W. Spangler, and J. Langendorf, "Quantification of Lithium-ion Cell Thermal Runaway Energetics," Sandia National Laboratories, Tech. Rep. January, 2016, SAND2016–0486. [Online]. Available: http://prod.sandia.gov/techlib/access-control.cgi/2016/160486.pdf (cit. on p. 15).

[48] T. Waldmann and M. Wohlfahrt-Mehrens, "Effects of rest time after Li plating on safety behavior—ARC tests with commercial high-energy 18650 Li-ion cells," *Electrochimica Acta*, vol. 230, pp. 454–460, Mar. 2017, ISSN: 00134686. DOI: 10.1016/j.electacta.2017.02.036. [Online]. Available: http://dx.doi.org/10.1016/j.electacta.2017.02.036%20http://linkinghub.elsevier.com/retrieve/pii/S0013468617302979 (cit. on p. 15).

[49] T. Waldmann, J. B. Quinn, K. Richter, M. Kasper, A. Tost, A. Klein, and M. Wohlfahrt-Mehrens, "Electrochemical, Post-Mortem, and ARC Analysis of Li-Ion Cell Safety in Second-Life Applications," *Journal of The Electrochemical Society*, vol. 164, no. 13, A3154–A3162, Oct. 2017, ISSN: 0013-4651. DOI: 10.1149/2.0961713jes. [Online]. Available: http://jes.ecsdl.org/lookup/doi/10.1149/2.0961713jes (cit. on p. 16).

[50] J. Liu, Z. Wang, J. Gong, K. Liu, H. Wang, and L. Guo, "Experimental Study of Thermal Runaway Process of 18650 Lithium-Ion Battery," *Materials*, vol. 10, no. 3, p. 230, Feb. 2017, ISSN: 1996-1944. DOI: 10.3390/ma10030230. [Online]. Available: http://www.mdpi.com/1996-1944/10/3/230 (cit. on p. 16).

[51] B. Lei, W. Zhao, C. Ziebert, N. Uhlmann, M. Rohde, and H. Seifert, "Experimental Analysis of Thermal Runaway in 18650 Cylindrical Li-Ion Cells Using an Accelerating Rate Calorimeter," *Batteries*, vol. 3, no. 2, p. 14, Apr. 2017, ISSN: 2313-0105. DOI: 10.3390/batteries3020014. [Online]. Available: http://www.mdpi.com/2313-0105/3/2/14 (cit. on pp. 16, 82).

[52] A. Kvasha, C. Gutiérrez, U. Osa, I. de Meatza, J. A. Blazquez, H. Macicior, and I. Urdampilleta, "A comparative study of thermal runaway of commercial lithium ion cells," *Energy*, vol. 159, pp. 547–557, 2018, ISSN: 03605442. DOI: 10.1016/j.energy.2018.06.173. [Online]. Available: https://

linkinghub.elsevier.com/retrieve/pii/S0360544218312386 (cit. on p. 16).

[53] A. Perea, A. Paolella, J. Dubé, D. Champagne, A. Mauger, and K. Zaghib, "State of charge influence on thermal reactions and abuse tests in commercial lithium-ion cells," *Journal of Power Sources*, vol. 399, no. July, pp. 392–397, 2018, ISSN: 03787753. DOI: 10.1016/j.jpowsour.2018.07.112. [Online]. Available: https://doi.org/10.1016/j.jpowsour.2018.07.112 (cit. on p. 16).

[54] H. M. Barkholtz, Y. Preger, S. Ivanov, J. Langendorf, L. Torres-Castro, J. Lamb, B. Chalamala, and S. R. Ferreira, "Multi-scale thermal stability study of commercial lithium-ion batteries as a function of cathode chemistry and state-of-charge," *Journal of Power Sources*, vol. 435, no. July, p. 226 777, Sep. 2019, ISSN: 03787753. DOI: 10.1016/j.jpowsour.2019.226777. [Online]. Available: https://doi.org/10.1016/j.jpowsour.2019.226777%20https://linkinghub.elsevier.com/retrieve/pii/S0378775319307487 (cit. on p. 16).

[55] T. T. D. Nguyen, S. Abada, A. Lecocq, J. Bernard, M. Petit, G. Marlair, S. Grugeon, and S. Laruelle, "Understanding the Thermal Runaway of Ni-Rich Lithium-Ion Batteries," *World Electric Vehicle Journal*, vol. 10, no. 4, p. 79, Nov. 2019, ISSN: 2032-6653. DOI: 10.3390/wevj10040079. [Online]. Available: https://www.mdpi.com/2032-6653/10/4/79 (cit. on p. 16).

[56] Z. Liao, S. Zhang, K. Li, M. Zhao, Z. Qiu, D. Han, G. Zhang, and T. G. Habetler, "Hazard analysis of thermally abused lithium-ion batteries at different state of charges," *Journal of Energy Storage*, vol. 27, no. November 2019, p. 101 065, 2020, ISSN: 2352-152X. DOI: 10.1016/j.est.2019.101065. [Online]. Available: https://doi.org/10.1016/j.est.2019.101065 (cit. on pp. 16, 80, 132).

[57] C. Zhao, J. Sun, and Q. Wang, "Thermal runaway hazards investigation on 18650 lithium-ion battery using extended volume accelerating rate calorimeter," *Journal of Energy Storage*, vol. 28, no. September 2019, p. 101 232, Apr. 2020, ISSN: 2352152X. DOI: 10.1016/j.est.2020.101232. [Online]. Available: https://doi.org/10.1016/j.est.2020.101232%20https:

//linkinghub.elsevier.com/retrieve/pii/S2352152X19311077 (cit. on p. 17).

[58] M. Lammer, A. Königseder, and V. Hacker, "Holistic methodology for characterisation of the thermally induced failure of commercially available 18650 lithium ion cells," *RSC Adv.*, vol. 7, no. 39, pp. 24 425–24 429, 2017, ISSN: 2046-2069. DOI: 10.1039/C7RA02635H. [Online]. Available: http://xlink.rsc.org/?DOI=C7RA02635H (cit. on p. 17).

[59] M. Lammer, A. Königseder, P. Gluschitz, and V. Hacker, "Influence of aging on the heat and gas emissions from commercial lithium ion cells in case of thermal failure," *Journal of Electrochemical Science and Engineering*, vol. 8, no. 1, p. 101, Mar. 2018, ISSN: 1847-9286. DOI: 10.5599/jese.476. [Online]. Available: http://pub.iapchem.org/ojs/index.php/JESE/article/view/476%20http://www.pub.iapchem.org/ojs/index.php/JESE/article/view/476 (cit. on p. 17).

[60] S. Koch, K. Birke, and R. Kuhn, "Fast Thermal Runaway Detection for Lithium-Ion Cells in Large Scale Traction Batteries," *Batteries*, vol. 4, no. 2, p. 16, Mar. 2018, ISSN: 2313-0105. DOI: 10.3390/batteries4020016. [Online]. Available: http://www.mdpi.com/2313-0105/4/2/16 (cit. on p. 18).

[61] S. Koch, A. Fill, and K. P. Birke, "Comprehensive gas analysis on large scale automotive lithium-ion cells in thermal runaway," *Journal of Power Sources*, vol. 398, no. July, pp. 106–112, Sep. 2018, ISSN: 03787753. DOI: 10.1016/j.jpowsour.2018.07.051. [Online]. Available: https://doi.org/10.1016/j.jpowsour.2018.07.051%20https://linkinghub.elsevier.com/retrieve/pii/S0378775318307687 (cit. on pp. 18, 19).

[62] G. Zhong, B. Mao, C. Wang, L. Jiang, K. Xu, J. Sun, and Q. Wang, "Thermal runaway and fire behavior investigation of lithium ion batteries using modified cone calorimeter," *Journal of Thermal Analysis and Calorimetry*, vol. 7, 2018, ISSN: 1388-6150. DOI: 10.1007/s10973-018-7599-7. [Online]. Available: http://link.springer.com/10.1007/s10973-018-7599-7 (cit. on p. 76).

[63] *Samsung Isn't the Only One with Lithium Ion Battery Problems. Just Ask NASA*, Wired.com. [Online]. Available: https://www.wired.com/2016/10/samsung-isnt-one-lithium-ion-problems-just-ask-nasa/ (visited on 10/27/2016) (cit. on p. 76).

[64] *Hannover: Explosion von E-Bike-Akku löst Parkhausbrand aus*, Heise.de. [Online]. Available: https://www.heise.de/newsticker/meldung/Hannover-Explosion-von-E-Bike-Akku-loest-Parkhausbrand-aus-3619564.html (visited on 02/01/2017) (cit. on p. 76).

[65] *Lithium-ion batteries believed to have started two separate home fires*, legalexaminer.com. [Online]. Available: https://farmingtonhills.legalexaminer.com/legal/defective-dangerous-products/lithium-ion-batteries-believed-to-have-started-two-separate-home-fires/ (visited on 05/01/2017) (cit. on p. 76).

[66] M. Deroover, *Wind power backup and storage batteries explode into flames and send a toxic cloud over the city of brussels*, wind-watch.org. [Online]. Available: https://www.wind-watch.org/news/2017/11/12/wind-power-backup-and-storage-batteries-explode-into-flames-and-send-a-toxic-cloud-over-the-city-of-brussels/ (visited on 11/12/2017) (cit. on p. 76).

[67] F. Lambert, *Tesla says Model S fire in France was due to 'electrical connection improperly tightened' by a human instead of robots*, electrek.co. [Online]. Available: https://ww.electrek.co/2016/09/09/tesla-fire-france-electrical-connection-improperly-tightened-human-robot/ (visited on 09/09/2016) (cit. on p. 76).

[68] F. Lambert, *Hyundai Kona EV exploded in a garage, blowing the door off*, electrek.co. [Online]. Available: https://ww.electrek.co/2019/07/27/hyundai-kona-ev-explodes-garage-blowing-door-off/ (visited on 06/27/2019) (cit. on pp. 76, 77).

[69] A. Blum and R. T. Long, "Full-scale Fire Tests of Electric Drive Vehicle Batteries," *SAE International Journal of Passenger Cars - Mechanical Systems*, vol. 8, no. 2, pp. 2015–01–1383, Apr. 2015, ISSN: 1946-4002. DOI:

10.4271/2015-01-1383. [Online]. Available: https://www.sae.org/content/2015-01-1383/ (cit. on p. 76).

[70] C. Petit Boulanger, J. Thomazo, B. Azmi, O. Labadie, B. Poutrain, M. Gentilleau, and H. Bazin, "A PARTNERSHIP BETWEEN RENAULT AND FRENCH FIRST RESPONDERS TO ENSURE SAFE INTERVENTION ON CRASH OR FIRE-DAMAGED ELECTRICAL VEHICLES.," in *24th ESV-Conference*, Gothenburg: U.S. DEPARTMENT OF TRANSPORTATION, 2015, pp. 1–7. [Online]. Available: http://www.nhtsa.gov/ESV (cit. on pp. 76, 79).

[71] R. T. Long Jr, A. F. Blum, T. J. Bress, and B. R. Cotts, "Best Practices for Emergency Response to Incidents Involving Electric Vehicles Battery Hazards : A Report on Full-Scale Testing Results," Fire Protection Research Foundation, QUINCY, MASSACHUSETTS, Tech. Rep., 2013. [Online]. Available: https://www.nfpa.org/News-and-Research/Data-research-and-tools/Emergency-Responders/Emergency-Response-to-Incident-Involving-Electric-Vehicle-Battery-Hazards (cit. on p. 76).

[72] O. Willstrand, "Fire Suppression Tests for Vehicle Battery Pack," RISE Research Institutes of Sweden, Tech. Rep. October, 2019, p. 10 (cit. on pp. 76, 124).

[73] R. Bisschop, O. Willstrand, F. Amon, and M. Rosengren, *Fire safety of lithium-ion batteries in road vehicles*, May. 2019, p. 105, ISBN: 9789188907783. DOI: 10.13140/RG.2.2.18738.15049 (cit. on p. 76).

[74] V. Somandepalli, K. Marr, and Q. Horn, "Quantification of Combustion Hazards of Thermal Runaway Failures in Lithium-Ion Batteries," *SAE International Journal of Alternative Powertrains*, vol. 3, no. 1, pp. 2014–01–1857, Apr. 2014, ISSN: 2167-4205. DOI: 10.4271/2014-01-1857. [Online]. Available: http://papers.sae.org/2014-01-1857/ (cit. on p. 77).

[75] *Grazer bei Explosion eines Akkus verletzt*, Telekurier Online Medien GmbH Co KG. [Online]. Available: https://kurier.at/chronik/oesterreich/grazer-bei-explosion-eines-akkus-verletzt/ (visited on 04/04/2020) (cit. on p. 77).

[76] M. B. Mckinnon and S. Kerber, "Four Firefighters Injured In Lithium-Ion Battery Energy Storage System Explosion - Arizona," UL Firefighter Safety Research Institute Columbia, MD 20145, Tech. Rep., 2020 (cit. on p. 77).

[77] W. Li, H. Wang, Y. Zhang, and M. Ouyang, "Flammability characteristics of the battery vent gas: A case of NCA and LFP lithium-ion batteries during external heating abuse," *Journal of Energy Storage*, vol. 24, no. May, p. 100 775, Aug. 2019, ISSN: 2352152X. DOI: 10.1016/j.est.2019.100775. [Online]. Available: https://doi.org/10.1016/j.est.2019.100775%20https://linkinghub.elsevier.com/retrieve/pii/S2352152X19301719 (cit. on pp. 77, 78).

[78] A. O. Said, C. Lee, S. I. Stoliarov, and A. W. Marshall, "Comprehensive analysis of dynamics and hazards associated with cascading failure in 18650 lithium ion cell arrays," *Applied Energy*, vol. 248, no. March, pp. 415–428, Aug. 2019, ISSN: 03062619. DOI: 10.1016/j.apenergy.2019.04.141. [Online]. Available: https://linkinghub.elsevier.com/retrieve/pii/S0306261919307561 (cit. on p. 77).

[79] *Verordnung explosionsfähige Atmosphären – VEXAT*, Bundesgesetzblatt, 2004. [Online]. Available: https://www.ris.bka.gv.at/eli/bgbl/II/2004/309 (cit. on pp. 78, 125).

[80] C. Essl, A. W. Golubkov, E. Gasser, M. Nachtnebel, A. Zankel, E. Ewert, and A. Fuchs, "Comprehensive Hazard Analysis of Failing Automotive Lithium-Ion Batteries in Overtemperature Experiments," *Batteries*, vol. 6, no. 2, p. 30, May 2020, ISSN: 2313-0105. DOI: 10.3390/batteries6020030. [Online]. Available: https://www.mdpi.com/2313-0105/6/2/30 (cit. on pp. 78, 80, 88).

[81] C. Essl, A. W. Golubkov, and A. Fuchs, "Comparing Different Thermal Runaway Triggers for Two Automotive Lithium-Ion Battery Cell Types," *Journal of The Electrochemical Society*, vol. 167, no. 13, p. 130 542, Oct. 2020, ISSN: 1945-7111. DOI: 10.1149/1945-7111/abbe5a. [Online]. Available: https://iopscience.iop.org/article/10.1149/1945-7111/abbe5a (cit. on p. 78).

[82] Y. Fernandes, A. Bry, and S. de Persis, "Identification and quantification of gases emitted during abuse tests by overcharge of a commercial Li-ion battery," *Journal of Power Sources*, vol. 389, no. April, pp. 106–119, Jun. 2018, ISSN: 03787753. DOI: 10.1016/j.jpowsour.2018.03.034. [Online]. Available: https://linkinghub.elsevier.com/retrieve/pii/S0378775318302581 (cit. on pp. 78, 79).

[83] F. Diaz, Y. Wang, R. Weyhe, and B. Friedrich, "Gas generation measurement and evaluation during mechanical processing and thermal treatment of spent Li-ion batteries," *Waste Management*, vol. 84, pp. 102–111, Feb. 2019, ISSN: 0956053X. DOI: 10.1016/j.wasman.2018.11.029. [Online]. Available: https://doi.org/10.1016/j.wasman.2018.11.029%20https://linkinghub.elsevier.com/retrieve/pii/S0956053X18307013 (cit. on p. 79).

[84] C. Forestier, A. Lecocq, A. Zantman, S. Grugeon, L. Sannier, G. Marlair, and S. Laruelle, "Study of the Role of LiNi 1/3 Mn 1/3 Co 1/3 O 2 /Graphite Li-Ion Pouch Cells Confinement, Electrolyte Composition and Separator Coating on Thermal Runaway and Off-Gas Toxicity," *Journal of The Electrochemical Society*, vol. 167, no. 9, p. 090 513, Apr. 2020, ISSN: 1945-7111. DOI: 10.1149/1945-7111/ab829e. [Online]. Available: https://iopscience.iop.org/article/10.1149/1945-7111/ab829e (cit. on p. 79).

[85] J. Diekmann, S. Doose, S. Weber, S. Münch, W. Haselrieder, and A. Kwade, "Development of a New Procedure for Nail Penetration of Lithium-Ion Cells to Obtain Meaningful and Reproducible Results," *Journal of The Electrochemical Society*, vol. 167, no. 9, p. 090 504, Mar. 2020, ISSN: 1945-7111. DOI: 10.1149/1945-7111/ab78ff. [Online]. Available: https://iopscience.iop.org/article/10.1149/1945-7111/ab78ff (cit. on p. 79).

[86] F. Larsson, S. Bertilsson, M. Furlani, I. Albinsson, and B.-E. Mellander, "Gas explosions and thermal runaways during external heating abuse of commercial lithium-ion graphite-LiCoO 2 cells at different levels of ageing," *Journal of Power Sources*, vol. 373, no. October 2017, pp. 220–231, Jan. 2018, ISSN: 03787753. DOI: 10.1016/j.jpowsour.2017.10.085. [Online]. Available:

http://linkinghub.elsevier.com/retrieve/pii/S0378775317314398 (cit. on p. 79).

[87] A. Nedjalkov, J. Meyer, M. Köhring, A. Doering, M. Angelmahr, S. Dahle, A. Sander, A. Fischer, and W. Schade, "Toxic Gas Emissions from Damaged Lithium Ion Batteries—Analysis and Safety Enhancement Solution," *Batteries*, vol. 2, no. 1, p. 5, Mar. 2016, ISSN: 2313-0105. DOI: 10.3390/batteries2010005. [Online]. Available: http://www.mdpi.com/2313-0105/2/1/5 (cit. on pp. 79, 130).

[88] A. Lecocq, M. Bertana, B. Truchot, and G. Marlair, "Comparison of the Fire Consequences of an Electric Vehicle and an Internal Combustion Engine Vehicle .," in *International Conference on Fires in Vehicles*, Boras: SP Technical Research Institute of Sweden, 2012, pp. 183–194 (cit. on p. 79).

[89] D. Sturk, L. Hoffmann, and A. Ahlberg Tidblad, "Fire Tests on E-vehicle Battery Cells and Packs," *Traffic Injury Prevention*, vol. 16, no. sup1, S159–S164, Jun. 2015, ISSN: 1538-9588. DOI: 10.1080/15389588.2015.1015117. [Online]. Available: http://www.tandfonline.com/doi/full/10.1080/15389588.2015.1015117 (cit. on p. 79).

[90] J. Sun, J. Li, T. Zhou, K. Yang, S. Wei, N. Tang, N. Dang, H. Li, X. Qiu, and L. Chen, "Toxicity, a serious concern of thermal runaway from commercial Li-ion battery," *Nano Energy*, vol. 27, pp. 313–319, Sep. 2016, ISSN: 22112855. DOI: 10.1016/j.nanoen.2016.06.031. [Online]. Available: http://dx.doi.org/10.1016/j.nanoen.2016.06.031%20http://linkinghub.elsevier.com/retrieve/pii/S2211285516302130 (cit. on p. 79).

[91] N. P. Lebedeva and L. Boon-Brett, "Considerations on the Chemical Toxicity of Contemporary Li-Ion Battery Electrolytes and Their Components," *Journal of The Electrochemical Society*, vol. 163, no. 6, A821–A830, Feb. 2016, ISSN: 0013-4651. DOI: 10.1149/2.0171606jes. [Online]. Available: http://jes.ecsdl.org/content/163/6/A821.full%20http://jes.ecsdl.org/lookup/doi/10.1149/2.0171606jes (cit. on pp. 80, 130).

[92] K. Xu, "Electrolytes and Interphases in Li-Ion Batteries and Beyond," *Chemical Reviews*, vol. 114, no. 23, pp. 11 503–11 618, Dec. 2014, ISSN: 0009-

2665. DOI: 10.1021/cr500003w. [Online]. Available: http://pubs.acs.org/doi/abs/10.1021/cr500003w (cit. on p. 80).

[93] M. Börner, A. Friesen, M. Grützke, Y. Stenzel, G. Brunklaus, J. Haetge, S. Nowak, F. Schappacher, and M. Winter, "Correlation of aging and thermal stability of commercial 18650-type lithium ion batteries," *Journal of Power Sources*, vol. 342, pp. 382–392, Feb. 2017, ISSN: 03787753. DOI: 10.1016/j.jpowsour.2016.12.041. [Online]. Available: http://linkinghub.elsevier.com/retrieve/pii/S0378775316317347 (cit. on p. 80).

[94] L. Benbrahim-Tallaa, B. Lauby-Secretan, D. Loomis, K. Z. Guyton, Y. Grosse, F. El Ghissassi, V. Bouvard, N. Guha, H. Mattock, K. Straif, I. I. Rusyn, S. M. Bartell, M. F. Cesta, W. Chiu, G. Cooper, J. C. DeWitt, M. Friesen, L. H. Lash, K. Steenland, L. Fritschi, C. M. Sergi, J. Hansen, F. L. Curieux, H. M. Bolt, S. Fukushima, G. Ichihara, K. Kamae, S. Kumagai, H. Tsuda, and K. Kjaerheim, "Carcinogenicity of perfluorooctanoic acid, tetrafluoroethylene, dichloromethane, 1,2-dichloropropane, and 1,3-propane sultone," *The Lancet Oncology*, vol. 15, no. 9, pp. 924–925, 2014, ISSN: 14745488. DOI: 10.1016/S1470-2045(14)70316-X (cit. on p. 80).

[95] H. M. Bolt and K. Golka, "1,3-Propane sultone, an extremely potent experimental carcinogen: what should be expected in humans?" *Toxicology Letters*, vol. 151, no. 1, pp. 251–254, Jun. 2004, ISSN: 03784274. DOI: 10.1016/j.toxlet.2003.12.073. [Online]. Available: http://linkinghub.elsevier.com/retrieve/pii/S0378427404000839 (cit. on p. 80).

[96] W. Weber, R. Wagner, B. Streipert, V. Kraft, M. Winter, and S. Nowak, "Ion and gas chromatography mass spectrometry investigations of organophosphates in lithium ion battery electrolytes by electrochemical aging at elevated cathode potentials," *Journal of Power Sources*, vol. 306, pp. 193–199, 2016, ISSN: 03787753. DOI: 10.1016/j.jpowsour.2015.12.025. [Online]. Available: http://linkinghub.elsevier.com/retrieve/pii/S0378775315306388 (cit. on p. 80).

[97] M. Grützke, S. Krüger, V. Kraft, B. Vortmann, S. Rothermel, M. Winter, and S. Nowak, "Investigation of the Storage Behavior of Shredded Lithium-Ion Batteries from Electric Vehicles for Recycling Purposes," *ChemSusChem*, vol. 8, no. 20, pp. 3433–3438, Oct. 2015, ISSN: 18645631. DOI: 10.1002/

cssc.201500920. [Online]. Available: http://doi.wiley.com/10.1002/cssc.201500920 (cit. on p. 80).

[98] D. Patel, J. B. Robinson, S. Ball, D. J. L. Brett, and P. R. Shearing, "Thermal Runaway of a Li-Ion Battery Studied by Combined ARC and Multi-Length Scale X-ray CT," *Journal of The Electrochemical Society*, vol. 167, no. 9, p. 090 511, Apr. 2020, ISSN: 1945-7111. DOI: 10.1149/1945-7111/ab7fb6. [Online]. Available: https://iopscience.iop.org/article/10.1149/1945-7111/ab7fb6 (cit. on p. 80).

[99] J. E. Salvaggio, "Inhaled particles and respiratory disease," *Journal of Allergy and Clinical Immunology*, vol. 94, no. 2, pp. 304–309, Aug. 1994, ISSN: 00916749. DOI: 10.1053/ai.1994.v94.a56009. [Online]. Available: https://linkinghub.elsevier.com/retrieve/pii/S0091674954000656 (cit. on p. 80).

[100] M. Mattenklott and N. Höfert, "Stäube an arbeitsplätzen und in der umwelt - Vergleich der begriffsbestimmungen," *Gefahrstoffe Reinhaltung der Luft*, vol. 69, no. 4, pp. 127–129, 2009, ISSN: 09498036 (cit. on pp. 80, 131).

[101] Kovachev, Schröttner, Gstrein, Aiello, Hanzu, Wilkening, Foitzik, Wellm, Sinz, and Ellersdorfer, "Analytical Dissection of an Automotive Li-Ion Pouch Cell," *Batteries*, vol. 5, no. 4, p. 67, Oct. 2019, ISSN: 2313-0105. DOI: 10.3390/batteries5040067. [Online]. Available: https://www.mdpi.com/2313-0105/5/4/67 (cit. on pp. 81, 83, 252).

[102] P. Gotcu and H. J. Seifert, "Thermophysical properties of LiCoO ¡sub¿2¡/sub¿ –LiMn ¡sub¿2¡/sub¿ O ¡sub¿4¡/sub¿ blended electrode materials for Li-ion batteries," *Phys. Chem. Chem. Phys.*, 2016, ISSN: 1463-9076. DOI: 10.1039/C6CP00887A. [Online]. Available: http://xlink.rsc.org/?DOI=C6CP00887A (cit. on pp. 81, 136).

[103] E. Schuster, C. Ziebert, A. Melcher, M. Rohde, and H. J. Seifert, "Thermal behavior and electrochemical heat generation in a commercial 40 Ah lithium ion pouch cell," *Journal of Power Sources*, vol. 286, pp. 580–589, 2015, ISSN: 03787753. DOI: 10.1016/j.jpowsour.2015.03.170. [Online]. Available: http://dx.doi.org/10.1016/j.jpowsour.2015.03.170 (cit. on p. 81).

[104] A. Loges, S. Herberger, P. Seegert, and T. Wetzel, "A study on specific heat capacities of Li-ion cell components and their influence on thermal management," *Journal of Power Sources*, vol. 336, pp. 341–350, Dec. 2016, ISSN: 03787753. DOI: 10.1016/j.jpowsour.2016.10.049. [Online]. Available: http://linkinghub.elsevier.com/retrieve/pii/S0378775316314410 (cit. on pp. 81–83).

[105] F. Richter, P. J. Vie, S. Kjelstrup, and O. S. Burheim, "Measurements of ageing and thermal conductivity in a secondary NMC-hard carbon Li-ion battery and the impact on internal temperature profiles," *Electrochimica Acta*, vol. 250, pp. 228–237, 2017, ISSN: 00134686. DOI: 10.1016/j.electacta.2017.07.173. [Online]. Available: http://dx.doi.org/10.1016/j.electacta.2017.07.173 (cit. on p. 81).

[106] A. Gaitonde and A. Nimmagadda, Amulya Marconnet, "Experimental characterization of thermal conductance across the separator-shell interface in dry cylindrical lithium ion batteries," in *Thermal and Thermomechanical Phenomena in Electronic Systems (ITherm)*, IEEE, 2017, pp. 1034–1039, ISBN: 9781509029945. DOI: 10.1109/ITHERM.2017.7992602 (cit. on pp. 81, 137).

[107] M. J. Lain, J. Brandon, and E. Kendrick, "Design strategies for high power vs. High energy lithium ion cells," *Batteries*, vol. 5, no. 4, 2019, ISSN: 23130105. DOI: 10.3390/batteries5040064 (cit. on pp. 81, 83).

[108] C. Z. Hu and J. D. Andrade, "Pyrolyzed, conducting kapton polyimide: An electrically conducting material," *Journal of Applied Polymer Science*, vol. 30, no. 11, pp. 4409–4415, 1985, ISSN: 10974628. DOI: 10.1002/app.1985.070301116 (cit. on p. 114).

[109] M. Egelhaaf, D. Kress, D. Wolpert, T. Lange, R. Justen, and H. Wilstermann, "Fire Fighting of Li-Ion Traction Batteries," *SAE International Journal of Alternative Powertrains*, vol. 2, no. 1, pp. 2013–01–0213, Apr. 2013, ISSN: 2167-4205. DOI: 10.4271/2013-01-0213. [Online]. Available: https://www.sae.org/content/2013-01-0213/ (cit. on p. 124).

[110] F. Larsson, P. Andersson, P. Blomqvist, A. Lor??n, and B. E. Mellander, "Characteristics of lithium-ion batteries during fire tests," *Journal of Power*

Sources, vol. 271, pp. 414–420, 2014, ISSN: 03787753. DOI: 10.1016/j.jpowsour.2014.08.027 (cit. on p. 124).

[111] P. Balachandran, "Gas dynamics for engineers," in *Gas dynamics for engineers*, Delhi: PHI Learning Private Limited, 2010, ch. Isentropic, pp. 70–71, ISBN: 978-81-203-4021-3 (cit. on p. 127).

[112] E. Lemmon, M. McLinden, and D. Friend, *"Thermophysical Properties of Fluid Systems" in NIST Chemistry WebBook*, P. Linstrom and W. Mallard, Eds. Gaithersburg MD: National Institute of Standards and Technology, 2018. DOI: 10.18434/T4D303 (cit. on p. 127).

[113] R. R. Kohlmeyer, G. A. Horrocks, A. J. Blake, Z. Yu, B. Maruyama, H. Huang, and M. F. Durstock, "Pushing the thermal limits of Li-ion batteries," *Nano Energy*, vol. 64, no. May 2020, p. 103 927, 2019, ISSN: 22112855. DOI: 10.1016/j.nanoen.2019.103927. [Online]. Available: https://doi.org/10.1016/j.nanoen.2019.103927 (cit. on p. 133).

[114] Y.-J. Kim, *Lgc's low voltage cell development*, Mainz, Germany: 8th Advanced Automotive Battery Conference, Jan. 31, 2018 (cit. on p. 133).

[115] V. Ruiz, A. Pfrang, A. Kriston, N. Omar, P. Van den Bossche, and L. Boon-Brett, "A review of international abuse testing standards and regulations for lithium ion batteries in electric and hybrid electric vehicles," *Renewable and Sustainable Energy Reviews*, vol. 81, no. June 2016, pp. 1427–1452, Jan. 2018, ISSN: 13640321. DOI: 10.1016/j.rser.2017.05.195. [Online]. Available: http://dx.doi.org/10.1016/j.rser.2017.05.195%20https://linkinghub.elsevier.com/retrieve/pii/S1364032117308250 (cit. on p. 133).

[116] V. Ruiz and A. Pfrang, "JRC exploratory research : Safer Li-ion batteries by preventing thermal propagation," Tech. Rep. March 2018, 2018, pp. 1–47. DOI: 10.2760/096975. [Online]. Available: https://ec.europa.eu/jrc/en/publication/jrc-exploratory-research-safer-li-ion-batteries-preventing-thermal-propagation (cit. on p. 134).

[117] A. Golubkov, "Initiation of Thermal Runaway With Different Heating Devices," in *Workshop: Safer Li-Ion Batteries by Preventing Thermal Propagation?*, Petten, 2018. [Online]. Available: https://ec.europa.eu/jrc/

en/event/workshop/workshop-safer-li-ion-batteries-preventing-thermal-propagation (cit. on p. 134).

[118] X. Feng, D. Ren, X. He, and M. Ouyang, "Mitigating Thermal Runaway of Lithium-Ion Batteries," *Joule*, vol. 4, no. 4, pp. 743–770, Apr. 2020, ISSN: 25424351. DOI: 10.1016/j.joule.2020.02.010. [Online]. Available: http://dx.doi.org/10.1016/j.joule.2020.02.010%20https://linkinghub.elsevier.com/retrieve/pii/S254243512030088X (cit. on p. 135).

[119] D. P. Finegan, E. Darcy, M. Keyser, B. Tjaden, T. M. M. Heenan, R. Jervis, J. J. Bailey, R. Malik, N. T. Vo, O. V. Magdysyuk, R. Atwood, M. Drakopoulos, M. DiMichiel, A. Rack, G. Hinds, D. J. L. Brett, and P. R. Shearing, "Characterising thermal runaway within lithium-ion cells by inducing and monitoring internal short circuits," *Energy Environ. Sci.*, vol. 10, no. 6, pp. 1377–1388, 2017, ISSN: 1754-5692. DOI: 10.1039/C7EE00385D. [Online]. Available: http://xlink.rsc.org/?DOI=C7EE00385D (cit. on pp. 135–137, 238, 239).

[120] E. Archibald, R. Kennedy, K. Marr, J. Jeevarajan, and O. Ezekoye, "Characterization of Thermally Induced Runaway in Pouch Cells for Propagation," *Fire Technology*, no. March, Mar. 2020, ISSN: 0015-2684. DOI: 10.1007/s10694-020-00974-2. [Online]. Available: https://doi.org/10.1007/s10694-020-00974-2%20http://link.springer.com/10.1007/s10694-020-00974-2 (cit. on pp. 135, 137, 138, 238, 239).

[121] L. Aiello, G. Kovachev, B. Brunnsteiner, M. Schwab, G. Gstrein, W. Sinz, and C. Ellersdorfer, "In situ measurement of orthotropic thermal conductivity on commercial pouch lithium-ion batteries with thermoelectric device," *Batteries*, vol. 6, no. 1, pp. 1–17, 2020, ISSN: 23130105. DOI: 10.3390/batteries6010010 (cit. on pp. 136, 137, 237).

[122] S. Gao, L. Lu, M. Ouyang, Y. Duan, X. Zhu, C. Xu, B. Ng, N. Kamyab, R. E. White, and P. T. Coman, "Experimental Study on Module-to-Module Thermal Runaway-Propagation in a Battery Pack," *Journal of The Electrochemical Society*, vol. 166, no. 10, A2065–A2073, Jun. 2019, ISSN: 0013-4651. DOI: 10.1149/2.1011910jes. [Online]. Available: https://iopscience.iop.org/article/10.1149/2.1011910jes (cit. on pp. 136–138).

[123] H. Wang, Z. Du, X. Rui, S. Wang, C. Jin, L. He, F. Zhang, Q. Wang, and X. Feng, "A comparative analysis on thermal runaway behavior of Li (Ni Co Mn) O2 battery with different nickel contents at cell and module level," *Journal of Hazardous Materials*, vol. 393, no. February, p. 122 361, Jul. 2020, ISSN: 03043894. DOI: 10.1016/j.jhazmat.2020.122361. [Online]. Available: https://doi.org/10.1016/j.jhazmat.2020.122361%20https://linkinghub.elsevier.com/retrieve/pii/S0304389420303496 (cit. on p. 136).

[124] S. Oswald, *Highly precise measurement of the heat conductivity of lithium ion battery cells perpendicular to the layer plane*, Mainz, Germany: Advanced Automotive Battery Conference, Jan. 25, 2018 (cit. on p. 137).

[125] S. Suresh and R. Stringfellow, "Final Technical Report Internal Short Circuits in Lithium-Ion Cells for PHEVs," TIAX LLC, Tech. Rep., 2014, p. 52. [Online]. Available: https://www.osti.gov/servlets/purl/1124078 (cit. on p. 137).

[126] Z. J. Zhang, P. Ramadass, and W. Fang, "18 – Safety of Lithium-Ion Batteries," in *Lithium-Ion Batteries Advances and Applications*, Elsevier, 2014, pp. 409–435, ISBN: 9780444595133. DOI: 10.1016/B978-0-444-59513-3.00018-2. [Online]. Available: http://dx.doi.org/10.1016/B978-0-444-59513-3.00018-2 (cit. on pp. 138, 139).

[127] S. Santhanagopalan, P. Ramadass, and J. (Zhang, "Analysis of internal short-circuit in a lithium ion cell," *Journal of Power Sources*, vol. 194, no. 1, pp. 550–557, Oct. 2009, ISSN: 03787753. DOI: 10.1016/j.jpowsour.2009.05.002. [Online]. Available: http://linkinghub.elsevier.com/retrieve/pii/S037877530900843X%20https://linkinghub.elsevier.com/retrieve/pii/S037877530900843X (cit. on pp. 139, 252).

[128] S. Koch, A. Fill, K. Kelesiadou, and K. P. Birke, "Discharge by short circuit currents of parallel-connected lithium-ion cells in thermal propagation," *Batteries*, vol. 5, no. 1, 2019, ISSN: 23130105. DOI: 10.3390/batteries5010018 (cit. on pp. 139, 140, 253).

[129] D. Sturk, L. Rosell, P. Blomqvist, and A. A. Tidblad, "Analysis of li-ion battery gases vented in an inert atmosphere thermal test chamber,"

Batteries, vol. 5, no. 3, pp. 1–17, 2019, ISSN: 23130105. DOI: 10.3390/batteries5030061 (cit. on p. 246).

[130] C. W. Wang, Y. B. Yi, A. M. Sastry, J. Shim, and K. A. Striebel, "Particle compression and conductivity in Li-ion anodes with graphite additives," *Journal of the Electrochemical Society*, vol. 151, no. 9, pp. 1–10, 2004, ISSN: 00134651. DOI: 10.1149/1.1783909 (cit. on p. 253).

[131] H. C. Shin, W. I. Cho, and H. Jang, "Electrochemical properties of carbon-coated LiFePO4 cathode using graphite, carbon black, and acetylene black," *Electrochimica Acta*, vol. 52, no. 4, pp. 1472–1476, 2006, ISSN: 00134686. DOI: 10.1016/j.electacta.2006.01.078 (cit. on p. 255).

[132] W. Guoping, Z. Qingtang, Y. Zuolong, and Q. MeiZheng, "The effect of different kinds of nano-carbon conductive additives in lithium ion batteries on the resistance and electrochemical behavior of the LiCoO2 composite cathodes," *Solid State Ionics*, vol. 179, no. 7-8, pp. 263–268, 2008, ISSN: 01672738. DOI: 10.1016/j.ssi.2008.01.015 (cit. on p. 255).

[133] D. Doughty and E. P. Roth, "A general discussion of Li Ion battery safety," *Electrochemical Society Interface*, vol. 21, no. 2, pp. 37–44, 2012. [Online]. Available: http://www.scopus.com/inward/record.url?eid=2-s2.0-84867753898%7B%5C&%7DpartnerID=40%7B%5C&%7Dmd5=19382decb891d60f28ef1049fca727ea (cit. on p. 260).

[134] A. Mauger, C. M. Julien, A. Paolella, M. Armand, and K. Zaghib, "Building Better Batteries in the Solid State : A Review," *Materials*, vol. 12, p. 3892, 2019. DOI: 10.3390/ma12233892 (cit. on p. 268).

[135] C. Weller, J. Pampel, S. Dörfler, H. Althues, and S. Kaskel, "Polysulfide Shuttle Suppression by Electrolytes with Low-Density for High-Energy Lithium–Sulfur Batteries," *Energy Technology*, vol. 1900625, pp. 1–12, 2019, ISSN: 2194-4288. DOI: 10.1002/ente.201900625 (cit. on p. 268).